Global Interpretation of ττ Events in the Context of the Standard Model and Beyond

Zur Erlangung des akademischen Grades eines

Doktors der Naturwissenschaften

von der KIT-Fakultät für Physik
des Karlsruher Instituts für Technologie (KIT)
angenommene

Dissertation

von

M. Sc. Artur Gottmann
aus St. Petersburg

Referenten: Priv.-Doz. Dr. Roger Wolf, Prof. Dr. Günter Quast
Institut für Experimentelle Teilchenphysik (ETP)

Tag der mündlichen Prüfung: 12. Juni 2020

Ich versichere hiermit, die vorliegende Arbeit selbstständig und nur unter Verwendung angegebener Hilfsmittel verfasst zu haben. Sämtliche Quellen, die in dieser Arbeit verwendet werden, habe ich an entsprechenden Stellen kenntlich gemacht.

Artur Gottmann

Karlsruhe, den 16.10.2020

Contents

1. Introduction

The nature of interactions between elementary particles nowadays is successfully described by the Standard Model of particle physics (SM), which is a quantum field theory exploiting the principle of local gauge invariance [1]. Its predictions cover a wide range of observed phenomena, comprising precision calculations and measurements of the anomalous magnetic moment of the electron, with uncertainties of the order of 10^{-11} [2, 3], the explanation of the radioactive β decay via the emission of a virtual massive W boson, which has been confirmed to exist by experiment [4], and the existence of quarks and gluons as elementary building blocks of neutrons, protons [5] and other hadrons.

One of the most recently studied predictions of the SM is the existence of the Higgs boson (h_{SM}) required to provide all known particles with their masses [6–8]. After the discovery of such a particle at the Large Hadron Collider (LHC) by two independent experiments, ATLAS [9] and CMS [10] in 2012, measurements of its properties have been carried out, including its mass of 125.38 ± 0.14 GeV [11], and couplings to fermions and gauge bosons [12]. While the mass is an unconstrained parameter of the SM, the coupling structure of the observed particle has been found to be compatible with the unique predictions for the h_{SM}, with a precision of the most recent measurements between a few and 15%, depending on the concrete coupling. These observations give justification to call the observed particle a Higgs boson (h_{obs}).

There is however strong belief to consider the h_{obs} only as part of an extended Higgs sector with significantly enriched phenomenology. This is supported by a series of shortcoming of the SM on the one and several assets of such extensions on the other hand. For example, gravity at the quantum level is not included in the SM, and will require a natural extension at scales, where such effects become more significant. The same is true for neutrino masses and the lack of explanation of dark matter, for which striking evidence emerged from astronomy and cosmology [13]. Possible solution to several of these shortcomings are offered by the concept of supersymmetry (SUSY) [14], which allows for the formulation of gravity as a quantum field theory and provides explanations for the existence of dark matter. In addition, the gauge couplings of the strong, weak, and electromagnetic interactions, that do not match in the SM, when evaluated at high energy scales with the help of renormalization group equations, can be unified above a certain unification scale pointing to a theoretically highly desired unified symmetry group to describe nature above that scale. In SUSY, an extended particle spectrum is introduced, including additional neutral (H, A) and charged ($H^{\pm}$) Higgs bosons, and yet undiscovered SUSY partners to the known SM particles.

Direct searches for additional, neutral heavy Higgs bosons were performed in several of their decay channels, including decays to a pair of top quarks [15], bottom quarks [16], W bosons [17], muons [18] and τ leptons [19]. The strongest constraints are given by the h, H, A $\rightarrow \tau\tau$ decay channel, which at the same time offers the highest sensitivity to investigate the coupling strength of the h_{obs} to fermions, with a current precision of 12% for the coupling to τ leptons [20, 21]. A SUSY model should therefore not only provide an

accurate prediction for the production and decay of the still unobserved Higgs bosons H and A. At the same time, it will be more and more challenged by the increasingly accurate measurement of the couplings of the h_{obs}, which is identified with the SUSY h, to τ leptons. This challenge will play an increasing role in the perspective of the LHC Run 3 and high luminosity LHC, where more data will lead to a precision of the h_{obs} coupling to τ leptons at the order of a few % [22].

Until now, the sensitivity to the coupling strength of the h_{obs} to τ leptons is exploited to its full potential only in highly tuned, dedicated analyses in the context of the SM interpretation. Parallel to these measurements, SUSY motivated Higgs boson searches are mostly focused on an inclusive and robust search strategies just for the heavy resonances. The main goal of this thesis is to develop a global interpretation of all analyzed $\tau\tau$ events in the full mass range. This analysis unifies both approaches to provide maximal sensitivity to constrain potential realizations of SUSY, but also general two Higgs doublet models (THDM). This strategy is in logic continuation of CMS searches for additional heavy neutral Higgs bosons in the context of the MSSM, which always included the contributions from the h in the statistical inference. It is anticipated to be the basis of the CMS legacy search for neutral heavy Higgs bosons in the context of the MSSM on the full LHC Run 2 dataset with 137 fb^{-1}, expected in 2021, laying path for searches of this kind based on the future Run 3 datasets and beyond.

The structure of this thesis is the following: In chapter 2, the theoretical concept of the SM and its minimal SUSY extension will be summarized with a focus on the Higgs sector. An overview over the CMS detector will be given in chapter 3, including a description of the most recent, so far not published, reconstruction techniques of particles relevant to the H $\to \tau\tau$ analysis. In chapter 4, preparations required for the H $\to \tau\tau$ analysis will be discussed, which is described in chapter 5, including a discussion of the obtained results. Conclusions are given in chapter 6.

2. The Standard Model and its Extensions

The Standard Model (SM) of particle physics and its extensions are quantum field theories (QFT) introducing a Lagrangian density $\mathcal{L}$ which is dependent on quantum fields $\phi(x)$ and their partial derivatives $\partial_\mu \phi(x)$ with respect to the Minkowski space-time $x_\mu = x = (t, -\vec{x})$. Based on the Lagrangian density, all rules about the particle evolution in the space-time, as well as their interactions with each other can be derived with the path integral formalism using perturbation theory techniques [23]. The resulting Feynman rules allow to compute the probabilities for processes, that lead from an initial to a final state, order by order in perturbation series. These computations are usually done in the reciprocal phase-space of the Minkowski space-time, the 4-momentum space with the 4-momentum vector $p_\mu = p = (E, -\vec{p})$. Thereby, the spacial coordinates $\vec{x}$ are connected to the 3-momentum $\vec{p}$, and the time t is connected to the energy E.

The scalar product for x_μ is defined in the following way, setting the constants for the speed of light and the reduced Planck constant to unity, $c = \hbar = 1$, and using Einstein's summation convention:

$$x_\mu x^\mu = g_{\mu\nu} x^\mu x^\nu = t^2 - \vec{x}^2, \qquad \left(g_{\mu\nu}\right) = diag(1, -1, -1, -1) \tag{2.1}$$

Here, the Lorentz metric $g_{\mu\nu}$ is used. The result on the right hand side of the equation is a Lorentz invariant quantity, also referred to a as a Lorentz scalar. This property also holds for the 4-momentum, resulting in the invariant mass squared, and is a property of the Lagrangian density $\mathcal{L}$ of a QFT.

In this chapter, the general aspects of the SM will be introduced in the first section, moving to one of the extensions beyond the SM (BSM), the Minimal Supersymmetric Extension of the SM (MSSM) in the next section. In the section after that, a special focus will be taken on the Higgs Sector of these models. The last two sections cover the topic of the calculation and simulation of processes within the SM and the MSSM.

2.1. Standard Model of Particle Physics

The SM describes the electromagnetic, the weak and the strong interactions between the elementary particles. The Lagrangian density of the SM can be decomposed as follows [1]:

$$\mathcal{L}_{SM} = \mathcal{L}_{Gauge} + \mathcal{L}_{Fermion} + \mathcal{L}_{Higgs} + \mathcal{L}_{Yukawa} + \mathcal{L}_{GF} + \mathcal{L}_{Ghost} \tag{2.2}$$

The $\mathcal{L}_{Gauge}$ term introduces the gauge fields, which give rise to carrier particles of the interactions, the gauge bosons with a spin polarization of ± 1, following therefore the Bose-Einstein spin statistic. The gauge fields result from three distinct, local gauge symmetry requirements imposed on the entire Lagrangian, following from the $U(1)_Y$, the $SU(2)_L$, and the $SU(3)_C$ symmetry groups. The term consists of expressions with field strength

tensors constructed from the gauge fields $B_\mu(x)$, $W_\mu^a(x)$ and $G_\mu^a(x)$, which correspond to the groups $U(1)_Y$, $SU(2)_L$ and $SU(3)_C$, respectively:

$$\mathcal{L}_{\text{Gauge}} = -\frac{1}{4} \cdot \left(B_{\mu\nu}B^{\mu\nu} + W_{\mu\nu}^a W^{a\mu\nu} + G_{\mu\nu}^a G^{a\mu\nu} \right) \tag{2.3}$$

$$B_{\mu\nu} = \partial_\mu B_\nu \quad - \quad \partial_\nu B_\mu$$
$$W_{\mu\nu}^a = \partial_\mu W_\nu^a \quad - \quad \partial_\nu W_\mu^a \quad - \quad g\epsilon^{abc}W_\mu^b W_\nu^c \quad a \in \{1,2,3\}$$
$$G_{\mu\nu}^a = \partial_\mu G_\nu^a \quad - \quad \partial_\nu G_\mu^a \quad - \quad g_s f^{abc}G_\mu^b G_\nu^c \quad a \in \{1,2,...,8\}$$

Thereby, g and g_s represent the weak $SU(2)_L$ and the strong gauge coupling constants, respectively. The field strength tensors $B_{\mu\nu}$, $W_{\mu\nu}^a$ and $G_{\mu\nu}^a$ describe the motion of the fields, and in case of the non-Abelian symmetry groups $SU(2)_L$ and $SU(3)_C$, the self-interactions of the gauge fields within a group. The number of different values, that the index a can take, corresponds to the number of the gauge fields and the number of the generators of the groups, which satisfy commutation relations containing the completely anti-symmetric tensor ϵ^{abc} or the structure constants of the $SU(3)_C$ group, f^{abc}:

$$SU(2)_L : [T_L^a, T_L^b] = i\epsilon^{abc}T_L^c, \qquad SU(3)_C : [T_C^a, T_C^b] = if^{abc}T_C^c$$

The fields B_μ and W_μ^a are combined in the context of the electroweak unification [24–26] to the physical fields corresponding to the photon, A_μ, to the charged $W^\pm$ bosons, $W_\mu^\pm$, and to the neutral Z boson, Z_μ:

$$\begin{pmatrix} W_\mu^+ \\ W_\mu^- \\ Z_\mu \\ A_\mu \end{pmatrix} = \begin{pmatrix} 1/\sqrt{2} & -i/\sqrt{2} & 0 & 0 \\ 1/\sqrt{2} & +i/\sqrt{2} & 0 & 0 \\ 0 & 0 & \cos\theta_W & -\sin\theta_W \\ 0 & 0 & \sin\theta_W & \cos\theta_W \end{pmatrix} \cdot \begin{pmatrix} W_\mu^1 \\ W_\mu^2 \\ W_\mu^3 \\ B_\mu \end{pmatrix} \tag{2.4}$$

The angle θ_W is the weak mixing angle, which can be defined through the coupling constants.

With the $\mathcal{L}_{\text{Fermion}}$ term, fermion fields are introduced to describe matter particles, which have a spin of $1/2$, and follow the Fermi-Dirac statistic. To accommodate for this, the fermions are arranged as spinor fields with 4 components, $\psi(x)$, reflecting the spin information and whether the fermion is a particle or an anti-particle. The spinor fields represent solutions to the Dirac equation of motion:

$$\left(i\gamma^\mu \partial_\mu - m_\psi \right) \psi = 0$$

The complex 4×4 matrices γ^μ act on the spinors and satisfy the anti-commutation relation $\{\gamma^\mu, \gamma^\nu\} = 2g^{\mu\nu} \cdot I_4$ with I_4 as the 4×4 identity matrix. With these matrices, it is possible to decompose a fermion spinor ψ into its left-handed and right-handed parts, ψ_L and ψ_R:

$$\psi_L = \frac{1}{2}\left(I_4 - \gamma^5 \right)\psi, \qquad \psi_R = \frac{1}{2}\left(I_4 + \gamma^5 \right)\psi, \qquad \gamma^5 = i\gamma^0\gamma^1\gamma^2\gamma^3$$

With this at hand, the weak interactions of the $SU(2)_L$ group can be defined, which act only on the left-handed parts of the fermion spinors. These are arranged into weak isospin

doublets, three doublets consisting of up-type and down-type quarks, and three doublets consisting of neutrinos and corresponding leptons:

$$\text{quarks: } Q_L \in \left\{ \begin{pmatrix} u'_L \\ d'_L \end{pmatrix}, \begin{pmatrix} c'_L \\ s'_L \end{pmatrix}, \begin{pmatrix} t'_L \\ b'_L \end{pmatrix} \right\}$$

$$\text{neutrinos \& leptons: } L_L \in \left\{ \begin{pmatrix} \nu_{e,L} \\ e_L \end{pmatrix}, \begin{pmatrix} \nu_{\mu,L} \\ \mu_L \end{pmatrix}, \begin{pmatrix} \nu_{\tau,L} \\ \tau_L \end{pmatrix} \right\}$$

The fields for the left-handed quarks are marked with ′ to point out, that these are the eigenstates of the weak interaction of $SU(2)_L$. These are different from the physical states of the quark fields, the mass eigenstates, which can be obtained by unitary transformations of the fields in the family space:

$$\begin{pmatrix} d_L \\ s_L \\ b_L \end{pmatrix} = U_L^d \begin{pmatrix} d'_L \\ s'_L \\ b'_L \end{pmatrix}, \quad \begin{pmatrix} u_L \\ c_L \\ t_L \end{pmatrix} = U_L^u \begin{pmatrix} u'_L \\ c'_L \\ t'_L \end{pmatrix}, \quad \begin{pmatrix} d_R \\ s_R \\ b_R \end{pmatrix} = U_R^d \begin{pmatrix} d'_R \\ s'_R \\ b'_R \end{pmatrix}, \quad \begin{pmatrix} u_R \\ c_R \\ t_R \end{pmatrix} = U_R^u \begin{pmatrix} u'_R \\ c'_R \\ t'_R \end{pmatrix} \tag{2.5}$$

$$U^\dagger U = \begin{pmatrix} 1 & 0 & 0 \\ 0 & 1 & 0 \\ 0 & 0 & 1 \end{pmatrix} \text{ for } U \in \left\{ U_L^d, U_L^u, U_R^d, U_R^u \right\}$$

To express weak interactions in terms of mass eigenstates, the Cabibbo-Kobayashi-Maskawa (CKM) mixing matrix V_{CKM} [27, 28] needs to be introduced to the corresponding term in the Lagrangian density:

$$\begin{pmatrix} \bar{u}'_L & \bar{c}'_L & \bar{t}'_L \end{pmatrix} \cdot \begin{pmatrix} d'_L \\ s'_L \\ b'_L \end{pmatrix} = \begin{pmatrix} \bar{u}_L & \bar{c}_L & \bar{t}_L \end{pmatrix} U_L^u \cdot U_L^{d,\dagger} \begin{pmatrix} d_L \\ s_L \\ b_L \end{pmatrix} = \begin{pmatrix} \bar{u}_L & \bar{c}_L & \bar{t}_L \end{pmatrix} \cdot V_{CKM} \cdot \begin{pmatrix} d_L \\ s_L \\ b_L \end{pmatrix}$$

$$= \begin{pmatrix} \bar{u}_L & \bar{c}_L & \bar{t}_L \end{pmatrix} \cdot \begin{pmatrix} V_{ud} & V_{us} & V_{ub} \\ V_{cd} & V_{cs} & V_{cb} \\ V_{td} & V_{ts} & V_{tb} \end{pmatrix} \cdot \begin{pmatrix} d_L \\ s_L \\ b_L \end{pmatrix}$$

Since neutrinos are considered as massless in the SM, right-handed neutrinos are not introduced. The simultaneous diagonalization of the lepton mass term and the weak interaction term can therefore be achieved. Without a loss of generality, mass eigenstates of leptons are also eigenstates of the weak interactions. However, there is evidence, that neutrinos are massive [29] and right-handed neutrinos need therefore be taken into account. The simplest extension of the SM would then involve the introduction of a mass term for the neutrinos and a mixing between the mass and weak interaction eigenstates, accomplished with the Pontecorvo-Maki-Nakagawa-Sakata (PMNS) mixing matrix [30, 31]. The kinetic term of the right-handed neutrinos would consist only of terms with partial derivatives, since these neutrinos would be sterile, without interactions of the SM.

The term for the weak interaction for the spinors Q_L and L_L is:

$$ig W_\mu^a T_L^a (Q_L + L_L) = ig W_\mu^a \frac{\tau^a}{2} (Q_L + L_L)$$

$$\tau^1 = \begin{pmatrix} 0 & 1 \\ 1 & 0 \end{pmatrix}, \qquad \tau^2 = \begin{pmatrix} 0 & -i \\ i & 0 \end{pmatrix}, \qquad \tau^3 = \begin{pmatrix} 1 & 0 \\ 0 & -1 \end{pmatrix}$$

The generators T^a of the SU(2)$_L$ group, which act on the weak isospin doublets, become Pauli matrices divided by 2 in their fundamental representation, $\tau^a/2$. The interaction of the fermion fields ψ to the weak field B_μ from the Abelian U(1)$_Y$ group can be expressed as:

$$ig'B_\mu Y \psi = ig'B_\mu Y \left(\psi_L + \psi_R\right)$$

Therein, g' and Y express the gauge coupling constant of U(1)$_Y$ and the weak hypercharge, respectively. Using the transformation into the physical electroweak fields from equation 2.4, the electroweak interactions with left-handed and right-handed fermions can be rewritten as follows:

$$i\left(gW_\mu^a \frac{\tau^a}{2} + g'B_\mu Y\right)(Q_L + L_L) =$$
$$i\left(\frac{g}{2}\left(\tau^+ W_\mu^+ + \tau^- W_\mu^-\right) + eQA_\mu + \frac{g}{\cos\theta_W}\left(\frac{\tau^3}{2} - Q\sin^2\theta_W\right)Z_\mu\right)(Q_L + L_L) \qquad (2.6)$$

$$e = g\sin\theta_W = g'\cos\theta_W$$
$$\tau^\pm = \frac{\tau^1 \pm i\tau^2}{\sqrt{2}}$$
$$Q = \frac{\tau^3}{2} + Y$$

$$ig'B_\mu Y \psi_R = i\left(eQA_\mu - \frac{g}{\cos\theta_W}Q\sin^2\theta_W Z_\mu\right)\psi_R \qquad (2.7)$$

The combination of the first two Pauli matrices to $\tau^\pm$ allows for charged currents, transforming a lower component of the weak isospin into the upper component and vice versa. The eigenvalues of the operator of the electric charge Q, the hypercharge Y, and the third generator of SU(2)$_L$ in its fundamental representation, $T_L^3 = \tau^3/2$, are given in table 2.1 for all fields of matter particles of the SM.

Quantum number	$\ell \in \{e, \mu, \tau\}$			$q^u \in \{u', c', t'\}$		$q^d \in \{d', s', b'\}$	
	ℓ_L	ℓ_R	$\nu_{\ell,L}$	q_L^u	q_R^u	q_L^d	q_R^d
T_L^3	-1/2	0	1/2	1/2	0	-1/2	0
Y	-1/2	-1	-1/2	1/6	2/3	1/6	-1/3
Q	-1	-1	0	2/3	2/3	-1/3	-1/3

Table 2.1.: Quantum numbers of the fields for all matter particles of the SM for the operators T_L^3, Y and Q.

In that way, all interactions of the fermions with photons, W and Z bosons are defined. The quark fields additionally take part in the strong interactions, mediated by the gauge

fields of the SU(3)$_C$ group. The physical quark fields are arranged into triplets q of the charge of the SU(3)$_C$, the color charge $c \in \{r, g, b\}$:

$$q = \begin{pmatrix} q^r \\ q^g \\ q^b \end{pmatrix}$$

In the fundamental representation of the SU(3)$_C$ group, the generators act on the quark triplets as halves of Gell-Mann matrices, $T_C^a = \lambda^a / 2$, defining, how the color charge of a quark is changed by interacting with the gluon gauge field G_μ^a corresponding to the generator:

$$ig_s G_\mu^a T_C^a q = ig_s G_\mu^a \frac{\lambda^a}{2} q$$

The discussed expressions of the interactions of the gauge bosons with the fermions ψ enter the Lagrangian $\mathcal{L}_{\text{Fermion}}$ with the following prescription:

$$i\bar{\psi}\gamma^\mu(...)_\mu\psi, \qquad \bar{\psi} = \psi^\dagger \gamma^0 \tag{2.8}$$

Together with the kinetic term for the fermions, $i\bar{\psi}\gamma^\mu\partial_\mu\psi$, the fermion Lagrangian reads:

$$\begin{aligned} \mathcal{L}_{\text{Fermion}} = & \sum_{\psi\in\text{fermions}} i\bar{\psi}\gamma^\mu\partial_\mu\psi + \sum_{q\in\text{quarks}} i\bar{q}\gamma^\mu ig_s G_\mu^a \frac{\lambda^a}{2} q \\ & + \sum_{Q_L} i\bar{Q}_L\gamma^\mu i \left(\frac{g}{2} \left(\tau^+ W_\mu^+ + \tau^- W_\mu^- \right) + eQA_\mu + \frac{g}{\cos\theta_W} \left(\frac{\tau^3}{2} - Q\sin^2\theta_W \right) Z_\mu \right) Q_L \\ & + \sum_{L_L} i\bar{L}_L\gamma^\mu i \left(\frac{g}{2} \left(\tau^+ W_\mu^+ + \tau^- W_\mu^- \right) + eQA_\mu + \frac{g}{\cos\theta_W} \left(\frac{\tau^3}{2} - Q\sin^2\theta_W \right) Z_\mu \right) L_L \\ & + \sum_{\ell\in\{e,\mu,\tau\}} i\bar{\ell}_R\gamma^\mu i \left(eQA_\mu - \frac{g}{\cos\theta_W} Q\sin^2\theta_W Z_\mu \right) \ell_R \\ & + \sum_{q\in\{u,d,c,s,t,b\}} i\bar{q}_R\gamma^\mu i \left(eQA_\mu - \frac{g}{\cos\theta_W} Q\sin^2\theta_W Z_\mu \right) q_R \end{aligned} \tag{2.9}$$

Up to now, every gauge boson and every fermion is considered to be massless, contradicting the observations [32]. To add the mass terms in a gauge invariant way, the Brout-Englert-Higgs mechanism [6–8] can be introduced to the Lagrangian, $\mathcal{L}_{\text{Higgs}}$, together with a Yukawa coupling term [33], $\mathcal{L}_{\text{Yukawa}}$, for the fermions. The details on these two terms will be discussed in section 2.3 for the SM and the MSSM together.

The remaining two terms in the Lagrangian, $\mathcal{L}_{\text{GF}}$ and $\mathcal{L}_{\text{Ghost}}$, describe the gauge fixing terms and the contributions of Faddeev-Popov ghosts [34], respectively. The gauge fixing is needed to be able to define the Feynman rules for that particular gauge choice. Depending on this choice, it may happen, that unphysical degrees of freedom are left for the non-Abelian groups, which are then accounted for by the ghost terms to allow for physically correct calculations of observables.

2.2. Minimal Supersymmetric Extension of the Standard Model

Although the Standard Model of particle physics describes the majority of quantum effects to a high precision, it should be considered as an effective theory which needs to be replaced by a more general concept for a number of reasons. First of all, the Standard Model is incomplete, since it does not describe gravity in a QFT approach. Gravitational quantum effects are expected to appear at the (reduced) Planck mass scale $M_P \approx 2.4 \cdot 10^{18}$ GeV, so latest at that scale, the Standard Model predictions should break down.

Furthermore, the SM does not provide a candidate for the dark matter, for which there is an evidence from cosmological observations [13].

One more reason is the hierarchy problem of the Higgs field in the SM [35]. Unlike for fermions and gauge bosons, the renormalized mass of the Higgs boson is very sensitive to new physics at large scales: Assuming for example, that a new particle would appear at the Planck scale with a mass of the order of this scale, its contribution to the self-energy corrections of the Higgs boson mass would be quadratic in the mass of the new particle. In consequence, to arrive at the small renormalized Higgs boson mass of about 125 GeV, a very precise cancellation between the bare, not renormalized mass and the corrections is required. Details on the renormalization procedure are presented in section 2.4.

Solutions to these problems can be introduced through an additional symmetry relating each boson with a fermion and vice versa [14, 36] which follows from the Poincaré algebra. Gravity can then be integrated into a larger concept with supersymmetry, like supergravity and string theory. The dark matter candidate can be provided by supersymmetric models by the lightest supersymmetric particle (LSP). Lastly, quadratic terms in the corrections to the renormalized Higgs boson mass can be removed by an exact cancellation between the contributions of a particle and its supersymmetric partner.

The particle content of the minimal supersymmetric extension of the Standard Model (MSSM) is arranged into supermultiplets containing pairs of fields, which represent the ordinary particles and their supersymmetric partner. Chiral supermultiplets are constructed for fermions and scalar Higgs fields, gauge supermultiplets for gauge bosons. The supersymmetric partners share the same quantum numbers as the corresponding ordinary particles, except for their spin. Since it is required, that $SU(2)_L$ is respected by all particles in the chiral supermultiplets involved in the electroweak interactions, one complex scalar supersymmetric partner is assigned to a left-handed fermion, and another partner is assigned to a right-handed fermion. In that way, each of the two fermion states with two degrees of freedom is accompanied by a scalar with two degrees of freedom.

Ordinary particles, their supersymmetric partners marked with a tilde ($\sim$), and the corresponding supermultiplets are summarized in tables 2.2 and 2.3. If the particles and their supersymmetric partners participate in the weak interaction, they are arranged as weak isospin doublets.

The names of supersymmetric partners are defined according to the type of the corresponding ordinary particle. In general, supersymmetric partners of fermions are called sfermions, with a further specification for quarks, leptons and neutrinos: squarks, sleptons and sneutrinos. The supersymmetric partners of the Higgs fields are called higgsinos.

The supersymmetric partners of gauge bosons are called gauginos, with further specification for the $SU(3)_C$, $SU(2)_L$ and $U(1)_Y$ symmetry groups: gluinos, winos and bino.

Gauginos are represented by fermion spinors with two degrees of freedom to cover the degrees of freedom of the gauge bosons correctly. Gluinos and bino need to be arranged as Majorana spinors in the 4-component notation to account for couplings to right-handed fields from the chiral supermultiplets. Winos can be handled as usual left-handed fermions.

Particle type	Spin 0	Spin 1/2	Supermultiplets
(s)quarks	$\tilde{Q}_\mathrm{L} = \begin{pmatrix} \tilde{q}_\mathrm{L}^u \\ \tilde{q}_\mathrm{L}^d \end{pmatrix}$	$Q_\mathrm{L} = \begin{pmatrix} q_\mathrm{L}^u \\ q_\mathrm{L}^d \end{pmatrix}$	$\begin{pmatrix} (\tilde{q}_\mathrm{L}^u, q_\mathrm{L}^u) \\ (\tilde{q}_\mathrm{L}^d, q_\mathrm{L}^d) \end{pmatrix}$
$q^u \in \{u', c', t'\}$	$\tilde{q}_\mathrm{R}^{u,*}$	$\bar{q}_\mathrm{R}^u$	$(\tilde{q}_\mathrm{R}^{u,*}, \bar{q}_\mathrm{R}^u)$
$q^d \in \{d', s', b'\}$	$\tilde{q}_\mathrm{R}^{d,*}$	$\bar{q}_\mathrm{R}^d$	$\left(\tilde{q}_\mathrm{R}^{d,*}, \bar{q}_\mathrm{R}^d\right)$
(s)neutrinos & (s)leptons	$\tilde{L}_\mathrm{L} = \begin{pmatrix} \tilde{\nu}_{\ell,\mathrm{L}} \\ \tilde{\ell}_\mathrm{L} \end{pmatrix}$	$L_\mathrm{L} = \begin{pmatrix} \nu_{\ell,\mathrm{L}} \\ \ell_\mathrm{L} \end{pmatrix}$	$\begin{pmatrix} (\tilde{\nu}_{\ell,\mathrm{L}}, \nu_{\ell,\mathrm{L}}) \\ (\tilde{\ell}_\mathrm{L}, \ell_\mathrm{L}) \end{pmatrix}$
$\ell \in \{e, \mu, \tau\}$	$\tilde{\ell}_\mathrm{R}^*$	$\bar{\ell}_\mathrm{R}$	$(\tilde{\ell}_\mathrm{R}^*, \bar{\ell}_\mathrm{R})$
Higgs(inos)	$H_u = \begin{pmatrix} H_u^+ \\ H_u^0 \end{pmatrix}$	$\tilde{H}_u = \begin{pmatrix} \tilde{H}_u^+ \\ \tilde{H}_u^0 \end{pmatrix}$	$\begin{pmatrix} (H_u^+, \tilde{H}_u^+) \\ (H_u^0, \tilde{H}_u^0) \end{pmatrix}$
	$H_d = \begin{pmatrix} H_d^0 \\ H_d^- \end{pmatrix}$	$\tilde{H}_d = \begin{pmatrix} \tilde{H}_d^0 \\ \tilde{H}_d^- \end{pmatrix}$	$\begin{pmatrix} (H_d^0, \tilde{H}_d^0) \\ (H_d^-, \tilde{H}_d^-) \end{pmatrix}$

Table 2.2.: Fields for fermions and Higgs fields, their supersymmetric partners and the corresponding supermultiplets for the MSSM. In case of right-handed fields ψ_R, the complex conjugate of the supersymmetric partner, marked with an asterisk ($*$), is assigned to the field $\bar{\psi}_\mathrm{R} = \psi_\mathrm{R}^\dagger \gamma^0$. Higgsinos are doublets of the weak isospin, so they correspond to left-handed Majorana fermions.

Particle type	Spin 1/2	Spin 1	Supermultiplets
gluinos, gluons	$\tilde{g}^a$	G_μ^a	$\left(\tilde{g}^a, G_\mu^a\right)$
winos, W's	$\tilde{W}^\pm, \tilde{W}^3$	$W_\mu^\pm, W_\mu^3$	$\left(\tilde{W}^\pm, W_\mu^\pm\right), \left(\tilde{W}^3, W_\mu^3\right)$
bino, B	$\tilde{B}$	B_μ	$\left(\tilde{B}, B_\mu\right)$

Table 2.3.: Fields for gauge bosons, their supersymmetric partners and the corresponding supermultiplets for the MSSM. In case of the neutral fields W_μ^3 and B_μ, the supersymmetric partners can be transformed into a zino ($\tilde{Z}$) and a photino ($\tilde{\gamma}$) as given in equation 2.4.

The MSSM Lagrangian density is completely defined by the allowed gauge transformations and the superpotential $\mathcal{W}$, which is a holomorphic function of the complex scalar fields treated as complex variables [36].

Additional terms of the MSSM Lagrangian density with respect to the SM, which respect gauge symmetries, can be subdivided into six groups: gauge interactions of sfermions, Higgs bosons, higgsinos and gauginos, terms with interactions of gauginos with a chiral supermultiplet pair, and terms with quartic interactions of the complex scalar fields of the chiral supermultiplets.

Sfermions are scalars, which participate in the same interactions as their ordinary partners, the fermions. A kinetic term for a scalar field ϕ is given by $(\partial_\mu \phi)^*(\partial^\mu \phi)$. In gauge theories, the partial derivative ∂_μ is extended to a covariant derivative D_μ, which involves interactions with gauge bosons. The interactions in $\mathcal{L}_{\text{Fermion}}$ in equation 2.9 are rearranged to write the interactions of sfermions in terms of covariant derivatives. These are summarized as follows:

$$D_\mu^{Q_L} = \partial_\mu + i g_s G_\mu^a \frac{\lambda^a}{2} + i \left(\frac{g}{2} \left(\tau^+ W_\mu^+ + \tau^- W_\mu^- \right) + eQA_\mu + \frac{g}{\cos \theta_W} \left(\frac{\tau^3}{2} - Q \sin^2 \theta_W \right) Z_\mu \right)$$

$$D_\mu^{q_R} = \partial_\mu + i g_s G_\mu^a \frac{\lambda^a}{2} + i \left(eQA_\mu - \frac{g}{\cos \theta_W} Q \sin^2 \theta_W Z_\mu \right)$$

$$D_\mu^{L_L} = D_\mu^H = \partial_\mu + i \left(\frac{g}{2} \left(\tau^+ W_\mu^+ + \tau^- W_\mu^- \right) + eQA_\mu + \frac{g}{\cos \theta_W} \left(\frac{\tau^3}{2} - Q \sin^2 \theta_W \right) Z_\mu \right)$$

$$D_\mu^{\ell_R} = \partial_\mu + i \left(eQA_\mu - \frac{g}{\cos \theta_W} Q \sin^2 \theta_W Z_\mu \right)$$

The gauge interactions of sfermions can then be written as given in equation 2.10:

$$\begin{aligned}
\mathcal{L}_{\text{Sfermion}} = &\sum_{\tilde{Q}_L} (D_\mu^{Q_L} \tilde{Q}_L)^\dagger (D^{\mu, Q_L} \tilde{Q}_L) \\
&+ \sum_{\tilde{q}_R^u} (D_\mu^{q_R} \tilde{q}_R^u)^\dagger (D^{\mu, q_R} \tilde{q}_R^u) + \sum_{\tilde{q}_R^d} (D_\mu^{q_R} \tilde{q}_R^d)^\dagger (D^{\mu, d_R} \tilde{q}_R^d) \\
&+ \sum_{\tilde{L}_L} (D_\mu^{L_L} \tilde{L}_L)^\dagger (D^{\mu, L_L} \tilde{L}_L) + \sum_{\tilde{\ell}_R} (D_\mu^{\ell_R} \tilde{\ell}_R)^\dagger (D^{\mu, \ell_R} \tilde{\ell}_R)
\end{aligned} \tag{2.10}$$

The hermitian conjugation marked with a dagger ($\dagger$) is used to cover the isospin multiplets of the SU(2)_L and SU(3)_C interactions. In case of isospin singlets, the hermitian conjugation becomes a complex conjugation.

The gauge interactions of the Higgs fields are part of the Lagrangian density of the MSSM Higgs sector, $\mathcal{L}_{\text{Higgs}}^{\text{MSSM}}$, and after electroweak symmetry breaking, these terms will become the mass terms of the gauge bosons and their interactions with the Higgs bosons. These terms are summarized as follows:

$$\begin{aligned}
\mathcal{L}_{\text{Higgs}}^{\text{MSSM}} &= (D_\mu^H H_u)^\dagger (D^{\mu, H} H_u) + (D_\mu^H H_d)^\dagger (D^{\mu, H} H_d) + \dots \\
&= \mathcal{L}_{\text{Higgs}}^{\text{kinetic}} + \dots
\end{aligned} \tag{2.11}$$

Contributions to $\mathcal{L}_{\text{Higgs}}^{\text{MSSM}}$ will be discussed in more detail in section 2.3.

The higgsinos are treated as left-handed fermions, such that equation 2.8 is used to

construct the term for the Lagrangian density:

$$\mathcal{L}_{\text{Higgsino}} = i\tilde{H}_u^\dagger \gamma^0 \gamma^\mu D_\mu^H \tilde{H}_u + i\tilde{H}_d^\dagger \gamma^0 \gamma^\mu D_\mu^H \tilde{H}_d \tag{2.12}$$

The same prescription applies to the gauginos summarized in the following:

$$\begin{aligned}
\mathcal{L}_{\text{Gaugino}} = {} & i\frac{1}{2}\tilde{g}^{a,\dagger}\gamma^0\gamma^\mu \left(\partial_\mu \tilde{g}^a + g_s f^{abc} G_\mu^b \tilde{g}^c \right) \\
& + i\tilde{W}^{a,\dagger}\gamma^0\gamma^\mu \left(\partial_\mu \tilde{W}^a + g\epsilon^{abc} W_\mu^b \tilde{W}^c \right) \\
& + i\frac{1}{2}\tilde{B}^\dagger\gamma^0\gamma^\mu \partial_\mu \tilde{B}
\end{aligned} \tag{2.13}$$

In the notation used in equation 2.13, the fields for the winos, $\tilde{W}^a$, are rotated with equation 2.4 to match the notation of the original fields W_μ^a ($a \in \{1,2,3\}$) of the SU(2)$_\text{L}$ group. The factor of 1/2 for the gluinos and bino is used to accommodate for the Majorana nature of the spinors.

The interactions of gauginos with a chiral supermultiplet pair (ϕ, ψ) are restricted to the particles, which share the same gauge group interactions, such that separate terms can be formulated for gluinos, winos and binos, as given in equation 2.14.

$$\begin{aligned}
\mathcal{L}_{\text{Gaugino}\leftrightarrow(\phi,\psi)} = {} & -\sqrt{2}g_s \sum_q \left(\tilde{g}^{a,\dagger}\gamma^0 \left(\tilde{q}^\dagger \frac{\lambda^a}{2} q \right) + \left(q^\dagger \gamma^0 \frac{\lambda^a}{2} \tilde{q} \right) \tilde{g}^a \right) \\
& - \sqrt{2}g \sum_{Q_\text{L}} \left(\tilde{W}^{a,\dagger}\gamma^0 \left(\tilde{Q}_\text{L}^\dagger \frac{\tau^a}{2} Q_\text{L} \right) + \left(Q_\text{L}^\dagger \gamma^0 \frac{\tau^a}{2} \tilde{Q}_\text{L} \right) \tilde{W}^a \right) \\
& - \sqrt{2}g \sum_{L_\text{L}} \left(\tilde{W}^{a,\dagger}\gamma^0 \left(\tilde{L}_\text{L}^\dagger \frac{\tau^a}{2} L_\text{L} \right) + \left(L_\text{L}^\dagger \gamma^0 \frac{\tau^a}{2} \tilde{L}_\text{L} \right) \tilde{W}^a \right) \\
& - \sqrt{2}g \sum_H \left(\tilde{W}^{a,\dagger}\gamma^0 \left(H^\dagger \frac{\tau^a}{2} \tilde{H} \right) + \left(\tilde{H}^\dagger \gamma^0 \frac{\tau^a}{2} H \right) \tilde{W}^a \right) \\
& - \sqrt{2}g' \sum_f \left(\tilde{B}^\dagger\gamma^0 \left(\tilde{f}^\dagger Y f \right) + \left(f^\dagger \gamma^0 Y \tilde{f} \right) \tilde{B} \right) \\
& - \sqrt{2}g' \sum_H \left(\tilde{B}^\dagger\gamma^0 \left(H^\dagger Y \tilde{H} \right) + \left(\tilde{H}^\dagger \gamma^0 Y H \right) \tilde{B} \right)
\end{aligned}$$

$$q \in \text{quarks} = \left\{ u_\text{L}', u_\text{R}', d_\text{L}', d_\text{R}', c_\text{L}', c_\text{R}', s_\text{L}', s_\text{R}', t_\text{L}', t_\text{R}', b_\text{L}', b_\text{R}' \right\}$$
$$f \in \text{fermions} = \text{quarks} \cup \left\{ e_\text{L}, e_\text{R}, \nu_{e,\text{L}}, \mu_\text{L}, \mu_\text{R}, \nu_{\mu,\text{L}}, \tau_\text{L}, \tau_\text{R}, \nu_{\tau,\text{L}} \right\}$$
$$Q_\text{L} \in \left\{ \begin{pmatrix} u_\text{L}' \\ d_\text{L}' \end{pmatrix}, \begin{pmatrix} c_\text{L}' \\ s_\text{L}' \end{pmatrix}, \begin{pmatrix} t_\text{L}' \\ b_\text{L}' \end{pmatrix} \right\}, \quad L_\text{L} \in \left\{ \begin{pmatrix} \nu_{e,\text{L}} \\ e_\text{L} \end{pmatrix}, \begin{pmatrix} \nu_{\mu,\text{L}} \\ \mu_\text{L} \end{pmatrix}, \begin{pmatrix} \nu_{\tau,\text{L}} \\ \tau_\text{L} \end{pmatrix} \right\}$$
$$H \in \{H_u, H_d\} \tag{2.14}$$

The hermitian conjugation for the complex scalar fields is again applied to account for the weak and strong isospin vectors, whereas the hermitian conjugation of spinors is applied in spinor and isospin space simultaneously.

The last term which follows from its invariance under gauge transformations is the quartic

coupling of the complex scalar fields. This term contributes to the scalar potential V of the MSSM:

$$V_{\text{Gauge}} = \frac{1}{2}g_s^2 \sum_q \left(\tilde{q}^\dagger \frac{\lambda^a}{2}\tilde{q}\right)^2$$
$$+ \frac{1}{2}g^2 \sum_{Q_L} \left(\tilde{Q}_L^\dagger \frac{\tau^a}{2}\tilde{Q}_L\right)^2 + \frac{1}{2}g^2 \sum_{L_L} \left(\tilde{L}_L^\dagger \frac{\tau^a}{2}\tilde{L}_L\right)^2 + \frac{1}{2}g^2 \sum_H \left(H^\dagger \frac{\tau^a}{2}H\right)^2$$
$$+ \frac{1}{2}g'^2 \sum_f \left(\tilde{f}^\dagger Y\tilde{f}\right)^2 + \frac{1}{2}g'^2 \sum_H \left(H^\dagger YH\right)^2 \tag{2.15}$$

The sums in equation 2.15 are performed in the same manner as in equation 2.14 and the same convention holds for the hermitian conjugation. The summation over the index a of symmetry group generators is performed implicitly, since the terms in the brackets are squared. The terms quartic in the Higgs fields will be considered in more detail in section 2.3.

By now, all terms in the MSSM Lagrangian density involving gauge couplings are formulated. The most general collection of the remaining terms, which are invariant both under gauge and supersymmetry transformations, can be derived from the superpotential $\mathcal{W}$ of the MSSM, which is holomorphic in the complex scalar fields of the MSSM. In consequence, a complex conjugate of a Higgs field, H^*, is not allowed in the superpotential, such that at least two Higgs doublets are required in supersymmetry, unlike it is the case in SM. The superpotential of the MSSM reads as follows:

$$\mathcal{W} = \hat{U}_R^\dagger Y_u^\dagger \hat{Q}_L \cdot H_u - \hat{D}_R^\dagger Y_d^\dagger \hat{Q}_L \cdot H_d - \hat{E}_R^\dagger Y_e^\dagger \hat{L}_L \cdot H_d + \mu H_u \cdot H_d, \quad Y_u, Y_d, Y_e \in \mathbb{C}^{3\times3}$$

$$\hat{U}_R = \begin{pmatrix} \tilde{u}_R' \\ \tilde{c}_R' \\ \tilde{t}_R' \end{pmatrix}, \quad \hat{D}_R = \begin{pmatrix} \tilde{d}_R' \\ \tilde{s}_R' \\ \tilde{b}_R' \end{pmatrix}, \quad \hat{E}_R = \begin{pmatrix} \tilde{e}_R \\ \tilde{\mu}_R \\ \tilde{\tau}_R \end{pmatrix}, \quad \hat{Q}_L = \begin{pmatrix} \begin{pmatrix} \tilde{u}_L' \\ \tilde{d}_L' \end{pmatrix} \\ \begin{pmatrix} \tilde{c}_L' \\ \tilde{s}_L' \end{pmatrix} \\ \begin{pmatrix} \tilde{t}_L' \\ \tilde{b}_L' \end{pmatrix} \end{pmatrix}, \quad \hat{L}_L = \begin{pmatrix} \begin{pmatrix} \tilde{\nu}_{e,L} \\ \tilde{e}_L \end{pmatrix} \\ \begin{pmatrix} \tilde{\nu}_{\mu,L} \\ \tilde{\mu}_L \end{pmatrix} \\ \begin{pmatrix} \tilde{\nu}_{\tau,L} \\ \tilde{\tau}_L \end{pmatrix} \end{pmatrix}$$

$$\text{Product of two weak isospin doublets: } J_1 \cdot J_2 = J_1^T \cdot \begin{pmatrix} 0 & 1 \\ -1 & 0 \end{pmatrix} \cdot J_2 \tag{2.16}$$

The vectors of weak isospin singlets $\hat{U}_R$, $\hat{D}_R$ and $\hat{E}_R$, the vectors of weak isospin doublets $\hat{Q}_L$ and $\hat{L}_L$, and the complex 3×3 matrices Y_u, Y_d and Y_e are arranged in the quark or lepton family space with three generations, such that in general, a mixing between the generations is allowed for the terms containing the matrices. The weak isospin singlet fields are hermitian conjugated to account for the vector structure in the family space. The product of two weak isospin doublets is defined such that the resulting expression is invariant under gauge transformations.

The entries of the matrices Y_u, Y_d and Y_e are dimensionless parameters, which correspond to Yukawa couplings to the Higgs bosons after electroweak symmetry breaking, as will be discussed in section 2.3. The parameter μ has the dimension of a mass and corresponds to the higgsino mass parameter.

The superpotential $\mathcal{W}$ in equation 2.16 is constructed assuming an additional discrete symmetry, the R-parity. The SM particles have +1 as eigenvalue of the corresponding parity operator, their supersymmetric partners obtain the eigenvalue -1. The motivation to assume R-parity conservation is to avoid processes, that change the number of quarks, leptons or neutrinos after transition from the initial to the final state. Such violations can lead to proton decays, for example $P \rightarrow e^+\pi^0$, which are constrained by experimental measurements: the lifetime of the proton is measured to be larger than about 10^{34} years [37].

The eigenvalue of R-parity operator $\mathcal{P}_R$ is defined from the total baryon number B, the total lepton number L and the spin S of a particle or its supersymmetric partner:

$$\mathcal{P}_R = (-1)^{3(B-L)+2S}$$

The total baryon number is +1/3 for left-handed quark supermultiplets, $-1/3$ for right-handed quark supermultiplets, and 0 for all other supermultiplets. The total lepton number is defined to be +1 for left-handed lepton and neutrino supermultiplets, -1 for right-handed lepton supermultiplets, and 0 for all other supermultiplets.

The introduction of R-parity conservation has several consequences to the phenomenology of the MSSM: Supersymmetric particles can only be produced in pairs in collider experiments. The LSP is then stable, such that it can serve as a dark matter candidate. As a consequence of these two points, each supersymmetric particle has a decay cascade, which involves the LSP as a final state at the end.

The prescription to obtain contributions to the Lagrangian density from the superpotential $\mathcal{W}$ involves its partial derivatives with respect to the complex scalar fields treated as complex variables. The first type of contributions involves second order derivatives of $\mathcal{W}$:

$$
\begin{aligned}
\mathcal{L}_{\mathcal{W}^{ij}} = -&\left(\sum_{ij} \psi_i \mathcal{W}^{ij} \psi_j + \sum_{kl} \bar{\psi}_k \mathcal{W}^{kl} \psi_l + \sum_{il} \psi_i \mathcal{W}^{il} \psi_l + \sum_{kj} \bar{\psi}_k \mathcal{W}^{kj} \psi_j \right) + h.c. \\
= -&\left(\sum_{ij} \psi_i \frac{\partial^2}{\partial \phi_i \partial \phi_j} \mathcal{W} \psi_j + \sum_{kl} \bar{\psi}_k \frac{\partial^2}{\partial \phi_k \partial \phi_l} \mathcal{W} \psi_l \right. \\
&\left. + \sum_{il} \psi_i \frac{\partial^2}{\partial \phi_i \partial \phi_l} \mathcal{W} \psi_l + \sum_{kj} \bar{\psi}_k \frac{\partial^2}{\partial \phi_k \partial \phi_j} \mathcal{W} \psi_j \right) + h.c.
\end{aligned}
\tag{2.17}
$$

(ϕ_i, ψ_i) right-handed fermion supermultiplets from table 2.2

(ϕ_j, ψ_j) left-handed fermion supermultiplets from table 2.2

$(\phi_k, \psi_k), (\phi_l, \psi_l)$ Higgs supermultiplets from table 2.2

The supermultiplets are taken exactly as defined in table 2.2, for example for the right-handed electron field, the supermultiplet is $(\tilde{e}_R^*, \bar{e}_R)$. In that way, all non-vanishing terms above are well defined and gauge-invariant. For instance, performing the double-sum over

the same indices results in terms equal to zero due to the structure of $\mathcal{W}$. The hermitian conjugated contributions ($h.c.$) are suppressed in equation 2.17. For the expressions in equation 2.17, it involves a complex conjugation of the derivatives of $\mathcal{W}$ and a conjugation of the spinor fields, for example: $\psi_i \mathcal{W}^{ij} \psi_j \rightarrow \bar{\psi}_j \mathcal{W}^{ij,*} \bar{\psi}_i$.

The first sum in $\mathcal{L}_{\mathcal{W}^{ij}}$ corresponds together with its hermitian conjugated version to Yukawa interactions between the fermions and the Higgs fields. The terms resulting from the seconds sum are higgsino mass terms with the corresponding mass parameter μ. The last two sums represent the interaction terms between the higgsino and a right-handed or left-handed pair of a fermion and its supersymmetric partner.

The second type of contributions is constructed from the first order derivatives of $\mathcal{W}$ and is part of the scalar potential V of the MSSM:

$$V = V_{\text{Gauge}} + V_{\mathcal{W}}$$

$$V_{\mathcal{W}} = \sum_i \mathcal{W}_i^* \mathcal{W}^i = \sum_i \left(\frac{\partial}{\partial \phi_i} \mathcal{W} \right)^* \frac{\partial}{\partial \phi_i} \mathcal{W} \tag{2.18}$$

ϕ_i scalar complex fields from table 2.2

The terms resulting from $V_{\mathcal{W}}$ can be separated into three groups: Terms without μ correspond to interactions between two equal or different sfermion pairs, to interactions between a Higgs field pair and a sfermion pair, or to quartic interactions of Higgs fields. Terms with one order of μ define cubic scalar couplings of Higgs fields with sfermion pairs. Lastly, terms with μ^2 correspond to Higgs mass terms.

All MSSM contributions to the Lagrangian density are defined by now, introducing only a few additional model parameters with respect to the ones known from the SM. However, the requirement of supersymmetry being exact leads to the requirement, that the masses of the SM particles and their supersymmetric partners must be equal. If this would be true, then a discovery of the supersymmetric partners should already have happened, for example a discovery of the selectron. Due to the lack of such discoveries, supersymmetry must be broken to provide a realistic description of particle physics [38].

Due to the Ferrara-Girardello-Palumbo mass sum rule [39], the spontaneous breaking of supersymmetry is not allowed to happen in the sector of the known interactions of the MSSM. Applied to the electron and its superpartners, with the simplifying assumption, that their chiral eigenstates are also mass eigenstates and do not mix with other scalars, the sum rule would require the following equation to be fulfilled after supersymmetry breaking in the sector of MSSM interactions:

$$m_{\tilde{e}_{\text{R}}}^2 + m_{\tilde{e}_{\text{L}}}^2 - 2m_e^2 = 0$$

This equation would imply, that the masses of the supersymmetric partners of the electron are either equal to the electron mass, or one of supersymmetric partners is lighter and the other one is heavier than the electron. Both cases are excluded by direct searches for SUSY particles, so the supersymmetry breaking can not be accomplished by the existing particle spectrum of the MSSM. In consequence, new fields need to be introduced to the MSSM to perform supersymmetry breaking.

A field is required, which obtains a vacuum expectation value after spontaneous supersymmetry breaking and provides a Goldstone boson, called goldstino. Furthermore, one

or several chiral supermultiplets, called messengers, are introduced to mediate the broken symmetry from the sector of the goldstino field to the MSSM sector. These chiral super-multiplets are the only fields, which interact with the field with the vacuum expectation value, such that its sector is often referred to as the hidden sector.

Several models exist to mediate the spontaneous supersymmetry breaking. In one approach, gravitational effects at the Planck mass scale M_P lead to supersymmetry breaking [40]. The global supersymmetry discussed so far is promoted to a local supersymmetry, such that gravity can be described in this framework by a spin 2 graviton and its supersymmetric partner with spin 3/2, gravitino. After supersymmetry breaking, the goldstino is absorbed by the gravitino, which then becomes massive. Loop corrections to the MSSM parameters involving the massive gravitino lead to increased masses of supersymmetric particles.

An alternative is provided by supersymmetry breaking through gauge interactions [41]. In its minimal realization, a new chiral supermultiplet is introduced as a messenger field between the source of the symmetry breaking in a hidden sector and the MSSM particle spectrum. This supermultiplet shares some of the gauge interactions of the MSSM. The supersymmetry breaking terms are then introduced to the Lagrangian density with loop corrections to the MSSM parameters. The energy scale, at which the new messenger particle becomes relevant, is chosen a few orders below the Planck mass scale, such that gravitational effects are irrelevant for the supersymmetry breaking.

Both approaches lead to a soft supersymmetry breaking to be able to maintain the solution to the hierarchy problem, avoiding terms in the supersymmetry breaking Lagrangian density $\mathcal{L}_\text{soft}$, which have dimensionless parameters. The most general Lagrangian density $\mathcal{L}_\text{soft}$, which is invariant under gauge transformations, is renormalizable, conserves R-parity, but breaks supersymmetry softly, has the following form:

$$
\begin{aligned}
\mathcal{L}_\text{soft} = &-\frac{1}{2}\left(M_1 \tilde{B}^\dagger \gamma^0 \tilde{B} + M_2 \tilde{W}^{a,\dagger}\gamma^0 \tilde{W}^a + M_3 \tilde{g}^{a,\dagger}\gamma^0 \tilde{g}^a\right) \\
&-\left(\hat{Q}_\text{L}^\dagger \boldsymbol{M}_Q^2 \hat{Q}_\text{L} + \hat{L}_\text{L}^\dagger \boldsymbol{M}_L^2 \hat{L}_\text{L} + \hat{U}_\text{R}^\dagger \boldsymbol{M}_U^2 \hat{U}_\text{R} + \hat{D}_\text{R}^\dagger \boldsymbol{M}_D^2 \hat{D}_\text{R} + \hat{E}_\text{R}^\dagger \boldsymbol{M}_E^2 \hat{E}_\text{R}\right) \\
&-\left(\hat{U}_\text{R}^\dagger \boldsymbol{A_u}\hat{Q}_\text{L}\cdot H_u - \hat{D}_\text{R}^\dagger \boldsymbol{A_d}\hat{Q}_\text{L}\cdot H_d - \hat{E}_\text{R}^\dagger \boldsymbol{A_e}\hat{L}_\text{L}\cdot H_d + c.c.\right) \\
&- m_{H_u}^2 H_u^* \cdot H_u - m_{H_d}^2 H_d^* \cdot H_d - \left(b_\text{soft} H_u \cdot H_d + c.c.\right)
\end{aligned}
\tag{2.19}
$$

The sfermion fields in equation 2.19 are arranged into vectors in the family space as it is done in equation 2.16. The hermitian conjugation of the gaugino spinors in the first line is applied to the spinor structure, whereas in case of the sfermion scalar fields it is used to take the weak isospin structure and the family space vectors into account. The product of weak isospin doublets is used as in equation 2.16. In the last two lines, the complex conjugated (*c.c.*) versions of the explicitly written terms are suppressed in the notation.

The first line in equation 2.19 represents the mass terms of the gauginos. It is important to note here, that these additional contributions to the gaugino masses are not connected to the mechanism of electroweak symmetry breaking described in section 2.3. In consequence, the couplings of the gauginos to the Higgs bosons remain to be driven by the term $\mathcal{L}_\text{Higgs}^\text{kinetic}$ from equation 2.11. In turn, gluinos do not have any couplings with the Higgs bosons, although they are massive after soft supersymmetry breaking.

The second line in equation 2.19 corresponds to the mass terms of the sfermions. The matrices $\boldsymbol{M}_Q^2$, $\boldsymbol{M}_L^2$, $\boldsymbol{M}_U^2$, $\boldsymbol{M}_D^2$ and $\boldsymbol{M}_E^2$ are 3×3 hermitian, complex matrices in the corre-

sponding family spaces, which contain entries of a dimension of squared mass and allow for a mixing between mass eigenstates in general.

The third line in equation 2.19 defines supersymmetry breaking couplings of sfermions to the Higgs bosons. The complex 3×3 matrices $\boldsymbol{A_u}$, $\boldsymbol{A_d}$ and $\boldsymbol{A_e}$ in the fermion family space have a dimension of mass and serve as supersymmetry breaking Yukawa couplings. Also with these matrices, a mixing within the fermion family spaces is allowed in general.

Finally, the last line of equation 2.19 describes the supersymmetry breaking terms, which enter the potential used for electroweak symmetry breaking.

All parameters of the soft supersymmetry breaking terms are related to a characteristic mass scale $m_{soft} \approx 1$ TeV to preserve the cancellation of the loop contributions to the Higgs bosons masses:

$$M_1, M_2, M_3, \boldsymbol{A_u}, \boldsymbol{A_d}, \boldsymbol{A_e} \approx m_{soft}$$
$$\boldsymbol{M_Q^2}, \boldsymbol{M_L^2}, \boldsymbol{M_U^2}, \boldsymbol{M_D^2}, \boldsymbol{M_E^2}, m_{H_u}^2, m_{H_d}^2, b_{soft} \approx m_{soft}^2$$

The full Lagrangian density of the MSSM can then be formulated as follows:

$$\begin{aligned}
\mathcal{L}_{MSSM} =& \mathcal{L}_{Sfermion} + \mathcal{L}_{Gaugino} + \mathcal{L}_{Higgsino} + \mathcal{L}_{Higgs}^{kinetic} + \mathcal{L}_{Gaugino \leftrightarrow (\phi, \psi)} + \mathcal{L}_{\mathcal{W}^{ij}} - V + \mathcal{L}_{soft} \\
&+ \mathcal{L}_{Fermion} + \mathcal{L}_{Gauge} \\
&+ \mathcal{L}_{GF}^{MSSM} + \mathcal{L}_{Ghost}^{MSSM}
\end{aligned} \tag{2.20}$$

The first line represents the contributions discussed in this section, the second line are terms from the SM discussed in section 2.1. The last line corresponds to gauge fixing and ghost terms which need to be extended from the SM formulation in section 2.1 to the MSSM. This model contains 105 MSSM parameters [42], which mostly result from soft supersymmetry breaking terms, and 19 parameters already contained in the SM Lagrangian density. The MSSM parameters can be reduced drastically by specifying the supersymmetry breaking mechanism and how it is exactly mediated to the MSSM sector, or by using simplifying assumptions, which are motivated by recent constraints from experimental measurements. With a reduced set of MSSM parameters, benchmark scenarios can be defined [43, 44], which represent specific phenomenological effects. The assumptions chosen for the benchmark scenario M_h^{125} [43] will be discussed in more detail in section 2.3.

2.3. Higgs Sector

As already indicated in section 2.1, mass terms for gauge bosons and for fermions can not be added explicitly to the Lagrangian density. Mass terms for $W^\pm$ and Z gauge bosons would have the form $m_W^2 W_\mu^+ W^{-\mu}$ and $m_Z^2 Z_\mu Z^\mu$, respectively. Such terms violate the gauge invariance of $SU(2)_L$. Similarly, fermion mass terms of the form $m_\psi \left(\bar{\psi}_R \psi_L + \bar{\psi}_L \psi_R \right)$ violate $SU(2)_L$ symmetry, since the left-handed and right-handed parts of the fermions transform differently under $SU(2)_L$.

A possible solution to this problem is the introduction of the Brout-Englert-Higgs mechanism [6−8] with its simplest realization in the SM. A new scalar field is introduced, that is part of the Higgs potential V_{Higgs}. The purpose of the potential is to provide a non-zero vacuum expectation value for the Higgs field at the minimum of the potential. The symmetry

of the model retained at a vacuum expectation value of zero is then spontaneously broken by the choice of the particular minimum. The number of broken degrees of freedom of the Higgs field become Goldstone bosons [45], which can be absorbed by gauge vector bosons as longitudinal degrees of freedom, making them massive.

For the electroweak sector $SU(2)_L \times U(1)_Y$, three of the four gauge bosons should obtain a mass. To accomplish this, a Higgs field is introduced to the SM as a weak isospin doublet of complex scalar fields:

$$H_{\text{SM}} = \begin{pmatrix} H_{\text{SM}}^+ \\ H_{\text{SM}}^0 \end{pmatrix} = \frac{1}{\sqrt{2}} \begin{pmatrix} h_{1,\text{SM}}^+ + i h_{2,\text{SM}}^+ \\ h_{1,\text{SM}}^0 + i h_{2,\text{SM}}^0 \end{pmatrix} \tag{2.21}$$

In that way, the Higgs field H_{SM} has four degrees of freedom and is invariant under $SU(2)_L \times U(1)_Y$. The eigenvalues of the corresponding operators T_L^3, Y and Q are given in table 2.4:

Quantum number	Higgs field	
	H_{SM}^+	H_{SM}^0
T_L^3	1/2	-1/2
Y	1/2	1/2
Q	1	0

Table 2.4.: Quantum numbers of the SM Higgs fields for the operators T_L^3, Y and Q.

The Higgs potential V_{Higgs} and the kinetic term of the Higgs field $\mathcal{L}_{\text{Higgs}}^{\text{kinetic}}$ are formulated together as the Higgs Lagrangian density $\mathcal{L}_{\text{Higgs}}^{\text{SM}}$ as follows:

$$\mathcal{L}_{\text{Higgs}}^{\text{SM}} = \mathcal{L}_{\text{Higgs}}^{\text{kinetic}} - V_{\text{Higgs}}$$

$$\mathcal{L}_{\text{Higgs}}^{\text{kinetic}} = \left(D_\mu^H H_{\text{SM}} \right)^\dagger \left(D^{\mu,H} H_{\text{SM}} \right)$$

$$V_{\text{Higgs}} = -\mu_{\text{SM}}^2 H_{\text{SM}}^\dagger H_{\text{SM}} + \lambda \left(H_{\text{SM}}^\dagger H_{\text{SM}} \right)^2 \tag{2.22}$$

Assuming that one of the four components of the Higgs field must be different from zero at the minimum of V_{Higgs}, this potential is minimized exactly when the following requirement is fulfilled:

$$H_{\text{SM}}^\dagger H_{\text{SM}} = \frac{\mu^2}{2\lambda} = \frac{v^2}{2} \tag{2.23}$$

The parameters μ and λ of the Higgs potential define the vacuum expectation value v. The non-vanishing vacuum expectation value can be chosen in any of the four components of the Higgs field. Since the vacuum is electrically neutral and symmetric under charge-parity ($\mathcal{CP}$) transformations, v is assigned to the parameterization of the real, neutral component of H_{SM}:

$$h_{1,\text{SM}}^0 = v + h_{\text{SM}} \quad \rightarrow \quad H_{\text{SM}} = \begin{pmatrix} H_{\text{SM}}^+ \\ \frac{1}{\sqrt{2}} \left(v + h_{\text{SM}} + i h_{2,\text{SM}}^0 \right) \end{pmatrix}$$

Expanding $\mathcal{L}^{\text{SM}}_{\text{Higgs}}$ in this parameterization results in a number of terms. All terms involving the Goldstone bosons H^+_{SM}, $H^-_{\text{SM}} = \left(H^+_{\text{SM}}\right)^*$ and $h^0_{2,\text{SM}}$ are unphysical and can be accounted for or even removed completely by introducing appropriate terms for gauge fixing. Therefore, only the terms with the vacuum expectation value v or Higgs boson field h_{SM} are considered in the following. The degrees of freedom, which corresponded to the three Goldstone bosons are absorbed by gauge transformations into the gauge boson fields $W^\pm_\mu$ and Z_μ.

The potential V_{Higgs} consists then of a mass term for the Higgs boson with $\text{m}^2_{h_{\text{SM}}} = 2\mu^2$, terms with trilinear and quartic Higgs boson self-couplings, and a constant offset which is neglected in further considerations:

$$
\begin{aligned}
V_{\text{Higgs}}|_{v+h_{\text{SM}}} &= \frac{\text{m}^2_{h_{\text{SM}}}}{4} h^2_{\text{SM}} \\
&+ \frac{\lambda}{4} h^4_{\text{SM}} + \frac{\mu^2}{v} h^3_{\text{SM}} \\
&- \frac{\cancel{\mu^2 v^2}}{4}
\end{aligned}
$$

The contributions with v or h_{SM} in the kinetic term $\mathcal{L}^{\text{kinetic}}_{\text{Higgs}}$ can be grouped into mass terms for the gauge bosons, trilinear coupling terms between the Higgs boson field and gauge boson pairs, quartic coupling terms between a Higgs boson pair and gauge boson pairs, and the remaining kinetic term for the Higgs boson with partial derivatives:

$$
\begin{aligned}
\mathcal{L}^{\text{kinetic}}_{\text{Higgs}}|_{v+h_{\text{SM}}} = \text{m}^2_{\text{W}} W^-_\mu W^{+\mu} &\qquad + \frac{\text{m}^2_{\text{Z}}}{2} Z_\mu Z^\mu \\
+ \frac{2\text{m}^2_{\text{W}}}{v} h_{\text{SM}} W^-_\mu W^{+\mu} &\quad + \frac{\text{m}^2_{\text{Z}}}{v} h_{\text{SM}} Z_\mu Z^\mu \\
+ \frac{\text{m}^2_{\text{W}}}{v^2} h^2_{\text{SM}} W^-_\mu W^{+\mu} &\quad + \frac{\text{m}^2_{\text{Z}}}{2v^2} h^2_{\text{SM}} Z_\mu Z^\mu \\
+ \frac{1}{2} \left(\partial_\mu h_{\text{SM}}\right) \left(\partial^\mu h_{\text{SM}}\right) &
\end{aligned}
$$

$$
\text{m}_{\text{W}} = \frac{gv}{2}, \qquad \text{m}_{\text{Z}} = \frac{gv}{2\cos\theta_W}
$$

Terms with the photon field A_μ cancel out exactly with the relations between the gauge coupling parameters e, g and g'. In consequence, the photon remains massless and does not couple to the Higgs boson field. This means, that after the spontaneous symmetry breaking procedure for the electroweak sector $\text{SU}(2)_\text{L} \times \text{U}(1)_\text{Y}$ demonstrated so far, the $\text{U}(1)_\text{em}$ symmetry of the electromagnetic interactions connected to A_μ remains. In contrast to that, the gauge boson fields $W^\pm_\mu$ and Z_μ obtain mass terms and couple to the Higgs boson field h_{SM}. The corresponding coupling strength is proportional to the squared mass, m^2_{W} and m^2_{Z}, respectively.

Mass terms for fermions are introduced with Yukawa interactions in a gauge invariant

way:

$$\mathcal{L}_{\text{Yukawa}}^{\text{SM}} = -\bar{L}_{\text{L}}Y_e E_{\text{R}}H_{\text{SM}} - \bar{Q}_{\text{L}}Y_d D_{\text{R}}H_{\text{SM}} - \bar{Q}_{\text{L}}Y_u U_{\text{R}} \begin{pmatrix} 0 & 1 \\ -1 & 0 \end{pmatrix} H_{\text{SM}}^* + h.c. \qquad (2.24)$$

$$U_{\text{R}} = \begin{pmatrix} u_{\text{R}}' \\ c_{\text{R}}' \\ t_{\text{R}}' \end{pmatrix}, \quad D_{\text{R}} = \begin{pmatrix} d_{\text{R}}' \\ s_{\text{R}}' \\ b_{\text{R}}' \end{pmatrix}, \quad E_{\text{R}} = \begin{pmatrix} e_{\text{R}} \\ \mu_{\text{R}} \\ \tau_{\text{R}} \end{pmatrix}, \quad Q_{\text{L}} = \begin{pmatrix} \begin{pmatrix} u_{\text{L}}' \\ d_{\text{L}}' \end{pmatrix} \\ \begin{pmatrix} c_{\text{L}}' \\ s_{\text{L}}' \end{pmatrix} \\ \begin{pmatrix} t_{\text{L}}' \\ b_{\text{L}}' \end{pmatrix} \end{pmatrix}, \quad L_{\text{L}} = \begin{pmatrix} \begin{pmatrix} \nu_{e,\text{L}} \\ e_{\text{L}} \end{pmatrix} \\ \begin{pmatrix} \nu_{\mu,\text{L}} \\ \mu_{\text{L}} \end{pmatrix} \\ \begin{pmatrix} \nu_{\tau,\text{L}} \\ \tau_{\text{L}} \end{pmatrix} \end{pmatrix}$$

The hermitian conjugation of the fields indicated by $\bar{\psi} = \psi^\dagger \gamma^0$, as well as in the terms suppressed in equation 2.24 with ($h.c.$), is applied in all relevant phase spaces simultaneously: the family space, the weak isospin space and the spinor space.

After electroweak symmetry breaking, $\mathcal{L}_{\text{Yukawa}}^{\text{SM}}$ is expanded in terms of the vacuum expectation value v and the Higgs boson field h_{SM}:

$$\mathcal{L}_{\text{Yukawa}}^{\text{SM}}|_{v+h_{\text{SM}}} = - \begin{pmatrix} \bar{e}_{\text{L}} & \bar{\mu}_{\text{L}} & \bar{\tau}_{\text{L}} \end{pmatrix} \cdot Y_e \cdot \begin{pmatrix} e_{\text{R}} \\ \mu_{\text{R}} \\ \tau_{\text{R}} \end{pmatrix} \left(\frac{v + h_{\text{SM}}}{\sqrt{2}} \right)$$

$$- \begin{pmatrix} \bar{d}_{\text{L}}' & \bar{s}_{\text{L}}' & \bar{b}_{\text{L}}' \end{pmatrix} \cdot Y_d \cdot \begin{pmatrix} d_{\text{R}}' \\ s_{\text{R}}' \\ b_{\text{R}}' \end{pmatrix} \left(\frac{v + h_{\text{SM}}}{\sqrt{2}} \right)$$

$$- \begin{pmatrix} \bar{u}_{\text{L}}' & \bar{c}_{\text{L}}' & \bar{t}_{\text{L}}' \end{pmatrix} \cdot Y_u \cdot \begin{pmatrix} u_{\text{R}}' \\ c_{\text{R}}' \\ t_{\text{R}}' \end{pmatrix} \left(\frac{v + h_{\text{SM}}}{\sqrt{2}} \right) + (h.c.)$$

The Yukawa coupling matrices Y_e, Y_u and Y_d have in general non-diagonal entries. To obtain mass terms for each fermion field, a transformation of the weak interaction eigenstates into mass eigenstates needs to be performed, as it was discussed in section 2.1 for equation 2.5. The diagonal mass matrices can be constructed as follows:

$$M_e = \frac{v}{\sqrt{2}} \cdot Y_e = diag\left(m_e, m_\mu, m_\tau\right)$$

$$M_d = \frac{v}{\sqrt{2}} \cdot U_{\text{L}}^d Y_d U_{\text{R}}^{d,\dagger} = diag\left(m_d, m_s, m_b\right)$$

$$M_u = \frac{v}{\sqrt{2}} \cdot U_{\text{L}}^u Y_u U_{\text{R}}^{u,\dagger} = diag\left(m_u, m_c, m_t\right)$$

The term $\mathcal{L}_{\text{Yukawa}}^{\text{SM}}|_{v+h_{\text{SM}}}$ obtains then a simple form, if expressed in terms of mass eigenstates:

$$\mathcal{L}_{\text{Yukawa}}^{\text{SM}}|_{v+h_{\text{SM}}} = -\left(1 + \frac{h_{\text{SM}}}{v}\right) \sum_{f \in \text{fermions}} m_f \cdot \left(\bar{f}_L f_R + \bar{f}_R f_L\right)$$

$$\text{fermions} = \{e, \mu, \tau, d, s, b, u, c, t\}$$

Additionally to the mass terms, couplings between the Higgs boson and fermion pairs are introduced, with a coupling strength proportional to the mass of the fermion m_f.

The phenomenology of the Higgs boson as predicted by the SM leads to the branching fractions and production cross-sections for proton-proton collisions at the centre of mass energy of $\sqrt{s}$ = 13 TeV shown in figure 2.1. The branching fraction of the H $\rightarrow \tau\tau$ decay belongs to the highest ones, since the τ lepton belongs to the third generation of the lepton family. As will be discussed in sections 3.2 and 4.3, the signatures of a $\tau\tau$ pair can be very well reconstructed, making the H $\rightarrow \tau\tau$ decay important for Higgs boson searches and measurements. The two most relevant Higgs production modes are the gluon fusion production and the vector boson fusion with two quarks in the final state. These production modes are represented on the right in figure 2.1 by the blue and red lines, respectively. A more detailed discussion on the dominant and subdominant production modes considered in the H $\rightarrow \tau\tau$ analysis will be given in section 4.2.
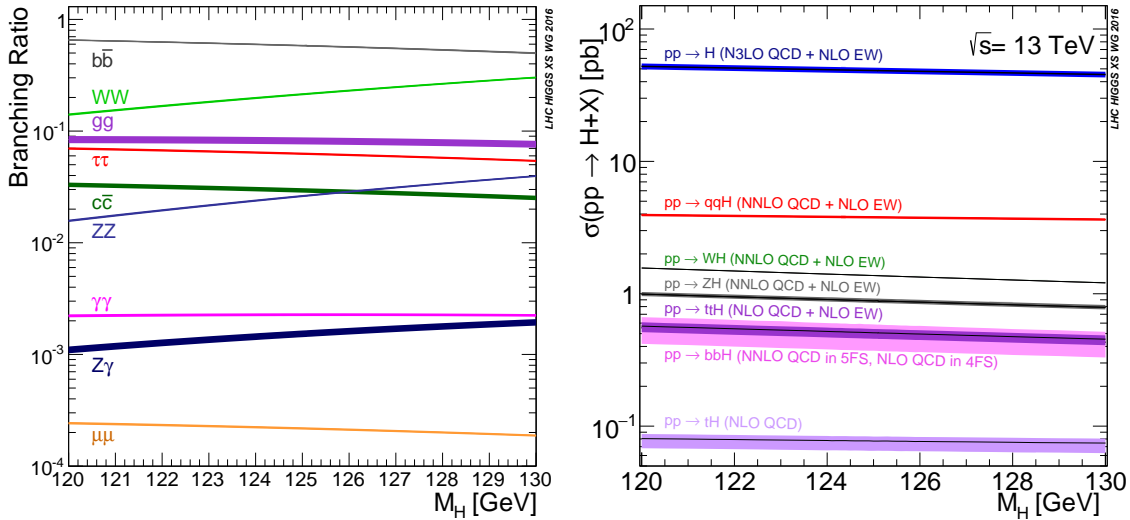
Figure 2.1.: Recent SM predictions for the branching fractions (left) and the production cross-sections (right) of the Higgs boson in the mass range [120, 130] GeV [46].

One of the simplest extensions of the SM Higgs sector is the Two-Higgs-Doublet-Model (THDM) [47, 48] with two SU(2)$_L$ Higgs doublets introduced to the Lagrangian density, which have the same eigenvalues as the SM Higgs doublet in table 2.4:

$$H_1 = \begin{pmatrix} H_1^+ \\ H_1^0 \end{pmatrix}, \qquad H_2 = \begin{pmatrix} H_2^+ \\ H_2^0 \end{pmatrix}$$

The most general, $\mathcal{CP}$ conserving Higgs potential in THDM, $V_{\text{Higgs}}^{\text{THDM}}$, has the following form:

$$V_{\text{Higgs}}^{\text{THDM}} = m_{11}^2 H_1^\dagger H_1 + m_{22}^2 H_2^\dagger H_2 - m_{12}^2 \left(H_1^\dagger H_2 + H_2^\dagger H_1 \right)$$
$$+ \frac{\lambda_1}{2} \left(H_1^\dagger H_1 \right)^2 + \frac{\lambda_2}{2} \left(H_2^\dagger H_2 \right)^2 + \lambda_3 H_1^\dagger H_1 H_2^\dagger H_2 + \lambda_4 H_1^\dagger H_2 H_2^\dagger H_1$$
$$+ \frac{\lambda_5}{2} \left(\left(H_1^\dagger H_2 \right)^2 + \left(H_2^\dagger H_1 \right)^2 \right) \tag{2.25}$$

The eight parameters introduced with $V_{\text{Higgs}}^{\text{THDM}}$ to the Lagrangian density can be chosen real. The non-vanishing minimum of the potential is chosen to be in the neutral, real components of the two Higgs doublets, such that these can be parameterized as:

$$H_1 = \begin{pmatrix} H_1^+ \\ \frac{1}{\sqrt{2}} (v_1 + h_1 + i\eta_1) \end{pmatrix}, \qquad H_2 = \begin{pmatrix} H_2^+ \\ \frac{1}{\sqrt{2}} (v_2 + h_2 + i\eta_2) \end{pmatrix} \tag{2.26}$$

Like in equation 2.23 for the SM Higgs potential, the parameters in $V_{\text{Higgs}}^{\text{THDM}}$ are related to each other by requiring two non-vanishing vacuum expectation values v_1 and v_2. This allows to define masses of the Higgs bosons in terms of a subset of the parameters of the potential and the vacuum expectation values. To separate the massless Goldstone bosons, which will be absorbed by the gauge bosons as in the SM, from the massive, physical Higgs bosons, linear combinations of the fields in equation 2.26 need to be constructed to match the mass eigenstates. In total, three combinations of the eight fields will become Goldstone bosons, the remaining five combinations will represent the physical Higgs boson spectrum of the THDM.

The electrically charged fields H_1^+ and H_2^+ can be combined to the massless charged Goldstone boson G^+ and the massive charged Higgs boson H^+ with the squared mass $m_{H^\pm}^2 = (m_{12}^2/v_1 v_2 - \lambda_4 - \lambda_5) \cdot (v_1^2 + v_2^2)$, which enters the tree level Lagrangian density. The oppositely charged counterparts of these fields can be obtained by complex conjugation: $G^- = (G^+)^*$, and $H^- = (H^+)^*$.

The fields η_1 and η_2, which are used to construct the imaginary, neutral parts of the Higgs doublets H_1 and H_2, have the massless neutral Goldstone boson G^0 and the massive pseudoscalar Higgs boson A as mass eigenstates. The field of the pseudoscalar Higgs boson obtains the squared mass $m_A^2 = (m_{12}^2/v_1 v_2 - 2\lambda_5) \cdot (v_1^2 + v_2^2)$.

Finally, the fields h_1 and h_2, which correspond to the real, neutral parts of the Higgs doublets, are used to build the two massive scalar Higgs bosons h and H with the former being the lighter one by convention.

The eight parameters in the Higgs potential $V_{\text{Higgs}}^{\text{THDM}}$ can be transformed into a different set of parameters, which directly influence the phenomenology of the model:

- Masses of the Higgs bosons: $m_{H^\pm}$, m_H, m_A and m_h
- The ratio of the vacuum expectation values: $v_2/v_1 = \tan \beta$
- The total vacuum expectation value v, defined by $v^2 = v_1^2 + v_2^2$
- The mixing angle α needed to rotate the fields h_1 and h_2 into scalar Higgs boson fields h and H
- The soft breaking mass parameter m_{12}

The remaining terms in the Higgs potential after the elimination of the Goldstone boson fields correspond to the trilinear and quartic couplings between the five physical Higgs

bosons [49]. In case of trilinear couplings, either the light scalar Higgs boson field h or the heavy scalar Higgs boson field H couples to Higgs boson pairs hh, HH, AA and H^+H^-. The quartic interactions consist of couplings between all possible Higgs boson pairs, which comprise the pairs mentioned before and the hH pair additionally, resulting in 14 different interaction vertices in total.

Kinetic contributions to the Higgs Lagrangian density involving the Higgs fields H_1 and H_2 are constructed in the same manner as in equation 2.22. The resulting mass terms for the gauge boson fields $W_\mu^\pm$ and Z_μ are of the same form as in SM, involving the total vacuum expectation value v. However, the interactions between the gauge bosons and the Higgs bosons are extended in a THDM. These interactions can separated into three types: interactions of one gauge boson and a Higgs boson pair, interactions of a Higgs boson with a gauge boson pair, and interactions of a Higgs boson pair with a gauge boson pair. The first type of interactions comprises the interaction of the boson field $W_\mu^\pm$ with a pair of a neutral and the charged Higgs boson field $H^\pm$. Beyond that, the Z boson field Z_μ couples to a pair with a scalar Higgs boson field and the pseudoscalar Higgs boson field A. The photon field A_μ, which is massless, therefore couples only to the pair of charged Higgs boson fields $H^\mp H^\pm$.

The second type of interactions involves only the couplings of neutral scalar Higgs boson fields, h and H, to a pair of massive gauge bosons, $W_\mu^+ W^{-\mu}$ or $Z_\mu Z^\mu$.

Finally, the interactions between a Higgs boson pair and a gauge boson pair can be summarized as follows: a pair of massive gauge bosons, $W_\mu^+ W^{-\mu}$ or $Z_\mu Z^\mu$, can interact with each of the Higgs boson pairs hh, HH, AA and H^+H^-, whereas a photon pair, $A_\mu A^\mu$, only interacts with the H^+H^- pair. A Z boson field can be combined with the W boson field, $Z_\mu W^{\pm\mu}$, to couple to a pair with a neutral Higgs boson and the charged Higgs boson $H^\pm$. The photon can be combined with the Z boson, $A_\mu Z^\mu$, to interact with H^+H^-, or with the W boson, $A_\mu W^{\pm\mu}$, to interact with a pair of a neutral Higgs boson and the charged Higgs boson $H^\pm$.

The way how fermions are coupled to the Higgs fields H_1 and H_2 via Yukawa coupling terms is not given a priori by the THDM and has to be chosen. By convention, the field H_2 is coupled to right-handed up-type quarks, U_R, as defined in the notation used in equation 2.24. After this, four different types of THDM Yukawa couplings are usually considered. In the type-1 THDM, the field H_2 is additionally coupled to right-handed leptons E_R and right-handed down-type quarks D_R. The field H_1 remains then without any couplings to fermions. In the type-2 THDM, which can be related to the Higgs sector of the MSSM, the right-handed leptons and down-type quarks are coupled to the field H_1. In the lepton-specific THDM, right-handed down-type quarks are coupled to the field H_2 and right-handed leptons to the field H_1, whereas it is chosen in the opposite way for the flipped THDM.

In case of the type-2 THDM, the contribution to the Lagrangian density, $\mathcal{L}_{\text{Yukawa}}^{\text{THDM}}$, would have the following form, using the notation of equation 2.24:

$$\mathcal{L}_{\text{Yukawa}}^{\text{THDM}} = -\bar{L}_L Y_e E_R H_1 - \bar{Q}_L Y_d D_R H_1 - \bar{Q}_L Y_u U_R \begin{pmatrix} 0 & 1 \\ -1 & 0 \end{pmatrix} H_2^* + h.c. \qquad (2.27)$$

After electroweak symmetry breaking, the elimination of the Goldstone bosons, and the transformation of the remaining Higgs fields and the fermions into their mass eigenstates,

the Yukawa coupling Lagrangian density from equation 2.27 can be simplified to:

$$\mathcal{L}_{\text{Yukawa}}^{\text{THDM}}|_{v,h,H,A,H^\pm} = -\sum_f \frac{\mathrm{m}_f}{v}\left(\bar{f}_{\mathrm{L}}f_{\mathrm{R}}\cdot\left(\zeta_h^f h + \zeta_H^f H\right) - i\bar{f}_{\mathrm{L}}\gamma^5 f_{\mathrm{R}}\cdot\zeta_A^f A\right)$$

$$-\sum_{q^d}\sum_{q^u}\frac{\sqrt{2}\,(V_{\text{CKM}})_{q^u q^d}}{v}H^+\cdot\left(\mathrm{m}_{q^u}\zeta_A^{q^u}\bar{q}_{\mathrm{R}}^u q_{\mathrm{L}}^d + \mathrm{m}_{q^d}\zeta_A^{q^d}\bar{q}_{\mathrm{L}}^u q_{\mathrm{R}}^d\right)$$

$$-\sum_\ell \frac{\sqrt{2}\mathrm{m}_\ell}{v}H^+\cdot\zeta_A^\ell\bar{\nu}_{\ell,\mathrm{L}}\ell_{\mathrm{R}}$$

$$+ h.c.$$

$$f\in\{e,\mu,\tau,d,s,b,u,c,t\}\,,$$
$$q^u\in\{u,c,t\}\,,\quad q^d\in\{d,s,b\}\,,\quad \ell\in\{e,\mu,\tau\}$$

The coupling structure of the scalar Higgs bosons h and H is $\mathcal{CP}$-even and is similar to the SM Higgs boson h_{SM}. The $\mathcal{CP}$-odd coupling structure of the pseudoscalar Higgs boson can be inferred from the additional factor $-i\gamma^5$ in the spinor space. The charged Higgs boson H^+ relates up- and down-type fermions with opposite chirality with each other, such that the CKM mixing matrix V_{CKM} is needed to account for the quark mass eigenstates properly.

The coupling prefactors for fermions ζ_ϕ^f are summarized together with the coupling prefactors for the gauge bosons ζ_ϕ^V in table 2.5. These factors depend on two parameters of the THDM, $\tan\beta$ and α.

	Fermions f and gauge bosons V		
Higgs boson	$f\in\{u,c,t\}$	$f\in\{d,s,b,e,\mu,\tau\}$	$V\in\left\{W_\mu^\pm,Z_\mu\right\}$
h	$\zeta_h^f = \cos\alpha/\sin\beta$	$\zeta_h^f = -\sin\alpha/\cos\beta$	$\zeta_h^V = \sin(\beta-\alpha)$
H	$\zeta_H^f = \sin\alpha/\sin\beta$	$\zeta_H^f = \cos\alpha/\cos\beta$	$\zeta_H^V = \cos(\beta-\alpha)$
A	$\zeta_A^f = 1/\tan\beta$	$\zeta_A^f = \tan\beta$	$\zeta_A^V = 0$

Table 2.5.: Coupling prefactors with respect to the SM expectation between the Higgs boson fields h, H and A, and the fermion and gauge boson fields for type-2 THDM.

The MSSM Higgs potential $V_{\text{Higgs}}^{\text{MSSM}}$ can be obtained from the scalar potential of the model, defined in equations 2.15 and 2.18:

$$V_{\text{Higgs}}^{\text{MSSM}} = \left(|\mu|^2 + m_{H_u}^2\right)H_u^\dagger H_u + \left(|\mu|^2 + m_{H_d}^2\right)H_d^\dagger H_d$$

$$+ b_{\text{soft}}\left(H_u^T\begin{pmatrix}0 & 1\\-1 & 0\end{pmatrix}H_d + H_u^\dagger\begin{pmatrix}0 & 1\\-1 & 0\end{pmatrix}H_d^*\right)$$

$$+ \frac{g^2+g'^2}{8}\left(H_u^\dagger H_u - H_d^\dagger H_d\right)^2 + \frac{g^2}{2}\left(H_u^\dagger H_d\right)^*\left(H_u^\dagger H_d\right) \tag{2.28}$$

The THDM Higgs potential can be transformed into the Higgs potential of the MSSM by relating the Higgs doublets and the parameters of the two models with each other in the following way:

$$V_{\text{Higgs}}^{\text{THDM}} = V_{\text{Higgs}}^{\text{MSSM}} \text{ for}$$

$$m_{11}^2 = |\mu|^2 + m_{H_d}^2$$
$$m_{22}^2 = |\mu|^2 + m_{H_u}^2$$
$$m_{12}^2 = b_{\text{soft}}$$
$$\lambda_1 = \lambda_2 = \frac{g^2 + g'^2}{4}$$
$$\lambda_3 = \frac{g^2 - g'^2}{4}$$
$$\lambda_4 = -\frac{g^2}{2}$$
$$\lambda_5 = 0$$

$$H_2 = H_u, \qquad H_1 = \begin{pmatrix} 0 & -1 \\ 1 & 0 \end{pmatrix} H_d^* \qquad (2.29)$$

Furthermore, the MSSM Yukawa coupling terms obtained from $\mathcal{L}_{\mathcal{W}^{ij}}$ in equation 2.17 can be transformed into the form used in equation 2.27 by using relations of the Higgs doublets from equation 2.29. This is demonstrated for up- and down-type quarks in the following:

$$-\bar{U}_{\text{R}} Y_u^\dagger Q_{\text{L}}^T \begin{pmatrix} 0 & 1 \\ -1 & 0 \end{pmatrix} H_u = -\bar{U}_{\text{R}} Y_u^\dagger Q_{\text{L}}^T \begin{pmatrix} 0 & 1 \\ -1 & 0 \end{pmatrix} H_2$$

$$= -\bar{U}_{\text{R}} Y_u^\dagger H_2^T \begin{pmatrix} 0 & -1 \\ 1 & 0 \end{pmatrix} Q_{\text{L}} = -\left(\bar{Q}_{\text{L}} Y_u U_{\text{R}} \begin{pmatrix} 0 & 1 \\ -1 & 0 \end{pmatrix} H_2^* \right)^\dagger$$

$$\bar{D}_{\text{R}}^\dagger Y_d^\dagger Q_{\text{L}}^T \begin{pmatrix} 0 & 1 \\ -1 & 0 \end{pmatrix} H_d = \bar{D}_{\text{R}}^\dagger Y_d^\dagger Q_{\text{L}}^T \begin{pmatrix} 0 & 1 \\ -1 & 0 \end{pmatrix}^2 H_1^*$$

$$= -\hat{D}_{\text{R}}^\dagger Y_d^\dagger H_1^\dagger Q_{\text{L}} = -\left(\bar{Q}_{\text{L}} Y_d D_{\text{R}} H_1 \right)^\dagger$$

In consequence, the MSSM Higgs sector has the same structure as the type-2 THDM, but with a few important differences. First of all, the parameters λ_i in the MSSM Higgs potential are completely determined by the SM gauge couplings, leaving four parameters introduced through $V_{\text{Higgs}}^{\text{MSSM}}$ to the tree-level Lagrangian density: μ, $m_{H_d}^2$, $m_{H_u}^2$ and b_{soft}. After electroweak symmetry breaking, the Higgs sector can be described by the mass of the pseudoscalar Higgs boson, m_A, the ratio of the vacuum expectation values, $\tan\beta$, and the total vacuum expectation value v. The latter is related to SM parameters by the Higgs couplings to the gauge bosons introduced with the kinetic terms of the Higgs doublets:

$$v^2 = \frac{2m_Z}{g^2 + g'^2}$$

This means, that only two new parameters are introduced by the tree-level MSSM Lagrangian density additionally, m_A and $\tan \beta$.

However, the enriched particle spectrum of the MSSM can have an influence on corrections to the Lagrangian density at higher orders as will be described in section 2.4. Such corrections include loops with supersymmetric particles. After the electroweak symmetry breaking, the Higgs bosons of the MSSM additionally couple to mass eigenstates of sfermions, higgsinos and gauginos. Thereby, the neutral higgsinos and neutral gauginos mix to mass eigenstates referred to as neutralinos. Similarly, the charged higgsinos and charge gauginos mix to mass eigenstates called charginos.

Due to the soft supersymmetry breaking, which deteriorates the exact cancellation of quadratic divergences in the Higgs boson mass corrections, the mass of the lightest scalar Higgs boson, m_h, can obtain values, which exceed the Z boson mass m_Z, such that the observed scalar Higgs boson with a mass at about 125 GeV becomes accessible to an MSSM interpretation. On the other hand, the extended particle spectrum with soft supersymmetry breaking leads to a large number of parameters introduced to the MSSM Higgs sector due to such corrections.

To study the MSSM Higgs sector systematically, a number of assumptions have been made based on current constraints from experiments, and on simplifying measures, which are not expected to change the phenomenology of the MSSM Higgs sector. These assumptions lead to the introduction of MSSM benchmark scenarios [43, 44]. One of them, the M_h^{125} scenario [43], will be discussed in detail in the context of this thesis.

One of the general assumptions of the M_h^{125} scenario is, that new sources of flavour violation are not introduced with the soft supersymmetry breaking terms from equation 2.19. In consequence, the mixing between the different flavours of sfermions is neglected. The effects from mass terms, as well as from the interaction terms with the Higgs bosons, can be then considered as small for the first and second generation sfermions in their family space. The sfermion squared mass matrices from $\mathcal{L}_{\text{soft}}$ are chosen in the following way, compatible with the latest sfermion searches:

$$
\boldsymbol{M}_Q^2 = diag\left(M_{\tilde{f}}^2, M_{\tilde{f}}^2, M_{Q_3}^2\right), \quad \boldsymbol{M}_L^2 = diag\left(M_{\tilde{f}}^2, M_{\tilde{f}}^2, M_{L_3}^2\right)
$$

$$
\boldsymbol{M}_U^2 = diag\left(M_{\tilde{f}}^2, M_{\tilde{f}}^2, M_{U_3}^2\right), \quad \boldsymbol{M}_D^2 = diag\left(M_{\tilde{f}}^2, M_{\tilde{f}}^2, M_{D_3}^2\right)
$$

$$
\boldsymbol{M}_E^2 = diag\left(M_{\tilde{f}}^2, M_{\tilde{f}}^2, M_{E_3}^2\right)
$$

$$
M_{\tilde{f}} = 2 \text{ TeV}, \qquad M_{Q_3} = M_{D_3} = M_{U_3} = 1.5 \text{ TeV}, \qquad M_{L_3} = M_{E_3} = 2 \text{ TeV} \qquad (2.30)
$$

The soft supersymmetry breaking Yukawa matrices from $\mathcal{L}_{\text{soft}}$ are reduced to the values of the third generation sfermions for the same reason:

$$
\boldsymbol{A}_u = diag\left(0, 0, A_t\right), \quad \boldsymbol{A}_d = diag\left(0, 0, A_b\right), \quad \boldsymbol{A}_e = diag\left(0, 0, A_\tau\right)
$$

$$
A_t = A_b = A_\tau, \qquad X_t = A_t - \frac{\mu}{\tan \beta} = 2.8 \text{ TeV} \qquad (2.31)
$$

The dimensionful Yukawa coupling parameters A_t, A_b and A_τ are chosen to be real. Instead of fixing these parameters directly, the mixing parameter X_t between the left- and right-handed stops is introduced and fixed to a value. This mixing parameter depends on the higgsino mass parameter μ and the ratio of the vacuum expectation values $\tan \beta$. Finally,

the higgsino and gaugino mass parameters are fixed to:

$$\mu = 1 \text{ TeV}, \qquad M_1 = 1 \text{ TeV}, \qquad M_2 = 1 \text{ TeV}, \qquad M_3 = 2.5 \text{ TeV} \qquad (2.32)$$

The remaining two free parameters can be chosen as the mass of the pseudoscalar Higgs boson m_A, and the ratio of the vacuum expectation values $\tan\beta$. To match the higher order calculations of the model, the parameters need to be defined in a fixed renormalization scheme. For μ and $\tan\beta$, the $\overline{\text{DR}}$ renormalization scheme is chosen, evaluated at the scale of the pole mass of the top quark, $m_t^{\text{pole}} = 172.5$ GeV, for the remaining parameters the on-shell renormalization scheme. More details on the schemes can be found in section 2.4. The masses of supersymmetric particles, which can influence the predictions for the Higgs boson masses, cross-sections and decay widths, are chosen high enough for the M_h^{125} scenario to resemble the phenomenology of a THDM Higgs sector. Furthermore, the scenario is required to provide a Higgs boson compatible with the SM prediction for the observed Higgs boson with a mass of 125 GeV. The corresponding Higgs boson is the light scalar h. Its properties will be studied in more detail and compared to the SM prediction in the following. Expected deviations can be roughly estimated from this comparison, such that these deviations can be exploited in the statistical inference of the H $\to \tau\tau$ analysis presented in chapter 5, when the data description by the MSSM hypothesis is compared to the description of the SM hypothesis.

The coupling prefactors in table 2.5, which are also valid for MSSM, can be considered in the decoupling limit of the MSSM: $m_A \gg m_Z$. In this case, the heavy scalar Higgs boson H and the pseudoscalar Higgs boson A become degenerate in mass and the light scalar h approaches the observation at 125 GeV. Additionally, the scalar mixing angle takes a simple form in this limit: $\alpha \to \beta - \pi/2$. In consequence, the couplings of the light scalar approach the SM prediction with $\zeta_h^i \to 1$. On the other hand, the coupling factors of the heavy scalar Higgs boson converge to the values of the pseudoscalar Higgs boson. This means, that couplings to down-type quarks and leptons are enhanced by $\tan\beta$, making the H/A $\to \tau\tau$ decays even more interesting for Higgs boson searches, as well as the heavy Higgs boson production associated with bottom quarks.

The SM predictions for the gluon fusion production of the Higgs boson with a mass of 125 GeV, its width and the branching fraction to a pair of τ leptons are given in table 2.6.

Quantity	Value
$m_{h_{\text{SM}}}$	125 GeV
BR($h_{\text{SM}} \to \tau\tau$)	0.06272
$\Gamma_{\text{tot}}^{\text{SM}}$	4.088 MeV
$\sigma(gg \to h_{\text{SM}})$	48.58 pb

Table 2.6.: SM predictions for the Higgs boson with a mass of 125 GeV, produced at a centre of mass energy of $\sqrt{s} = 13$ TeV [46].

A relative comparison is performed between the M_h^{125} predictions and the SM predictions for these quantities in the $(m_A, \tan\beta)$ plane as illustrated in figure 2.2. For all considered quantities, the relevant parameter space is set by mass values of the light scalar Higgs boson, which are within the theoretical uncertainty, $m_h \in [122, 128]$ GeV [50, 51]. The area, where this condition is not satisfied, is shown as a red hashed contour, with a variation of

m_h from 122 GeV down to 110 GeV for most of the parameter points.

The deviation of the gluon fusion cross-section in the area with $m_h \in [122, 128]$ GeV is about 2% smaller than the SM expectation for parameter points with $m_A \gtrsim 200$ GeV. For points with m_A below 200 GeV, the values start to exceed the lower 5% threshold.
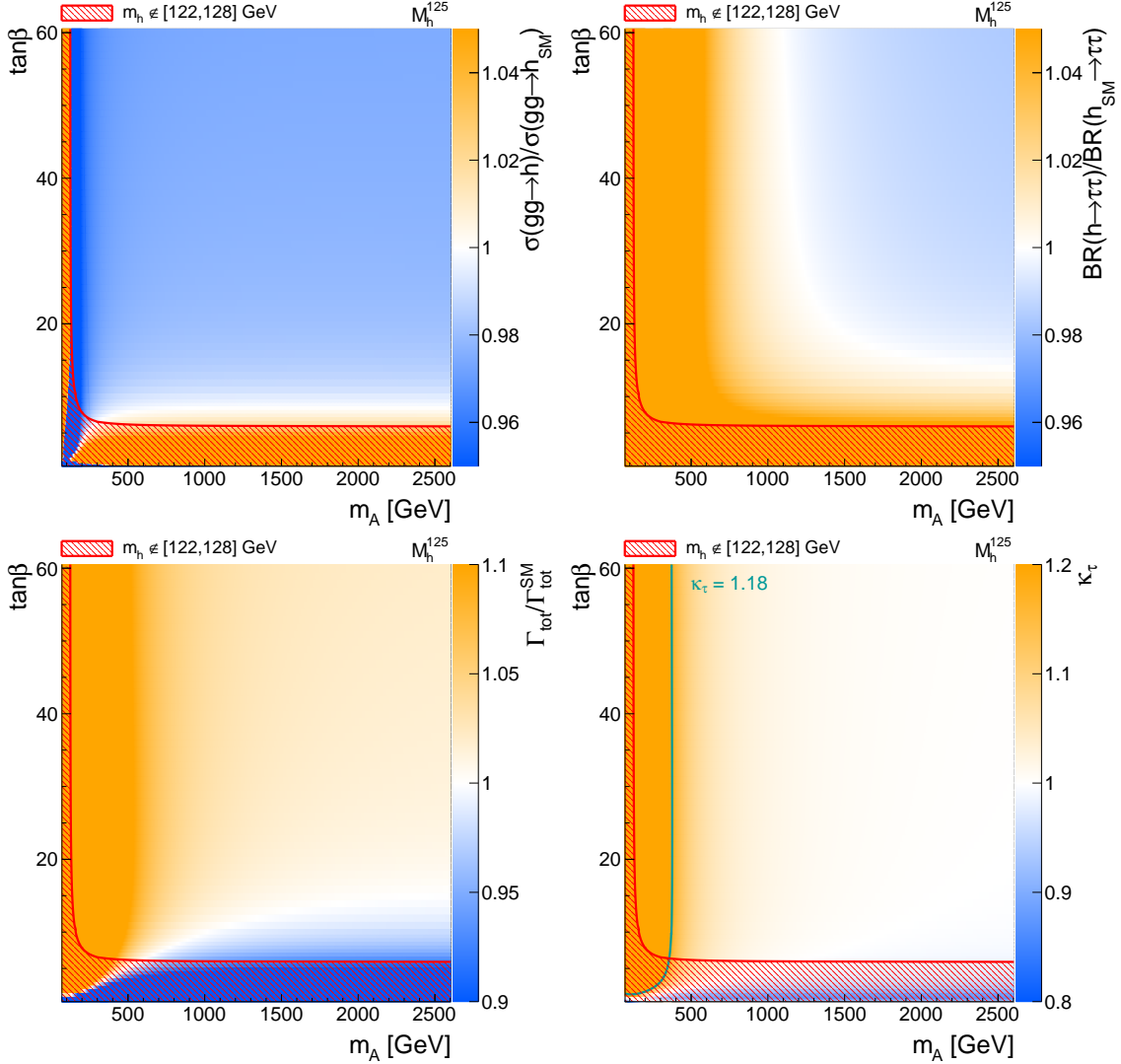

Figure 2.2.: MSSM predictions from M_h^{125} scenario [43] for $\sigma(gg \rightarrow h)$ (top left), BR $(h \rightarrow \tau\tau)$ (top right), Γ_{tot} (bottom left) and κ_τ (bottom right) are shown, relative to the SM expectation for a Higgs boson with a mass of 125 GeV. The parameter space area excluded by the theoretical uncertainty on m_h is marked with a red hashed contour. For κ_τ, an exclusion shown with a dark cyan line results from the 95% confidence interval on κ_τ from combined measurements of the properties of the observed Higgs boson [12].

For the branching fraction comparison, the MSSM prediction is within 2% around the SM prediction for points from the relevant $(m_A, \tan\beta)$ area, which have additionally $m_A \gtrsim 700$ GeV and $\tan\beta \gtrsim 10$. Beyond that region, the values for MSSM BR $(h \rightarrow \tau\tau)$ exceed the upper 5% threshold.

In summary, an overall deviation of up to 5% with respect to the SM is expected for the product $\sigma(gg \to h) \cdot BR(h \to \tau\tau)$ for large values of m_A. In the intermediate region with m_A between 200 and 700 GeV, the MSSM prediction for the light scalar Higgs boson can deviate stronger from the SM expectation.

The last quantity considered in the comparison is the total width of the light scalar Higgs boson, which is within 5% in the relevant parameter space and $m_A \gtrsim 600$ GeV. Below this threshold, the values for Γ_{tot} begin to rise and exceed the upper 10% threshold.

With the provided information on Γ_{tot} and $BR(h \to \tau\tau)$, the relative coupling κ_τ can be computed:

$$\kappa_\tau^2 = \frac{\Gamma_{tot} \cdot BR(h \to \tau\tau)}{\Gamma_{tot}^{SM} \cdot BR(h_{SM} \to \tau\tau)}$$

The resulting values for κ_τ shown at the bottom right of figure 2.2 can be compared with the corresponding constraints from a multi-parameter scan performed in the context of combined measurements of the properties of the observed Higgs boson [12]. The resulting confidence interval is $\kappa_\tau \in [0.65, 1.18]$ at 95% confidence level. It can be concluded, that based only on the published κ_τ constraints, most of the parameter space with $m_A \lesssim 350$ GeV can be excluded. This means, that provided a good sensitivity to the observed Higgs boson with a mass of 125 GeV, exclusions on benchmark scenarios in the $(m_A, \tan\beta)$ parameter space can be improved by taking the light scalar Higgs boson into account in the signal modelling.

In chapter 5, the sensitivity to the observed Higgs boson that can be obtained from full Run 2 data in the $H \to \tau\tau$ analysis, and the impact of deviations from the SM prediction on the exclusion limits of the M_h^{125} scenario will be discussed in more detail and quantified.

2.4. Higher Order Calculations in Perturbation Theory

After the Feynman rules were defined [1, 49], they can be used to compute the amplitudes of processes like the ones illustrated as Feynman diagrams in figure 2.3 for muon pair production through electron pair annihilation and Compton scattering. Each of the external lines, the vertices, and the internal lines corresponds to a mathematical expression of the corresponding Feynman rule. At each vertex, energy and momentum conservation is assumed, so that the 4-momenta transfers in the tree level Feynman diagrams in figure 2.3 are defined at each line by the incoming and outgoing particles.

The amplitude, also referred to as the matrix element $\mathcal{M}$, is the sum of all diagrams. The probability of a process is proportional to the squared matrix element, $|\mathcal{M}|^2$. The matrix element $\mathcal{M}$ is usually given for an explicit configuration of incoming and outgoing 4-momenta and of spin and polarization of the corresponding external states. In case these states are not prepared for a specific spin or polarization, $|\mathcal{M}|^2$ needs to be averaged over the spins and polarizations of the initial states, and summed over the spins and polarizations of the final states. This procedure is often denoted by $\overline{|\mathcal{M}|^2}$.

From $\overline{|\mathcal{M}|^2}$, the general form to compute a cross-section or decay rate of a process can be formulated in differential form as follows:

$$dw_{i \to f} = \frac{(2\pi)^4 \cdot \delta^4 \left(\sum_f q_f - \sum_i p_i\right) \cdot \overline{|\mathcal{M}|^2}(\{q_f, p_i\}) \cdot dLIPS(\{q_f\})}{F(\{p_i\})} \tag{2.33}$$
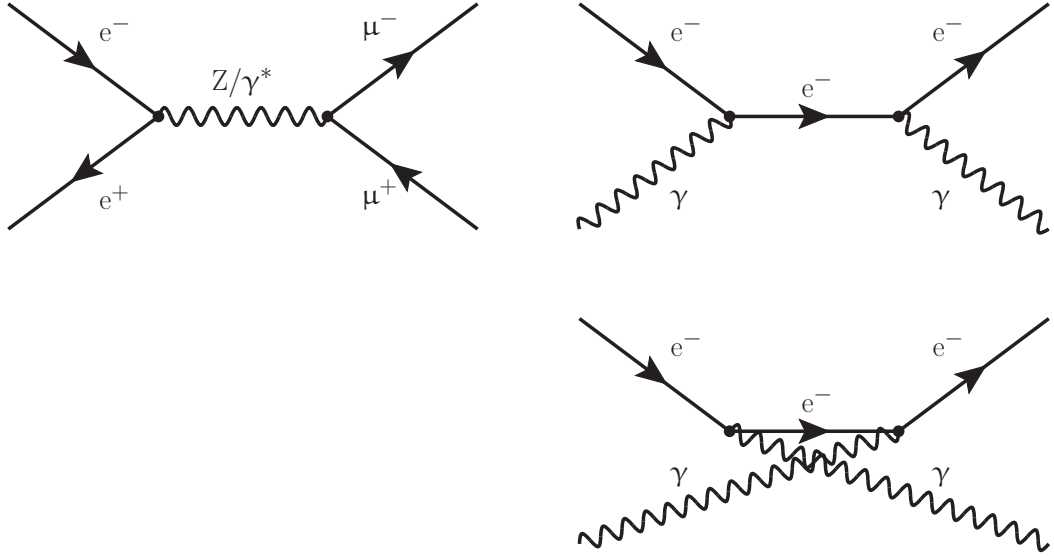
Figure 2.3.: Feynman diagrams for muon pair production through electron pair annihilation, $e^+e^- \rightarrow \mu^+\mu^-$ (left) and Compton scattering (right). Fermions are represented by straight lines with arrows, a Z boson, an excited photon γ^* or a real photon γ by wavy lines. Internal lines between two vertices shown as black dots correspond to propagators, external lines to initial states on the left or to final states on the right of a diagram. In case of Compton scattering, two different transitions are possible between the initial and final states, such that these have to be added to obtain the corresponding matrix element.

The transition rate $\mathrm{dw}_{i \rightarrow f}$ from an initial to a final state is composed of several building blocks: the squared matrix element $\overline{|\mathcal{M}|^2}$, which depends on the 4-momenta of the initial states p_i and the final states q_f, the Møller flux factor F [52] computed from 4-momenta p_i of the prepared initial states, and the Lorentz-invariant phase space dLIPS [53] defined for the final states. Dirac's Delta function $(2\pi)^4 \cdot \delta^4 \left(\sum_f q_f - \sum_i p_i \right)$ ensures the conservation of the total 4-momentum of the system during the integration over dLIPS. This integration can be performed over the entire phase space to obtain inclusive transition rates, or over its slices in an observable of interest, to determine the dependence of the transition rate on this observable.

Tree level Feynman diagrams contribute to their processes at leading order (LO) in the couplings involved in the vertices. Each vertex term is proportional to the square root of the coupling constants, $\sqrt{\alpha_{em}}$ for the electromagnetic interactions, $\sqrt{\alpha_w}$ for the weak interactions, and $\sqrt{\alpha_s}$ for the strong interactions. The coupling constants are defined as functions of the gauge coupling constants e, g and g_s. In natural units, they read:

$$\alpha_{em} = \frac{e^2}{4\pi}, \qquad \alpha_w = \frac{g^2}{4\pi}, \qquad \alpha_s = \frac{g_s^2}{4\pi} \tag{2.34}$$

Additional corrections to the leading order contribution, which are at the next order in one of the coupling constants α_i, correspond to diagrams with the same initial and final states, but extended with one vertex of the interaction proportional to $\sqrt{\alpha_i}$. Such corrections

comprise virtual contributions, which do not have an influence on the initial and final states of the process, and emissions of particles from the initial or the final states, which can alter their kinematic properties.
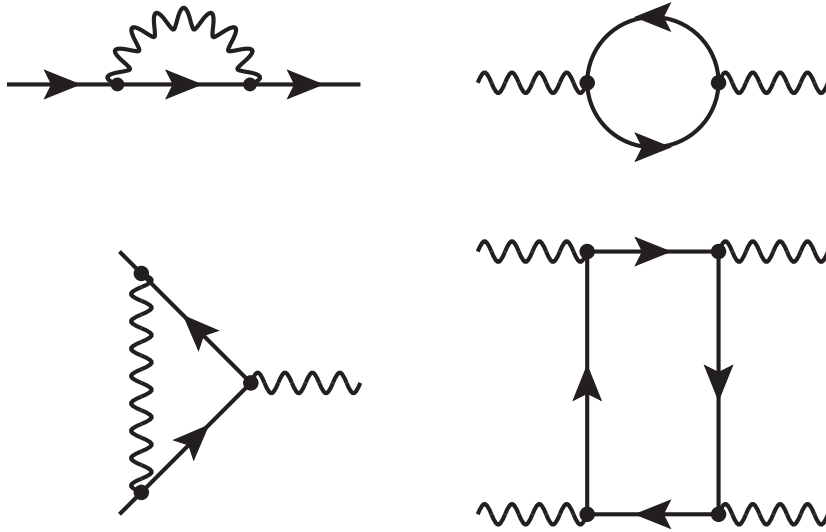
Figure 2.4.: Examples of virtual contributions to tree level diagrams at higher orders of perturbation: fermion self energy (top left), vacuum polarization of the photon (top right), vertex correction (bottom left), and a generic box diagram with a fermion loop (bottom right). The momentum transfer within the loops needs to be integrated over its entire phase space, leading to divergent terms.

The virtual contributions shown in figure 2.4, consist of modifications of internal lines, referred to as self energy of a particle and in case of the gauge bosons also as vacuum polarization, of modifications of vertices, and generic loop diagrams. These contributions involve closed loops, such that the 4-momentum transfer within each loop needs to be integrated out over the entire 4-momentum phase-space. In consequence, divergences are introduced to the calculation of higher order (HO) Feynman diagrams containing loops, called infrared for the vanishing momentum transfers within the loop, $q^2 \rightarrow 0$, and ultraviolet for $q^2 \rightarrow \infty$.

Ultraviolet divergences can be mitigated with the technique of dimensional regularization [54], changing from the four space-time dimensions to a slightly smaller value, $d = 4 \rightarrow d = 4 - 2\epsilon$. To preserve the dimension of the matrix element, a renormalization scale μ_R is introduced, which corrects the integral dimension via a multiplicative factor of $\mu_R^{2\epsilon}$. After evaluating the integral for $d = 4 - 2\epsilon$ and expanding the resulting terms at $\epsilon \rightarrow 0$, divergent terms can be isolated and summarized in counter-terms, which are used to renormalize the coupling constants, the masses and the fields of the Lagrangian density, such that the renormalized quantities are finite. The renormalized Lagrangian density $\mathcal{L}_{HO}$ is then the difference between the tree level Lagrangian density $\mathcal{L}$ and the counter-terms $\mathcal{L}_{ct}$:

$$\mathcal{L}_{HO} = \mathcal{L} - \mathcal{L}_{ct}$$

If the renormalization is possible by a finite amount of renormalized parameters for all orders of perturbation in $\sqrt{\alpha_i}$, the theory is called renormalizable, as it is the case for

the SM and the MSSM. The definition of the counter-terms depends on the particular renormalization scheme used. Common schemes comprise the on-shell scheme (OS), in which the counter-terms are defined such that the renormalized mass corresponds to the mass pole in the propagator of the considered field, the modified version of the minimal subtraction scheme ($\overline{\text{MS}}$) [55–57], and the dimensional reduction scheme ($\overline{\text{DR}}$) [58], which is similar to ($\overline{\text{MS}}$), but with a modified dimensional regularization procedure, which preserves the invariance of supersymmetric Lagrangian densities.

After fixing the renormalization scheme, the values for the renormalized quantities, which correspond to physical observables, can be set to finite, experimentally measured values. The measurements are required to be performed at a fixed scale $\mu_{R,i}^0$, which is typical for the momentum transfers involved in the measured process. Since the renormalized quantities depend on the scales $\mu_{R,i}$, the measured reference value for the renormalized quantity at $\mu_{R,i}^0$ can be connected to its value at any scale $\mu_{R,i}$ using renormalization group equations [59, 60]. This leads to the effect of running coupling constants [61, 62] and running masses [63], reflecting the changing behaviour of the interactions of the theory at different energy transfers.

For the electromagnetic coupling α_{em} in quantum electrodynamics (QED), the reference measurement corresponds to the limit of vanishing momentum transfer $q^2 \to 0$ and is measured to be the fine-structure constant $\alpha_{em}(q^2 \to 0) \approx 1/137$ from non-relativistic quantum mechanics. At higher momentum transfers, α_{em} increases.

In case of the couplings from non-Abelian interactions, like α_w for the weak interactions and α_s for the strong interactions of quantum chromodynamics (QCD), the couplings decrease with increasing momentum transfer, leading to the effect called asymptotic freedom. For small momentum transfers $q^2 \to 0$, the weak coupling is suppressed by the mass of the W boson, so that in this limit, the Fermi's theory of weak interactions between fermions can be established as an effective theory, which describes for example the β decay of nucleons [64]. The reference measurement of α_w is usually performed at momentum transfers around the Z boson mass, $q^2 = m_Z^2$.

In case of QCD interactions with massless gluons as gauge bosons, the running of α_s obtained from perturbative calculations breaks down at the scale $\Lambda_{QCD} \approx 0.3$ GeV, where the strong coupling α_s reaches unity, so that the perturbation series connected to it becomes divergent. This is an indication, that quantum chromodynamics is non-perturbative in this regime and quarks can not be considered as free particles any more, leading to their confinement to composed hadron states. Also in case of α_s, its reference value is usually determined at $q^2 = m_Z^2$ from experimental measurements.

For leptons, which do not interact strongly, the pole mass can be measured unambiguously and used as the reference point for the running mass. On the other hand, pole masses of the quarks can not be measured precisely due to their confinement and non-perturbative contributions, such that the pole mass is not well-defined. Photons and gluons, which are massless and obey the Ward-Takahashi identity [65–67], do not acquire mass corrections through renormalization, whereas this is the case for the massive W, Z and Higgs bosons.

In figure 2.5 it is shown, how the running of MSSM parameters can be used to study the resulting effects at different energy scales. On the left, the running of the coupling constants of the $SU(3)_C \times SU(2)_L \times U(1)_Y$ interactions is shown, parameterized as $\alpha_1 = \frac{5}{3} \frac{1}{\cos \theta_W} \alpha_{em}$, $\alpha_2 = \alpha_W$, and $\alpha_3 = \alpha_s$ to match the required definitions in the context of grand unification [36]. For the SM case, the couplings do not unify at high energy scales. However, the MSSM has an appropriate particle spectrum to introduce a kink into the evolution of the

coupling constants, such that they can be unified at a scale $Q \approx 10^{16}$ GeV in the shown example. This result is considered to be a favourable feature of supersymmetric models. On the right of figure 2.5, the running of the reduced set of MSSM mass parameters is shown as it would be the case in the framework of supergravity with gravity-mediated supersymmetry breaking. At the scale $Q = 1.5 \cdot 10^{16}$ GeV, common mass parameters m_0, μ and $m_{1/2}$ are chosen to control the evolution of sfermion masses, the mass parameters of the Higgs potential, and the gaugino masses. The mass parameter of the field H_u becomes negative at the electroweak scale $Q \approx 100$ GeV, indicating the electroweak symmetry breaking.
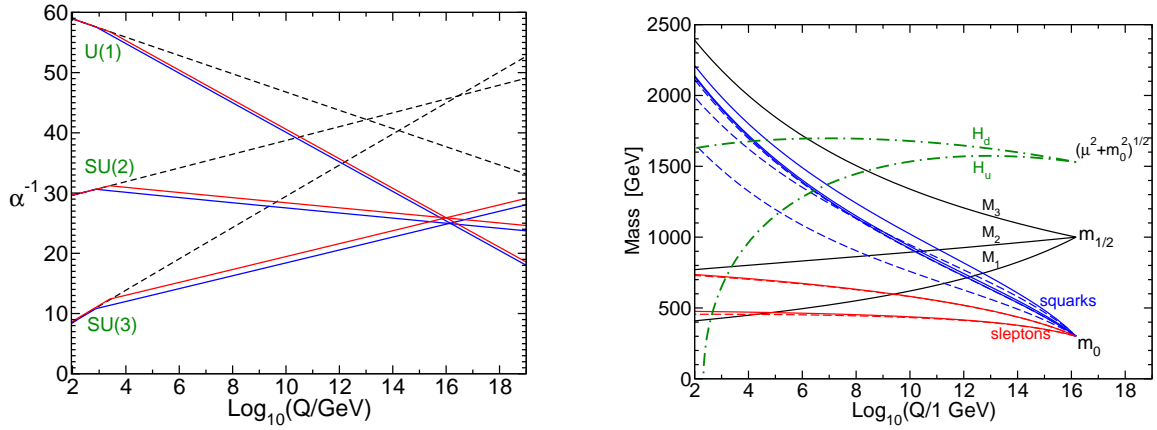
Figure 2.5.: Illustrative examples of running couplings (left) and running mass parameters (right) in the MSSM [36]. On the left, the running of the couplings α_1 for $U(1)_Y$, α_2 for $SU(2)_L$, and α_3 for $SU(3)_C$ is shown. The dashed black lines representing the SM evolution do not unify at high energy scales Q. In contrast to that, the solid lines representing MSSM have a kink, which leads to a unification at $Q \approx 10^{16}$ GeV. For the MSSM examples, the sparticle masses are chosen to be equal to introduce a single distinct kink into the coupling constant evolution, at about 750 GeV (blue) or at about 2.5 GeV (red). On the right, the evolution of mass parameters of MSSM in the supergravity framework is shown. At a scale $Q = 1.5 \cdot 10^{16}$ GeV, the common MSSM parameters m_0, μ and $m_{1/2}$ are fixed. Green dashed-dotted lines represent the resulting evolution of the mass parameters of the Higgs potential of the fields H_u and H_d. Black solid lines represent the evolution of the gaugino masses, blue lines the evolution of squark masses, and red lines the evolution of slepton and sneutrino masses. Dashed sfermion lines correspond to the third generation in the fermion family space, solid lines to the remaining first two generations.

Additionally to the infrared divergences from virtual contributions, emissions of soft or collinear photons or gluons lead to divergent terms in the calculations of matrix elements. The divergences can be identified again with dimensional regularization in case of infrared and collinear divergences, in a dimension of the space-time slightly higher than four, $d = 4 \rightarrow d = 4 + 2\epsilon$. If these divergences do not cancel each other by resummation at all orders [68, 69], for instance in calculations of QCD processes without a sum over all possible initial states, they are controlled by the factorization scale μ_F introduced through dimensional regularization. The evolution from one scale to another is defined by the

Dokshitzer-Gribov-Lipatov-Altarelli-Parisi (DGLAP) equations [70–74] describing the splitting of a parton (gluon or quark) into a pair of partons and is connected to the parton distribution functions (p.d.f.'s) of composite hadron states. The scale μ_F can be understood as the energy threshold, below which the energy of gluons is considered as soft or collinear. In that way, a factorization of physics at low energies described by DGLAP equations and p.d.f.'s from physics at high energies calculated in perturbative QCD is achieved.

In consequence, for each process to be calculated, a renormalization scale μ_R and a factorization scale μ_F needs to be chosen, which describe the typical energy transfer of the process and its separation from physics at low energies, respectively. This choice is a priori arbitrary and is assigned with uncertainties obtained from variations of these scales by factors 0.5 and 2 with respect to the nominal choice. Such variations are mostly relevant for QCD calculations and are usually referred to as QCD scale uncertainties. Furthermore, if finite quark mass values m_q are required, they are varied within their uncertainties on non-perturbative effects.

To provide predictions for processes in proton-proton collisions, several calculations need to be done additionally to the computation of the matrix element described so far covering production cross-sections and decay widths with equation 2.33. Starting from the protons, the momentum fraction x needs to be determined, which is carried by the partons of the proton entering the interaction of the hard process at a certain squared momentum transfer scale q^2. This is accomplished by the p.d.f.'s, which are obtained from fits to data at fixed scales q_0^2 [75]. The evolution to the scale of the considered hard process, q^2 is made possible with DGLAP equations. The models used for p.d.f.'s are phenomenological, and are accounted for by corresponding uncertainties, including a variation of the chosen reference value for the strong coupling, $\alpha_s(m_Z^2)$.

The parton splitting functions in the DGLAP equations can be used to simulate the emission of multiple partons, referred to as parton showering, for the incoming and outgoing partons of the hard process. Parton showers are often simulated separately from the simulation of the hard process from the matrix element. In case of NLO simulation of the hard process, emissions can also be simulated at the level of the matrix element, such that a proper matching between the parton shower simulation and the matrix element calculation is needed to avoid possible double-counting [76]. Parton showering is performed, until a scale is reached, at which non-perturbative QCD effects are not negligible anymore. From this point on, hadronization of the partons is performed, with subsequent decays of the final state hadrons. Finally, soft interactions of the proton remnants with each other and with the partons participating in the hard process, referred to as the underlying event, has to be taken into account. The parameters of the models used for the description of the underlying event are adapted to measurements of data collected from collisions with soft interactions and summarized in parameter tunes [77]. The steps of parton showering, hadronization, simulation of hadron decays, and the description of the underlying event are often covered by the same software [78–80].

3. CMS Experiment at LHC

The Compact Muon Solenoid (CMS) experiment is one of the four major experiments of the Large Hadron Collider (LHC) at the Conseil Européen pour la Recherche Nucléaire (CERN) near Geneva, Switzerland. To perform collisions of proton pairs at the collision point of the CMS detector, bunches of about 10^{11} protons are accelerated by various pre-accelerators to intermediate energies, before they are accelerated in the LHC ring. There, each of them reaches an energy of 6.5 TeV. The two beams of proton bunches accelerated in opposite directions are crossed every 25 ns, leading to multiple proton-proton collisions per bunch crossing at a centre of mass energy $\sqrt{s} = 13$ TeV. As shown in figure 3.1, the protons are first accelerated by the linear accelerator LINAC 2, then they enter three ring pre-accelerators, the BOOSTER accelerator at first, followed by the Proton Synchrotron (PS), and the Super Proton Synchrotron (SPS).
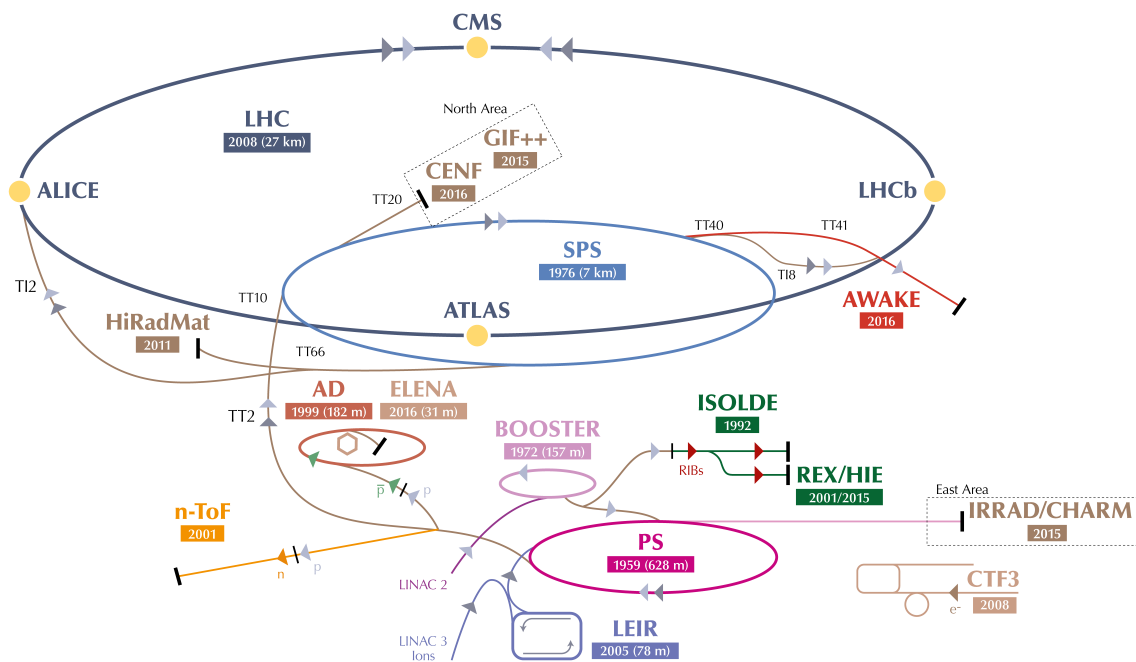
Figure 3.1.: A schematic view of the accelerator complex [81] at CERN.

The orientation of the coordinate system used at the CMS experiment is defined as follows: The x-axis is oriented towards the ring center, the y-axis is chosen to show upwards, and the z-axis points into the direction of the beam that is accelerated anti-clockwise in the LHC ring. Additionally, the azimuth angle $\phi \in [-\pi, \pi]$ and the polar angle $\theta \in [0, \pi]$ are introduced, with $\phi = 0$ in the direction of the x-axis, and $\theta = 0$ in direction of the z-axis. The pseudorapidity $\eta = -\ln \tan(\theta/2)$ is used in particle physics to have an approximation for the rapidity y of the flight direction of a particle in case its mass is negligible.

3.1. Detector Subsystems

The CMS [82] detector is built to cover as much of the solid angle around the interaction point as possible for a collision of two proton beams with equal energy. The detector has a cylindrically symmetrical design consisting of a barrel around the beam pipe and endcaps closing the forward regions of the detector. Because of this symmetry, particle momenta $\vec{p}$ are provided in terms of their transverse part $\vec{p}_T$, and the component along the beam axis p_z. The transverse momentum $\vec{p}_T$ is usually given by its magnitude p_T and angle ϕ. The detector subsystems used in the barrel and endcap of CMS are shown in its schematic view in figure 3.2.
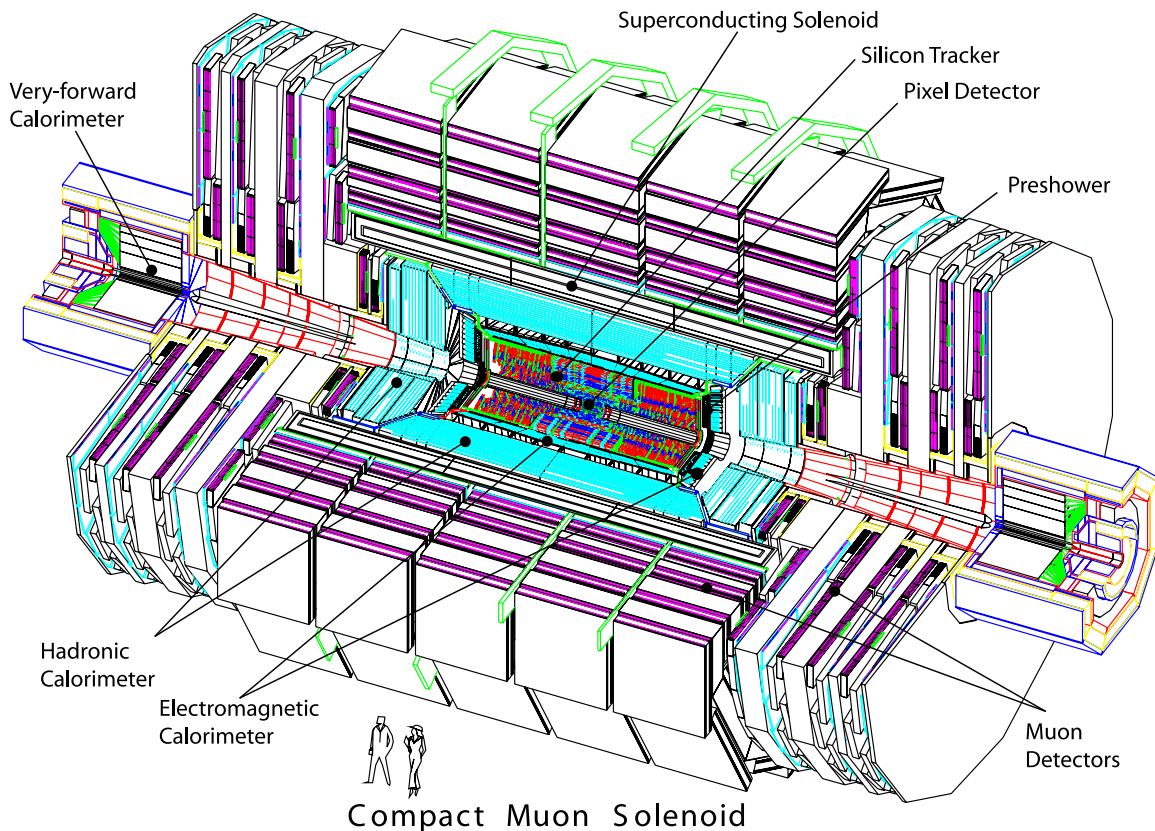
Figure 3.2.: A schematic view of the CMS detector [82] showing the positions of its sub-systems.

The subsystem closest to the beam pipe is the inner tracking system consisting of the pixel tracker and the strip tracker to measure trajectories of charged particles, followed by the electromagnetic calorimeters (ECAL) to stop particles interacting electromagnetically, electrons and photons. In case of the endcap region, an electromagnetic preshower calorimeter is placed between the inner tracking system and the endcap ECAL. The electromagnetic calorimeters are enclosed by the hadronic calorimeters (HCAL) to stop predominantly strongly interacting particles. The HCAL in the endcap is extended with a forward calorimeter to increase the coverage of the CMS detector. The HCAL in the barrel is surrounded by a superconducting solenoid magnet, providing a homogeneous magnetic field of 3.8 T in direction of the z-axis within the solenoid. The magnetic flux outside the solenoid is captured by an iron yoke in the opposite direction with 2 T. Muon chambers

are placed into the gaps in the iron yoke to allow the detection of muons that traversed all previous detectors as minimum ionizing particles (MIPs).

Several upgrades of the CMS detector were planned and performed before and during the Run 2 data-taking period. The update of the Level 1 trigger system [83] was ready before the start of the Run 2 data-taking. The upgraded pixel detector in the inner tracking system [84] was ready at the beginning of 2017. The upgrades of the hadronic calorimeters [85] and the extension of the muon detection system by gas electron multipliers (GEMs) [86] were performed step by step during Run 2 and are continued after the data-taking.

3.1.1. Inner Tracking System
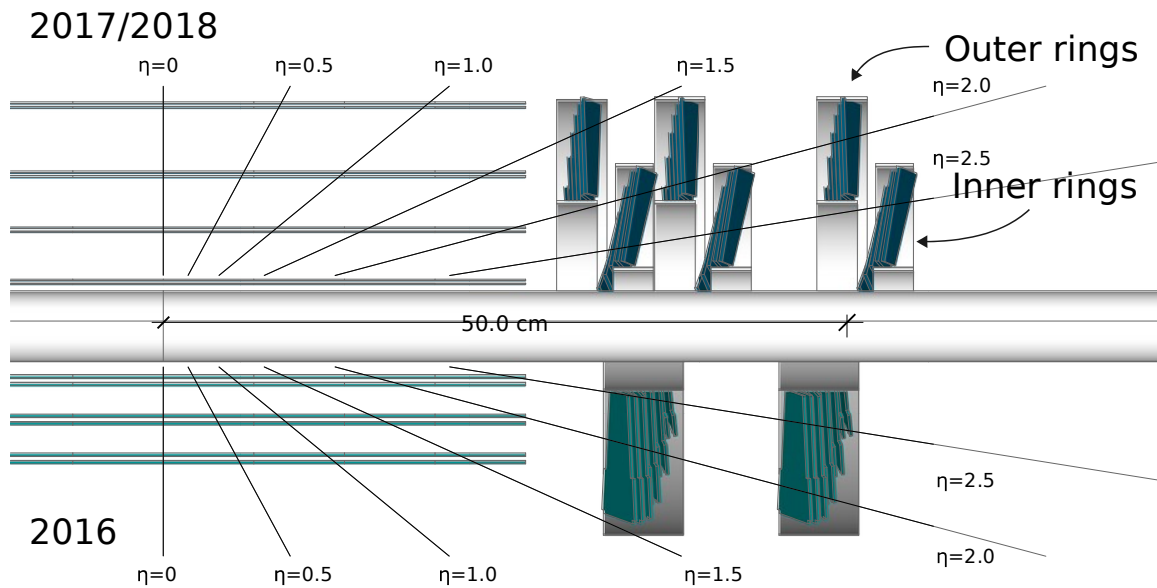
Figure 3.3.: A schematic view of the pixel tracker [84] shown along the beam axis. The layout used during the data-taking in 2016 is shown below the beam pipe, consisting of three barrel layers and two endcap disks. The layout of the upgraded pixel tracker used from 2017 on consisting of four barrel layers and three endcap disks is shown above the beam pipe. Each of the upgraded endcap disks has an inner and an outer ring.

The innermost part of the inner tracking system is the pixel detector consisting of silicon modules, which allow a three-dimensional reconstruction of the point, where a charged particle traverses the module, referred to as a reconstructed hit. The layout of the pixel tracker is shown in figure 3.3 for both of its versions used during the Run 2 data-taking, the version used during 2016 and the upgraded version used in 2017 and 2018. During the 2016 data-taking period, the pixel tracker consisted of three barrel layers and two endcap disks. During the upgrade between the 2016 and the 2017 data-taking periods, the barrel layers of the pixel tracker were replaced by four new layers and the endcap disks by three new disks with a different structure consisting of an inner and an outer ring for each of the disks. The upgrade allows to reconstruct tracks with up to four hits within the pixel detector in the tracker sensitive region of $|\eta| < 2.5$. One of the main goals of the pixel tracker upgrade is to reduce the misreconstruction rate in an environment with about 50

interactions happening at the same time while retaining or even improving the efficiency of real tracks. As shown later for the entire tracking system in figure 3.5, this goal was accomplished.

The barrel layers are organized in arrays of modules with rectangular silicon chips of about 0.01 mm^2, referred to as pixels, whereas the modules of the endcap disks are arranged in blades in a turbine-like geometry. This concept allows a resolution of about 10 μm in the transverse direction with respect to the beam pipe for the reconstruction of hits, and a resolution of about 20 μm in the direction along the beam pipe. A three-dimensional hit is reconstructed from the charge distribution of neighbouring pixels, with an average efficiency greater than 99% [87].
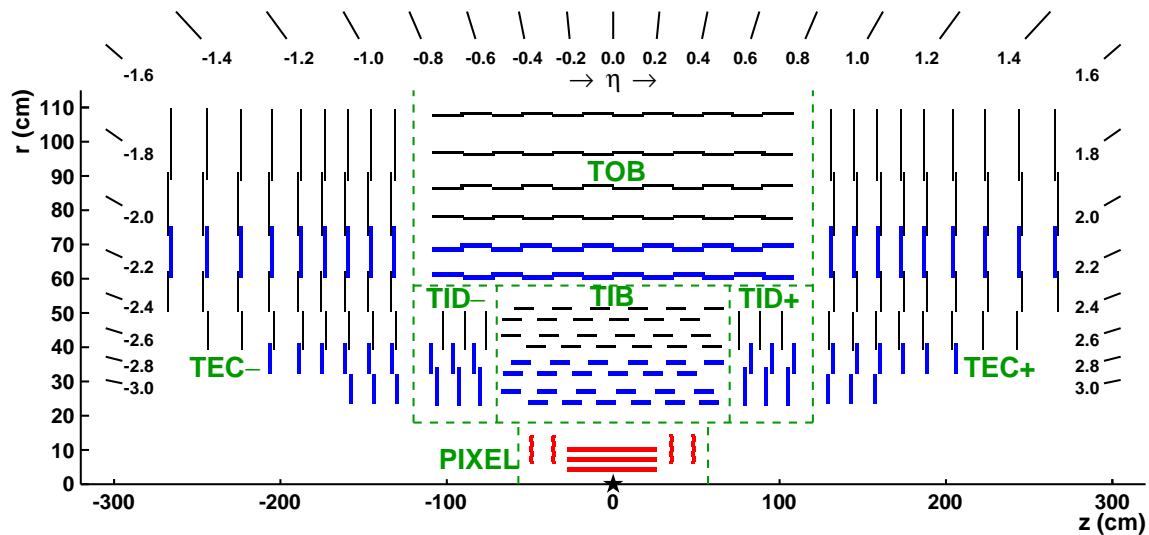
Figure 3.4.: A schematic view of the inner tracking system [87]. The pixel tracker (the version used during data-taking in 2016) is marked in red. The different regions of the strip tracker are separated from each other by green dashed lines and marked with green abbreviations. Thin black lines correspond to strip modules, which are only able to reconstruct two-dimensional hits, whereas the thick blue lines represent strip modules capable of three-dimensional hit reconstruction. This is achieved by combining two strip modules into one and rotating them against each other by 100 mrad.

The pixel tracker is enclosed by the strip tracker with a layout as shown in figure 3.4. The inner and outer regions of the strip tracker consist of strip module layers in the barrel regions and strip module disks in the endcap parts of the detector. Two types of strip modules are used in all strip tracker regions: To allow the reconstruction of a three-dimensional hit in the strip tracker, two strip modules are combined to a stereo strip module, with the single modules rotated by 100 mrad against each other. Such strip modules are marked with thick blue lines in figure 3.4. The remaining strip modules, marked by thin black lines, provide only a two-dimensional hit reconstruction in the (r, φ) plane for the strip modules of the barrel layers and in the (φ, z) plane for the strip modules of the disks in the barrel and endcap. The achieved resolution of the strip tracker spans from 20 μm to 50 μm depending on the considered region and direction. A particle traversing the strip tracker is able to pass about 10 of its modules, which have a hit

reconstruction efficiency of 99%, if they are active for readout during a proton-proton collision [87].
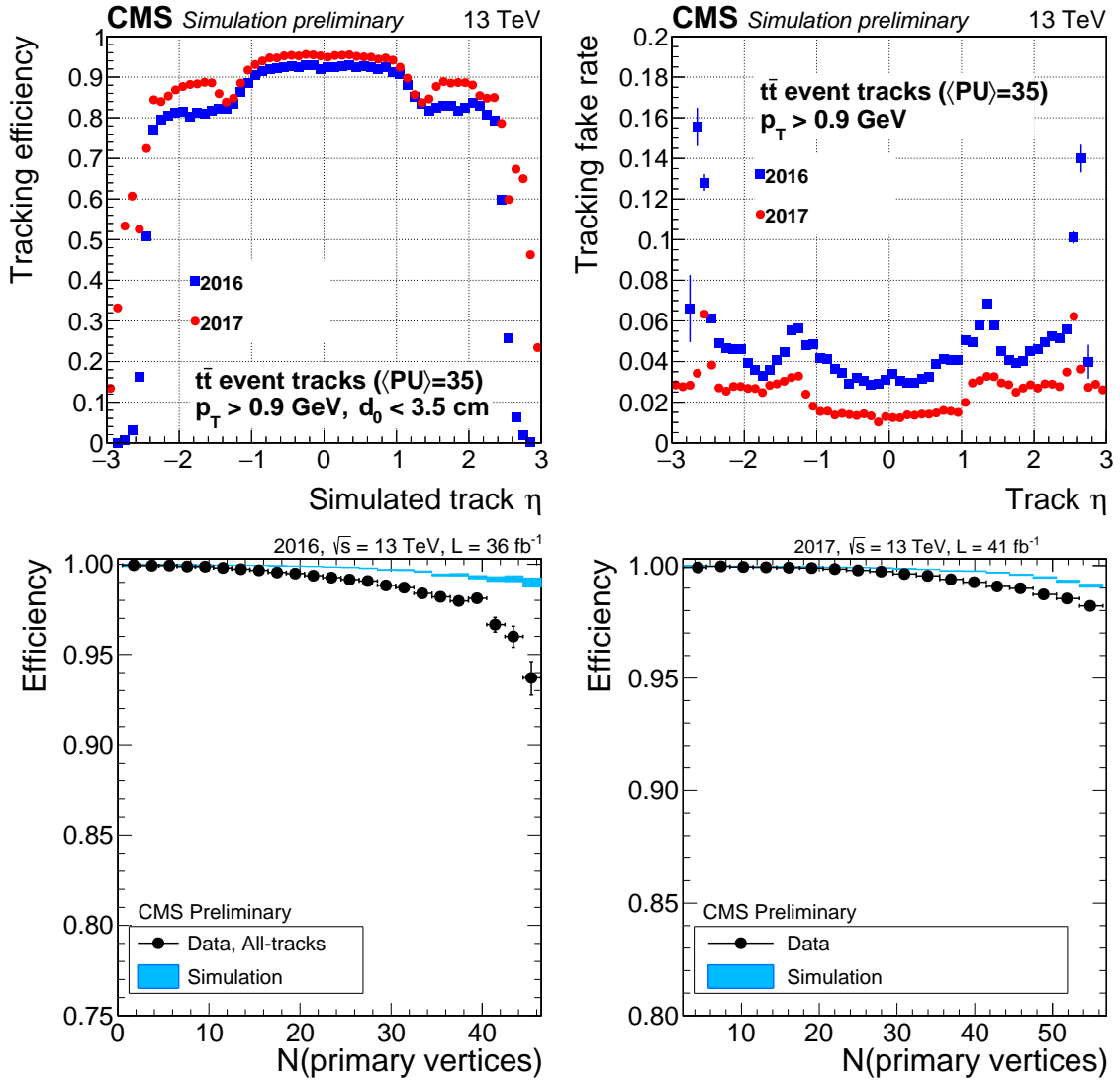
Figure 3.5.: Tracking efficiency measurements based on simulation (top) [88] and on measurements with Z → μμ events using the tag and probe method (bottom) [89, 90] for the 2016 and 2017 data-taking periods.

Comparisons of tracking efficiencies between the 2016 and 2017 data-taking periods are presented in figure 3.5. The tracking efficiency at the top left and the misreconstruction rate at the top right are based on tracks from simulated events of top quark pair production [88]. These efficiencies are computed for events with an average number of additional interactions of ⟨PU⟩ = 35. Comparing the 2017 with respect to the 2016 data-taking period, the tracking efficiency is improved and extended to higher pseudorapidity while the misreconstruction rate is reduced significantly. Comparing the tracking efficiency measured with the tag and probe method on Z → μμ events in 2016 [89] at the bottom left with the same measurement for 2017 [90] at the bottom right as a function of the number of reconstructed interaction points, N(primary vertices), an improvement from 2016 to

2017 can be seen for N(primary vertices) > 40. These measurements indicate the positive influence of the upgrade performed for the pixel detector on the reconstruction efficiency of all physics objects related to tracks, like electrons, muons, and charged hadrons, and on the b-tagging efficiency of jets [91].

3.1.2. Electromagnetic Calorimeters

The ECAL enclosing the tracker consists of a barrel (EB) and an endcap region (EE), as well as the preshower calorimeter placed prior to the EE as shown in figure 3.6. For the preshower calorimeter, two planes of silicon strip detectors are used with a lead absorber disk in between. For EE and EB, homogeneous lead tungstate ($PbWO_4$) crystals were chosen to provide a radiation hard detector material both with showering and scintillating properties. Electromagnetic showers within $PbWO_4$ crystals are characterized by a short radiation length of 0.89 cm, and a short Molière radius of 2.2 cm. To measure the light from the crystals, which is emitted to 80% within 25 ns, silicon avalanche photodiodes are used in the EB and vacuum phototriodes in the EE. Because of its properties, the use of $PbWO_4$ allowed to place the ECAL inside the solenoid, contributing in that way to the compact design of the CMS detector.
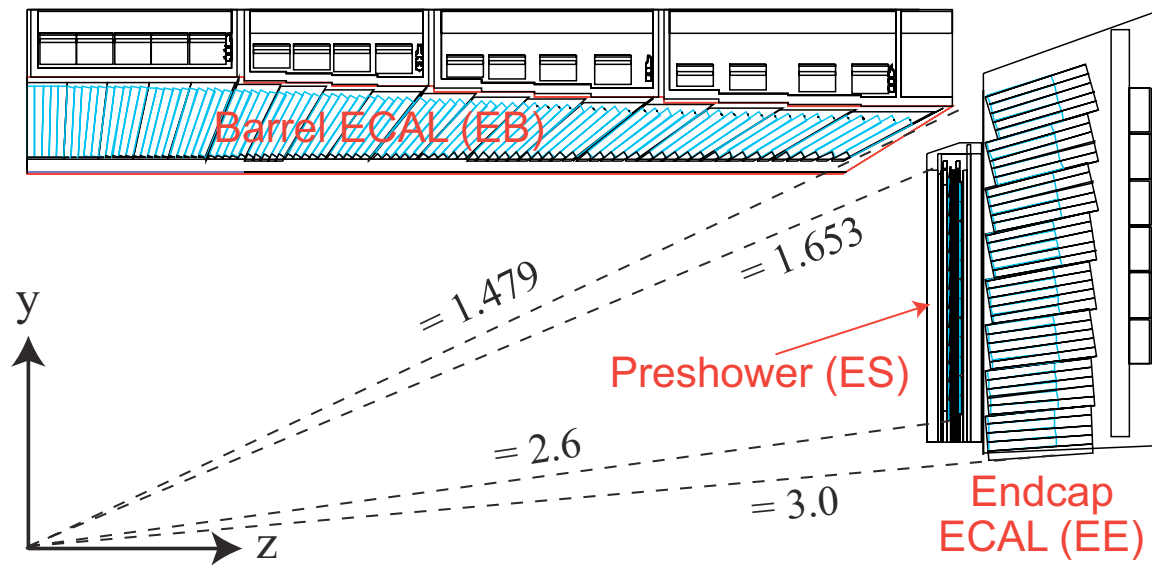
Figure 3.6.: Schematic view of the electromagnetic calorimeters used at CMS [82].

The radiation resistant electromagnetic calorimeters of CMS provide a fast measurement of deposited energy with a fine granularity of the electromagnetic showers caused by interacting particles entering the detector. A relative energy resolution of about 1.5% is expected for energies between 10 and 50 GeV of the traversing electron or photon, whereas at higher energies, a resolution of 0.4% can be achieved. Although a full coverage of the pseudorapidity region $|\eta| < 3$ is provided, gaps between the barrel and the endcap calorimeters left for the readout electronics lead to a decrease in efficiency for particles traversing the region $|\eta| \in [1.44, 1.56]$.

3.1.3. Hadronic Calorimeters

The HCAL is arranged into four components shown in figure 3.7. The barrel (HB) and the endcap (HE) calorimeters enclose the ECAL and fill the remaining space left inside the magnetic coil. A hadronic calorimeter placed outside the magnetic coil (HO) is constructed to collect and stop particles punching through the system of calorimeters and the magnetic coil. The HO is used for hadron rejection within the muon reconstruction. The last component is placed into the forward region of the detector (HF) to extend the pseudorapidity coverage to $|\eta| < 5$, allowing the reconstruction of forward jets and an improved reconstruction of the missing transverse energy.
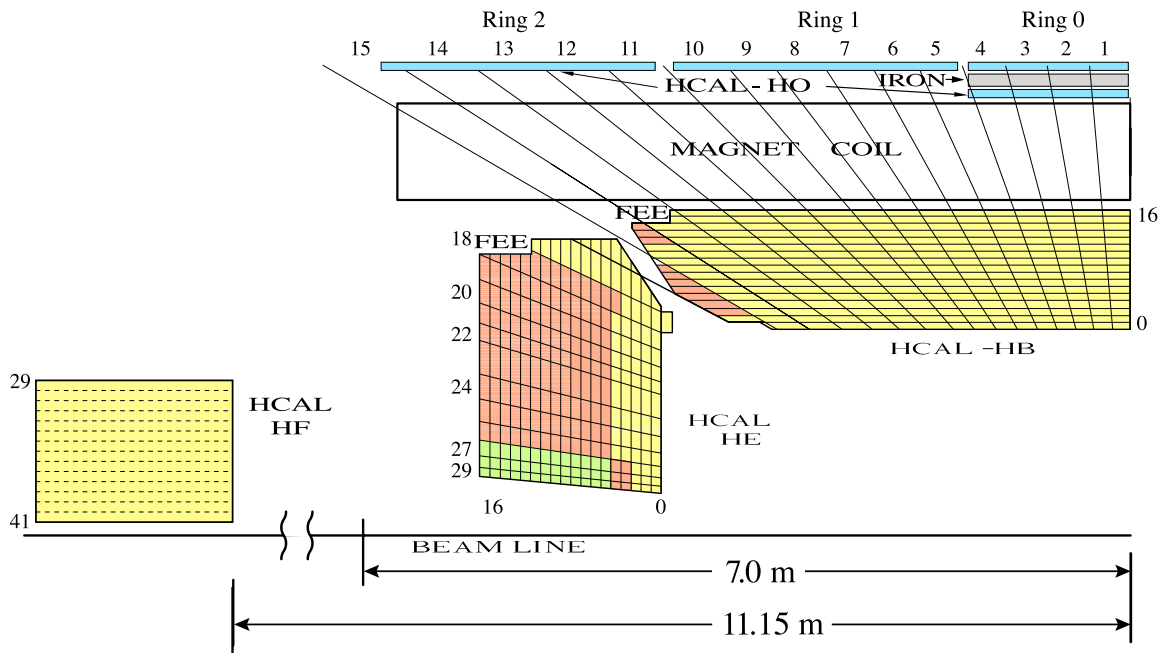
Figure 3.7.: Schematic view of the hadronic calorimeters used at CMS [85].

Both the HB and HE are designed as sampling calorimeters with brass used as the absorber material and plastic scintillator tiles in between. The light from the tiles is guided through fibres to the multi-channel hybrid photodiodes serving for photodetection. In the context of the HCAL upgrade, these will be replaced by silicon photomultipliers after Run 2 data-taking, including the corresponding readout electronics. The HO is composed of up to two scintillator planes within the gaps in the iron yoke, which is used as absorber material. The HF is a sampling calorimeter based on steel as absorber material and quartz fibres for signal production. The Cherenkov light produced by traversing particles in the quartz fibres is guided to the photomultipliers upgraded from a single to a dual readout during Run 2 data-taking. The expected design energy resolution of the HCAL for traversing hadrons is from 20 to 30% for energies between 20 and 50 GeV saturating to 10% for higher energies.

3.1.4. Muon Detection System

The muon detection system is composed of three main types of detectors as shown in figure 3.8. The aluminium drift tubes (DTs) are arranged in chambers in the gaps of the

barrel iron yoke covering a pseudorapidity of $|\eta| < 1.2$. The chambers contain planes of drift tubes for measurement of the r, ϕ and the z position of the traversing charged particles. Such a particle would ionize the gas within a tube, so that electrons would move to positively charged wires in the electric field of the tube, producing a signal by hitting a wire. Combining the timing information and the positions of the wires hit in the subsequent tubes, the trajectory of a traversing particle can be reconstructed. The spacial resolution of the drift tubes is of the order of 0.1 mm and the direction is measured with a precision of 1 mrad.

For the endcap region, cathode strip chambers (CSCs) are used extending the pseudorapidity coverage to $|\eta| < 2.4$. In contrast to the drift tubes, which perform best in a homogeneous magnetic field and at a low rate of traversing particles, cathode strip chambers can be operated reliably in an inhomogeneous magnetic field and under hard radiation conditions. The chambers filled with gas consist of positively charged anode wires crossed perpendicularly by negatively charged cathode strips. A charged particle traversing the chamber ionizes the gas, leading to electrons moving towards the anodes and creating an avalanche. At the same time, positively charged ions move towards the cathode strips. This technique allows a reconstruction of two position coordinates in the endcap. The spacial resolution of the cathode strip chambers is as for the drift tubes of the order of 0.1 mm and the direction is measured with an angular resolution of about 10 mrad.

Resistive plate chambers (RPCs) are used both in the barrel and the endcaps up to a pseudorapidity of $|\eta| < 1.6$ to perform complementary and very fast measurements of about 1 ns for traversing charged particles, ideal to make fast trigger decisions. Each chamber contains two plates with opposite charge made from resistive plastic and separated by gas. After a charged particle has crossed the chamber, electrons from ionization move towards the anode plate creating avalanche electrons, which pass the plate and hit metallic strips put on top of the anode plate.

In the context of the upgrade of the CMS detector for high luminosity conditions, an extension of the endcap muon system is required to handle the large rate of incoming particles and still trigger muons with high efficiency. Tests of a new measurement technique with gas electron multipliers (GEMs) were performed during the 2018 data-taking year to install the full set of the new detectors during the shutdown after Run 2. The position of a tested GEM chamber during Run2 is illustrated by a red box in figure 3.8.

The muon detection system of CMS allows for a reconstruction of muons, which have a relative momentum resolution of 1% in the barrel and 3% in the endcap for transverse momenta $\lesssim 100$ GeV [92].

3.2. Reconstruction of Physics Objects

The focus of this section is the reconstruction of physics objects performed after the raw data has been collected based on decisions of the trigger system described in section 3.3. This reconstruction is referred to as offline reconstruction, and allows to use more time-consuming algorithms.

At first, the reconstruction of tracks and vertices will be described [87], followed by a general introduction of isolation criteria used for high-level physics objects like electrons, muons, and τ leptons. The reconstructed tracks are a vital input to the reconstruction of muons [92] and electrons [93] discussed next. Reconstructed muons and electrons are
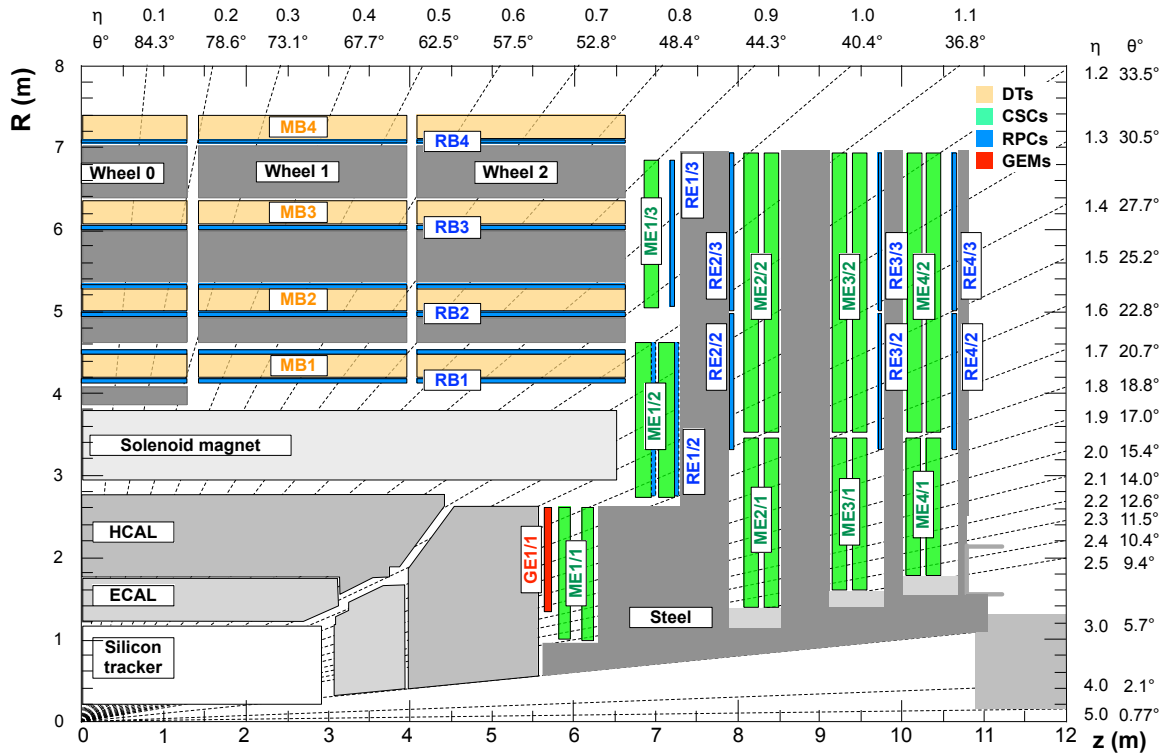
Figure 3.8.: Schematic view of the muon detection system used at CMS [86].

subsequently used in the particle flow (PF) algorithm [94], which allows to reconstruct physics objects unambiguously by correlating information across all detector subsystems. Based on the resulting PF candidates, jets are formed using the anti-k_T algorithm [95] and missing transverse energy $\vec{p}_T^{\,miss}$ is reconstructed [96]. Reconstructed jets are tagged according to their flavour to distinguish between jets induced by a light quark or gluon, jets induced by a charm quark, and jets induced by a bottom quark [97]. Furthermore, jets are used to start the reconstruction of hadronic τ lepton decays, referred to as τ_h candidates [98].

3.2.1. Tracks and Vertices

After the hits in the pixel and strip tracking systems have been reconstructed [87], the reconstruction of tracks is performed with an iterative tracking algorithm. In each iteration, the combinatorical track finder (CTF) algorithm is used for track reconstruction [87, 99], which consists of the following steps:

1. Track seeds are found, which contain collections of multiple pixel and/or strip hits.
2. Initial sets of parameters and uncertainties are determined from the seeds for the extrapolation of a trajectory expected from a charged particle to find hits in the remaining layers of the tracking system.
3. The trajectory is extrapolated and matching hits are added to the collection of the seeding hits. With each new hit in the collection, the parameters of the trajectory are updated by a fit.

4. After all matching hits were found, a final trajectory fit is performed to obtain the best possible set of parameters for the track.

5. The track is accepted or rejected based on criteria to the final track parameters.

6. In case the track is accepted, the associated hits are removed from the collection of unassigned hits.

In total, about ten iterations are performed to reconstruct tracks from the inner tracking system [94], depending on the data-taking year. The main differences between each iteration are the way the track seeds are determined, and the selection criteria imposed on the tracks. The individual iterations are summarized in table 3.1.

| | Track seeding | | |
Iteration	Pixel	Strip	Targeted tracks
0	4	0	high p_T (2017 & 2018)
1	3	0	high p_T
2	3	0	high p_T displaced (b hadron decays)
3	3	0	low p_T
4	2	0	high p_T, low quality
5		3	displaced
6, 7	0	2, 3	very displaced (interactions with detector material)
8		2	inside high p_T jets
9, 10	muon detector		muon tracks

Table 3.1.: Iterations used to reconstruct tracks in the inner tracking system [94]. The last two iterations are not seeded by hits in the pixel or strip trackers, but by muon detector subsystems.

Due to the upgrade of the inner tracker system after the data-taking year 2016, additional layers and disks in the pixel tracker have become available, leading to an additional iteration for the track reconstruction during the data-taking years 2017 and 2018 based on seeds with four hits in the pixel tracker and targeting high p_T tracks. Subsequent iterations are common between all Run 2 data-taking years. Iterations 1 to 3 are based on triplets of hits in the pixel tracker, targeting additional high p_T tracks, tracks from b hadron decays, and low p_T tracks. The reduced amount of unassigned hits in the pixel and strip trackers after these iterations allows to recover high p_T tracks with low quality seeded by pairs of hits in the pixel tracker. Further iterations target displaced tracks, high p_T tracks within jets, which can share individual hits with each other, and tracks which can be seeded by muon detector subsystems.

Next, the reconstruction of all proton-proton interaction points within the same bunch crossing, referred to as primary vertices, is performed, based on a selection of reconstructed tracks and the estimated position of the bunch crossing, the beam spot [87]. The selected tracks are required to have an impact parameter significance with respect to the beam spot smaller than 5, at least 2 reconstructed hits in the pixel tracker, and at least 5 reconstructed hits in the entire inner tracker. The trajectory fit of each selected track is required to have

$\chi^2/N_{dof} < 20$.

After the track selection, a clustering based on the distance of closest approach between the considered track and the beam spot along the beam axis is performed, based on the deterministic annealing algorithm [100]. An analogon to the free energy from statistical mechanics is defined to move from the hypothesis of a single vertex with all tracks assigned to it to a system of multiple vertices by lowering a temperature parameter. At the last step of the algorithm, a final assignment of each selected track to exactly one vertex is achieved.

After the clustering, the vertex candidates with at least two associated tracks are fitted with the adaptive vertex fitter [101] to obtain the vertex position and its covariance matrix. The number of degrees of freedom of a vertex is computed as given in equation 3.1 and serves as its quality criterion. The track weights w_i are associated to each track by the vertex fitting algorithm and correspond to the probability of a track to belong to the reconstructed vertex.

$$N_{dof}^{vtx} = \sum_{i \in tracks} w_i - 3 \tag{3.1}$$

After their reconstruction, primary vertices are ordered by the p_T^2 sum over the associated tracks and p_T^{miss}. The vertex with the highest p_T^2 sum is assumed to be the one corresponding to the hard interaction process and is referred to as the primary vertex (PV) in the following. The remaining vertices usually correspond to soft interactions within a single bunch crossing, referred to as pileup vertices (PU).

3.2.2. Isolation Criteria

Isolation criteria are introduced to reconstructed physics objects to distinguish between particles, which are accompanied by many other particles, such that they can form together a jet, from particles with a surrounding environment containing only a few particles. The second type of particles is referred to as isolated and they are likely to be produced by mechanisms other than jet formation from gluons or quarks, making isolated particles of particular relevance for physics measurements and searches. Isolated particles can for example originate from Higgs boson decays.

The isolation can be defined based on the amount of additional energy in the ECAL and HCAL or the sum of the transverse momenta of additional tracks in a (η, ϕ) cone around the considered particle ℓ, for example $\Delta R = \sqrt{\Delta\phi^2 + \Delta\eta^2} < 0.3$:

$$I^{calo}(\ell) = \sum_{\Delta R < 0.3} E_{ECAL} + E_{HCAL}, \qquad I^{track}(\ell) = \sum_{\Delta R < 0.3} p_T(track) \tag{3.2}$$

However, $I^{calo}(\ell)$ can contain undesired contributions from PU, whereas $I^{track}(\ell)$ does not account for the energy from neutral particles. To account for the shortcomings of $I^{calo}(\ell)$ and $I^{track}(\ell)$, two additional isolation definitions are introduced based on PF candidates discussed in detail in subsection 3.2.5, which comprise photons, and charged and neutral hadrons.

Charged hadrons $h^\pm$ can be easily assigned to PV and PU. For neutral particles, such as photons γ and neutral hadrons h^0, this is not possible, and therefore, a correction is applied to account for contributions from PU on a statistical basis.

For the $\Delta\beta$-corrected isolation, the ratio between the energy of neutral particles and the energy of charged hadrons from PU is assumed to be $\Delta\beta = 0.5$, leading to the following definition:

$$I^{\Delta\beta}(\ell) = \sum_{h^{\pm}_{PV}} p_T(h^{\pm}_{PV}) + \max\left(0, \sum_{h^0} p_T(h^0) + \sum_{\gamma} p_T(\gamma) - \Delta\beta \cdot \sum_{h^{\pm}_{PU}} p_T(h^{\pm}_{PU})\right),$$

$$\forall\, PF \in \{h^{\pm}_{PV}, h^{\pm}_{PU}, h^0, \gamma\} : \Delta R(\ell, PF) < 0.4 \tag{3.3}$$

An alternative correction for PU contributions is derived using the information on the pileup density ρ in a collision event and the average effective area A_{eff} [102]. Thereby, ρ represents a per-event measure for any form of diffuse contamination from PU to energy or momentum sums like the isolation, and A_{eff} a measure of the susceptibility of these sums to the contamination, in general dependent on the rapidity y and the azimuth angle ϕ in the detector. In case of the isolation, y and ϕ are given by the considered particle ℓ:

$$I^{A_{eff}}(\ell) = \max\left(0, \sum_{h^{\pm}_{PV}} p_T(h^{\pm}_{PV}) + \sum_{h^0} p_T(h^0) + \sum_{\gamma} p_T(\gamma) - \rho \cdot A_{eff}(\ell)\right),$$

$$\forall\, PF \in \{h^{\pm}_{PV}, h^0, \gamma\} : \Delta R(\ell, PF) < 0.3 \tag{3.4}$$

The pileup density is calculated for each collision event with the grid-based method for background estimation using `FastJet` software package [103]. The configuration for `FastJet` is as follows:

- Grid spacing in the (y, ϕ) plane is required to be 0.55,
- the threshold on rapidity is $|y| < 5.0$,
- and all PF candidates are used as input.

The area A_{eff} is determined from simulation by extracting the linear dependence of the p_T sum of neutral particles on ρ for given values of y and ϕ.

In the context of this thesis, requirements on the isolation of a particle ℓ are usually defined relative to its p_T:

$$I^i_{rel}(\ell) = I^i(\ell)/p_T(\ell), \qquad i \in \{calo, track, \Delta\beta, A_{eff}\} \tag{3.5}$$

3.2.3. Muons

A muon usually traverses through the full detector leaving hits in the inner tracker system, energy from ionization in the ECAL and HCAL, and hits in the muon system. The standard track reconstruction algorithm described in subsection 3.2.1 does not account for bremsstrahlung radiated off the muon. However, for muons the bremsstrahlung effect is considered to be negligible in most cases. In the following, the reconstruction of the muon signature in the CMS detector will be described.

After the reconstruction of the inner track hits in the pixel and strip tracker subsystems and the outer track hits in the RPC, CSC and DT muon systems, three main approaches are used to construct muon tracks.

Standalone muon tracks

For this approach, only the hits in the outer tracking muon system are used in the reconstruction to obtain trajectories with the Kalman Filter technique [99], starting with seeds composed from groups of hits in DT and CSC segments.

Tracker muon tracks

Tracks in the inner tracking system reconstructed by the iterative approach described in subsection 3.2.1 are matched to the reconstructed hits in the DT and CSC muon systems by extrapolation through the CMS detector and magnetic field. If such a matching succeeds for tracks with transverse momentum $p_T > 0.5$ GeV and total momentum $p > 2.5$ GeV, the matched tracks are declared as tracker muon tracks. The spacial distance between the reconstructed hit in the muon system and the intersection point between the extrapolated track and the muon system is considered as one of the muon track quality metrics.

Global muon tracks

Standalone muon tracks and tracker muon tracks are matched by propagating both tracks to a common surface and comparing the spacial distance. In case of a successful matching, the hits from both tracks are fitted using the Kalman filter to obtain a global muon track.

Tracker muons have the largest efficiency, in particular in detector regions, which are not covered well by the muon system, such that the efficiency to reconstruct a muon in more than the innermost muon station is decreased. However, tracker muons can have a larger contamination by hadrons reaching the first layer of the muon system.

Global muons have a smaller efficiency, but the best momentum resolution, because the information from the full detector is used. Since more than one muon station is traversed by the muon, global muons are less contaminated by hadrons, resulting in a much purer collection of muons.

If a muon is reconstructed both as a global and a tracker muon, it is merged to a single physics object.

The reconstructed tracker and global muons are processed further with the PF algorithm. Additional criteria described in detail in subsection 3.2.5 are checked to define a muon as a PF candidate. This can serve as quality criterion in addition to the usual metrics for the quality of the reconstructed muons.

The χ^2 of the muon track fit and the fraction of its valid hits are part of the set of variables used as quality metrics. A kink finding algorithm splits a muon track and computes a χ^2 value to check, whether the track is more compatible with a single track or with two separate tracks. In case of a global muon track, the matching between the tracker and the standalone tracks is quantified with a χ^2 value. In addition, the compatibility between the tracker muon track and the muon system segments is quantified by values between 0 and 1. Additional criteria can be imposed on the transverse and longitudinal impact parameters d_{xy} and d_z between the primary vertex and the track extrapolated to the vertex position. To create stricter identification criteria, the number of hits in the muon system used in the global track fit, N_{hits}^{MD}, is considered, as well as the number of muon stations associated to the track, N_{MS}. For the tracker muon track used for the global track fit, the number of hits in the pixel tracker, N_{hits}^{pixel}, as well as the number of hits in the inner tracking system in

total, $N_{hits}^{tracker}$, are used as quality metrics.

The quality criteria are combined into several muon identification (ID) working points. Criteria to be fulfilled for three working points used in this thesis will be discussed in the following.

Loose muon ID

- The muon is a PF candidate,
- and reconstructed as global or as tracker muon.

Medium muon ID

- The muon fulfills the loose ID,
- the fraction of valid hits in the inner tracking system is greater than 0.8.
- In case the muon is global, it must fulfill:
    - a requirement on the track fit quality, $\chi^2/N_{dof} < 3$,
    - the matching between the standalone and tracker muon track, $\chi^2 < 12$,
    - the kink finder compatibility, $\chi^2 < 20$,
    - and the segment compatibility to be greater than 0.303.
- Otherwise, it is a tracker muon and its segment compatibility is required to be greater than 0.451.

Tight muon ID

- The muon is a PF candidate and is reconstructed as global muon,
- the global track fit is required to have $\chi^2/N_{dof} < 10$.
- Additional requirements are defined for the muon system: $N_{hits}^{MD} > 0$, $N_{MS} > 1$,
- the inner tracking system: $N_{hits}^{pixel} > 0$, $N_{hits}^{tracker} > 5$,
- and the impact parameters: $d_{xy} < 2$ mm, $d_z < 5$ mm.

The momentum reconstruction of the muon is performed by using information from four different track fits of the reconstructed muon. The best of the four track fits is selected for the muon, based on the relative uncertainty on the p_T obtained from the track fit and its goodness of fit criterion.

In the first fit approach, only the hits in the inner tracking system are used for momentum extraction. This approach works well for muons with $p_T < 200$ GeV, where the contribution from the muon system to the measurement is marginal. The second approach exploits the hits in the inner tracking system and the innermost muon station, which contains hits from the muon track. The third approach is used for muon stations with high occupancy, where the track is refitted only with hits compatible with the extrapolated trajectory. In the most sophisticated fourth approach, an attempt is made to account for energy losses in the muon stations causing significant bending of the trajectory.

The isolation of muons is determined using the $\Delta\beta$-corrected definition from equation 3.3.

3.2.4. Electrons

Due to the presence of the magnetic field, the trajectory of electrons traversing the detector is strongly bent, leading to a high probability of an emission of bremsstrahlung photons.

In consequence, an electron looses up to 80% of its energy in the inner tracking system, before it is stopped in the ECAL.

An electron is expected to have the following signature in the detector: a main track traversing the inner tracking system up to the ECAL, energy deposits in the ECAL with a large spread across ϕ and a small spread across η, additional separate ECAL deposits from high energetic photon emissions, and accompanying tracks from e^+e^- conversions of bremsstrahlung photons.

The reconstruction of an electron can be divided into five main steps:

1. Energy deposits of the electron in the ECAL are reconstructed, using the energy clustering algorithm adapted for the PF reconstruction [94]. These energy deposits are referred to as PF clusters in the following.
2. PF clusters in the ECAL are combined to ECAL superclusters with an energy equal to the sum of the PF cluster energies and an energy weighted position in the (η, ϕ) plane. The combination follows an optimized pattern in (η, ϕ), specific for the reconstruction of electrons and photons.
3. A dedicated track reconstruction takes place with a version of the algorithm discussed in subsection 3.2.1, which is adapted to account for the large amount of bremsstrahlung photons.
4. PF clusters and ECAL superclusters are linked to the electron tracks to construct electron objects.
5. Bremsstrahlung photons and their conversions are added to the electron object, and the associated ECAL supercluster is updated accordingly.

The track reconstruction algorithm for electrons is based on a Gaussian-sum filter (GSF) [104] algorithm, which is more computationally intensive than CTF. For this reason, the GSF algorithm is performed on a subset of all reconstructed hits in the inner tracking system, initiated from hit collections referred to as electron track seeds. The seeds are determined using an ECAL-based and a track-based approach.

In the ECAL-based approach, an electron trajectory is propagated through the inner tracking system to PV, starting from an ECAL supercluster position, which fulfills specified energy requirements. The intersection points between the innermost layers of the inner tracking system and the helix trajectory are used to start a search within (ϕ, z) windows for hits in the inner tracking system, which have served as seeds for the CTF reconstruction and are summarized in table 3.1. In case of a successful match for two or more hits, the resulting hit collection is declared as an ECAL-based seed.

The track seeds used for the CTF reconstruction are reconsidered for the track-based electron track seeding. If the quality of a CTF track is sufficient and it is matching to a PF cluster in the ECAL, the corresponding seeding hits are directly selected for further quality requirements. Otherwise, the seeding hits are refitted with the GSF algorithm to account for the possible photon radiation. If the refitted track matches to a PF cluster in the ECAL, its seeding hits are selected for further quality requirements. The quality requirements for the selected seeds involve a multivariate analysis of the quality of the corresponding tracks and the level of matching of these tracks to PF clusters in the ECAL. If the selected track seeds pass these quality requirements, they are declared as track-based seeds.

The main track reconstruction is performed with the GSF algorithm with the following main difference to the Kalman Filter technique: The energy loss of an electron traversing

the tracker material is modelled by the Bethe-Heitler function instead of a Gaussian. This function is approximated by a sum of Gaussians. Starting from each selected electron track seed, a trajectory is propagated to the next layer in the inner tracking system to match the intersection between the tracker module surface and the trajectory to a reconstructed hit. The matching parameters are relaxed to account for energy losses of the electron. In case that more than one hit are matched, multiple trajectory hypotheses are tested. The trajectory resulting from the updated set of hits is propagated and updated with the same procedure to the next layers repeatedly, until the last layer in the inner tracking system is reached. After all hits of a track are collected, these hits are fitted with the GSF algorithm to obtain the track parameters.

Next, the reconstructed electron tracks are combined with the matching ECAL energy deposits. In case of ECAL-based track seeding, the seeding supercluster is checked for the match. The electron tracks with track-based seeds are matched to a PF cluster in the ECAL.

A specific bremsstrahlung recovery is performed for the reconstructed electron [94]. In the region, where the reconstructed electron track is traversing the material of the inner tracking system, tangential lines are propagated to the ECAL and checked for an intersection with a PF cluster. This would indicate a high energetic bremsstrahlung photon. Due to the probability of up to 60% for a photon to convert in the tracking material, the tangential lines are also checked for a match with a pair of secondary GSF tracks, which in turn match to PF clusters in the ECAL, indicating a pair of electrons from photon conversion [105]. After imposing quality criteria to the potential bremsstrahlung photons and photon conversions, the ECAL cluster of the electron (the supercluster or the PF cluster) is updated with the additional PF clusters to a new, refined ECAL supercluster.

To obtain the best possible estimate for the electron momentum, an energy and momentum calibration is performed during the electron reconstruction, which can be separated into three main steps: At first, the energy of each PF cluster is calibrated, then, the energy of the corresponding supercluster, and finally, the combination of the ECAL energy and track measurements of the electron. The PF cluster calibration is based on fits of analytical functions of the energy and η of the PF cluster to the corresponding distribution of the true energy in simulation, whereas the supercluster, and the final energy and momentum calibration are performed by using multivariate techniques.

For the electron isolation, the definition from equation 3.4 is used, requiring a calculation of A_{eff} from simulated events to construct the PU correction. For electrons, A_{eff} is derived in bins of the pseudorapidity of the electron supercluster $\eta(e)$. This approximation of the rapidity y is used because of the negligible mass of electrons with respect to $p_T(e) \gtrsim 20$ GeV. The dependence of A_{eff} on ϕ is also considered as negligible. For a given $|\eta(e)|$ range, A_{eff} is derived as follows:

1. A 2-dimensional distribution is constructed for the p_T sum of neutral hadrons and photons, and the pileup density ρ.
2. For each slice of the distribution in ρ, the one-sided 90% quantile is computed, starting from a neutral p_T sum of zero.
3. The slope of the linear part of the resulting function of ρ, starting at values $\rho \gtrsim 10$ GeV, is the effective area A_{eff}.

In the table 3.2, the determined values for A_{eff} are shown in bins of $|\eta(e)|$.

Bin of the pseudorapidity $|\eta(e)|$	Effective area A_{eff}
$|\eta(e)| \in [0, 1)$	0.1440
$|\eta(e)| \in [1, 1.479)$	0.1562
$|\eta(e)| \in [1.479, 2)$	0.1032
$|\eta(e)| \in [2, 2.2)$	0.0859
$|\eta(e)| \in [2.2, 2.3)$	0.1116
$|\eta(e)| \in [2.3, 2.4)$	0.1321
$|\eta(e)| \in [2.4, 2.5)$	0.1654

Table 3.2.: The effective area A_{eff} determined in bins of the electron supercluster pseudorapidity $|\eta(e)|$.

Several variables are chosen for the electron identification to define the quality of the reconstructed electron. The majority of these variables can be subdivided into four categories: shower shape, track quality, track to cluster matching, and the conversion identification [105].

The main shower shape variable, $\sigma_{i\eta i\eta}$, is used to check, whether the full energy deposit in a 5×5 set of ECAL crystals around the seeding ECAL crystal in (η, ϕ) is compatible with one or more particles:

$$\sigma_{i\eta i\eta}^2 = A_{\text{crystal}} \cdot \frac{\sum_i^{5 \times 5} w_i \cdot \left(i\eta_i - \overline{i\eta}\right)^2}{\sum_i^{5 \times 5} w_i}, \qquad w_i = 4.7 + \log\left(\frac{E_i}{E_{5 \times 5}}\right) \qquad (3.6)$$

The coordinate $i\eta$ is an integer number of an ECAL crystal in the η direction, $\overline{i\eta}$ refers to the energy weighted mean of the individual crystal positions in the 5×5 set, and $E_{5 \times 5}$ is the energy sum of the 5×5 set. The value of $\sigma_{i\eta i\eta}$ is normalized to the approximate size of a crystal A_{crystal}. Similarly, $\sigma_{i\phi i\phi}$ is defined. Supporting variables, that belong to the shower shape category, are listed in the following:

- A measure for the circularity of an electromagnetic shower, $1 - E_{1 \times 5}/E_{5 \times 5}$. The corresponding 1×5 set of ECAL crystals is extended in the local $i\phi$ direction within the ECAL.
- The ratio $R_9 = E_{3 \times 3}/E_{\text{SC}}^{\text{raw}}$ of the energy of the 3×3 crystal set around the seeding crystal, $E_{3 \times 3}$, over the uncorrected supercluster energy, $E_{\text{SC}}^{\text{raw}}$.
- The ratio of the preshower energy assigned to the supercluster over its uncorrected energy, $E_{\text{SC}}^{\text{PS}}/E_{\text{SC}}^{\text{raw}}$.
- The ratio of the hadronic energy in the HCAL in a cone of $\Delta R < 0.15$ around the electron supercluster position over the supercluster energy, H/E_{SC}.
- The spacial widths of the supercluster in the η and ϕ directions, $\Delta\eta_{\text{SC}}$ and $\Delta\phi_{\text{SC}}$.

The track quality is determined by the following variables:

- The track fit quality of the GSF track and the associated CTF track, χ_{GSF}^2 and χ_{CTF}^2.
- The number of hits associated with these tracks, $N_{\text{hits}}^{\text{GSF}}$ and $N_{\text{hits}}^{\text{CTF}}$.
- The number of lost hits within the GSF track, $N_{\text{lost}}^{\text{GSF}}$.

- The energy loss caused by bremsstrahlung $f_{brem} = (p_{in} - p_{out})/p_{in}$.

The energy loss is computed from the estimates of the electron momenta before and after bremsstrahlung. The former momentum p_{in} is calculated from the curvature of the track trajectory near the interaction point, the latter momentum p_{out} from the trajectory extrapolated from the outer part of the track to the ECAL surface.
The quality of the track to cluster matching can be quantified in terms of differences between energies and momenta definitions, and spacial differences in η and ϕ. The variables constructed for that purpose are listed in the following:

- The ratio $R_{EoP}^{in} = E_{SC}/p_{in}$ is the best estimate for the state of the electron before bremsstrahlung emission.
- Similarly, the ratio $R_{EoP}^{out} = E_{PF}/p_{out}$ refers to the best estimate of the electron state after bremsstrahlung emission. The energy E_{PF} corresponds to the PF cluster nearest to the intersection point of the electron trajectory and the ECAL surface.
- The difference $1/E_{SC} - 1/p_{in}$, used in particular for explicit requirements on this variable.

- The trajectory for the part of the electron track near the interaction point is extrapolated to the ECAL surface, such that its spacial distance to the supercluster position can be defined, $\Delta\eta_{in}$ and $\Delta\phi_{in}$.
- An alternative of the spacial difference in η is defined by using the position of seeding PF cluster instead of the supercluster, $\Delta\eta_{in}^{seed}$. This is done to avoid biases, that could be introduced by the supercluster position.
- The trajectory of the electron track part near the ECAL is extrapolated to the ECAL surface, and its intersection point is compared to the η position of the seeding PF cluster, $\Delta\eta_{out}$.

Variable category	Set of variables
General	calibrated electron p_T, supercluster $\eta(e)$, pileup density ρ
Shower shape	$\sigma_{i\eta i\eta}$, $\sigma_{i\phi i\phi}$, $1 - E_{1\times5}/E_{5\times5}$, R_9, E_{SC}^{PS}/E_{SC}^{raw}, H/E_{SC}, $\Delta\eta_{SC}$, $\Delta\phi_{SC}$
Track quality	χ^2_{GSF}, χ^2_{CTF}, N_{hits}^{GSF}, N_{hits}^{CTF}, N_{lost}^{GSF}, f_{brem}
Track to cluster matching	R_{EoP}^{in}, R_{EoP}^{out}, $1/E_{SC} - 1/p_{in}$, $\Delta\eta_{in}$, $\Delta\phi_{in}$, $\Delta\eta_{out}$
Conversion identification	conversion vertex probability

Table 3.3.: Categorized variables used for the multivariate electron identification. Details are given in the text.

In table 3.3, a summary of the discussed variables is given, which are used for a multivariate electron identification based on a boosted decision tree (BDT), which is trained on simulated

$Z \to$ ee events with the XGBoost software [106]. The 90% efficiency working point of the BDT is defined as a function of the electron p_T. Additionally, six categories are introduced by using three $\eta(e)$ and two electron p_T regions, summarized in table 3.4 together with the p_T dependent lower thresholds on the BDT discriminator output.

	$p_T \in [5, 10)$ GeV	$p_T \geq 10$ GeV
$|\eta(e)| \in [0, 0.8)$	$2.77 - 8.163 \cdot \exp(-p_T/3.82)$	$5.92 - 9.32 \cdot \exp(-p_T/13.48)$
$|\eta(e)| \in [0.8, 1.479)$	$1.86 - 11.86 \cdot \exp(-p_T/2.19)$	$5.02 - 8.79 \cdot \exp(-p_T/13.13)$
$|\eta(e)| \in [1.479, 2.5)$	$1.73 - 17.01 \cdot \exp(-p_T/2.02)$	$4.17 - 9.01 \cdot \exp(-p_T/13.20)$

Table 3.4.: Requirements on the BDT discriminator for the 90% efficiency working point of the multivariate electron identification. The lower thresholds depend on the electron p_T and the six categories in electron p_T and supercluster $\eta(e)$.

Explicit requirements on the quality variables for the veto working point of the electron identification are summarized in table 3.5.

Variable	$|\eta(e)| \in [0, 1.479)$	$|\eta(e)| \in [1.479, 2.5)$
$\sigma_{i\eta i\eta}$	< 0.0126	< 0.0457
$|\Delta\eta_{in}^{seed}|$	< 0.00463	< 0.00814
$|\Delta\phi_{in}|$	< 0.148	< 0.19
H/E_{SC}	$< 0.05 + \frac{1.16\ \text{GeV}}{E_{SC}} + 0.0324 \cdot \frac{\rho}{E_{SC}}$	$< 0.05 + \frac{2.54\ \text{GeV}}{E_{SC}} + 0.183 \cdot \frac{\rho}{E_{SC}}$
$I_{rel}^{\Delta\beta}(e)$	$< 0.198 + \frac{0.506\ \text{GeV}}{p_T}$	$< 0.203 + \frac{0.96\ \text{GeV}}{p_T}$
$|1/E_{SC} - 1/p_{in}|$	$< 0.209\ \text{GeV}^{-1}$	$< 0.132\ \text{GeV}^{-1}$
N_{lost}^{GSF}	≤ 2	≤ 3
conversion veto	passed	passed

Table 3.5.: Explicit requirements for the veto working point of the electron identification. The thresholds are defined in two supercluster $\eta(e)$ regions and depend on variables used for electron identification.

3.2.5. Particle Flow Algorithm

The main goal of the particle flow (PF) algorithm [94] is to reconstruct and identify particles in the detector unambiguously by using the complete information provided by the different detector subsystems. The inputs for the PF algorithm are reconstructed tracks and vertices described in subsection 3.2.1, reconstructed muons described in subsection 3.2.3, and

information from the calorimeters. Within the PF algorithm, electrons are reconstructed as described in subsection 3.2.4, with relaxed requirements on the electron quality. These electrons are referred to as PF electrons, and are a superset of electrons used further for the data analysis.

These inputs are used to reconstruct all PF candidates consisting of muons, electrons, photons, and charged and neutral hadrons. First, the reconstruction of PF clusters in the calorimeters will be described, followed by a description of particle identification with a linking algorithm, which combines the information from the tracks, calorimeters and the muon detector subsystem.

Energy deposits are reconstructed in the barrel and endcap parts of the ECAL and HCAL, in the preshower calorimeter and in the HF. Electromagnetic and hadronic energy deposits in an HF cell are directly considered as energy clusters. For other detector subsystems, a clustering algorithm is used:

1. Calorimeter cells are determined, which can be used as seeds to start the reconstruction algorithm, referred to as cluster seeds. They are required to exceed a certain minimum energy threshold, and to have the maximum energy compared to the adjacent cells.
2. Starting from the cluster seeds, adjacent cells are aggregated, as long as their energy exceeds energy thresholds specified for the calorimeter region. In this way, energy clusters are constructed.
3. Based on these energy clusters, PF clusters are reconstructed based on a Gaussian mixture model described in the following.

In this model, it is assumed, that the energy deposits in each of the M calorimeter cells of the constructed energy cluster result from N Gaussian energy deposits distributed over the (η, ϕ) plane. The parameters of the model are the amplitudes A_i and the mean positions $\vec{\mu}_i$ of the Gaussians, whereas the width σ of each Gaussian is fixed to a value specific to the calorimeter considered. An iterative approach is used to determine the parameters with two steps in each iteration.

At first, the expected fraction f_{ij} of the measured energy E_j of the calorimeter cell at position $\vec{c}_j$ is computed in terms of parameters of the Gaussians and the calorimeter cell positions:

$$f_{ij} = \frac{A_i \cdot \exp\left[-(\vec{c}_j - \vec{\mu}_i)^2/(2\sigma^2)\right]}{\sum_{k=1}^{N} A_k \cdot \exp\left[-(\vec{c}_j - \vec{\mu}_k)^2/(2\sigma^2)\right]} \tag{3.7}$$

For the first iteration, the seed cell values for the energy and the position are taken as parameters A_i and $\vec{\mu}_i$ to compute f_{ij}.

In the second step, the expected values for the parameters are computed in terms of the fraction values f_{ij}, the measured energies E_j and the measured positions $\vec{c}_j$:

$$A_i = \sum_{j=1}^{M} f_{ij} \cdot E_j, \qquad \vec{\mu}_i = \sum_{j=1}^{M} f_{ij} \cdot E_j \vec{c}_j \tag{3.8}$$

Using these values as the initial fit parameters, a maximum likelihood fit of the Gaussian model based on f_{ij} from equation 3.7 is performed to the shape of the considered energy

cluster. The obtained values for A_i and $\vec{\mu}_i$ after the fit are used for the computation of f_{ij} in the next iteration. This procedure is repeated until convergence.

After that, the obtained N Gaussians are declared as PF clusters. Due to the requirements imposed on the energy of each calorimeter cell to enter the PF clustering, the resulting PF cluster energies usually are biased towards lower values. A calibration is performed using simulated photon events for the ECAL and simulated neutral hadron events for the HCAL, depending on the energy and the pseudorapidity of the particles and using analytic functions.

The main goal of the linking algorithm is to create PF blocks from the reconstructed elements provided as input information. For each link between two elements, a distance is defined to quantify the quality of the link.

At first, tracks are linked to PF clusters in the ECAL and HCAL. If multiple PF clusters in the HCAL are matched to one track, or several tracks are matched to one PF cluster in the ECAL, then only the link to the nearest object is kept. As explained in subsection 3.2.4, bremsstrahlung photons and their conversions are recovered during the electron reconstruction. Corresponding PF clusters and tracks are linked within the PF algorithm to the matching GSF track.

The finest granularity is provided by the preshower calorimeter, followed by the ECAL, and HCAL, such that the cluster to cluster matching is started with the preshower. If several PF clusters of a less granular calorimeter are matched to one PF cluster of a more granular calorimeter, then only the link to the nearest cluster is kept.

The remaining links are created among tracks compatible with a displaced interaction vertex, among tracks in the inner tracking system and the muon detector subsystem, and among elements created during the electron reconstruction, such as a supercluster in the ECAL, which is translated into links between associated PF clusters.

Starting from the established PF blocks, the particle reconstruction and identification begins with muons, as described in subsection 3.2.3. Isolated muons are declared as PF muons, if the relative track and calorimeter isolations defined in equation 3.2 fulfill the requirements of $I_{rel}^{track}(\mu) < 0.1$ and $I_{rel}^{calo}(\mu) < 0.1$. Muons, which do not fulfill these isolation criteria, are required to fulfill the tight identification working point instead, and to have either at least three associated track segments in the muon detector subsystems or calorimeter deposits associated to the muon track, which are compatible with an ionization from a muon. Muons, which do not fulfill this selection, are kept in case their standalone track is of high quality or in case they have a large number of hits in the muon detector systems. After all PF muons are identified, the corresponding elements in the PF blocks are not used in further processing.

Electrons and isolated photons are reconstructed from the remaining PF blocks. Based on the reconstructed components described in subsection 3.2.4 the seeds for the PF candidates are chosen. The electron PF candidate is seeded by a GSF track in case that the associated cluster is not linked to more than three additional tracks. A photon PF candidate is seeded by an ECAL supercluster, which is exceeding a threshold on its transverse energy $E_T > 10$ GeV and is not linked to any GSF track.

For ECAL-based electrons, the requirement $H/E_{SC} < 0.1$ is imposed. The momenta and directions of the electrons and photons are assigned after all bremsstrahlung photons are collected and associated to the PF candidates and the total energy and momentum are calibrated.

Electron PF candidates are kept, if they satisfy identification criteria summarized in a

multivariate BDT discriminator, trained for different detector regions and using isolation information for an isolated electron or without this information to target non-isolated electrons.

Photon PF candidates are kept, if they are sufficiently isolated from tracks and other ECAL clusters, and their energy distribution and the ratio between the HCAL and ECAL are compatible with a photon shower.

All reconstructed elements associated to the selected electron and photon PF candidates are not used in further processing. In addition, tracks identified to be from a photon conversion, but not associated to a PF candidate, are also removed from the PF blocks due to the high probability of these tracks being misreconstructed.

In the next step, the reconstruction of potential jet constituents is performed: charged and neutral hadrons, non-isolated photons and non-isolated muons.

Within acceptance of the inner tracking system $|\eta| < 2.5$, PF blocks with PF clusters from the ECAL and HCAL, but without a link to a track, are directly declared as non-isolated photons (ECAL) and neutral hadrons (HCAL).

Beyond the tracker acceptance, the charged and neutral hadrons can not be distinguished, so the assignment of ECAL clusters to photons is no longer justified. Therefore, the PF blocks with links between the ECAL and HCAL cluster are assigned to a neutral or charged hadron, whereas PF blocks containing only ECAL clusters are assumed to be from a photon. The energies of the classified neutral hadrons and non-isolated photons are calibrated using the PF cluster calibration. The clusters in the HF are directly considered as HF photons and HF hadrons without calibration.

The remaining PF blocks contain PF clusters in the HCAL linked to one or more tracks, which in turn may be linked to the remaining PF clusters in the ECAL. Each of the PF clusters in the ECAL is linked at most to one of these tracks. Such PF blocks are assigned to recovered muons, photons, charged hadrons, or neutral hadrons, based on the best compatibility of the calibrated energy and momenta of the PF blocks to one of the listed particle types.

At this level, all PF candidates are reconstructed. However, the event description is extended and corrected by using information of the full event. Particles from secondary vertices are identified and are summarized and recalibrated as a primary charged hadron, in case of an existing incoming track for the secondary vertex. Additionally, misidentified charged hadrons and muons are corrected, based on the reconstructed $\vec{p}_T^{\text{miss}}$.

3.2.6. Jets and Missing Transverse Energy

To reduce the effect of contamination from PU [107], the PF candidates collection is adjusted in two ways: charged hadron subtraction (CHS) [108, 109] and pileup per particle identification (PUPPI) [109, 110].

The main idea of the charged hadron subtraction is to identify tracks of particles coming from PU and remove the associated PF candidates from the input collection used in the jet reconstruction. The vertex fit for PU discussed in subsection 3.2.1 is required to have a minimum number of degrees of freedom, $N_{\text{dof}}^{\text{vtx}} > 4$ to be used in the CHS method. A track of a charged PF candidate associated to such PU is required to have a track fit with $\chi^2/N_{\text{dof}} < 20$. If this is the case, the PF candidate is removed from the input to the jet reconstruction. The reduced PF candidate collection resulting from this method is referred to as the PF+CHS collection.

Based on this collection, jets are reconstructed using the anti-k_T algorithm [95] as implemented in the `FastJet` software package [103]. Starting from the PF candidate with the highest p_T, this algorithm performs a recursive combination of particle pairs, if they fulfill a requirement on the distance measures:

$$d_{ij} = \min\left(\frac{1}{k_{T,i}^2}, \frac{1}{k_{T,j}^2}\right) \cdot \frac{\Delta R_{ij}^2}{r^2},$$

$$d_{iB} = \frac{1}{k_{T,i}^2}, \tag{3.9}$$

$$\Delta R_{ij}^2 = (y_i - y_j)^2 + (\phi_i - \phi_j)^2$$

In each recursion step, the distance metric d_{ij} is computed for an intermediate jet i, and a PF candidate j. In the first iteration, the jet i corresponds to a single PF candidate. The value of d_{ij} is compared with the metric d_{iB}, computed for the jet i. If $d_{ij} < d_{iB}$, the jet i is combined with the PF candidate j, and is passed to the next recursion step. Otherwise, the jet i is considered as reconstructed and the recursive combination stops. After the formation of the jet, its associated PF candidates are removed from the input collection of the PF candidates and the algorithm starts again from the PF candidate with the highest p_T.

The quantities $k_{T,l}$ in equation 3.9 refer to the transverse momenta of the considered jets or PF candidates $l \in \{i, j\}$, y_l and ϕ_l are defined as their rapidities and azimuth angles, respectively. The choice of the radius parameter is $r = 0.4$ for the jets considered in the context of this thesis. The algorithm is collinear and infrared safe.

To suppress misreconstructed jets [107], identification criteria are defined for jets derived from the PF+CHS collection. The explicit requirements are summarized in table 3.6, using variables based on the multiplicities and the fraction of different types of PF candidates within a jet. The efficiency for genuine jets is above 99%, whereas the background rejection is at about 98%.

In the PUPPI approach, the information of the surrounding area of each PF candidate is investigated to assign a probability, that this particle is from the hard interaction process of PV. Similarly to the CHS method, charged PF candidates are assigned to PV or to PU. Charged PF candidates from PV obtain directly a weight of $w_{PUPPI} = 1$, charged PF candidates from PU a weight of $w_{PUPPI} = 0$. All remaining charged PF candidates are without any vertex assignment. In case their impact parameter in the beam direction, d_z is smaller than 0.3 cm, such charged PF candidates obtain a weight of $w_{PUPPI} = 1$, otherwise $w_{PUPPI} = 0$. In this way, all charged PF candidates are provided with a weight.

In the following, the weight assignment to the remaining neutral PF candidates is described. A metric α_i based on the information from the surrounding area has to be defined, with which PF candidates from PU can be distinguished from PF candidates from PV. At CMS [109], α_i is defined by:

$$\alpha_i = \log\left(\sum_{j \neq i, \, \Delta R_{ij} < 0.4} \left(\frac{p_T(j)}{\Delta R_{ij}}\right)^2\right) \begin{cases} j = P_{PV}^{\pm} & \text{for } |\eta_i| < 2.5 \\ j = \text{PF candidate} & \text{for } |\eta_i| \geq 2.5 \end{cases} \tag{3.10}$$

$$\Delta R_{ij}^2 = (\eta_i - \eta_j)^2 + (\phi_i - \phi_j)^2$$

For a considered PF candidate i, a sum over the PF candidates j is performed, with the squared ratio between their transverse momenta $p_T(j)$ and their distance to the PF can-

$|\eta|$ region	Jet variable	data-taking year		
		2016	2017	2018
$|\eta| \in [0, 2.4]$	Charge hadron fraction	> 0	> 0	> 0
	Charged multiplicity	> 0	> 0	> 0
	Electron fraction	< 0.99	-	-
	Neutral hadron fraction	< 0.99	< 0.9	< 0.9
	Photon fraction	< 0.99	< 0.9	< 0.9
	Number of all particles	> 1	> 1	> 1
$|\eta| \in (2.4, 2.6]$	Charged hadron fraction	-	-	> 0
	Charged multiplicity	-	-	> 0
	Neutral hadron fraction	< 0.99	< 0.9	< 0.9
	Photon fraction	< 0.99	< 0.9	< 0.9
	Number of all particles	> 1	> 1	> 1
$|\eta| \in (2.6, 2.7]$	Charged multiplicity	-	-	> 0
	Neutral hadron fraction	< 0.99	< 0.9	< 0.9
	Photon fraction	< 0.99	< 0.9	< 0.99
	Number of all particles	> 1	> 1	-
$|\eta| \in (2.7, 3]$	Photon fraction	> 0.01	$\in (0.02, 0.9)$	$\in (0.02, 0.9)$
	Neutral hadron fraction	< 0.98	-	-
	Number of neutral particles	> 2	> 2	> 2
$|\eta| \in (3, 4.7)$	Photon fraction	< 0.9	< 0.9	< 0.9
	Neutral hadron fraction	-	> 0.02	> 0.2
	Number of neutral particles	> 10	> 10	> 10

Table 3.6.: Explicit requirements to construct jet identification criteria to suppress misre-constructed jets, dependent on the data-taking year.

didate i in the (η, ϕ) plane, ΔR_{ij}. Within the acceptance of the inner tracking system, $|\eta_i| < 2.5$, the sum is performed over all charged PF candidates from PV, $P_{PV}^{\pm}$, in a cone $\Delta R_{ij} < 0.4$ around the PF candidate i. Outside the tracker acceptance, all PF candidates are taken, which are inside the cone. In case that there are no PF candidates present within the cone around the PF candidate i, the PF candidate is directly associated to PU with $\alpha_i = 0$. The metric α_i is transformed into a quantity, which can be interpreted as the probability of the PF candidate i to originate from PV. This translation is performed in two steps. At first, estimators for the median $\bar{\alpha}_{PU}$ and the spread σ_{PU}^2 are computed, based on the distribution of α_i for charged PF candidates i from PU. The spread σ_{PU}^2 is computed as follows:

$$\sigma_{PU}^2 = \frac{1}{N_{PU}} \cdot \sum_{i=1}^{N_{PU}} (\alpha_i - \bar{\alpha}_{PU})^2 \qquad (3.11)$$

The quantity N_{PU} refers to the number of the charged PF candidates from PU. The values for $\bar{\alpha}_{PU}$ and σ_{PU}^2 are measured for PF candidates with $|\eta| < 2.5$. Beyond that region, extrapolation factors derived from simulation are applied, resulting in an $|\eta|$ dependent median $\bar{\alpha}_{PU}(|\eta|) = SF_{\alpha}(|\eta|) \cdot \bar{\alpha}_{PU}$ and spread $\sigma_{PU}^2(|\eta|) = SF_{\sigma}^2(|\eta|) \cdot \sigma_{PU}^2$. These scale factors

	$A(|\eta|)$	$B(|\eta|)$	$SF_\alpha(|\eta|)$	$SF_\sigma(|\eta|)$
$|\eta| \in [0, 2.5)$	0.2 GeV	0.015 GeV	1	1
$|\eta| \in [2.5, 3)$	2.0 GeV	0.13 GeV	0.9	1.2
$|\eta| \in [3, 5)$	2.0 GeV	0.13 GeV	0.75	0.95

Table 3.7.: Parameters used by the PUPPI algorithm, which are dependent on predefined $|\eta|$ regions.

are summarized in table 3.7.

In the second step, a new quantity is defined, which is assumed to follow a χ^2 distribution with one degree of freedom for values of α_i greater than $\bar{\alpha}_{PU}(|\eta|)$:

$$\chi_i^2 = \begin{cases} (\alpha_i - \bar{\alpha}_{PU}(|\eta_i|))^2 / \sigma_{PU}^2(|\eta_i|) & \alpha_i > \bar{\alpha}_{PU}(|\eta_i|) \\ 0 & \alpha_i \le \bar{\alpha}_{PU}(|\eta_i|) \end{cases} \tag{3.12}$$

Using the χ^2 cumulative distribution function with one degree of freedom, $F(\cdot; N_{dof} = 1)$, an intermediate weight is computed by $w_i = F(\chi_i^2; N_{dof} = 1)$, if $\chi_i^2 > 0$ for neutral PF candidates i. In case of $\chi_i^2 = 0$, the final weight is set to 0. Furthermore, the final weight is set to 0, if $w_i < 0.01$ or if the requirement $w_i \cdot p_T(i) > A(|\eta_i|) + B(|\eta_i|) \cdot N_{vtx}$ is not fulfilled. The quantity N_{vtx} refers to the number of all primary vertices well reconstructed in the event, whereas the parameters A and B are defined for the different $|\eta|$ regions, as summarized in table 3.7.

To conclude, the final weight $w_{PUPPI}(i)$ for a PF candidate i is defined by:

$$w_{PUPPI}(i) = \begin{cases} 1 & i = P_{PV}^\pm \\ 0 & i = P_{PU}^\pm \\ 0 & i = P^0 \text{ and } w_i < 0.01 \\ 0 & i = P^0 \text{ and } w_i \cdot p_T(i) \le A(|\eta_i|) + B(|\eta_i|) \cdot N_{vtx} \\ w_i & \text{otherwise} \end{cases} \tag{3.13}$$

$$w_i = \begin{cases} F(\chi_i^2; N_{dof} = 1) & \chi_i^2 > 0 \\ 0 & \chi_i^2 = 0 \end{cases}$$

Here, $P_{PV}^\pm$ refers to a charged PF candidate from PV, $P_{PU}^\pm$ to a charged PF candidate from PU, and P^0 to a neutral PF candidate. PF candidates with $w_{PUPPI} = 0$ are removed from the list of PF candidates, resulting in a reduced PF candidates collection, referred to as the PUPPI collection in the following.

The PUPPI collection is used to define the missing transverse energy $\vec{p}_T^{miss}$ [96]:

$$\vec{p}_T^{miss} = - \sum_{i \in PUPPI} w_{PUPPI}(i) \cdot \vec{p}_T(i) \tag{3.14}$$

3.2.7. Jet Tagging

To distinguish jets by their flavour, especially for heavy flavour quarks, like the bottom and the charm quark, specific jet tagging algorithms have been developed [97]. These

algorithms are based on the track displacement information with respect to PV for tracks associated with the jet, on the distance of such a track with respect to the axis of the jet, and on the compatibility of this track with secondary vertices reconstructed with algorithms adapted to jet tagging.

Secondary vertices

The reconstruction of secondary vertices is performed on all reconstructed tracks with transverse momentum of $p_T > 0.8$ GeV and longitudinal impact parameter of $d_z < 0.3$ cm, using the inclusive vertex finding (IVF) explained in the following.

1. Track seeds are determined from which the secondary vertex reconstruction can be started. Such tracks are required to have a three-dimensional impact parameter with $d_{3D} \geq 0.05$ cm and a significance of the transverse impact parameter with $d_{xy}/\sigma_{d_{xy}} \geq 1.2$.
2. A track is clustered to a seeding track, if they are closest to each other at the point of their closest approach, and if this distance and the angle between the two tracks fulfills predefined requirements.
3. The tracks of each cluster are fitted with the adaptive vertex fitter [101], which was also used for the reconstruction of primary vertices.
4. After the fit, the distance between PV and each secondary vertex is tested, requiring the transverse and three-dimensional distances to have significances of at least 2.5 and 0.5, respectively. Secondary vertices fulfilling this requirement are selected for further processing.
5. Overlapping vertices are reduced to one vertex, if they share 70% of their tracks or if the significance of the distance between the two vertices is less than 2. For the remaining secondary vertices, tracks being more compatible with PV are removed from the set of tracks associated with the considered secondary vertex.
6. The reduced sets of tracks are refitted, the resulting final secondary vertices are checked again for overlaps, requiring less than 20% of shared tracks for a vertex pair and a distance significance greater than 10.
7. The remaining secondary vertices are associated to jets, if they fulfill $\Delta R < 0.3$ for the jet axis and flight direction of the secondary vertex, which is defined by the vector connecting PV and the secondary vertex.

The most recent discriminator created to identify the jet flavour at CMS is the `DeepJet` tagger [111] based on a deep neural network [112] (DNN). It takes advantage of the high level variables computed for a jet, as well as the properties of each PF candidate and each secondary vertex associated to it. The properties of up to 25 charged PF candidates, up to 25 neutral PF candidates and up to four secondary vertices are provided to the DNN for training.

Inputs to DNN

The high level properties assigned to each jet consist of the following quantities:

- $p_T(jet)$ and $\eta(jet)$,

- the numbers of charged and neutral PF candidates of the jet, N_{PV} and N_{p^0},
- number of primary vertices N_{vtx},
- and quantities related to tracks and secondary vertices associated with the jet.

For each charged PF candidate, track related properties are provided to the DNN, including

- transverse and three-dimensional impact parameters and their significances,
- distance between the track and jet axis at the point of closest approach,
- $\Delta\eta$ and ΔR between the track and jet momentum,
- track momentum in and perpendicular to the direction of the jet axis,
- and quality metrics for the track, like its χ^2.

For neutral PF candidates, the inputs comprise

- the type of the PF candidate, being either a neutral hadron or photon,
- and ratio between the hadronic and total energy.

Input quantities common among all PF candidates are

- the separation in ΔR between the momentum and the jet axis,
- ratio between the p_T of the PF candidate and the $p_T(\text{jet})$,
- weight assigned by the PUPPI method,
- and ΔR between the PF candidate momentum and the flight direction of the associated secondary vertex, if available.

The set of variables related to secondary vertices includes

- p_T of the secondary vertex,
- ΔR between its flight direction and the jet axis,
- number of associated tracks,
- quality of the vertex fit,
- impact parameters and their significances with respect to PV,
- energy ratio between the secondary vertex and the jet,
- angle θ between the momentum $\vec{p}(\text{SV})$ and flight direction of the secondary vertex,
- and the corrected secondary vertex mass, m_{SV}^{corr}.

Based on the invariant mass $m(\text{SV})$ and momentum $p(\text{SV})$ of the secondary vertex derived from its 4-momentum, m_{SV}^{corr} is defined as:

$$m_{SV}^{corr} = \sqrt{m^2(SV) + p^2(SV) \cdot \sin^2(\theta)} + p(SV) \cdot \sin(\theta) \tag{3.15}$$

DNN architecture

The input quantities of charged and neutral PF candidates, and secondary vertices are arranged into arrays of each type. The elements of the array are sorted by increasing significance of their displacement with respect to PV, or by increasing p_T, assuming the

strongest separation power between jet flavours for most displaced PF candidates or secondary vertices.

For the architecture of the DNN, a set of layers is used, which is referred to as a hidden layer. It consists of

- a layer with trainable parameters with the rectified linear unit (ReLU) [113] activation function,
- followed by a batch normalization layer,
- and a dropout layer with a rate of 0.1 [112].

The input arrays of each type are processed through up to four dense hidden layers with a decreasing amount of nodes. The resulting three arrays are processed through a hidden layer containing a recurrent neural network with long short-term memory [112]. This allows to reduce the array of charged PF candidates to 150 DNN features, the array with neutral PF candidates to 50 features, and the array with secondary vertices to 50 features. These three sets of features are concatenated with the set of high level properties of the jet, and together, these features are passed through seven hidden layers with a few 100 nodes per layer, followed by an output layer with seven nodes, activated by the softmax function [114]

$$S(z)_i = \frac{e^{z_i}}{\sum_j e^{z_j}}, \qquad z = (z_1, ..., z_7) \in \mathbb{R}^7. \tag{3.16}$$

The output nodes represent the probability of a jet to correspond to a certain type, as defined in table 3.8. The training of the DNN is performed on a balanced set of simulated jets for each type, with p_T distributions reweighted to the p_T distribution of b-jets.

The cross entropy is chosen as the loss function used within training process, the optimizer for the training is the Adam [115] algorithm, and the training was performed for 50 iterations.

Probability symbol	Jet	
$\mathbb{P}_{bb}$		two or more b hadrons
$\mathbb{P}_{b_{lep}}$		exactly one b hadron decaying into leptons
$\mathbb{P}_b$	contains	exactly one b hadron decaying into hadrons
$\mathbb{P}_{cc}$		two or more c hadrons
$\mathbb{P}_c$		exactly one c hadron
$\mathbb{P}_{uds}$	is induced by	light quarks
$\mathbb{P}_g$		a gluon

Table 3.8.: Definitions of jet types used for the classification with the `DeepJet` discriminator. The jet types are defined in an exclusive way.

In consequence, the resulting probability, that the jet is a b-jet, can be computed as $\mathbb{P}_{b\text{-jet}} = \mathbb{P}_{bb} + \mathbb{P}_{b_{lep}} + \mathbb{P}_b$. A jet is considered as b-tagged, if the probability $\mathbb{P}_{b\text{-jet}}$ is greater than the threshold of the chosen working point, given in table 3.9. The loose, medium and tight working points are defined to have a mistagging rate of 10%, 1% and 0.1%, respectively, for jets induced by light quarks or gluons with p_T between 80 and 120 GeV.

Working point	Requirement on the probability $\mathbb{P}_{\text{b-jet}}$		
	2016	2017	2018
loose	> 0.06	> 0.05	> 0.05
medium	> 0.31	> 0.30	> 0.28
tight	> 0.72	> 0.75	> 0.73

Table 3.9.: Definitions of year dependent working points for tagging b-jets with the `DeepJet` discriminator. Detail are given in the text.

3.2.8. Hadronic Decays of Tau Leptons

The reconstruction of hadronic decays of τ leptons, denoted as τ_h, starts with a jet as seeding object [98]. It is based on the hadron plus strips (HPS) algorithm, exploiting the specific signatures of τ_h with one or more charged hadrons and additional neutral hadrons. The neutral hadrons are mostly pions, π^0, which decay into pairs of photons before reaching active detector material. These photons have a high conversion probability, such that electron pairs can appear in the τ_h final state. The signature of the photons and electron pairs from photon conversions are clustered into strips in the (η, ϕ) plane. Up to three charged hadrons may be identified for a τ_h, as well as up to two neutral pions. The decay mode (DM) of τ_h is computed by counting the number of charged hadrons, $N_{h^\pm}$, identified within the seeding jet and the number of neutral pions N_{π^0}, given as

$$DM = 5 \cdot (N_{h^\pm} - 1) + N_{\pi^0}, \qquad N_{h^\pm} \in \{1, 2, 3\}, \qquad N_{\pi^0} \in \{0, 1, 2\}. \qquad (3.17)$$

Decay mode values $DM \in \{0, 1, 2, 10, 11\}$ correspond to existing hadronic decays of τ leptons, whereas the remaining values $DM \in \{5, 6, 7\}$ may occur, if for example one of the charged hadrons is not reconstructed. Since these decay modes are highly contaminated by QCD multijet background, the decay modes $DM \in \{5, 6, 7\}$ are rejected in the τ_h identification used for this thesis and are not considered in the following.

To be assigned as a charged hadron to τ_h, a charged hadron within the seeding jet is required to have a transverse momentum $p_T > 0.5$ GeV and to be compatible with PV by fulfilling a requirement on its transverse impact parameter of the track, $d_{xy} < 0.1$ cm.

To recover as much energy of τ_h deposited in the ECAL as possible, a dynamic strip reconstruction is performed. Particles coming from nuclear interactions of the involved charged hadrons with the detector material, as well as the electrons and photons from multiple scattering and bremsstrahlung from the photon conversions of $\pi^0 \to \gamma\gamma$ decays, are taken into account by this technique.

The strip reconstruction starts with the electron or the photon (e/γ) candidate with the highest p_T, which has not been assigned to any strip yet. Its position in the (η, ϕ) plane and transverse momentum are assigned to the new strip. In the following iterations in the reconstruction of this strip, the e/γ candidate with the next highest p_T is taken to check requirements on its distance to the current strip in the (η, ϕ) plane for $\Delta\eta$ and $\Delta\phi$, given as

$$\Delta\eta < f(p_T(e/\gamma)) + f(p_T(\text{strip})), \qquad f(p_T) = 0.2 \cdot \left(\frac{p_T}{1 \text{ GeV}}\right)^{-0.66}$$

$$\Delta\phi < g(p_T(e/\gamma)) + g(p_T(\text{strip})), \qquad g(p_T) = 0.35 \cdot \left(\frac{p_T}{1 \text{ GeV}}\right)^{-0.71} \qquad (3.18)$$

The functions f and g were derived from the distances of simulated e/γ candidates to the corresponding simulated τ_h in η and ϕ, depending on $p_T(e/\gamma)$. In that way, a dynamic adaption of the $(\Delta\eta, \Delta\phi)$ window is established to collect e/γ candidates into a strip. If the considered e/γ candidate fulfills the requirements in equation 3.18, it is merged into the strip cluster. The size of the new strip is checked to be within the boundaries $\Delta\eta_{strip} \in [0.05, 0.15]$ and $\Delta\phi_{strip} \in [0.05, 0.3]$, and its position and p_T are updated, using a p_T weighted average for the position defined as

$$
\begin{aligned}
\eta_{strip} &= \frac{1}{p_T(strip)} \cdot \sum_{e/\gamma \in strip} p_T(e/\gamma) \cdot \eta_{e/\gamma} \\
\phi_{strip} &= \frac{1}{p_T(strip)} \cdot \sum_{e/\gamma \in strip} p_T(e/\gamma) \cdot \phi_{e/\gamma}
\end{aligned}
\tag{3.19}
$$

The updated strip is propagated to the merging iteration of the next e/γ candidate highest in p_T within the dynamic $(\Delta\eta, \Delta\phi)$ window. The procedure is repeated, until no e/γ candidates are present within the $(\Delta\eta, \Delta\phi)$ window to be added to the currently considered strip. In that case, the elements of the reconstructed strip are removed from the list of available e/γ candidates for the considered τ_h candidate and the reconstruction of the next strip is initiated, beginning with the e/γ candidate with the highest p_T left in the list.

After both the charged hadron candidates and strips are reconstructed, they are combined to several τ_h hypotheses, depending on the best matching decay mode. For the simplest decay mode, DM = 0, for which only one charged hadron is available and no strips are reconstructed, the mass of the charged hadron candidate is assigned directly to the mass of the visible decay products of the τ lepton, m_{τ_h}. For the remaining decay modes, it is required, that m_{τ_h} is within a decay mode dependent mass window, given as

$$
\begin{aligned}
&\text{DM} = 1,\ h^\pm\pi^0: &&m_{\tau_h} \in (0.3\ \text{GeV} - \Delta m_{strip},\ m^{max}_{DM=1}) \\
&\text{DM} = 2,\ h^\pm\pi^0\pi^0: &&m_{\tau_h} \in (0.4\ \text{GeV} - \Delta m_{strip},\ m^{max}_{DM=2}) \\
&\text{DM} \in \{10, 11\},\ h^\pm h^\mp h^\pm(\pi^0): &&m_{\tau_h} \in (0.8\ \text{GeV}, 1.5\ \text{GeV})
\end{aligned}
$$

$$
\begin{aligned}
m^{max}_{DM=1} &= 1.3\ \text{GeV} \cdot \sqrt{\frac{p_T(\tau_h)}{100\ \text{GeV}}} + \Delta m_{strip}, &&m^{max}_{DM=1} \in [1.3\ \text{GeV}, 4.2\ \text{GeV}] \\
m^{max}_{DM=2} &= 1.2\ \text{GeV} \cdot \sqrt{\frac{p_T(\tau_h)}{100\ \text{GeV}}} + \Delta m_{strip}, &&m^{max}_{DM=2} \in [1.2\ \text{GeV}, 4\ \text{GeV}]
\end{aligned}
$$

$$
\begin{aligned}
\Delta m_{strip} &= \sqrt{\left(\frac{\partial m_{\tau_h}}{\partial \eta_{strip}} \cdot f(p_T(strip))\right)^2 + \left(\frac{\partial m_{\tau_h}}{\partial \phi_{strip}} \cdot g(p_T(strip))\right)^2} \\
\frac{\partial m_{\tau_h}}{\partial \eta_{strip}} &= \frac{p_z(strip) \cdot E_{\tau_h} - p_z(\tau_h) \cdot E_{strip}}{m_{\tau_h}} \\
\frac{\partial m_{\tau_h}}{\partial \phi_{strip}} &= \frac{(p_x(\tau_h) - p_x(strip)) \cdot p_y(strip) - (p_y(\tau_h) - p_y(strip)) \cdot p_x(strip)}{m_{\tau_h}},
\end{aligned}
\tag{3.20}
$$

where Δm_{strip} corresponds to the amount of mass added to the hadronic system of the τ lepton by the e/γ candidates from the strips of the τ_h. The upper thresholds $m^{max}_{DM=1}$ and

$m_{DM=2}^{max}$ are restricted to specified ranges.

After this procedure, several τ_h candidates available for each jet undergo further quality criteria. At first, the total charge of the charged hadron candidates is required to be equal to ±1. Additionally they must be within the signal cone, $\Delta R < \Delta R_{sig}$, defined as

$$\Delta R_{sig} = 3 \text{ GeV}/p_T(\tau_h), \qquad \Delta R_{sig} \in [0.05, 0.1], \qquad (3.21)$$

where it is limited to a specified range. The position of the strip is required to be within the signal cone of the τ_h candidate, whereas the strip area itself may exceed it. If multiple τ_h candidates are still left after imposing these quality criteria, the one with the highest p_T is chosen to have at most one reconstructed τ_h per jet.

The signature of a τ_h candidate can also be caused by jets, electrons and muons. To reduce the amount of misidentified τ_h candidates, a multivariate identification procedure has been developed [116], based on a convolutional deep neural network [112] (DNN). The DNN is trained on balanced sets of simulated candidates for the four classes to be distinguished: genuine τ_h candidates and misidentified τ_h candidates from jets, electrons or muons. These τ_h candidates are selected to have $p_T > 20$ GeV, $|\eta| < 2.3$, and a longitudinal impact parameter $|d_z| < 0.2$ cm.

For the training, both the high level information based on the properties of the reconstructed τ_h candidate, and the information from detector subsystems assigned to the PF candidates of the τ_h or the nearby reconstructed electrons and muons are used. To account for the amount of contributions from PU, the pileup density ρ is added to the set of variables used for training. All variables are transformed to values in $[-1, 1]$.

High level information

The high level properties provided with the τ_h candidate can be grouped as follows:

- Quantities related to the 4-momentum of τ_h, including its constituents $p_T(\tau_h)$, η_{τ_h}, ϕ_{τ_h} and m_{τ_h}, and quantities derived from it, like $E_{\tau_h}/p_T(\tau_h)$, and the ratio between the energy of the τ_h deposited in the ECAL and total energy, $E_{\tau_h}^{ECAL}/E_{\tau_h}$.
- Number of constituents of the τ_h candidate, $N_{h^\pm}$, N_{π^0}, and N_γ.
- Sums of p_T of PF candidates around τ_h within $\Delta R < 0.3$ or $\Delta R < 0.5$, as introduced in subsection 3.2.2.
- Quantities related to the impact parameters, their significances, and quality of the track of the charged hadron with the highest p_T, that is part of τ_h.
- Distance in (η, ϕ) of τ_h constituents with respect to the τ_h candidate.
- Pileup density ρ.

Information on the surrounding environment of the τ_h candidate

All reconstructed particles, that are within the signal cone $\Delta R < \Delta R_{sig}$ or isolation cone $\Delta R < 0.5$ with respect to the τ_h candidate, are considered to compile the information on its surrounding environment. The position of nearby particles is mapped onto 11×11 and 21×21 grids in the $(\Delta\eta, \Delta\phi)$ plane for the signal and isolation cones. The sizes of the cells in the grids are chosen to be $(\Delta\eta, \Delta\phi) = (0.02, 0.02)$ for the signal and $(\Delta\eta, \Delta\phi) = (0.05, 0.05)$ for the isolation cone.

Each property of the reconstructed particles is filled into the grids based on the $(\Delta\eta, \Delta\phi)$

values. In that way, images of the surrounding environment of the τ_h candidate are constructed from properties of nearby particles. The particles are separated into three groups, such that six grids in total are created from the information on the reconstructed particles. The groups are summarized as

- muons (subsections 3.2.3 and 3.2.5),
- electrons and photons (subsections 3.2.4 and 3.2.5),
- and charged and neutral hadrons (subsection 3.2.5).

DNN architecture

As in case of the `DeepJet` tagger described in subsection 3.2.7, a set of layers is used for the DNN architecture, which is referred to as a hidden layer. It contains

- a batch normalization layer,
- followed by a layer with trainable parameters and a parametric rectified linear unit (PReLU) [113] activation function,
- and a dropout layer with a rate of 0.2.

The architecture of the DNN can be split into three main steps.

At first, the set of quantities of each cell of the six grids, extended with the $p_T(\tau_h)$, η_{τ_h} and ρ, and the set of high level quantities are processed through several dense hidden layers of the same size independently from each other.

To connect the individual grid cells with each other, convolution hidden layers are used, merging a 3×3 block of cells into a single number in each hidden layer.

In the last step, the convoluted features from the six grids and the features from high level properties provided with τ_h are concatenated and processed through four dense hidden layers, followed by an output layer with four nodes and a softmax activation function. From the resulting four probabilities $\mathbb{P}_{\tau_h}$, $\mathbb{P}_{jet}$, $\mathbb{P}_e$ and $\mathbb{P}_\mu$, a discriminator $D_{\tau_h}^\alpha$ between being a genuine τ_h candidate or one of the sources of misidentification α is computed by

$$D_{\tau_h}^\alpha = \frac{\mathbb{P}_{\tau_h}}{\mathbb{P}_{\tau_h} + \mathbb{P}_\alpha}, \qquad \alpha \in \{jet, e, \mu\} \tag{3.22}$$

The trainable parameters of the DNN are optimized by the Adam algorithm with the Nesterov momentum as metric, using a custom loss function based on the focal loss [117]. For the application, the DNN after a training process of seven epochs is used. Different working points were defined based on the discriminators $D_{\tau_h}^\alpha$, given in table 3.10.

Working point name	Requirement on the discriminator		
	$D^{jet}_{\tau_h}$	$D^e_{\tau_h}$	$D^\mu_{\tau_h}$
VVVLoose	> 0.260	> 0.063	
VVLoose	> 0.425	> 0.169	
VLoose	> 0.598	> 0.363	> 0.106
Loose	> 0.785	> 0.682	> 0.216
Medium	> 0.883	> 0.885	> 0.555
Tight	> 0.931	> 0.968	> 0.875
VTight	> 0.957	> 0.986	
VVTight	> 0.973	> 0.993	

Table 3.10.: Definitions of the working points for the discriminators between the genuine τ_h candidate and a misidentified τ_h candidate. The efficiency to recognize a genuine τ_h candidate is highest for the VVVLoose working point, decreasing with each row in the table and lowest for the VVTight working point. For the discrimination against muons, only four working points were defined.

3.3. Trigger System

The rate of all proton-proton collision events happening each 25 ns is too high to be stored. Therefore, a trigger system is required to reduce the amount of data by selecting events of interest for measurements of SM particles or searches for new physics. The trigger is concepted in two parts. The Level 1 (L1) trigger is a hardware-based trigger taking advantage of the possibility to construct specific algorithms with field programmable gate arrays (FPGAs). The rate is reduced from 40 MHz to 100 kHz by the L1 trigger with a decision whether to keep an event or not taken within less than 1 µs. The second part of the trigger system, the high level trigger (HLT), is purely software-based running on a computer farm close to the CMS detector. The HLT reduces the rate further to 100 Hz.

3.3.1. Hardware-Based Level 1 Trigger
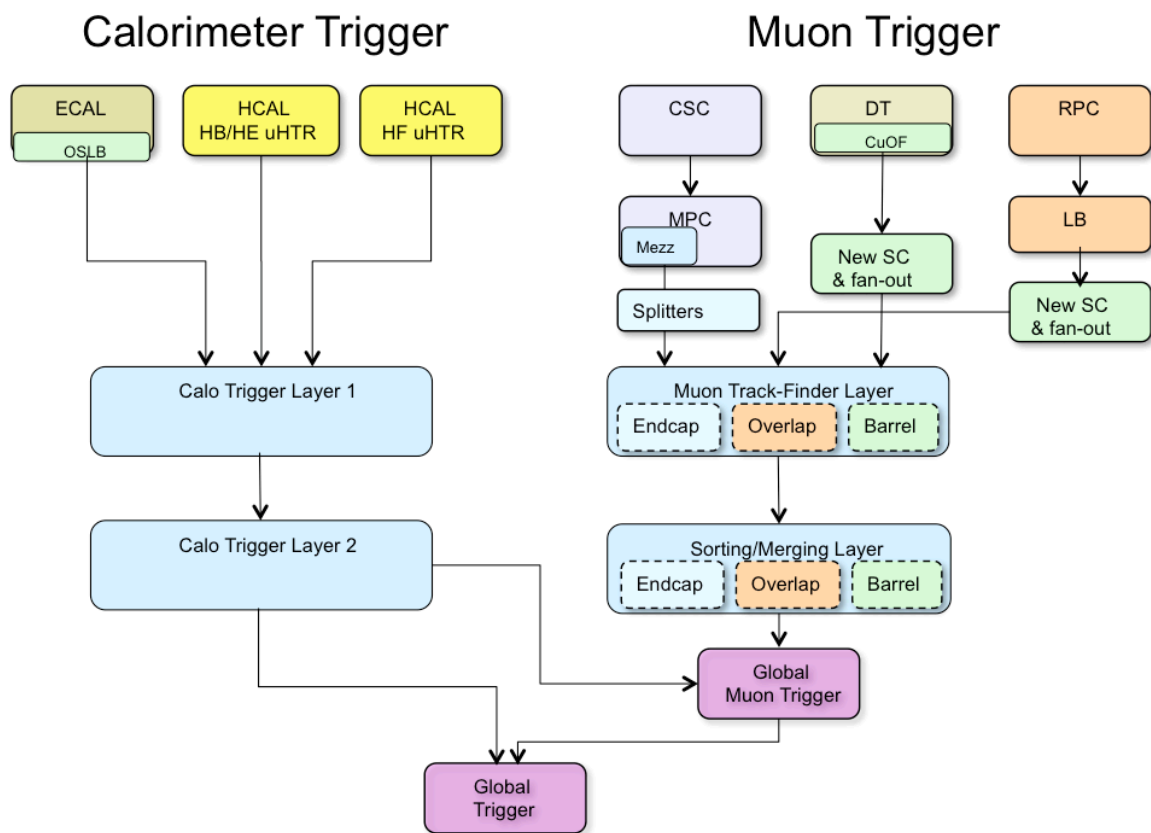
Figure 3.9.: A workflow scheme for the upgraded Level 1 trigger at CMS [83].

The workflow of the hardware-based Level 1 trigger including the corresponding updates installed before 2016 is shown in figure 3.9. To allow a decision within 1 µs, the information from the calorimeters and the muon detection subsystems are used, while the tracker is omitted in the concept of the L1 trigger. The information from the calorimeters and the muon system is at first processed separately for each of the two systems and is unified at the end into a global L1 trigger decision. In case that at least one of the L1 algorithms accepts the event, the full detector readout is stored for the HLT. The global L1 trigger is flexible enough to combine the information of several L1 physics objects, for example a

lepton pair from a Higgs or gauge boson decay.

Within the L1 calorimeter trigger, the energy deposits from the ECAL and HCAL are processed through two trigger layers. In the first layer, the energy deposits in the calorimeters are calibrated and sorted, whereas the second layer is responsible for the reconstruction of physics objects such as electrons, photons, τ_h candidates, or jets, and various energy sums used for isolation requirements or an estimate of p_T^{miss} in the detector. The reconstructed physics objects are required to fulfill predefined selection criteria, for example on their quality, isolation, p_T or η.

The L1 muon trigger takes advantage of the redundant measurements made by the three detector systems, DTs, CSCs and RPCs. The pre-processed hits in the muon detectors are passed to three different track finder algorithms for the barrel region with $|\eta| < 0.83$, the overlap region, where all three detectors are available, and the endcap region with $|\eta| > 1.2$. The reconstructed tracks are then processed through the next layer sorting the muons, removing duplicates and applying selection criteria. In the final step of the muon trigger, calorimeter information is used for the remaining muon candidates to check for their isolation.

3.3.2. Software-Based High Level Trigger

The high level trigger (HLT) system, also referred to as online reconstruction, is purely software-based, with similar reconstruction algorithms as introduced in section 3.2, but optimized to fulfill the constraints given by the fixed output rate of a few 100 Hz. The L1 physics objects are used as seeds to start the reconstruction with higher granularity and precision.

For muons [92], one of the used algorithms takes the L1 seeds to start the standalone muon reconstruction and match the resulting muons with the tracker information in a limited readout region defined by the muon trajectory extrapolated from the muon detectors to the inner tracking system. If tracks are found to be within this region, the track parameters are updated to match a global muon trajectory. Another muon reconstruction algorithm similar to tracker muon algorithm, matches tracks to the L1 seeds within an (η, ϕ) window. Once the muons are reconstructed, isolation variables are computed from ECAL clusters, HCAL clusters and charged tracks with the pileup correction based on effective areas, as introduced in equation 3.4. The trigger decisions are based on requirements on the muon isolation, p_T and η.

In case of the electrons, ECAL clusters are reconstructed around the electromagnetic L1 seeds and tracks in the surrounding area are matched to these clusters. Identification and isolation criteria introduced in subsection 3.2.4 are applied to derive trigger decisions for electrons.

Before an optimized version of the HPS algorithm was introduced and commissioned during the 2018 data-taking period [118], a cone-based reconstruction of τ_h candidates was performed at the HLT level [98]. The energy depositions in the ECAL and HCAL within $\Delta R < 0.8$ around each L1 τ_h candidate seed are considered. Narrow jets are reconstructed using the anti-k_T algorithm with the distance parameter r = 0.2 to build preliminary τ_h candidates. Additional isolation requirements are imposed on these candidates, based on tracks reconstructed from pixel detector hits around the preliminary τ_h candidate. The final τ_h reconstruction is then started from PF jets reconstructed near the remaining preliminary τ_h candidates. The PF algorithm used here is optimized for the HLT reconstruction. A p_T

dependent signal cone and isolation cone are defined to reconstruct the final τ_h candidate and to compute isolation variables and transverse energy sums, based on the PF candidates of the used jet. These variables, as well as p_T and η of the final τ_h candidate are used to derive the trigger decision.

The individual sets of requirements to create a trigger decision for the HLT are referred to as HLT paths, whereas the physics objects reconstructed in this process as HLT objects.

4. Preparations for the H $\to \tau\tau$ analysis

For the H $\to \tau\tau$ analysis presented in this thesis, the data collected at CMS between the years 2016 and 2018 of the Run 2 data-taking is used. The integrated luminosity of the data certified as good for physics analyses was measured separately for each data-taking year. The measured values are $L_{int.}^{2016} = 35.9$ fb^{-1}, $L_{int.}^{2017} = 41.5$ fb^{-1} and $L_{int.}^{2018} = 59.7$ fb^{-1} with relative uncertainties of 2.5%, 2.3% and 2.5% for the data-taking years 2016, 2017 and 2018, respectively [119–121]. A total amount of 137 fb^{-1} of recorded data is used for the analysis.

τ lepton decay	fraction	$\tau\tau$ final state	fraction	$\tau\tau$ final state	fraction
$\tau \to \mu\nu_\tau\nu_\mu$	17.39%	$\mu\tau_h(3\nu)$	22.5%	$\tau_h\tau_h(2\nu)$	42%
$\tau \to e\nu_\tau\nu_e$	17.82%	$e\tau_h(3\nu)$	23.1%	$ee(4\nu)$	3%
$\tau \to \tau_h\nu_\tau$	64.79%	$e\mu(4\nu)$	6.2%	$\mu\mu(4\nu)$	3.2%

Table 4.1.: Branching fractions of the τ lepton decays and $\tau\tau$ final states [32].

As shown in table 4.1, there are six possible final states for $\tau\tau$ events, as can be obtained from the decays of the τ lepton. The most probable $\tau\tau$ final state is $\tau_h\tau_h$ with only two neutrinos, that contribute to p_T^{miss}, such that the $\tau_h\tau_h$ pair carries a significant fraction of the $\tau\tau$ pair energy. The $e\tau_h$ and $\mu\tau_h$ following next profit from a good energy and momentum resolution of reconstructed electrons and muons, having at the same time a large branching fraction. The $e\mu$ final state also profits from the good resolution of electrons and muons, but additionally to the small branching fraction, it has a large contribution to p_T^{miss} from neutrinos, such that the energy of the $e\mu$ pair has a larger spread.
The ee and $\mu\mu$ final states are not considered as sensitive to H $\to \tau\tau$, since the H $\to \tau\tau \to$ ee or H $\to \tau\tau \to \mu\mu$ signal is expected to be suppressed by the Z $\to$ ee and Z $\to \mu\mu$ processes. In the following, the preparations preliminary to the H $\to \tau\tau$ analysis will be discussed, including the expected contributions of physics processes, selection of the sensitive final states, and the corresponding corrections and uncertainties assigned to the expected processes.

4.1. Background Estimation Methods

The main contributions to the signal sensitive final states $\mu\tau_h$, $e\tau_h$, $\tau_h\tau_h$ and $e\mu$ summarized in table 4.2 comprise the following processes:

- The production of a Z boson decaying into the desired Z $\to \tau\tau$ final state or other leptonic final states which are not identified correctly, mainly from Z $\to$ ee or Z $\to \mu\mu$ decays. The Z boson may be produced by a fermion pair annihilation, or a

| | ττ final state | | | |
Background process	$e\tau_h$	$\mu\tau_h$	$\tau_h\tau_h$	$e\mu$
$Z \to \tau\tau$	27%	46%	33%	20%
$Z \to \ell\ell$, $\ell \in \{e, \mu\}$	9%	2%	1%	1%
$t\bar{t}$	18%	13%	< 1%	54%
$W \to \ell\nu$, $\ell \in \{e, \mu\}$	42%	36%	< 1%	3%
QCD			66%	11%
Di-boson & single-t	4%	3%	< 1%	11%

Table 4.2.: Background contributions to ττ final states selected for the data-taking year 2018.

fusion of two electroweak vector bosons, with typically two well separated quark jets accompanying the Z boson in the final state.

- The production of a W boson contributes in particular to the semileptonic final states $\mu\tau_h$ and $e\tau_h$, where the muon or the electron from the W boson is paired with a jet misidentified as a τ_h candidate. Also the W boson is produced either by a fermion pair annihilation or a fusion of two electroweak vector bosons.
- The top pair production contributes mostly to the events with b-tagged jets. The subsequent decays of the two W bosons resulting from the $t\bar{t}$ pair decay define the signal final state the process contributes to, mostly appearing in $e\mu$.
- Contributions from the non-resonant production of two vector bosons or from the single top production are also most prominent in the $e\mu$ final state.
- Remaining events are expected to originate from events with multijet topology, exclusively from the strong interactions, where the jets are misidentified as the signal final states. This background has a significant contribution to the $\tau_h\tau_h$ final state, and is referred to as the QCD multijet background or just QCD.

All these processes are estimated using techniques described in the following subsections.

4.1.1. Genuine ττ final states

The τ embedding technique [122] to estimate genuine ττ final states was already used in public Run 2 analyses of CMS [19, 21]. As illustrated in figure 4.1, the method consists of four steps. At first, $Z \to \mu\mu$ events are selected. Then, the reconstructed hits in the inner tracking system and the muon detector subsystem from the muon, and the energy deposits in the calorimeters associated to the muon trajectory are removed from the reconstructed event record. This step is referred to as $Z \to \mu\mu$ cleaning. The kinematic properties of the selected $\mu\mu$ pair are used to simulate the decay of a ττ system in an otherwise empty detector. The modified selected event and the simulated ττ decay are merged into a single, hybrid event at the level of reconstructed tracks and calorimeter deposits, followed by the reconstruction of physics objects based on the hybrid information.
There are several advantages of this background estimation method, the most important ones are mentioned in the following:

- Estimated processes are not affected by the luminosity uncertainty, since the τ
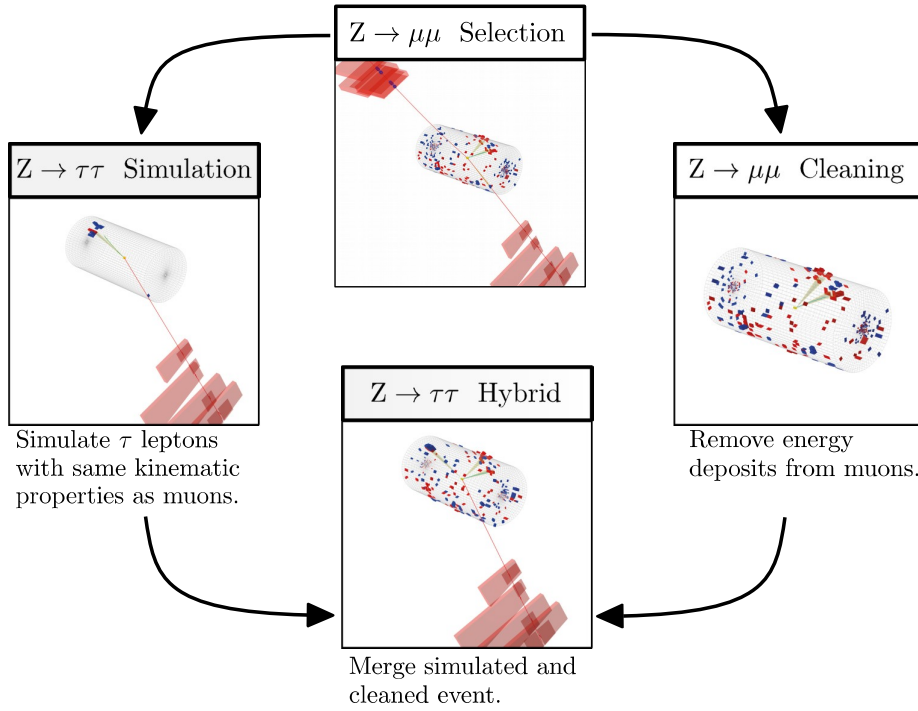
Figure 4.1.: A schematic view of the τ embedding method consisting of four steps [122].

- embedded dataset scales with the recorded data.
- The description of interactions from PU, the underlying event, and the jets originate from data, such that no corrections are required.
- All data-taking specific effects, like a temporary outage of a detector module, unexpectedly large detector noise, or effects because of the detector aging, are naturally included in the τ embedded event record.

The effects introduced by the τ embedding technique due to the replacement of the selected muons from data by simulated τ lepton decays, as well as corresponding corrections and uncertainties specific to the τ embedding technique are discussed for each of the four steps in more detail in the following.

Muon Pair Selection

A muon pair is required to be of a good quality on one hand, but on the other hand, its selection should loose enough to reduce biases that may be introduced by it. Furthermore, the requirements should match the ones from analyses using the samples derived from the τ embedding method.

Globally reconstructed muons are selected with $p_T = 17(8)$ GeV for the (sub-)leading muon, $|\eta| < 2.4$, and an impact parameter in direction of the beam axis of $dz < 0.2$ cm. These muons are required to be matched to an HLT path with similar requirements, be associated to PV, and to fulfill the very loose working point of I_{rel}^{track} at the HLT level. Furthermore, the $\mu\mu$ system selected by the HLT path is required to have a mass of $m_{\mu\mu} > 3.8(8)$ GeV for the 2016 (2017 and 2018) data-taking year(s). The reconstructed muon pair passing all these requirements should have an invariant mass $m_{\mu\mu} > 20$ GeV, and the two muons should be of opposite charge. If multiple pairs fulfill the requirements, the pair closest to

the Z boson mass is chosen to be used for the further steps.
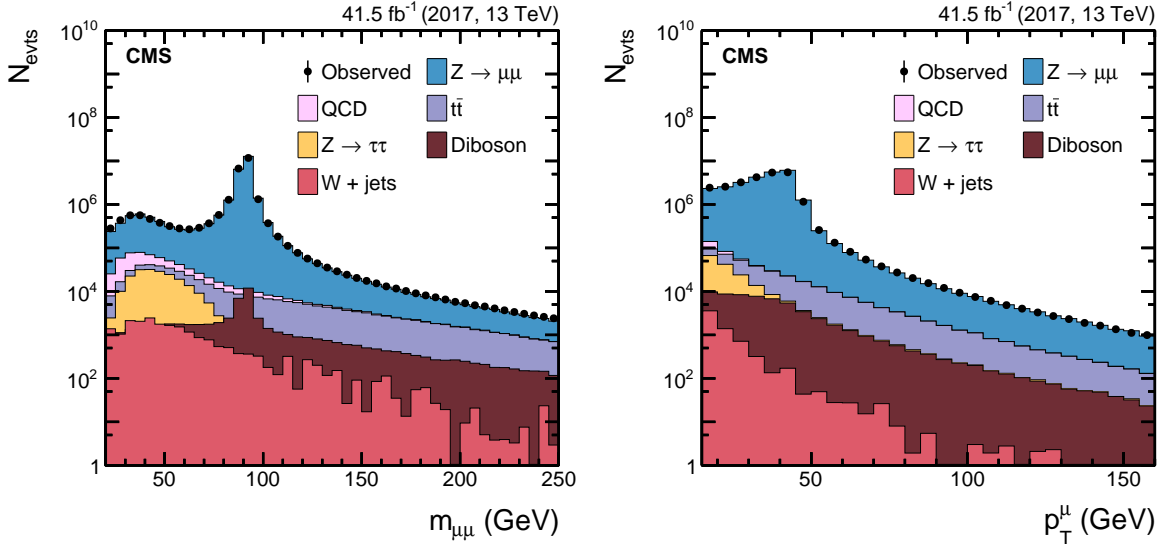
Figure 4.2.: Distributions of the invariant mass of the di-muon system, $m_{\mu\mu}$, on the left and the transverse momentum of the subleading muon, p_T^μ, on the right, with the expected contributions to the selected di-muon events of the 2017 data [122].

As shown in figure 4.2, the major contribution to this selection is the $Z \rightarrow \mu\mu$ decay with a fraction of 97% of the total amount of expected events. However, at higher values of $m_{\mu\mu}$ and p_T^μ, other processes start to contribute, most prominently the production of top quark pairs, $t\bar{t}$, and the production of two vector bosons or a single top quark, referred to as Diboson. If at least one b-tagged jet is required in addition, the contribution from $t\bar{t}$ is increased up to 25%. Such contributions contain not only the desired decays into prompt muons, but also muons from τ lepton decays, and particles misidentified as muons. These contributions are found to have a negligible impact on the final set of the hybrid τ embedded events.

Less important are contributions located at lower muon p_T, like the $Z \rightarrow \tau\tau \rightarrow \mu\mu$ process, the production of a W boson accompanied by jets (W + jets), and the QCD multijet background. Since the selected muons of these processes are replaced by τ leptons, which decay into final states with at least one neutrino, both $m_{\mu\mu}$ and muon p_T are shifted to lower values. In consequence, such events have a negligible impact on the final set of hybrid τ embedded events.

To account for the $\mu\mu$ contributions in addition to the $Z \rightarrow \mu\mu$ decay in the final set of τ embedded samples, which are replaced by $\tau\tau$ pairs, corresponding contributions estimated with simulated samples are rejected to avoid double-counting. These comprise genuine $\tau\tau$ pairs from $t\bar{t}$ and Diboson.

In case of $t\bar{t}$, an uncertainty is introduced to the τ embedded samples, in which the estimated contribution to genuine $\tau\tau$ pairs is modified by an addition or subtraction of simulated $t\bar{t}$ events scaled with 0.1.

The discussed $\mu\mu$ selection can introduce biases, the most prominent example is the muon reconstruction and identification efficiency as a function of the muon η. To demonstrate this, the efficiency measurements of the loose and tight working points of the muon ID are illustrated in figure 4.3. The tight working point (left) is similar to the $\mu\mu$ selection, since
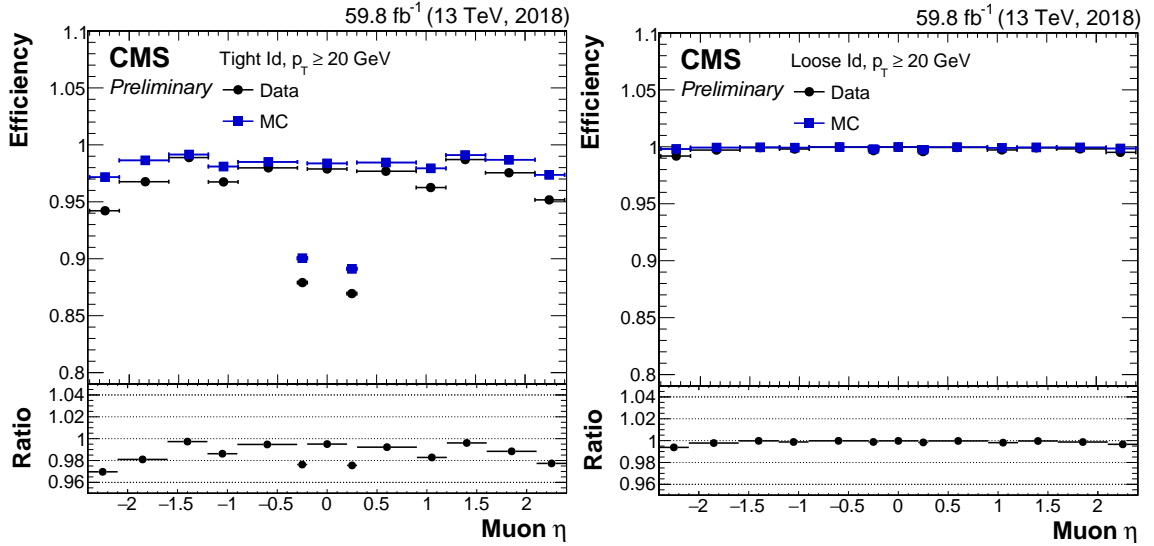
Figure 4.3.: Measurements of the muon identification efficiency for the tight (left) and loose (right) working points of muon ID as a function of muon η for 2018 data in black and for corresponding simulation (MC) in blue [123].

only globally reconstructed muons are selected. In contrast to that, the loose working point (right) selects tracker muons in addition.

The measured efficiency of the loose working point is mostly flat as function of muon η, whereas the efficiency of the tight working point drops for certain η regions not well covered by the muon detector subsystem.

To compensate for this effect [124], the data efficiency $\epsilon_{\mu\mu}$ of the muon pair selection used for τ embedding is measured as a function of muon p_T and $|\eta|$. A correction is introduced to the τ embedded events as the inverse of the total selection efficiency, $1/\epsilon_{\mu\mu}$, computed for the reconstructed ττ final state matched to the two simulated τ leptons replacing the two muons from data. A normalization uncertainty of 4% is assigned to this correction, corresponding to its total averaged magnitude.

The total selection efficiency $\epsilon_{\mu\mu}$ is computed from two types of efficiencies: the efficiency of the HLT requirements, ϵ_{HLT}, and the efficiency of selecting a globally reconstructed muon $\epsilon_{sel.}$. The efficiency of the HLT requirements is measured separately for each of the two muon legs building the HLT decision, one leg with the higher threshold $p_T > 17$ GeV, ϵ_{17}, and the other leg with the lower threshold $p_T > 8$ GeV, ϵ_8, using the tag and probe technique. The efficiency of the HLT requirements ϵ_{HLT} and the total selection efficiency $\epsilon_{\mu\mu}$ are computed in the following way given two reconstructed muons as input which are denoted with μ_1 and μ_2:

$$\epsilon_{HLT} = \epsilon_8(\mu_1) \cdot \epsilon_{17}(\mu_2) + \epsilon_8(\mu_2) \cdot \epsilon_{17}(\mu_1) - \epsilon_{17}(\mu_1) \cdot \epsilon_{17}(\mu_2)$$
$$\epsilon_{\mu\mu} = \epsilon_{HLT} \cdot \epsilon_{sel.}(\mu_1) \cdot \epsilon_{sel.}(\mu_2)$$

The subtraction of the third term in the equation for ϵ_{HLT} avoids double-counting in the overlap region of the two possible combinations, how the muons could invoke the trigger decision, expressed by the first two terms in the equation. The measured efficiencies ϵ_8, ϵ_{17} and $\epsilon_{sel.}$ are shown in figure 4.4 for 2018 data selected for τ embedding. As expected, the

efficiencies are lower for $|\eta_\mu| \in [0.1, 0.3)$ compared to the efficiencies in the $|\eta_\mu| \in [0.3, 0.8)$ region.
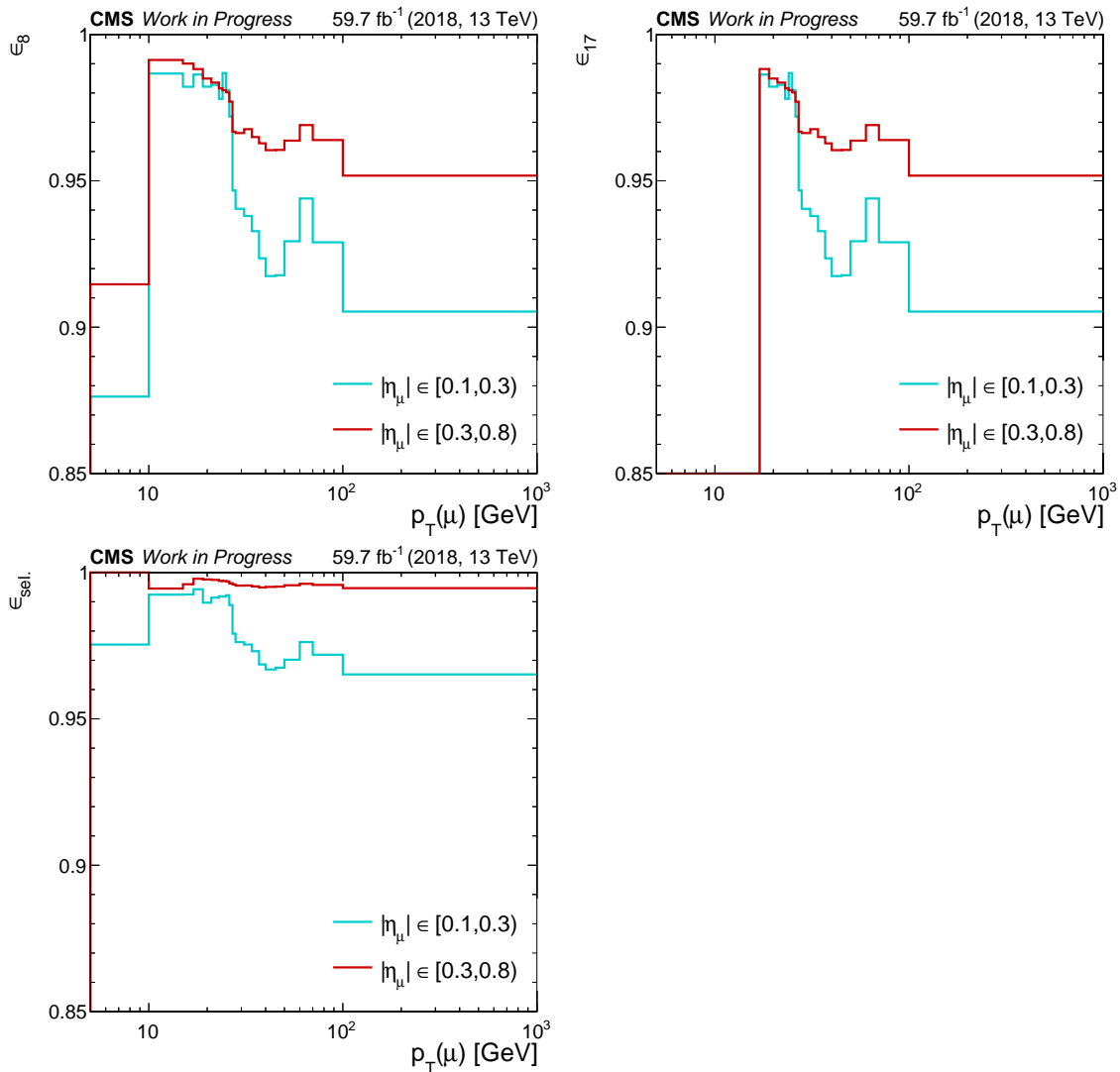
Figure 4.4.: Measurements of the muon efficiencies (top left) ϵ_8, (top right) ϵ_{17} and (bottom left) $\epsilon_{sel.}$ as functions of $p_T(\mu)$ for different regions of $|\eta_\mu|$.

Muon Pair Cleaning

The reconstructed hits in the inner tracking system and the muon chambers associated to the two selected muons are removed from the event record and the calorimeter energy deposits, which are crossed by the muon trajectory are corrected for the expected energy deposited by the muon as a minimum ionizing particle (MIP). After the removal, a part of the reconstruction algorithms is applied to the cleaned event record to obtain the remaining tracks and calorimeter clusters needed for the last step of the τ embedding technique. The main advantage of the removal of the hits and the energy deposits associated with the selected muons is that it is performed at an early level of the reconstruction. At this level, the complexity of the event record is small compared to a completely reconstructed

event, discussed in section 3.2. In consequence, the complex connections between different reconstructed elements, like tracks, PF clusters or jet constituents, can be constructed from the cleaned event record in a straight-forward way using the same reconstruction algorithms. Residual effects of the $Z \rightarrow \mu\mu$ cleaning were studied in detail and are discussed in the following.

If the reconstructed hits of the tracks in the inner tracking system or the muon chambers are shared among multiple tracks, the cleaning of a shared reconstructed hit will result in a remaining track with a lower quality or it will not be reconstructed. This effect may persist after the injection of simulated τ leptons, because their visible decay products could move into a different direction than the original muons. Such tracks are reconstructed in one of the latest iterations of the track reconstruction, as discussed in subsection 3.2.1, and expected to appear within jets. For this reason, possible detoriations by the $Z \rightarrow \mu\mu$ cleaning are therefore neglected. However, for future high luminosity collisions with much more tracks expected in the inner tracking system, this effect has to be reassessed. The energy deposits, which are removed from the calorimeters, correspond mainly to ionization induced by traversing muons. Bremsstrahlung photons, which are produced through the interaction of the muons with the detector material, and which enter the calorimeters not in the vicinity of the muon trajectory, are not recovered by the muon reconstruction algorithm, and therefore, are not removed from the data event record. In consequence, these energy deposits would remain in the event and introduce differences in the energy surrounding the embedded leptons. In that way, the remaining energy deposits have an influence on p_T sums, used for example to compute the lepton isolation. The introduced differences were studied and found to be of about a few 100 MeV in the total energy sum around the embedded lepton, which is small enough to be neglected compared to the statistical accuracy of the used data.

Simulation of Lepton Pairs

In addition to the simulation of $\tau\tau$ final states, dedicated control samples are provided for validation purposes, in which the selected muons are replaced by simulated electrons or muons. The 4-momenta of the two selected muons undergo several corrections before being assigned to the leptons to be simulated. At first, they need to be corrected for the mass difference between the muon and τ lepton or electron mass, denoted in the following with ℓ. The muon momenta are boosted into the center-of-mass frame of the di-muon system, and the corrected energy E_ℓ and the magnitude of the 3-momentum $|\vec{p}_\ell|$ are derived from the assumption of the corresponding lepton mass:

$$E_\ell = \frac{m_{\mu\mu}}{2}, \qquad |\vec{p}_\ell| = \sqrt{E_\ell^2 - m_\ell^2}, \qquad \ell \in \{e, \tau\}$$

The 3-momentum $\vec{p}_\ell$ is rescaled to match the corrected magnitude and the 4-momentum $(E_\ell, \vec{p}_\ell)$ is boosted back into the laboratory frame.

The next correction has been estimated using a simulated $Z \rightarrow \mu\mu$ dataset for validation, where the two selected reconstructed muons are replaced by simulated muons with exactly the same kinematic properties to undergo detector simulation and reconstruction. This leads to a broadening of the peak in the invariant mass spectrum of the di-muon system $m_{\mu\mu}$ and is corrected for the production of datasets with τ leptons [124].

The effects resulting from the final state radiation (FSR) of the muons from the original

$Z \rightarrow \mu\mu$ decay were studied as well. The FSR is not taken into account by the muon reconstruction, such that the peak of the $m_{\mu\mu}$ distribution and the p_T of the two reconstructed muons selected for the τ embedding method is shifted to lower values. To avoid additional FSR, it is explicitly disabled for the simulation of the embedded leptons.

In that way, the photons from FSR of the selected muons remain untouched in the data event record with the consequence, that FSR is underestimated for electrons and overestimated for τ leptons.

The broadening of the mass peak due to the additional reconstruction of the embedded leptons, as well as the FSR effects are found to be negligible compared to the magnitude of the energy scale and resolution uncertainties introduced to the selected $\tau\tau$ final states of the $H \rightarrow \tau\tau$ analysis.

Before starting the simulation of the leptons, the interaction point, at which the simulated leptons should be produced, is set to the reconstructed primary vertex of the muons from data [125].

While the embedded muons and electrons enter the detector simulation without further changes, the decay of the τ leptons is simulated with `Pythia 8.2` [80] beforehand, including the hadronization of quarks and gluons for τ_h candidates. To increase the size of the datasets created by the τ embedding technique, the vectorial 3-momentum sum over all visible decay products of the simulated τ leptons needs to fulfill requirements on its p_T and η which are chosen to be close to the ones used in the $H \rightarrow \tau\tau$ analysis. To pass these requirements, the simulation of the τ decays is performed $N = 1000$ times. If at least one of the trials is successful, the event is stored and the last successful trial is passed to the detector simulation, otherwise the event is rejected.

In that way, the kinematic distributions of the τ decay products are biased, such that the simulated events passing the p_T and η thresholds are accepted with higher probability. To correct for this effect, the number of successfully simulated trials k is counted and a correction weight $p = k/N$ is stored to approximate the probability of the $\tau\tau$ decay with given kinematic properties. The accomplished oversampling is about a factor of 5 for the $\tau_h\tau_h$ final state, 15 for the $\mu\tau_h$ and $e\tau_h$ final states, and 50 for the $e\mu$ final state.

The simulation of the CMS detector is based on the `GEANT4` [126] software simulating the behaviour of particles entering the active detector material. After the detector simulation, the information of the simulated event record is the same as it would be provided during data-taking.

The trigger simulation is performed on this event record. For the HLT simulation, it is important to provide the information on the position of the beam crossing, as well as the position of the reconstructed vertex from data [127]. The main reason for this is an event record resulting from two leptons and an otherwise empty detector, leading to a more difficult vertex reconstruction with decreased vertex quality.

The response of HLT paths is expected to be different as well for the same reason. For example, isolation sums of the simulated leptons will be close to zero. To mitigate this, corrections are derived for the HLT efficiency, in the same way as for the simulation, discussed in more detail in section 4.3. After the HLT simulation, those reconstruction algorithms are run, that provide reconstructed tracks and other constituents seeding the reconstruction of physics objects like reconstructed clusters in the calorimeters.

Creation of the Hybrid Event Record

After all tracks in the inner tracking system and the muon chambers, and the calorimeter clusters have been reconstructed for the cleaned and simulated event records separately, the corresponding collections are merged into one for each type of the reconstructed objects. If two calorimeter clusters are reconstructed at the same position in both records, their energy is summed and they are considered as one cluster. After this, the reconstruction of the physics objects and primary vertices is continued based on the hybrid collections, including the recomputation of the missing transverse energy $\vec{p}_T^{\,miss}$.

The unification of the simulated and cleaned event records is performed at a later stage: the beginning of physics object reconstruction. Ideally, the hybrid event creation would be performed at the same level as the cleaning of the muon pair, but this is not possible in the current version of the reconstruction software. The reason for this are the limitations imposed by the way, how the information on the alignment and calibration of the CMS detector is stored.

To reduce the amount of stored information per event, the measurements of the detector alignment and calibration are stored for certain intervals of time and independent from the event records. The event records are then assigned to the corresponding time interval to restore this information during the event reconstruction.

The detector calibration records contain all information on the response of the various subdetector modules, relating the signal from electronics with energy or position measurements. The detector alignment records define the global position of the detector, the location of different detector modules with respect to each other, and how the deformation of their surface looks like at a certain point of time.

This allows to translate the local coordinates of the hits in the inner tracking system and the muon chambers, and the local coordinates of the energy deposits in the calorimeters into global spacial coordinates with respect to the collision point of the CMS detector. Deviations of a few μm can already lead to a mismatch between a track in the pixel tracker and a track in the strip tracker originating from the same particle [128].

Both event records may have overlapping hits or energy deposits, which can not be handled separately with different alignment and calibration records within the same reconstruction sequence. In consequence, the hybrid event record needs to be processed with one consistent alignment and calibration information set. The information on the simulated embedded leptons must be interpreted with the alignment and calibration record from data. While the differences in the detector calibration are expected to be too small to change the position of reconstructed hits and the energy clusters significantly, the differences in the tracker alignment lead to significant effects on track reconstruction performance. The best solution would be to perform the detector simulation directly with the alignment and calibration records from data. This is an open task and should be pursued as one of the main preparations for the high luminosity LHC.

The unification of the cleaned and simulated event records is therefore started at a stage of the reconstruction, at which the relevant objects are already translated into the global coordinate system. While effects from using a different alignment information is avoided for the reconstruction of the physics objects in that way, it still persists, if detector-related quantities are accessed, for example in the identification algorithms of electrons and τ_h candidates.

The last main limitation to be mentioned is the fact, that the trigger reconstruction se-

quences are performed only on the simulated event record. This restricts the calculation of the trigger decisions to the two embedded leptons. Currently, this approach covers the main HLT paths of interest, but more specialized HLT paths using the information on jets and p_T^{miss} in addition to the lepton pair are not properly simulated. The integration of all HLT reconstruction sequences into the τ embedding workflow is another main task for the future.

Within these limitations, the τ embedding technique provides a robust and well behaving estimation of genuine τ leptons in the $\tau\tau$ final states after the application of all relevant corrections, as demonstrated in the corresponding publications [19, 21, 122].

4.1.2. Jets Misidentified as τ_h Candidates

The estimation method of background contributions with at least one τ_h candidate from a misidentified jet (Jet $\to \tau_h$) was introduced at CMS in the context of the measurement of the $Z \to \tau\tau$ cross-section [129] and then successfully used in $H \to \tau\tau$ analyses [19, 21].
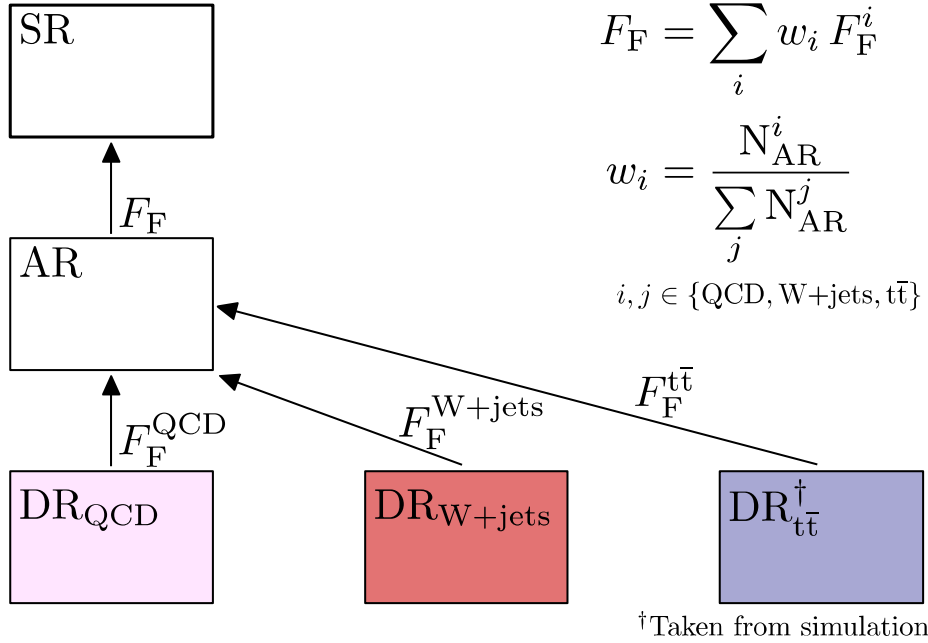
Figure 4.5.: An illustration of the estimation method for contributions of jets misidentified as τ_h candidates [129].

The main idea of the method is illustrated in figure 4.5 and is based on the assumption, that the ratio between the isolated τ_h candidates and non-isolated τ_h candidates, both coming from jets after the same selection, is unique and depends only on $p_T(\tau_h)$. This ratio is considered in separate phase-space regions of categories based on the number of additional jets in the event, N_{jets}, and, if required, on the separation in ΔR between the constituents of the considered $\tau\tau$ pair. Any other quantity or selection is assumed not to have an impact on this ratio, denoted as F_F in the following.

Given this factor, the contribution of jets misidentified as τ_h candidates to the signal region (SR) with isolated τ_h candidates can be derived using data from a region with non-isolated misidentified τ_h candidates, referred to as the application region (AR).

The F_F value can be determined in a region with a different selection enriching the contribution of jets misidentified as τ_h candidates. This region is called determination region (DR) in the following.

After selecting events into the $\mu\tau_h$ and $e\tau_h$ final states, three main processes are identified to contribute to Jet $\rightarrow \tau_h$:

- QCD multijet background (QCD),
- W boson production accompanied by jets, with a subsequent decay of the W boson into a lepton and its neutrino (W + jets),
- and top quark pair production ($t\bar{t}$).

For the $\tau_h\tau_h$ final state, the jets misidentified as τ_h candidates are assumed to originate entirely from QCD.

The AR defined for the H $\rightarrow \tau\tau$ analysis can have significant contributions from other processes than Jet $\rightarrow \tau_h$, denoted with non-Jet $\rightarrow \tau_h$. All contributions to the AR are accounted for by their fractions relative to the total yield in the AR, which are estimated from data, simulation, and τ embedding.

As the assumption of this method, that the F_F value is only dependent on $p_T(\tau_h)$, is not exactly true, correction factors were derived in the corresponding regions. The exact procedure of this F_F method, as well as the assignment of uncertainties, will be described for each considered final state in more detail in the following.

The explicit details on the selection of events into $\mu\tau_h$, $e\tau_h$ and $\tau_h\tau_h$ final states are described in section 4.3. This subsection is focused on the differences of AR and DR with respect to SR. The procedure to derive F_F described in the following is valid for the three final states in general, but demonstrated on the example of $\mu\tau_h$ and $\tau_h\tau_h$ final states of data-taking in 2018.

F_F in $\mu\tau_h$ and $e\tau_h$

The AR of the $\mu\tau_h$ and $e\tau_h$ final states differ from SR only by the isolation requirement on the τ_h candidate, expressed by the discriminator of τ_h candidates against jets, which is introduced in subsection 3.2.8. The Tight working point of the discriminator is chosen for the SR, AR is selected by requiring the τ_h candidate not to meet the Tight working point, but to pass the VLoose working point.

The determination region for QCD is defined by requiring a same-sign $\tau\tau$ pair instead of an opposite-sign pair and by restricting the relative isolation to $I_{rel}(\ell) \in [0.05, 0.15]$, $\ell \in \{e, \mu\}$. The calculation of F_F^{QCD} is performed as follows:

1. All expected contributions other than QCD are subtracted from data, based on τ embedding and simulation.
2. The numbers of events of remaining isolated and non-isolated τ_h candidates are calculated in bins of $p_T(\tau_h)$ for the $N_{jets} = 0$, $N_{jets} = 1$, and $N_{jets} \geq 2$ categories.
3. Ratios of these numbers for each category are computed to obtain the F_F^{QCD} value in bins of $p_T(\tau_h)$.
4. The binned F_F^{QCD} is fitted with a set of analytic functions, leading to a continuous F_F^{QCD} with uncertainties, shown in figure 4.6 on the left.
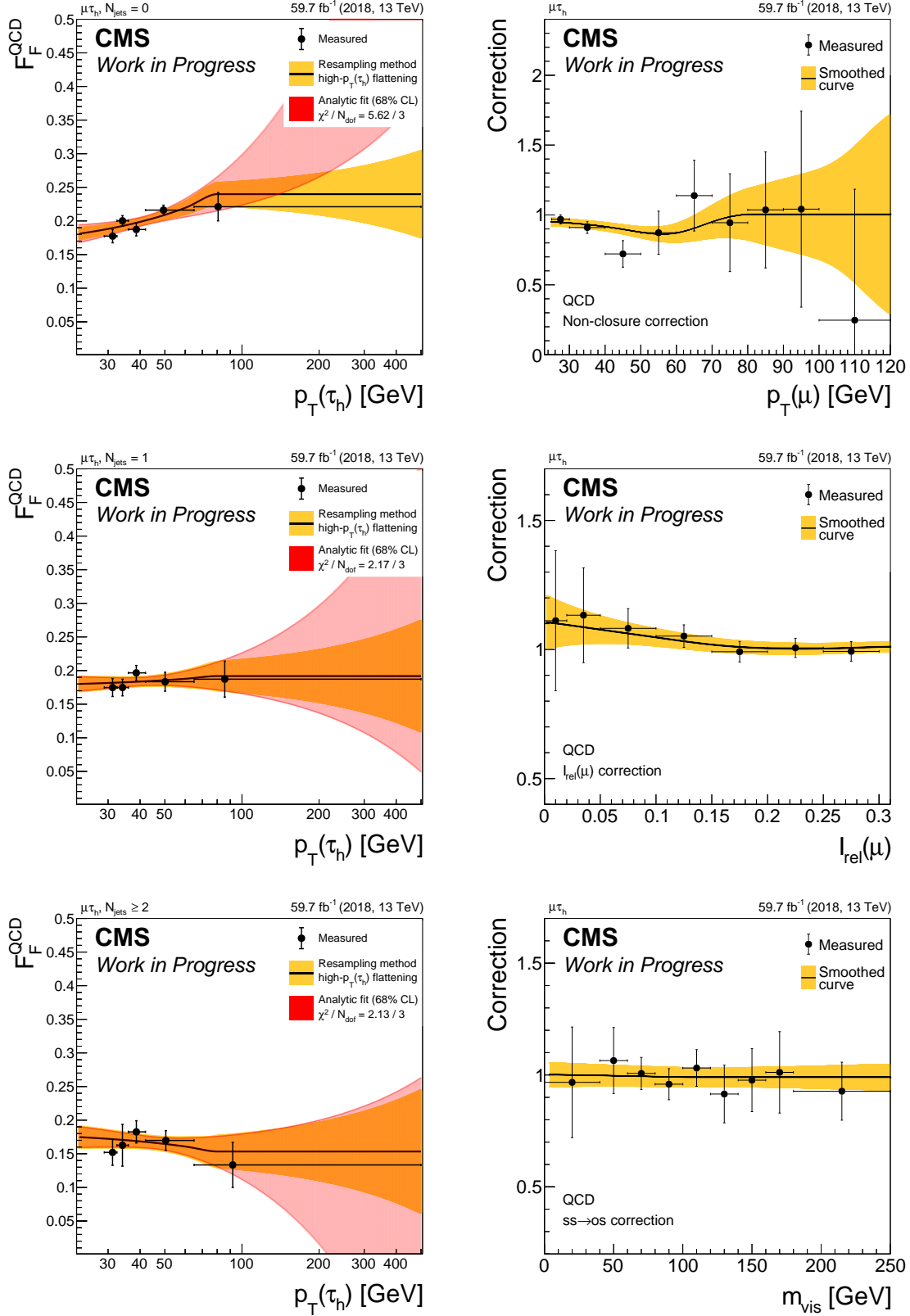
Figure 4.6.: F_F^{QCD} and corrections for the $\mu\tau_h$ final state of the data-taking in 2018. Left: Values of F_F^{QCD} as a function of $p_T(\tau_h)$ for (top) $N_{jets} = 0$, (middle) $N_{jets} = 1$, and (bottom) $N_{jets} \geq 2$. Right: Corrections for F_F^{QCD}, covering the non-closure in (top) $p_T(\mu)$ and (middle) $I_{rel}(\mu)$, and (bottom) the extrapolation from the same-sign to the opposite-sign region, as function of m_{vis}.

The derived F_F^{QCD} functions are investigated for a non-closure in distribution of the transverse momentum of the lepton, $p_T(\ell)$ ($\ell \in \{e, \mu\}$). Furthermore, the extrapolation from DR to SR is considered.

One correction factor is derived as function of the relative isolation of the lepton, $I_{rel}(\ell)$ ($\ell \in \{e, \mu\}$), to account for the different requirement on this quantity in DR. Additionally, the correction for the extrapolation from the same-sign into the opposite sign region is determined as function of the visible invariant mass of the $\tau\tau$ pair, m_{vis}.

At first, F_F^{QCD} is considered in bins of $p_T(\ell)$:

1. Contributions other than from QCD are subtracted from data.
2. Remaining events with non-isolated τ_h candidates are weighted with F_F^{QCD}.
3. The derived distribution represents the contribution of isolated τ_h candidates from QCD.
4. It is compared with the expected distribution from remaining events with isolated τ_h candidates.
5. The ratio $C[p_T(\ell)]$ is smoothed with a Gaussian kernel to obtain a continuous correction function.

To determine the correction on $I_{rel}(\ell)$ extrapolation, the relative isolation requirement of DR is relaxed to the interval $[0, 0.3)$ and the same procedure as for $C[p_T(\ell)]$ is performed to obtain the correction function $C[I_{rel}(\ell)]$. This time, the events with non-isolated τ_h candidates are weighted with $F_F^{QCD} \cdot C[p_T(\ell)]$.

The correction for the extrapolation from the same-sign to the opposite-sign region is determined by using the derivation procedure of F_F^{QCD} and its non-closure correction in $p_T(\ell)$ in a region with relaxed lepton isolation, $I_{rel}(\ell) \in [0.15, 0.25)$. This region is separated into three parts equivalent to the nominal DR, AR, and SR. The derived distribution of m_{vis} is compared to the expected one in the SR equivalent, obtained from subtracting contributions other than QCD from data. A continuous ratio of these distributions, $C^{ss \to os}[m_{vis}]$, is obtained from smoothing the binned ratio.

In consequence, the final, corrected F_F^{QCD} value is a function of five quantities:

$$F_F^{QCD}[N_{jets}, p_T(\tau_h), p_T(\ell), I_{rel}(\ell), m_{vis}] =$$
$$F_F^{QCD}[N_{jets}, p_T(\tau_h)] \cdot C[p_T(\ell)] \cdot C[I_{rel}(\ell)] \cdot C^{ss \to os}[m_{vis}] \qquad (4.1)$$

The correction factors are shown in figure 4.6 on the right.

The determination region for $W + \text{jets}$ differs from the signal region only by two requirements. To enrich the $W + \text{jets}$ contribution and to suppress the contributions from the Z boson production, the transverse mass between the lepton and the missing transverse energy is required to be greater than 70 GeV:

$$m_T(\ell, p_T^{miss}) = \sqrt{2 \cdot p_T(\ell) \cdot p_T^{miss} \cdot [1 - \cos \Delta\phi(\vec{p}_T(\ell), \vec{p}_T^{miss})]} \geq 70 \text{ GeV}$$

For the signal region, the requirement on the transverse mass is $m_T(\ell, p_T^{miss}) < 70$ GeV. The second requirement to suppress the contribution from top quark pair production is imposed on the number of b-tagged jets, $N_{b\text{-tag}} = 0$, which is not applied in the signal region.
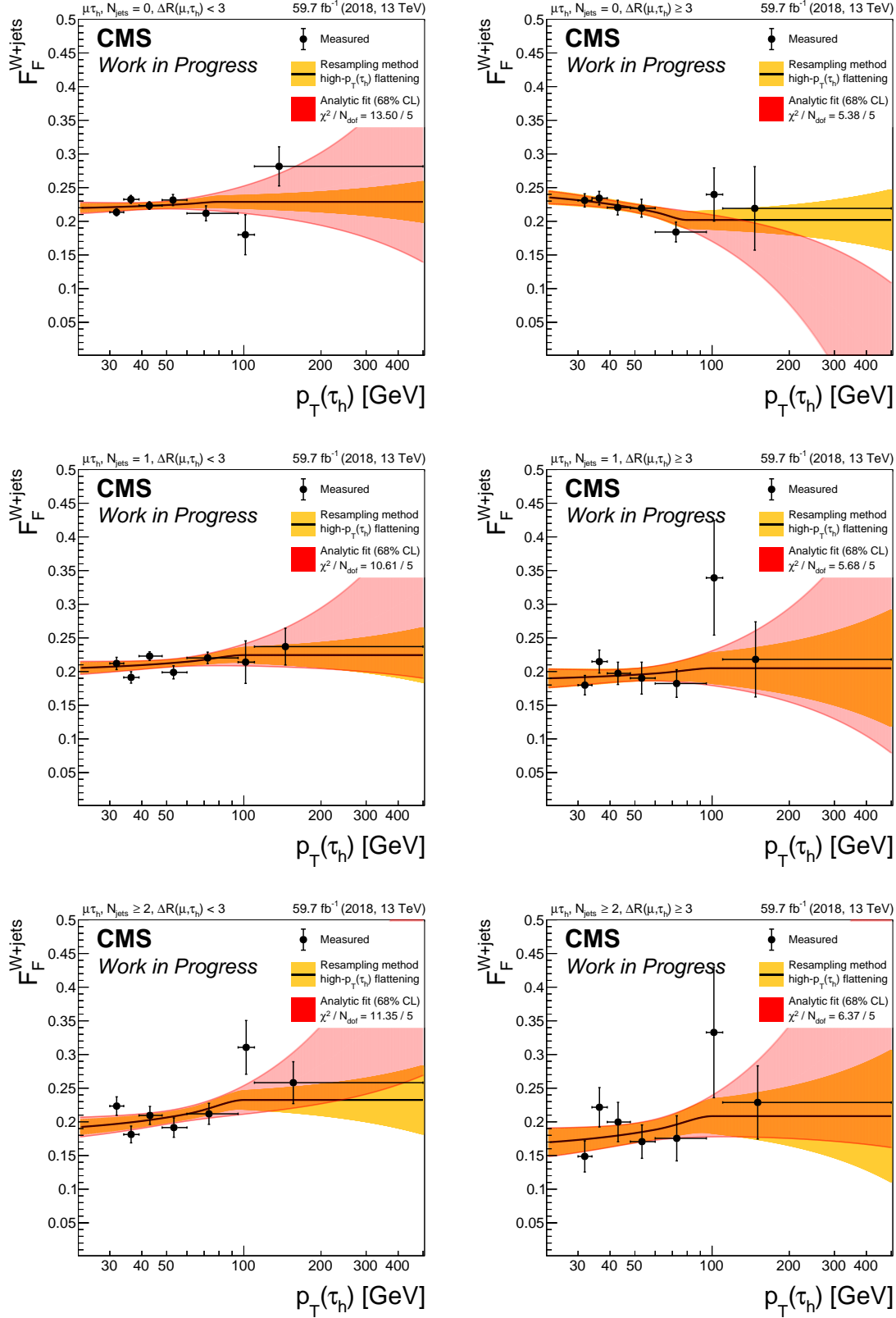
Figure 4.7.: F_F^{W+jets} values as a function of $p_T(\tau_h)$ in categories of N_{jets} and $\Delta R(\mu, \tau_h)$ for the $\mu\tau_h$ final state of the data-taking in 2018. On the left, N_{jets} categories with $\Delta R(\mu, \tau_h) < 3$ are shown, on the right with $\Delta R(\mu, \tau_h) \geq 3$. N_{jets} categories are constructed for (top) $N_{jets} = 0$, (middle) $N_{jets} = 1$, and (bottom) $N_{jets} \geq 2$.

The function F_F^{W+jets} depending on $p_T(\tau_h)$ is derived in six different categories, constructed from the requirements on N_{jets} and $\Delta R(\ell, \tau_h)$:

- Three categories $N_{jets} = 0$, $N_{jets} = 1$, and $N_{jets} \geq 2$ are further separated by
- $\Delta R(\ell, \tau_h) < 3$ and $\Delta R(\ell, \tau_h) \geq 3$.

The F_F^{W+jets} values shown in figure 4.7 are derived in an equivalent way to F_F^{QCD}. The QCD contribution, which needs to be subtracted from data, is estimated by changing to the same-sign region of the DR for W + jets.

The derived F_F^{W+jets} functions are investigated for non-closure in $p_T(\ell)$, and the extrapolation for $m_T(\ell, p_T^{miss})$ is measured as a function m_{vis}. The correction $C[p_T(\ell)]$ is derived in an equivalent way as $C[m_{vis}]$ for F_F^{QCD}.

Due to the absence of a region with $m_T(\ell, p_T^{miss}) < 70$ GeV, which is pure enough in W + jets, the correction for the extrapolation in $m_T(\ell, p_T^{miss})$, is derived using simulation and recalculating F_F^{W+jets} and $C[p_T(\ell)]$ based on it.

The rederived functions are applied to events with non-isolated τ_h candidates from the W + jets simulation and compared with events with isolated τ_h candidates from W + jets simulation in bins of m_{vis}. The ratio is smoothed with a Gaussian kernel to obtain the correction factor $C^{m_T(\ell, p_T^{miss})}[m_{vis}]$. The final F_F^{W+jets} value is a function of five quantities:

$$F_F^{W+jets}[N_{jets}, \Delta R(\ell, \tau_h), p_T(\tau_h), p_T(\ell), m_{vis}] =$$
$$F_F^{W+jets}[N_{jets}, \Delta R(\ell, \tau_h), p_T(\tau_h)] \cdot C[p_T(\ell)] \cdot C^{m_T(\ell, p_T^{miss})}[m_{vis}] \quad (4.2)$$

The correction factors are shown in figure 4.8.
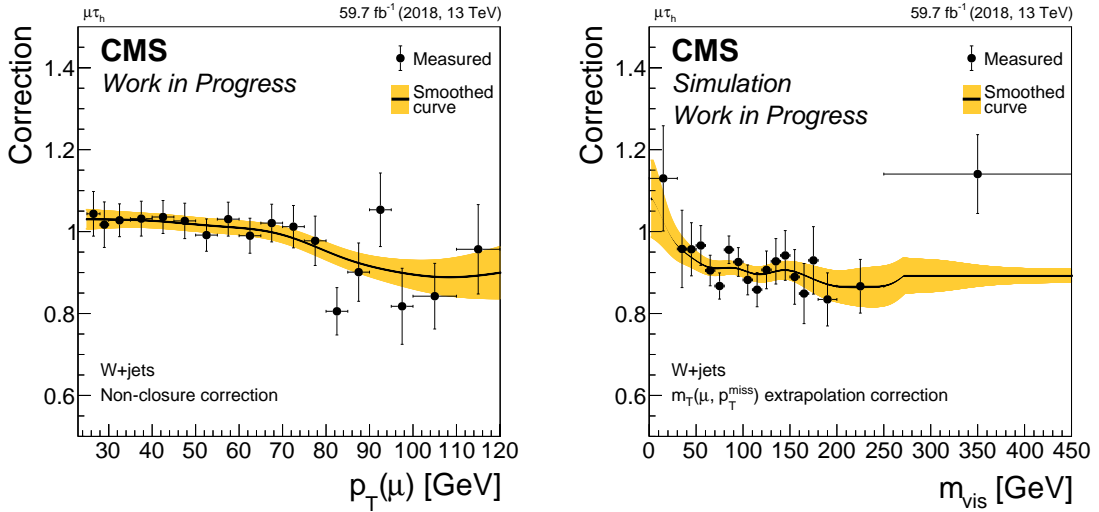
Figure 4.8.: Corrections for F_F^{W+jets} as functions of (left) $p_T(\mu)$, and of (right) m_{vis} covering the $m_T(\mu, p_T^{miss})$ extrapolation for the $\mu\tau_h$ final state of the data-taking in 2018.

The contribution to Jet $\to \tau_h$ from top quark pair production is estimated from simulation due to the absence of pure enough determination regions in the $\mu\tau_h$ and $e\tau_h$ final states. This means, that DR of $t\bar{t}$ consists of the signal region with isolated τ_h candidates and

AR with non-isolated τ_h candidates. The ratio of the distributions in bins of $p_T(\tau_h)$ is fitted with a set of analytic functions to obtain a continuous $F_F^{t\bar{t}}$ function in two categories defined by $N_{jets} \leq 1$ and $N_{jets} \geq 2$. The functions $F_F^{t\bar{t}}$ are investigated for non-closure in bins of m_{vis} and a continuous correction factor $C[m_{vis}]$ is derived. The final $F_F^{t\bar{t}}$ function depends on three quantities:

$$F_F^{t\bar{t}}[N_{jets}, p_T(\tau_h), m_{vis}] = F_F^{t\bar{t}}[N_{jets}, p_T(\tau_h)] \cdot C[m_{vis}] \qquad (4.3)$$

The resulting uncorrected $F_F^{t\bar{t}}$ functions and the corresponding correction in m_{vis} are shown in figure 4.9.
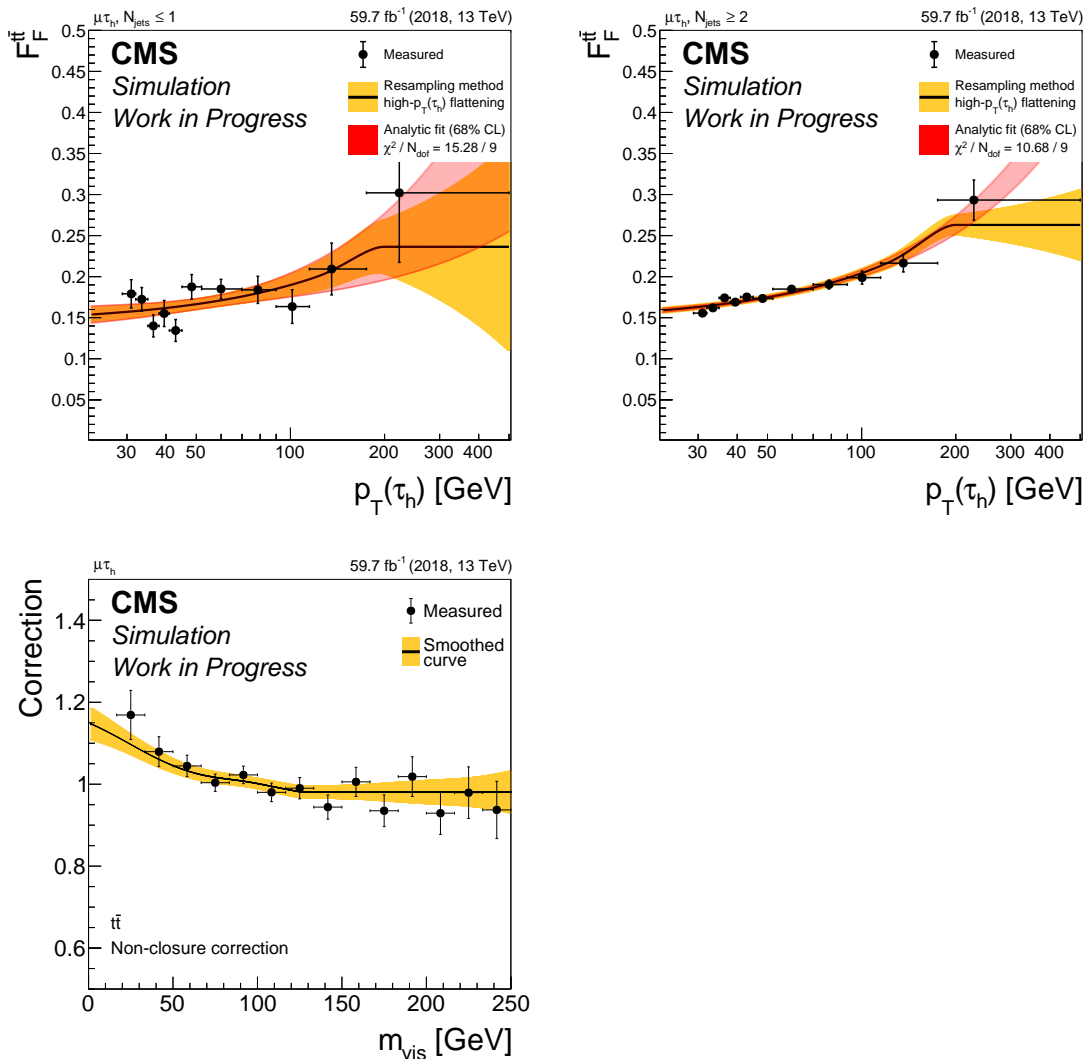
Figure 4.9.: $F_F^{t\bar{t}}$ and its correction for the $\mu\tau_h$ final state of the data-taking in 2018. Top: The uncorrected $F_F^{t\bar{t}}$ value as a function of $p_T(\tau_h)$ for (left) $N_{jets} \leq 1$ and (right) $N_{jets} \geq 2$. Bottom left: Correction of $F_F^{t\bar{t}}$ in m_{vis}.

After the individual functions F_F^i have been determined, they are combined by using fractions of expected contributions to the AR.

$$F_F = f_{QCD} \cdot F_F^{QCD} + f_{W+jets} \cdot F_F^{W+jets} + f_{t\bar{t}} \cdot F_F^{t\bar{t}}, \qquad f_{QCD} + f_{W+jets} + f_{t\bar{t}} = 1 \qquad (4.4)$$

The relative fractions f_i are determined in bins of $m_T(\ell, p_T^{miss})$ to separate the different contributions well from each other. They are obtained by determining relevant contributions to the AR: QCD, W + jets, $t\bar{t}$ and processes without jets misidentified as τ_h candidates. The intermediate fractions obtained from these contributions are renormalized, such that equation 4.4 is fulfilled.

The estimation of the jets misidentified as τ_h candidates in the signal region, denoted with Jet $\rightarrow \tau_h$ reads then as follows:

$$\text{Jet} \rightarrow \tau_h(\text{SR}) = \text{Data}(\text{AR}) \cdot F_F - \text{non-Jet} \rightarrow \tau_h(\text{AR}) \cdot F_F \tag{4.5}$$

The multiplication with the F_F value must be understood as event-wise. To avoid double-counting, events with a τ_h candidate being a misidentified jet must be rejected in each simulated process, since already covered by the F_F method.

In total 26 shape altering uncertainties are introduced per final state, obtained from

- the resampling of the fits of uncorrected F_F^i by varying the data points within their statistical uncertainties,
- subtraction of non-Jet $\rightarrow \tau_h$ contributions,
- smoothed uncertainty band of each correction,
- each derived correction by not applying it or applying it twice,
- and the application of fractions in the AR.

Furthermore, two normalization uncertainties are introduced for each category of a final state to cover changes in the yield of the Jet $\rightarrow \tau_h$ contribution.

F_F in $\tau_h\tau_h$

The main contribution of jets misidentified as τ_h candidates in the $\tau_h\tau_h$ final state is expected to come from QCD multijet background. This reduces the number of determination regions to a single one.

On the other hand, it has to be taken into account, that each of the two τ_h candidates in this final state may come from a misidentified jet, such that an event is used twice during determination of F_F^{QCD} and its corrections.

As for $\mu\tau_h$ and $e\tau_h$ final states, an isolated τ_h candidate is defined by passing the Tight working point of the discriminator against jets, while a non-isolated τ_h candidate is required to fail the Tight, but pass the VLoose working point.

An event in the $\tau_h\tau_h$ final state is required to have exactly one isolated, and one non-isolated τ_h candidate to be used in the DR of F_F^{QCD}. Additionally, the two τ_h candidates are required to have the same charge. The procedure to derive F_F^{QCD} is similar to the one for $\mu\tau_h$ and $e\tau_h$ final states:

- Uncorrected F_F^{QCD} functions are derived by subtracting contributions other than QCD from data in DR and fitting the ratio of binned $p_T(\tau_h)$ distributions of isolated and non-isolated τ_h candidates. This is done for three categories in N_{jets}: $N_{jets} = 0$, $N_{jets} = 1$, and $N_{jets} \geq 2$.
- First non-closure correction $C[m_{vis}]$ is derived in bins of m_{vis} by applying F_F^{QCD} to the distribution for non-isolated τ_h candidates and comparing it with the distribution for isolated τ_h candidates in DR.

- A second non-closure correction $C[2^{nd}\,p_T(\tau_h)]$ is determined as function of the transverse momentum of the second τ_h candidate, using this time $F_F^{QCD} \cdot C[m_{vis}]$.
- The last correction $C^{ss \to os}[m_{vis}]$ covers the extrapolation from the same-sign to the opposite-sign region, measured in bins of m_{vis} in the region, where both τ_h candidates are non-isolated.

The derived F_F^{QCD} functions and the corresponding corrections are shown in figure 4.10. The final, corrected F_F^{QCD} function depends on four quantities:

$$
\begin{aligned}
F_F^{QCD}[N_{jets}, p_T(\tau_h), m_{vis}, 2^{nd}\,p_T(\tau_h)] = \\
F_F^{QCD}[N_{jets}, p_T(\tau_h)] \cdot C[m_{vis}] \cdot C[2^{nd}\,p_T(\tau_h)] \cdot C^{ss \to os}[m_{vis}] \quad (4.6)
\end{aligned}
$$

For the total F_F function it must be taken into account, that two τ_h candidates are available in the $\tau_h \tau_h$ final state by applying a factor of $1/2$:

$$
F_F = \frac{1}{2} \cdot \begin{cases} F_F^{QCD}[\text{leading } \tau_h, \ldots] & \text{non-isolated leading } \tau_h \\ F_F^{QCD}[\text{subleading } \tau_h, \ldots] & \text{non-isolated subleading } \tau_h \\ F_F^{QCD}[\text{leading } \tau_h, \ldots] + F_F^{QCD}[\text{subleading } \tau_h, \ldots] & \text{both non-isolated} \end{cases}
$$

(4.7)

The contribution of jets misidentified as τ_h candidates to the signal region is estimated by applying F_F event-wise to data in the AR and subtracting contributions other than QCD from data.

$$
\text{Jet} \to \tau_h(SR) = \text{Data}(AR) \cdot F_F - \text{non-Jet} \to \tau_h(AR) \cdot F_F \quad (4.8)
$$

For the $\tau_h \tau_h$ final state, 10 shape altering uncertainties are introduced, evaluated for each non-isolated τ_h candidate and based on:
.

- the resampling of the fits of uncorrected F_F^{QCD} by varying the data points within their statistical uncertainties,
- subtraction of non-Jet $\to \tau_h$ contributions,
- smoothed uncertainty band of each correction,
- and each derived correction by not applying it or applying it twice.

Additionally, two normalization uncertainties are introduced for each category of the $\tau_h \tau_h$ final state to cover changes in the yield of the Jet $\to \tau_h$ contribution.
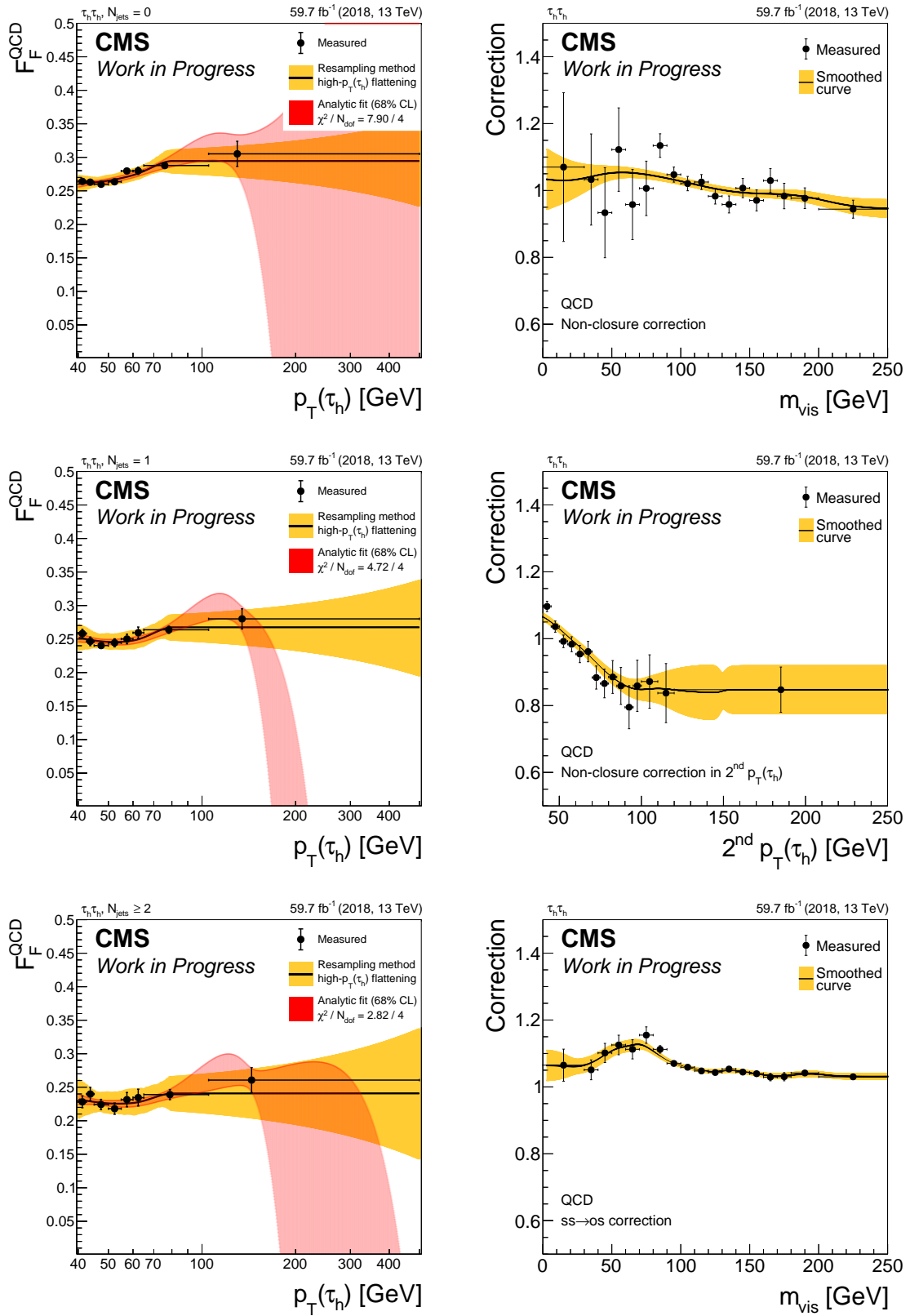
Figure 4.10.: F_F^{QCD} and corrections for the $\tau_h\tau_h$ final state of the data-taking in 2018. Left: Values of F_F^{QCD} as a function of $p_T(\tau_h)$ for (top) $N_{jets} = 0$, (middle) $N_{jets} = 1$, and (bottom) $N_{jets} \geq 2$. Right: Corrections for F_F^{QCD}, covering the non-closure in (top) m_{vis} and (middle) the second $p_T(\tau_h)$, and (bottom) the extrapolation from the same-sign to the opposite-sign region, as function of m_{vis}.

4.1.3. QCD Multijet Background in the eμ Final State

The QCD multijet background in the eμ final state can be estimated from a shape determination region (DR) with a same-sign lepton pair. The basic assumption of such a method is that the distribution of any quantity of interest in the region with a same-sign lepton pair is the same as in the signal region (SR) with oppositely charged leptons. Only the absolute yield may be different and would need an extrapolation factor measured in a region with a looser isolation requirement on one of the leptons, in eμ usually chosen to be the muon. The QCD shape is estimated in the same-sign DR by subtracting all expected contributions from data based on τ embedding and simulation in bins of a quantity of interest:

$$QCD(SR) = Data(DR) \cdot \epsilon_{QCD} - non\text{-}QCD(DR) \cdot \epsilon_{QCD} \qquad (4.9)$$

In the simplest possible approach, the shape is scaled with a constant extrapolation factor from a same-sign region to an opposite-sign region and is used as an estimate of the QCD contribution in the signal region.

However, this was found insufficient [21], and the extrapolation factor is derived as a function of muon and electron p_T, N_{jets}, and $\Delta R(e, \mu)$. This extended extrapolation factor ϵ_{QCD} is constructed to mitigate the violation of the assumption, that the QCD shape is unique for the same-sign and opposite-sign regions.

Three regions are considered additionally to the signal and QCD shape determination regions for this measurement based on the relative isolations of the electron and muon, given as follows.

$$
\begin{aligned}
&SR: & I_{rel}(\mu) < 0.2, && I_{rel}(e) < 0.15, && \text{opposite-sign eμ} \\
&DR: & I_{rel}(\mu) < 0.2, && I_{rel}(e) < 0.15, && \text{same-sign eμ} \\
&R1: & I_{rel}(\mu) \in [0.2, 0.5), && I_{rel}(e) < 0.15 \\
&R2: & I_{rel}(\mu) \in [0.2, 0.5), && I_{rel}(e) \in [0.15, 0.5) \\
&R3: & I_{rel}(\mu) < 0.2, && I_{rel}(e) \in [0.15, 0.5)
\end{aligned}
$$

In the R1 region, an initial measurement of the extrapolation factor ϵ_{QCD} is performed in three categories $N_{jets} = 0$, $N_{jets} = 1$, and $N_{jets} \geq 2$, as a second order polynomial of $\Delta R(e, \mu)$. For each $\Delta R(e, \mu)$ bin, the ratio between the numbers of events with an opposite-sign and a same-sign pair is built, subtracting the expected non-QCD contributions from the data events. The factor ϵ_{QCD} is parameterized with

$$\epsilon_{QCD}[\Delta R(e, \mu)] = p0 + p1 \cdot (\Delta R(e, \mu) - 3) + p2 \cdot (\Delta R(e, \mu) - 3)^2$$

for each category in N_{jets}, and the corresponding parameter estimates are given in table 4.3.

The uncertainties of $\epsilon_{QCD}[\Delta R(e, \mu)]$ on the parameters are propagated to the estimate and used as systematic uncertainties for each N_{jets} category, resulting in 9 uncertainties in total. The factor $\epsilon_{QCD}[N_{jets}, \Delta R(e, \mu)]$ is investigated in the transverse momenta of the electron and muon. For this purpose, the distribution of the QCD contribution to the same-sign events of the region R1 is estimated by subtracting the expected non-QCD events based on τ embedding and simulation from data and reweighting all events with the derived

	Parameter estimates		
Category	p0	p1	p2
$N_{jets} = 0$	1.96 ± 0.05	-0.16 ± 0.02	-0.12 ± 0.02
$N_{jets} = 1$	2.01 ± 0.03	-0.32 ± 0.02	-0.04 ± 0.01
$N_{jets} \geq 2$	1.76 ± 0.04	-0.36 ± 0.02	-0.01 ± 0.01

Table 4.3.: Measured parameters for the extrapolation factor ϵ_{QCD} in three N_{jets} categories for the data-taking year 2018.

extrapolation factors. The obtained distribution in bins of $(p_T(\mu), p_T(e))$ is compared to the expected QCD distribution from the opposite-sign events in data after subtracting the opposite-sign non-QCD contributions. The ratio of the expected and the obtained distributions is used as a correction, $C[p_T(\mu), p_T(e)]$.

The two regions with a looser electron isolation, R2 and R3, are used to derive the corrections for the extrapolation from the regions with the loosely isolated muons, R1 and R2, to the regions with the isolated muons, R3, SR and DR. This is done by deriving in each of the two regions the QCD extrapolation factors in bins of $(p_T(\mu), p_T(e))$ with the same procedure as described before. The ratio of the QCD extrapolation factor in the region R3 and the QCD extrapolation factor in the region R2 is taken as the correction for the extrapolation between the isolation regions, $C^{iso}[p_T(\mu), p_T(e)]$. An additional uncertainty is introduced to this correction by applying it in quadrature or not at all.

The final extrapolation factor is then a function of the four quantities, as given in the following equation:

$$\epsilon_{QCD}[N_{jets}, \Delta R(e, \mu), p_T(\mu), p_T(e)] =$$
$$\epsilon_{QCD}[N_{jets}, \Delta R(e, \mu)] \cdot C[p_T(\mu), p_T(e)] \cdot C^{iso}[p_T(\mu), p_T(e)] \quad (4.10)$$

4.1.4. Simulation-Based Estimation

The simulation of proton-proton collisions is performed using Monte Carlo (MC) event generators, such as `Pythia 8.2` [80], `Madgraph 5 aMC@NLO` [130] and `POWHEG` [131], as discussed in section 2.4. For parton showering, hadronization, and the simulation of the underlying event, `Pythia 8.2` is chosen. The specific tunes of parameterization of the underlying event is configured with dedicated measurements [132]. The evaluation of p.d.f.'s is performed with the `NNPDF3.0` [133] and `NNPDF3.1` [134] sets.

After these steps, a single proton-proton collision with a specific process is simulated up to the level of final state particles. At this point, the detector simulation with `GEANT4` [126] is performed to obtain the hits and energy deposits of the simulated particles traversing the CMS detector subsystems in a magnetic field. Next, the simulation of pileup interactions needs to be performed. This is done by simulating minimum bias events with `Pythia 8.2` up to the detector simulation with `GEANT4`, and mixing them with the simulated hard scattering event. The number of additional interactions to be mixed is determined in two steps:

1. A random real value λ is picked from a given distribution of the total number of interactions adapted to the one expected in data.

2. A integer $N \sim P(\lambda)$ is thrown from a Poisson distribution P using λ as its parameter.
3. The number $N - 1$ defines the number of additional interactions to be mixed.

After the pileup mixing, the simulated detector response is expected to be as it will be during the data-taking. In the final step, the simulation of the trigger system decisions and the subsequent reconstruction of the event record are performed.

The expected yield $N_{exp.}$ of a process $X \rightarrow Y$ with a production cross-section σ_X and a branching fraction BR_Y can be computed from a dataset with a number of simulated events $N_{sim.}$ for a given integrated luminosity $L_{int.}$ as follows:

$$N_{exp.} = L_{int.} \cdot \sigma_X \cdot BR_Y / N_{sim.}$$

Consequently, a simulated dataset needs to be reweighted to the right luminosity and cross-section to match the number of events in data recorded by the experiment. For a proper combination of the luminosity measurements for all data-taking years, the total uncertainties on the luminosity are split into individual sources, which are partially correlated across the years. The uncertainties are summarized in table 4.4.

Uncertainty source	2016	2017	2018
	±2.2%	0	0
Uncorrelated	0	±2.0%	0
	0	0	±1.5%
X-Y factorization	±0.9%	±0.8%	±2.0%
Length scale	0	±0.3%	±0.2%
Beam-Beam deflection	±0.4%	±0.4%	0
Dynamic β	±0.5%	±0.5%	0
Beam current calibration	0	±0.3%	±0.2%
Ghosts and satellites	±0.4%	±0.1%	0

Table 4.4.: Uncertainties for the integrated luminosity split by individual sources [119–121].

Uncertainties are also available for the calculation of the cross-section and branching fraction, which are assigned to each simulated process, as discussed in section 2.4. In consequence, these uncertainties are required to be taken into account for each simulation-based estimation in the statistical inference.

Furthermore, a reweighting is needed, if the distribution of the total number of interactions in the simulated events does not correspond to data. The distribution in data can be derived from the instantaneous luminosity $L_{inst.}$ of a single bunch crossing, the total inelastic cross-section of a proton-proton collision, $\sigma_{inel.} = 69.2$ mb [135], and the frequency of how often a proton bunch traverses the full circle of the LHC ring within a second, f. The average total number of interactions λ can then be computed from data as follows:

$$\lambda = \frac{L_{inst.} \cdot \sigma_{inel.}}{f}$$

The distributions of the total number of interactions in data for the three data-taking years, as well as the corresponding distribution for the simulated dataset used for the 2018

data-taking are shown in figure 4.11. The correction weights are obtained by dividing the normalized data distribution by the normalized distribution in the simulated dataset of the corresponding data-taking year.
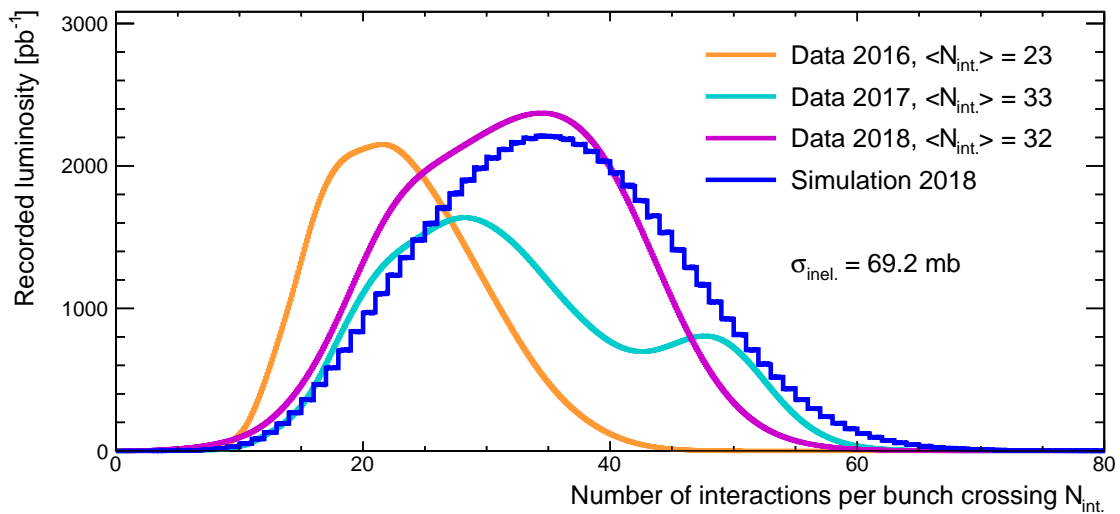
Figure 4.11.: The distribution of the total number of interactions in data for the three data-taking years and for the simulation of the data-taking in 2018 [119–121].

The last general correction for processes estimated with simulation to be considered is specific to the data-taking years 2016 and 2017 and is referred to as the prefiring correction. Due to issues in the propagation of timing from the ECAL to the L1 trigger system, a significant fraction of L1 trigger objects from a considered bunch crossing can be assigned to the previous one for the pseudorapidity region $|\eta| > 2$. In that way, the L1 trigger would fire on the event from the previous bunch crossing.

This event is likely to be uninteresting and would in the end be rejected by the HLT. On the other hand, the subsequent event in the correct bunch crossing would not only have missing L1 trigger objects in the mentioned ECAL region, but will be completely rejected by L1 due to the fact, that if the L1 fires, the next bunch crossing - in that case the correct one - is not stored at all. This effect is not modelled in the simulation for the 2016 and 2017 data-taking years and is corrected by the measured probability for a simulated event not to cause the prefiring of the L1. This total probability is computed from single prefiring probabilities measured for photons and jets in bins of transverse momenta and pseudorapidity.

The contributions from the Z boson production, that are not modelled neither by the τ embedding nor by the F_F method, are estimated from simulation. The hard scattering process of the events with $Z \rightarrow \ell\ell$ is simulated using the `Madgraph 5 aMC@NLO` Monte-Carlo generator at the leading order (LO) in the strong coupling constant of QCD, α_s, with next-to-leading order (NLO) electroweak corrections. The total yield is scaled to the corresponding products of the cross-sections and the branching fractions for each subcontribution to the Z boson production given in table 4.5 with the associated uncertainties.

The transverse momentum of the Z boson is not modelled correctly at LO. Therefore, the modelling is corrected in a $Z \rightarrow \mu\mu$ control region, where the reconstructed transverse momentum of Z boson should have the best precision. The correction is measured in bins

Subcontribution	$\sigma \cdot$ BR in pb	Uncertainty
Drell-Yan $Z \to \ell\ell$, $m_Z > 50$ GeV	6077.22, `FEWZ 3.1` [136], NNLO QCD, NLO EW	4% [136]
Electroweak $Z \to \ell\ell$, $m_Z > 50$ GeV	4.321, from generator, LO QCD, NLO EW	4%
Drell-Yan $Z \to \ell\ell$, $m_Z \in (10, 50]$ GeV	18810, from generator (NLO), NLO QCD, NLO EW	4%

Table 4.5.: Individual subcontributions of the Z boson production taken into account for the $H \to \tau\tau$ analysis, with the products of cross-sections and branching fractions with the associated uncertainties.

of the mass of the muon pair, m($\mu\mu$), with values greater than 50 GeV and over the full spectrum of the transverse momentum of the $\mu\mu$ system. The correction is derived such that the normalization of the $Z \to \mu\mu$ contribution is preserved. The uncertainties for the correction factors are defined by not applying the correction and applying it twice.

The production of the W boson, both through the annihilation of fermions and through the fusion of two vector bosons, is also simulated with `Madgraph 5 aMC@NLO` Monte-Carlo generator at LO QCD with NLO electroweak corrections. This contribution is used in the eμ final state, where it is not covered by a data-driven estimate as it is the case in other $\tau\tau$ final states. The total yield is scaled for each subcontribution to the corresponding product of the cross-section and the branching fraction, listed in table 4.6.

Subcontribution	$\sigma \cdot$ BR in pb	Uncertainty
ff $\to W^\pm \to \ell v$	61526.7, `FEWZ 3.1` [136], NNLO QCD, NLO EW	4% [136]
Electroweak $W^- \to \ell^- \bar{v}$ $m_W > 50$ GeV	23.24, from generator, LO QCD, NLO EW	4%
Electroweak $W^+ \to \ell^+ v$ $m_W > 50$ GeV	29.59, from generator, LO QCD, NLO EW	4%

Table 4.6.: Individual subcontributions of the W boson production taken into account for the $H \to \tau\tau$ analysis, with the products of cross-sections and branching fractions with the associated uncertainties.

The top quark pair production is modelled with the `POWHEG` Monte-Carlo generator at NLO QCD, while the inclusive cross-section $\sigma_{t\bar{t}} = 831.76$ pb is known up to the NNLO precision in QCD with the soft gluon resummation at the level of next-to-next to leading logarithms (NNLL), and a corresponding relative uncertainty of 6% [137]. The yield of the datesets is scaled to this cross-section accordingly. To account for interference effects at NLO level, negative event weights are provided by the `POWHEG` tool. The total number of the simulated

events is then computed from these weights w_i as follows:

$$N_{\text{sim.}} = \sum_{i \in \text{events}} \frac{w_i}{|w_i|}$$

The distribution of the transverse momentum p_T of the top quarks from $t\bar{t}$ production is expected to be mismodelled and is therefore corrected with an empirical approach using an analytic function based on the procedure of the published parton level results [138, 139]. A scale factor is derived as a function of parton level p_T of a simulated top quark:

$$SF[p_T(t)] = \exp\left[0.088 - 8.7 \cdot 10^{-3} \cdot \frac{p_T(t)}{1\,\text{GeV}} + 9.2 \cdot 10^{-6} \cdot \left(\frac{p_T(t)}{1\,\text{GeV}}\right)^2\right]$$

An event weight $w_{t\bar{t}}$ is computed from the transverse momenta of the top quark, t, and the anti-top quark, $\bar{t}$ of the top quark pair production.

$$w_{t\bar{t}} = \sqrt{SF[p_T(t)] \cdot SF[p_T(\bar{t})]}$$

This weight corrects only the shape of the distribution. Since $t\bar{t}$ is considered as a background, a simplified uncertainty prescription is used by not applying the correction and applying it twice.

Subcontribution	$\sigma \cdot$ BR in pb	Uncertainty
W^+W^-	118.7 [140], NNLO QCD, NLO EW	5%
$W^\pm Z$	27.57, from generator, LO QCD	5%
ZZ	12.14, from generator, LO QCD	5%
Single t, t-channel	136.02, HATHOR [141, 142], NLO QCD	5%
Single $\bar{t}$, t-channel	80.95, HATHOR [141, 142], NLO QCD	5%
Single t or $\bar{t}$, W associated	71.7 [143], NNLO QCD	5%

Table 4.7.: Individual subcontributions of the boson pair and single top quark production taken into account for the H $\rightarrow \tau\tau$ analysis, with the products of cross-sections and branching fractions with the associated uncertainties.

The last set of simulated contributions corresponds to the production of a boson pair and a single top quark in two dominant channels, the t-channel in which the top quark is

accompanied by a quark, and the W-t channel in which the top quark is associated with a W boson. The boson pair production is simulated with `Pythia 8.2` at LO precision in QCD, the single top contributions with `POWHEG` at NLO precision in QCD. The yields of each of the contribution is scaled to the corresponding cross-section, listed in table 4.7 with uncertainties. As for the $t\bar{t}$ production, the negative weights of the single top contribution need to be accounted for in $N_{sim.}$.

4.2. Modelling of the Higgs Boson Signal

All general points made at the beginning of subsection 4.1.4 for the simulation-based background are valid for the signal modelling with Monte Carlo event generators. For the modelling of the Standard Model (SM) Higgs boson production at a mass $m_H = 125$ GeV, the `POWHEG` generator was used to obtain $H \rightarrow \tau\tau$ and $H \rightarrow WW \rightarrow 2\ell2\nu$ decays with different production modes at NLO QCD precision. The production of samples for the Minimal Supersymmetric Extension of the Standard Model (MSSM) relies on `Pythia 8.2` at LO precision in QCD and on `Madgraph 5 aMC@NLO` at NLO precision in QCD with NLO electroweak (EW) corrections.

4.2.1. SM Higgs Boson Contributions

The different production modes, that are taken into account in the $H \rightarrow \tau\tau$ analysis are given in table 4.8 together with the cross-sections.

Production mode	Cross-seciton in pb	QCD precision	EW precision
Gluon fusion	48.58	N^3LO	NLO
Vector boson fusion	3.782	NNLO	NLO
Z associated	0.8839	NNLO	NLO
W^+ associated	0.84	NNLO	NLO
W^- associated	0.5328	NNLO	NLO
$t\bar{t}$ associated	0.5071	NLO	NLO

Table 4.8.: Cross-sections of individual production modes for the SM Higgs boson at $m_H = 125$ GeV used in the analysis, calculated for a centre of mass energy $\sqrt{s} = 13$ TeV [46].

The branching fractions for the $H \rightarrow \tau\tau$ and $H \rightarrow WW \rightarrow 2\ell2\nu$ decays correspond to $BR(H \rightarrow \tau\tau) = 6.272 \cdot 10^{-2}$ and $BR(H \rightarrow WW \rightarrow 2\ell2\nu) = 2.268 \cdot 10^{-2}$ for a Higgs boson mass of $m_H = 125$ GeV [32, 46]. These branching fractions are subject to uncertainties resulting from variations of the QCD scale, the strong coupling parameter α_s, and the variation due to finite quark masses used in the calculation, m_q. The uncertainties are summarized in table 4.9, together with the total uncertainties obtained from the squared sum of the individual uncertainties.

The production modes of the $H \rightarrow \tau\tau$ decay are combined into three contributions according to their signatures and the sensitivity of the $H \rightarrow \tau\tau$ analysis to them.

The most dominant contribution is gluon fusion production, denoted as ggH in the following. While mostly produced alone, the Higgs boson can be accompanied by one or more

Decay channel	relative uncertainty in %			
	QCD scale	m_q	α_s	total
H $\rightarrow$ $\tau\tau$	1.17	0.99	0.62	1.65
H $\rightarrow$ WW $\rightarrow$ 2ℓ2ν	0.99	0.99	0.66	1.55

Table 4.9.: Branching fraction uncertainties for a Higgs boson with a mass m_H = 125 GeV [46]. The total uncertainty results from the quadratic sum of the uncertainties of the three individual sources and is used in the analysis.

jets due to gluon emissions from the initial state. The resulting signature with one distinct and high energetic jet and a boosted Higgs boson recoiling against it is the one to which the analysis is most sensitive to.

The second set of production modes with a specific signature is the one, where the H $\rightarrow$ $\tau\tau$ analysis is in particular sensitive to: a Higgs boson accompanied by two quark jets, denoted as qqH in the following. These jets may be well separated in η as they result from the vector boson fusion or more collimated, coming from a decay of a single vector boson resonance into a pair of quarks, Z $\rightarrow$ q$\bar{q}$ and W $\rightarrow$ q'$\bar{q}$, which recoil against the Higgs boson. Thus, the latter signature results from the production modes with an associated vector boson in its hadronic final state.

In consequence, qqH can alternatively be expressed as:

$$qqH = (VBF + V \rightarrow qq)\,H$$

The two contributions ggH and qqH constitute the main two signals targeted by the H $\rightarrow$ $\tau\tau$ analysis with a measurement of the signal strength. The remaining contributions with associated vector bosons decaying to leptons and neutrinos and the t$\bar{t}$ associated production are minor signal contributions taken into account in the analysis, but with an expected yield fixed to the SM expectation. The H $\rightarrow$ WW $\rightarrow$ 2ℓ2ν decay, which is a non-negligible background to the eμ final state, is also taken into account, fixed to the SM expectation.

To apply an extended scheme of uncertainties, the two main signals ggH and qqH are considered in the context of simplified template cross-sections (STXS) [144], which are illustrated in figure 4.12. The STXS allow to define theoretical predictions for a set of individual phase space regions selected based on Higgs boson p_T and η, jet multiplicities N_{jets}, the mass of two jets, m_{jj}, and the p_T of the system combined from the Higgs boson and accompanying jets, which is denoted with Hjj. These quantities are evaluated with the `Rivet` tool [145] based on the information from the `POWHEG` generator.

Dedicated uncertainties can then be defined for each of the phase space regions, resulting in a set of more differential uncertainties. An analysis, which is sensitive to a specific phase space region, like ggH with one jet and a large Higgs boson p_T, would then be only sensitive to the corresponding uncertainty, while the remaining ones will have no impact on the result.
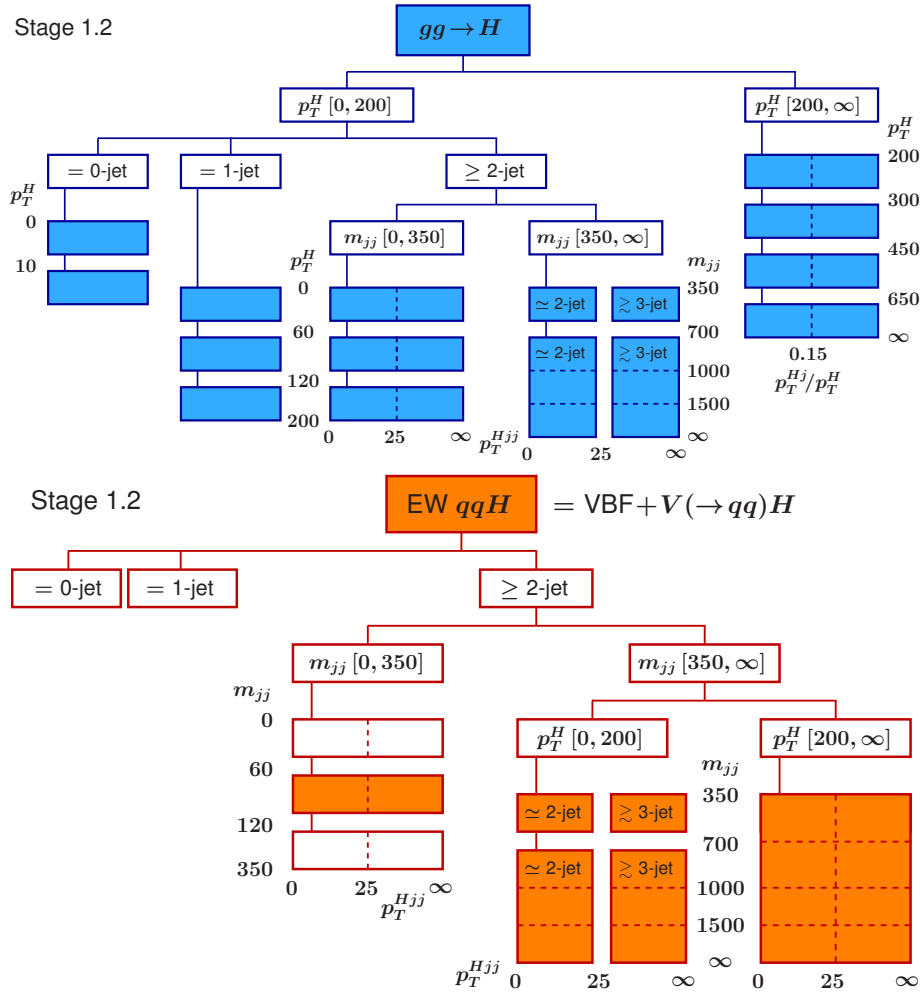
Figure 4.12.: STXS for (top) ggH and (bottom) qqH [144]. Stage 1.2 is updated with respect to the published Stage 1.1 with a finer binning in $p_T(H)$ beyond 200 GeV, for ggH. All phase space regions are shown for $|\eta(H)| < 2.5$, the forward region with $|\eta(H)| \geq 2.5$ is not shown, but is considered as an individual phase space region as well. Dashed lines represent a finer phase space binning defined for uncertainties.

In this context, a special treatment is made for the ggH contribution to the $H \to \tau\tau$ decay including a specific set of corrections and uncertainties. A reweighting scheme is provided to move from the NLO QCD precision of the events generated by POWHEG to the NNLO precision in QCD and a proper matching of parton showers achieved by POWHEG NNLOPS [146]. The corresponding event weights are determined in bins of the Higgs boson p_T and the number of jets. Using the reweighted contribution, a scheme is provided to cover all uncertainties related to the QCD scale used in the theory predictions, covering nine different sources [46].

A first set of four uncertainty sources is summarized in table 4.10 and consists of the uncertainties on the total yield of events from gluon fusion, two uncertainties on the migration across jet multiplicities, N_{jets}, and on the resummation scheme used in the computations [147].

An additional uncertainty covers the variation of the top quark mass, $\Delta\sigma_{m(t)}$, for the top

Uncertainty source	uncertainty in %		
	$N_{jets} = 0$	$N_{jets} = 1$	$N_{jets} \geq 2$, non-VBF
Total yield, $\Delta\sigma_{ggH}$	±3.81	±5.23	±8.87
Resummation, $\Delta\sigma_{res}$	±0.10	±4.51	±8.87
Migration for $N_{jets} : 0 \leftrightarrow \geq 1$, $\Delta\sigma_{01}$	∓4.15	±7.92	±4.44
Migration for $N_{jets} : 1 \leftrightarrow \geq 2$, $\Delta\sigma_{12}$		∓6.81	±18.2

Table 4.10.: Uncertainties on the total yield of the gluon fusion Higgs boson production for the QCD scale variation $\Delta\sigma_{ggH}$, the choice of the soft gluon resummation scheme $\Delta\sigma_{res}$ and the migration between jet multiplicities, $\Delta\sigma_{01}$ and $\Delta\sigma_{12}$. In case of $\Delta\sigma_{01}$ and $\Delta\sigma_{12}$, opposite signs indicate an anti-correlation between the jet multiplicities.

quark in the loop of the gluon fusion process. This uncertainty is applied to events with a Higgs boson fulfilling $p_T(H) > 160$ GeV. The variation of one standard deviation is rising linearly from 0% at $p_T(H) = 160$ GeV to 37% at $p_T(H) = 500$ GeV and remains at 37% for higher $p_T(H)$ values.

To account for migrations between different regions in $p_T(H)$ due to changes in the QCD scale, two uncertainties have been defined to cover such effects around $p_T(H) \sim 60$ GeV and around $p_T(H) \sim 120$ GeV for events with one or more jets, $N_{jets} \geq 1$, consistent with the STXS shown in figure 4.12. A variation of one standard deviation for the migration uncertainties is defined as follows:

- For a given $p_T(H)$ and smaller values, the variation has a constant value.
- For larger values of $p_T(H)$ it rises linearly until a second $p_T(H)$ threshold is reached.
- For $p_T(H)$ values above the second threshold, the variation remains at the reached value.

The defined $p_T(H)$ values and the corresponding variations are given in table 4.11.

Uncertainty source	N_{jets}	variation	$p_T(H)$ threshold
$p_T(H) \sim 60$ migration	1	-10%	20 GeV
		+10%	100 GeV
	≥ 2	-10%	0 GeV
		+10%	180 GeV
$p_T(H) \sim 120$ migration	≥ 1	-1.6%	90 GeV
		+14%	160 GeV

Table 4.11.: Uncertainty variations at given $p_T(H)$ thresholds for the $p_T(H)$ migration uncertainties for different jet multiplicities.

All uncertainties discussed so far are applied to events, which do not have a VBF signature, defined by the STXS. As shown in figure 4.12, the VBF signature in an event is defined by a Higgs boson with $|\eta(H)| < 2.5$ and $p_T(H) < 200$ GeV, two or more jets with $p_T(jet) > 30$

30 GeV, and a di-jet mass $m_{jj} \geq 350$ GeV for the two jets with the highest p_T.

The events from gluon fusion production with a VBF signature are supplied with two uncertainties specific for this phase space:

- The first uncertainty is a 20% variation of the total yield of events with a VBF signature,
- and the second uncertainty covers the migration of events from the region with low transverse momentum of the system composed from the Higgs boson and the two leading jets, $p_T(Hjj) < 25$ GeV, to the region with high $p_T(Hjj) \geq 25$ GeV. A variation of one standard deviation of the uncertainty is defined such, that the yield of events with a VBF signature and $p_T(Hjj) < 25$ GeV is changed by -32%, while it is changed by 23.5% in the region with $p_T(Hjj) \geq 25$ GeV.

A similar uncertainty scheme is applied to the qqH contribution, consisting of a total yield uncertainty for the change of the QCD scale and nine migration uncertainties based on N_{jets}, $p_T(H)$, $p_T(Hjj)$, and m_{jj}. The relative variations of one standard deviation are determined for each phase space region defined by the STXS visualized for qqH in figure 4.12. The average value for the variation of the uncertainty on the total yield equals to 0.38% for all events of the qqH contribution. The variation values for the uncertainties on the migration in N_{jets}, $p_T(Hjj)$ and $p_T(H)$ are given in table 4.12. The values are in most cases stable across the STXS phase space regions for qqH, with one exception: for events with $p_T(Hjj) \geq 25$ GeV, the variation value strongly depends on the $p_T(H)$ and m_{jj} phase space region.

Uncertainty source	average uncertainty or uncertainty range in %	
N_{jets} with selection $|\eta(H)| < 2.5$	$N_{jets} \leq 1$: ∓ 1.02	$N_{jets} \geq 2$: ± 0.89
$p_T(Hjj)$ with selection $|\eta(H)| < 2.5$, $N_{jets} \geq 2$	$p_T(Hjj) < 25$ GeV: ∓ 3.15	$p_T(Hjj) \geq 25$ GeV: $\pm[0.69, 6.04]$
$p_T(H)$ with selection $|\eta(H)| < 2.5$, $N_{jets} \geq 2$, $m_{jj} \geq 350$ GeV	$p_T(H) < 200$ GeV: ± 0.03	$p_T(H) \geq 200$ GeV: ∓ 0.26

Table 4.12.: Values for the variation of one standard deviation for the migration uncertainties in N_{jets}, $p_T(Hjj)$ and $p_T(H)$. For N_{jets} and $p_T(H)$, the variations stay stable across all phase space regions. In case of $p_T(Hjj)$, the correlation of this quantity to $p_T(H)$ and m_{jj} leads to phase space dependent values for regions with $p_T(Hjj) \geq 25$ GeV. The variation value is largest for low m_{jj}, decreasing with higher m_{jj}. Furthermore, it is larger for $p_T(H) \geq 200$ GeV than for $p_T(H) < 200$ GeV in the same m_{jj} phase space region.

The last set of qqH specific uncertainties is for the migrations in m_{jj} shown in table 4.13. The values are stable across the different phase space regions. A variation of one standard deviation covers a migration from a region with lower m_{jj} to all regions with higher m_{jj}.

Events affected by migration in m_{jj}: $|\eta(H)| < 2.5$, $N_{jets} \geq 2$, $m_{jj} \geq m_{jj}^{sel}$			
m_{jj}^{sel} in GeV	m_{jj}^{unc} in GeV	average uncertainty in %	
		$m_{jj} < m_{jj}^{unc}$	$m_{jj} \geq m_{jj}^{unc}$
0	60	∓17.7	±0.49
60	120	∓7.24	±0.36
120	350	∓1.55	±0.51
350	700	∓0.68	±0.43
700	1000	∓1.01	±0.48
1000	1500	∓0.43	±0.37

Table 4.13.: Values for the variation of one standard deviation for the migration uncertainties in m_{jj} around the phase space border m_{jj}^{unc}. The uncertainties are defined in the way, such that a migration from a lower m_{jj} region to all higher m_{jj} regions is considered, leading to the selection with m_{jj}^{sel}.

Additionally to these QCD scale related uncertainties for the ggH and qqH contributions to the $H \to \tau\tau$ decay, normalization uncertainties are introduced for the variation of the strong coupling parameter α_s and the variation of different sets of uncertainties on parton distribution functions (p.d.f.). These uncertainties affect only the total yield of the contributions. For all other contributions to the $H \to \tau\tau$ decay, as well as for gluon fusion and vector boson fusion production of the Higgs boson with the $H \to WW \to 2\ell2\nu$ decay, a set of three uncertainties is considered, which change the total yield of the corresponding contribution: the QCD scale uncertainty, the uncertainty for the α_s variation and the uncertainty on the p.d.f.'s. The values for one standard deviation of the uncertainties affecting the total yield of the contributions are given in table 4.14, together with the resulting total uncertainty.

Contribution		relative uncertainty in %			
		QCD scale	α_s	p.d.f. choice	total
Gluon fusion		-	1.9	2.6	3.2
VBF + V($\to$qq)		-	2.1	0.5	2.2
Z($\to \ell\ell/\nu\nu$) associated	$H \to \tau\tau$	3.8	1.3	0.9	4.2
$W^\pm(\to \ell\nu)$ associated		0.7	1.7	0.9	2.0
$t\bar{t}$ associated		9.2	3.0	2.0	9.9
Gluon fusion	$H \to WW \to 2\ell2\nu$	4.0	1.9	2.6	5.1
Vector boson fusion		0.4	2.1	0.5	2.2

Table 4.14.: Uncertainties affecting the total yield of the considered contribution with three distinct sources combined into a total uncertainty used for the analysis [46].

4.2.2. MSSM Higgs Boson Contributions

In contrast to the measurements of the properties of the observed Higgs boson at 125 GeV, a search for one or more additional Higgs bosons requires a coverage of a wide mass range.

In the Higgs boson search presented in this thesis, about 30 simulated samples are used with Higgs boson masses ranging from 110 GeV to 3.2 TeV for each considered production mode. For intermediate masses, a template morphing technique is used, explained in detail later in this subsection.

To be as model-independent as possible, the search for additional Higgs boson resonances is usually kept inclusive in the selection and categorization, The production modes targeted by the analysis are chosen to be the ones with the highest expected cross-section. This covers gluon fusion, denoted with ggϕ, and the production of the Higgs boson associated with bottom quarks, denoted with bbϕ, which is significantly enhanced in certain theoretical scenarios, as explained in section 2.3. In the context of the MSSM, the contribution of the light scalar Higgs boson h from VBF + V $\rightarrow$ (qq) is taken additionally into account, denoted with qqh.

The ggϕ production mode is simulated using `Pythia 8.2` with LO precision in QCD. The simulation of the Higgs boson is configured using a fixed set of SUSY parameters in the SUSY Les Houches Accord (SLHA) format [148, 149], which are computed using `FeynHiggs` [150]. To reach NLO precision, event weights are computed, which depend on $p_T(\phi)$. These weights are used to reweight the p_T distribution from LO `Pythia 8.2` to the expected p_T spectrum from `POWHEG` at NLO QCD based on a THDM Higgs boson model at fixed reference values of the parameters, in particular the mass of the Higgs boson m_ϕ, the mixing angle α of the scalar Higgs boson mass matrix, and the ratio of the vacuum expectation values $\tan \beta$.

The bbϕ contribution is modelled using `Madgraph 5 aMC@NLO` with fixed MSSM parameters at NLO precision in QCD assuming the 4-flavour scheme for the proton. Since a difference between the NLO predictions of `Madgraph 5 aMC@NLO` and `POWHEG` has been observed [46], an additional uncertainty is introduced to account for the difference in acceptance in the categories with and without b-tagged jets by varying the shower scale parameter Q_{sh} and the QCD scale in `Madgraph 5 aMC@NLO` by a factor of two.

Signal Template Morphing

To obtain binned distributions for the MSSM signals at intermediate masses, which are not simulated with Monte-Carlo generators, the template morphing technique is performed. The required mass m_ϕ of the Higgs boson serves as the morphing parameter. At first, the neighbouring mass values are determined, denoted with m_ϕ^- and m_ϕ^+, for which the binned distributions for statistical inference are obtained from simulated samples. The required mass value is then between these neighbouring masses: $m_\phi \in [m_\phi^-, m_\phi^+]$.

To estimate the distribution of the discriminator D for an intermediate Higgs boson mass, the cumulative distribution functions (CDFs) are derived from the probability density functions (PDFs) of D for the neighbouring masses m_ϕ^- and m_ϕ^+. An illustrative example for the distributions of the discriminator (top left) and the corresponding CDFs (top right) is given in figure 4.13.

In the next step, value pairs of D are determined, (D^-, D^+), which correspond to the same value of the two CDFs. To obtain continuous CDFs from the histograms, the probability values are linearly interpolated between the probability values at the bin edges of the CDF histograms. This is indicated by thick red and blue lines in the diagram of figure 4.13 (top right). The CDF values at the leftmost edges with the same value of one CDF histogram are then projected onto the other CDF, so that the discriminator value for the same probability
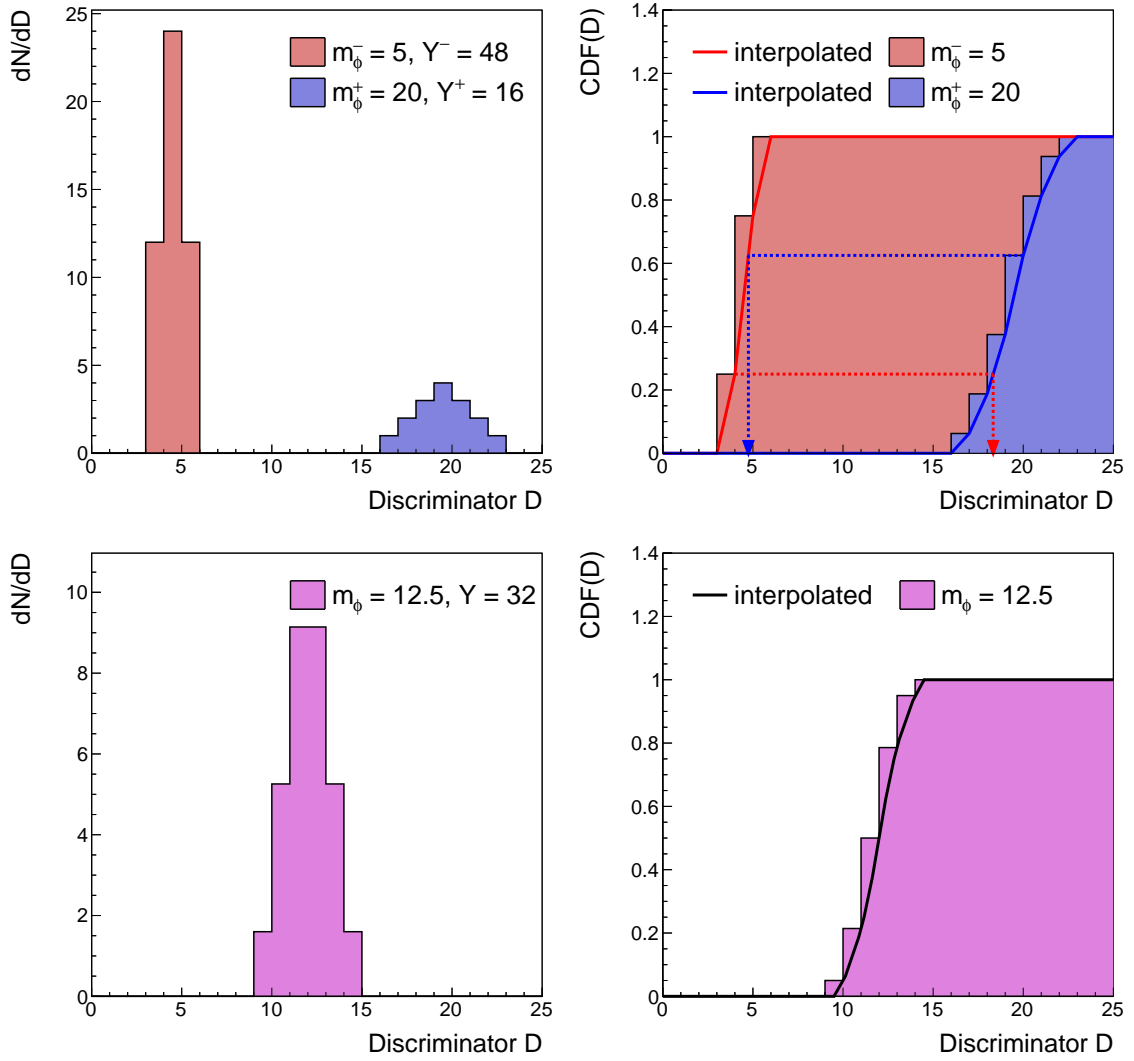
Figure 4.13.: An illustrative example to explain the method of signal template morphing. Details are given in the text.

can be obtained from linear interpolation between the bin edges, choosing the leftmost probability value for bins with equal values. This is illustrated with dashed red and blue arrows in figure 4.13 (top right). In that way, a value pair of D is built, consisting of the value from the edge for one of the two CDFs and the interpolated discriminator value from the other CDF, both with the same probability value.

The CDF for the intermediate m_ϕ is computed from the discriminator value pairs using

$$D = D^- + (m_\phi - m_\phi^-) \cdot \frac{D^+ - D^-}{m_\phi^- - m_\phi^-},$$

and the corresponding probabilities. This interpolation is accurate, as long as the change in the shape and the yield of the distribution of D is correlated with the change in mass m_ϕ.

In table 4.15, the values D^-, D^+, the derived value D, and the probability values corresponding to the three discriminator values are shown for the example from figure 4.13.

D⁻	D⁺	D	CDF(D)
3	16	9.5	0
3.25	17	10.125	0.0625
3.75	18	10.875	0.1875
4	18.3333	11.1667	0.25
4.25	19	11.625	0.375
4.75	20	12.375	0.625
5	20.6667	12.8333	0.75
5.25	21	13.125	0.8125
5.75	22	13.875	0.9375
6	23	14.5	1

Table 4.15.: Values of the discriminator with the same cumulative probability value for the distributions of the small, large and intermediate Higgs boson mass of the illustrative example. The intermediate mass is chosen to be $m_\phi = 12.5$ in this example.

Next, the obtained CDF needs to be mapped onto the binning used for the discriminator D. This is done by using the derived discriminator values and the corresponding probabilities and linearly interpolating these to a continuous probability function. Then, this function is evaluated for discriminator values of the edges of each histogram bin. The obtained CDF histogram is then turned into a PDF by building difference quotients for each histogram bin from the CDF values at the left and right edges:

$$PDF(bin) = \frac{CDF^{right}(bin) - CDF^{left}(bin)}{bin\ width} \tag{4.11}$$

In the last step, the obtained PDF for the intermediate Higgs boson mass is scaled to the interpolated yield Y using

$$Y = Y^- + (m_\phi - m_\phi^-) \cdot \frac{Y^+ - Y^-}{m_\phi^- - m_\phi^-}, \tag{4.12}$$

with the yields Y^- and Y^+ obtained from the discriminator distributions of the neighbouring Higgs boson masses. The derived continuous CDF, the corresponding CDF histogram, and the resulting distribution of D are shown at the bottom of figure 4.13.

This procedure is applied to the nominal distribution of a discriminator as well as to the distributions resulting from systematic uncertainties altering the shape of the discriminator distribution. In case of normalization uncertainties, equation 4.12 is used to interpolate the magnitude of the normalization change if it is dependent on m_ϕ. The signal template morphing is based on CDFs to make a smooth transition between the discriminator distributions preserving cumulative probabilities.

Corrections and Uncertainties for ggϕ

The main correction applied to each MSSM ggϕ expectation is the reweighting from LO to NLO QCD precision based on $p_T(\phi)$ [151]. At LO QCD precision modelled by

`Pythia 8.2`, the transverse momentum of the Higgs boson originates from initial state radiation of the partons (ISR). The matrix element of the hard scattering process itself, illustrated in figure 4.14, is expected to lead to $p_T(\phi) = 0$ due to momentum conservation in the collinear approximation. The loop consists of heavy, strongly interacting particles, which interact with the incoming gluons on one hand and with the Higgs boson on the other hand. Assuming only SM particles in the loop, which would be valid for the SM and THDM models, the most significant contributions would originate from the top and bottom quark. Extending the particle spectrum with MSSM particles, the quark superpartners, squarks, can also contribute to the loop, mostly with stop and sbottom loops, indicated in the Feynman diagrams in the middle and at the right of figure 4.14. However, these contributions are suppressed by $1/m_{\tilde{q}}$ in the matrix element, if considering the limit of high squark masses $m_{\tilde{q}} \gg m_h$ with respect to the mass of the light Higgs boson [152].
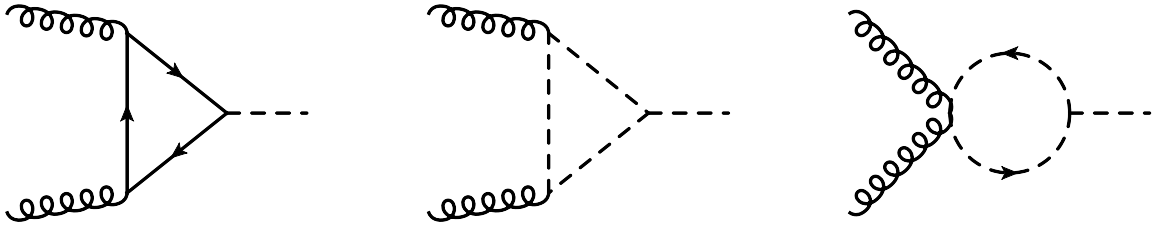
Figure 4.14.: Feynman diagrams of the gluon fusion Higgs boson production at LO QCD precision of the matrix element [152]. On the left, only quarks contribute to the loop, mainly top and bottom quarks because of their high mass. The diagrams in the middle and on the right represent possible contributions from quark superpartners, squarks, mainly stop and sbottom superpartners. These SUSY contributions are suppressed by the masses of the SUSY particles, which are expected to be above several TeV.

In summary, the main contributions to the LO cross-section proportional to the squared matrix element can be reduced to three contributions: the contribution with only the top quark in the loop, σ_t, the contribution with only the bottom quark in the loop, σ_b, and the top-bottom interference term, σ_{tb}. The decomposition of the total cross-section $\sigma_{gg\phi}$ is given by:

$$\sigma_{gg\phi} = \sigma_t + \sigma_b + \sigma_{tb} \tag{4.13}$$

Corrections at NLO QCD enter into the calculation of the matrix element by additional contributions of particles which interact via the strong interaction with the coupling parameter α_s. An additional order in α_s corresponds to up to two additional interaction vertices to be added to the LO Feynman diagram. The corrections can be separated into loop corrections, corrections to vertices and corrections leading to emissions of additional real particles, with the latter type being able to alter the Higgs boson transverse momentum on the level of the matrix element. If R-parity conservation is assumed, supersymmetric particles can only be produced in pairs. As one of the consequences, the only possible real emission at NLO QCD is an emission of a gluon or a quark. Example Feynman diagrams with gluon emissions at NLO QCD are shown in figure 4.15, with particles in the loop being quarks or squarks of top or bottom flavour.

If real emissions are introduced into the gluon fusion Higgs boson production process,
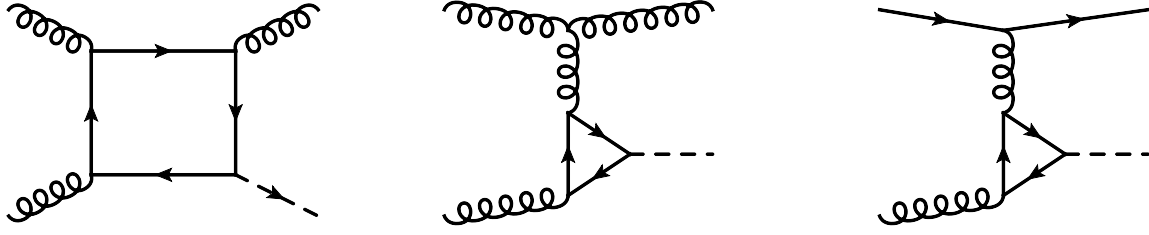
Figure 4.15.: Example Feynman diagrams for NLO QCD corrections with real emissions of quarks or gluons [152]. In general, the particles in the loop may be both the top and bottom quarks, as well as their superpartners. The diagrams in the middle and on the right can be rotated by 90° to obtain another example of a real emission.

logarithms $\log(p_T(\phi)/m_\phi)$ enter the fixed order computation of the matrix element, leading to a divergence for small Higgs boson transverse momentum, $p_T(\phi) \to 0$. To mitigate this divergence, a resummation of the logarithmic terms to all orders is needed to obtain finite results. It is possible to factorize the resummed logarithms as an exponential factor in the collinear limit $p_T(\phi) \to 0$ from the remaining hard scattering process. An energy scale μ_{res} needs to be introduced, up to which the resummed result is accurate. In the approach of the POWHEG Monte-Carlo generator, the matching between the resummed result valid for low $p_T(\phi)$ and the fixed order result valid for high $p_T(\phi)$ is performed dynamically by introducing a damping factor d:

$$d = \frac{\mu_{res}^2}{\mu_{res}^2 + p_T^2(\phi)} \tag{4.14}$$

The parts of the squared matrix element, which differ between the resummed and the fixed order results, are then multiplied by d and $1-d$ respectively to preserve the total inclusive cross-section at any scale μ_{res}. In consequence, an anti-correlation is introduced between the low $p_T(\phi)$ and high $p_T(\phi)$ regimes by changes of μ_{res}. It was found [151], that the resummation scale μ_{res} is not only dependent on the Higgs boson mass m_ϕ, but also on the mass of the quark in the loop, m_q. Therefore, the derivation of the Higgs boson transverse momentum distribution is considered as a multi-scale problem, involving the mass of the Higgs boson, its p_T, and m_q. To take this into account, the individual $p_T(\phi)$-dependent contributions in equation 4.13 are computed at three different scales μ_{res}^t, μ_{res}^b and μ_{res}^{tb}, depending on the involved quark flavours in the contributions. Following the proposed approach [151, 153], the optimal scales have been derived for a Higgs boson mass range $m_\phi \in [80, 3200]$ GeV as shown in figure 4.16. These scales are used to derive the individual $p_T(\phi)$ spectrum at NLO QCD precision for each of the top, bottom and interference terms contributing to the total $p_T(\phi)$ spectrum.

The three contributions to the cross-section are proportional to the Yukawa coupling factors ζ_ϕ^q of the quarks, as for example introduced in table 2.5, involved in the loops of the squared matrix elements:

$$\sigma_t \sim \left(\zeta_\phi^t\right)^2, \qquad \sigma_b \sim \left(\zeta_\phi^b\right)^2, \qquad \sigma_{tb} \sim \zeta_\phi^t \cdot \zeta_\phi^b.$$

This allows to encode a coupling structure different from the SM through the Yukawa coupling factors, as long as it is ensured, that the main contribution to the total cross-
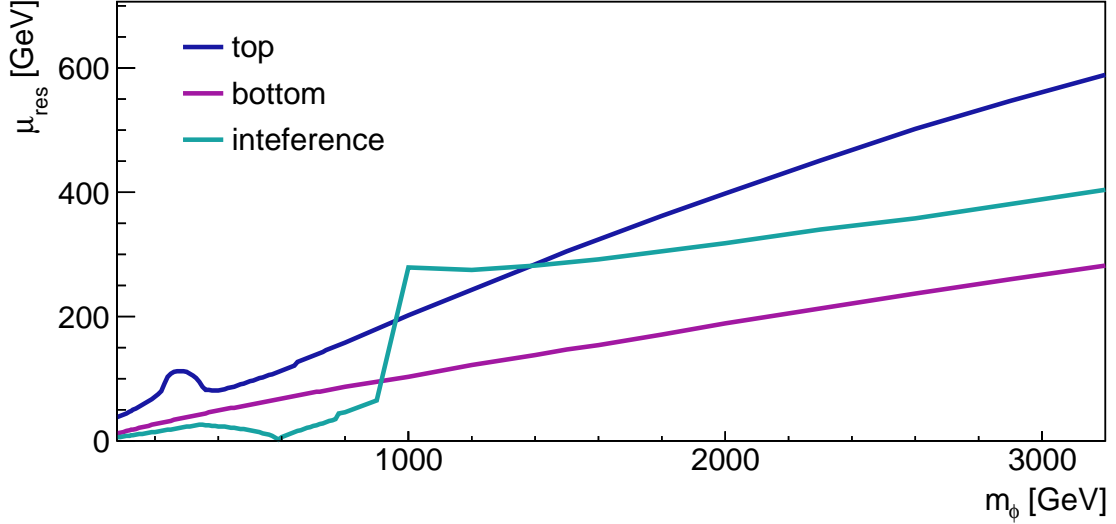
Figure 4.16.: Resummation scales derived for Higgs boson masses between 80 and 3200 GeV, used in the simulation of POWHEG for the contributions to the gluon fusion production from the top quark, bottom quark in the loop and the interference term.

section as a function of $p_T(\phi)$ originates from top and bottom quarks in the loop. This is for example given in THDM. The Yukawa couplings in THDM are functions of several parameters, depending on the Higgs boson in question. For the two scalar Higgs bosons, $\phi \in \{h, H\}$, the coupling factors depend on m_ϕ, $\tan\beta$, and the mixing angle α. In case of the pseudoscalar Higgs boson, A, the Yukawa couplings depend only on m_A and $\tan\beta$. The cross-section at a different point in the parameter space of a model, $\sigma_{gg\phi}^{NLO}$, is obtained by reweighting of the individual contributions with ratios between the target Yukawa coupling factors ζ_ϕ^q and the reference Yukawa coupling factors $\bar{\zeta}_\phi^q$:

$$
\sigma_{gg\phi}^{NLO} = \left(\frac{\zeta_\phi^t}{\bar{\zeta}_\phi^t}\right)^2 \cdot \sigma_t + \left(\frac{\zeta_\phi^b}{\bar{\zeta}_\phi^b}\right)^2 \cdot \sigma_b + \frac{\zeta_\phi^t \cdot \zeta_\phi^b}{\bar{\zeta}_\phi^t \cdot \bar{\zeta}_\phi^b} \cdot \sigma_{tb}
$$

$$
= \sigma_t^{NLO} \qquad + \sigma_b^{NLO} \qquad + \sigma_{tb}^{NLO}
$$

(4.15)

The Monte-Carlo generation can therefore be restricted to a fixed set of reference parameters $\tan\beta$ and α. In the context of this thesis, `Pythia 8.2` samples at LO QCD precision were reweighted to distributions predicted by `POWHEG` for Higgs bosons h, H or A, and for contributions σ_t, σ_b or σ_{tb} from a THDM simulation.

With this setup, various THDM models can be tested by reweighing from one reference set of THDM parameters to another at NLO QCD precision. To be able to describe the MSSM with a type-2 THDM inspired Higgs sector, it is necessary to estimate the effect of SUSY particles in the loop of the gluon fusion process, as well as the NLO QCD corrections from SUSY particles. In figure 4.17, examples are shown for such corrections. Some of these corrections, like shown in the diagram on the left of figure 4.17, can be considered as a modification of the Yukawa coupling of the quark in the loop to the Higgs boson. The

most relevant of such modifications is the one for the Yukawa coupling of the bottom quark, often referred to as the Δ_b correction [43, 154]. The remaining effects of the NLO QCD corrections related to SUSY were studied for several heavy Higgs boson masses and model parameters and found to be below 5% in the $p_T(\phi)$ distribution [155]. It is decided to consider only the Δ_b correction as relevant for the description of the $p_T(\phi)$ spectrum of a MSSM Higgs boson.
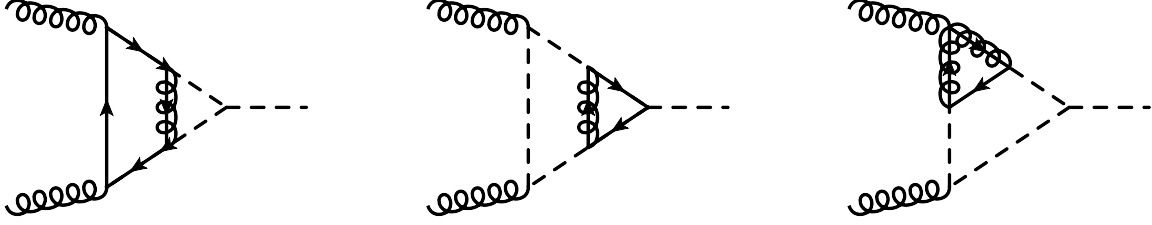
Figure 4.17.: Example Feynman diagrams showing NLO QCD corrections involving SUSY particles [152]. The diagram on the left can be expressed as a modified Yukawa coupling between the quarks in the loop and the Higgs boson. Such a procedure is not possible for the diagrams in the middle and on the right.

For a model-independent search of a single Higgs boson, SM couplings to the top and to the bottom are assumed, leading to the choice of the Yukawa coupling factors in equation 4.15 $\zeta_\phi^t = \zeta_\phi^b = 1$.

Depending on the considered model and the mass of the Higgs boson, m_ϕ, an inclusive value of the product of the cross-section and the branching fraction, $\sigma \cdot BR$, might by known at a higher precision in QCD, than the NLO QCD precision differential in $p_T(\phi)$, which is obtained from the reweighting method. To account for this, the reweighting of simulated events is adapted to the form given as:

$$\sigma_{gg\phi} = \sigma \cdot BR \cdot \left(\frac{\sigma_t^{NLO}}{\sigma_{gg\phi}^{NLO}} \cdot D_t + \frac{\sigma_b^{NLO}}{\sigma_{gg\phi}^{NLO}} \cdot D_b + \frac{\sigma_{tb}^{NLO}}{\sigma_{gg\phi}^{NLO}} \cdot D_{tb} \right) \qquad (4.16)$$

To elevate the simulated LO samples to NLO precision, the following steps are performed:

1. Discriminator distributions D_t, D_b and D_{tb} are obtained from simulated events reweighted with the ratio of the normalized $p_T(\phi)$ distributions between the NLO and LO expectation, for example, from `POWHEG` and `Pythia 8.2`.
2. The yields of the discriminator distributions are normalized unity.
3. The normalized distributions are combined to one contribution by multiplying each with the fraction expected to contribute to the total cross-section of the considered model at NLO QCD precision.
4. After that, the resulting distribution is scaled to the inclusive $\sigma \cdot BR$ value with the highest available QCD precision, leading to the reweighted distribution $\sigma_{gg\phi}$.

The mass points m_ϕ and the corresponding scales μ_{res}^t, μ_{res}^b and μ_{res}^{tb} shown in figure 4.16 are used to produce the $p_T(\phi)$ spectrum for each of the three THDM Higgs bosons h, H and A with the reference parameters in equation 4.17, for each of the contributions σ_t, σ_b

and σ_i separately.

$$\alpha = \pi/4, \qquad \tan \beta = \begin{cases} 50 & \phi = H \\ 15 & \phi \in \{h, A\} \end{cases} \tag{4.17}$$

The corresponding reference Yukawa coupling factors $\bar{\zeta}^t_\phi$ and $\bar{\zeta}^b_\phi$ are functions of these parameters and are summarized in table 4.16.

top coupling	bottom coupling
$\bar{\zeta}^t_h = 0.71$	$\bar{\zeta}^b_h = -10.63$
$\bar{\zeta}^t_H = 0.71$	$\bar{\zeta}^b_H = 35.36$
$\bar{\zeta}^t_A = 1/15$	$\bar{\zeta}^b_A = 15$

Table 4.16.: Yukawa coupling factors computed for a reference set of THDM model parameters given in equation 4.17. These parameters are used to produce simulated datasets with `POWHEG` at NLO precision in QCD for the contributions to the loop of the gluon fusion process by the top quark, the bottom quark and their interference. The transverse momentum distributions of Higgs bosons in these datasets allow to derive weights for the simulated events from `Pythia 8.2` at LO precision in QCD.
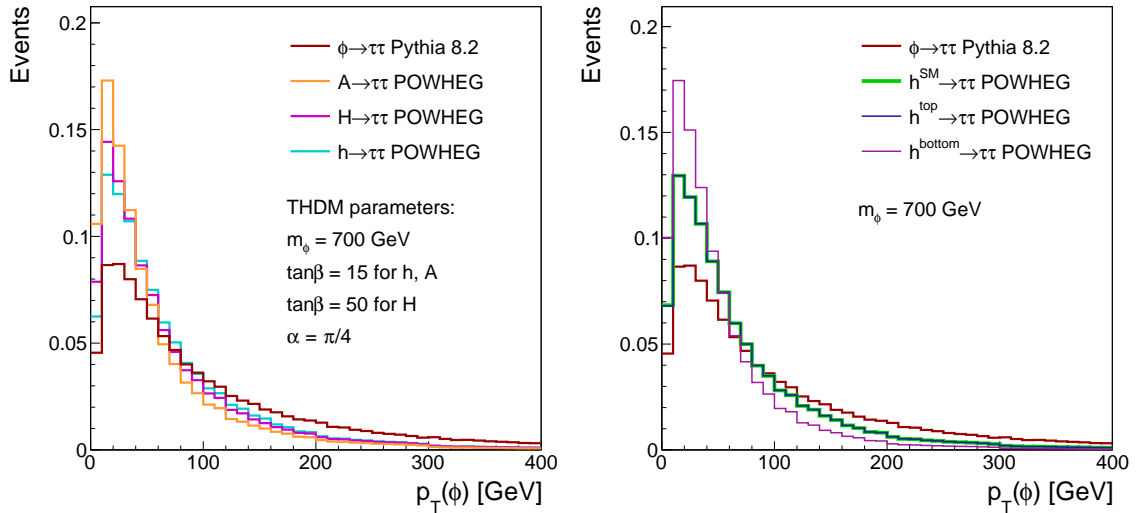
Figure 4.18.: Transverse momentum distributions of a Higgs boson with a mass of 700 GeV, shown for LO QCD precision from `Pythia 8.2`, of NLO QCD from `POWHEG` for the THDM reference parameter set on the left, and for contributions with SM couplings, top or bottom quark only on the right.

In figure 4.18 (left), the $p_T(\phi)$ distribution at LO QCD from `Pythia 8.2` with a Higgs boson mass $m_\phi = 700$ GeV is compared to the NLO prediction of `POWHEG` for all three THDM Higgs bosons h, H and A with the same mass and for the reference set of THDM parameters listed in equation 4.17. In general, the description of $p_T(\phi)$ with `POWHEG` at

NLO QCD is observed to be softer, than the ISR modelled by `Pythia 8.2`. Furthermore, the contribution with the top quark in the loop leads to a harder $p_T(\phi)$ spectrum than the contribution from the bottom quark in the loop. In consequence, the hardest distribution obtained with the Yukawa coupling factors from table 4.16 is expected for the light scalar Higgs boson, h, followed by heavy scalar H. The pseudoscalar Higgs boson A has the softest $p_T(\phi)$ spectrum.

On the right of figure 4.18, the $p_T(\phi)$ distribution of a Higgs boson with $m_\phi = 700$ GeV at LO QCD from `Pythia 8.2` is shown together with the distribution from a Higgs boson with SM couplings, with only the top quark and with only the bottom quark in the loop at the same Higgs boson mass. As expected, the SM-like distribution is dominated by the top quark contribution.
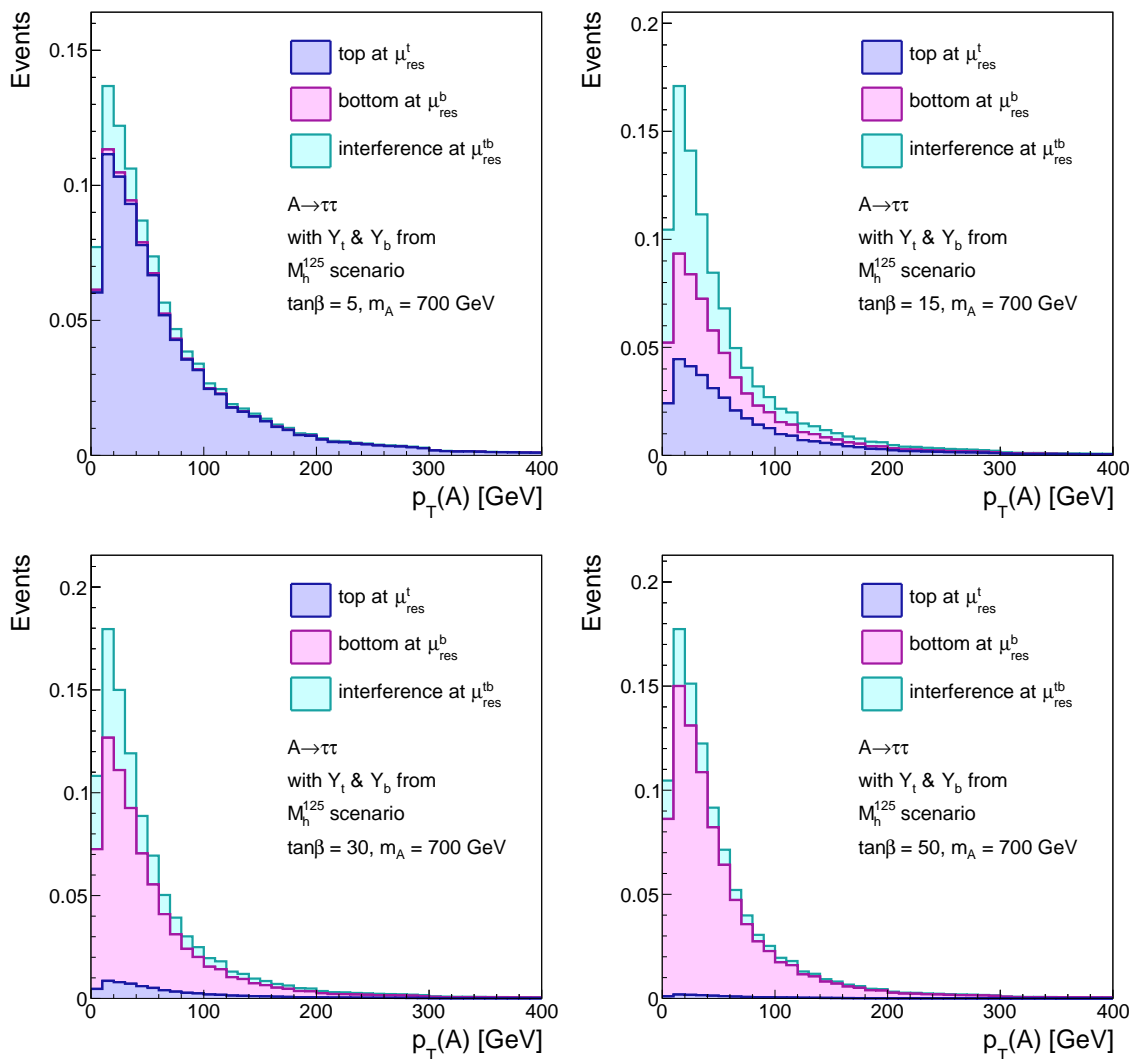
Figure 4.19.: Contributions to the $p_T(A)$ spectrum of the pseudoscalar Higgs boson, evaluated for a mass at 700 GeV and $\tan\beta \in \{5, 15, 30, 50\}$ with Yukawa coupling factors from the M_h^{125} MSSM benchmark scenario [43].

To check the effect of reweighting from one $\tan\beta$ parameter value to another, the transverse momentum distributions of the pseudoscalar Higgs boson, $p_T(A)$ are shown in figure 4.19

for $\tan\beta \in \{5, 15, 30, 50\}$ and a mass $m_A = 700$ GeV. The distributions are obtained from events simulated with `Pythia 8.2`, reweighted to the expectation from the M_h^{125} MSSM benchmark scenario [43] by using the Yukawa coupling factors ζ_A^t and ζ_A^b predicted by this model. Moving from low to high $\tan\beta$ values, so from left to right and from top to bottom of figure 4.19, the composition of the total $p_T(A)$ spectrum changes. For low $\tan\beta$, the contribution with the top quark in the loop is most dominant. At $\tan\beta = 15$, all three contributions share equal importance, whereas for high values of $\tan\beta$, the bottom quark loop contribution is most dominant. In consequence, the $p_T(A)$ spectrum is softer at high $\tan\beta$ and harder at low $\tan\beta$.

If considered in the context of an MSSM scenario, the estimated $gg\phi$ contribution is provided with normalization uncertainties for p.d.f.'s, uncertainties from α_s variations, and QCD scale uncertainties, that are dependent on the parameters of the MSSM, m_A and $\tan\beta$.

Corrections and Uncertainties for bbϕ

To describe the Higgs boson production associated with bottom quarks, a proper flavour scheme needs to be chosen: Either four quark flavours are assumed to be contained in the accelerated protons together with gluons, up, down, charm and strange quarks, or five flavours, adding the bottom quark to the proton description. The four-flavour scheme (4FS) Feynman diagrams at LO QCD are shown on the left and in the middle of figure 4.20, the five-flavour scheme (5FS) diagram at LO QCD on the right.
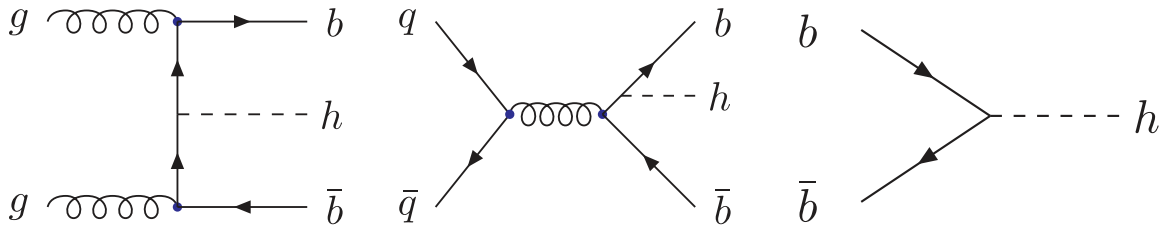
Figure 4.20.: Feynman diagrams for the Higgs boson fusion production associated with bottom quarks at leading order in QCD [156]. On the left and in the middle, diagrams from 4FS, on the right, a 5FS diagram are shown.

Already the LO diagrams show differences between the two schemes: the 4FS diagrams involves two strong interaction vertices, whereas the 5FS diagram does not involve QCD interactions. Furthermore, the schemes have different assumptions on the bottom quark. In 4FS, the bottom quark does not appear in the initial state, and is handled with a finite mass in the calculations. In contrast to that, the bottom quark in the 5FS has to be treated as massless to appear in the initial state [157].

At NLO QCD precision, virtual vertex and loop corrections, as well as real emissions of quarks or gluons contribute additionally to the total matrix element of the production process. For the 4FS, all terms up to the order α_s^3 contribute to NLO, whereas the 5FS NLO terms consist only of terms up to the order α_s. Virtual loop corrections to the diagram in the 4FS can contain not only the bottom quark, but also the top quark in the loop. If the Higgs boson is radiated off by the quark in the loop, the total 4FS cross-section is then composed of terms different in the Yukawa coupling structure. The terms can be grouped into contributions with bottom Yukawa coupling factor squared, $\zeta_\phi^b \cdot \zeta_\phi^b$, and with

the product of the top and bottom Yukawa coupling factors, $\zeta_\phi^b \cdot \zeta_\phi^t$ [157].

Also for the simulation of $bb\phi$ production, large logarithms need to be taken into account. As it is the case for `POWHEG` [158], this is controlled by a scale parameter in `Madgraph 5 aMC@NLO` [157], the shower scale parameter Q_{sh}. By fixing this parameter to a certain value, an upper bound is defined for the energy scale allowed for the parton shower. The exact value of the scale is determined on an event-by-event basis from a distribution with a peak at about $Q_{sh}/2$. This procedure allows to control the validity of soft and collinear emissions simulated with `Madgraph 5 aMC@NLO` and a proper matching to the expected fixed order calculation at high $p_T(\phi)$. The particular choice of Q_{sh} has an influence not only on the $p_T(\phi)$ distribution, but also on the kinematic properties of the bottom quarks and the resulting b-tagged jets.

The effect on the b-jet acceptance was tested for variations of the Q_{sh} parameter and the factorization and renormalization scales μ_F and μ_R. The migration between the categories without any b-tagged jets and categories with at least one b-tagged jet was considered as a function of the Higgs boson mass m_ϕ produced in association with bottom quarks. The relative deviations from the nominal yield per category introduced as uncertainties are shown in figure 4.21.
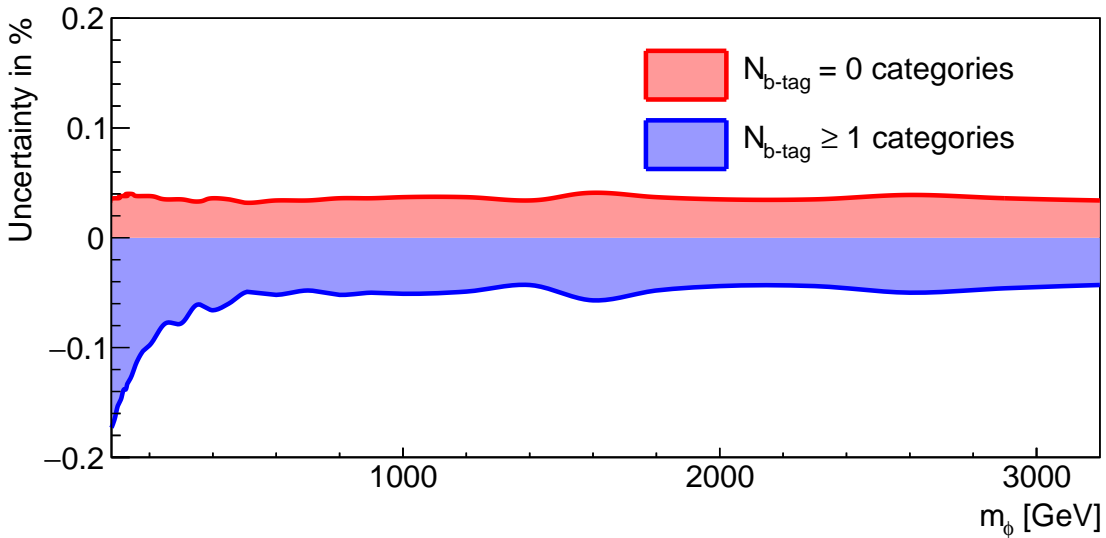
Figure 4.21.: Uncertainty on the migration between the categories without any b-tagged jets and the categories with at least one b-tagged jet due to the variation of the scale parameter Q_{sh} and the factorization and the renormalization scales μ_F and μ_R, shown as a function of m_ϕ. An anti-correlation between the categories can be observed, illustrating the migration effects.

This uncertainty is assumed to be sufficient to cover the changes in the acceptance due to the scale variations considered. However, if a categorization is planned to be introduced, which is dependent on $p_T(\phi)$, the uncertainty due to the change of the scales should be reconsidered as a function of $p_T(\phi)$.

The cross-section for $bb\phi$ production can be computed assuming different flavour schemes. For description of differential quantities through simulation of events with `Madgraph 5 aMC@NLO`, the 4FS is found to lead to a better description [157]. For the inclusive cross-section, however, the contributions from both schemes are matched consistently to each

other, if considered in a MSSM benchmark scenario [43]. In this matching scheme, the contribution of $\zeta_\phi^b \cdot \zeta_\phi^t$ terms is neglected, since it is vanishing for high $\tan\beta$, and the region with low $\tan\beta$ values is dominated by the gluon fusion production. The cross-section values for bbϕ production predicted by MSSM scenarios are provided by an uncertainty reflecting the variations of the p.d.f. parameters, the α_s coupling and the QCD scales involved into the computation of the cross-section in both schemes.

Estimation of the light scalar Higgs boson h

In the context of the MSSM interpretation of $\tau\tau$ final states, the MSSM prediction of the light scalar Higgs boson h, which is associated with the observed Higgs boson at 125 GeV, is estimated for bbh, ggh and qqh production modes. For bbh, the signal is estimated as discussed previously. For the dominant contributions from ggh and qqh, the simulated SM prediction is normalized to the expected MSSM value for $\sigma \cdot \mathrm{BR}$ in the $(m_A, \tan\beta)$ parameter space, using values shown in figure 2.2. In that way it is ensured, that the kinematic properties of h are compatible with the SM expectation. This approach is considered as valid as long as the mass of the light scalar is within the theoretical uncertainty, $m_h \in [122, 128]$ GeV.

In case of qqh, the reweighting factor for the cross-section needs to be computed from the Yukawa couplings provided with the M_h^{125} MSSM scenario:

$$\zeta_H^t = \sin\alpha/\sin\beta$$
$$\Rightarrow \alpha = \arcsin\left(\zeta_H^t \cdot \sin\left(\arctan\left(\tan\beta\right)\right)\right)$$
$$\zeta_h^V = \sin(\beta - \alpha) = \sin\left(\arctan\left(\tan\beta\right) - \arcsin\left(\zeta_H^t \cdot \sin\left(\arctan\left(\tan\beta\right)\right)\right)\right) \quad (4.18)$$

The value of ζ_h^V in the parameter region of M_h^{125} with $m_h \in [122, 128]$ GeV is found to be near 1, as expected. The total reweighting factor $\zeta_h^V \cdot \zeta_h^V \cdot \mathrm{BR}(h \rightarrow \tau\tau)/\mathrm{BR}(h_{SM} \rightarrow \tau\tau)$ is used to obtain the MSSM prediction.

4.3. Selection of $\tau\tau$ events

All reconstructed physics objects discussed in section 3.2 are selected to enrich the $H \rightarrow \tau\tau$ signal over different backgrounds. At first, the selection of leptons will be discussed, which are used to create the signal pair and define event-based vetoes. After this, the construction of the $\tau\tau$ pair is explained in general, followed by the selection of jets and corrections to the missing transverse energy. At the end of this section, the selection into the $\mu\tau_h$, $e\tau_h$, $\tau_h\tau_h$ and $e\mu$ final states is discussed.

4.3.1. Lepton Selection

Prior to the selection of leptons, the energies of the reconstructed electrons, muons, and τ_h candidates are corrected and assigned with corresponding uncertainties. A relative energy shift Δp_μ due to such a correction or uncertainty is applied to the entire 4-momentum p_μ of the considered lepton ℓ in the following way:

$$p'_\mu(\ell) = \left(1 + \Delta p_\mu(\ell)\right) \cdot p_\mu(\ell) \quad (4.19)$$

The energy of the muons is expected to be precise compared to electrons and τ_h candidates. Therefore, nor corrections are applied to the muon 4-momenta neither there are any uncertainties assigned. The muons undergo three different selections consisting of kinematic and quality criteria:

- The first and strictest selection is used for the signal $\tau\tau$ pair.
- The second, looser selection is used to prevent an overlap between the $\tau\tau$ final states described in subsection 4.3.4.
- The last and loosest selection is used only in the $\mu\tau_h$ final state to suppress the $Z \to \mu\mu$ background.

The selection requirements are summarized in table 4.17 using criteria introduced in subsection 3.2.3.

	Muon candidates for			
	Signal pair		Overlap veto	$Z \to \mu\mu$ veto
kinematic properties	$p_T(\mu) > 20(10)$ GeV $\|\eta(\mu)\| < 2.1(2.4)$	$\mu\tau_h(e\mu)$, $\mu\tau_h(e\mu)$	$p_T(\mu) > 10$ GeV, $\|\eta(\mu)\| < 2.4$	$p_T(\mu) > 15$ GeV, $\|\eta(\mu)\| < 2.4$
isolation in $\Delta R < 0.4$	$I_{rel}^{\Delta\beta} < 0.15(0.2)$	$\mu\tau_h(e\mu)$	$I_{rel}^{\Delta\beta} < 0.3$	$I_{rel}^{\Delta\beta} < 0.3$
identification	Medium WP		Medium WP	Loose WP
impact parameters	$d_{xy} < 0.045$ cm, $d_z < 0.2$ cm		$d_{xy} < 0.045$ cm, $d_z < 0.2$ cm	$d_{xy} < 0.045$ cm, $d_z < 0.2$ cm

Table 4.17.: Selection requirements applied to muons.

For electrons, the energy corrections and uncertainties are derived separately for the energy scale and the resolution for each event [159, 160] using a multivariate BDT regression for data and simulation. The scale is corrected for in data, such that the $Z \to ee$ peak is located at $m_Z = 91.188$ GeV [32] as used in the simulation. The resolution is corrected in simulation to match the measured resolution in data. Scale and resolution uncertainties are applied both to simulation and treated as correlated across the years.

The effects of the corrections and uncertainty shifts on the distribution of the invariant mass of the electron pair in a $Z \to ee$ enriched region of the data-taking year 2017 are illustrated in figure 4.22.

One the left, the following effects are visible after applying the corrections:

- The data distribution is shifted to lower values by the correction, as can also be seen in the ratio of the lower panel, where in case of the data distributions, the corrected data is divided by uncorrected data.
- The simulated (MC) distribution is broader after the correction, as can be seen in the ratio plot, where corrected simulation is divided by uncorrected simulation.

- After the correction, the corrected data and MC distributions agree better, shown with black dots in the ratio plot, where corrected data is divided by corrected MC.
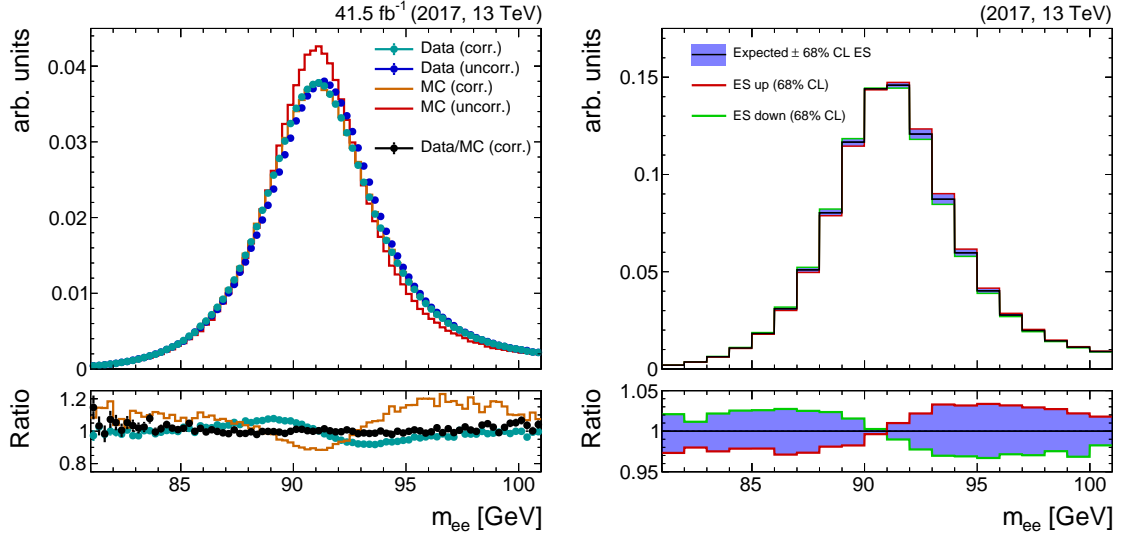
Figure 4.22.: Effects of the corrections (left) and uncertainty variations (right) [159, 160] on the invariant mass of an electron pair in a $Z \rightarrow ee$ enriched control region for the data-taking year 2017. Details are given in the text.

In the right figure, the scale uncertainty variation is shown, compared to the corrected expectation. The green line corresponds to a shift to lower values, the red line to a shift to higher values of m_{ee}. The uncertainties on the resolution are not shown due to their negligible effect.

In case of the estimation of genuine τ lepton pairs described in subsection 4.1.1, the electron energy scale and resolution are expected to be different from the description both in data and simulation. For this purpose, separate corrections to the energy scale of the electrons and corresponding uncertainties are determined, neglecting resolution effects. The summary of these corrections and uncertainties is given in table 4.18.

Detector region	Data-taking year		
	2016	2017	2018
$\lvert\eta(e)\rvert < 1.479$	$-0.24 \pm 0.50\%$	$-0.07 \pm 0.50\%$	$-0.33 \pm 0.50\%$
$\lvert\eta(e)\rvert \geq 1.479$	$-0.70 \pm 1.25\%$	$-1.13 \pm 1.25\%$	$-0.56 \pm 1.25\%$

Table 4.18.: Energy scale corrections and uncertainties estimated for electrons in τ embedded events. The uncertainty shift is chosen differently for the ECAL barrel and ECAL endcap regions, defined by $\eta(e)$ of the supercluster. The uncertainties are treated as correlated across the two detector regions and across the years.

After the energy of the electrons has been corrected, three sets of selection requirements to the electrons are defined, in an equivalent way as for muons, summarized in table 4.19 using criteria from subsection 3.2.4:

- The first and strictest selection is used for the signal $\tau\tau$ pair.
- The second, looser selection is used to prevent an overlap between the $\tau\tau$ final states described in subsection 4.3.4.
- The last and loosest selection is used only in the $e\tau_h$ final state to suppress the $Z \to ee$ background.

	Electron candidates for			
	Signal pair		Overlap veto	Z → ee veto
kinematic properties	$p_T(e) > 29(17)$ GeV $\|\eta(e)\| < 2.1(2.4)$	$e\tau_h(e\mu)$, $e\tau_h(e\mu)$	$p_T(e) > 10$ GeV, $\|\eta(e)\| < 2.5$	$p_T(e) > 15$ GeV, $\|\eta(e)\| < 2.5$
isolation in $\Delta R < 0.3$	$I_{rel}^{A_{eff}} < 0.15$		$I_{rel}^{A_{eff}} < 0.3$	$I_{rel}^{A_{eff}} < 0.3$
identification	MVA based, 90% efficiency WP		MVA based, 90% efficiency WP	cut based, veto WP
track quality	$N_{lost\ hits} \leq 1$		$N_{lost\ hits} \leq 1$	N.A.
conversion veto	passed		passed	N.A.
impact parameters	$d_{xy} < 0.045$ cm, $d_z < 0.2$ cm		$d_{xy} < 0.045$ cm, $d_z < 0.2$ cm	$d_{xy} < 0.045$ cm, $d_z < 0.2$ cm

Table 4.19.: Selection requirements applied to electrons. Selection criteria not applied are marked with N.A.

Corrections and uncertainties are determined and evaluated differently for genuine τ_h candidates, or muons, electrons, or jets misidentified as τ_h candidates. In case of genuine τ_h candidates, they are determined for each of the two estimation methods, the τ embedding method for the backgrounds and the simulation based estimation for the signal.

The energy scale of genuine τ_h candidates is determined separately for each reconstructed decay mode in a $Z \to \tau\tau$ enriched region of the $\mu\tau_h$ selection, which is discussed in detail in subsection 4.3.4. The resulting relative shifts for the corrections and uncertainties with respect to the uncorrected 4-momenta of the genuine τ_h candidates are given in table 4.20. The corrections and uncertainties depend on the decay mode of the τ_h candidate, and the considered data-taking year.

The decay modes of the τ_h candidates with only one charged particle, DM $\in \{0, 1, 2\}$, can have a signature similar to reconstructed muons or electrons. In consequence, $Z \to ee$ and $Z \to \mu\mu$ processes can contribute to the selection of the $e\tau_h$ and $\mu\tau_h$ final states by an electron or a muon misidentified as a τ_h candidate. Despite the fact, that the rejection efficiency of such events is high for the discriminators discussed in subsection 3.2.8, a

data-taking year Energy scale shift for	2016	2017 simulation	2018
DM = 1	$-1.0^{+0.7}_{-0.6}\%$	$+0.7^{+1.0}_{-0.6}\%$	$-1.6^{+0.7}_{-0.7}\%$
DM $\in \{1, 2\}$	$-0.1^{+0.4}_{-0.3}\%$	$+0.2^{+0.5}_{-0.4}\%$	$-0.3^{+0.4}_{-0.4}\%$
DM = 10	$+0.8^{+0.7}_{-0.4}\%$	$+0.2^{+0.5}_{-0.5}\%$	$-1.1^{+0.5}_{-0.5}\%$
DM = 11	$+0.1^{+1.0}_{-1.0}\%$	$-0.5^{+1.6}_{-1.0}\%$	$+0.1^{+1.1}_{-0.9}\%$
Energy scale shift for		τ embedding	
DM = 1	$-0.2^{+0.5}_{-0.5}\%$	$+0.0^{+0.4}_{-0.4}\%$	$-0.3^{+0.4}_{-0.4}\%$
DM $\in \{1, 2\}$	$-0.2^{+0.2}_{-0.3}\%$	$-1.2^{+0.5}_{-0.2}\%$	$-0.6^{+0.4}_{-0.3}\%$
DM = 10	$-1.3^{+0.3}_{-0.5}\%$	$-0.8^{+0.4}_{-0.5}\%$	$-0.7^{+0.3}_{-0.3}\%$
DM = 11	$-1.3^{+0.3}_{-0.5}\%$	$-0.8^{+0.4}_{-0.5}\%$	$-0.7^{+0.3}_{-0.3}\%$

Table 4.20.: Energy scale corrections and uncertainties for genuine τ_h candidates for each of the three data-taking years 2016, 2017 and 2018. Details are given in the text.

non-negligible contribution remains because of the relatively high Z → ee and Z → μμ rates. Such τ_h candidates reconstructed from electrons or muons require a dedicated energy scale correction and corresponding uncertainties, which are measured in Z → ee and Z → μμ enriched regions of eτ_h and μτ_h final states, respectively. The energy scale corrections and uncertainties were measured for the decay modes separately, and in case of electrons misidentified as τ_h candidates, the energy scale was found to be different between the barrel and endcap regions of the detector. The resulting corrections and uncertainties are given in table 4.21 and in table 4.22.

	Data-taking year		
Decay mode	2016	2017	2018
DM = 0	$+0.0 \pm 1.0\%$	$-0.2 \pm 1.0\%$	$-0.2 \pm 1.0\%$
DM $\in \{1, 2\}$	$-0.5 \pm 1.0\%$	$-0.8 \pm 1.0\%$	$-1.0 \pm 1.0\%$

Table 4.21.: Energy scale corrections and uncertainties for muons misidentified as τ_h candidates in simulated Z → μμ samples for each of the three data-taking years 2016, 2017 and 2018. Details are given in the text.

After the energy of all reconstructed τ_h candidates has been corrected, these are selected as specified for the μτ_h, eτ_h and $\tau_h\tau_h$ final states in table 4.23.

| | Decay mode | | | |
| | DM = 0 | | DM ∈ {1, 2} | |
year	$|\eta| \leq 1.5$	$|\eta| > 1.5$	$|\eta| \leq 1.5$	$|\eta| > 1.5$
2016	$+0.7^{+0.8}_{-1.0}$ %	$-3.5^{+1.8}_{-1.1}$ %	$+3.4^{+1.2}_{-2.5}$ %	$+5.0^{+6.6}_{-5.7}$ %
2017	$+0.9^{+1.4}_{-0.9}$ %	$-2.6^{+2.2}_{-1.4}$ %	$+1.2^{+2.1}_{-1.0}$ %	$+1.5^{+6.5}_{-5.0}$ %
2018	$+1.4^{+0.9}_{-0.6}$ %	$-3.1^{+2.8}_{-1.2}$ %	$+1.9^{+1.3}_{-1.6}$ %	$-1.5^{+5.5}_{-4.3}$ %

Table 4.22.: Energy scale corrections and uncertainties for electrons misidentified as τ_h candidates in simulated $Z \to ee$ samples for each of the three data-taking years 2016, 2017 and 2018 separately. Details are given in the text.

| | τ_h candidates for | | |
	$\mu\tau_h$	$e\tau_h$	$\tau_h\tau_h$
kinematic properties	$p_T(\tau_h) > 30$ GeV $\|\eta(\tau_h)\| < 2.1$	$p_T(\tau_h) > 30$ GeV $\|\eta(\tau_h)\| < 2.1$	$p_T(\tau_h) > 40$ GeV $\|\eta(\tau_h)\| < 2.1$
discriminator against jets	Tight WP	Tight WP	Tight WP
discriminator against muons	Tight WP	VLoose WP	VLoose WP
discriminator against electrons	VVLoose WP	Tight WP	VVLoose WP
impact parameters	$d_z < 0.2$ cm	$d_z < 0.2$ cm	$d_z < 0.2$ cm

Table 4.23.: Selection requirements applied to τ_h candidates for $\mu\tau_h$, $e\tau_h$ and $\tau_h\tau_h$ final states using quality criteria and criteria for kinematic properties defined in subsection 3.2.8.

4.3.2. Signal Pair Selection

The candidates for the signal pair selected as given in table 4.17 for muons, table 4.19 for electrons, and table 4.23 for τ_h candidates, are combined to $\tau\tau$ pairs suitable for each of the $\mu\tau_h$, $e\tau_h$, $\tau_h\tau_h$ and $e\mu$ final states. The constituents of these pairs are required to be separated in the (η, ϕ) plane by $\Delta R > 0.5$ in final states with a τ_h and by $\Delta R > 0.3$ in the $e\mu$ final state. The remaining pairs are associated to each final state using the following algorithm:

1. For each $\tau\tau$ pair $\tau_1\tau_2$, the isolation measure is compared between the first $\tau\tau$ pair

constituents, τ_1. The pair with the more isolated τ_1 is moved forward in the sorted list, unless the isolation of τ_1 is too similar between the two pairs. In that case:

2. Compare the transverse momentum between the first $\tau\tau$ pair constituents, $p_T(\tau_1)$. The pair with the higher $p_T(\tau_1)$ is elevated in the sorted list, unless $p_T(\tau_1)$ is too similar between the two pairs. In that case:

3. For each $\tau\tau$ pair $\tau_1\tau_2$, the isolation measure between the second $\tau\tau$ pair constituents, τ_2, is compared. The pair with the more isolated τ_2 is elevated in the sorted list, unless the isolation of τ_2 is too similar between the two pairs. In that case:

4. Compare the transverse momentum between the second $\tau\tau$ pair constituents, $p_T(\tau_2)$. The pair with the higher $p_T(\tau_2)$ is elevated in the sorted list.

The isolation measure is chosen to be the $\Delta\beta$ corrected isolation, $I_{rel}^{\Delta\beta}$, for the muons and the relative isolation with the effective area correction, $I_{rel}^{A_{eff}}$, for electrons. For both isolation definitions, the smaller the value the more isolated the muon or the electron. In case of τ_h candidates, the discriminator against jets, $D_{\tau_h}^{jet}$, includes an isolation measure with higher values for more isolated τ_h candidates. The definition of pair constituents as first or as second is final state dependent and follows this order: muons, electrons, τ_h candidates. In the $\tau_h\tau_h$ final state, two versions of a $\tau\tau$ pair are used in the sorted list, with the two τ_h constituents exchanged in their position.

In that way, the most isolated $\tau\tau$ pair is assumed to be at the beginning of the sorted list and is chosen to be the signal $\tau\tau$ pair. Next, the signal $\tau\tau$ pair is checked to match the HLT physics objects for the triggers assigned to the considered final state, the pair constituents are corrected for differences in efficiencies and are assigned with the corresponding efficiency uncertainties.

HLT Matching

Depending on the final state, and the chosen HLT paths, only one or both $\tau\tau$ pair constituents are required to match to a lepton reconstructed by the HLT. The relevant HLT physics objects consist of muons, electrons and τ_h candidates reconstructed as discussed in subsection 3.3.2 and which fulfill the requirements of the considered HLT path. For final states with a τ_h, the $\tau\tau$ pair constituents are considered as matched, if they are located within $\Delta R < 0.5$ with respect to the HLT physics object. For the eμ final state, the threshold is chosen as $\Delta R < 0.3$. Furthermore, $|\eta|$ requirements of the HLT path are also imposed on the signal pair constituents, while in case of the p_T requirements of the HLT path, a higher threshold than for the HLT path requirement is taken, being above by 1 GeV for muons and by 5 GeV for electrons and τ_h candidates to avoid a large fraction of the trigger turn-on region.

Efficiencies for Muons, Electrons and τ_h Candidates

In general, the total efficiency ϵ of selecting an electron, muon or τ_h with a good quality can be decomposed as follows:

$$\epsilon = \epsilon(\text{reco}) \cdot \epsilon(\text{id}|\text{reco}) \cdot \epsilon(\text{iso}|\text{id}) \cdot \epsilon(\text{trg}|\text{iso}) \qquad (4.20)$$

At first the reconstruction efficiency $\epsilon(\text{reco})$ of the considered physics object is measured. After that, the identification efficiency $\epsilon(\text{id}|\text{reco})$ of the reconstructed physics object is determined. Depending on the identification working point of the reconstructed object, its

isolation efficiency $\epsilon(\text{iso}|\text{id})$ is measured. The last step is the measurement of the trigger efficiency $\epsilon(\text{trg}|\text{iso})$ of the reconstructed object, which depends both on its isolation and its identification working point.
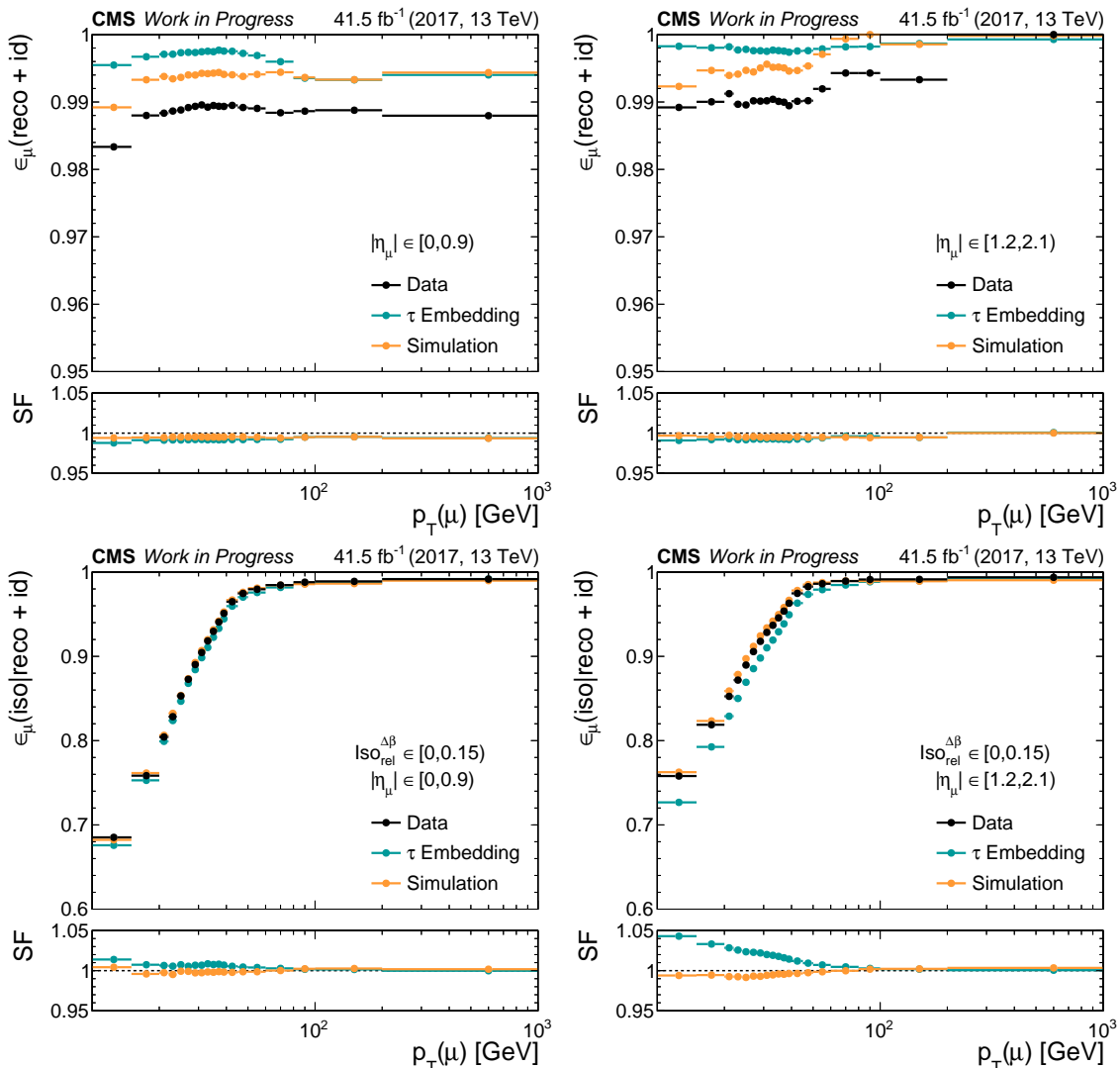
Figure 4.23.: Muon reconstruction and identification efficiencies, $\epsilon_\mu(\text{reco} + \text{id})$ (top), and isolation efficiencies $\epsilon_\mu(\text{iso}|\text{reco} + \text{id})$ (bottom), measured for data, τ embedding and simulation from the data-taking year 2017 as functions of $p_T(\mu)$ and $|\eta_\mu|$. Isolation efficiencies are measured for $I_{\text{rel}}^{\Delta\beta} \in [0, 0.15)$. On the left, a central detector region, $|\eta_\mu| \in [0, 0.9)$, is shown, on the right, a more forward region, $|\eta_\mu| \in [1.2, 2.1]$. The scale factor (SF) to data is shown in the lower panels of the figures.

In case of muons, the reconstruction efficiency $\epsilon(\text{reco})$ and the identification efficiency $\epsilon(\text{id}|\text{reco})$ are reorganized into the efficiency of the track of the muon in the inner tracking system $\epsilon(\text{track})$ and the efficiency of the remaining muon reconstruction and the subsequent muon identification, $\epsilon(\text{reco} + \text{id}|\text{track})$. The reconstruction efficiency of a muon track in the inner tracking system exceeds 99% [87], therefore the equation 4.20 can be

simplified in the case of muons to:

$$\epsilon_\mu = \epsilon_\mu(\text{reco} + \text{id}) \cdot \epsilon_\mu(\text{iso}|\text{reco} + \text{id}) \cdot \epsilon_\mu(\text{trg}|\text{iso}) \qquad (4.21)$$

The muon efficiencies in the equation above are measured in a $Z \to \mu\mu$ control region with the tag and probe method. The tag muon is selected using the signal requirements in table 4.17. Another muon is considered as the probe, when it passes loose requirements on kinematic properties, is well separated from the tag muon, and it is building together with the tag muon an oppositely charged muon pair with an invariant mass $m_{\mu\mu} \in [65, 115]$ GeV. The probe muon is tested to fulfill the identification, isolation and trigger requirements to measure the three efficiencies $\epsilon_\mu(\text{reco} + \text{id})$, $\epsilon_\mu(\text{iso}|\text{reco} + \text{id})$ and $\epsilon_\mu(\text{trg}|\text{iso})$, respectively. The efficiencies are measured as functions of the transverse momentum $p_T(\mu)$ and the magnitude of the pseudorapidity $|\eta_\mu|$ of the muon for events from data, simulation and from the τ embedding method. An example of the efficiency for the reconstruction and identification of the muon, $\epsilon_\mu(\text{reco} + \text{id})$, is shown in figure 4.23 at the top for the data-taking year 2017 as a function of $p_T(\mu)$ for a central and a forward region of the CMS detector.

Based on muon pairs passing the signal identification requirements, the isolation efficiency, $\epsilon_\mu(\text{iso}|\text{reco} + \text{id})$, is measured in a similar way. Depending on the signal final state, the isolated region is chosen for the probe muon to correspond to $I_{\text{rel}}^{\Delta\beta} \in [0, 0.15)$ or to $I_{\text{rel}}^{\Delta\beta} \in [0, 0.2)$ for $\mu\tau_h$ or $e\mu$, respectively. An example of measured isolation efficiency of the muon is shown in figure 4.23 at the bottom for the data-taking year 2017.
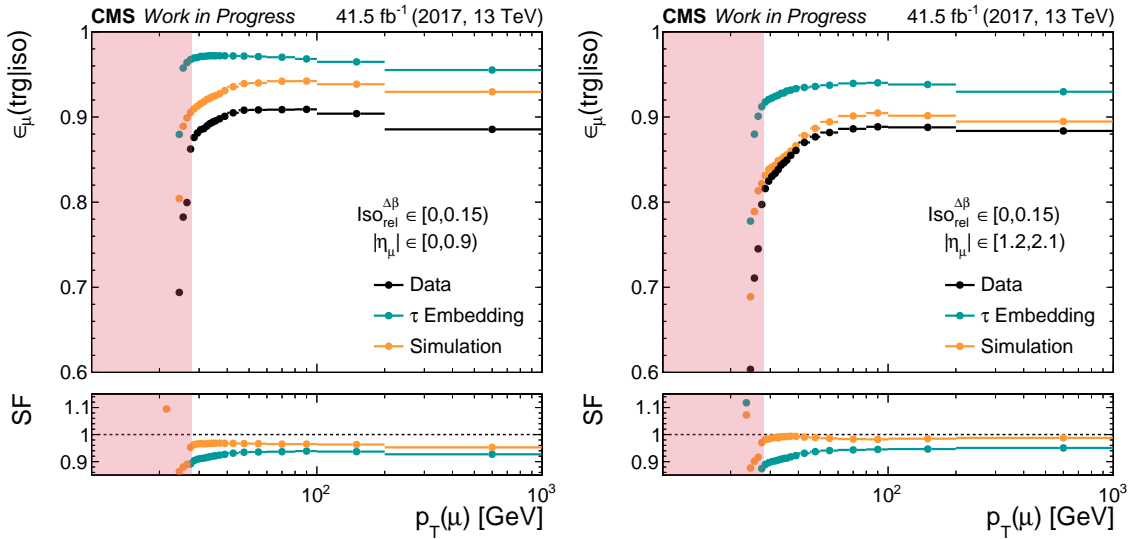
Figure 4.24.: Muon HLT path efficiencies for an HLT selecting a muon with $p_T(\mu) \geq 27$ GeV, $\epsilon_\mu(\text{trg}|\text{iso})$, measured for data, τ embedding and simulation from the data-taking year 2017 as functions of $p_T(\mu)$ and $|\eta_\mu|$ in the isolated region $I_{\text{rel}}^{\Delta\beta} \in [0, 0.15)$. On the left, a central detector region, $|\eta_\mu| \in [0, 0.9)$, is shown, on the right, a more forward region, $|\eta_\mu| \in [1.2, 2.1)$. The scale factor (SF) to data is shown in the lower panels of the figures. The red filled area excludes the turn-on region of the HLT path at $p_T(\mu) \leq 28$ GeV which is not considered in the analysis for this trigger path.

For muons passing both the identification and isolation requirements of the signal selection, the HLT path efficiency is measured. The HLT paths with muons used in the analysis cover different algorithms, searching only for a muon, for a pair consisting of a muon and a τ_h for the $\mu\tau_h$ final state, or for a pair of an electron and a muon for the $e\mu$ final state. For the latter two types of HLT paths, the measurement of each pair leg is performed separately, assuming a factorization of the legs. An example of an efficiency measurement for an HLT path targeting only a muon is shown in figure 4.24 for the data-taking year 2017.

For electrons, the set of efficiencies to be measured corresponds to the one given in equation 4.20. A $Z \to ee$ enriched region is chosen for the measurements with the tag and probe method, following the signal requirements for the tag electron and requiring loose criteria on kinematic properties for the probe electron. Furthermore, the invariant mass of the electron pair is required to be in the region of the $Z \to ee$ peak, $m_{ee} \in [65, 115]$ GeV. As for muons, electrons are tested to fulfill the considered identification, isolation and trigger requirements of the signal electron selection in table 4.19 to measure subsequently each component of the total efficiency. The efficiencies are measured as function of the transverse momentum of the electron, $p_T(e)$ and of the pseudorapidity of the ECAL supercluster associated to the electron, η_e. An example for the electron reconstruction efficiency, $\epsilon_e(\text{reco})$, is shown in figure 4.25 for the data-taking year 2017 [160]. In case of events from τ embedding, a 100% electron reconstruction efficiency is assumed and possible biases due to this assumption are expected to be covered by subsequent efficiency measurements.
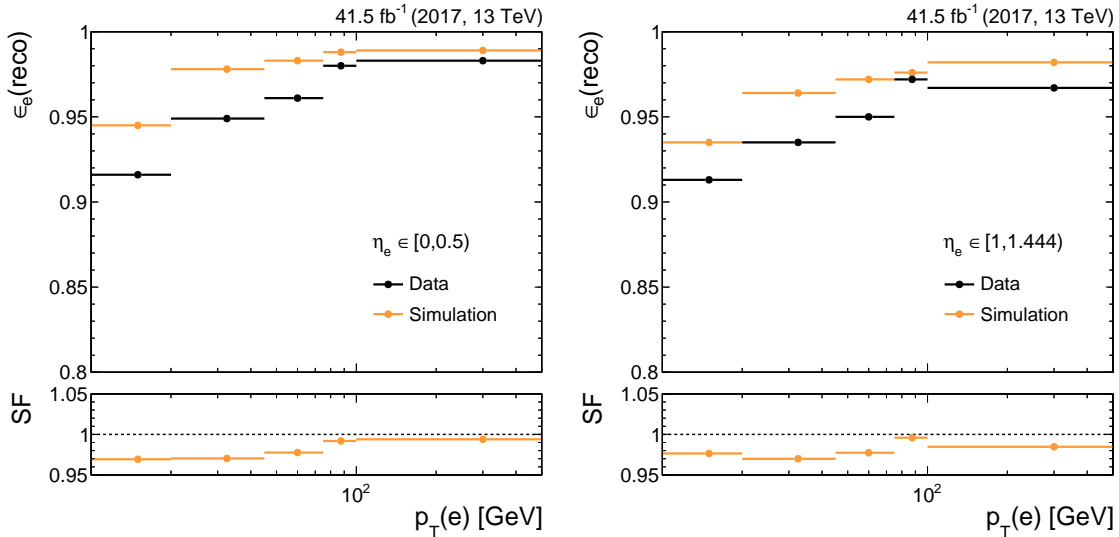
Figure 4.25.: Electron reconstruction efficiencies, $\epsilon_e(\text{reco})$, measured for data and simulation from the data-taking year 2017 as functions of $p_T(e)$ and η_e [160]. On the left, a central detector region, $\eta_e \in [0, 0.5)$, is shown, on the right, a more forward region, $\eta_e \in [1, 1.444)$. The scale factor (SF) to data is shown in the lower panels of the figures.

For all reconstructed electrons, the identification efficiency, $\epsilon_e(\text{id}|\text{reco})$, is measured. An example is shown in figure 4.26 at the top for the data-taking year 2017. The reconstructed electrons passing identification requirements, are subject of the isolation efficiency mea-

surement, $\epsilon_e(\mathrm{iso|id})$. An example for the data-taking year 2017 is shown in figure 4.26 at the bottom.
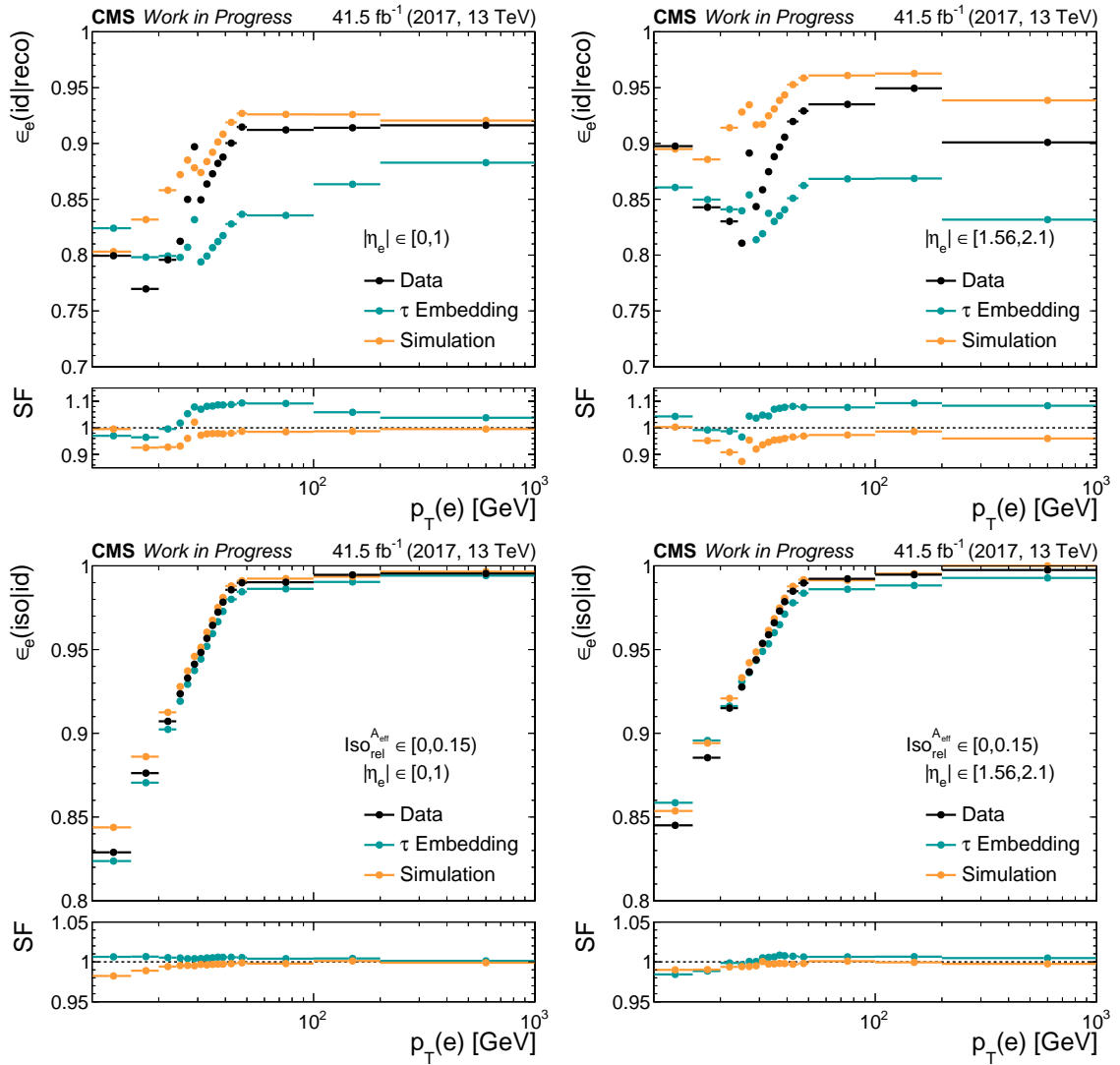
Figure 4.26.: Electron identification efficiencies, $\epsilon_e(\mathrm{id|reco})$ (top), and isolation efficiencies $\epsilon_e(\mathrm{iso|id})$ (bottom), measured for data, τ embedding and simulation from the data-taking year 2017 as functions of $p_T(e)$ and $|\eta_e|$. Isolation efficiencies are measured for $I_{rel}^{A_{eff}} \in [0, 0.15]$. On the left, a central detector region, $|\eta_e| \in [0, 1)$, is shown, on the right, a more forward region, $|\eta_e| \in [1.56, 2.1]$. The scale factor (SF) to data is shown in the lower panels of the figures.

Finally, reconstructed electrons passing identification and isolation requirements are considered for the efficiency measurements of HLT paths, $\epsilon_e(\mathrm{trg|iso})$. As for muons, different HLT paths are used in the analysis to trigger on electrons: there are HLT paths targeting only an electron, targeting a pair of an electron and a τ_h for the $e\tau_h$ final state, or targeting a pair of an electron and a muon for the $e\mu$ final state. Also here, a factorization of the pair legs is assumed. An example of an efficiency measurement for an HLT algorithm searching only for an electron is shown in figure 4.27. An additional scale factor of 0.991 is applied to events passing HLT paths with a single electron or with an $e\tau_h$ pair for

data-taking in 2017 to account for the too small vertex acceptance in z direction, when matching tracks to an ECAL supercluster. The reason for this was a too small uncertainty on the beamspot measurement in z direction at the beginning of the data-taking in 2017, which was used to define the vertex acceptance region for the HLT paths with electrons.
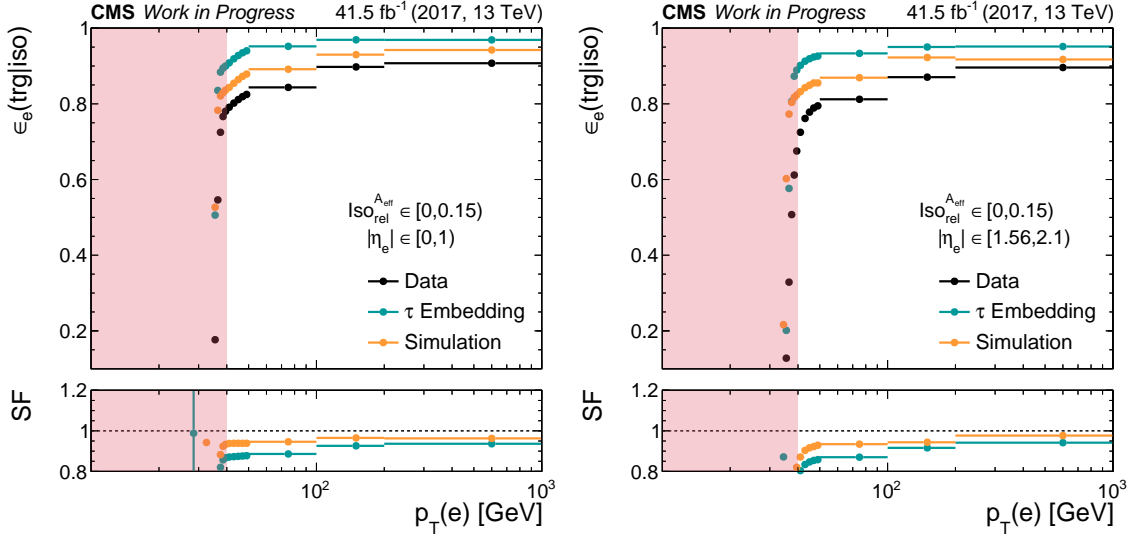
Figure 4.27.: Electron HLT path efficiencies selecting an electron with $p_T(e) \geq 35$ GeV, $\epsilon_e(\text{trg}|\text{iso})$, measured for data, τ embedding and simulation from the data-taking year 2017 as functions of $p_T(e)$ and $|\eta_e|$ in the isolated region $I_{\text{rel}}^{A_{\text{eff}}} \in [0, 0.15)$. On the left, a central detector region, $|\eta_e| \in [0, 1)$, is shown, on the right, a more forward region, $|\eta_e| \in [1.56, 2.1)$. The scale factor (SF) to data is shown in the lower panels of the figures. The red filled area excludes the turn-on region of the HLT path at $p_T(e) \leq 40$ GeV which is not considered in the analysis for this trigger path.

A global normalization uncertainty of 2% is assumed for the reconstruction, identification, and isolation efficiencies of muons and electrons, separately for each of the physics objects. This uncertainty is correlated across the years and correlated with 50% between processes from simulation and the τ embedded events due to the fact, that the measurement of the efficiencies itself is performed in the same way, whereas the description of the physics objects in τ embedded events is expected to be different due to the simulation of the $\tau\tau$ pair in an empty detector.

For the HLT paths involving muons and electrons, a normalization uncertainty is applied to the events passing the requirements related to an HLT path selection, for each of the physics objects. For HLT paths constructed only for either a muon or an electron, a 2% uncertainty is applied for each physics object separately. For the HLT path targeting the eμ pair, a total uncertainty of 2% is applied. In case of HLT paths for the $\mu\tau_h$ and eτ_h final states, a normalization uncertainty of 2% is chosen to account for the muon or electron leg of the HLT paths, which fire for the $\tau\tau$ pair.

These normalization uncertainties on HLT path efficiencies are treated as uncorrelated across the years and uncorrelated between simulation and τ embedding, with the latter choice due to the expectation of large differences in HLT reconstruction observed between simulated and τ embedded events.

The total efficiency for τ_h candidates is decomposed into two contributions: a single measurement for the efficiency of the reconstruction, identification, and isolation of the τ_h candidate, $\epsilon_{\tau_h}(\text{id})$, and the efficiency of the HLT paths involving a τ_h object, $\epsilon_{\tau_h}(\text{trg}|\text{id})$:

$$\epsilon_{\tau_h} = \epsilon_{\tau_h}(\text{id}) \cdot \epsilon_{\tau_h}(\text{trg}|\text{id}) \tag{4.22}$$

Similar to the energy scale measurements, the measurement of $\epsilon_{\tau_h}(\text{id})$ depends on the true physics object which is reconstructed as a τ_h candidate. For electrons and muons, which are reconstructed as τ_h candidates, the background rejection efficiency of the discriminators against electrons and muons defined in subsection 3.2.8 is measured in $Z \rightarrow ee$ and $Z \rightarrow \mu\mu$ enriched regions as a function of the magnitude of the pseudorapidity of the τ_h object, $|\eta_{\tau_h}|$.

data-taking year	2016		2017		2018	
working point (WP)	VVLoose	Tight	VVLoose	Tight	VVLoose	Tight
			Scale factor (SF)			
$|\eta_{\tau_h}| \in [0, 1.46)$	1.38	1.22	1.11	1.22	0.91	1.47
$|\eta_{\tau_h}| \in (1.558, 2.3)$	1.29	1.47	1.03	0.93	0.91	0.66
			Uncertainty relative to SF			
$|\eta_{\tau_h}| \in [0, 1.46)$	$\pm 31\%$		$\pm 26\%$		$\pm 18\%$	
$|\eta_{\tau_h}| \in (1.558, 2.3)$	$\pm 22\%$		$\pm 41\%$		$\pm 30\%$	

Table 4.24.: Scale factors from simulation to data for electrons reconstructed as τ_h candidates as a function of $|\eta_{\tau_h}|$ for each data-taking year and for the two working points considered in the analysis. The gap between the barrel and the endcap of the detector, $|\eta_{\tau_h}| \in [1.46, 1.558]$, remains uncorrected due to a bad modelling of electrons in this region. Relative uncertainties for the scale factors are given for the Tight working point used in the $e\tau_h$ final state.

In table 4.24, the scale factors from simulation to data for the background rejection efficiency of the discriminator against electrons is shown for all three data-taking years and the working points considered for the signal selection of $\mu\tau_h$, $e\tau_h$ and $\tau_h\tau_h$ final states given in table 4.23. The most dominant contribution to events with electrons reconstructed as τ_h candidates is the $Z \rightarrow ee$ process in the $e\tau_h$ final state. This process is assigned with an additional set of normalization uncertainties for each η_{τ_h} region from table 4.24, uncorrelated across the data-taking years.

In a similar way, the background rejection efficiency of the discriminator against muons is presented in table 4.25. The dominant contribution to events with muons reconstructed as τ_h candidates in the $\mu\tau_h$ final state, the $Z \rightarrow \mu\mu$ process, is also assigned with an additional set of normalization uncertainties for each η_{τ_h} region defined in table 4.25, uncorrelated across the data-taking years.

For genuine τ_h candidates from the τ embedding method and from simulation, the efficiency of the discriminator against jets is measured in the $\mu\tau_h$ final state enriched in $Z \rightarrow \tau\tau$ events as a function of the transverse momentum $p_T(\tau_h)$ and the decay mode of the τ_h object. Since the DNN outputs representing the probabilities to identify the reconstructed τ_h as a true τ_h, jet, muon or electron sum up to 1, the discriminators from

data-taking year	2016		2017		2018	
working point (WP)	VLoose	Tight	VLoose	Tight	VLoose	Tight
			Scale factor (SF)			
$\|\eta_{\tau_h}\| \in [0, 0.4)$	1.25	1.38	1.12	0.92	1.00	0.81
$\|\eta_{\tau_h}\| \in [0.4, 0.8)$	0.96	0.72	0.76	0.79	1.08	1.02
$\|\eta_{\tau_h}\| \in [0.8, 1.2)$	1.29	1.34	0.99	0.67	1.04	0.92
$\|\eta_{\tau_h}\| \in [1.2, 1.7)$	0.92	1.03	0.75	1.07	0.95	0.83
$\|\eta_{\tau_h}\| \in [1.7, 2.3)$	5.01	5.05	4.44	4.08	5.58	4.52
			Uncertainty relative to SF			
$\|\eta_{\tau_h}\| \in [0, 0.4)$		$\pm\ 9\%$		$\pm18\%$		$\pm19\%$
$\|\eta_{\tau_h}\| \in [0.4, 0.8)$		$\pm42\%$		$\pm32\%$		$\pm34\%$
$\|\eta_{\tau_h}\| \in [0.8, 1.2)$		$\pm20\%$		$\pm39\%$		$\pm24\%$
$\|\eta_{\tau_h}\| \in [1.2, 1.7)$		$\pm63\%$		$\pm42\%$		$\pm57\%$
$\|\eta_{\tau_h}\| \in [1.7, 2.3)$		$\pm17\%$		$\pm21\%$		$\pm20\%$

Table 4.25.: Scale factors from simulation to data for muons reconstructed as τ_h candidates as a function of $|\eta_{\tau_h}|$ for each data-taking year and for the two working points considered in the analysis. Relative uncertainties for the scale factors are given for the Tight working point used in the $\mu\tau_h$ final state.

equation 3.22 are correlated with each other. In consequence, the measured efficiencies for each working point of the discriminator against jets chosen in signal selection of τ_h candidates depend additionally on the working points chosen for the discriminator against electrons and muons. It was found, that the discriminator against electrons has stronger effects on the discriminator against jets and the additional dependence is taken into account.

In the $\tau_h\tau_h$ final state, the scale factors for the efficiency of selecting genuine τ_h candidates depend only on the decay mode of the τ_h object due to high thresholds on the transverse momentum $p_T(\tau_h) > 40$ GeV, as given in table 4.23 and the resulting reduction of the $p_T(\tau_h)$ dependence of the scale factors in the considered $p_T(\tau_h)$ range. A summary of the scale factors with their uncertainties used in the $\tau_h\tau_h$ final state is given in table 4.26 for the selection of τ_h candidates passing the Tight working point of the discriminator against jets. The scale factors are measured using the VVLoose working point of the discriminator against electrons as it is chosen for the $\tau_h\tau_h$ final state.

For the $\mu\tau_h$ and $e\tau_h$ final states, the $p_T(\tau_h)$ dependent scale factors are chosen due to lower thresholds. An example of the scale factor measurements with corresponding uncertainties is given in figure 4.28 for the data-taking year 2017 and the Tight working point of the discriminator against jets.

The uncertainties given in table 4.26 are applied uncorrelated for each decay mode combination in the $\tau_h\tau_h$ final state. For the two remaining final states with τ_h candidates, $\mu\tau_h$ and $e\tau_h$, the p_T dependent uncertainties in figure 4.28 are treated correlated across the final states, but uncorrelated for each p_T bin. To cover effects from the correlation between the different choices of the discriminators against jets, electrons and muons, an additional normalization uncertainty is introduced uncorrelated across the $\mu\tau_h$, $e\tau_h$ and $\tau_h\tau_h$ final states with an amplitude of 1% for $\mu\tau_h$ and $e\tau_h$, and 1.4% for $\tau_h\tau_h$.

data-taking year	2016	2017	2018
Scale factor for		simulation	
DM $= 1$	0.90 ± 0.05	0.87 ± 0.05	1.05 ± 0.06
DM $\in \{1, 2\}$	0.98 ± 0.05	0.94 ± 0.05	0.96 ± 0.05
DM $= 10$	0.79 ± 0.04	0.83 ± 0.05	0.95 ± 0.06
DM $= 11$	0.78 ± 0.05	0.65 ± 0.04	0.90 ± 0.06
Scale factor for		τ embedding	
DM $= 1$	0.91 ± 0.05	0.91 ± 0.06	1.01 ± 0.06
DM $\in \{1, 2\}$	0.96 ± 0.05	1.05 ± 0.06	1.00 ± 0.06
DM $= 10$	0.92 ± 0.06	0.96 ± 0.07	1.13 ± 0.07
DM $= 11$	0.83 ± 0.05	0.79 ± 0.05	0.97 ± 0.06

Table 4.26.: Scale factors from simulation and τ embedding to data for genuine τ_h objects selected with the Tight WP of the discriminator against jets as a function of the decay mode (DM) of the τ_h candidate for each data-taking year. The uncertainties are given as symmetric up- and downward variations with respect to the nominal scale factors.
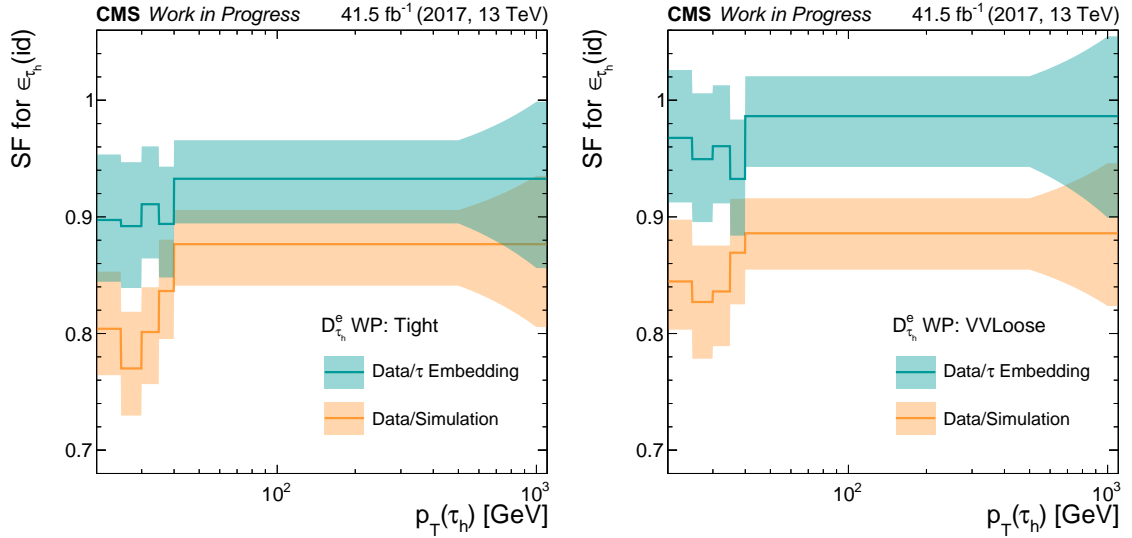
Figure 4.28.: Scale factors from simulation and τ embedding to data for genuine τ_h objects selected with the Tight WP of the discriminator against jets as a function of the transverse momentum $p_T(\tau_h)$ for the data-taking year 2017. On the left, the measurement using the Tight WP of the discriminator against electrons ($D^e_{\tau_h}$ WP : Tight) is given, as it is used in the $e\tau_h$ final state. On the right, the measurement with the VVLoose WP of the discriminator against electrons ($D^e_{\tau_h}$ WP : VVLoose) is shown, as it is used in the $\mu\tau_h$ final state. The uncertainties are illustrated as semi-transparent bands around the nominal scale factors shown as solid lines.

All uncertainties related to the efficiency of selecting genuine τ_h candidates, $\epsilon_{\tau_h}(\mathrm{id})$, are

treated uncorrelated across the data-taking years, but correlated to 50% between simulation and τ embedding.

The τ_h objects passing the identification requirements of the signal pair selection are passed to the measurement of the HLT path efficiencies. The HLT paths with τ_h objects as targets cover $\mu\tau_h$, $e\tau_h$ and $\tau_h\tau_h$ pairs in the $H \to \tau\tau$ analysis considered in this thesis. Possible extensions of the HLT selection to paths targeting one boosted τ_h or a $\tau_h\tau_h$ pair accompanied by a jet pair were studied and are expected to increase the sensitivity in the search for heavy Higgs bosons or the sensitivity to the VBF production of the observed Higgs boson, respectively.

Assuming a factorization of the total HLT path efficiency into a product of efficiencies of each of the two legs of the pair, the HLT efficiency of a single τ_h leg is measured in the $\mu\tau_h$ final states enriched in $Z \to \tau\tau$ events with appropriate $\mu\tau_h$ monitoring HLT paths designed for efficiency measurements. The τ_h leg HLT efficiencies are measured in bins of transverse momentum, $p_T(\tau_h)$, in categories defined by the decay mode of the τ_h object, and are fitted with analytic functions, that model a trigger turn-on.

In the next step, corrections to the measured efficiency curves are determined in (η, ϕ) bins to cover effects related to single, inefficient detector modules in the detector subsystems. An example measurement for the τ_h leg of a $\tau_h\tau_h$ HLT path combination of the data-taking year 2017 is shown in figure 4.29 for a subset of decay modes, $DM \in \{0, 10\}$.

For each τ_h object leg of the HLT paths used in $\mu\tau_h$, $e\tau_h$, and $\tau_h\tau_h$ final states, p_T dependent uncertainties are introduced for each decay mode individually, based on the uncertainties of the analytic functions for the derived scale factors, as shown in figure 4.29 in the lower panels. These HLT path uncertainties are treated uncorrelated across the data-taking years and uncorrelated between simulation and τ embedding.

Additional efficiency corrections are applied to events from the τ embedding method due to the expected differences in reconstruction of τ_h candidates and electrons performed in an empty detector except the simulated $\tau\tau$ process. In case of τ_h objects, reconstruction efficiency scale factors are derived as functions of the number of reconstructed charged hadrons, $N_{h^\pm}$, and the number of reconstructed neutral pions, N_{π^0}, assigned to each τ_h object. The total scale factor is expressed as follows:

$$SF_{tot} = [SF_{h^\pm}]^{N_{h^\pm}} \cdot [SF_{\pi^0}]^{N_{\pi^0}}$$

$$N_{h^\pm} = \begin{cases} 1, & DM \in \{0, 1, 2\} \\ 3, & DM \in \{10, 11\} \end{cases}$$

$$N_{\pi^0} = \begin{cases} 0, & DM \in \{0, 10\} \\ 1, & DM \in \{1, 2, 11\} \end{cases}$$

The scale factors are measured in a $Z \to \tau\tau$ enriched region of the $\mu\tau_h$ final state with the following values and uncertainties:

$$SF_{h^\pm} = 0.975 \pm 0.008 \qquad SF_{\pi^0} = 1.051 \pm 0.014$$

The variations on the individual scale factors are treated as uncorrelated uncertainties on the τ_h reconstruction efficiency. For the $\tau_h\tau_h$ final state, the scale factors computed for each τ_h object are multiplied with each other to result in an event-wise scale factor.

For electrons, non-closure corrections were introduced to HLT path efficiencies, if artificially low efficiencies were observed, particularly low in the endcap region for electrons with $p_T(e) < 35$ GeV.
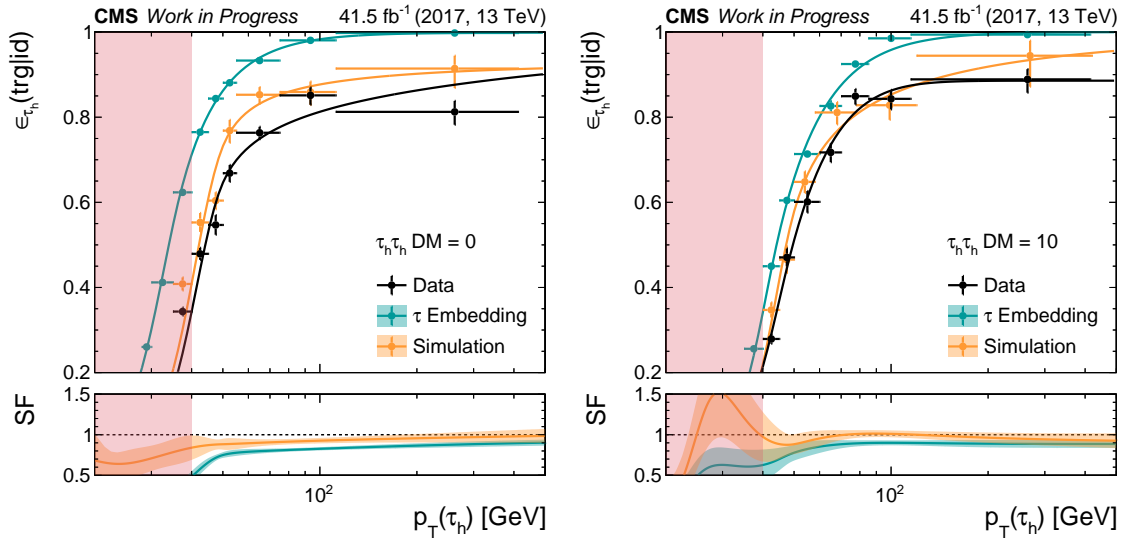
Figure 4.29.: Efficiencies for the HLT paths selecting a $\tau\tau$ pair in the $\tau_h\tau_h$ final state, measured for one τ_h leg assuming factorization, are shown for the data-taking year 2017. The efficiencies depend on the decay mode of the τ_h object (DM) and the transverse momentum, $p_T(\tau_h)$. On the left, the measurement for DM = 0 is shown, on the right, for DM = 10. The fitted analytic functions, as well as the binned measurements are shown in the main plot for data, τ embedding and simulation. The scale factors (SF) to data derived from the analytic functions are illustrated in the lower panels together with their uncertainty bands. The red filled area covers the region with $p_T(\tau_h) \leq 40$ GeV not used in the analysis for this HLT path combination. The fitted analytic functions are additionally corrected for differences in HLT efficiency along the (η, ϕ) plane.

4.3.3. Selection of Jets and Missing Transverse Energy

Jets, which are reconstructed as explained in subsection 3.2.6, are at first corrected for the energy scale and energy resolution. In case of the data-taking year 2017, the jets are additionally preselected prior to the corrections to reduce jets coming from detector noise in the ECAL system. The corresponding selection rejects jets with transverse momentum $p_T(jet) < 50$ GeV and pseudorapidity $|\eta_{jet}| \in (2.65, 3.139)$. The energy scale corrections are applied both to data and simulation in different steps [161].

At first, measures additionally to the charged hadron subtraction (CHS) are taken to reduce the contribution of pileup to the jets. Next, the effects from the detector response and the underlying event are corrected based on calibration using simulated events. Residual differences between simulation and data are corrected for with results from a combination of measurements in di-jet, multijet events, and events with $Z \rightarrow \ell\ell$ accompanied by jets as functions of the transverse momentum and the pseudorapidity of the jet. Finally, corrections related to the jet flavour are measured in simulation and applied both to data and simulation.

Different uncertainty sources are assigned to the energy scale corrections, which are additionally subdivided into different detector regions based on the pseudorapidity of the corrected jets. These uncertainty sources are summarized in the list below.

- Total flat uncertainty components related to limited statistics in the energy scale correction measurements, to the uncertainty on the reference scale, and to the corrections for initial and final state radiation.
- Uncertainty related to the differences in the simulation of parton showering and underlying event extrapolated to high jet p_T.
- Two uncertainties covering the response variation to single particles in jets, for ECAL and HCAL separately, extrapolated to high jet p_T.
- Uncertainty related to the differences in responses to jets, depending on the jet flavour.
- Time dependence during the data-taking, resulting from the aging of the detector.
- Relative uncertainties of the jet energy resolution as function of jet pseudorapidity η_{jet} in bins $[1.3, 2.5, 3.0, \infty]$.
- Relative uncertainties due to differences in models applied to the jet transverse momentum distribution, $p_T(jet)$ in bins of pseudorapidity $\eta_{jet} : [0, 1.3, 2.5, 3.0, \infty]$.
- Relative uncertainties due to differences between measurements of residual corrections needed for data as a function of η_{jet}.
- Relative uncertainties due to initial and final state radiation as a function of η_{jet}.
- Relative uncertainties due to limited statistics in determination of uncertainties of initial and final state radiation, for uncertainties in the endcap region, $\eta_{jet} \in [1.3, 3.0)$, and forward region, $\eta_{jet} \in [3.0, \infty)$.
- A flat uncertainty for remaining differences between data and simulation due to pileup after pileup corrections have been applied.
- Uncertainties on pileup corrections as functions of $p_T(jet)$, estimated in pseudorapidity bins $\eta_{jet} : [0, 1.3, 2.5, 3.0, \infty]$.

These uncertainties are grouped into a reduced set of 11 uncertainties based on the correlations between the sources, the covered detector regions in pseudorapidity η_{jet}, and the correlations between the data-taking years.

The energy resolution of jets in data is measured to be worse than as expected from simulation [161]. For this reason, an additional, stochastic smearing of the 4-momenta is applied based on scale factors s_{JER} and the expected energy resolution σ_{JER} measured as functions of jet transverse momentum, its pseudorapidity and the pileup density:

$$\Delta p_\mu(jet) \cdot p_\mu(jet) = \left(\sigma \sim \mathrm{Gauss}(0, \sigma_{JER})\right) \cdot \sqrt{s_{JER}^2 - 1}$$

The value σ is drawn from a Gaussian distribution. The variations of the scale factors s_{JER} are summarized into one uncertainty for the jet energy resolution.

The corrected jets are selected into two different collections summarized in table 4.27. Common to both collections are the general jet identification and the overlap rejection with the selected $\tau\tau$ pair. The general jets are required to have larger transverse momentum, but are allowed to be in the forward region of the detector, while the b-tagged jets are allowed to have a lower transverse momentum, but are limited to the detector region covered by the inner tracking system.

The b-tagged jets from simulation are further corrected for the differences in b-tagging efficiencies between data and simulation using analysis specific efficiency measurements and general scale factors. The efficiencies are measured in the signal regions of $\mu\tau_h$, $e\tau_h$, $\tau_h\tau_h$ and $e\mu$ final states as functions of the transverse momentum and the pseudorapidity of the jet for jets induced by bottom quarks, charm quarks, and for light jets, which are

selection	general jets	b-tagged jets
Kinematic properties	$p_T(\text{jet}) > 30$ GeV, $|\eta_{\text{jet}}| < 4.7$	$p_T(\text{jet}) > 20$ GeV, $|\eta_{\text{jet}}| < 2.5(2.4)$
Jet identification	ID from table 3.6	ID from table 3.6
Overlap rejection	selected $\tau\tau$ pair	selected $\tau\tau$ pair
B-tagging		medium WP from table 3.9

Table 4.27.: Selection of jets and b-tagged jets. The pseudorapidity requirement for the b-tagged jets is dependent on the data-taking year with a threshold of 2.4 for 2016 and a threshold of 2.5 for 2017 and 2018.

induced by light quarks or gluons. The exact definition of these jets is given in table 3.8. An example of the b-tagging efficiencies for the data-taking years 2016 and 2018 is given in figure 4.30.

Based on these efficiencies and provided scale factors, the jets in simulated events are corrected to the data b-tagging efficiency on a jet-by-jet basis [97]. In case a jet is b-tagged and the corresponding b-tagging scale factor (SF) is smaller than 1, the b-tagging is removed with a probability of $1 - \text{SF}$. In case a jet is not b-tagged, but passes the remaining selection criteria for a b-tagged jet, it is considered as b-tagged with a probability $(1 - \text{SF})/(1 - 1/\epsilon)$, if $\text{SF} \geq 1$. Here, the efficiency ϵ refers to the efficiencies as shown in figure 4.30.

The scale factors for jets induced by bottom or charm quarks are determined from a combination of measurements in regions enriched with multijet events, events enriched with jets containing muons, and events enriched with a top quark pair with final states containing one or two leptons. The scale factors for light jets are determined from a measurement in a multijet enriched region. The uncertainties are based on the total variations of the scale factors. Variations of scale factors for jets induced by bottom or charm quarks are considered as correlated to 100%, leading to the uncertainty on the b-tagging efficiency. An uncorrelated uncertainty for the misidentification of a light jet being b-tagged is constructed from the total variation of the scale factor for light jets.
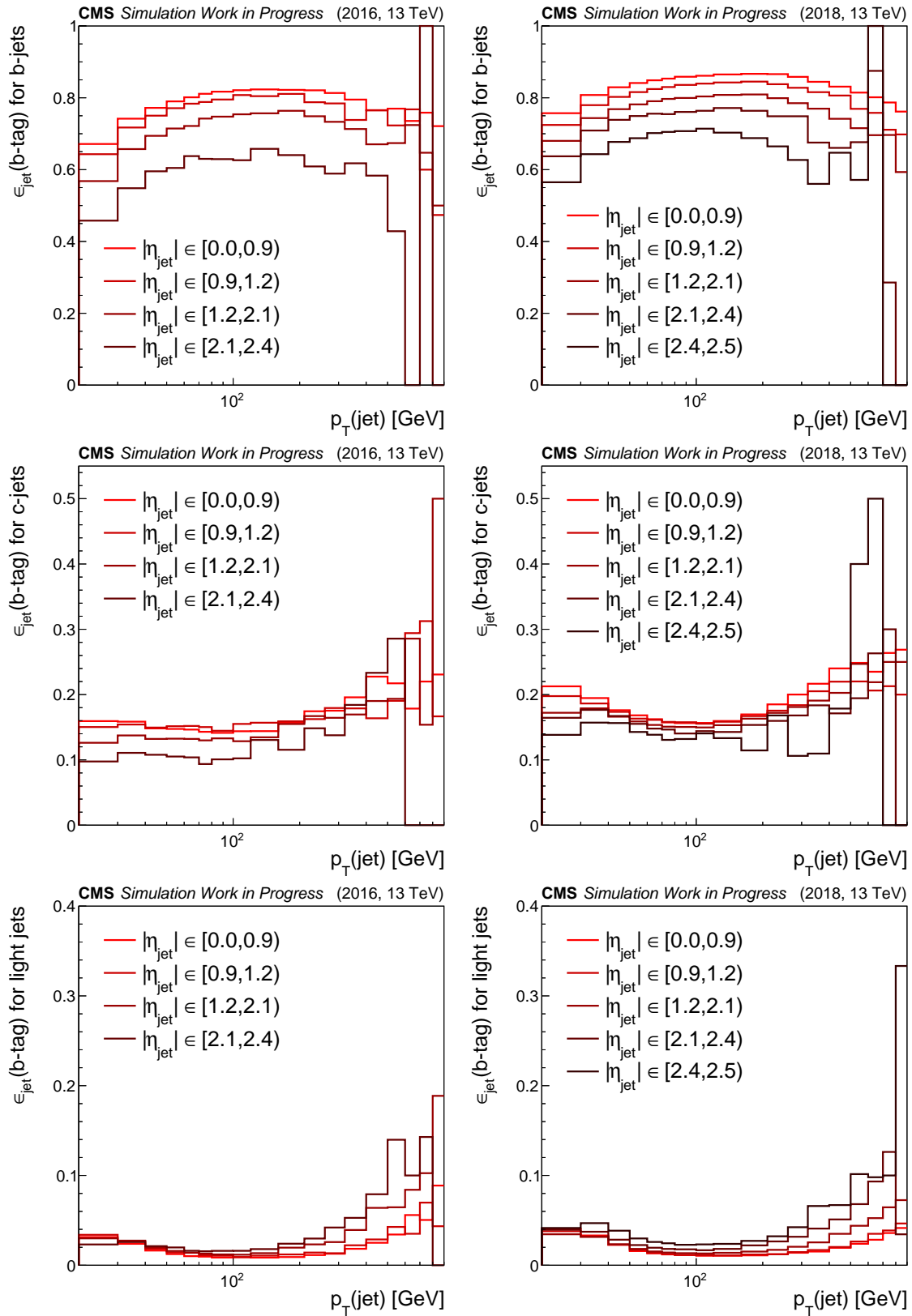
Figure 4.30.: B-tagging efficiencies in simulation for tagging jets induced by bottom quarks (top), charm quarks (middle), and light quarks or gluons (bottom), as functions of jet transverse momentum, $p_T(jet)$ and the jet pseudorapidity η_{jet} for the data-taking years 2016 (left) and 2018 (right).

The variations applied to the 4-momenta of the $\tau\tau$ pair, which result from the corresponding energy corrections and uncertainties, are propagated to the missing transverse energy reconstructed with the PUPPI method discussed in subsection 3.2.6, $\vec{p}_T^{\,miss}$. Further corrections and uncertainties assigned to $\vec{p}_T^{\,miss}$ in simulation depend on the particular simulated process.

In case that there is no single boson resonance recoiling against the jets of the hard process, both the jet energy corrections and uncertainties are propagated to the PF candidates clustered into these jets and used in $\vec{p}_T^{\,miss}$ calculation. Additionally, an uncertainty is assigned to $\vec{p}_T^{\,miss}$ due to the unclustered energy in an event, which may come for example from detector noise.

In case of simulated events with a recoiling boson resonance, as it is the case for events with the processes $Z \rightarrow \ell\ell$, $W \rightarrow l\nu$, $H \rightarrow \tau\tau$ and $H \rightarrow WW \rightarrow 2\ell2\nu$, only the jet energy corrections are propagated to $\vec{p}_T^{\,miss}$. Additionally, recoil corrections are derived and assigned with uncertainties in the $Z \rightarrow \mu\mu$ control region, where real contributions to $\vec{p}_T^{\,miss}$ are expected to vanish.

For the measurement of recoil corrections, $\vec{p}_T^{\,miss}$ split into two contributions parallel, $\hat{e}_\parallel(Z)$, and perpendicular, $\hat{e}_\perp(Z)$, to the reconstructed transverse momentum of the Z boson, $\vec{p}_T(Z)$, which corresponds to the transverse momentum of the di-muon system, $\vec{p}_T(\mu\mu)$, in the control region:

$$\vec{p}_T^{\,miss} = p_\parallel^{miss} \cdot \hat{e}_\parallel(Z) + p_\perp^{miss} \cdot \hat{e}_\perp(Z)$$

The distributions of $p_\parallel^{miss}$ and $p_\perp^{miss}$ are expected to be centered around 0 GeV and are measured for data and simulation in the region around the Z boson peak, $m_{\mu\mu} \in (70, 110)$ GeV, in categories constructed from the number of jets, N_{jets}, and the transverse momentum of the Z boson, $p_T(\mu\mu)$:

- N_{jets} category bins: $[0, 1, 2, \infty]$.
- $p_T(\mu\mu)$ category bins: $[0, 10, 20, 30, 50, \infty]$ GeV.

The corrections are determined from the differences in distributions between data and simulation with the quantile mapping technique: Values of the quantities with equal probabilities given by the corresponding cumulative distributions are connected with each other by a mapping function. Since the exact orientation of the $\vec{p}_T^{\,miss}$ component perpendicular to the transverse momentum of the Z boson is arbitrary, the distribution of the magnitude, $|p_\perp^{miss}|$, is considered for quantile mapping. An example of the distributions is shown in figure 4.31 for the data-taking year 2016 in the $N_{jets} = 0$, $p_T(\mu\mu) \in [0, 10]$ GeV and $N_{jets} = 1$, $p_T(\mu\mu) > 50$ GeV categories. For the distributions in data, all contributions other than from $Z \rightarrow \mu\mu$ are subtracted.
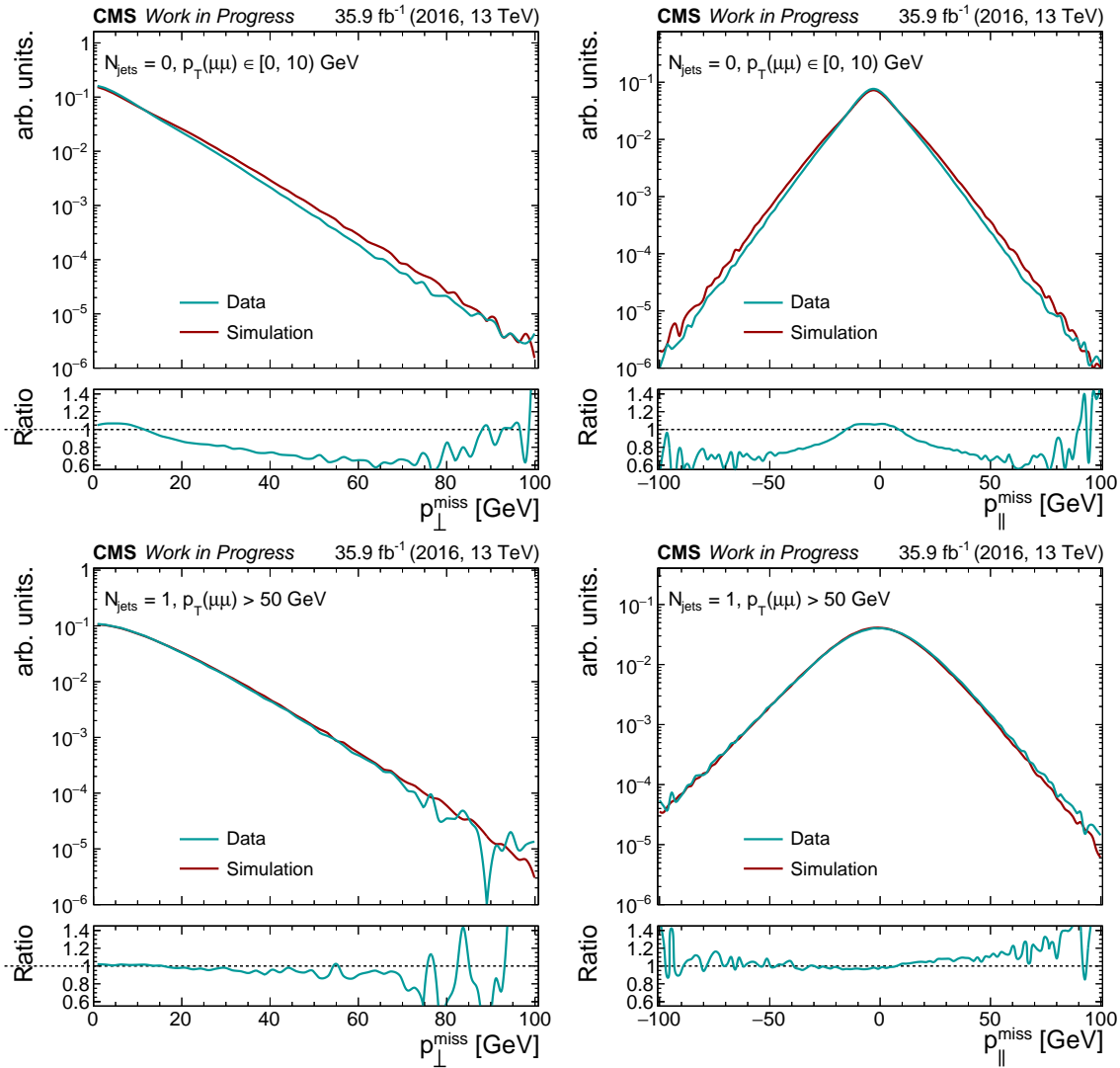
Figure 4.31.: Distributions of $|p_\perp^{miss}|$ (left) and $p_\parallel^{miss}$ (right) for the data-taking year 2016 for two different categories, top and bottom row respectively. For data distributions, all processes other than $Z \to \mu\mu$ are subtracted. All distributions are normalized to unity. The lower panels of the figures show the ratio between data and simulation.

Additionally to these distributions, the mean of the relative hadronic recoil with respect to the Z boson $\vec{p}_T$ is determined in simulation as a preparation for the uncertainty measurement. The hadronic recoil $\vec{H}_T$ is computed from $\vec{p}_T^{miss}$ by adding it to the reconstructed Z boson $\vec{p}_T$ and switching the sign of the result:

$$\vec{H}_T = -\left(\vec{p}_T(Z) + \vec{p}_T^{miss}\right)$$

As for the derivation of the $\vec{p}_T^{miss}$ corrections, the hadronic recoil is split into two components parallel and perpendicular to the $\vec{p}_T$ of the Z boson, $H_\parallel$ and $H_\perp$. For each simulated $Z \to \mu\mu$ event, the parallel component of the hadronic recoil is divided by the magnitude of the simulated transverse momentum of the Z boson, $p_T^{sim}(Z)$. The mean of the negative

value of this ratio is computed for each $(N_{jets}, p_T^{sim}(Z))$ category across the events passing the corresponding selection criteria. An example of the resulting values is shown for the data-taking years 2017 and 2018 in figure 4.32, which are expected to be centered at 1, if the hadronic recoil would be perfectly compensated by the Z boson $\vec{p}_T$. Deviations from the unity, seen for low $p_T^{sim}(Z)$ and in the $N_{jets} = 0$ category, indicate, that some of the information on jets is lost during the reconstruction of $\vec{p}_T^{miss}$. This mean serves as a measure for this bias and is used for the computation of the uncertainty.
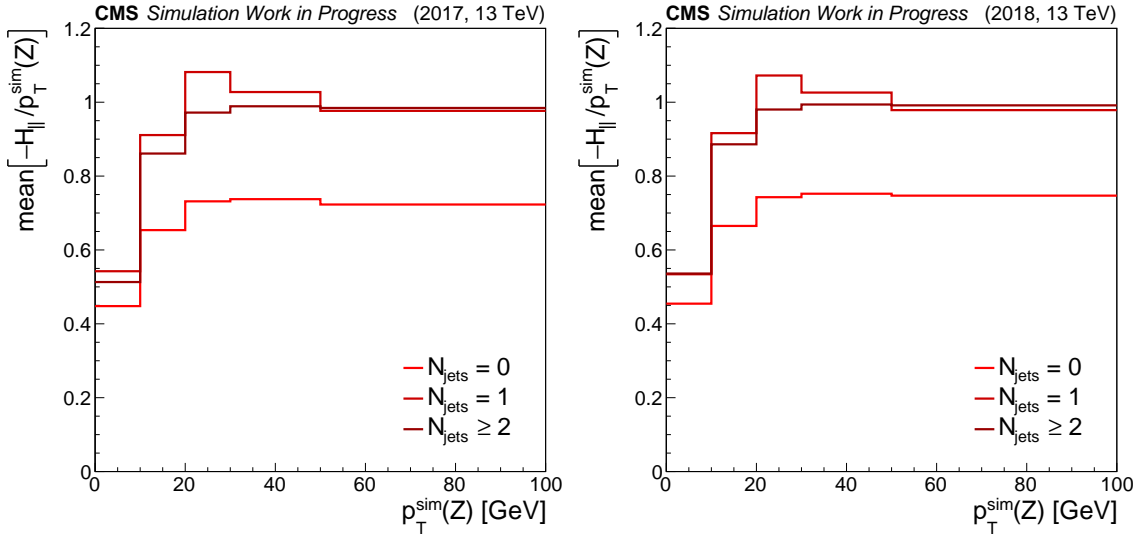
Figure 4.32.: The mean of the ratio between the hadronic recoil component parallel to the reconstructed Z boson $\vec{p}_T$, and the magnitude of the simulated transverse momentum of the Z boson, $p_T^{sim}(Z)$. The values are shown for the three N_{jets} categories and as a function of $p_T^{sim}(Z)$, binned in the same manner as the corresponding categorization, and chosen for the data-taking years 2017 and 2018. For the application of these measurements, the values at the bin edges of the histograms are linearly interpolated.

After these measurements, the corrections are applied to all simulated samples with a single resonance R, using the magnitude of its simulated transverse momentum $p_T^{sim}(R)$. This allows to generalize to cases with true $\vec{p}_T^{miss}$ contributions from the resonance, in particular, when τ decays are involved. In this case, the real contribution from the simulated neutrinos is subtracted from $\vec{p}_T^{miss}$ to obtain the artificial contribution to missing transverse energy, $\vec{p}_T^{miss}(art)$, as it is the case for the measurement in the $Z \rightarrow \mu\mu$ control region:

$$\vec{p}_T^{miss}(art) = \vec{p}_T^{miss} - \sum_\nu \vec{p}_T^{sim}(\nu)$$

This artificial contribution is split into two components parallel and perpendicular to $\vec{p}_T^{sim}(R)$, $p_\parallel^{miss}(art)$ and $p_\perp^{miss}(art)$. The components are corrected from simulation to data using the quantile mapping with the corresponding distributions of $|p_\perp^{miss}|$ and $p_\parallel^{miss}$ from the measurement and then building back $\vec{p}_T^{miss}$ from the corrected components.

The uncertainties on $\vec{p}_T^{miss}$ are estimated from the hadronic recoil, which is computed for a

resonance R in a more general way based on simulated $\vec{p}_T$:

$$\vec{H}_T = -\left(\vec{p}_T^{\,sim}(R) - \sum_\nu \vec{p}_T^{\,sim}(\nu) + \vec{p}_T^{\,miss} \right)$$

This hadronic recoil is split into two components parallel and perpendicular to $\vec{p}_T^{\,sim}(R)$, $H_\parallel$ and $H_\perp$. The values are varied in two different ways, changing the response and the resolution of the hadronic recoil.

In case of the variation of the recoil response, only the parallel component is changed, based on the mean values shown in figure 4.32, evaluated for the corresponding $(N_{jets}, p_T^{sim}(R))$ category:

$$H_\parallel^{new} = H_\parallel + shift \cdot mean\left[-H_\parallel / p_T^{sim}(Z) \right] \cdot p_T^{sim}(R)$$

A positive value of the shift would pull the parallel component of the hadronic more into the direction of the $\vec{p}_T^{\,sim}(R)$.

For the variation of the recoil resolution, both components are changed:

$$H_\parallel^{new} = H_\parallel + shift \cdot \left(H_\parallel - mean\left[-H_\parallel / p_T^{sim}(Z) \right] \cdot p_T^{sim}(R) \right)$$

$$H_\perp^{new} = (1 + shift) \cdot H_\perp$$

For a positive value of the shift, the distributions of the components would be smeared out with respect to their expected mean values. The simpler formula for $H_\perp$ results from the assumption, that the distribution is centered around 0 GeV.

The initial shift values are at first chosen to be $\pm10\%$, applied to the simulated $Z \to \mu\mu$ events in the corresponding control region, and determined in a maximum likelihood fit for each N_{jets} category, resulting in values given in table 4.28. The shift values are extracted from the pulls on the variations, preserving the correlations between the N_{jets} categories. In that way, two uncertainties are introduced for the recoil corrections of $\vec{p}_T^{\,miss}$ for each data-taking year, treated as uncorrelated across the years.

category	response			resolution		
	2016	2017	2018	2016	2017	2018
$N_{jets} = 0$	-1.79%	-1.47%	-1.51%	+1.60%	+1.12%	+2.64%
$N_{jets} = 1$	+0.72%	-1.06%	-1.56%	+0.78%	+5.13%	+5.82%
$N_{jets} \geq 2$	+0.66%	-0.32%	-1.78%	+0.53%	-2.56%	+5.16%

Table 4.28.: Shifts determined by maximum likelihood fits in N_{jets} categories in the $Z \to \mu\mu$ enriched control region for the response and resolution variations of the hadronic recoil.

The last correction related to $\vec{p}_T^{\,miss}$ description are event filters for events with an artificially large $\vec{p}_T^{\,miss}$, which is identified to come from several systematic sources, including noise in the HCAL and the ECAL, interactions of beam particles with the detector material and bad reconstruction of muons [96].

4.3.4. Selection of ττ Final States

After all physics objects were selected and the corresponding corrections are known, the final state specific selection is finalized by introducing the explicit HLT paths to be used for each final state and by ensuring the reduction of the overlap between the final states and the control regions.

μτ_h

In the $\mu\tau_h$ final state, the possible overlap with the other signal final states and the $Z \to \mu\mu$ control region needs to be reduced. For this purpose, the corresponding collections of muons in table 4.17 and electrons table 4.19 are used. The overlap veto collection of the muon is at first checked, whether it contains the muon from the signal pair and if so, it is removed it. If there are still additional muons in this collection left, this would indicate an overlap with the $Z \to \mu\mu$ control region and the event is rejected. Similarly, if any electrons are found in the event, which pass the overlap veto selection, the event is rejected due to the possible overlap with the $e\tau_h$ and $e\mu$ final states. Additionally, muons oppositely charged from the $Z \to \mu\mu$ veto collection are combined to a pair. If the pair constituents are additionally well separated, fulfilling the $\Delta R > 0.15$ criterion, the event is rejected to further reduce the overlap with the $Z \to \mu\mu$ control region and suppress the $Z \to \mu\mu$ contamination.

The HLT path selection for the $\mu\tau_h$ final state consists of a path selecting one muon and a path firing, if a $\mu\tau_h$ pair can be found. The first HLT path requires an isolated muon with a threshold on the transverse momentum depending on the data-taking year, $p_T(\mu) > 22$ GeV in 2016 and $p_T(\mu) > 27$ GeV in 2017 and 2018. The thresholds on the matched reconstructed muons are then chosen 1 GeV above. For the latter $\mu\tau_h$ HLT path, the isolated muon is required to have $p_T(\mu) > 19$ GeV in 2016 and $p_T(\mu) > 20$ GeV in 2017 and 2018. For all years, this muon is required to have a pseudorapidity of $|\eta_\mu| < 2.1$ in the HLT path. To avoid an overlap with the first HLT path, the additional criteria on the matched reconstructed muons are $p_T(\mu) \in (20, 23]$ GeV in 2016 and $p_T(\mu) \in (21, 28]$ GeV in 2017 and 2018. Furthermore, the isolated τ_h object in the $\mu\tau_h$ HLT path is required to pass $|\eta_{\tau_h}| < 2.1$ for all data-taking years, $p_T(\tau_h) > 20$ GeV in 2016 and $p_T(\tau_h) > 27$ GeV. The matched reconstructed τ_h candidates are additionally required to have a transverse momentum $p_T(\tau_h) > 30$ GeV in 2016 and $p_T(\tau_h) > 32$ GeV in 2017 and 2018.

eτ_h

For the $e\tau_h$ final state, the overlap reduction is performed in a similar manner as for the $\mu\tau_h$ final state: The electrons passing the overlap veto selection are compared to the electron of the selected signal pair and if a match was found, the corresponding electron is removed from the collection. If after this some electrons still remain in the collection, the event is rejected to reduce the overlap with the $Z \to ee$ control region. If muons are contained in the overlap veto collection, the event is also rejected to avoid overlap with $\mu\tau_h$ and $e\mu$ final states. Electrons from the $Z \to ee$ veto collection are combined to pairs, if their charge is opposite and they are well separated with $\Delta R > 0.15$. If at least one such pair is created, the event is rejected to further reduce the overlap with the $Z \to ee$ control region and suppress the $Z \to ee$ contamination.

Also for the $e\tau_h$ final state, a combination of HLT paths targeting only an electron and

an eτ_h pair is used. The first HLT path requires an isolated electron with $|\eta_e| < 2.1$ for all years and $p_T(e) > 25$ GeV in 2016, $p_T(e) > 35$ GeV in 2017 and $p_T(e) > 32$ GeV in 2018. A threshold on the transverse momentum higher by 5 GeV is applied to the matched reconstructed electrons. In the eτ_h HLT path, the isolated electron is required to have $p_T(e) > 24$ GeV and $|\eta_e| < 2.1$ for all data-taking years. Also in this case, the overlap to the former HLT path is avoided by a requirement on the transverse momentum of the matched reconstructed electrons, $p_T(e) \in (29, 30]$ GeV for 2016, $p_T(e) \in (29, 40]$ GeV for 2017 and $p_T(e) \in (29, 37]$ GeV for 2018. The HLT path requirements on the τ_h object consist of a pseudorapidity threshold of $|\eta_{\tau_h}| < 2.1$ for all data-taking years and a $p_T(\tau_h)$ threshold of 20 GeV in 2016 and 30 GeV in 2017 and 2018. To avoid the turn-on region of the HLT path with the τ_h object, the $p_T(\tau_h)$ thresholds on the matched reconstructed τ_h candidates are increased, resulting in $p_T(\tau_h) > 30$ GeV in 2016 and $p_T(\tau_h) > 35$ GeV in 2017 and 2018.

$\tau_h\tau_h$

In the $\tau_h\tau_h$ final state, only the overlap veto collections of electrons and muons are used to reduce the overlap with the eτ_h and $\mu\tau_h$ final states. In case any of the two lepton types is found in the event, it is rejected.

Throughout all data-taking years, HLT paths firing for a pair of two isolated τ_h candidates with $p_T(\tau_h) > 35$ GeV and $|\eta_{\tau_h}| < 2.1$ are used in the $\tau_h\tau_h$ final state. An additional requirement on the transverse momentum of the matched reconstructed τ_h candidates, $p_T(\tau_h) > 40$ GeV, is used to ensure, that the reconstructed τ_h candidates passing the selection are in the plateau region of the efficiency curve of the HLT paths.

eμ

In case of the eμ final state, the overlap veto collections of electrons and muons are checked, whether they contain the electron and the muon from the selected signal pair, respectively. If any additional leptons are contained in one of the two collections, the event is rejected to avoid an overlap with both the $Z \rightarrow$ ee and the $Z \rightarrow \mu\mu$ control regions and suppress the contamination by $Z \rightarrow$ ee and $Z \rightarrow \mu\mu$.

For the eμ final state, a combination of two HLT paths firing on an eμ pair is used, which is similar across the data-taking years. The two HLT paths are designed such, that either the isolated electron or the isolated muon should have the lower threshold on the transverse momentum, $p_T(e) > 12$ GeV and $p_T(\mu) > 8$ GeV, respectively. For these soft leptons, an additional p_T threshold is imposed on the matched reconstructed objects, $p_T(e) > 17$ GeV and $p_T(\mu) > 10$ GeV. The lepton with the higher p_T threshold in the HLT paths is chosen commonly: $p_T(e/\mu) > 23$ GeV. Also in this case, the matched reconstructed leptons are required to pass higher thresholds, $p_T(e) > 28$ GeV and $p_T(\mu) > 24$ GeV.

5. Categorization and Statistical Inference

In this chapter, the categorization of the events selected for the $H \rightarrow \tau\tau$ analyses, the procedures of statistical inference, and the results obtained from it will be discussed. The definition of the main control regions, and the signal regions used in all analyses will be discussed in the following, the more analysis-specific categorization will be discussed in sections 5.1, 5.2, and 5.3.

A control region for top quark pair production is obtained in the eµ final state by making use of the D_ζ variable defined as follows:

$$D_\zeta = p_\zeta^{\text{miss}} - 0.85 \cdot p_\zeta^{\text{vis}}, \quad p_\zeta^{\text{vis}} = \left(\vec{p}_T(e) + \vec{p}_T(\mu)\right) \cdot \hat{\zeta}, \quad p_\zeta^{\text{miss}} = \vec{p}_T^{\text{miss}} \cdot \hat{\zeta}, \quad (5.1)$$

where the normalized vector $\hat{\zeta}$ represents the bisectional direction between the transverse momentum vectors of the electron, $\vec{p}_T(e)$, and the muon, $\vec{p}_T(\mu)$. The numerical factor of -0.85 in the linear combination of the two projections p_ζ^{miss} and p_ζ^{vis} is chosen such, that the $Z \rightarrow \tau\tau$ and $H \rightarrow \tau\tau$ distributions are peaking approximately at zero. To enrich events from top quark pair production and isolate the $H \rightarrow WW$ contribution to the eµ final state, a requirement of $D_\zeta < -35$ GeV is imposed. The distribution of this variable for the data-taking year 2018 is shown in figure 5.1 (left).
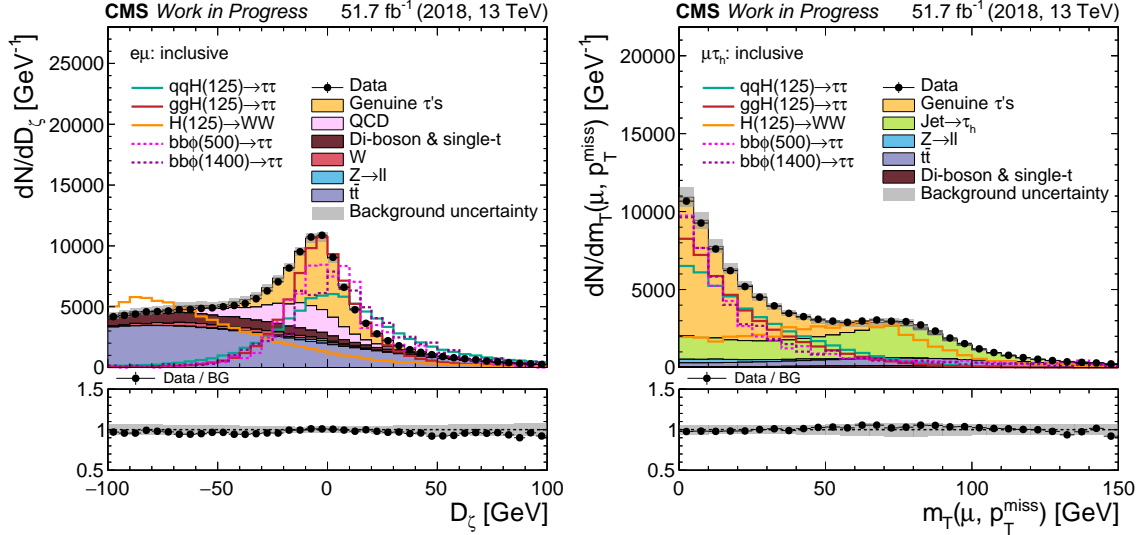
Figure 5.1.: Distributions of the variables used for categorization, (left) D_ζ in the eµ final state and (right) $m_T(\mu, p_T^{\text{miss}})$ in the $\mu\tau_h$ final state of the data-taking year 2018 for data and expected signals and backgrounds. The background contributions are stacked. The SM $H \rightarrow \tau\tau$, BSM $\phi \rightarrow \tau\tau$ and SM $H \rightarrow WW$ signals are rescaled for shape comparison in the upper panel of the figures. The grey background uncertainty bands include both statistical and systematic uncertainties in the state before a maximum likelihood fit.

Two additional control regions are introduced in the $\mu\tau_h$ and $e\tau_h$ final states to constrain the uncertainties on the $W \to \ell\nu$ estimation from the F_F method, using the transverse mass of the system constructed from the transverse momentum of the lepton and the missing transverse energy, $m_T(e/\mu, p_T^{miss})$. Its general definition is given below:

$$m_T(\ell_1, \ell_2) = \sqrt{2 \cdot p_T(\ell_1) \cdot p_T(\ell_2) \cdot (1 - \cos\Delta\phi(\ell_1, \ell_2))} \tag{5.2}$$

The angle $\Delta\phi(\ell_1, \ell_2)$ is the difference in azimuth angle between the two physics objects ℓ_1 and ℓ_2. To enrich the $W \to \ell\nu$ background, $m_T(e/\mu, p_T^{miss}) \geq 70$ GeV is required. The distribution of $m_T(\mu, p_T^{miss})$ for the $\mu\tau_h$ channel for the data-taking year 2018 is shown in figure 5.1 (right). The chosen discriminator for statistical inference in the control regions is the total transverse mass introduced in section 5.2. The remaining events are assigned to signal regions of the $\mu\tau_h$, $e\tau_h$, $\tau_h\tau_h$ and $e\mu$ final states.

To model uncertainties, two procedures are used, depending on the nature of the uncertainty. Uncertainties, which change only the normalization of a distribution, are modelled with a single nuisance parameter θ, which follows the log-normal (lnN) distribution with the probability density function

$$lnN\,(\theta; \mu, \sigma) = \frac{1}{\sqrt{2\pi}\sigma\theta} \cdot \exp\left(-\frac{(\ln(\theta) - \mu)^2}{2\sigma^2}\right).$$

The parameter μ is chosen to be $\mu = 0$, and the parameter σ corresponds to the relative variation of the considered systematic uncertainty. This means, that $\ln(\theta)$ follows a Gaussian distribution with a mean equal to 0, and a standard deviation equal to σ. Normalization uncertainties are used to cover multiplicative corrections to the expected yield of a distribution, for example, efficiency corrections.

The second type of uncertainties can alter both the shape and the normalization of the discriminator distribution. For such uncertainties, each histogram bin of the normalized discriminator distribution is interpolated with a function between the systematic downward variation, the nominal distribution, and the systematic upward variation, and is extrapolated linearly beyond the variations. The function is chosen to be a sixth order polynomial to obtain an interpolation function and derivatives of it which are smooth enough [162]. The bin interpolations are controlled by a single nuisance parameter, which is assumed to be distributed according to a Gaussian with the mean and standard deviation equal to 0 and 1, respectively. The change in normalization of the shape uncertainty is accounted for by a linear interpolation of the distribution yields on a logarithmic scale and is controlled by the same nuisance parameter.

To account for the finite number expected background events in each histogram bin, a third type of uncertainty is added to the uncertainty model, estimated with the Barlow-Beeston approach [163, 164], using a single, Gaussian distributed parameter, which is applied to the total expected background yield in the considered histogram bin. These uncertainties are a special case of shape altering uncertainties.

The setup of the uncertainty model common for all $H \to \tau\tau$ analyses considered in this thesis is shown in table 5.1 for normalization uncertainties and table 5.2 for shape altering uncertainties.

The processes provided with the uncertainties are abbreviated as follows:

- Background from genuine τ pairs: EMB
- Jets misidentified as τ_h candidates: Jet $\rightarrow \tau_h$
- Estimation of the QCD multijet background: QCD
- Processes estimated by simulation: MC
- $Z \rightarrow \ell\ell$ contributions with $\ell \in \{e, \mu\}$:   ZL
- Top quark pair production without genuine τ pairs: TTL
- Di-Boson and single top production without genuine τ pairs: VVL
- $W \rightarrow \ell\nu$ contributions with $\ell \in \{e, \mu\}$:   W

Uncertainty source	number of θ_j	relative variation	affected processes	details on correlations
Luminosity	7	0 to 2.2%	MC	100% across years for 1 parameter
e ID & Iso	1	2%	MC, EMB in $e\tau_h$, $e\mu$	100% across years, 50% between MC, EMB
μ ID & Iso	1	2%	MC, EMB in $\mu\tau_h$, $e\mu$	100% across years, 50% between MC, EMB
τ_h ID ($\mu\tau_h$)	1	1%	MC, EMB	50% between MC, EMB
τ_h ID ($e\tau_h$)	1	1%	MC, EMB	50% between MC, EMB
τ_h ID ($\tau_h\tau_h$)	1	1.4%	MC, EMB	50% between MC, EMB
$\sigma_{t\bar{t}}$	1	6%	TTL	100% across years
$\sigma_{\text{Di-boson \& single-t}}$	1	5%	VVL	100% across years
$\sigma_{Z\rightarrow\ell\ell}$	1	4%	ZL	100% across years
$\sigma_{W\rightarrow\ell\nu}$	1	4%	W	100% across years
HLT μ-leg ($\mu\tau_h$)	2	2%	MC, EMB	0% between MC, EMB
HLT e-leg ($e\tau_h$)	2	2%	MC, EMB	0% between MC, EMB
HLT ($e\mu$)	1	2%	MC, EMB	0% between MC, EMB
$\mu \rightarrow \tau_h$ rejection	5	9 to 63%	ZL in $\mu\tau_h$	
$e \rightarrow \tau_h$ rejection	2	18 to 41%	ZL in $e\tau_h$	
$\mu\mu$ selection	1	4%	EMB	
Jet $\rightarrow \tau_h$ estimation	2 per category	3.7 to 9.5%	Jet $\rightarrow \tau_h$ in $\mu\tau_h$, $e\tau_h$, $\tau_h\tau_h$	0% across categories

Table 5.1.: Normalization uncertainties common to the H $\rightarrow \tau\tau$ analyses discussed in sections 5.1, 5.2, and 5.3, modelled as nuisance parameters θ_j, which follow a log-normal (lnN) distribution. If not stated otherwise, the uncertainties are treated as uncorrelated across the years.

Uncertainty source	number of θ_i	affected processes	details on correlations
Prefiring	1	MC in 2016, 2017	100% across years
Z → ℓℓ reweighting	1	ZL	100% between 2017, 2018
t$\bar{\text{t}}$ reweighting	1	TTL	100% across years
τ_h ID (one τ_h)	5	MC, EMB in $\mu\tau_h$, eτ_h	50% between MC, EMB
τ_h ID (two τ_h candidates)	4	MC, EMB in $\tau_h\tau_h$	50% between MC, EMB
τ_h energy scale	4	MC, EMB in $\mu\tau_h$, eτ_h, $\tau_h\tau_h$	50% between MC, EMB
$\mu \to \tau_h$ energy scale	2	ZL in $\mu\tau_h$	
e $\to \tau_h$ energy scale	4	ZL in eτ_h	
Electron energy scale, resolution	2	MC in eτ_h, eμ	100% across years
Electron energy scale	1	EMB in eτ_h, eμ	100% across years
Jet energy scale, resolution	12	MC	100% across years for 6 parameters
$\vec{p}_T^{\text{miss}}$ unclustered energy	1	TTL, VVL	100% across years
$\vec{p}_T^{\text{miss}}$ recoil scale, resolution	2	ZL, W, signal MC	
HLT τ_h-leg ($\mu\tau_h$, eτ_h, $\tau_h\tau_h$)	4 per final state	MC, EMB in $\mu\tau_h$, eτ_h, $\tau_h\tau_h$	0% between MC, EMB 0% across final states
B-tagging	2	MC	
t$\bar{\text{t}}$ contamination	1	EMB	
τ_h decay mode reconstruction	2	EMB in $\mu\tau_h$, eτ_h, $\tau_h\tau_h$	
QCD estimation	10	QCD in eμ	
Jet → τ_h estimation	26 in $\mu\tau_h$, eτ_h 10 in $\tau_h\tau_h$	Jet → τ_h in $\mu\tau_h$, eτ_h, $\tau_h\tau_h$	0% across final states

Table 5.2.: Shape altering uncertainties common to the H → ττ analyses discussed in sections 5.1, 5.2, and 5.3, modelled as nuisance parameters θ_i. If not stated otherwise, the uncertainties are treated as uncorrelated across the years.

For each uncertainty source, the number of nuisance parameters, the processes affected by the uncertainty, as well as details on the correlations used for the considered uncertainty are given in the two tables. In case of the normalization uncertainties, the relative variation of the yield is given in addition.

To improve the stability of the statistical inference, as well as to avoid artificial constraints on nuisance parameters, all shape altering uncertainties, which do not significantly change the shape of the distribution of the chosen discriminator in a considered category, are transformed into normalization uncertainties. The decision is taken by a comparison of a systematic variation with the statistical uncertainties of the nominal distribution, pointing to the possible fraction of statistical fluctuations in the variation.

The presented uncertainty model is used for the statistical inference based on a binned maximum likelihood approach. The observed number of events n_k in each histogram bin of the discriminator distribution is assumed to follow a Poisson distribution, leading to the following definition of the likelihood evaluated for the total number of data events n:

$$L\left(n | \mu \cdot s\left(\theta\right) + b\left(\theta\right)\right) = \prod_{i \in \text{shape}} \text{Gauss}\left(\theta_i; 0, 1\right) \prod_{j \in \text{lnN}} \text{lnN}\left(\theta_j; 0, \sigma_j\right)$$
$$\prod_{k \in \text{bins}} \text{Poisson}\left(n_k; \mu \cdot s_k\left(\{\theta_i\}, \{\theta_j\}\right) + b_k\left(\{\theta_i\}, \{\theta_j\}\right)\right) \qquad (5.3)$$

The expected number of events $\mu \cdot s_k\left(\{\theta_i\}, \{\theta_j\}\right) + b_k\left(\{\theta_i\}, \{\theta_j\}\right)$ of each histogram bin k is constructed from the background expectation b_k and the signal expectation s_k which is scaled by the signal strength parameter μ. The corresponding Poisson distribution evaluated for the number of observed events n_k corresponds to the probability of observing n_k events, given the expected number of events in that bin. The signal and background expectations depend on the nuisance parameters altering the shape of the histogram, θ_i, or changing its normalization, θ_j. The values of these nuisance parameters are not known exactly, but with an uncertainty, and following a Gaussian or lnN distribution. To account for this, the product of the Poisson probabilities is multiplied additionally with the corresponding distributions of the nuisance parameters.

In the simplest application of the maximum likelihood approach, the likelihood is maximized with respect to all parameters to extract the signal strength μ of the expected signal at the global maximum of the likelihood function, the best estimate value $\hat{\mu}$. The analysis-specific variations of this procedure will be discussed in more detail in the following sections.

5.1. SM H $\to \tau\tau$ analysis

Measurements of the properties of the observed Higgs boson with the mass of 125 GeV, referred to as SM measurements in the following, focus on enriching the expected SM Higgs boson signal at this particular mass. For that purpose, a mass related discriminator is chosen, designed to separate backgrounds from the SM H $\to \tau\tau$ expectation, the SVfit $\tau\tau$ mass $m_{\tau\tau}$ in the classic version of the algorithm [165]. This algorithm is a likelihood based method to determine the full 4-momentum of the Higgs boson, including the undetectable contributions from neutrinos in τ decays, using the 4-momenta of the visible final states, the missing transverse energy vector, and its covariance matrix [96] as input. The separation power of this quantity is compared to the total transverse mass of the $\tau\tau$ system, m_T^{tot},

which is used for the BSM $H \to \tau\tau$ search and explained in more detail in section 5.2. The comparison is performed in a category sensitive to VBF Higgs boson production, as shown in figure 5.2. The better separation of the SM $H \to \tau\tau$ expectation from the $Z \to \tau\tau$ background for $m_{\tau\tau}$ is visible by eye.
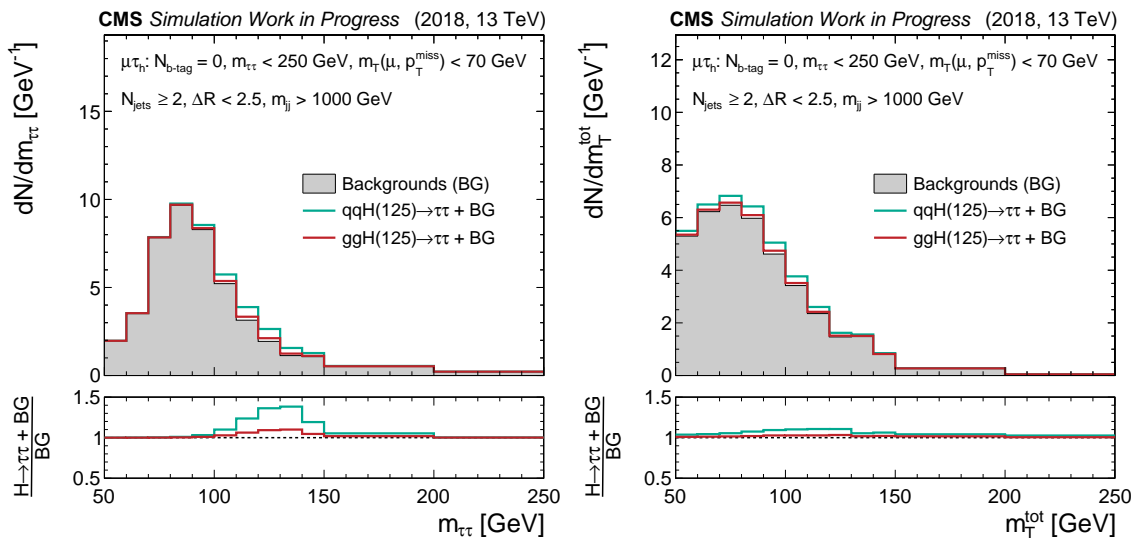
Figure 5.2.: Distributions of the discriminators (left) $m_{\tau\tau}$ and (right) m_T^{tot} in the same category sensitive to the SM VBF signal. The signal distribution for $m_{\tau\tau}$ has a better resolution, allowing to discriminate the signal better from backgrounds.
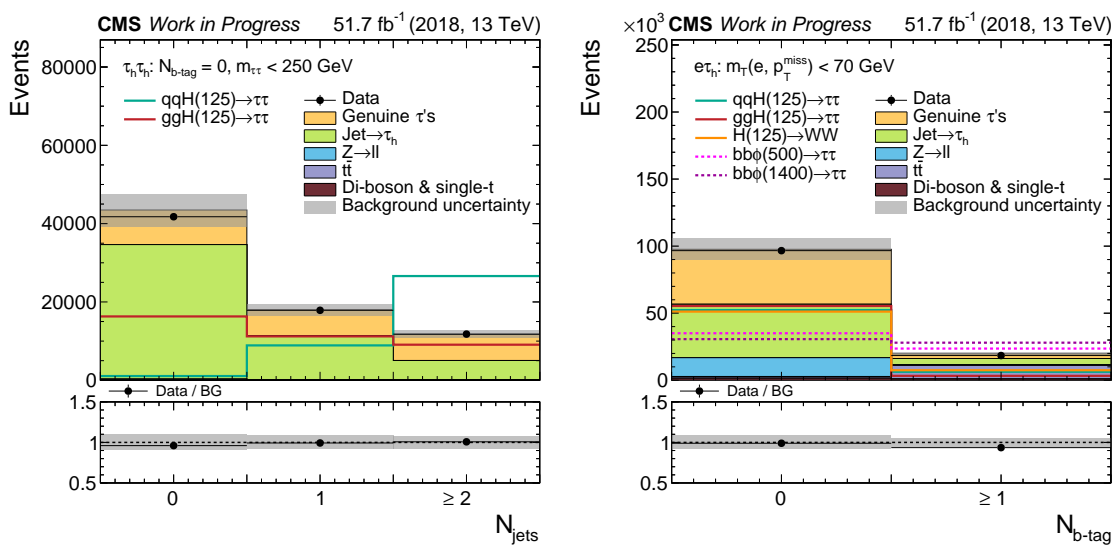
Figure 5.3.: Distributions of the variables used for categorization, (left) N_{jets} in the $\tau_h\tau_h$ final state and (right) $N_{b\text{-tag}}$ in the $e\tau_h$ final state of the data-taking year 2018 for data and expected signals and backgrounds. The SM $H \to \tau\tau$, BSM $\phi \to \tau\tau$ and SM $H \to WW$ signals are rescaled for shape comparison in the upper panel of the figures. The grey background uncertainty bands include both statistical and systematic uncertainties in the state before a maximum likelihood fit.

For the SM measurement, the signal regions of the $\mu\tau_h$, $e\tau_h$, $\tau_h\tau_h$, and $e\mu$ final states

defined at the beginning of chapter 5 are further refined by requiring $N_{b\text{-tag}} = 0$ and $m_{\tau\tau} < 250$ GeV. The first requirement is imposed to suppress the background from top quark pair production, concentrated at $N_{b\text{-tag}} \geq 1$ as can be seen in figure 5.3 (right) for the $e\tau_h$ final state. The second requirement is imposed to separate the SM measurement from the high mass region to allow for a combination of categories sensitive to the observed Higgs boson at 125 GeV with categories used for the search of additional heavy Higgs boson resonances, as will be discussed in section 5.3.
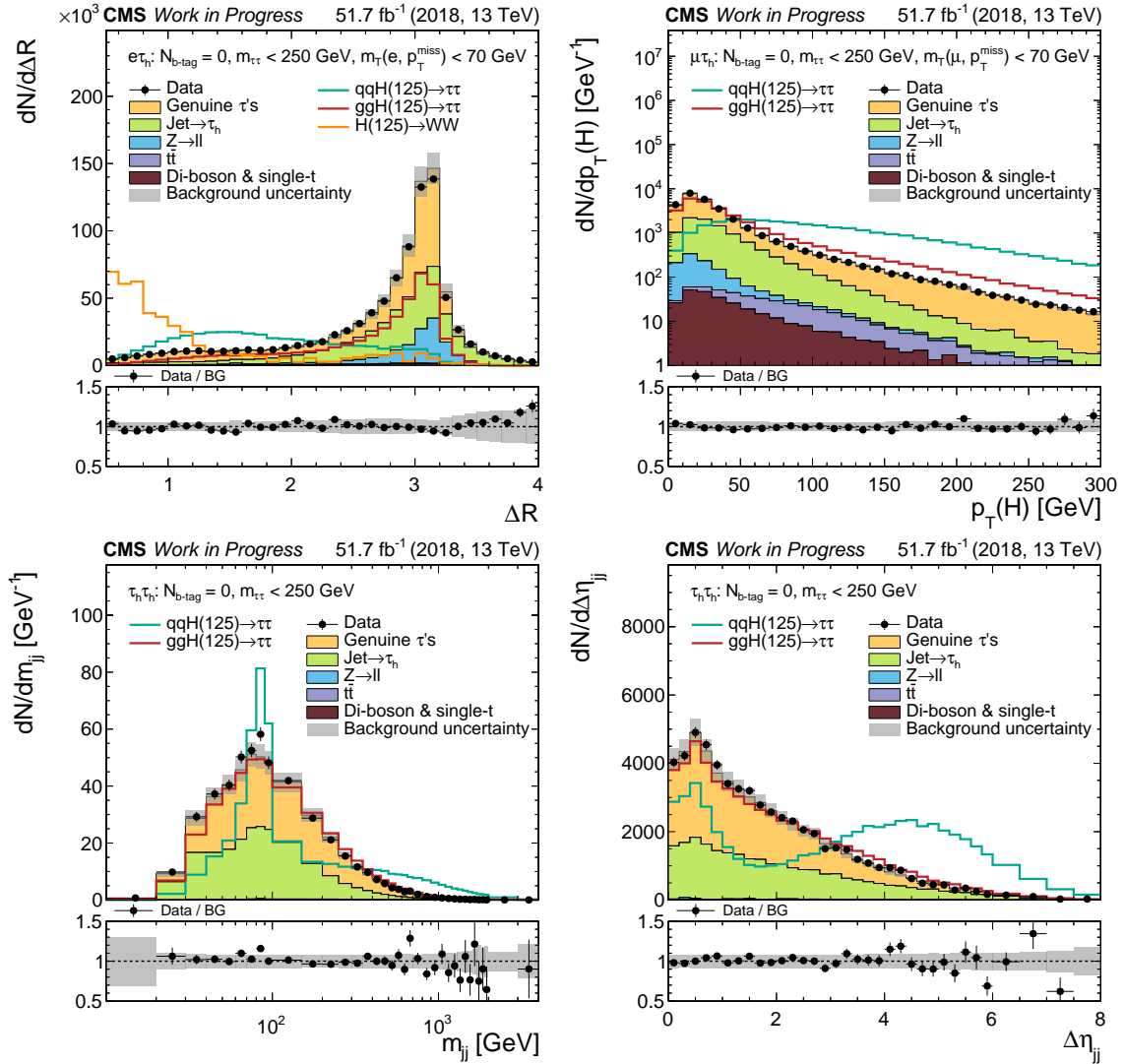
Figure 5.4.: Distributions of the variables used for categorization, (top left) ΔR in the $e\tau_h$ final state, (top right) $p_T(H)$ in the $\mu\tau_h$ final state, (bottom left) m_{jj}, and (bottom right) $\Delta\eta_{jj}$ in the $\tau_h\tau_h$ finale state of the data-taking year 2018 for data and expected signals and backgrounds. The SM $H \rightarrow \tau\tau$ and $H \rightarrow WW$ signals are rescaled for shape comparison in the upper panel of the figures. The grey background uncertainty bands include both statistical and systematic uncertainties in the state before a maximum likelihood fit.

The signal region for the SM measurement is divided into categories based on quantities, which depend on the kinematic properties of the selected $\tau\tau$ pair, and properties of the jets

that accompany the $\tau\tau$ pair in the event. The first step of the categorization is based on the number of selected jets, N_{jets}, sorting events into categories with zero, one or at least two jets. As shown in figure 5.3 (left) for the $\tau_h\tau_h$ final state of the data-taking in 2018, signal events from VBF Higgs boson production have mostly two jets, whereas events from gluon fusion Higgs boson production, as well as from the major backgrounds, have usually not more than one jet.

Further categorization is based on the separation between the $\tau\tau$ pair in the (η, ϕ) plane, ΔR, and the reconstructed estimate of the Higgs boson $p_T(H)$, which is the magnitude of the vectorial sum of visible $\vec{p}_T$ of the $\tau\tau$ pair and $\vec{p}_T^{miss}$. The categorization with ΔR allows in particular to isolate events with contributions from Jet $\to \tau_h$ in the final states with a τ_h candidate. Events with at least two jets are categorized based on jet related quantities, the invariant mass of the two jets with the highest p_T, m_{jj}, and their separation in η, $\Delta\eta_{jj}$. For the $e\mu$, $\mu\tau_h$ and $e\tau_h$ final states, specific categorizations are introduced based on D_ζ and $m_T(e/\mu, p_T^{miss})$. The distributions of additional quantities used for categorization are shown in figure 5.4 for ΔR in the $e\tau_h$ final state, for $p_T(H)$ in the $\mu\tau_h$ final state, and for m_{jj} and $\Delta\eta_{jj}$ in the $\tau_h\tau_h$ final state, taken from the data-taking year 2018.

The requirements used for the categorization of the signal regions in the $\mu\tau_h$ and $e\tau_h$ final states are summarized in figure 5.5. The final states are indicated by the large filled blue box at the top. The boxes framed in blue represent intermediate selection steps. The filled blue boxes represent the final category definition. The filled boxes with numbers to the left/right indicate the binning in the given quantity. The bins are defined such, that they include (exclude) the smaller (larger) boundary value.
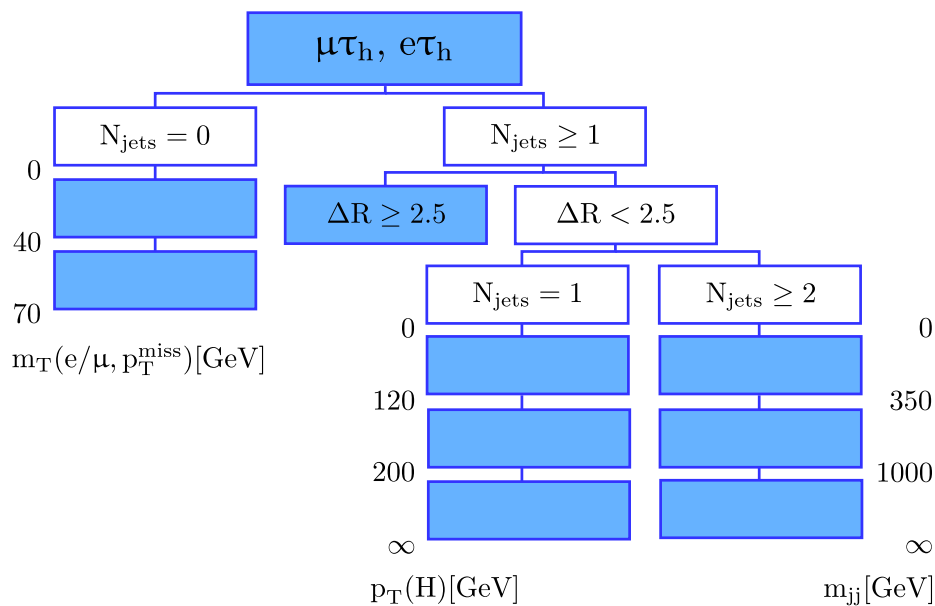
Figure 5.5.: Categorization applied to the signal region refined for the SM measurement in the $\mu\tau_h$ and $e\tau_h$ final states. Details are given in the text.

The requirements used for the categorization of the signal region of the $\tau_h\tau_h$ final state are given in figure 5.6. A similar visualization as in figure 5.5 is used. Additionally, small filled red boxes with requirements on ΔR or $\Delta\eta_{jj}$ indicate the categorization based on a second variable. The dashed red line represents a unification of the corresponding two regions into one category.
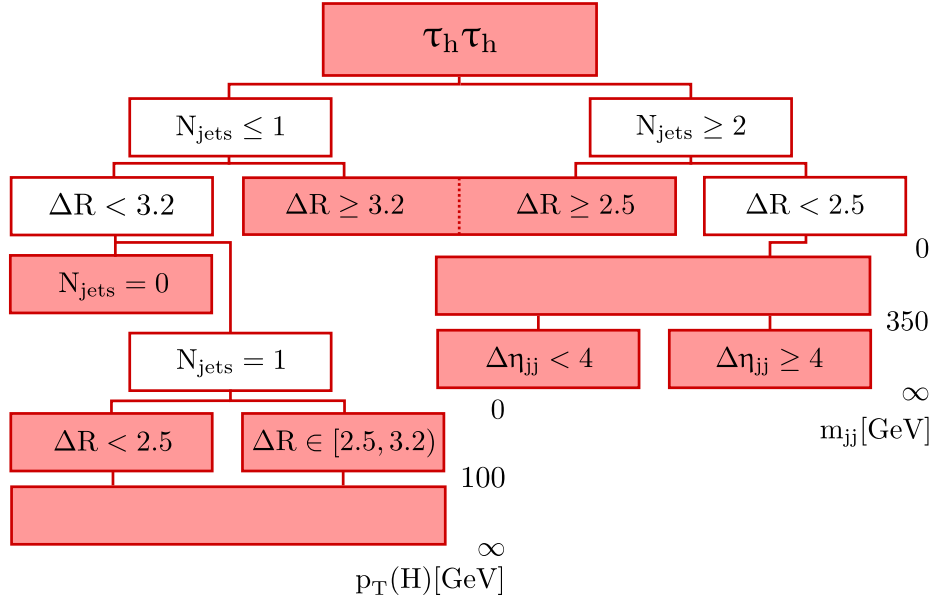
Figure 5.6.: Categorization applied to the signal region refined for the SM measurement in the $\tau_h\tau_h$ final state. Details are given in the text.

The signal region of the $e\mu$ final state is categorized as given in figure 5.7. A similar visualization as in figures 5.5 and 5.6 is used.
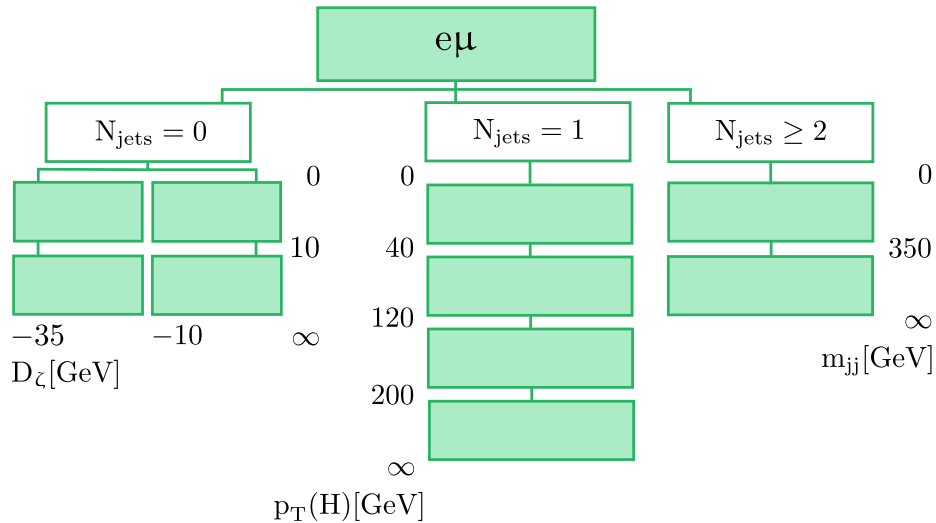
Figure 5.7.: Categorization applied to the signal region refined for the SM measurement in the $e\mu$ final state. Details are given in the text.

In addition to the uncertainty model summarized in tables 5.1 and 5.2, uncertainties specific to the SM Higgs boson signal are introduced. As before, two types of uncertainties are used, summarized in table 5.3 for normalization uncertainties, and in table 5.4 for shape altering effects. The following abbreviations for the Higgs boson production processes are used, where necessary:

- W boson associated production with $W \to \ell\nu$ WH
- Z boson associated production with $Z \to \ell\ell$ and $Z \to \nu\nu$ ZH
- VBF production and W,Z boson associated production with $W,Z \to qq$ qqH
- Gluon fusion   ggH
- $t\bar{t}$ associated production   ttH

Uncertainty source	number of nuisance parameters	relative variation	affected processes
BR($H \to \tau\tau$)	3	0.6% to 1.7%	$H \to \tau\tau$
BR($H \to WW$)	3	0.6% to 1%	$H \to WW$
σ_{ggH} (QCD scale)	1	3.9	ggH ($H \to WW$)
σ_{ggH} (p.d.f.)	1	3.2%	ggH
σ_{qqH} (QCD scale)	1	0.5%	qqH ($H \to WW$)
σ_{qqH} (p.d.f.)	1	2.1%	qqH
$\sigma_{WH,ZH}$ (QCD scale, p.d.f.)	2	0.8 to 1.8%	WH, ZH
σ_{ttH} (QCD scale, p.d.f.)	2	3.6 to 8%	ttH

Table 5.3.: Normalization uncertainties specific to the SM Higgs boson signals, modelled as nuisance parameters, which follow a log-normal (lnN) distribution. The nuisance parameters are treated as 100% correlated across the years.

Uncertainty source	number of nuisances parameters	affected processes
σ_{ggH} (QCD scale)	9	ggH ($H \to \tau\tau$)
σ_{qqH} (QCD scale)	10	qqH ($H \to \tau\tau$)

Table 5.4.: Shape altering uncertainties specific to the SM Higgs boson signals. The nuisance parameters are treated as 100% correlated across the years.

In the context of the SM measurement, the signal strengths of the two main production modes, μ_{ggH} and μ_{qqH}, as well as their combination to the signal strength μ are measured in the SM $H \to \tau\tau$ analysis. The remaining contributions to the $H \to \tau\tau$ and $H \to WW \to 2\ell2\nu$ signals are fixed to their SM expectations. Of relevance for the analysis are the results of the signal strengths, their constraints, the significance of the results, and the correlation between μ_{ggH} and μ_{qqH}.

To obtain these results, the likelihood function of equation 5.3 is extended to the negative

logarithmic likelihood ratio

$$q_\mu = -2 \cdot \Delta \ln L(\mu) = -2 \cdot \ln \left(\frac{L(n|\mu \cdot s(\hat{\hat{\theta}}_\mu) + b(\hat{\hat{\theta}}_\mu))}{L(n|\hat{\mu} \cdot s(\hat{\theta}) + b(\hat{\theta}))} \right). \tag{5.4}$$

The denominator in the likelihood ratio represents the global maximum of the likelihood, from which the best estimate $\hat{\mu}$ can be extracted. The numerator in the ratio corresponds to a local maximum of the likelihood for a fixed value of μ. Based on this log-likelihood ratio and for a fixed value of μ, the probability to obtain an observed result q_μ^{obs} or larger can be computed, if the distribution of q_μ is known. This probability is usually referred to as p-value and computed as follows for a known distribution $f(q_\mu)$:

$$p_\mu = \int_{q_\mu^{obs}}^{\infty} f(q_\mu) dq_\mu \tag{5.5}$$

An example for such a p-value is related to the significance of a signal, computed for $\mu = 0$ and a distribution $f(q_0)$ under the assumption of no signal. The significance is directly related to the probability to obtain the result q_0^{obs} or larger due to a fluctuation from backgrounds. The smaller the p-value p_0, the higher the significance Z, which can be computed from p_0 and given in multiples of a standard deviation of a normal distribution:

$$Z = \sqrt{2} \cdot err^{-1}(2 \cdot p_0 - 1) \approx \hat{\mu}/\hat{\sigma}, \qquad \Phi(x) = \frac{1}{2} \left(1 + err \left(\frac{x}{\sqrt{2}} \right) \right),$$

where err^{-1} is the inverse of the error function, which is related to the cumulative Gaussian distribution Φ.

Provided that the likelihood is evaluated for a large number of events [166], the log-likelihood ratio from equation 5.4 can be approximated by the following term:

$$q_\mu = -2 \cdot \Delta \ln L(\mu) \approx \frac{(\mu - \hat{\mu})^2}{\hat{\sigma}^2} \tag{5.6}$$

The square root of the variance of the best estimate signal strength, $\hat{\sigma}^2$, corresponds then to the constraint on the signal strength measurement. This approximation leads to the following consequences:

- The log-likelihood ratio q_μ follows a non-central χ^2 distribution with one degree of freedom for fixed μ, such that p-values can be computed easily with this analytic approximation, for example for the significance Z. Furthermore, the quantiles of the χ^2 distribution are directly related to the values of q_μ, allowing the construction of confidence intervals and regions, covering for example 68% or 95% of the possible values of q_μ drawn from $f(q_\mu)$.
- While scanning q_μ, the constraint $\hat{\sigma}$ can be found by searching for the crossing of the parabolic approximation in equation 5.6 with $q_\mu = 1$.
- In case of multiple signals, the covariance matrix of the corresponding signal strength parameters μ_i can be computed from second order derivatives of the log-likelihood ratio, $\partial^2/\partial\mu_i\partial\mu_j (\Delta \ln L)$. In that way, correlations between the signals can be approximated.

Distributions of the discriminating variables are shown for a selection of categories, which enter the statistical inference. For the data-taking year 2018, background (BG) enriched categories discussed at the beginning of this chapter are shown in figure 5.8, and categories for SM H → ττ signal extraction in figures 5.9, 5.10, 5.11, and 5.12 for the eμ, eτ$_h$, μτ$_h$, and τ$_h$τ$_h$ final states. Background uncertainties shown in the figures correspond to the quadratic sum of statistical and systematic uncertainties after performing a maximum likelihood fit of the inclusive signal strength μ. Data is in well agreement with expected signal and background contributions within the uncertainties. Categories with N$_{jets}$ = 0 collect ggH signal, which does not contribute to categories with N$_{jets}$ ≥ 1. Categories with N$_{jets}$ = 1 have an increased sensitivity to ggH, and in case of large p$_T$(H), they become relevant also for qqH. Categories with N$_{jets}$ ≥ 2 are sensitive to both signals, with an increased sensitivity to qqH in case of requirements on m$_{jj}$ and Δη$_{jj}$.
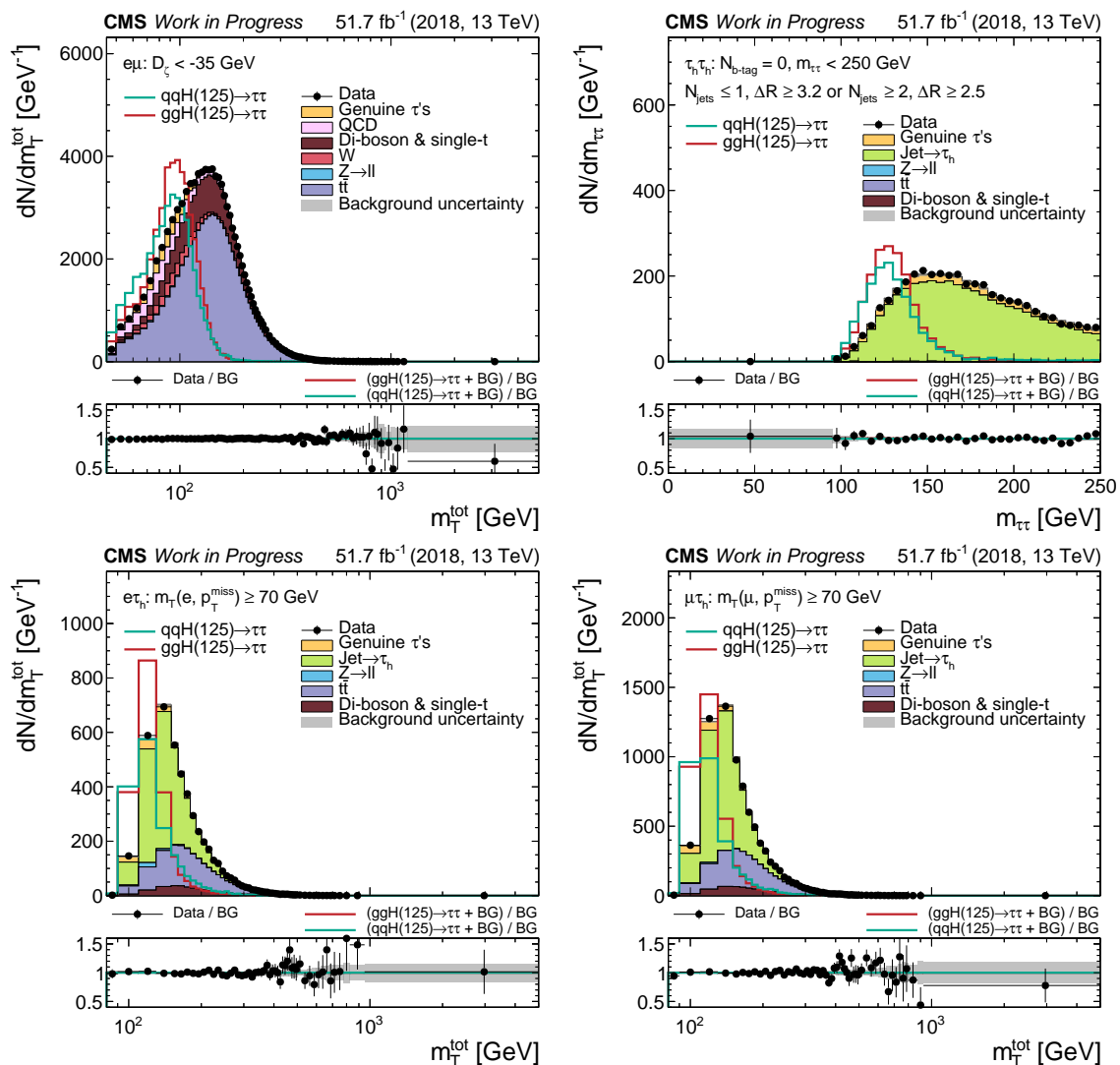
Figure 5.8.: Distributions of m$_{ττ}$ and m$_T^{tot}$ for eμ, τ$_h$τ$_h$, eτ$_h$, and μτ$_h$ in control regions of data-taking in 2018. Expected SM H → ττ signal, rescaled for shape comparison in the upper panels, is shown with data and stacked background (BG). Grey uncertainty bands illustrate the total BG uncertainty after a maximum likelihood fit for μ. In the lower panel, SM H → ττ is scaled to SM expectation.
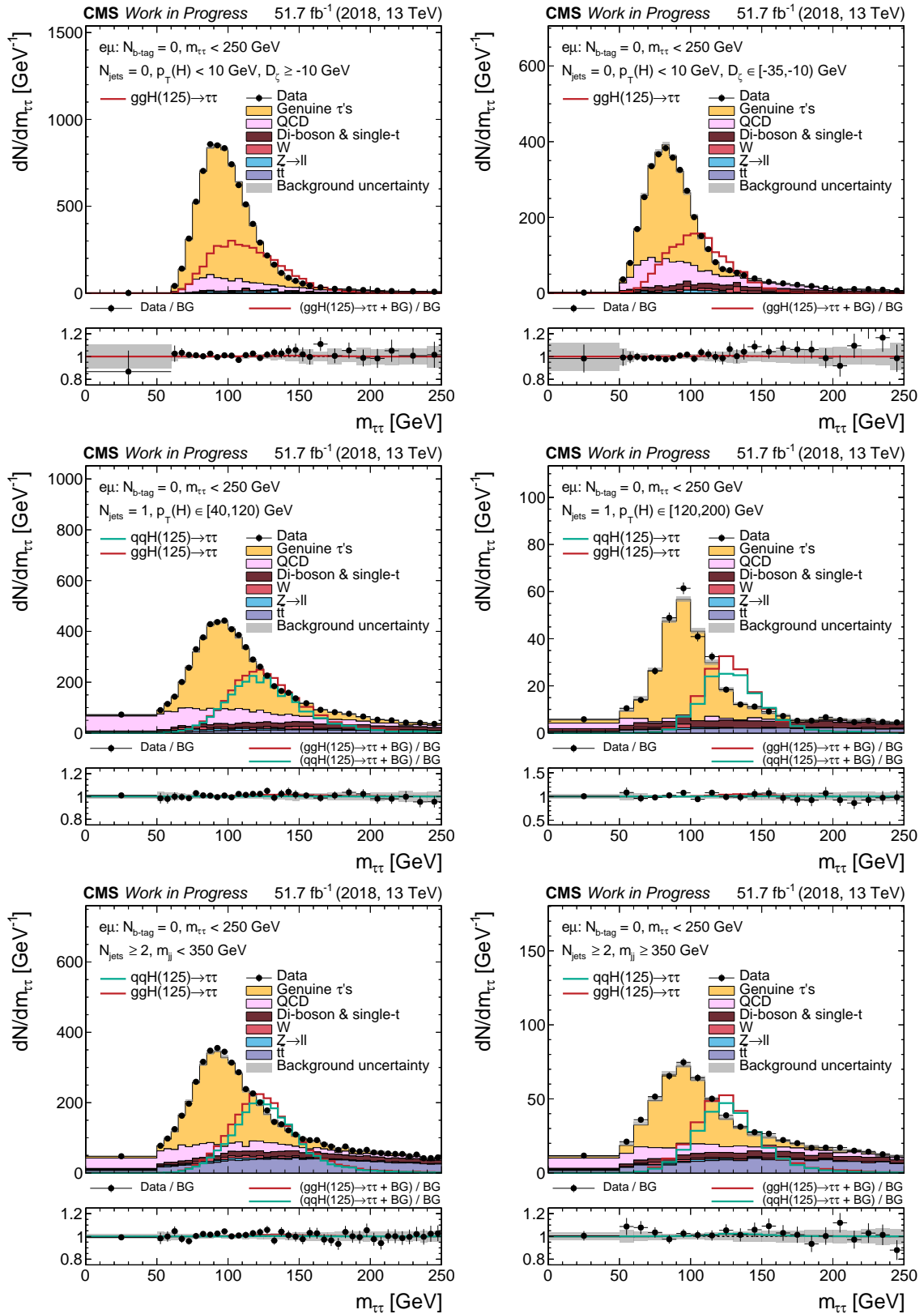
Figure 5.9.: Distributions of $m_{\tau\tau}$ for eμ in six selected categories of data-taking in 2018. Expected SM H $\to \tau\tau$ signal, rescaled for shape comparison in the upper panels, is shown with data and stacked background (BG). Grey uncertainty bands illustrate the total BG uncertainty after a maximum likelihood fit for μ. In the lower panel, SM H $\to \tau\tau$ is scaled to SM expectation.
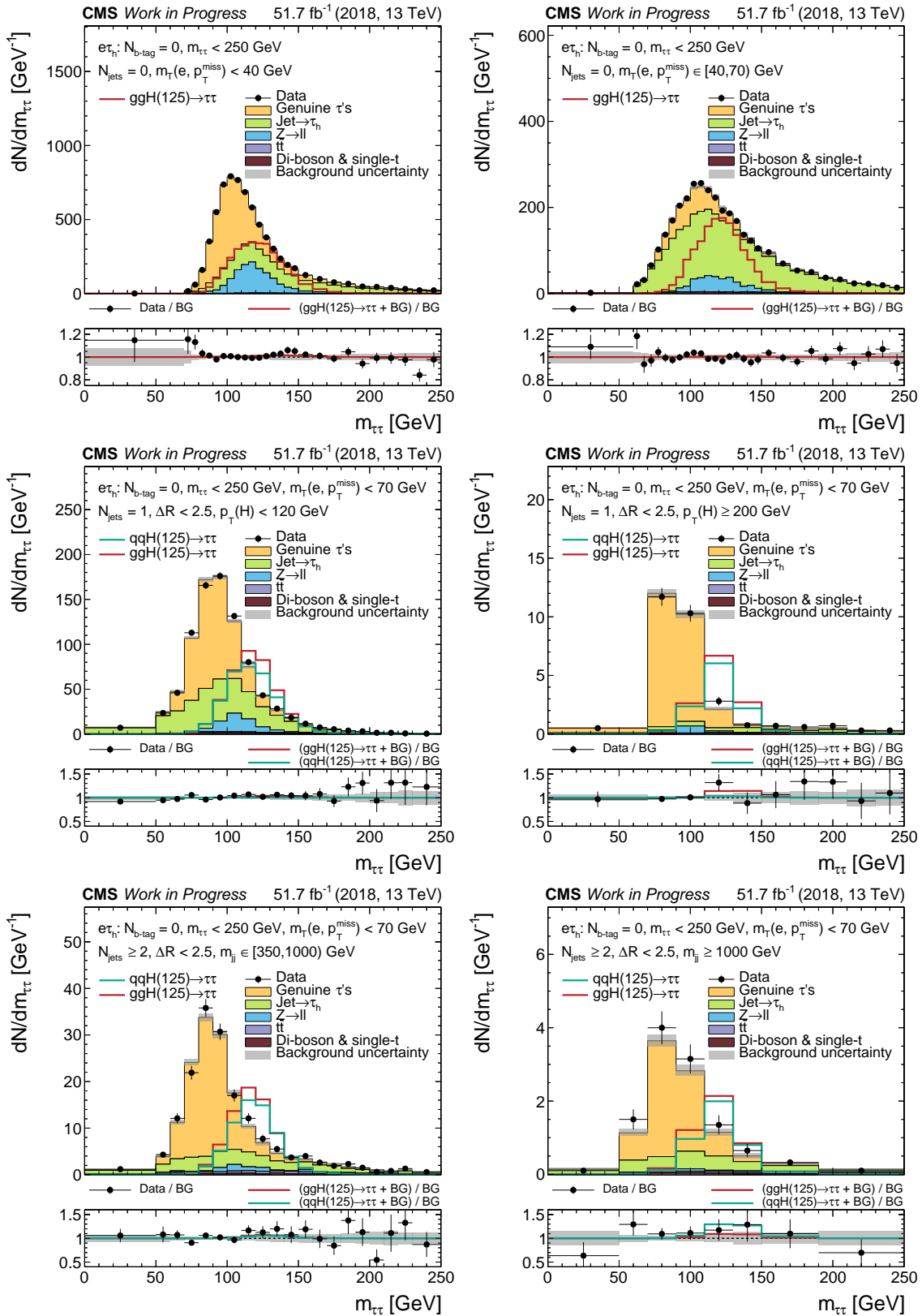
Figure 5.10.: Distributions of $m_{\tau\tau}$ for $e\tau_h$ in six selected categories of data-taking in 2018. Expected SM $H \to \tau\tau$ signal, rescaled for shape comparison in the upper panels, is shown with data and stacked background (BG). Grey uncertainty bands illustrate the total BG uncertainty after a maximum likelihood fit for μ. In the lower panel, SM $H \to \tau\tau$ is scaled to SM expectation.
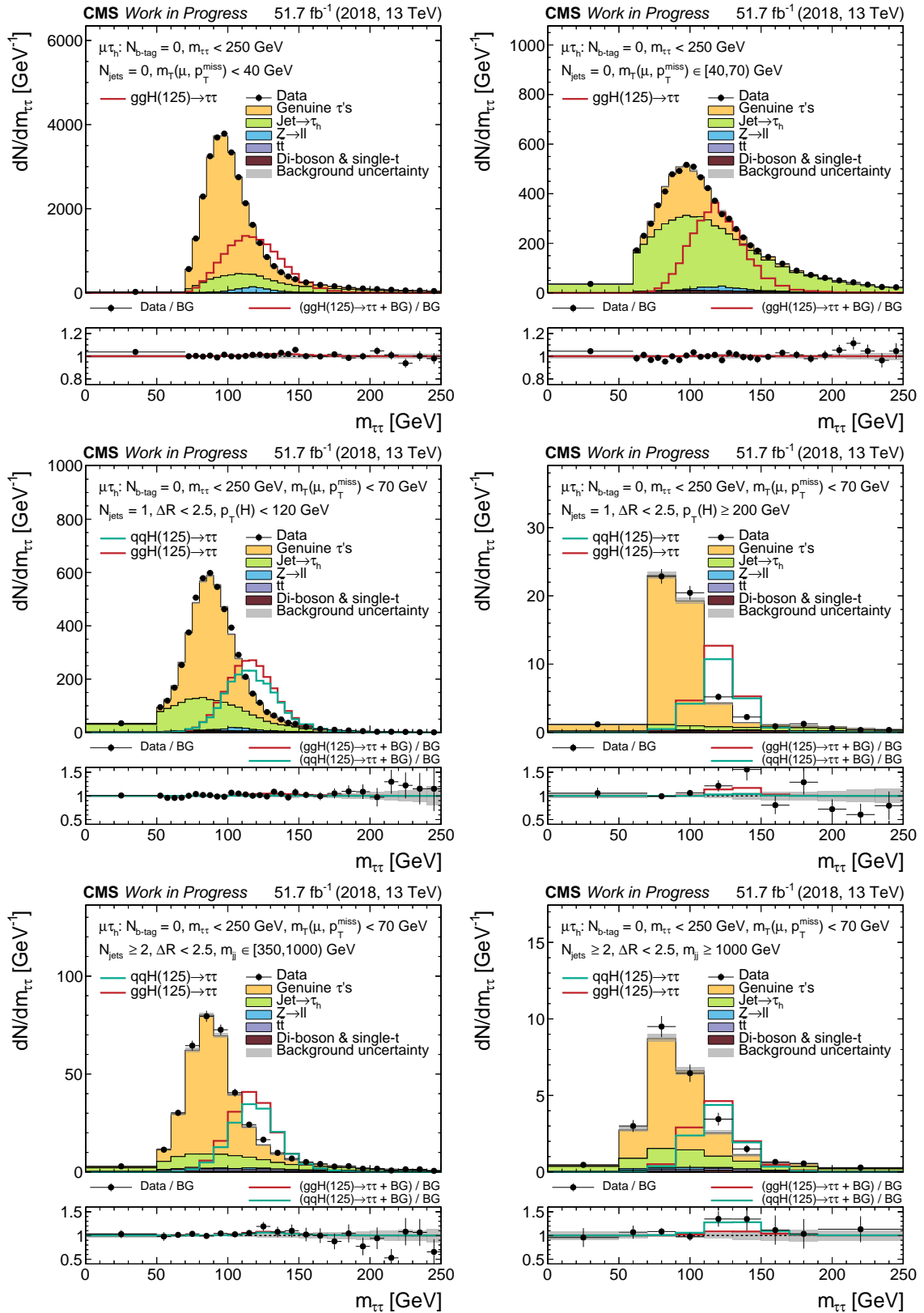
Figure 5.11.: Distributions of $m_{\tau\tau}$ for $\mu\tau_h$ in six selected categories of data-taking in 2018. Expected SM $H \to \tau\tau$ signal, rescaled for shape comparison in the upper panels, is shown with data and stacked background (BG). Grey uncertainty bands illustrate the total BG uncertainty after a maximum likelihood fit for μ. In the lower panel, SM $H \to \tau\tau$ is scaled to SM expectation.
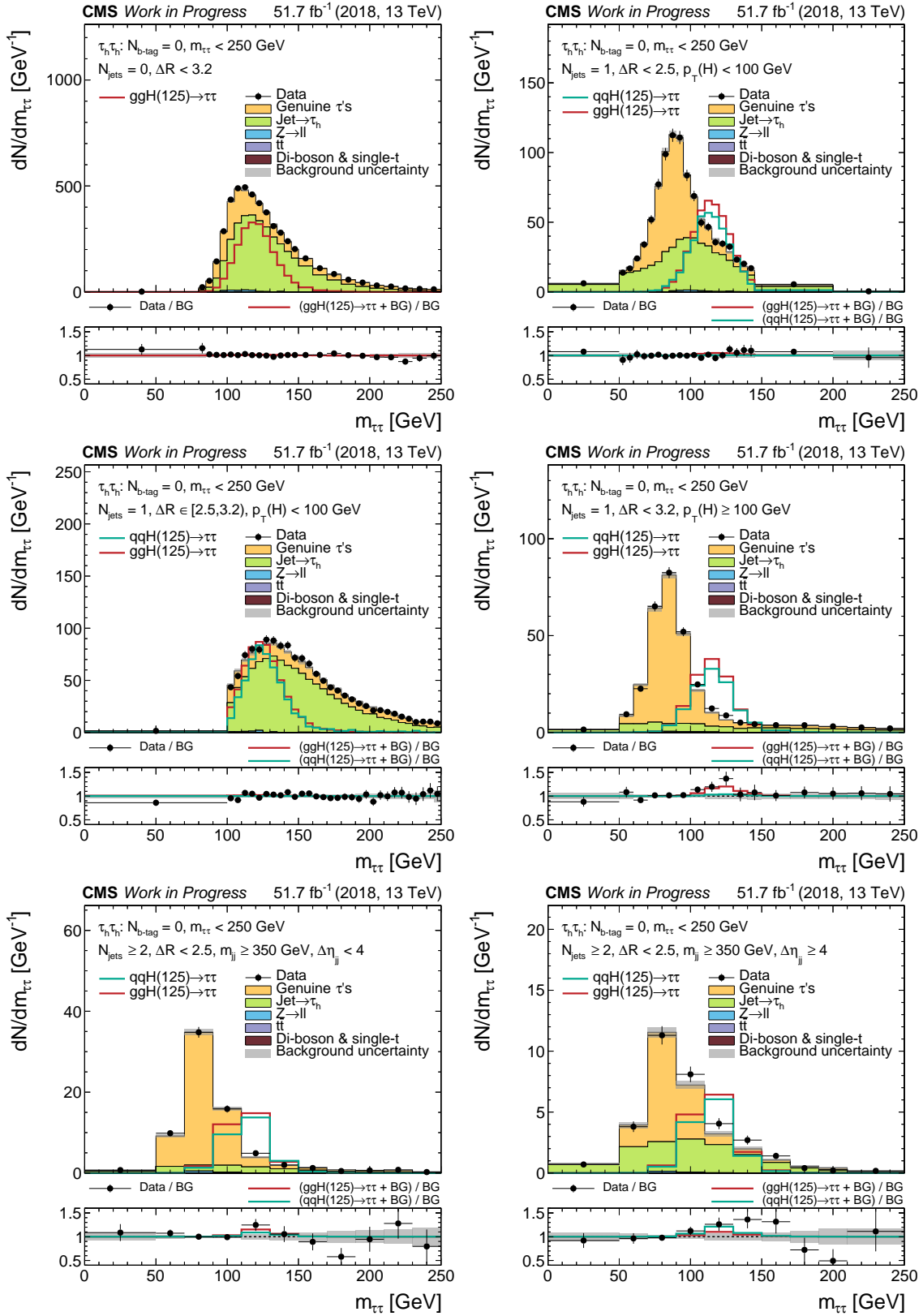
Figure 5.12.: Distributions of $m_{\tau\tau}$ for $\tau_h\tau_h$ in six selected categories of data-taking in 2018. Expected SM $H \rightarrow \tau\tau$ signal, rescaled for shape comparison in the upper panels, is shown with data and stacked background (BG). Grey uncertainty bands illustrate the total BG uncertainty after a maximum likelihood fit for μ. In the lower panel, SM $H \rightarrow \tau\tau$ is scaled to SM expectation.

Results for signal strengths μ, μ_{ggH} and μ_{qqH} are shown in figure 5.13. These comprise the constraints and corresponding scans of the likelihood ratios for all signal strengths, and in addition, significances Z for μ_{ggH} and μ_{qqH} in multiples of a standard deviation σ, as well as the correlation ρ between these two parameters of interest. In case of the analysis with two signals, ggH and qqH, one of the signal strength parameters is always free floating, while the other parameter is scanned. In that way, the freely floating parameter takes its best estimate value for a given fixed value of the scanned parameter. The significances are evaluated in the same way, setting the signal strength parameter to be studied to 0, while the other one is floating. The correlation between μ_{ggH} and μ_{qqH} is computed from the second derivatives of the log-likelihood ratio with respect to these two parameters.

$$Z_{ggH} = 6.1(5.0)\sigma$$

$$Z_{qqH} = 1.9(3.8)\sigma$$

$$\rho(ggH, qqH) = -40(42)\%$$
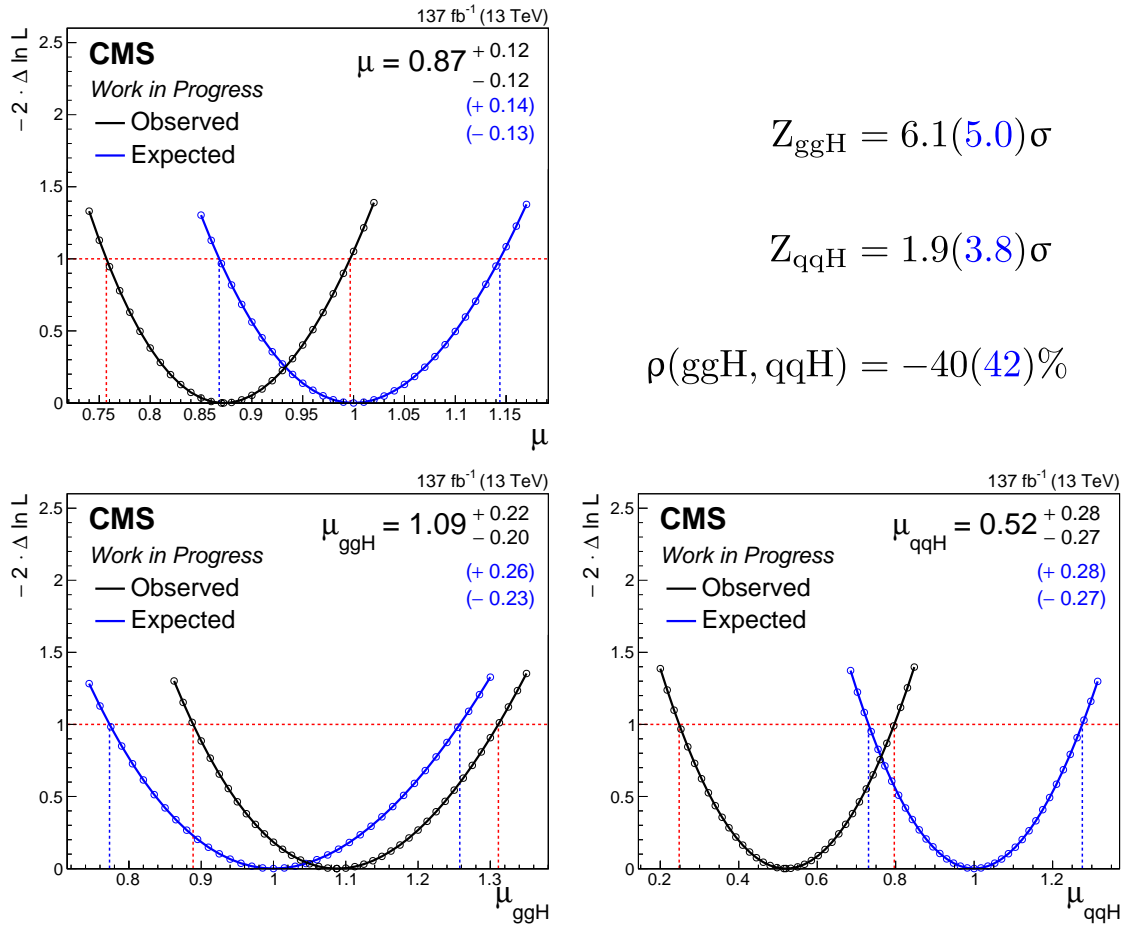
Figure 5.13.: Observed (expected) results of the SM $H \rightarrow \tau\tau$ measurement on the full Run 2 data. The log-likelihood scans of signal strength parameters μ, μ_{ggH} and μ_{qqH} shown as black (blue) curves in the figures at the top left and bottom are checked for a crossing with 1, indicated by the dashed lines. The crossings are projected onto the axis of the signal strength parameter to obtain the signal strength constraints given at the top right corner of each figure. The observed (expected) significances Z_{ggH} and Z_{qqH}, as well as the correlation $\rho(ggH, qqH)$, are given at the top right in black (blue).

The obtained results of the SM $H \rightarrow \tau\tau$ measurement on the full Run 2 data demonstrate, that a high sensitivity to the two main Higgs boson production modes, μ_{ggH} and μ_{qqH},

can be achieved with a proper categorization, allowing to test the effective couplings to gluons, τ leptons and electroweak vector bosons. Provided with such a high sensitivity, the contribution of a light scalar Higgs boson at about 125 GeV should be taken consistently into account to exploit the full potential of the $H \to \tau\tau$ analysis for BSM interpretations in form of benchmark scenarios [43, 44].

The observed results are consistent with the SM expectation, within 1σ for μ and μ_{ggH}, and within 2σ for μ_{qqH}. The smooth course of the observed and expected log-likelihood scans point to a stable and converging statistical inference of the presented analysis.

5.2. Classic BSM H $\to \tau\tau$ analysis

The following BSM search for Higgs bosons in $\tau\tau$ final states is inspired by the $H \to \tau\tau$ search on the 2016 data published by CMS [19]. The categorization of the signal regions introduced at the beginning of chapter 5 is performed using three quantities: $N_{b\text{-}tag}$, $m_T(e/\mu, p_T^{miss})$ in the $\mu\tau_h$ and $e\tau_h$ final states, and D_ζ in the $e\mu$ final state. The main categorization is performed based on $N_{b\text{-}tag}$ to define categories enriched with the signal from b-associated production. An additional, more final state specific categorization is applied to each of the $\mu\tau_h$, $e\tau_h$ and $e\mu$ final states. The requirements used for categorization are visualized in figure 5.14 for the $\mu\tau_h$ and $e\tau_h$ (blue), the $\tau_h\tau_h$ (red), and the $e\mu$ (green) final states in a similar way as shown before in figures 5.5, 5.6, and 5.7.
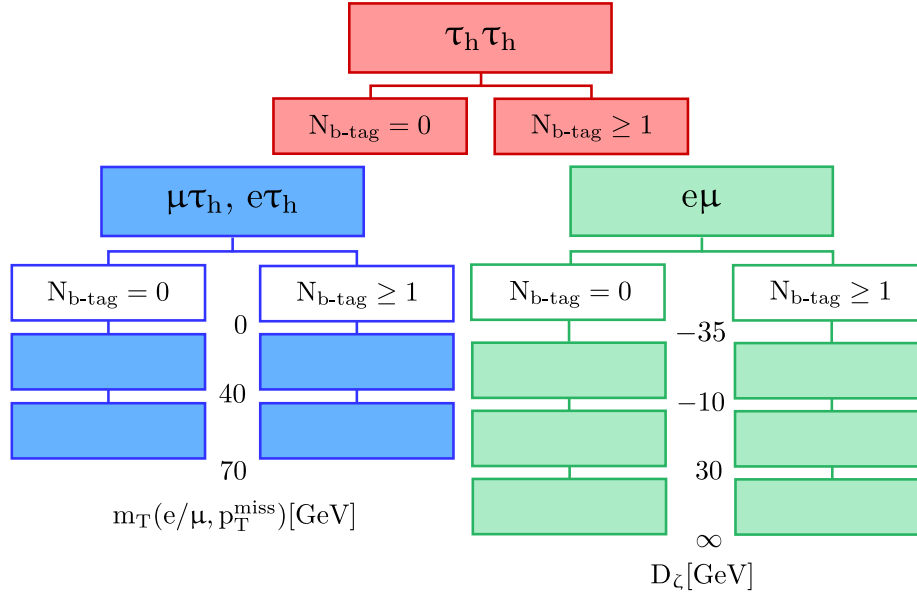
Figure 5.14.: Categorization applied to the signal regions of the BSM search for Higgs bosons in the $\tau\tau$ final states. Details are given in the text.

The discriminator chosen for the BSM search is the total transverse mass computed for the visible $\tau\tau$ pair $\tau_1\tau_2 \in \{\mu\tau_h, e\tau_h, \tau_h\tau_h, e\mu\}$, defined as follows:

$$m_T^{tot} = \sqrt{m_T^2(\tau_1, p_T^{miss}) + m_T^2(\tau_2, p_T^{miss}) + m_T^2(\tau_1, \tau_2)} \tag{5.7}$$

Thereby, the transverse mass defined in equation 5.2 is used to compute the individual parts of m_T^{tot}. This variable is well suited for the search for heavy Higgs bosons in particular

because of small tails of its distribution at high mass values, despite the fact, that its resolution at low mass values is weaker than for $m_{\tau\tau}$. A comparison of the two discriminators is given in figure 5.15.
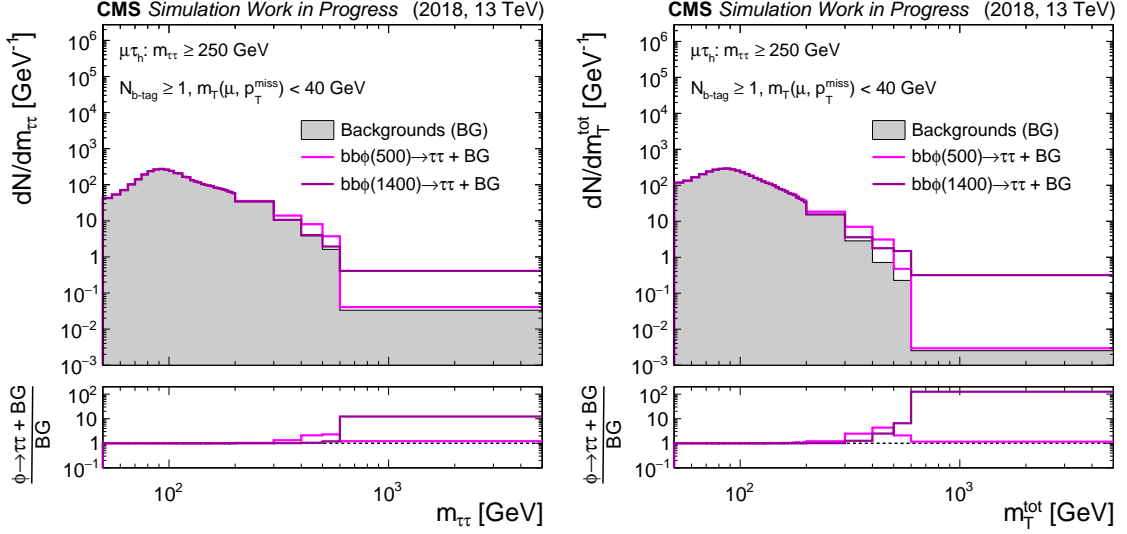
Figure 5.15.: Distributions of the discriminators $m_{\tau\tau}$ and m_T^{tot} in a category used in the BSM high mass search, enriched by events with b-tagged jets. The m_T^{tot} distribution has smaller high mass tails, allowing for a better discrimination of heavy Higgs boson signals from the background.

In addition to the uncertainties introduced in tables 5.1, 5.2, 5.3 and 5.4, the BSM samples of the b-associated production are equipped with mass-dependent normalization uncertainties which are anti-correlated between the categories with at least one b-tagged jet and the categories without a b-tagged jet. If predictions for the cross-sections and the branching fractions from a BSM model are provided, then additional normalization uncertainties are included [43, 44]. In case of gluon fusion production, QCD scale and p.d.f. + α_s uncertainties are used. For b-associated production, a single uncertainty is used to account for all theoretical variations of the prediction.

Results of the BSM search are presented in form of upper limits on the yield for a model-independent search of a single resonance, and in form of exclusion contours in the $(m_A, \tan\beta)$ parameter plane of the M_h^{125} scenario [43], which serves as a proxy for several specific BSM scenarios with a THDM inspired Higgs sector.

Both representations of the results are obtained with the CL_s method [167–169]. For this purpose, the p-values of two hypotheses are computed, p_μ for the hypothesis to be tested and p_0 for the reference hypothesis for a given test statistic q_μ, assuming different distributions of q_μ for each of the hypotheses. The CL_s value is then defined as the ratio of the two p-values, compared with a fixed confidence level $1 - \alpha = 95\%$. A yield prediction or parameter point is excluded, if the CL_s value falls below α:

$$CL_s = \frac{p_\mu}{p_0} = \frac{\int_{q_\mu^{obs}}^{\infty} f(q_\mu|\mu)dq_\mu}{\int_{q_\mu^{obs}}^{\infty} f(q_\mu|0)dq_\mu} \leq \alpha = 0.05$$

To examine the sensitivity of an analysis, the CL_s value is computed for the quantiles from the expected distribution of the test statistic assuming the reference hypothesis. The

median quantile coincides with the most probable value of the test statistic, if the reference hypothesis would be true. The other four quantile values are correspond to the 68% and 95% confidence intervals around the median. For a better understanding and interpretation of the corresponding CL_s values, an illustrative example will be discussed in the following, based on Gaussian distributions with different parameters, shown in figure 5.16.
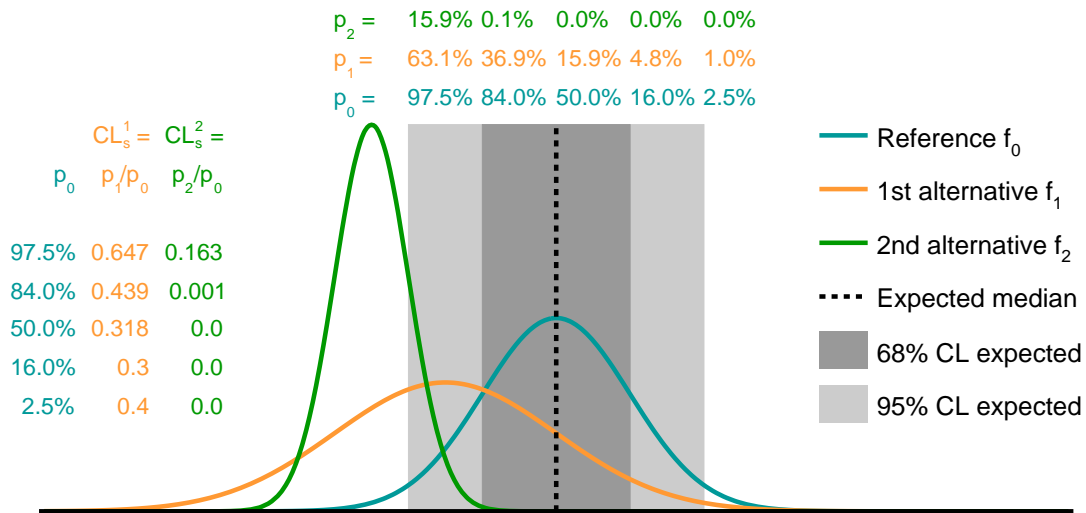
Figure 5.16.: Illustrative example of the CL_s method based on Gaussian distributions of a test statistic, assuming a reference hypothesis f_0, and two alternative hypotheses, one with a broader Gaussian distribution f_1, and another one with a narrower Gaussian distribution f_2.

Assuming that the distributions of the test statistic are known, the quantiles can be directly obtained from the distribution of the reference hypothesis f_0 with known p-values, shown in figure 5.16. Then, these quantiles can be used to integrate over the distributions of the alternative hypotheses to obtain the corresponding p-values, given for the first alternative hypothesis based on f_1, and for the second alternative hypothesis based on f_2.

After comparing the resulting CL_s values with the 0.05 threshold, it can be concluded, that the first alternative hypothesis can not be excluded by any of the five quantiles, while the second hypothesis is excluded by all quantiles but the one corresponding to $p_0 = 97.5\%$. Assuming, that the alternative hypotheses f_1 and f_2 correspond to fixed values of a parameter of interest $\mu = 1$ and $\mu = 2$, the smaller value of the parameter is expected to be outside of each exclusion contour, while the larger value of the parameter is expected to lie between the exclusion contours corresponding to $p_0 = 97.5\%$ and $p_0 = 84\%$.

The CL_s values for the different expected quantiles can be interpreted as a measure, how well the alternative hypotheses can be distinguished from the reference hypothesis, and because of that, also as a measure for the sensitivity of the given analysis.

A specific feature of the CL_s value is, that the exclusion of the alternative hypothesis depends on the ability to model the data by the reference hypothesis. In case of a bad description leading to a low value of p_0, the CL_s value is increased, so that the alternative may not be excluded despite of a low p-value. This effect can be observed for the 1st alternative hypothesis in the illustrative example, if comparing p_1 with CL_s^1.

The reference hypothesis of the model-independent BSM search for a single Higgs boson

is chosen to be the background expectation together with the SM Higgs boson signal. In this case, the log-likelihood ratio of equation 5.4 is used in a modified version

$$q_\mu = -2 \cdot \ln \left(\frac{L(n|\mu \cdot s_{BSM}(\hat{\hat{\theta}}_\mu) + s_{SM}(\hat{\hat{\theta}}_\mu) + b(\hat{\hat{\theta}}_\mu))}{L(n|\hat{\mu} \cdot s_{BSM}(\hat{\theta}) + s_{SM}(\hat{\theta}) + b(\hat{\theta}))} \right),$$ (5.8)

which allows again to use asymptotic formulae for the computation of the upper limits [166].

Two production processes are used to model the model-independent contribution of a Higgs boson like resonance ϕ: b-associated production and gluon fusion assuming coupling factors ζ_ϕ^t and ζ_ϕ^b as predicted by the SM for a given mass m_ϕ. Each of the two signal contributions is scaled to a yield corresponding to a product of the cross-section and branching fraction of 1 pb. In that way, upper limits on the two signal strengths $\mu_{gg\phi}$ and $\mu_{bb\phi}$ are given in pb, so that they can be interpreted as upper limits on the product of the cross-section and branching fraction, $\sigma(\phi) \cdot BR(\phi \rightarrow \tau\tau)$.

To compute these limits, one of the signal strengths is considered as the main parameter of interest, which is scanned to reach a CL_s of 0.05, while the other one is left floating to obtain its best estimate value for a given value of the main parameter.

The distributions of the discriminating variable m_T^{tot} are shown in figures 5.17, 5.18, 5.19, and 5.20 for the BSM categories of the eμ, eτ_h, $\mu\tau_h$, and $\tau_h\tau_h$ final states. Distributions of the BSM Higgs boson resonances at a mass of 500 GeV produced via gluon fusion (ggϕ) or in association with bottom quarks (bbϕ) with $\sigma \cdot BR = 1$ pb are added on top of the total background and compared to data. The lower panels of the figures show always the summed expectation of signal and background, and data, both divided by the total background. Background uncertainties correspond to the quadratic sum of statistical and systematic uncertainties after performing a maximum likelihood fit for the signal strengths $\mu_{gg\phi}$ and $\mu_{bb\phi}$. Comparing the expectation consisting of the signals at $m_\phi = 500$ GeV scaled to $\sigma \cdot BR = 1$ pb and background with data, it can be concluded, that data is compatible with background within the uncertainties, and the signal with $\sigma \cdot BR = 1$ pb is expected to be excluded.

The eμ final state has the smallest sensitivity to the BSM signal, mostly from the categories with $N_{b\text{-tag}} = 0$, whereas in categories with $N_{b\text{-tag}} \geq 1$, the signal is suppressed by the large contribution from the t$\bar{t}$ background. Higher sensitivity is given in the eτ_h and $\mu\tau_h$ final states, shared equally between ggϕ and bbϕ in categories with $N_{b\text{-tag}} = 0$, and with an increased amount of bbϕ signal in categories with $N_{b\text{-tag}} > 0$. Thereby, the sensitivity is mainly driven by categories with $m_T(e/\mu, p_T^{miss}) < 40$ GeV, whereas the other two categories are supposed to collect the remaining signal. The $\tau_h\tau_h$ final state has the best sensitivity, shared between the ggϕ and bbϕ equally in the category with $N_{b\text{-tag}} = 0$, while for $N_{b\text{-tag}} \geq 1$, bbϕ is the main signal.
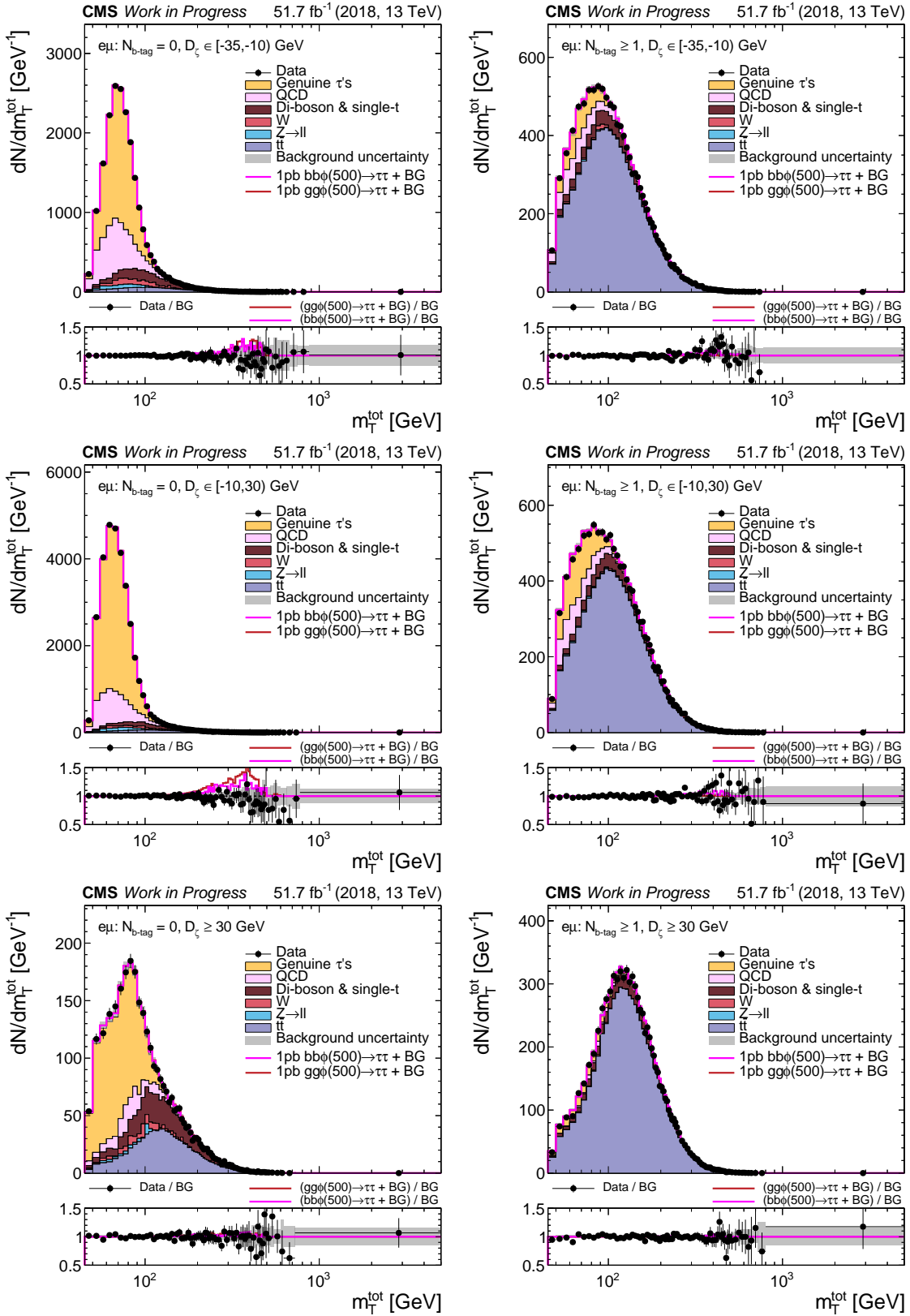
Figure 5.17.: Distributions of m_T^{tot} for eμ in BSM categories of data-taking in 2018. Stacked expected background (BG) and BSM signals ggφ and bbφ with $m_\phi = 500$ GeV and $\sigma \cdot BR = 1$ pb on top of BG are compared with data. Grey uncertainty bands illustrate the total BG uncertainty after a maximum likelihood fit for $\mu_{gg\phi}$ and $\mu_{bb\phi}$. In the lower panels, the ratio to BG is shown.
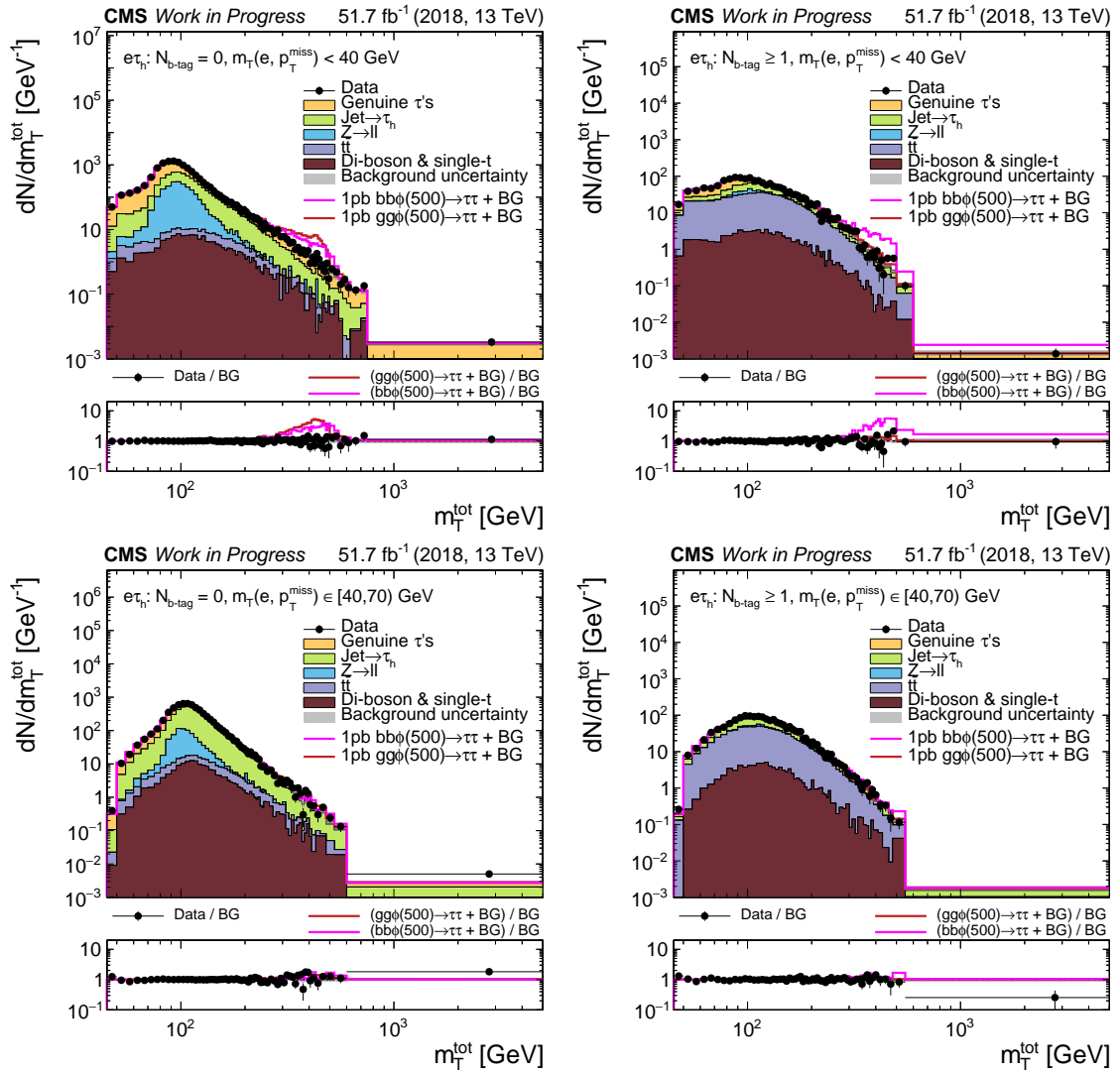
Figure 5.18.: Distributions of m_T^{tot} for $e\tau_h$ in BSM categories of data-taking in 2018. Stacked expected background (BG) and BSM signals $gg\phi$ and $bb\phi$ with $m_\phi = 500$ GeV and $\sigma \cdot BR = 1$ pb on top of BG are compared with data. Grey uncertainty bands illustrate the total BG uncertainty after a maximum likelihood fit for $\mu_{gg\phi}$ and $\mu_{bb\phi}$. In the lower panels, the ratio to BG is shown.
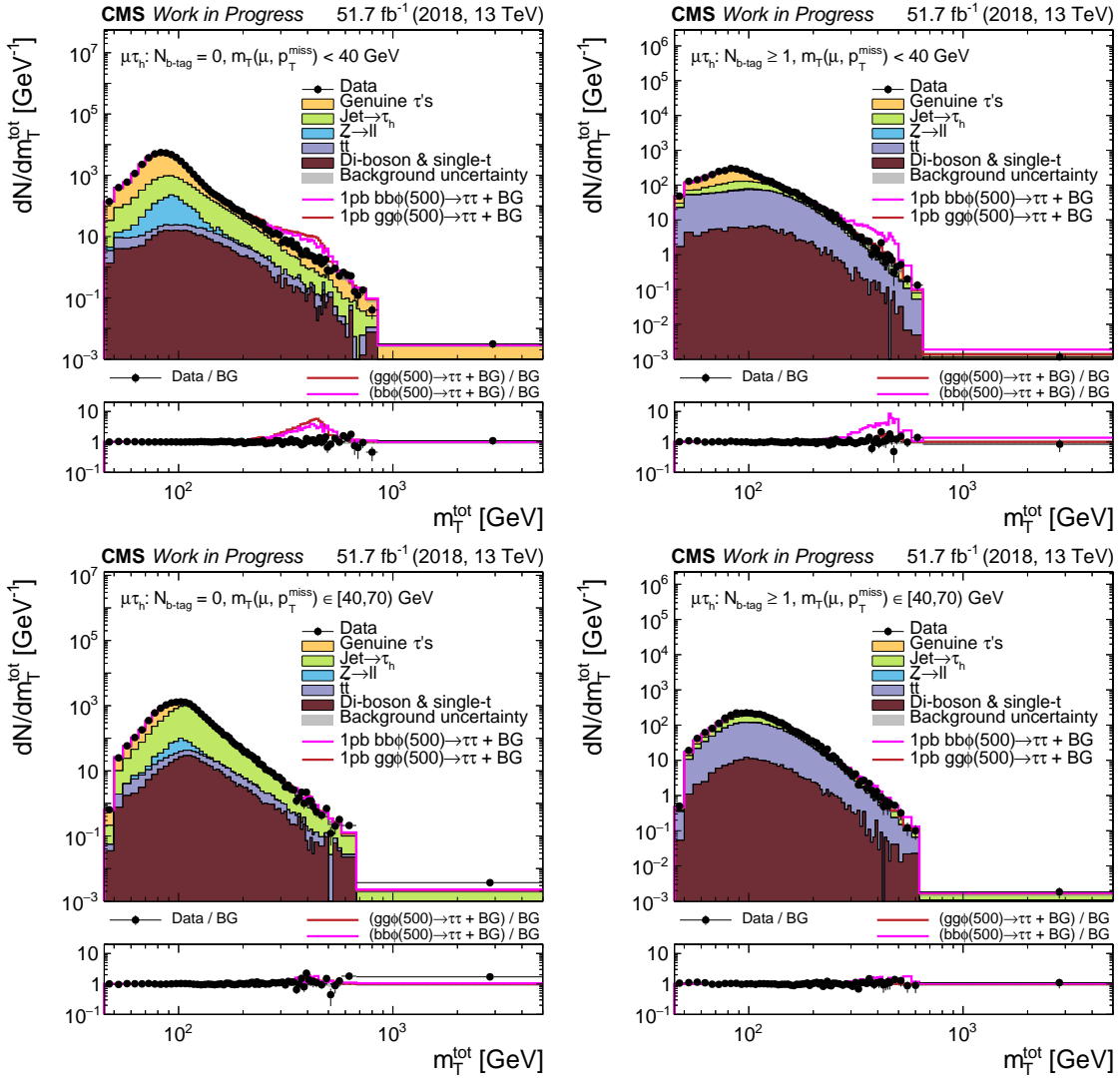
Figure 5.19.: Distributions of m_T^{tot} for $\mu\tau_h$ in BSM categories of data-taking in 2018. Stacked expected background (BG) and BSM signals $gg\phi$ and $bb\phi$ with $m_\phi = 500$ GeV and $\sigma \cdot BR = 1$ pb on top of BG are compared with data. Grey uncertainty bands illustrate the total BG uncertainty after a maximum likelihood fit for $\mu_{gg\phi}$ and $\mu_{bb\phi}$. In the lower panels, the ratio to BG is shown.
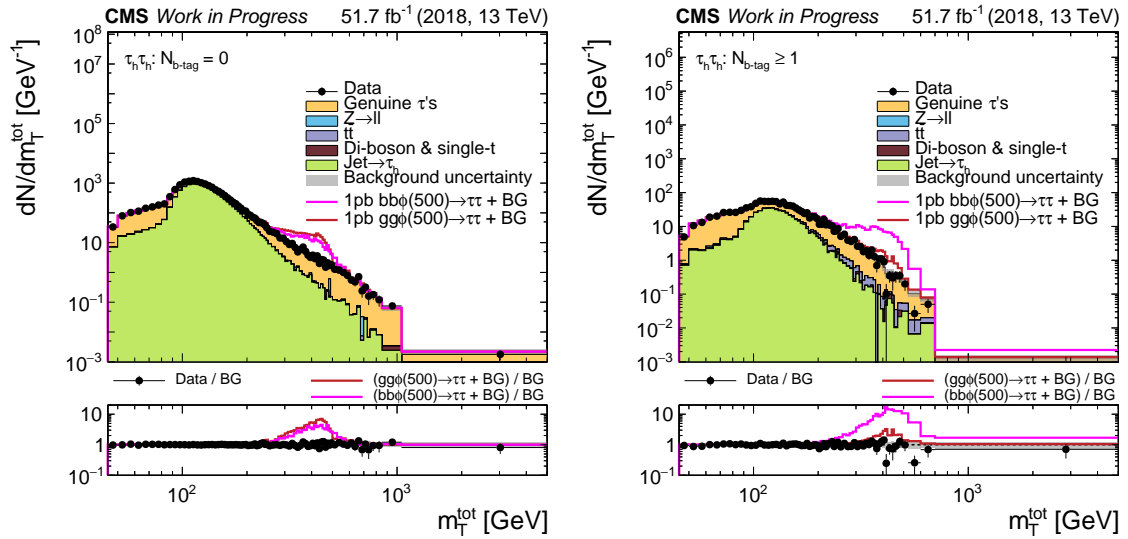
Figure 5.20.: Distributions of m_T^{tot} for $\tau_h\tau_h$ in BSM categories of data-taking in 2018. Stacked expected background (BG) and BSM signals $gg\phi$ and $bb\phi$ with $m_\phi = 500$ GeV and $\sigma \cdot BR = 1$ pb on top of BG are compared with data. Grey uncertainty bands illustrate the total BG uncertainty after a maximum likelihood fit for $\mu_{gg\phi}$ and $\mu_{bb\phi}$. In the lower panels, the ratio to BG is shown.

In figure 5.21, results for the upper limits on $\sigma \cdot BR$ are shown for (left) $gg\phi$ and (right) $bb\phi$ in a mass range $m_\phi \in [110, 3200]$ GeV. At the top, the results are restricted to the 2016 dataset to compare to the expected limits from the CMS publication on the same dataset [19]. At the bottom, the result on the full Run 2 dataset is shown, compared with the corresponding expectation from the ATLAS experiment [170]. The comparison for the 2016 dataset at the top of the figure reveals, that several improvements to the analysis have been made since the CMS publication, including

- a more efficient identification of electrons and τ_h candidates,
- a more efficient b-tagging method,
- the usage of a $\vec{p}_T^{\,miss}$ definition with a better resolution,
- the switch to the τ embedding method to estimate backgrounds from genuine τ pairs,
- improved corrections on the jet energy scale and resolution,
- and a more accurate uncertainty model.

These improvements can explain the stronger expected limits obtained on the same dataset for masses up to $m_\phi \approx 1600$ GeV.

Compared to the results from the ATLAS experiment, the obtained expected upper limits are computed in a wider mass range and are stronger in the mass region $m_\phi \in [110, 700]$ GeV, and consistent with the expected upper limits from ATLAS for higher mass values, where the shape information of the discriminator chosen for statistical inference plays a minor role.

Green and yellow filled bands represent the 68% and 95% expected confidence bands, which are determined with the procedure illustrated with figure 5.16. They can be interpreted as uncertainties on the expected median limit.

Observed upper limits are compatible with the SM expectation within 3σ standard deviations, with a few mass points sligly beyond the 95% confidence intervals, which corresponds to 2σ fluctuations from the SM hypothesis. Observed limits stronger than the expected by more than 2σ point to residual mismodelling in the background model in the relevant region of m_T^{tot}. In consequence, the excess of about 2σ for ggφ at masses $m_\phi \in [600, 1000]$ GeV in the limits for entire Run 2 data can be explained by such a mismodelling.
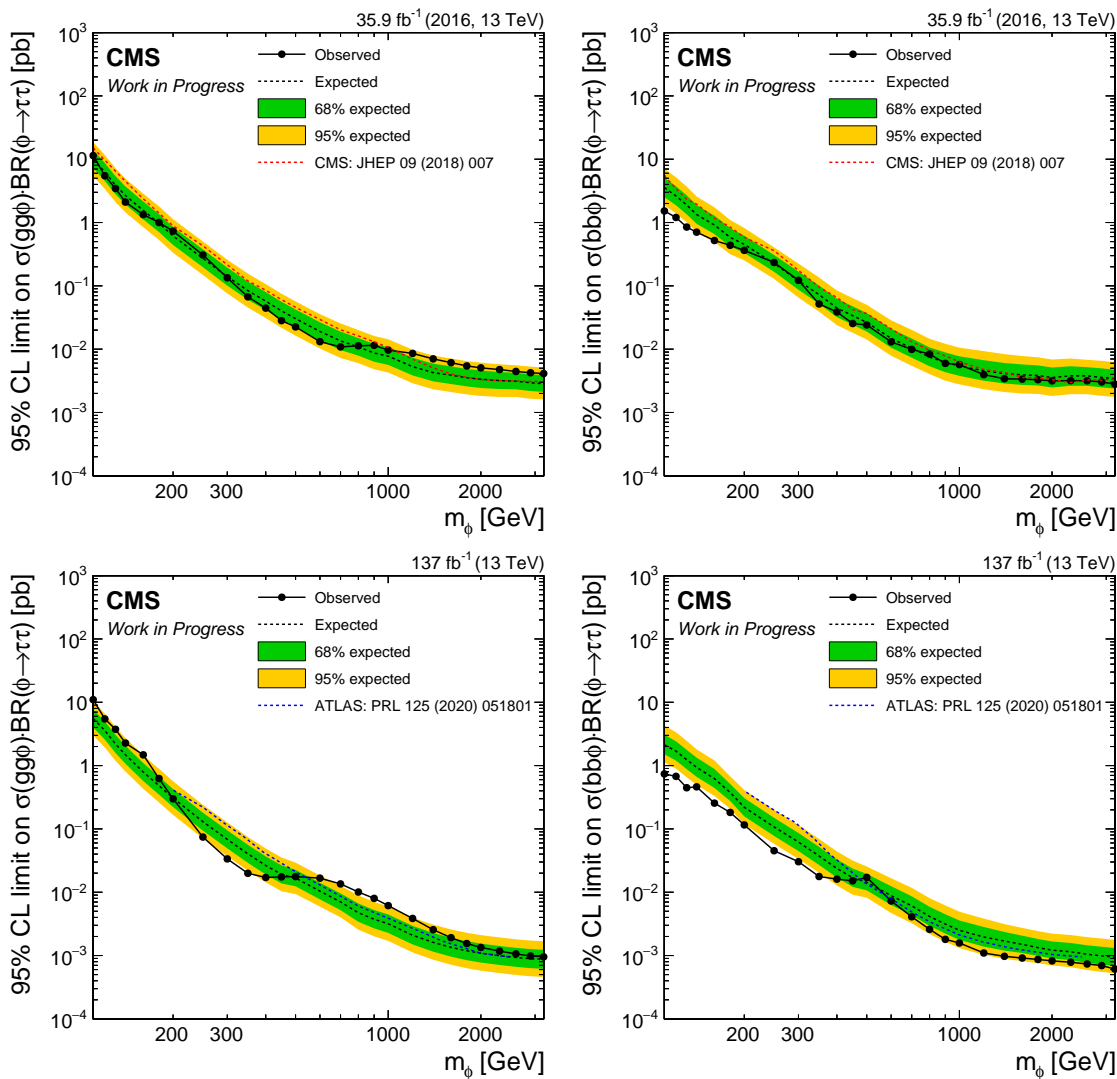
Figure 5.21.: Model-independent upper limits at 95% confidence level on (left) gluon fusion and (right) b-associated production σ · BR of a Higgs boson φ with mass m_ϕ for (top) 2016 data and (bottom) the entire Run 2 data. The black dashed line represents the median of the expected upper limit, while the green and yellow bands show the 68% and 95% confidence intervals for a given value of m_ϕ. Black dots connected with black solid lines correspond to observed limits. Expected results from (red) CMS [19] and (blue) ATLAS [170] are shown as dashed lines for comparison.

For model-dependent exclusion limits on the M_h^{125} scenario [43], the test statistic depends on the signal model used for the statistical inference. Two setups are used to model the signal:

- only heavy Higgs bosons: $H, A \rightarrow \tau\tau$
- full signal spectrum: $h, H, A \rightarrow \tau\tau$

For the first setup, the BSM definition of the test statistic q_μ in equation 5.8 can be directly used to calculate the CL_s value, so that for $\mu > 0$ the contribution from the BSM model is added on top of the SM expectation and for $\mu = 0$, all BSM contributions vanish. In case of the second setup exploiting the full signal spectrum of the BSM scenario M_h^{125}, one of the Higgs bosons, usually the light scalar h, is expected to be compatible with the SM expectation. Consequently, the SM expectation is replaced by the prediction from the BSM model, so that a redefinition of the likelihood is implied:

$$L(\mu) = L(n|\mu \cdot s_{BSM}(\theta) + (1 - \mu) \cdot s_{SM}(\theta) + b(\theta))$$

With this likelihood definition, the test statistic with the log-likelihood ratio q_μ from equation 5.8 becomes ill-defined, since the global best estimate in the denominator of the ratio is allowed to take values of μ different from 1 or 0, leading to a mixture of the Higgs boson expected from the SM with the light scalar h of the BSM model. To avoid this, a new test statistic $q_{(B)SM}$ is defined, which can then be transformed into a difference of two log-likelihood ratios q_1 and q_0 with the likelihood definition from above:

$$
\begin{aligned}
q_{(B)SM} &= -2 \cdot \ln\left(\frac{L(n|s_{BSM}(\hat{\theta}_1) + b(\hat{\theta}_1))}{L(n|s_{SM}(\hat{\theta}_0) + b(\hat{\theta}_0))}\right) \\
&= -2 \cdot \ln\left(\frac{L(n|s_{BSM}(\hat{\theta}_1) + b(\hat{\theta}_1)) \cdot L(n|\hat{\mu} \cdot s_{BSM}(\hat{\theta}) + (1 - \hat{\mu}) \cdot s_{SM}(\hat{\theta}) + b(\hat{\theta}))}{L(n|s_{SM}(\hat{\theta}_0) + b(\hat{\theta}_0)) \cdot L(n|\hat{\mu} \cdot s_{BSM}(\hat{\theta}) + (1 - \hat{\mu}) \cdot s_{SM}(\hat{\theta}) + b(\hat{\theta}))}\right) \\
&= -2 \cdot \ln\left(\frac{L(n|s_{BSM}(\hat{\theta}_1) + b(\hat{\theta}_1))}{L(n|\hat{\mu} \cdot s_{BSM}(\hat{\theta}) + (1 - \hat{\mu}) \cdot s_{SM}(\hat{\theta}) + b(\hat{\theta}))}\right) \\
&\quad + 2 \cdot \ln\left(\frac{L(n|s_{SM}(\hat{\theta}_0) + b(\hat{\theta}_0))}{L(n|\hat{\mu} \cdot s_{BSM}(\hat{\theta}) + (1 - \hat{\mu}) \cdot s_{SM}(\hat{\theta}) + b(\hat{\theta}))}\right) \\
&= q_1 - q_0
\end{aligned}
\tag{5.9}
$$

This adapted test statistic allows on one hand to test two signal hypotheses against each other, which have overlapping predictions, and on the other hand, its distribution can be estimated by asymptotic formulae, as it is the case for the log-likelihood ratio q_μ, since $q_{(B)SM}$ is related to it.

The resulting exclusion contours for M_h^{125} benchmark scenario in the $(m_A, \tan\beta)$ parameter space are shown in figure 5.22 for parameter values $m_A \in [110, 2600]$ GeV and $\tan\beta \in [2, 60]$.

On the left, a signal composition with only the heavy Higgs bosons H and A is used. The confidence level bands are small with respect to variations in m_A or in $\tan\beta$, which both change the yield and shape of the signal contributions from the heavy Higgs bosons H and A. Because of a similar BSM signal modelling, these expected results can be compared

with results from the ATLAS experiment [170]. The analysis presented in this thesis is competitive with the results from ATLAS, as can be concluded from figure 5.22 (left). However, it must be taken into account, that the additional uncertainties on the cross-section and branching fraction predictions provided with the M_h^{125} benchmark scenario are treated differently in the ATLAS analysis [171], such that the comparison done for model-independent results shown in figure 5.21 (bottom) can not be translated directly into the comparison shown in figure 5.22 (left).

Exclusion contours for the setup with the full Higgs boson spectrum are shown on the right of figure 5.22. Due to the low sensitivity to the light scalar Higgs boson h, the results are similar to the ones on the left of figure 5.22. An additional comparison with expected limits from the CMS publication for 2016 data [19] is shown for this setup. The results of this thesis in figure 5.22 (right) based on full Run 2 data allow to exclude the entire considered parameter space below $m_A \lesssim 350$ GeV, and to push the expected exclusion contour towards higher values of m_A.

Observed CL_s limits in both setups are consistent with the SM expectation. The excess for $m_A \in [600, 1000]$ GeV expected from model-independent results for ggϕ shown in figure 5.21 (bottom left) is within the 95% confidence band, corresponding in this case to a fluctuation of less than 2σ. This can be partly explained by the introduction of model-dependent uncertainties on the cross-section and branching fraction predictions, which are not available in the model-independent case. Furthermore, the dominant contribution for the parameter point $(m_A, \tan\beta) = (700$ GeV$, 8)$ is from the b-associated production, being greater than gluon fusion by 1.2 for A and 2.9 for H in the M_h^{125} scenario.
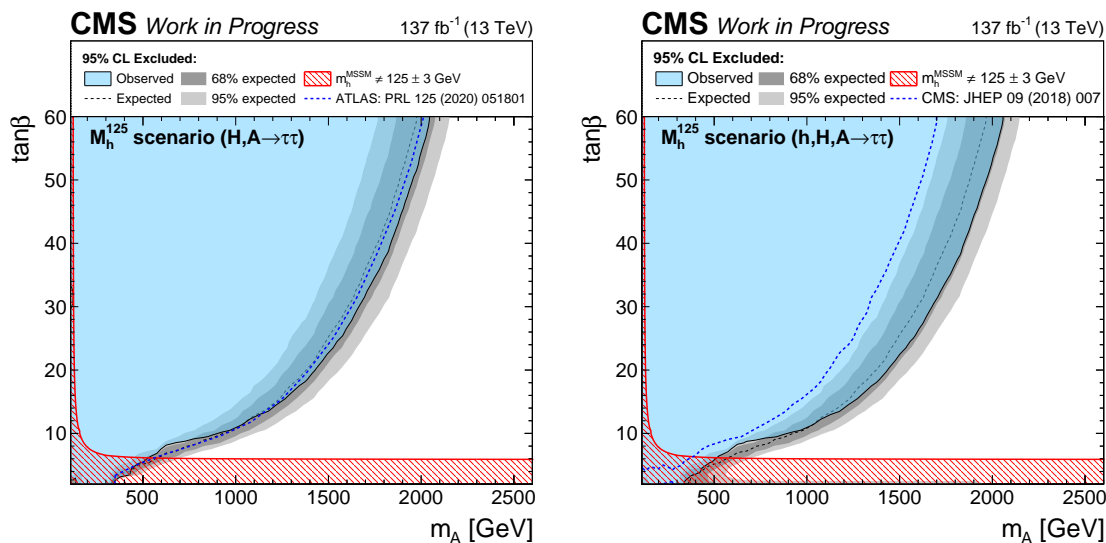
Figure 5.22.: CL_s exclusion contours in $(m_A, \tan\beta)$ for M_h^{125} using the classic BSM categorization for the signal regions of all $\tau\tau$ final states. On the left, only the heavy Higgs bosons are used in the signal model, whereas on the right, the full Higgs spectrum is tested, including the light scalar Higgs boson h. The filled area corresponds to the parameter space excluded by observed CL_s limits, the dashed black line to the median expected exclusion contour, and the grey shaded bands to the 68% and 95% confidence intervals. The median expected results are compared with expected exclusion contours from (left) ATLAS [170], and (right) CMS [19], shown as dashed blue lines.

An additional test of the sensitivity to the light scalar Higgs boson is performed by changing the yield of the ggh and qqh MSSM contributions by $\pm 10\%$. The impact of this change is illustrated by signal distributions of m_T^{tot} expected for the SM and for the MSSM, which are obtained from a weighted sum over the distributions of m_T^{tot} in each category. The weight is computed per category as the ratio between SM signal yield expectation and the sum of the SM signal yield with the total background yield, $h_{SM}/(h_{SM} + BG)$. It is used to reweight both the SM and the MSSM expectation in each category. The MSSM parameters are chosen to be $m_A = 1500$ GeV and $\tan \beta = 15$ to reduce the nominal yield difference between the expectations from MSSM and SM, as can be seen in figure 2.2 for (top left) the gluon fusion cross-section and (top right) $h \to \tau\tau$ branching fraction.

The resulting signal distributions for the MSSM expectation of ggh and qqh compared with respect to the corresponding SM expectation are shown in figure 5.23 on the left, together with the corresponding expected exclusion contours on the right. At the top of figure 5.23, the nominal expectation from the M_h^{125} scenario is shown, corresponding to the results in figure 5.22 on the right. In the middle of figure 5.23 the $+10\%$ variation of the MSSM signal yield is illustrated, at the bottom of figure 5.23, the -10% variation.

As discussed in subsection 4.2.2, the MSSM predictions for ggh and qqh are constructed from the distribution of the SM prediction for the Higgs boson at 125 GeV, reweighted to $\sigma \cdot BR$ predicted by the M_h^{125} scenario. This is done to avoid possible differences in the properties of the Higgs boson resulting from different software used to simulate the process. In consequence, the approximated prediction for ggh and qqh always corresponds to a mass of 125 GeV, which does not hold for the region in the $(m_A, \tan \beta)$ parameter space marked with the red hashed contour with $m_h \neq 125 \pm 3$ GeV.

Despite the strong deviation of the manually varied signal yield expected from the MSSM, the expected CL_s exclusion contours do not change significantly in the parameter space with $m_h = 125 \pm 3$ GeV. This is expected, since the analysis presented in this section is mainly designed for a search for heavy Higgs boson resonances. In the following section 5.3, it will be shown, how the sensitivity to yield changes of the light scalar Higgs boson can be increased by combining the BSM and SM inspired categories.
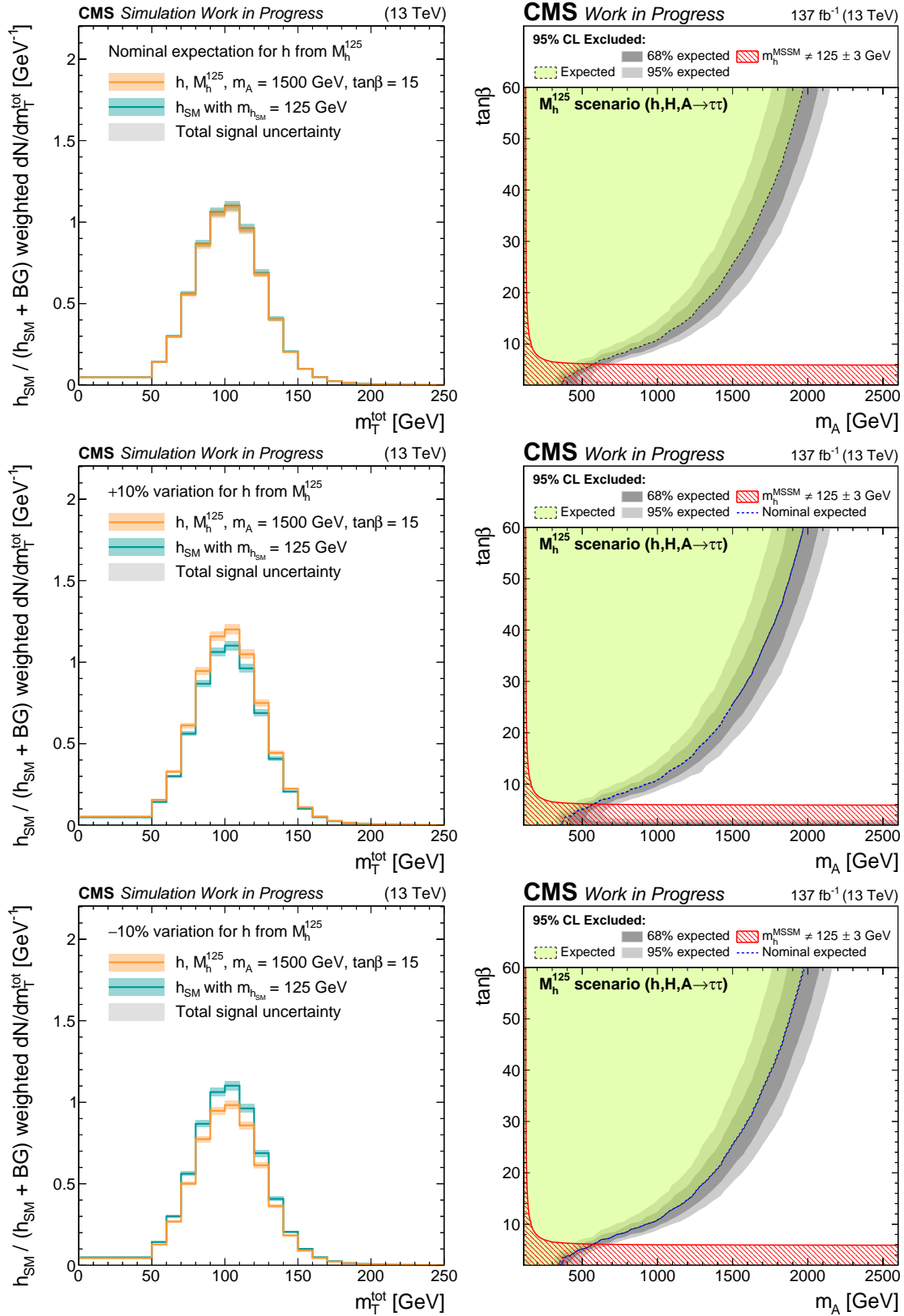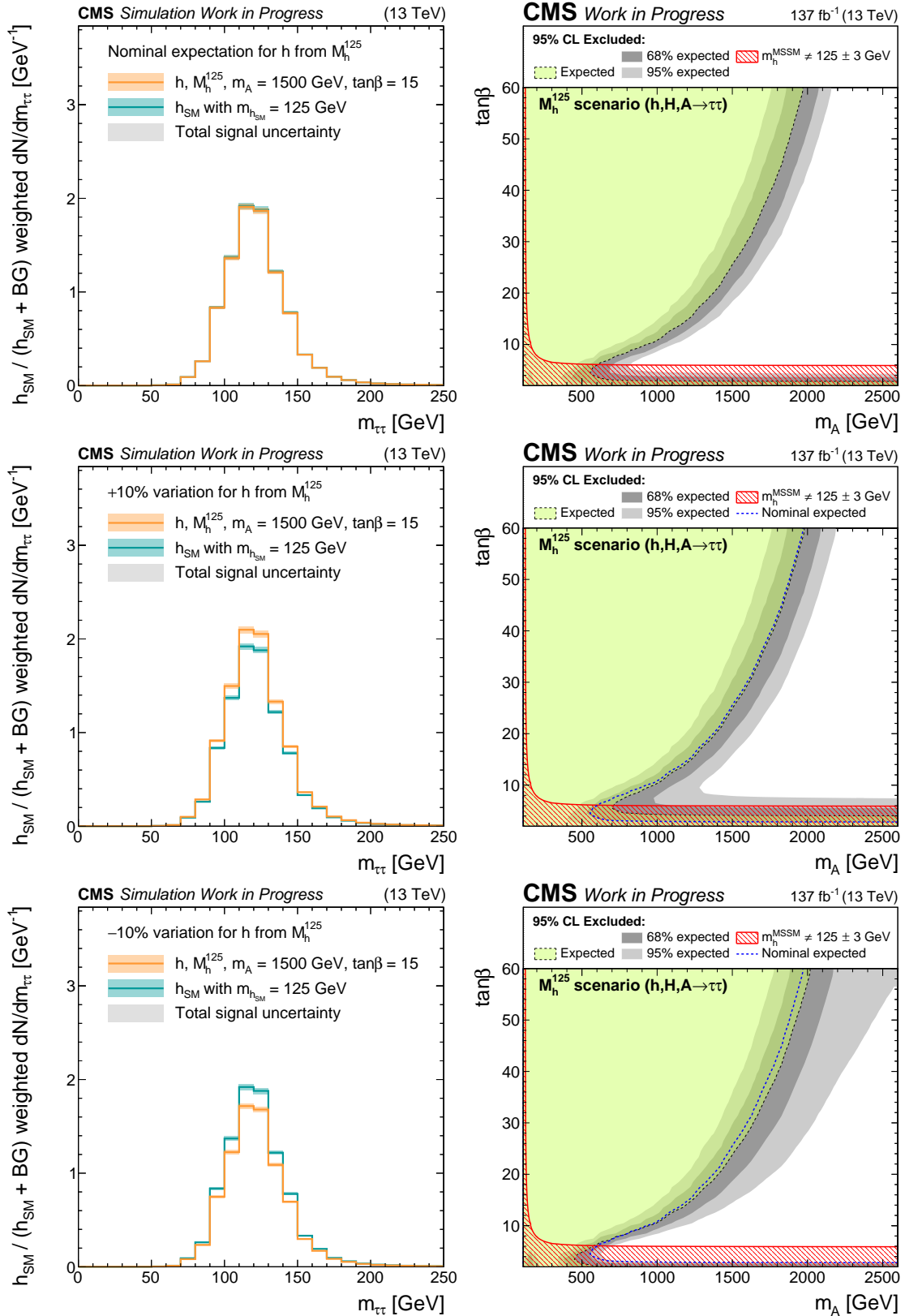
Figure 5.23.: Illustration of the impact of yield changes in the signal distributions (left) on the CL$_s$ exclusion contours of the M_h^{125} scenario (right), using the H $\rightarrow \tau\tau$ analysis with BSM categorization. The nominal MSSM yield for ggh and qqh (top) is changed by (middle) +10% and (bottom) −10%. Details are given in the text.

5.3. BSM H $\rightarrow \tau\tau$ analysis including SM categories

To include the SM categories into the BSM analysis, the signal regions of all $\tau\tau$ final states are divided into three parts, based on $N_{\text{b-tag}}$ and $m_{\tau\tau}$. The SM categories of section 5.1 are left unchanged, so that for events with $N_{\text{b-tag}} = 0$, a high mass region is created by the requirement $m_{\tau\tau} \geq 250$ GeV, where the BSM categorization from section 5.2 is applied. The BSM categories for events with $N_{\text{b-tag}} \geq 1$ remain unchanged.

The signal modelling is chosen dependent on the categorization to simplify the technical setup for the statistical inference. For the SM categories, where the contributions from ggh and qqh are most relevant, only these signals are used in the signal model. The high mass region with $N_{\text{b-tag}} = 0$ is expected to be most sensitive to the heavy Higgs bosons H, A in the ggϕ and bbϕ production modes. The $N_{\text{b-tag}} \geq 1$ region, as well as the three control regions, are equipped with the full signal model of the three neutral Higgs bosons. This simplification has the consequence, that the sensitivity to the heavy Higgs bosons H and A with $m_H, m_A \lesssim 200$ GeV is reduced, since they would also contribute to the total signal yield in the SM categories. On the other hand, the sensitivity of the SM categories is expected to be driven by the ggh and qqh processes, so this simplification is considered justified. The signal assignment to the categories is summarized in table 5.5.

	Categorization	Signal ggh, qqh	H, A	bbh
$N_{\text{b-tag}} = 0$, $m_{\tau\tau} < 250$ GeV	(SM)	✓	✗	✗
$N_{\text{b-tag}} = 0$, $m_{\tau\tau} \geq 250$ GeV	(BSM)	✗	✓	✗
$N_{\text{b-tag}} \geq 1$	(BSM)	✓	✓	✓
	Control regions	✓	✓	✓

Table 5.5.: Assignment of BSM signals to the SM and BSM categories.

In figures 5.24 and 5.25, m_T^{tot} distributions from BSM categories with $N_{\text{b-tag}} = 0$ are shown, which were additionally required to contain only events, that fulfill $m_{\tau\tau} \geq 250$ GeV, to be able to include the SM categories into the analysis. The difference with respect to the corresponding categories without the requirement on $m_{\tau\tau}$ from section 5.2 is visible for low m_T^{tot} values with reduced contributions from the background with genuine τ pairs and the Jet $\rightarrow \tau_h$ background.

The M_h^{125} prediction of the heavy Higgs boson resonances H and A for parameters $m_A = 700$ GeV and $\tan\beta = 30$ is shown in these distributions as signal. For this parameter point, the two heavy Higgs bosons are degenerate in mass and the MSSM cross-sections for the b-quark associated production and gluon fusion are modified by the high $\tan\beta$ value, such that the b-quark associated production is dominating:

$$\frac{\sigma_{\text{bbH}}}{\sigma_{\text{ggH}}} \approx 30 \qquad \frac{\sigma_{\text{bbA}}}{\sigma_{\text{ggA}}} \approx 17$$

$$\text{for } (m_A, \tan\beta) = (700 \text{ GeV}, 30) \text{ in } M_h^{125}$$

In consequence, a single Higgs boson resonance is expected as a reconstructed signature, resulting mostly from the b-quark associated production. This is verified by the figures showing categories sensitive to this signal.

Figure 5.24.: Distributions of m_T^{tot} in the BSM categories with $N_{b\text{-tag}} = 0$ and $m_{\tau\tau} \geq 250$ GeV of (top and bottom left) $e\mu$ and (bottom right) $\tau_h\tau_h$. The signal prediction of the M_h^{125} scenario at $(m_A, \tan\beta) = (700 \text{ GeV}, 30)$ for the heavy Higgs bosons H and A is shown as signal, resulting in a single mass degenerate resonance dominated by the b-quark associated production. The signal is added on top of the stacked background expectation and compared with data. Grey uncertainty bands illustrate the total BG uncertainty after a maximum likelihood fit performed for the fixed $(m_A, \tan\beta)$ values.

Figure 5.25.: Distributions of m_T^{tot} in the BSM categories with $N_{b\text{-}tag} = 0$ and $m_{\tau\tau} \geq 250$ GeV of (top) $e\tau_h$ and (bottom) $\mu\tau_h$. The signal prediction of the M_h^{125} scenario at $(m_A, \tan\beta) = (700\text{ GeV}, 30)$ for the heavy Higgs bosons H and A is shown as signal, resulting in a single mass degenerate resonance dominated by the b-quark associated production. The signal is added on top of the stacked background expectation and compared with data. Grey uncertainty bands illustrate the total BG uncertainty after a maximum likelihood fit performed for the fixed $(m_A, \tan\beta)$ values.
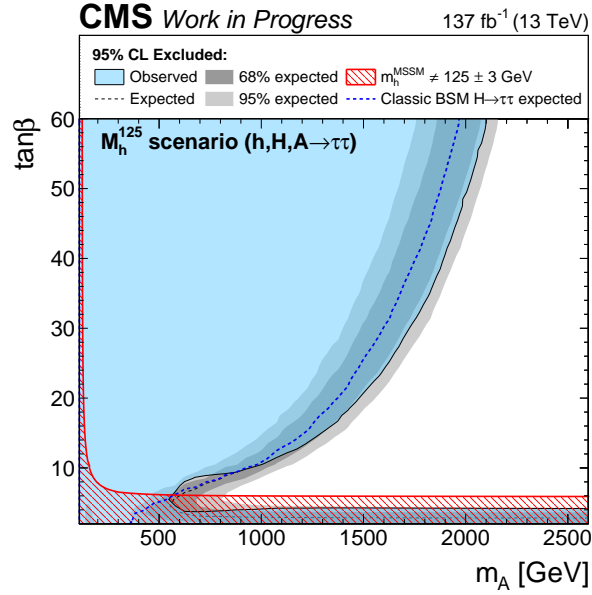
Figure 5.26.: CL_s exclusion contours in $(m_A, \tan\beta)$ for M_h^{125} using the categorization and signal composition given in table 5.5. The median expected results are compared with the expected exclusion contour for classic BSM categorization shown in figure 5.22 (right), shown as a dashed blue line.

Results for the model-dependent exclusion contours of the M_h^{125} scenario are shown in figure 5.26. Within the eligible parameter space satisfying the requirement $m_h \in [122, 128]$ GeV, these results are compatible with figure 5.22. These findings are consistent with the exclusion at the bottom right of figure 2.2 constructed from constraints on the coupling κ_τ, which are obtained from combined measurements of the properties of the observed Higgs boson at 125 GeV [12]. On the other hand, the exclusion is extended for low $\tan\beta$ values, for which the yield prediction from M_h^{125} deviates significantly from SM, in addition to the mass difference.

A similar test as illustrated by figure 5.23 is performed to demonstrate the increased sensitivity to $\pm 10\%$ changes in the yield of the MSSM expectation for ggh and qqh. The resulting signal distributions of $m_{\tau\tau}$ from the SM categories, which are illustrated for $m_A = 1500\,\text{GeV}$ and $\tan\beta = 15$, and the corresponding exclusion contours in the $(m_A, \tan\beta)$ parameter plane are shown in figure 5.27.

Due to the optimized categorization, the effective $h_{SM}/(h_{SM}+BG)$ weighted yield of the SM and MSSM signals is increased by $\approx 40\%$ with respect to the test performed in figure 5.23. In addition, the discriminator $m_{\tau\tau}$ allows to collect more events per bin than m_T^{tot} due to a better resolution for $m_{\tau\tau} \leq 250\,\text{GeV}$. In consequence, the changes of $\pm 10\%$ applied to the expected MSSM yield are more significant relative to the total signal uncertainty and increase the impact on the exclusion contours significantly.

This is best visible for the exclusion contours corresponding to quantiles with $p_0 = 16\%$ and $p_0 = 2.5\%$ of the 68% and 95% confidence bands. In case of the upward yield variation in figure 5.27 (middle), these contours are moved up for low $\tan\beta$, and to the right for the remaining values of $\tan\beta$. For the downward yield variation in figure 5.27 (bottom), both contours are moved even more to the right, such that the one corresponding to $p_0 = 2.5\%$ reaches the $(m_A, \tan\beta) = (2600\,\text{GeV}, 60)$ corner of the parameter space.

Figure 5.27.: Illustration of the impact of yield changes in the signal distributions (left) on the $\mathrm{CL_s}$ exclusion contours of the $\mathrm{M_h^{125}}$ scenario (right), using the BSM $H \to \tau\tau$ analysis with SM categories. The nominal MSSM yield for ggh and qqh (top) is changed by (middle) +10% and (bottom) −10%. Details are given in the text.

6. Conclusions

The scope of this thesis has been an ansatz for the global analysis of all $\tau\tau$ events measured by CMS, in the full range of the invariant $\tau\tau$ mass. This ansatz unifies dedicated measurements of the properties of the observed Higgs boson (h_{obs}) in the explicit Standard Model (SM) interpretation, with traditional robust searches for additional neutral heavy Higgs bosons in the $h, H, A \rightarrow \tau\tau$ decay channel in the context of the minimal supersymmetric extension of the SM (MSSM). The MSSM serves as a proxy for general two Higgs doublet (THDM) extensions of the SM Higgs sector. In the SM interpretation, the h_{obs} is associated with the SM Higgs boson (h_{SM}). In the MSSM interpretation, the h_{obs} is usually associated with the lightest neutral MSSM Higgs boson, h.

In consequence, two analyses and their combination have been presented and discussed throughout this thesis: A measurement of the stage-0 simplified template cross-sections (STXS) [144] for gluon fusion and vector boson fusion (VBF) in the SM interpretation, and a traditional search for additional neutral heavy Higgs bosons in the MSSM interpretation. Both analyses are based on the full LHC Run 2 dataset obtained from proton-proton collisions at a centre of mass energy of 13 TeV with an integrated luminosity of 137 fb^{-1}. The backgrounds to these analyses are obtained to up to 90% from data.

The presented work benefits from the experience gained with and synergies used across the following analysis projects pursued and brought to publication by the CMS collaboration, during this Ph.D.:

- the development of the τ embedding technique for the estimation of the most dominant background for analyses in $\tau\tau$ final states, the production of genuine $\tau\tau$ pairs from non-Higgs boson SM processes like $Z \rightarrow \tau\tau$ [122],
- the search for additional neutral Higgs bosons in the $\tau\tau$ final states [19],
- and the measurement of STXS of the observed Higgs boson in the $H \rightarrow \tau\tau$ decay channel in the SM interpretation [21].

Both analyses have been performed from front to end in the four most sensitive $\tau\tau$ final states $\tau_h\tau_h$, $\mu\tau_h$, $e\tau_h$, and $e\mu$. Auxiliary measurements, reconstruction and identification techniques, and the modelling of signal and background contributions to the $\tau\tau$ final states were studied in detail and brought to their state-of-the-art realization within the CMS collaboration.

The analyses presented throughout this thesis are meant to have blueprint character for future measurements of CMS. They are simpler than the individual measurements, which have been published, in a few aspects, focusing on the main goal of unification of the two approaches. Once this unified paradigm is established, the individual parts of the analysis may grow again in complexity.

Based on the full Run 2 dataset, the SM analysis presented in this thesis reaches an observed (expected) significance of 6.1(5.0)σ and 1.9(3.8)σ for each of the two corresponding dominant production modes, gluon fusion and VBF, in the SM interpretation. In conse-

quence, the resulting expected sensitivity is competitive with the currently published results from CMS, which are more sophisticated in their technique, but based on smaller datasets [20, 21].

The search for additional neutral heavy Higgs bosons in the $H \to \tau\tau$ decay channel shows a significant improvement with respect to the currently published expected results from CMS [19], and is competitive with the latest expected results from ATLAS [170].

Both analyses are combined to investigate the benefit of extending the search for heavy resonances with a measurement of properties of the presumed boson h, in the MSSM interpretation. For this purpose, the predictions of the main MSSM production modes gluon fusion and b-quark associated production were supplemented with the VBF prediction for the boson h for the very first time in the course of this thesis in close collaboration with the LHC Higgs Cross-Section Working Group (LHCHXSWG) and the theory department at KIT (ITP).

With the introduced global interpretation of $\tau\tau$ events, a highly discriminating role of the coupling of the boson h to τ leptons for variations within ±10% was demonstrated. In perspective of combined Run 2 and Run 3 datasets and with refined analysis techniques, this sensitivity can be brought to variations as small as ±2-3% and thus provide the strongest constraints on potential realization of supersymmetry.

The demonstration of such a global analysis in $\tau\tau$ final states can be extended by other final states with sensitivity to any of the bosons h, H or A. Such sophisticated analyses based on explicit benchmark models for physics beyond the SM will provide an important complement to the generic analyses of the coupling structure of the h_{obs} in form of effective field theories.

The first version of the presented analyses was handed in in a blind state according to CMS scientific rules. After the Ph.D. defense, it was agreed upon with the referees to prepare the analyses for unblinding and present them in front of CMS. The results in this final version of the dissertation were approved by convenors of the CMS collaboration in the context of a thesis approval. This thesis is anticipated to serve as the basis for the upcoming CMS search for additional neutral heavy Higgs bosons in the MSSM or general THDM models, planned for publication in 2021.

During the Run 3 of the LHC, several conceptional refinements have the potential to increase the outlined sensitivity of the presented $H \to \tau\tau$ analyses even further and beyond the bare increase in luminosity. In the following, only three examples will be given:

- The acceptance of the search for additional heavy Higgs bosons in the $\tau\tau$ final states can be significantly increased, if events are taken into account, which are selected with a trigger designed for boosted hadronic τ lepton decays [172]. The expected increase in sensitivity is of the order of 10 to 20%.
- A multivariate classification of $\tau\tau$ events based on neural networks [173] has proven to provide an increased sensitivity [21] to h_{obs}, with the possibility to decrease the number of categories. An extension of this approach to Higgs bosons with masses between 100 GeV and 4 TeV is in principle possible and could be revisited [174].
- Subtleties in the way the CMS detector alignment and calibration are currently mapped into the τ embedding method are currently the limiting factor in the precision of the method [124, 125, 127, 128]. Envisaged improvements at this end might well lead to control of this background at the level of 1-2% in the kinematic distributions, leading to an unprecedented level of precision of $\tau\tau$ analyses.

176

Bibliography

[1] J. C. Romão and J. P. Silva, "A Resource for Signs and Feynman Diagrams of the Standard Model", *Int. J. Mod. Phys. A* **27** (2012) 1230025, `doi:10.1142/S0217751X12300256`, `arXiv:1209.6213`.

[2] T. Aoyama, M. Hayakawa, T. Kinoshita, and M. Nio, "Tenth-Order QED Contribution to the Electron g-2 and an Improved Value of the Fine Structure Constant", *Phys. Rev. Lett.* **109** (2012) 111807, `doi:10.1103/PhysRevLett.109.111807`, `arXiv:1205.5368`.

[3] T. Aoyama, M. Hayakawa, T. Kinoshita, and M. Nio, "Tenth-Order Electron Anomalous Magnetic Moment — Contribution of Diagrams without Closed Lepton Loops", *Phys. Rev. D* **91** (2015), no. 3, 033006, `doi:10.1103/PhysRevD.91.033006`, `arXiv:1412.8284`, [Erratum: *Phys. Rev. D* **96** (2017) 019901, `doi:10.1103/PhysRevD.96.019901`].

[4] L. Di Lella and C. Rubbia, "The Discovery of the W and Z Particles", volume 23, pp. 137–163, 2015, `doi:10.1142/9789814644150\_0006`.

[5] Y.-B. Yang et al., "Proton Mass Decomposition from the QCD Energy Momentum Tensor", *Phys. Rev. Lett.* **121** (2018), no. 21, 212001, `doi:10.1103/PhysRevLett.121.212001`, `arXiv:1808.08677`.

[6] P. W. Higgs, "Broken Symmetries, Massless Particles and Gauge Fields", *Phys. Lett.* **12** (1964) 132–133, `doi:10.1016/0031-9163(64)91136-9`.

[7] P. W. Higgs, "Broken Symmetries and the Masses of Gauge Bosons", *Phys. Rev. Lett.* **13** (1964) 508–509, `doi:10.1103/PhysRevLett.13.508`.

[8] F. Englert and R. Brout, "Broken Symmetry and the Mass of Gauge Vector Mesons", *Phys. Rev. Lett.* **13** (1964) 321–323, `doi:10.1103/PhysRevLett.13.321`.

[9] ATLAS Collaboration, "Observation of a New Particle in the Search for the Standard Model Higgs Boson with the ATLAS Detector at the LHC", *Phys. Lett. B* **716** (2012) 1–29, `doi:10.1016/j.physletb.2012.08.020`, `arXiv:1207.7214`.

[10] CMS Collaboration, "Observation of a New Boson at a Mass of 125 GeV with the CMS Experiment at the LHC", *Phys. Lett. B* **716** (2012) 30–61, `doi:10.1016/j.physletb.2012.08.021`, `arXiv:1207.7235`.

[11] CMS Collaboration, "A Measurement of the Higgs Boson Mass in the Diphoton Decay Channel", *Phys. Lett. B* **805** (2020) 135425, `doi:10.1016/j.physletb.2020.135425`, `arXiv:2002.06398`.

[12] CMS Collaboration, "Combined Higgs Boson Production and Decay Measurements with up to 137 fb^{-1} of Proton-Proton Collision Data at $\sqrt{s}$ = 13 TeV", CMS-PAS-HIG-19-005.

[13] K. Freese, "Review of Observational Evidence for Dark Matter in the Universe and in Upcoming Searches for Dark Stars", *EAS Publ. Ser.* **36** (2009) 113–126, `doi:10.1051/eas/0936016`, `arXiv:0812.4005`.

[14] H. P. Nilles, "Supersymmetry, Supergravity and Particle Physics", *Phys. Rept.* **110** (1984) 1–162, `doi:10.1016/0370-1573(84)90008-5`.

[15] CMS Collaboration, "Search for Heavy Higgs Bosons Decaying to a Top Quark Pair in Proton-Proton Collisions at $\sqrt{s}$ = 13 TeV", *JHEP* **04** (2020) 171, `doi:10.1007/JHEP04(2020)171`, `arXiv:1908.01115`.

[16] CMS Collaboration, "Search for Beyond the Standard Model Higgs Bosons Decaying into a b$\bar{\text{b}}$ Pair in pp Collisions at $\sqrt{s}$ = 13 TeV", *JHEP* **08** (2018) 113, `doi:10.1007/JHEP08(2018)113`, `arXiv:1805.12191`.

[17] CMS Collaboration, "Search for a Heavy Higgs Boson Decaying to a Pair of W Bosons in Proton-Proton Collisions at $\sqrt{s}$ = 13 TeV", *JHEP* **03** (2020) 034, `doi:10.1007/JHEP03(2020)034`, `arXiv:1912.01594`.

[18] CMS Collaboration, "Search for MSSM Higgs Bosons Decaying to $\mu^+\mu^-$ in Proton-Proton Collisions at $\sqrt{s}$ = 13 TeV", *Phys. Lett. B* **798** (2019) 134992, `doi:10.1016/j.physletb.2019.134992`, `arXiv:1907.03152`.

[19] CMS Collaboration, "Search for Additional Neutral MSSM Higgs Bosons in the $\tau\tau$ Final State in Proton-Proton Collisions at $\sqrt{s}$ = 13 TeV", *JHEP* **09** (2018) 007, `doi:10.1007/JHEP09(2018)007`, `arXiv:1803.06553`.

[20] CMS Collaboration, "Observation of the Higgs Boson Decay to a Pair of τ Leptons with the CMS Detector", *Phys. Lett. B* **779** (2018) 283–316, `doi:10.1016/j.physletb.2018.02.004`, `arXiv:1708.00373`.

[21] CMS Collaboration, "Measurement of Higgs Boson Production and Decay to the $\tau\tau$ Final State", CMS-PAS-HIG-18-032.

[22] M. Cepeda et al., "Report from Working Group 2: Higgs Physics at the HL-LHC and HE-LHC", volume 7, pp. 221–584, 12, 2019, `arXiv:1902.00134`, `doi:10.23731/CYRM-2019-007.221`.

[23] R. Rivers, "Path Integral Methods in Quantum Field Theory", Cambridge Monographs on Mathematical Physics, Cambridge University Press, 1988, `doi:10.1017/CBO9780511564055`.

[24] S. Glashow, "Partial Symmetries of Weak Interactions", *Nucl. Phys.* **22** (1961) 579–588, `doi:10.1016/0029-5582(61)90469-2`.

[25] A. Salam and J. C. Ward, "Electromagnetic and Weak Interactions", *Phys. Lett.* **13** (1964) 168–171, `doi:10.1016/0031-9163(64)90711-5`.

[26] S. Weinberg, "A Model of Leptons", *Phys. Rev. Lett.* **19** (1967) 1264–1266, `doi:10.1103/PhysRevLett.19.1264`.

[27] N. Cabibbo, "Unitary Symmetry and Leptonic Decays", *Phys. Rev. Lett.* **10** (1963) 531–533, `doi:10.1103/PhysRevLett.10.531`.

[28] M. Kobayashi and T. Maskawa, "CP Violation in the Renormalizable Theory of Weak Interaction", *Prog. Theor. Phys.* **49** (1973) 652–657, `doi:10.1143/PTP.49.652`.

[29] M. Gonzalez-Garcia and Y. Nir, "Neutrino Masses and Mixing: Evidence and Implications", *Rev. Mod. Phys.* **75** (2003) 345–402, `doi:10.1103/RevModPhys.75.345`, `arXiv:hep-ph/0202058`.

[30] B. Pontecorvo, "Inverse Beta Processes and Nonconservation of Lepton Charge", *Sov. Phys. JETP* **7** (1958) 172–173, `http://jetp.ac.ru/cgi-bin/dn/e_007_01_0172.pdf`.

[31] Z. Maki, M. Nakagawa, and S. Sakata, "Remarks on the Unified Model of Elementary Particles", *Prog. Theor. Phys.* **28** (1962) 870–880, `doi:10.1143/PTP.28.870`.

[32] Particle Data Group Collaboration, "Review of Particle Physics", *Phys. Rev. D* **98** (2018), no. 3, 030001, `doi:10.1103/PhysRevD.98.030001`.

[33] H. Yukawa, "On the Interaction of Elementary Particles I", *Proc. Phys. Math. Soc. Jap.* **17** (1935) 48–57, `doi:10.1143/PTPS.1.1`.

[34] L. Faddeev and V. Popov, "Feynman Diagrams for the Yang-Mills Field", *Phys. Lett. B* **25** (1967) 29–30, `doi:10.1016/0370-2693(67)90067-6`.

[35] S. Weinberg, "Implications of Dynamical Symmetry Breaking", *Phys. Rev. D* **13** (1976) 974–996, `doi:10.1103/PhysRevD.13.974`, [Addendum: *Phys. Rev. D* **19** (1979) 1277–1280, `doi:10.1103/PhysRevD.19.1277`].

[36] S. P. Martin, "A Supersymmetry Primer", volume 21, pp. 1–153, 2010, `arXiv:hep-ph/9709356`, `doi:10.1142/9789814307505_0001`.

[37] Super-Kamiokande Collaboration, "Search for Proton Decay via $P \rightarrow e^+ \pi^0$ and $P \rightarrow \mu^+ \pi^0$ in a Large Water Cherenkov Detector", *Phys. Rev. Lett.* **102** (2009) 141801, `doi:10.1103/PhysRevLett.102.141801`, `arXiv:0903.0676`.

[38] L. Girardello and M. T. Grisaru, "Soft Breaking of Supersymmetry", *Nucl. Phys. B* **194** (1982) 65, `doi:10.1016/0550-3213(82)90512-0`.

[39] S. Ferrara, L. Girardello, and F. Palumbo, "A General Mass Formula in Broken Supersymmetry", *Phys. Rev. D* **20** (1979) 403, `doi:10.1103/PhysRevD.20.403`.

[40] P. Nath, R. L. Arnowitt, and A. H. Chamseddine, "Gravity Induced Symmetry Breaking and Ground State of Local Supersymmetric GUTs", *Phys. Lett. B* **121** (1983) 33–36, `doi:10.1016/0370-2693(83)90196-X`.

[41] G. Giudice and R. Rattazzi, "Theories with Gauge Mediated Supersymmetry Breaking", *Phys. Rept.* **322** (1999) 419–499, `doi:10.1016/S0370-1573(99)00042-3`, `arXiv:hep-ph/9801271`.

[42] S. Dimopoulos and D. W. Sutter, "The Supersymmetric flavor problem", *Nucl. Phys. B* **452** (1995) 496–512, `doi:10.1016/0550-3213(95)00421-N`, `arXiv:hep-ph/9504415`.

[43] E. Bagnaschi et al., "MSSM Higgs Boson Searches at the LHC: Benchmark Scenarios for Run 2 and Beyond", *Eur. Phys. J. C* **79** (2019), no. 7, 617, `doi:10.1140/epjc/s10052-019-7114-8`, `arXiv:1808.07542`.

[44] H. Bahl, S. Liebler, and T. Stefaniak, "MSSM Higgs Benchmark Scenarios for Run 2 and Beyond: The Low $\tan\beta$ Region", *Eur. Phys. J. C* **79** (2019), no. 3, 279, `doi:10.1140/epjc/s10052-019-6770-z`, `arXiv:1901.05933`.

[45] J. Goldstone, A. Salam, and S. Weinberg, "Broken Symmetries", *Phys. Rev.* **127** (1962) 965–970, `doi:10.1103/PhysRev.127.965`.

[46] LHC Higgs Cross Section Working Group Collaboration, "Handbook of LHC Higgs Cross Sections: 4. Deciphering the Nature of the Higgs Sector", `doi:10.23731/CYRM-2017-002`, `arXiv:1610.07922`.

[47] T. Lee, "A Theory of Spontaneous T Violation", *Phys. Rev. D* **8** (1973) 1226–1239, `doi:10.1103/PhysRevD.8.1226`.

[48] G. Branco et al., "Theory and Phenomenology of Two-Higgs-Doublet Models", *Phys. Rept.* **516** (2012) 1–102, `doi:10.1016/j.physrep.2012.02.002`, `arXiv:1106.0034`.

[49] J. F. Gunion, H. E. Haber, G. L. Kane, and S. Dawson, "The Higgs Hunter's Guide", volume 80, 2000.

[50] G. Degrassi et al., "Towards High Precision Predictions for the MSSM Higgs Sector", *Eur. Phys. J. C* **28** (2003) 133–143, `doi:10.1140/epjc/s2003-01152-2`, `arXiv:hep-ph/0212020`.

[51] B. Allanach et al., "Precise Determination of the Neutral Higgs Boson Masses in the MSSM", *JHEP* **09** (2004) 044, `doi:10.1088/1126-6708/2004/09/044`, `arXiv:hep-ph/0406166`.

[52] C. Møller, "General Properties of the Characteristic Matrix in the Theory of Elementary Particles 1", *D. Kgl Danske Vidensk. Selsk. Mat.-Fys. Medd.* **23** (1945), no. 1, `http://gymarkiv.sdu.dk/MFM/kdvs/mfm%2020-29/mfm-23-1.pdf`.

[53] O. Skjeggestad, "Notes on Phase Space", `doi:10.5170/CERN-1964-013-V-2.1`.

[54] G. 't Hooft and M. Veltman, "Regularization and Renormalization of Gauge Fields", *Nucl. Phys. B* **44** (1972) 189–213, `doi:10.1016/0550-3213(72)90279-9`.

[55] G. 't Hooft, "Dimensional Regularization and the Renormalization Group", *Nucl. Phys. B* **61** (1973) 455–468, `doi:10.1016/0550-3213(73)90376-3`.

[56] S. Weinberg, "New Approach to the Renormalization Group", *Phys. Rev. D* **8** (1973) 3497–3509, `doi:10.1103/PhysRevD.8.3497`.

[57] W. A. Bardeen, A. Buras, D. Duke, and T. Muta, "Deep Inelastic Scattering Beyond the Leading Order in Asymptotically Free Gauge Theories", *Phys. Rev. D* **18** (1978) 3998, `doi:10.1103/PhysRevD.18.3998`.

[58] W. Siegel, "Supersymmetric Dimensional Regularization via Dimensional Reduction", *Phys. Lett. B* **84** (1979) 193–196, `doi:10.1016/0370-2693(79)90282-X`.

[59] H. Arason et al., "Renormalization Group Study of the Standard Model and its Extensions. 1. The Standard Model", *Phys. Rev. D* **46** (1992) 3945–3965, `doi:10.1103/PhysRevD.46.3945`.

[60] D. Castano, E. Piard, and P. Ramond, "Renormalization Group Study of the Standard Model and its Extensions. 2. The Minimal Supersymmetric Standard Model", *Phys. Rev. D* **49** (1994) 4882–4901, `doi:10.1103/PhysRevD.49.4882`, `arXiv:hep-ph/9308335`.

[61] D. S. M. Alves, J. Galloway, J. T. Ruderman, and J. R. Walsh, "Running Electroweak Couplings as a Probe of New Physics", *JHEP* **02** (2015) 007, `doi:10.1007/JHEP02(2015)007`, `arXiv:1410.6810`.

[62] A. Deur, S. J. Brodsky, and G. F. de Teramond, "The QCD Running Coupling", *Prog. Part. Nucl. Phys.* **90** (2016) 1–74, `doi:10.1016/j.ppnp.2016.04.003`, `arXiv:1604.08082`.

[63] Z.-z. Xing, H. Zhang, and S. Zhou, "Updated Values of Running Quark and Lepton Masses", *Phys. Rev. D* **77** (2008) 113016, `doi:10.1103/PhysRevD.77.113016`, `arXiv:0712.1419`.

[64] E. Fermi, "Trends to a Theory of β Radiation. (In Italian)", *Nuovo Cim.* **11** (1934) 1–19, `doi:10.1007/BF02959820`.

[65] J. C. Ward, "An Identity in Quantum Electrodynamics", *Phys. Rev.* **78** (1950) 182, `doi:10.1103/PhysRev.78.182`.

[66] Y. Takahashi, "On the Generalized Ward Identity", *Nuovo Cim.* **6** (1957) 371, `doi:10.1007/BF02832514`.

[67] N. Nakanishi, "Ward-Takahashi Identities in Quantum Field Theory with Spontaneously Broken Symmetry", *Prog. Theor. Phys.* **51** (1974) 1183–1192, `doi:10.1143/PTP.51.1183`.

[68] T. Kinoshita, "Mass Singularities of Feynman Amplitudes", *J. Math. Phys.* **3** (1962) 650–677, `doi:10.1063/1.1724268`.

[69] T. Lee and M. Nauenberg, "Degenerate Systems and Mass Singularities", *Phys. Rev.* **133** (1964) B1549–B1562, `doi:10.1103/PhysRev.133.B1549`.

[70] V. Gribov and L. Lipatov, "Deep Inelastic e p Scattering in Perturbation Theory", *Sov. J. Nucl. Phys.* **15** (1972) 438–450.

[71] V. Gribov and L. Lipatov, "e⁺e⁻ Pair Annihilation and Deep Inelastic e p Scattering in Perturbation Theory", *Sov. J. Nucl. Phys.* **15** (1972) 675–684.

[72] L. Lipatov, "The Parton Model and Perturbation Theory", *Sov. J. Nucl. Phys.* **20** (1975) 94–102.

[73] G. Altarelli and G. Parisi, "Asymptotic Freedom in Parton Language", *Nucl. Phys. B* **126** (1977) 298–318, `doi:10.1016/0550-3213(77)90384-4`.

[74] Y. L. Dokshitzer, "Calculation of the Structure Functions for Deep Inelastic Scattering and e⁺e⁻ Annihilation by Perturbation Theory in Quantum Chromodynamics", *Sov. Phys. JETP* **46** (1977) 641–653, `http://jetp.ac.ru/cgi-bin/dn/e_046_04_0641.pdf`.

[75] J. Butterworth et al., "PDF4LHC Recommendations for LHC Run II", *J. Phys. G* **43** (2016) 023001, `doi:10.1088/0954-3899/43/2/023001`, `arXiv:1510.03865`.

[76] M. Schönherr, "Parton Shower Matching and Merging", *PoS* **CORFU2017** (2018) 110, `doi:10.22323/1.318.0110`, `arXiv:1804.10643`.

[77] CMS Collaboration, "Extraction and Validation of a new Set of CMS PYTHIA8 Tunes from Underlying-Event Measurements", *Eur. Phys. J. C* **80** (2020), no. 1, 4, `doi:10.1140/epjc/s10052-019-7499-4`, `arXiv:1903.12179`.

[78] M. Bahr et al., "Herwig++ Physics and Manual", *Eur. Phys. J. C* **58** (2008) 639–707, `doi:10.1140/epjc/s10052-008-0798-9`, `arXiv:0803.0883`.

[79] J. Bellm et al., "Herwig 7.0/Herwig++ 3.0 Release Note", *Eur. Phys. J. C* **76** (2016), no. 4, 196, `doi:10.1140/epjc/s10052-016-4018-8`, `arXiv:1512.01178`.

[80] T. Sjöstrand et al., "An Introduction to PYTHIA 8.2", *Comput. Phys. Commun.* **191** (2015) 159–177, `doi:10.1016/j.cpc.2015.01.024`, `arXiv:1410.3012`.

[81] E. Mobs, "The CERN Accelerator Complex. Complexe des Accélérateurs du CERN", OPEN-PHO-ACCEL-2016-009, General Photo.

[82] CMS Collaboration, "CMS Physics: Technical Design Report Volume 1: Detector Performance and Software", CERN-LHCC-2006-001, CMS-TDR-8-1.

[83] CMS Collaboration, "CMS Technical Design Report for the Level-1 Trigger Upgrade", CERN-LHCC-2013-011, CMS-TDR-12, CMS-TDR-012.

[84] CMS Collaboration, "CMS Technical Design Report for the Pixel Detector Upgrade", `doi:10.2172/1151650`.

[85] CMS Collaboration, "CMS Technical Design Report for the Phase 1 Upgrade of the Hadron Calorimeter", `doi:10.2172/1151651`.

[86] A. Colaleo, A. Safonov, A. Sharma, and M. Tytgat, "CMS Technical Design Report for the Muon Endcap GEM Upgrade", CERN-LHCC-2015-012, CMS-TDR-013.

[87] CMS Collaboration, "Description and Performance of Track and Primary-Vertex Reconstruction with the CMS Tracker", *JINST* **9** (2014), no. 10, P10009, `doi:10.1088/1748-0221/9/10/P10009`, `arXiv:1405.6569`.

[88] CMS Collaboration, "2017 Tracking Performance Plots", CMS-DP-2017-015.

[89] CMS Collaboration, "Muon Tag and Probe Efficiency on 2016 Data", CMS-DP-2016-043.

[90] CMS Collaboration, "Muon Tracking Efficiency using Tag and Probe Method for 2017 Dataset", CMS-DP-2019-004.

[91] CMS Collaboration, "Performance of b Tagging Algorithms in Proton-Proton Collisions at 13 TeV with Phase 1 CMS Detector", CMS-DP-2018-033.

[92] CMS Collaboration, "Performance of the CMS Muon Detector and Muon Reconstruction with Proton-Proton Collisions at $\sqrt{s} = 13$ TeV", *JINST* **13** (2018), no. 06, P06015, `doi:10.1088/1748-0221/13/06/P06015`, `arXiv:1804.04528`.

[93] CMS Collaboration, "Performance of Electron Reconstruction and Selection with the CMS Detector in Proton-Proton Collisions at $\sqrt{s} = 8$ TeV", *JINST* **10** (2015), no. 06, P06005, `doi:10.1088/1748-0221/10/06/P06005`, `arXiv:1502.02701`.

[94] CMS Collaboration, "Particle-Flow Reconstruction and Global Event Description with the CMS Detector", *JINST* **12** (2017), no. 10, P10003, `doi:10.1088/1748-0221/12/10/P10003`, `arXiv:1706.04965`.

[95] M. Cacciari, G. P. Salam, and G. Soyez, "The Anti-k_t Jet Clustering Algorithm", *JHEP* **04** (2008) 063, `doi:10.1088/1126-6708/2008/04/063`, `arXiv:0802.1189`.

[96] CMS Collaboration, "Performance of Missing Transverse Momentum Reconstruction in Proton-Proton Collisions at $\sqrt{s} = 13$ TeV using the CMS Detector", *JINST* **14** (2019), no. 07, P07004, `doi:10.1088/1748-0221/14/07/P07004`, `arXiv:1903.06078`.

[97] CMS Collaboration, "Identification of Heavy-Flavour Jets with the CMS Detector in pp Collisions at 13 TeV", *JINST* **13** (2018), no. 05, P05011, `doi:10.1088/1748-0221/13/05/P05011`, `arXiv:1712.07158`.

[98] CMS Collaboration, "Performance of Reconstruction and Identification of τ Leptons Decaying to Hadrons and ν_τ in pp Collisions at $\sqrt{s} = 13$ TeV", *JINST* **13** (2018), no. 10, P10005, `doi:10.1088/1748-0221/13/10/P10005`, `arXiv:1809.02816`.

[99] R. Frühwirth, "Application of Kalman Filtering to Track and Vertex Fitting", *Nucl. Instrum. Meth. A* **262** (1987) 444–450, `doi:10.1016/0168-9002(87)90887-4`.

[100] K. Rose, "Deterministic Annealing for Clustering, Compression, Classification, Regression, and Related Optimization Problems", *IEEE Proc.* **86** (1998), no. 11, 2210–2239, `doi:10.1109/5.726788`.

[101] R. Frühwirth, W. Waltenberger, and P. Vanlaer, "Adaptive Vertex Fitting", *J. Phys. G* **34** (2007) N343, `doi:10.1088/0954-3899/34/12/N01`.

[102] M. Cacciari and G. P. Salam, "Pileup Subtraction using Jet Areas", *Phys. Lett. B* **659** (2008) 119–126, `doi:10.1016/j.physletb.2007.09.077`, `arXiv:0707.1378`.

[103] M. Cacciari, G. P. Salam, and G. Soyez, "FastJet User Manual", *Eur. Phys. J. C* **72** (2012) 1896, `doi:10.1140/epjc/s10052-012-1896-2`, `arXiv:1111.6097`.

[104] W. Adam, R. Frühwirth, A. Strandlie, and T. Todorov, "Reconstruction of Electrons with the Gaussian Sum Filter in the CMS Tracker at LHC", *eConf* **C0303241** (2003) TULT009, `doi:10.1088/0954-3899/31/9/N01`, `arXiv:physics/0306087`.

[105] CMS Collaboration, "Performance of Photon Reconstruction and Identification with the CMS Detector in Proton-Proton Collisions at $\sqrt{s}$ = 8 TeV", *JINST* **10** (2015), no. 08, P08010, `doi:10.1088/1748-0221/10/08/P08010`, `arXiv:1502.02702`.

[106] T. Chen and C. Guestrin, "XGBoost: A Scalable Tree Boosting System", `doi:10.1145/2939672.2939785`, `arXiv:1603.02754`.

[107] CMS Collaboration, "Jet Algorithms Performance in 13 TeV Data", CMS-PAS-JME-16-003.

[108] CMS Collaboration, "Pileup Removal Algorithms", CMS-PAS-JME-14-001.

[109] CMS Collaboration, "Pileup Mitigation at CMS in 13 TeV Data", *JINST* **15** (2020), no. 09, P09018, `doi:10.1088/1748-0221/15/09/P09018`, `arXiv:2003.00503`.

[110] D. Bertolini, P. Harris, M. Low, and N. Tran, "Pileup per Particle Identification", *JHEP* **10** (2014) 059, `doi:10.1007/JHEP10(2014)059`, `arXiv:1407.6013`.

[111] CMS Collaboration, "Performance of the DeepJet b Tagging Algorithm using 41.9 fb^{-1} of Data from Proton-Proton Collisions at 13TeV with Phase 1 CMS Detector", CMS-DP-2018-058.

[112] I. Goodfellow, Y. Bengio, and A. Courville, "Deep Learning", MIT Press, 2016, `http://www.deeplearningbook.org`.

[113] K. He, X. Zhang, S. Ren, and J. Sun, "Delving Deep into Rectifiers: Surpassing Human-Level Performance on ImageNet Classification", `arXiv:1502.01852`.

[114] F. Chollet et al., "Keras", 2015, `https://keras.io`.

[115] D. P. Kingma and J. Ba, "Adam: A Method for Stochastic Optimization", `arXiv:1412.6980`.

[116] CMS Collaboration, "Performance of the DeepTau Algorithm for the Discrimination of Taus against Jets, Electron, and Muons", CMS-DP-2019-033.

[117] T.-Y. Lin et al., "Focal Loss for Dense Object Detection", `arXiv:1708.02002`.

[118] CMS Collaboration, "2018 Tau Trigger Reconstruction Comparison", CMS-DP-2018-035.

[119] CMS Collaboration, "CMS Luminosity Measurements for the 2016 Data Taking Period", CMS-PAS-LUM-17-001.

[120] CMS Collaboration, "CMS Luminosity Measurement for the 2017 Data-Taking Period at $\sqrt{s}$ = 13 TeV", CMS-PAS-LUM-17-004.

[121] CMS Collaboration, "CMS Luminosity Measurement for the 2018 Data-Taking Period at $\sqrt{s}$ = 13 TeV", CMS-PAS-LUM-18-002.

[122] CMS Collaboration, "An Embedding Technique to Determine $\tau\tau$ Backgrounds in Proton-Proton Collision Data", *JINST* **14** (2019), no. 06, P06032, `doi:10.1088/1748-0221/14/06/P06032`, `arXiv:1903.01216`.

[123] CMS Collaboration, "Muon Reconstruction Performance during Run II", CMS-DP-2019-022.

[124] J. Bechtel, "Cross-Check of the CMS Search for Additional MSSM Higgs Bosons in the di-τ Final State using $\mu \to \tau$ Embedded Events", ETP-KA/2017-31, Master's thesis, Karlsruhe Institute of Technology (KIT), 2017.

[125] A. Akhmetshin, "Embedding - a Data Driven Method to Estimate the Z $\to \tau\tau$ Background in the H $\to \tau\tau$ Searches", IEKP-KA/2016-23, Master's thesis, Karlsruhe Institute of Technology (KIT), 2016.

[126] GEANT4 Collaboration, "GEANT4: A Simulation Toolkit", *Nucl. Instrum. Meth. A* **506** (2003) 250–303, `doi:10.1016/S0168-9002(03)01368-8`.

[127] S. Brommer, "Production of Hybrid Data Samples for Data Driven Background Determination in the H $\to \tau\tau$ Channel", ETP-KA/2019-05, Master's thesis, Karlsruhe Institute of Technology (KIT), 2019.

[128] P. Ahrens, "Implementation of the Electron Identification in $\mu \to \tau$ Embedded Hybrid Events", ETP-KA/2018-11, Master's thesis, Karlsruhe Institute of Technology (KIT), 2018.

[129] CMS Collaboration, "Measurement of the Z$\gamma^* \to \tau\tau$ Cross Section in pp Collisions at $\sqrt{s}$ = 13 TeV and Validation of τ Lepton Analysis Techniques", *Eur. Phys. J. C* **78** (2018), no. 9, 708, `doi:10.1140/epjc/s10052-018-6146-9`, `arXiv:1801.03535`.

[130] J. Alwall et al., "The Automated Computation of Tree-Level and Next-to-Leading Order Differential Cross Sections, and their Matching to Parton Shower Simulations", *JHEP* **07** (2014) 079, `doi:10.1007/JHEP07(2014)079`, `arXiv:1405.0301`.

[131] S. Alioli, P. Nason, C. Oleari, and E. Re, "A General Framework for Implementing NLO Calculations in Shower Monte Carlo Programs: The POWHEG BOX", *JHEP* **06** (2010) 043, `doi:10.1007/JHEP06(2010)043`, `arXiv:1002.2581`.

[132] R. Gupta, "Underlying Event Measurements at CMS", in *Proceedings, 17th Conference on Elastic and Diffractive Scattering (EDS Blois 2017): Prague, Czech Republic, June 26-30, 2017*, `arXiv:1711.00785`.

[133] NNPDF Collaboration, "Parton Distributions for the LHC Run II", *JHEP* **04** (2015) 040, `doi:10.1007/JHEP04(2015)040`, `arXiv:1410.8849`.

[134] NNPDF Collaboration, "Parton Distributions from High-Precision Collider Data", *Eur. Phys. J. C* **77** (2017), no. 10, 663, `doi:10.1140/epjc/s10052-017-5199-5`, `arXiv:1706.00428`.

[135] CMS Collaboration, "Measurement of the Inelastic Proton-Proton Cross Section at $\sqrt{s} = 13$ TeV", *JHEP* **07** (2018) 161, `doi:10.1007/JHEP07(2018)161`, `arXiv:1802.02613`.

[136] Y. Li and F. Petriello, "Combining QCD and Electroweak Corrections to Dilepton Production in FEWZ", *Phys. Rev. D* **86** (2012) 094034, `doi:10.1103/PhysRevD.86.094034`, `arXiv:1208.5967`.

[137] M. Czakon and A. Mitov, "Top++: A Program for the Calculation of the Top-Pair Cross-Section at Hadron Colliders", *Comput. Phys. Commun.* **185** (2014) 2930, `doi:10.1016/j.cpc.2014.06.021`, `arXiv:1112.5675`.

[138] CMS Collaboration, "Measurement of Differential Cross Sections for Top Quark Pair Production using the Lepton+Jets Final State in Proton-Proton Collisions at 13 TeV", *Phys. Rev. D* **95** (2017), no. 9, 092001, `doi:10.1103/PhysRevD.95.092001`, `arXiv:1610.04191`.

[139] CMS Collaboration, "Measurement of the Differential Cross Section for $t\bar{t}$ Production in the Dilepton Final State at $\sqrt{s} = 13$ TeV", CMS-PAS-TOP-16-011.

[140] T. Gehrmann et al., "W^+W^- Production at Hadron Colliders in Next to Next to Leading Order QCD", *Phys. Rev. Lett.* **113** (2014), no. 21, 212001, `doi:10.1103/PhysRevLett.113.212001`, `arXiv:1408.5243`.

[141] M. Aliev et al., "HATHOR: Hadronic Top and Heavy Quarks Cross Section Calculator", *Comput. Phys. Commun.* **182** (2011) 1034–1046, `doi:10.1016/j.cpc.2010.12.040`, `arXiv:1007.1327`.

[142] P. Uwer, "Hadronic Single Top-Quark Production: Updated Predictions and Uncertainty Estimates", *PoS* **LHCP2016** (2016) 166, `doi:10.22323/1.276.0166`.

[143] N. Kidonakis, "Theoretical Results for Electroweak-Boson and Single-Top Production", *PoS* **DIS2015** (2015) 170, `doi:10.22323/1.247.0170`, `arXiv:1506.04072`.

[144] N. Berger et al., "Simplified Template Cross Sections - Stage 1.1", `arXiv:1906.02754`.

[145] A. Buckley et al., "Rivet User Manual", *Comput. Phys. Commun.* **184** (2013) 2803–2819, `doi:10.1016/j.cpc.2013.05.021`, `arXiv:1003.0694`.

[146] K. Hamilton, P. Nason, and G. Zanderighi, "Finite Quark-Mass Effects in the NNLOPS POWHEG+MiNLO Higgs Generator", *JHEP* **05** (2015) 140, `doi:10.1007/JHEP05(2015)140`, `arXiv:1501.04637`.

[147] R. Boughezal et al., "Combining Resummed Higgs Predictions Across Jet Bins", *Phys. Rev. D* **89** (2014), no. 7, 074044, `doi:10.1103/PhysRevD.89.074044`, `arXiv:1312.4535`.

[148] P. Z. Skands et al., "SUSY Les Houches Accord: Interfacing SUSY Spectrum Calculators, Decay Packages, and Event Generators", *JHEP* **07** (2004) 036, `doi:10.1088/1126-6708/2004/07/036`, `arXiv:hep-ph/0311123`.

[149] B. Allanach et al., "SUSY Les Houches Accord 2", *Comput. Phys. Commun.* **180** (2009) 8–25, `doi:10.1016/j.cpc.2008.08.004`, `arXiv:0801.0045`.

[150] H. Bahl et al., "Precision Calculations in the MSSM Higgs-Boson Sector with FeynHiggs 2.14", *Comput. Phys. Commun.* **249** (2020) 107099, `doi:10.1016/j.cpc.2019.107099`, `arXiv:1811.09073`.

[151] E. Bagnaschi and A. Vicini, "The Higgs Transverse Momentum Distribution in Gluon Fusion as a Multiscale Problem", *JHEP* **01** (2016) 056, `doi:10.1007/JHEP01(2016)056`, `arXiv:1505.00735`.

[152] R. V. Harlander, F. Hofmann, and H. Mantler, "Supersymmetric Higgs Production in Gluon Fusion", *JHEP* **02** (2011) 055, `doi:10.1007/JHEP02(2011)055`, `arXiv:1012.3361`.

[153] E. Bagnaschi et al., "Resummation Ambiguities in the Higgs Transverse-Momentum Spectrum in the Standard Model and Beyond", *JHEP* **01** (2016) 090, `doi:10.1007/JHEP01(2016)090`, `arXiv:1510.08850`.

[154] M. Carena et al., "Complementarity between Nonstandard Higgs Boson Searches and Precision Higgs Boson Measurements in the MSSM", *Phys. Rev. D* **91** (2015), no. 3, 035003, `doi:10.1103/PhysRevD.91.035003`, `arXiv:1410.4969`.

[155] J. Metwally, "Determination of the Transverse Momentum Distribution for the Production of THDM and MSSM Higgs Bosons via Gluon Fusion at Next-To-Leading Order using POWHEG", ETP-KA/2018-07, Master's thesis, Karlsruhe Institute of Technology (KIT), 2018.

[156] J. M. Campbell et al., "Higgs Boson Production in Association with Bottom Quarks", in *Physics at TeV Colliders. Proceedings, Workshop, Les Houches, France, May 26-June 3, 2003*, `arXiv:hep-ph/0405302`.

[157] M. Wiesemann et al., "Higgs Production in Association with Bottom Quarks", *JHEP* **02** (2015) 132, `doi:10.1007/JHEP02(2015)132`, `arXiv:1409.5301`.

[158] B. Jäger, L. Reina, and D. Wackeroth, "Higgs Boson Production in Association with b Jets in the POWHEG BOX", *Phys. Rev. D* **93** (2016), no. 1, 014030, `doi:10.1103/PhysRevD.93.014030`, `arXiv:1509.05843`.

[159] CMS Collaboration, "Electron and Photon Performance in CMS with the Full 2016 Data Sample", CMS-DP-2017-004.

[160] CMS Collaboration, "Electron and Photon Performance in CMS with the Full 2017 Data Sample and Additional 2016 Highlights for the CALOR 2018 Conference", CMS-DP-2018-017.

[161] CMS Collaboration, "Jet Energy Scale and Resolution in the CMS Experiment in pp Collisions at 8 TeV", *JINST* **12** (2017), no. 02, P02014, `doi:10.1088/1748-0221/12/02/P02014`, `arXiv:1607.03663`.

[162] "Combine: CMS Higgs Combination Toolkit", `https://cms-analysis.github.io/HiggsAnalysis-CombinedLimit`.

[163] R. J. Barlow and C. Beeston, "Fitting using Finite Monte Carlo Samples", *Comput. Phys. Commun.* **77** (1993) 219–228, `doi:10.1016/0010-4655(93)90005-W`.

[164] J. Conway, "Incorporating Nuisance Parameters in Likelihoods for Multisource Spectra", in *Proceedings, PHYSTAT 2011 Workshop on Statistical Issues Related to Discovery Claims in Search Experiments and Unfolding, CERN, Geneva, Switzerland 17-20 January 2011*, pp. 115–120, `doi:10.5170/CERN-2011-006.115`, `arXiv:1103.0354`.

[165] L. Bianchini et al., "Reconstruction of the Higgs Mass in Events with Higgs Bosons Decaying into a Pair of τ Leptons using Matrix Element Techniques", *Nucl. Instrum. Meth. A* **862** (2017) 54–84, `doi:10.1016/j.nima.2017.05.001`, `arXiv:1603.05910`.

[166] G. Cowan, K. Cranmer, E. Gross, and O. Vitells, "Asymptotic Formulae for Likelihood-Based Tests of New Physics", *Eur. Phys. J. C* **71** (2011) 1554, `doi:10.1140/epjc/s10052-011-1554-0`, `arXiv:1007.1727`, [Erratum: *Eur. Phys. J. C* **73** (2013) 2501, `doi:10.1140/epjc/s10052-013-2501-z`].

[167] A. L. Read, "Presentation of Search Results: The CL(s) Technique", *J. Phys. G* **28** (2002) 2693–2704, `doi:10.1088/0954-3899/28/10/313`.

[168] E. Gross, "LHC Statistics for Pedestrians", in *PHYSTAT-LHC Workshop on Statistical Issues for LHC Physics*, pp. 205–212, `doi:10.5170/CERN-2008-001.205`.

[169] B. Mistlberger and F. Dulat, "Limit Setting Procedures and Theoretical Uncertainties in Higgs Boson Searches", `arXiv:1204.3851`.

[170] ATLAS Collaboration, "Search for Heavy Higgs Bosons Decaying into two Tau Leptons with the ATLAS Detector using pp Collisions at $\sqrt{s} = 13$ TeV", *Phys. Rev. Lett.* **125** (2020), no. 5, 051801, `doi:10.1103/PhysRevLett.125.051801`, `arXiv:2002.12223`.

[171] P. Bechtle et al., "HiggsBounds-5: Testing Higgs Sectors in the LHC 13 TeV Era", `arXiv:2006.06007`.

[172] M. Burkart, "Application of Novel Trigger Selections to Precision Analyses of Higgs Boson Decays to τ Leptons", ETP-KA/2019-09, Master's thesis, Karlsruhe Institute of Technology (KIT), 2019.

[173] S. Wunsch, "A Novel Strategy for the Standard Model $H \rightarrow \tau\tau$ Analysis with Emphasis on Minimizing Systematic Uncertainties in Presence of Modern Multi-Variate Methods", ETP-KA/2017-26, Master's thesis, Karlsruhe Institute of Technology (KIT), 2017.

[174] S. Wozniewski, "Development of Multivariate Analysis Methods for Enhancing the Sensitivity to Supersymmetric Higgs Bosons in the $H \to \tau\tau$ Decay Channel", IEKP-KA/2017-18, Master's thesis, Karlsruhe Institute of Technology (KIT), 2017.

A. Distributions of Variables

A.1. Categorization Variables
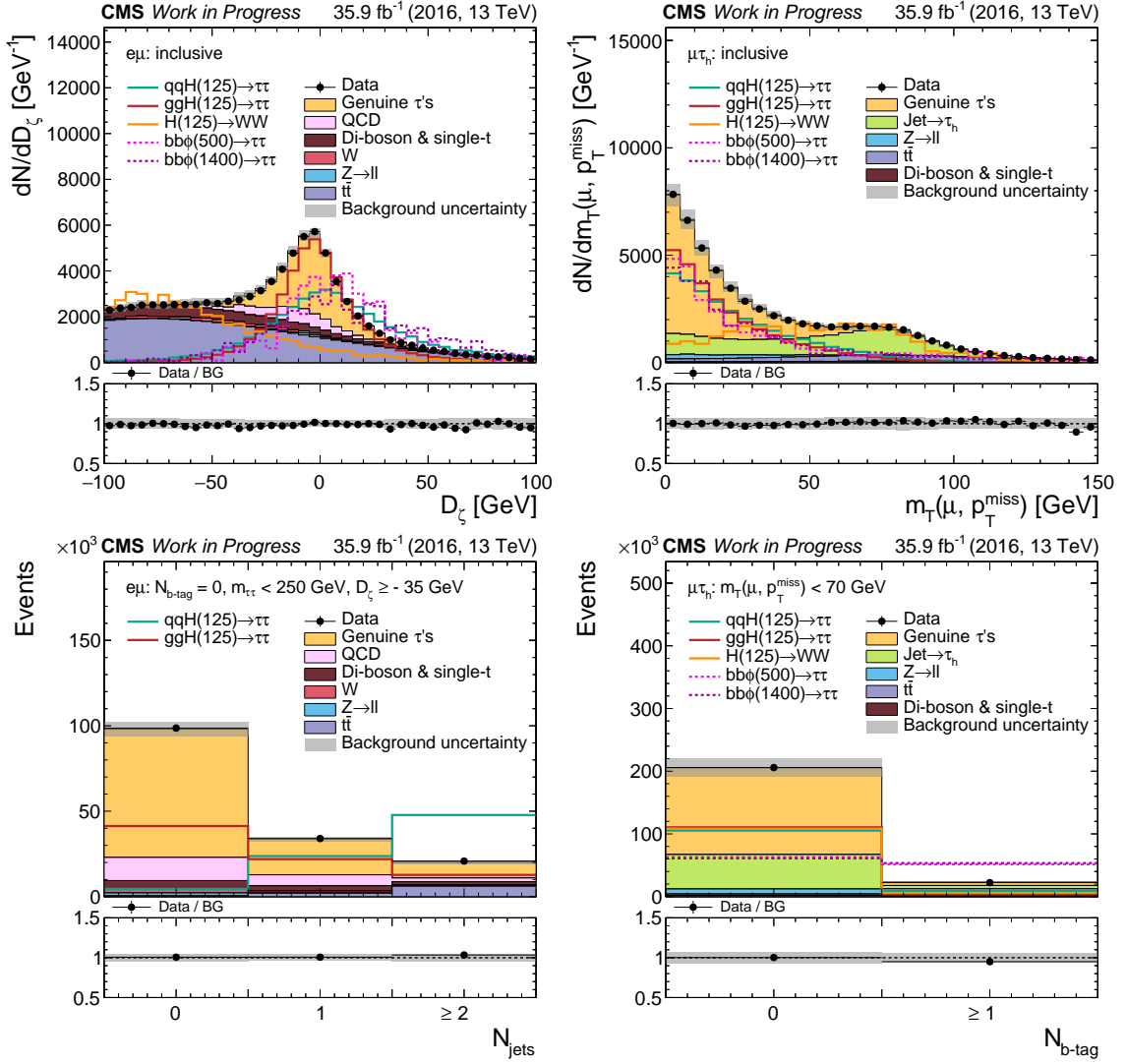
Figure A.1.: Distributions of the variables used for categorization for data and expected signals and backgrounds. The background contributions are stacked. The SM H → ττ, BSM φ → ττ and SM H → WW signals are rescaled for shape comparison in the upper panel of the figures. The grey background uncertainty bands include both statistical and systematic uncertainties in the state before a maximum likelihood fit.
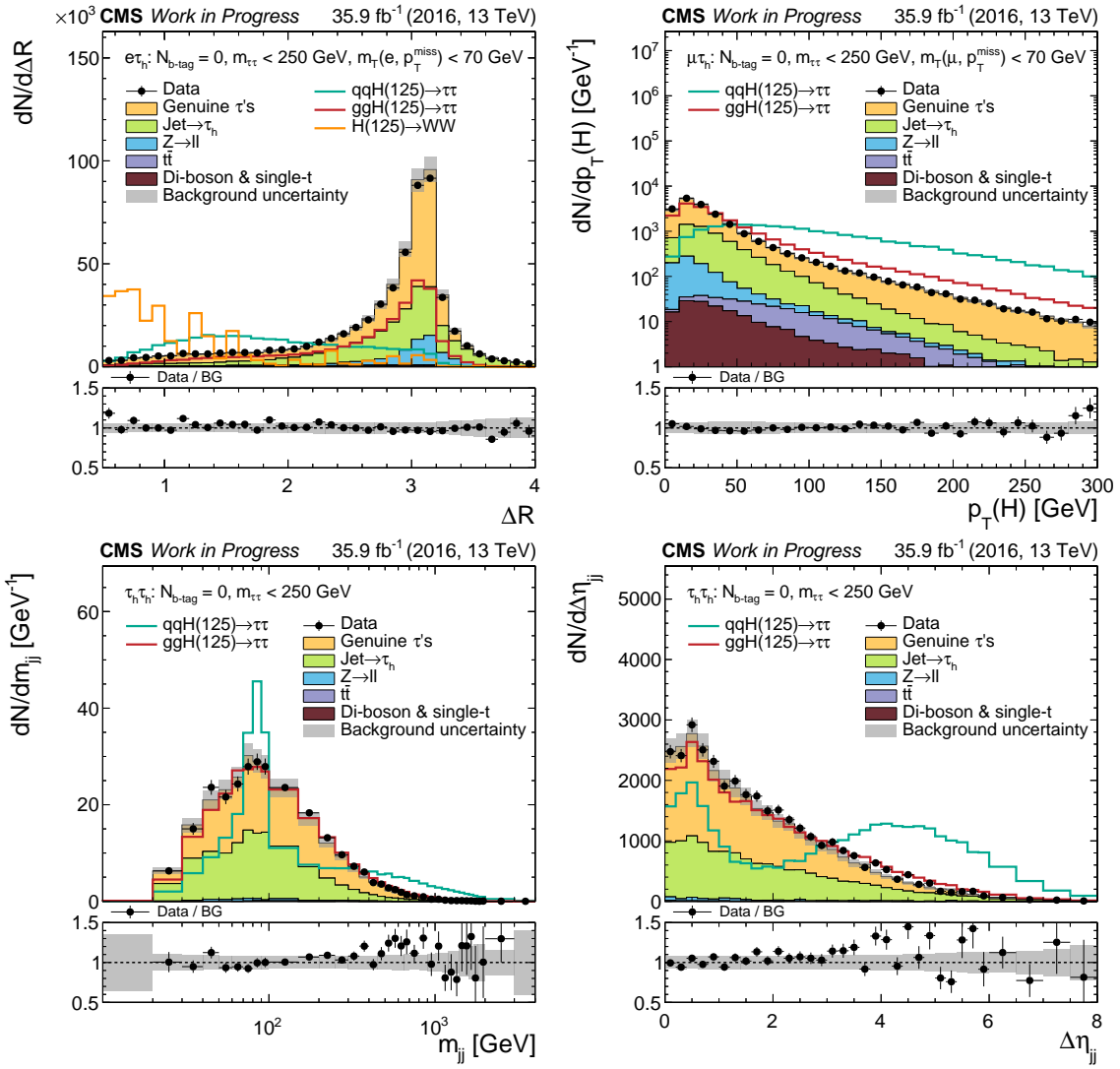
Figure A.2.: Distributions of the variables used for categorization for data and expected signals and backgrounds. The background contributions are stacked. The SM H → ττ and H → WW signals are rescaled for shape comparison in the upper panel of the figures. The grey background uncertainty bands include both statistical and systematic uncertainties in the state before a maximum likelihood fit.
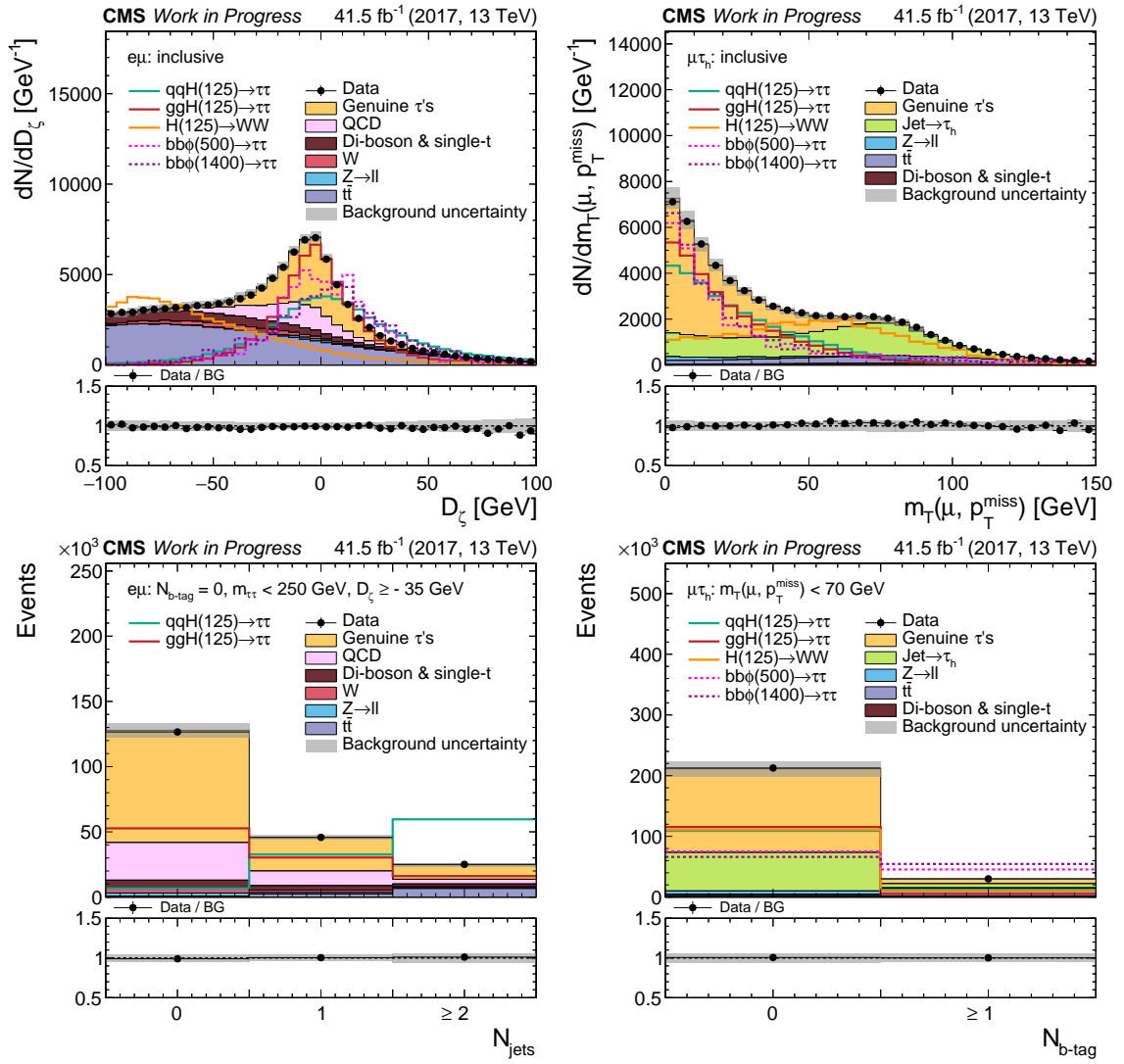
Figure A.3.: Distributions of the variables used for categorization for data and expected signals and backgrounds. The background contributions are stacked. The SM H → ττ, BSM φ → ττ and SM H → WW signals are rescaled for shape comparison in the upper panel of the figures. The grey background uncertainty bands include both statistical and systematic uncertainties in the state before a maximum likelihood fit.
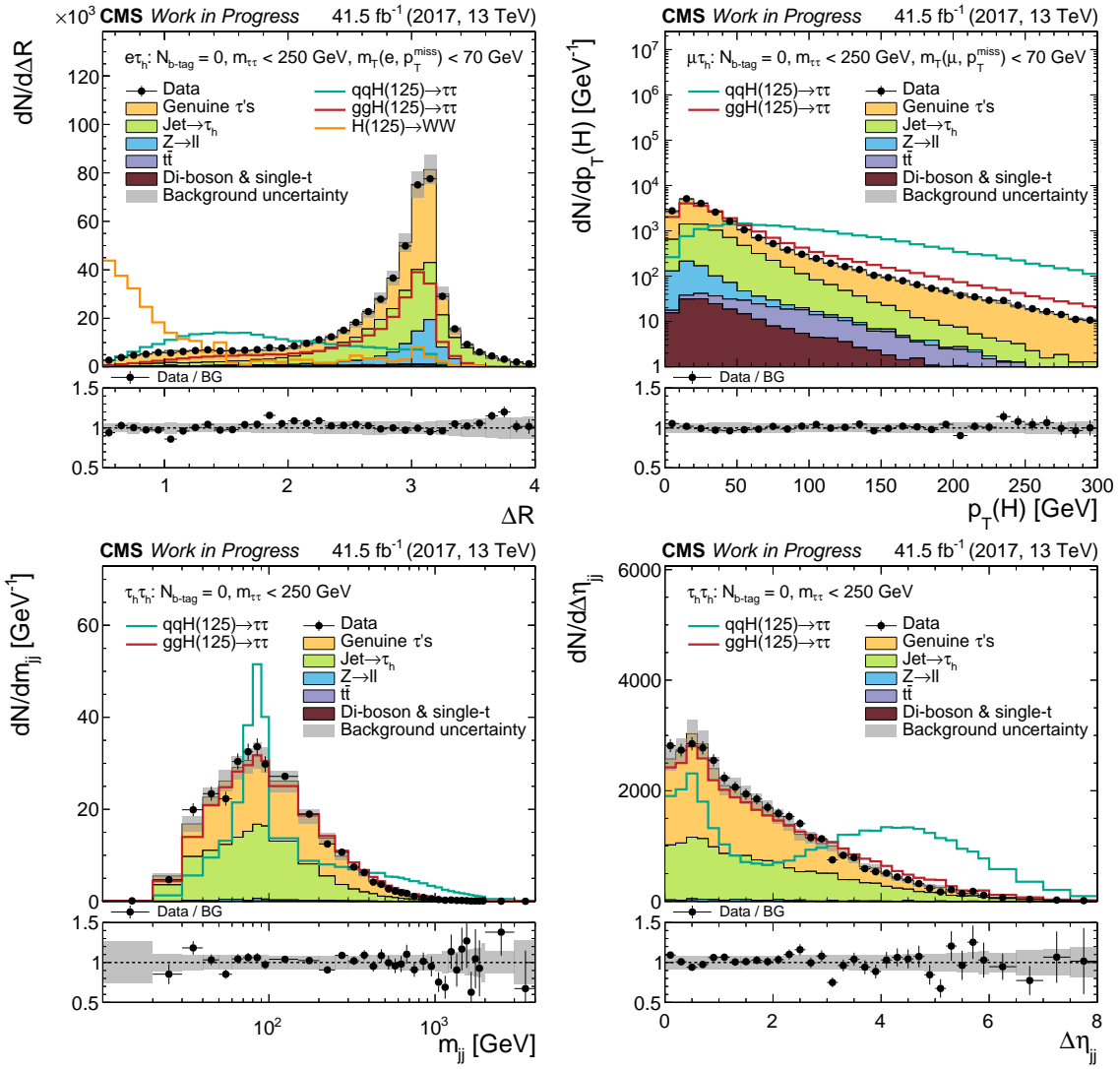
Figure A.4.: Distributions of the variables used for categorization for data and expected signals and backgrounds. The background contributions are stacked. The SM H → ττ and H → WW signals are rescaled for shape comparison in the upper panel of the figures. The grey background uncertainty bands include both statistical and systematic uncertainties in the state before a maximum likelihood fit.
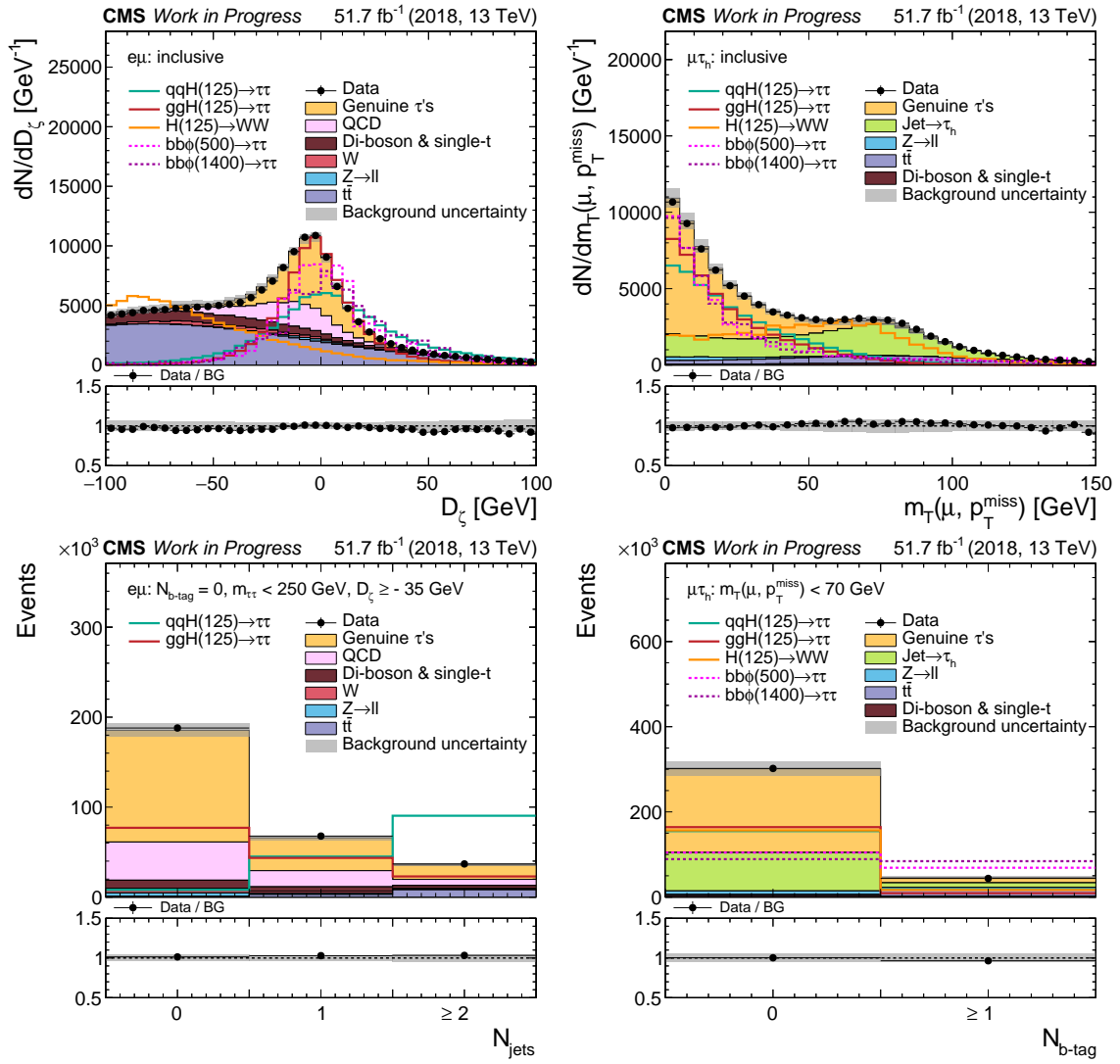
Figure A.5.: Distributions of the variables used for categorization for data and expected signals and backgrounds. The background contributions are stacked. The SM H → ττ, BSM φ → ττ and SM H → WW signals are rescaled for shape comparison in the upper panel of the figures. The grey background uncertainty bands include both statistical and systematic uncertainties in the state before a maximum likelihood fit.
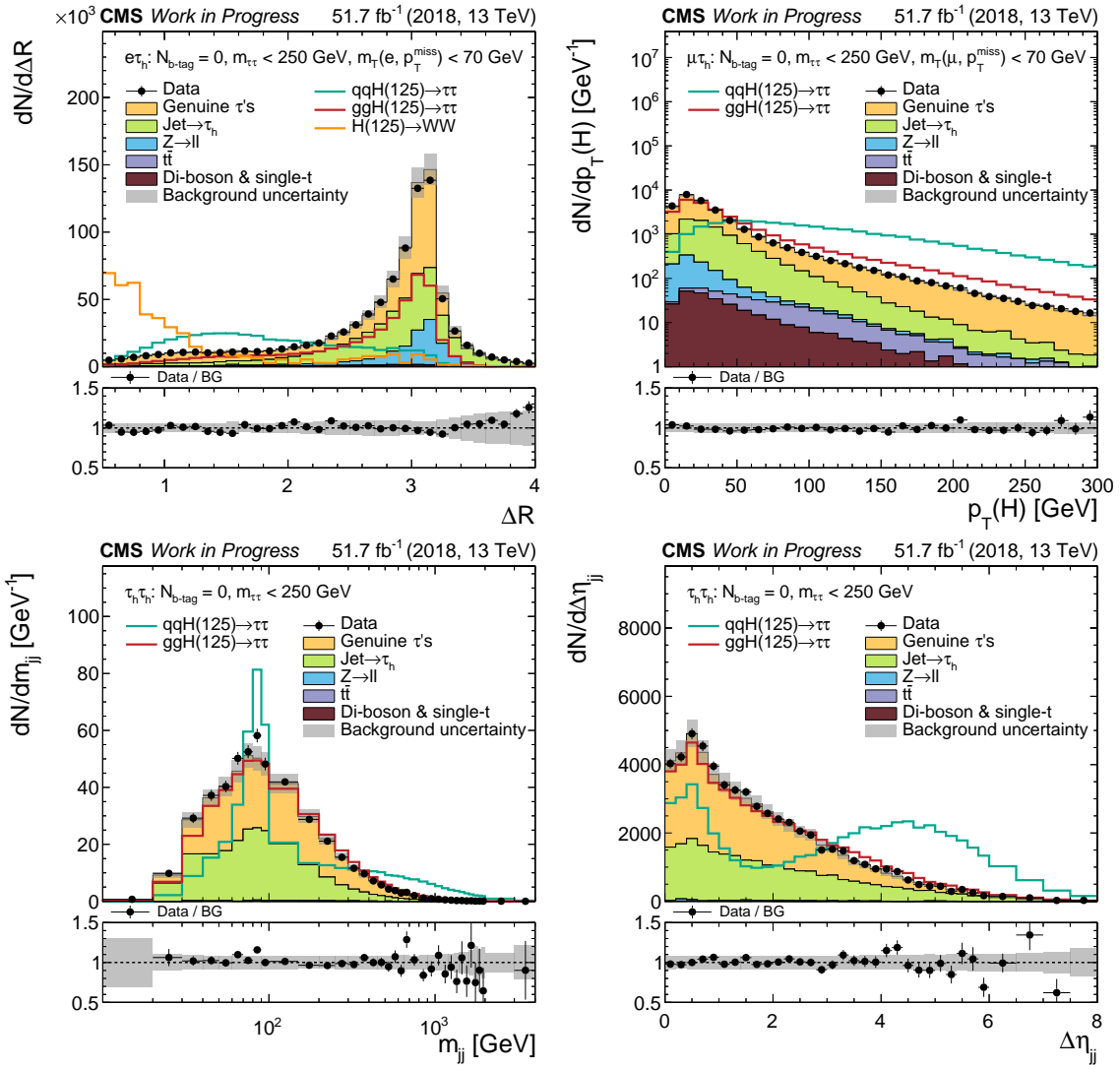
Figure A.6.: Distributions of the variables used for categorization for data and expected signals and backgrounds. The background contributions are stacked. The SM H → ττ and H → WW signals are rescaled for shape comparison in the upper panel of the figures. The grey background uncertainty bands include both statistical and systematic uncertainties in the state before a maximum likelihood fit.

A.2. m_T^{tot} and $m_{\tau\tau}$ in Control Regions
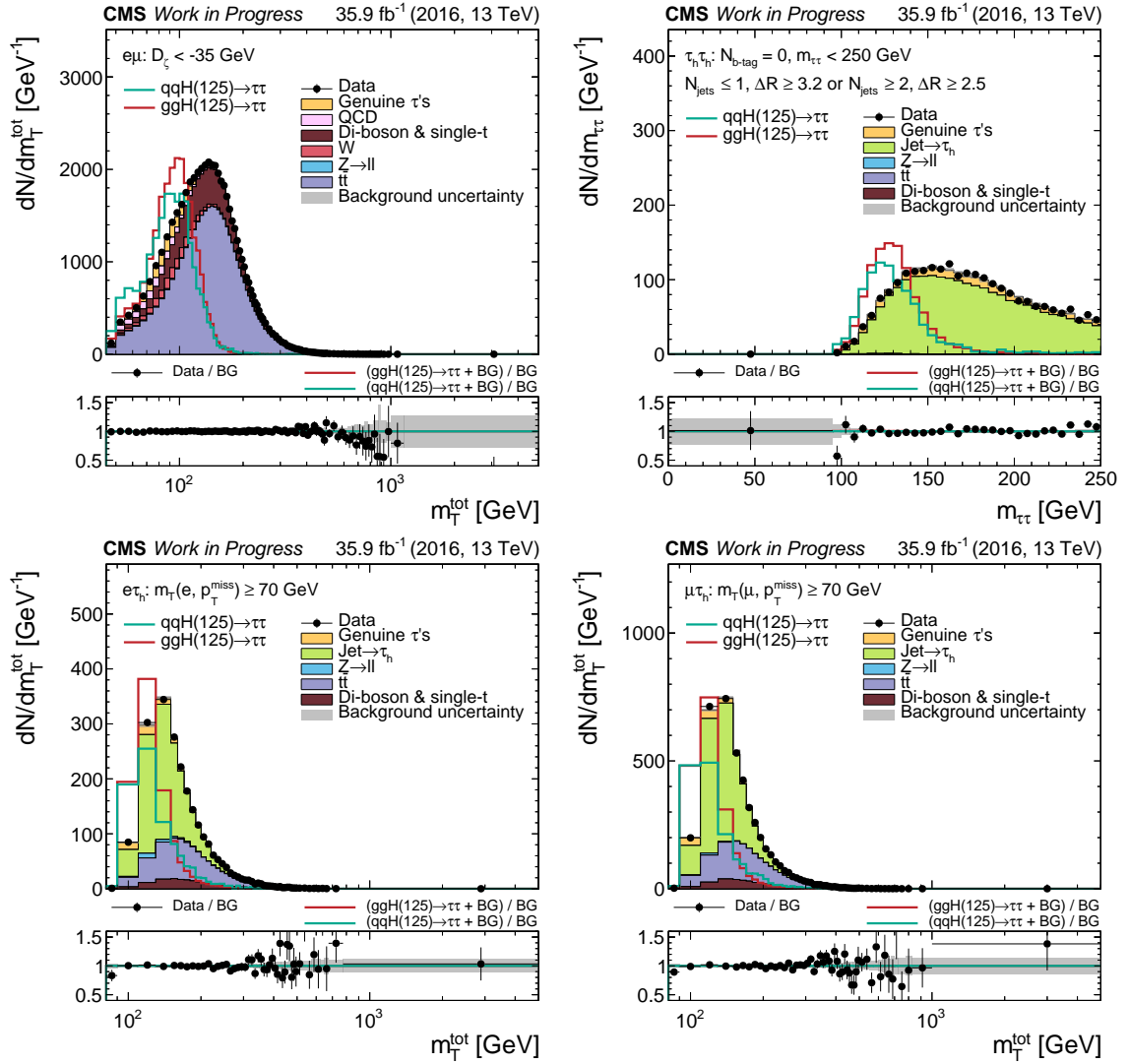
Figure A.7.: Distributions of the (top right) $m_{\tau\tau}$ and (top left and bottom) m_T^{tot} for the (top left) eμ, (top right) $\tau_h\tau_h$, (bottom left) eτ_h, and (bottom right) μτ_h final states in control regions. Expected SM H → ττ signal, rescaled for shape comparison in the upper panels, is shown with data and stacked background (BG). Grey uncertainty bands illustrate the total BG uncertainty after a maximum likelihood fit for signal strength μ. In the lower panel, SM H → ττ is scaled to SM expectation.

Figure A.8.: Distributions of the (top right) $m_{\tau\tau}$ and (top left and bottom) m_T^{tot} for the (top left) eμ, (top right) $\tau_h\tau_h$, (bottom left) eτ_h, and (bottom right) $\mu\tau_h$ final states in control regions. Expected SM H $\rightarrow \tau\tau$ signal, rescaled for shape comparison in the upper panels, is shown with data and stacked background (BG). Grey uncertainty bands illustrate the total BG uncertainty after a maximum likelihood fit for signal strength μ. In the lower panel, SM H $\rightarrow \tau\tau$ is scaled to SM expectation.
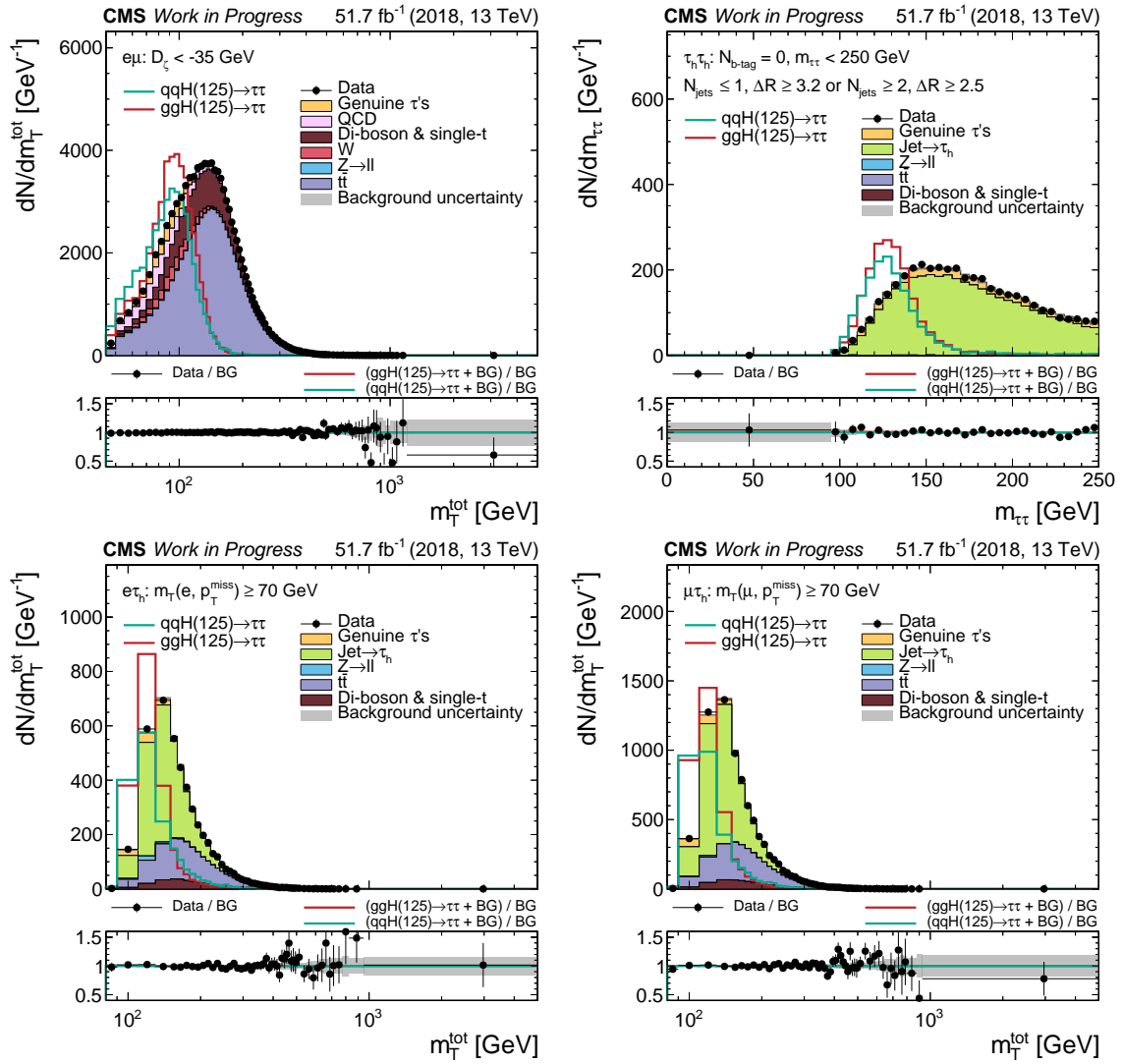
Figure A.9.: Distributions of the (top right) $m_{\tau\tau}$ and (top left and bottom) m_T^{tot} for the (top left) eµ, (top right) $\tau_h\tau_h$, (bottom left) eτ_h, and (bottom right) µτ_h final states in control regions. Expected SM H $\rightarrow \tau\tau$ signal, rescaled for shape comparison in the upper panels, is shown with data and stacked background (BG). Grey uncertainty bands illustrate the total BG uncertainty after a maximum likelihood fit for signal strength µ. In the lower panel, SM H $\rightarrow \tau\tau$ is scaled to SM expectation.

A.3. $m_{\tau\tau}$ in SM Categories (eμ)
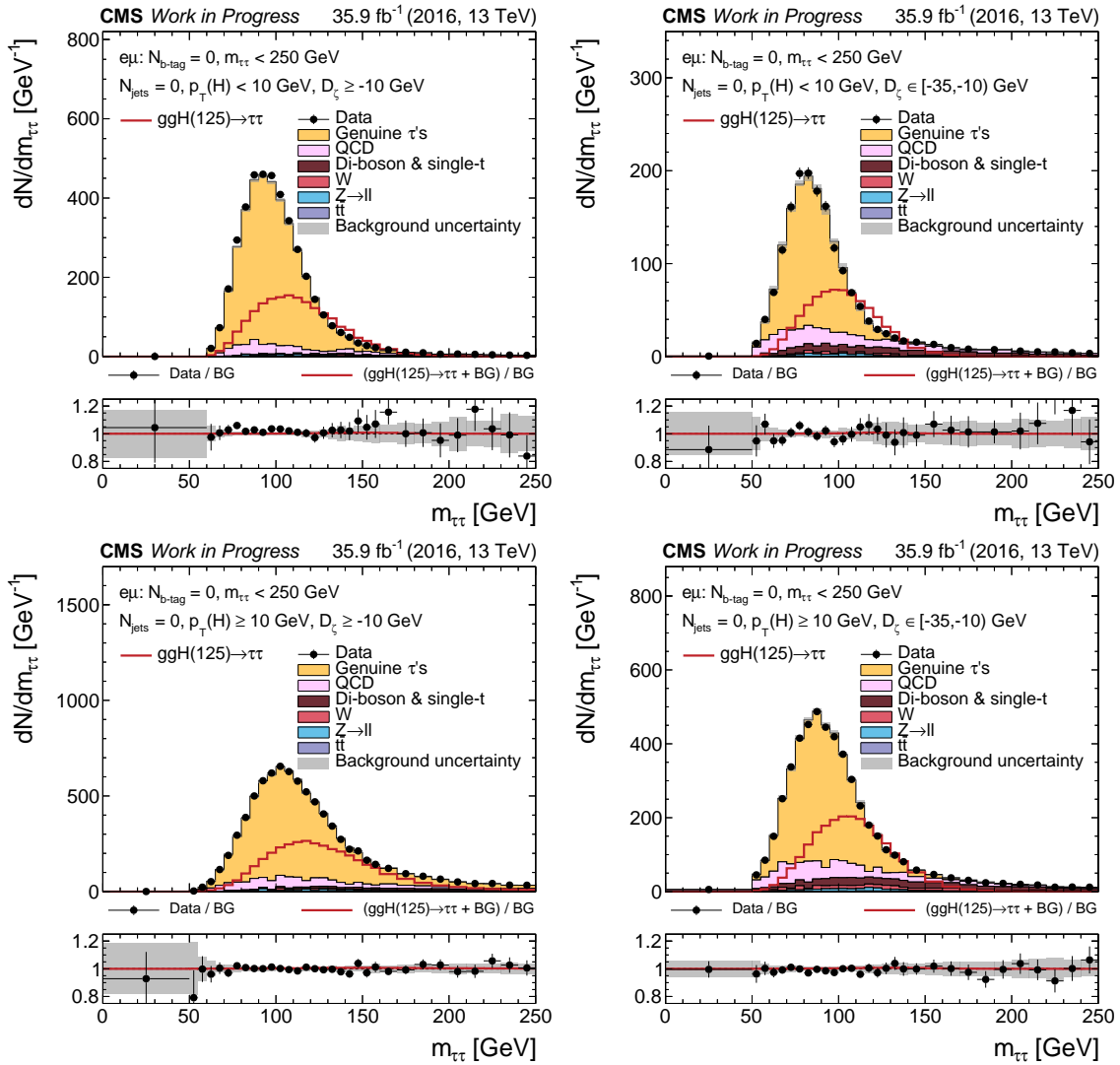
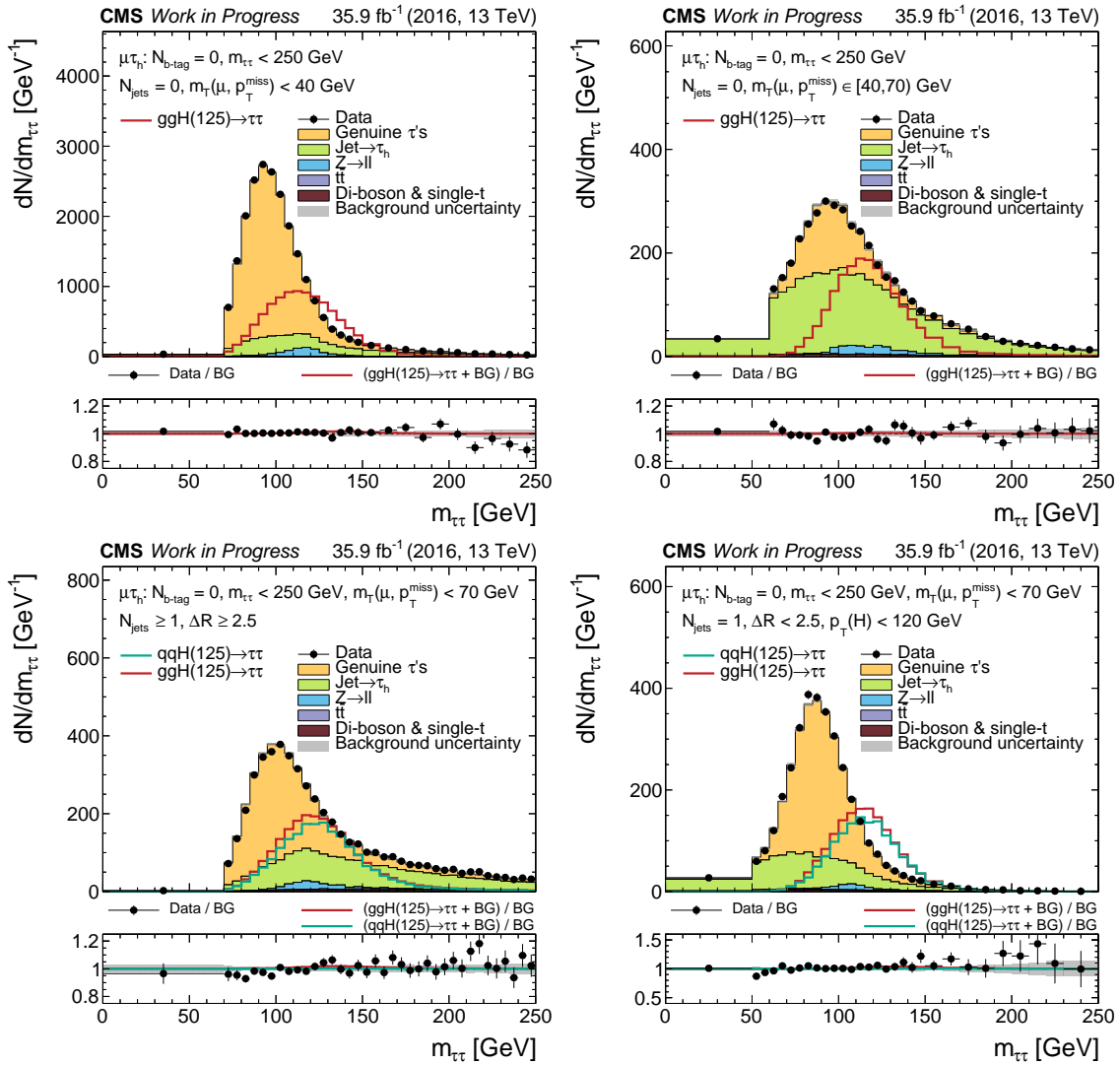Figure A.10.: Distributions of $m_{\tau\tau}$ for the eμ final state. Expected SM H $\rightarrow \tau\tau$ signal, rescaled for shape comparison in the upper panels, is shown with data and stacked background (BG). Grey uncertainty bands illustrate the total BG uncertainty after a maximum likelihood fit for signal strength μ. In the lower panel, SM H $\rightarrow \tau\tau$ is scaled to SM expectation.
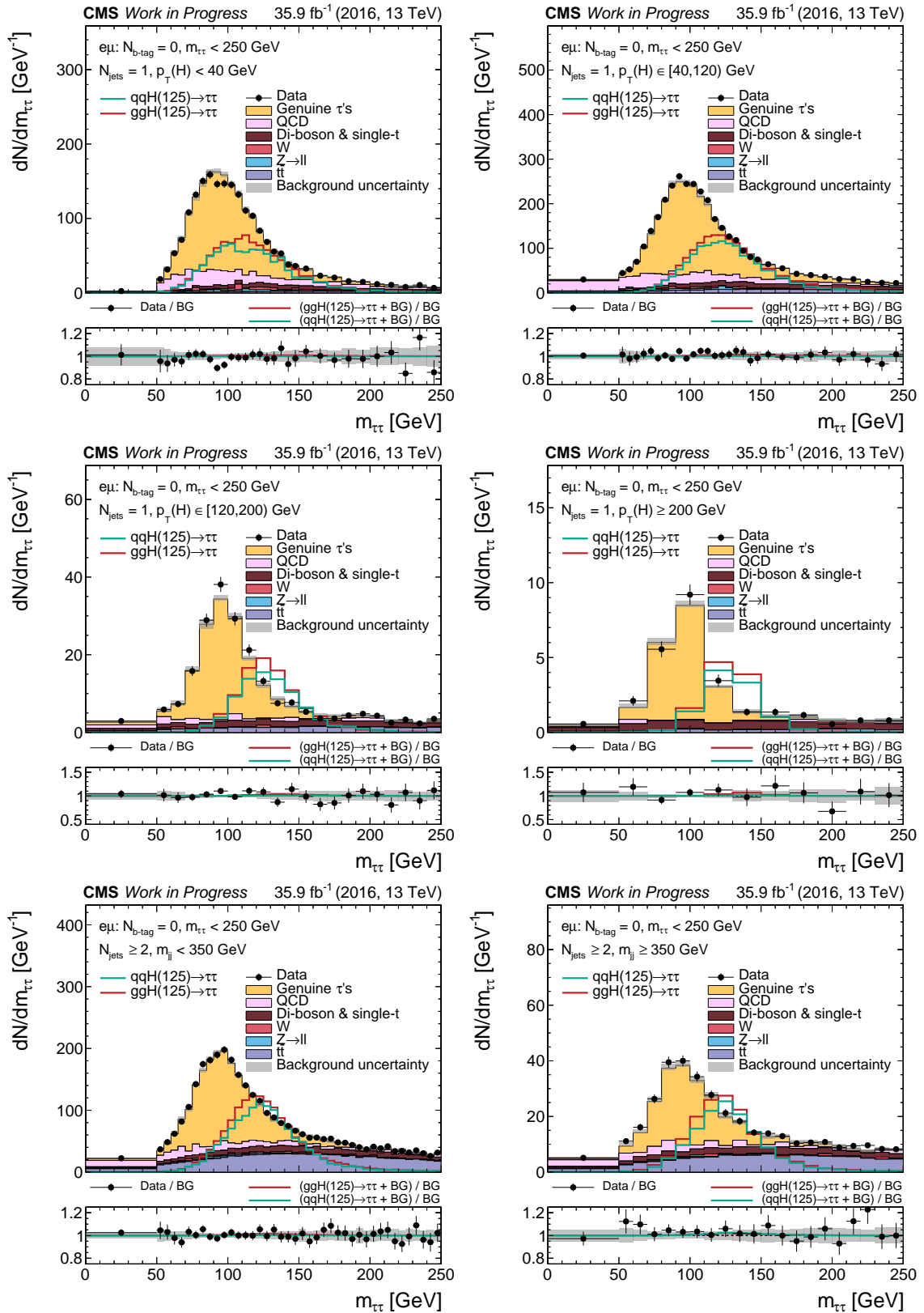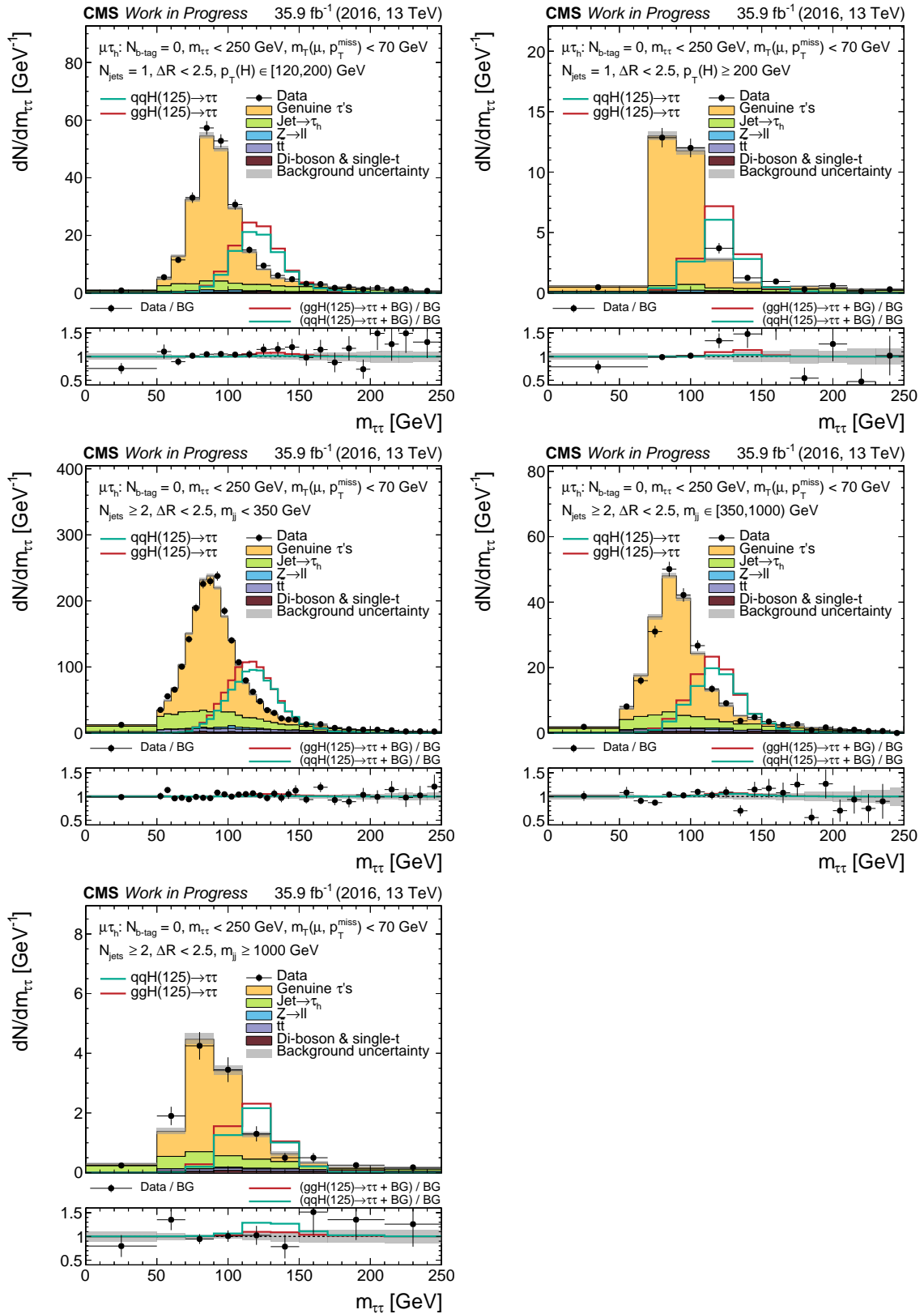
Figure A.11.: Distributions of $m_{\tau\tau}$ for the eμ final state. Expected SM H → ττ signal, rescaled for shape comparison in the upper panels, is shown with data and stacked background (BG). Grey uncertainty bands illustrate the total BG uncertainty after a maximum likelihood fit for signal strength μ. In the lower panel, SM H → ττ is scaled to SM expectation.
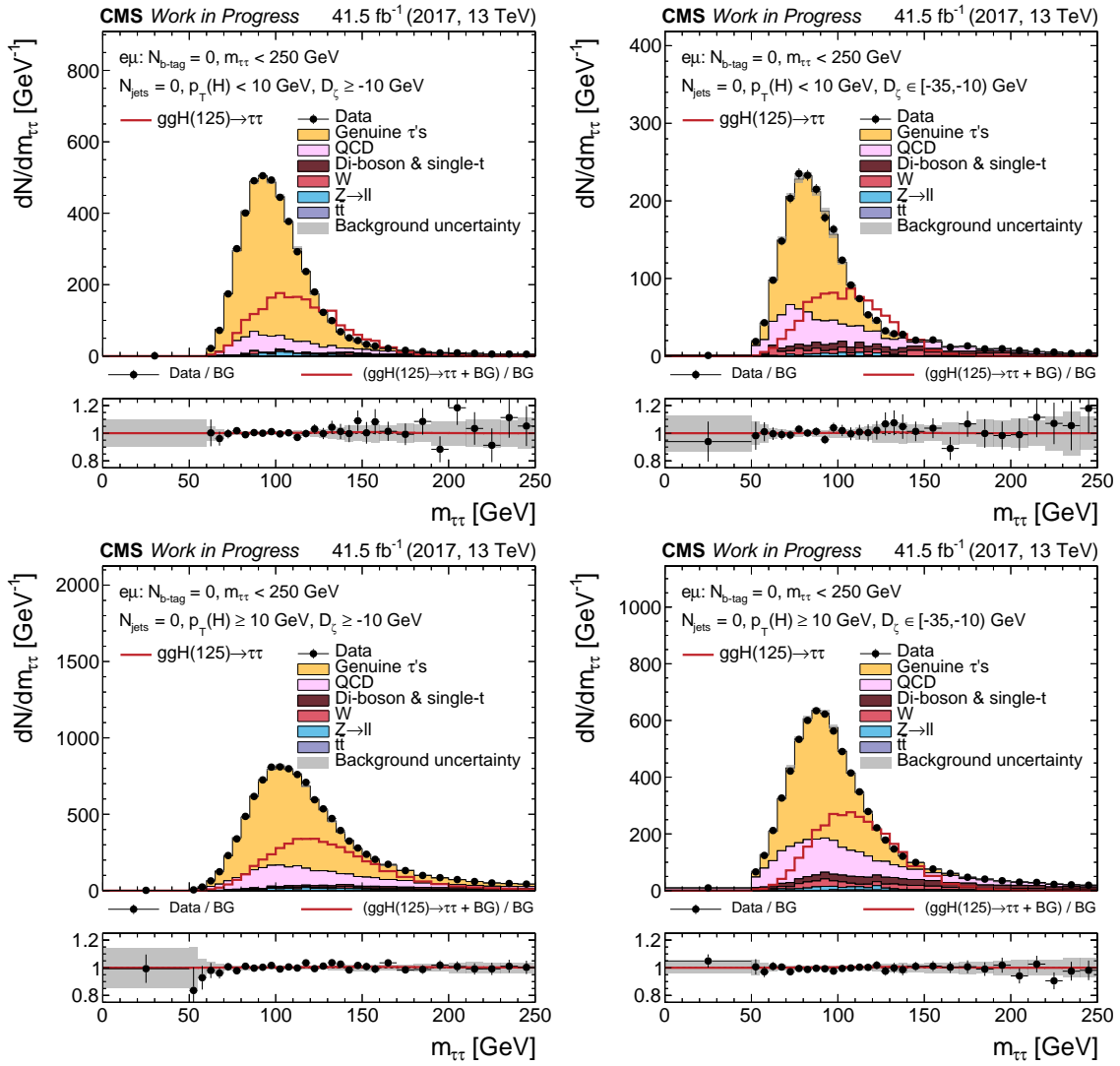
Figure A.12.: Distributions of $m_{\tau\tau}$ for the eμ final state. Expected SM H → ττ signal, rescaled for shape comparison in the upper panels, is shown with data and stacked background (BG). Grey uncertainty bands illustrate the total BG uncertainty after a maximum likelihood fit for signal strength μ. In the lower panel, SM H → ττ is scaled to SM expectation.
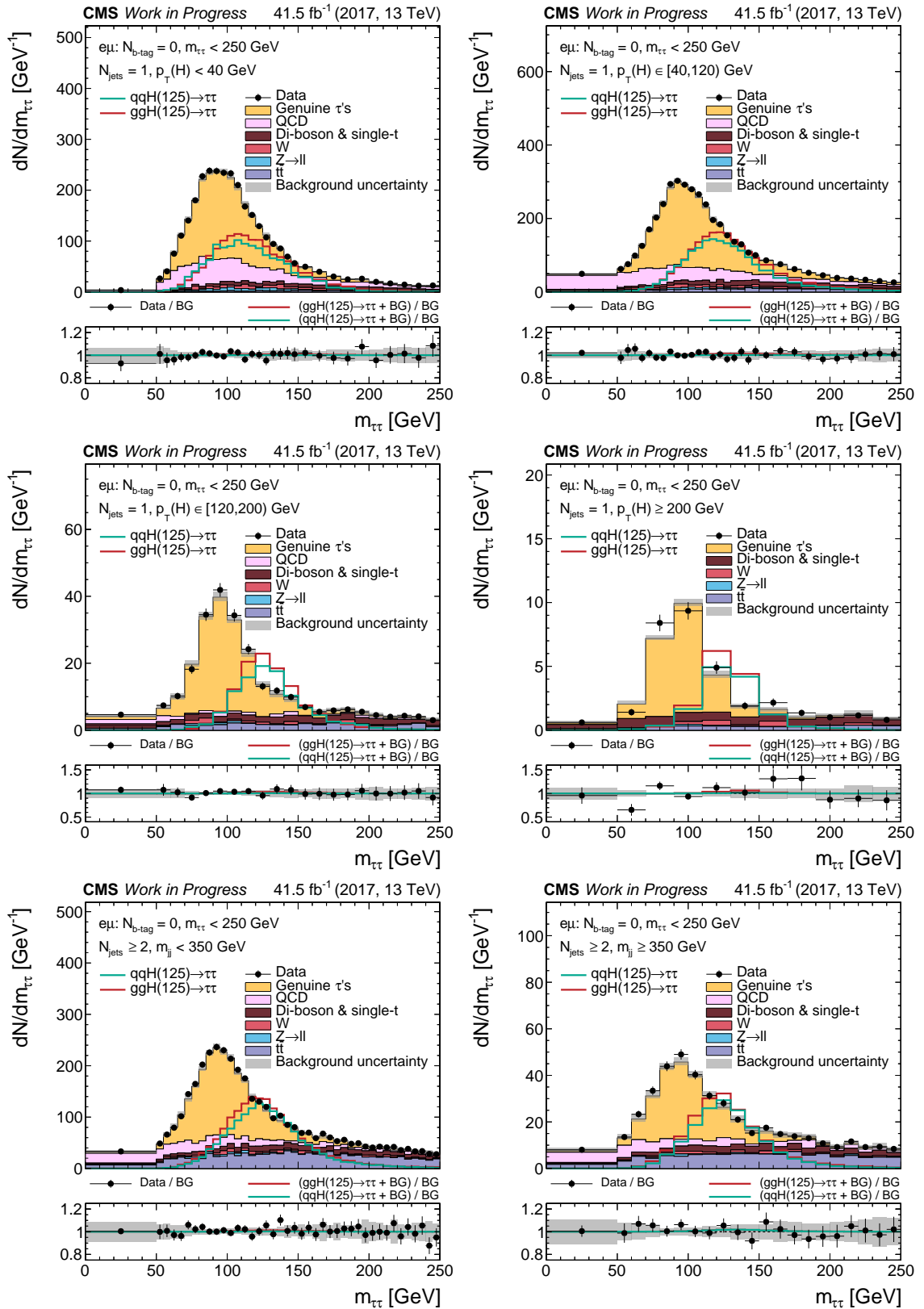
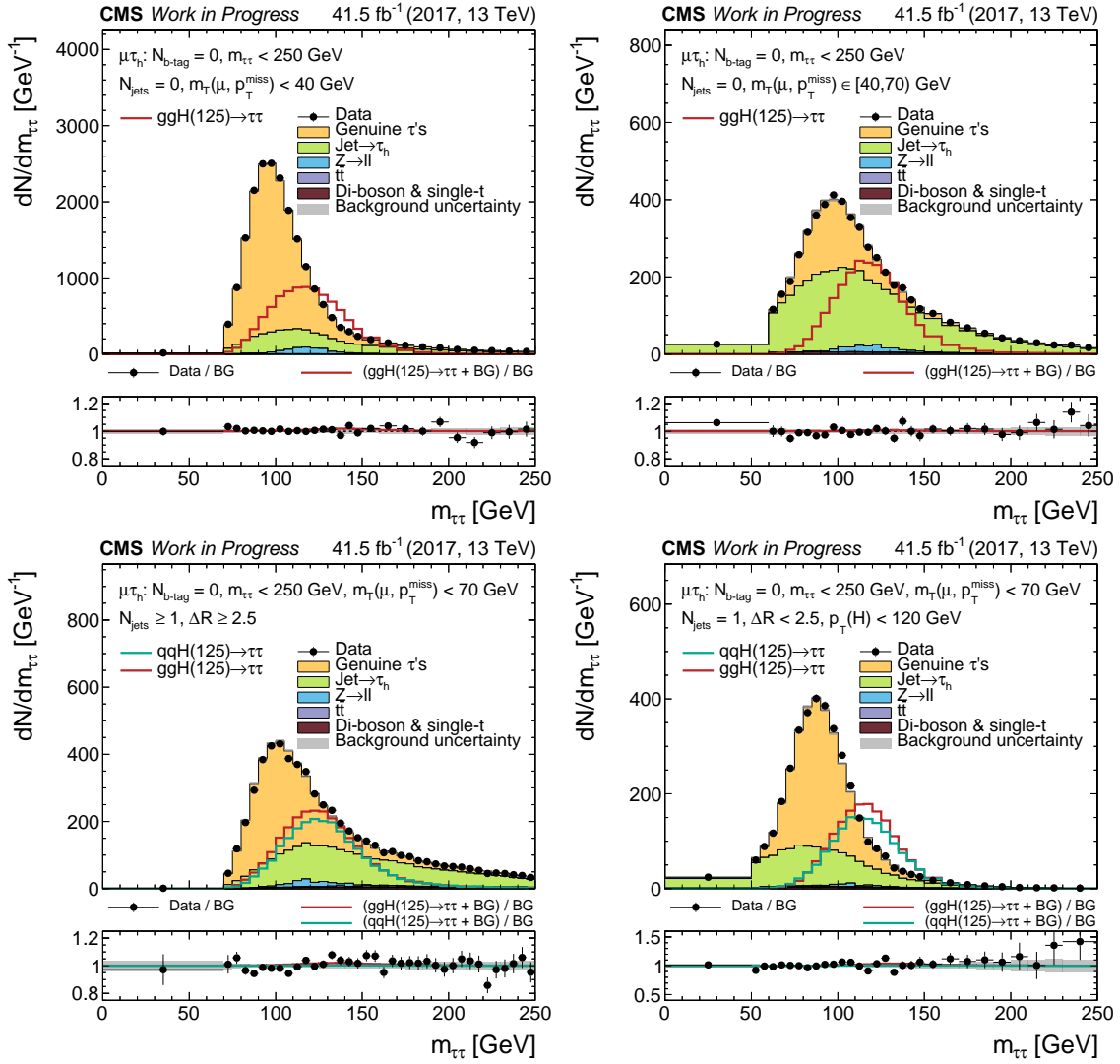Figure A.13.: Distributions of $m_{\tau\tau}$ for the eμ final state. Expected SM H → ττ signal, rescaled for shape comparison in the upper panels, is shown with data and stacked background (BG). Grey uncertainty bands illustrate the total BG uncertainty after a maximum likelihood fit for signal strength μ. In the lower panel, SM H → ττ is scaled to SM expectation.
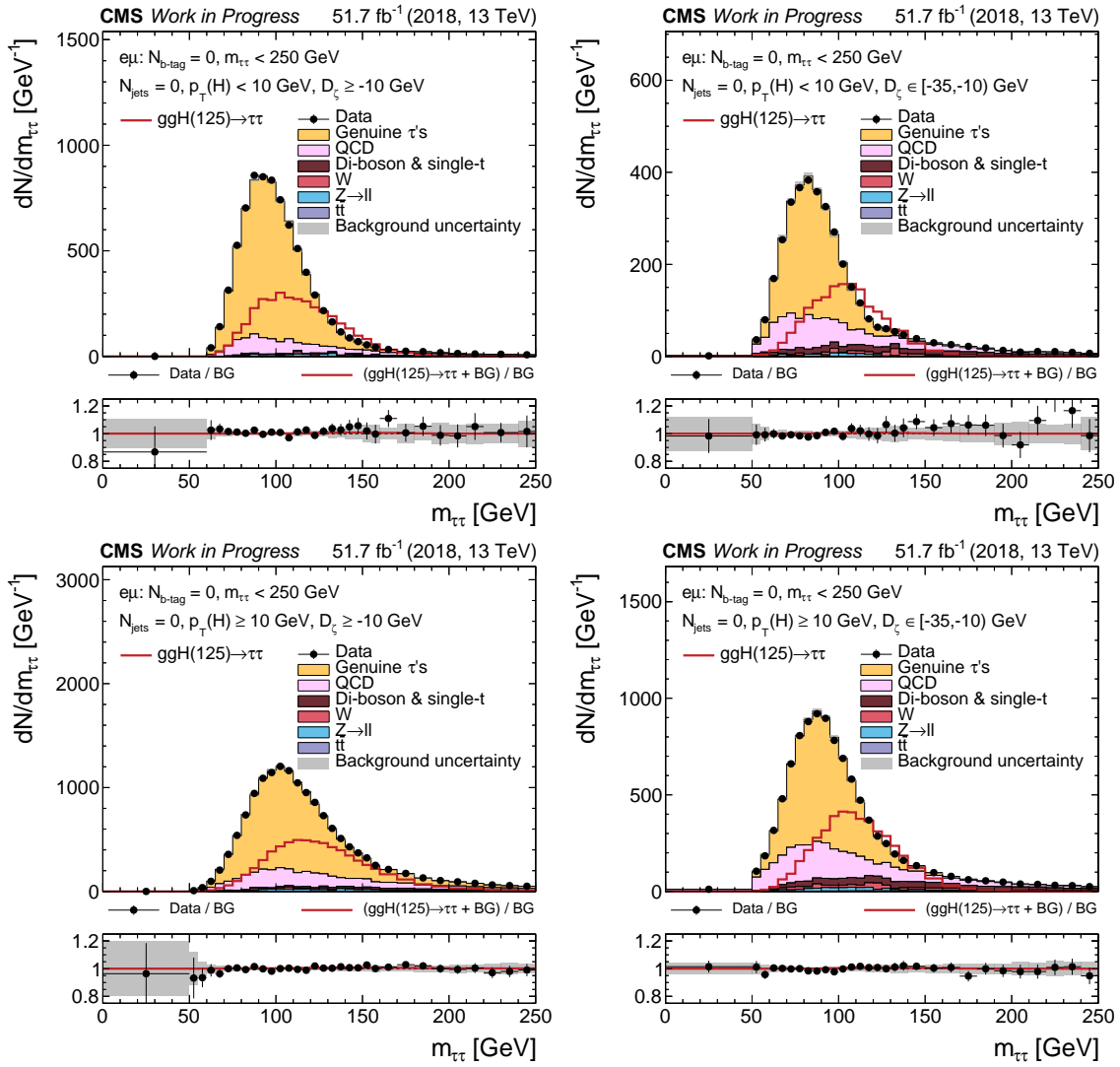
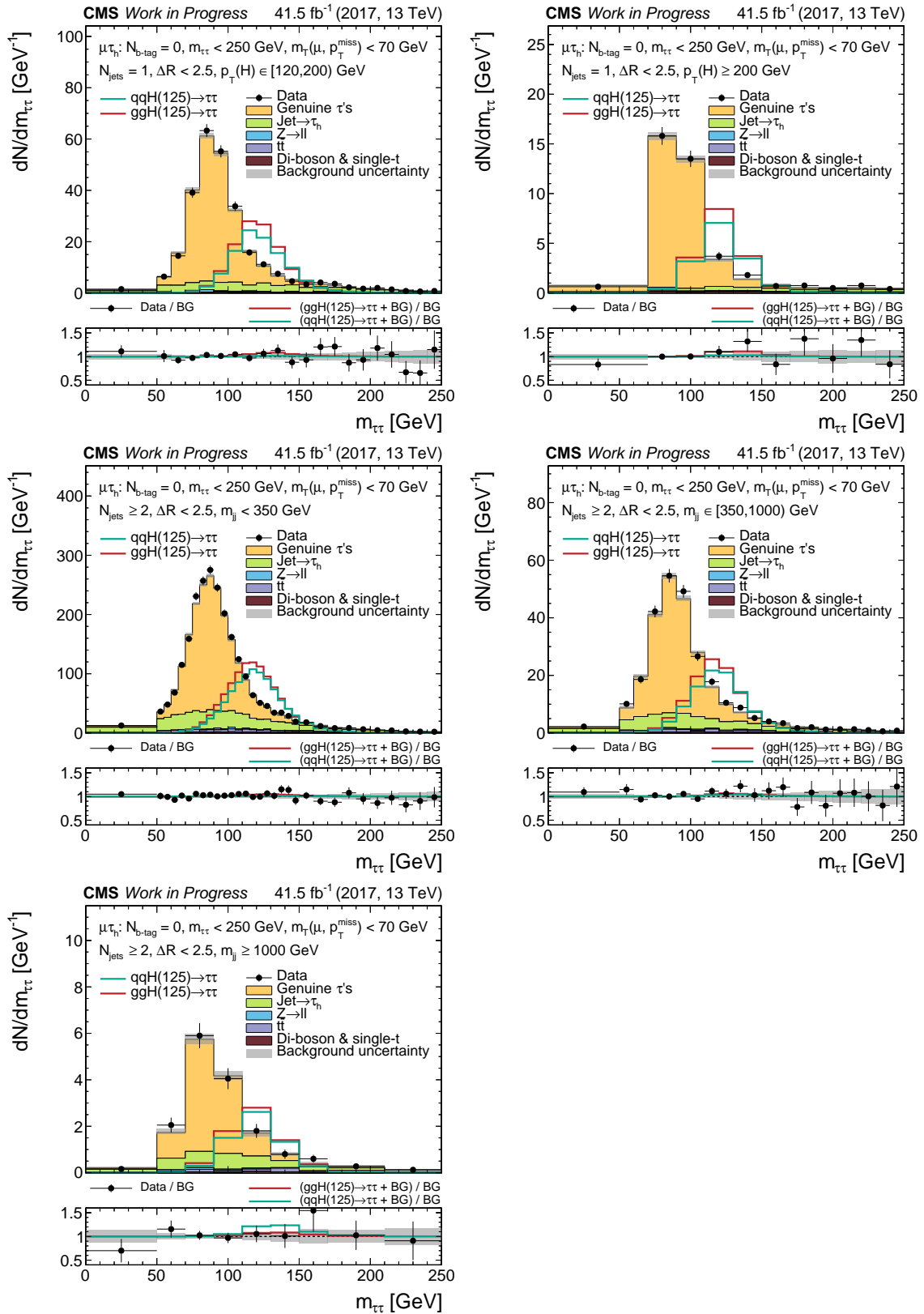Figure A.14.: Distributions of $m_{\tau\tau}$ for the eμ final state. Expected SM H → ττ signal, rescaled for shape comparison in the upper panels, is shown with data and stacked background (BG). Grey uncertainty bands illustrate the total BG uncertainty after a maximum likelihood fit for signal strength μ. In the lower panel, SM H → ττ is scaled to SM expectation.
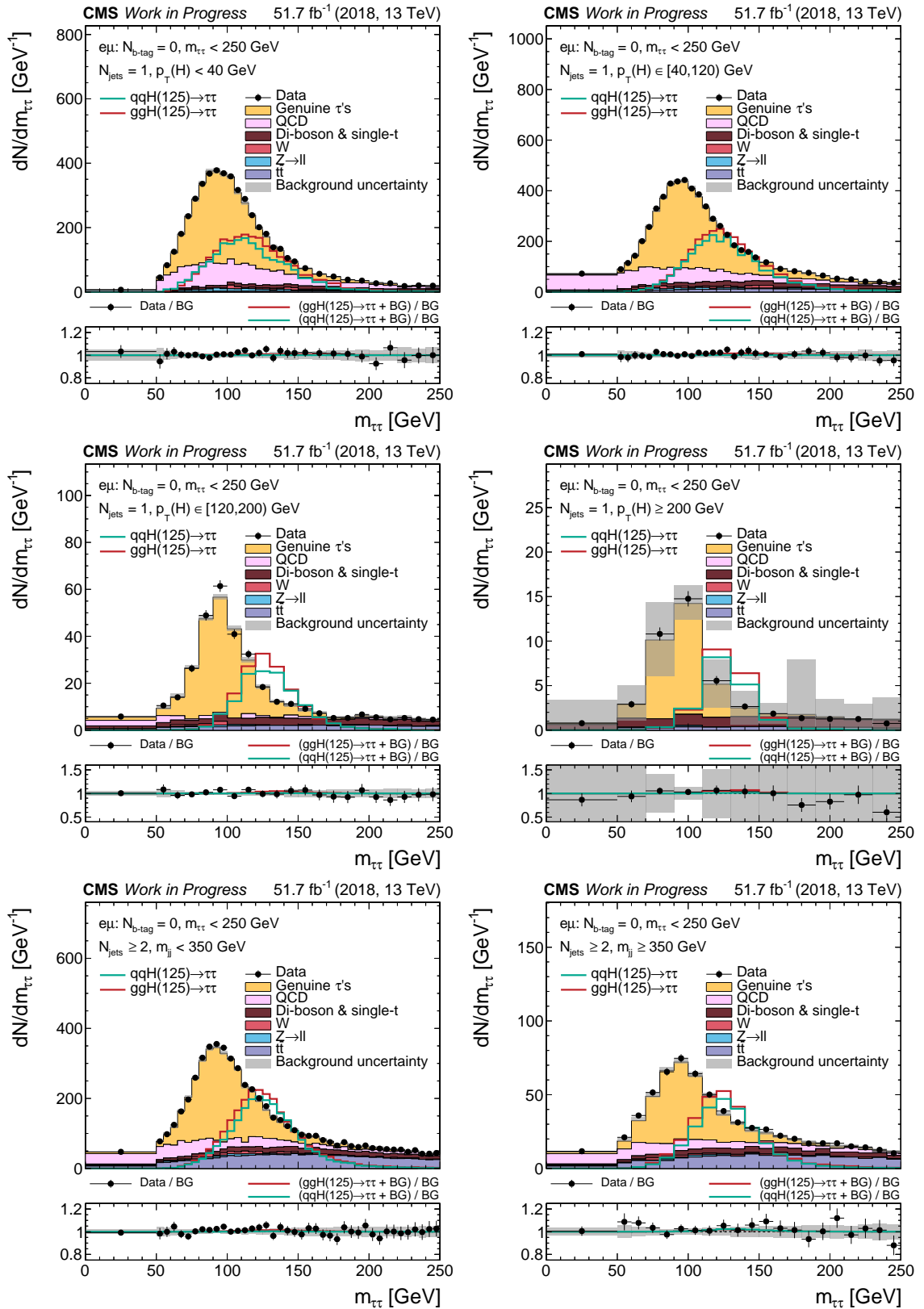
Figure A.15.: Distributions of $m_{\tau\tau}$ for the eμ final state. Expected SM H → ττ signal, rescaled for shape comparison in the upper panels, is shown with data and stacked background (BG). Grey uncertainty bands illustrate the total BG uncertainty after a maximum likelihood fit for signal strength μ. In the lower panel, SM H → ττ is scaled to SM expectation.
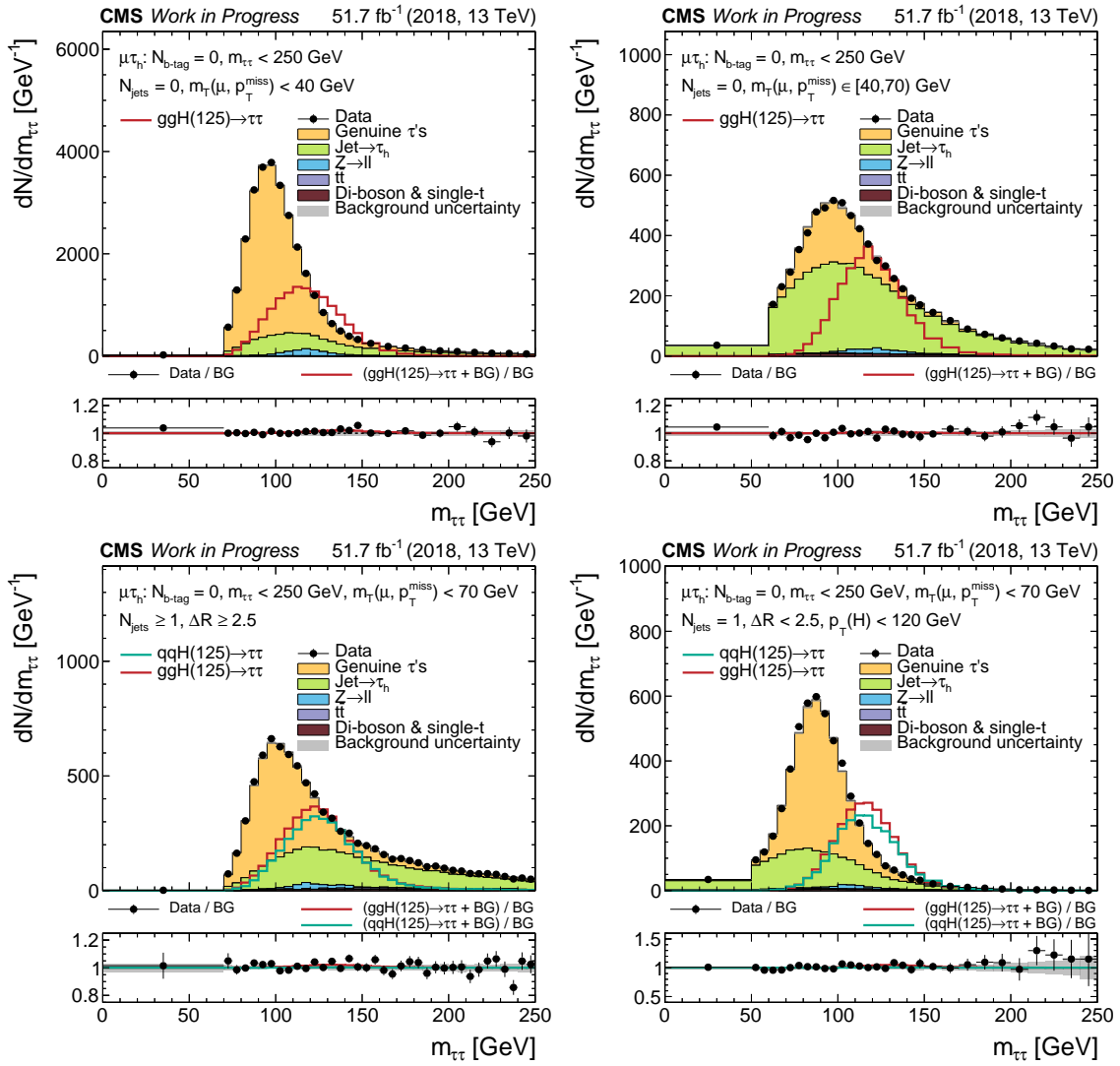
A.4. $m_{\tau\tau}$ in SM Categories ($e\tau_h$)
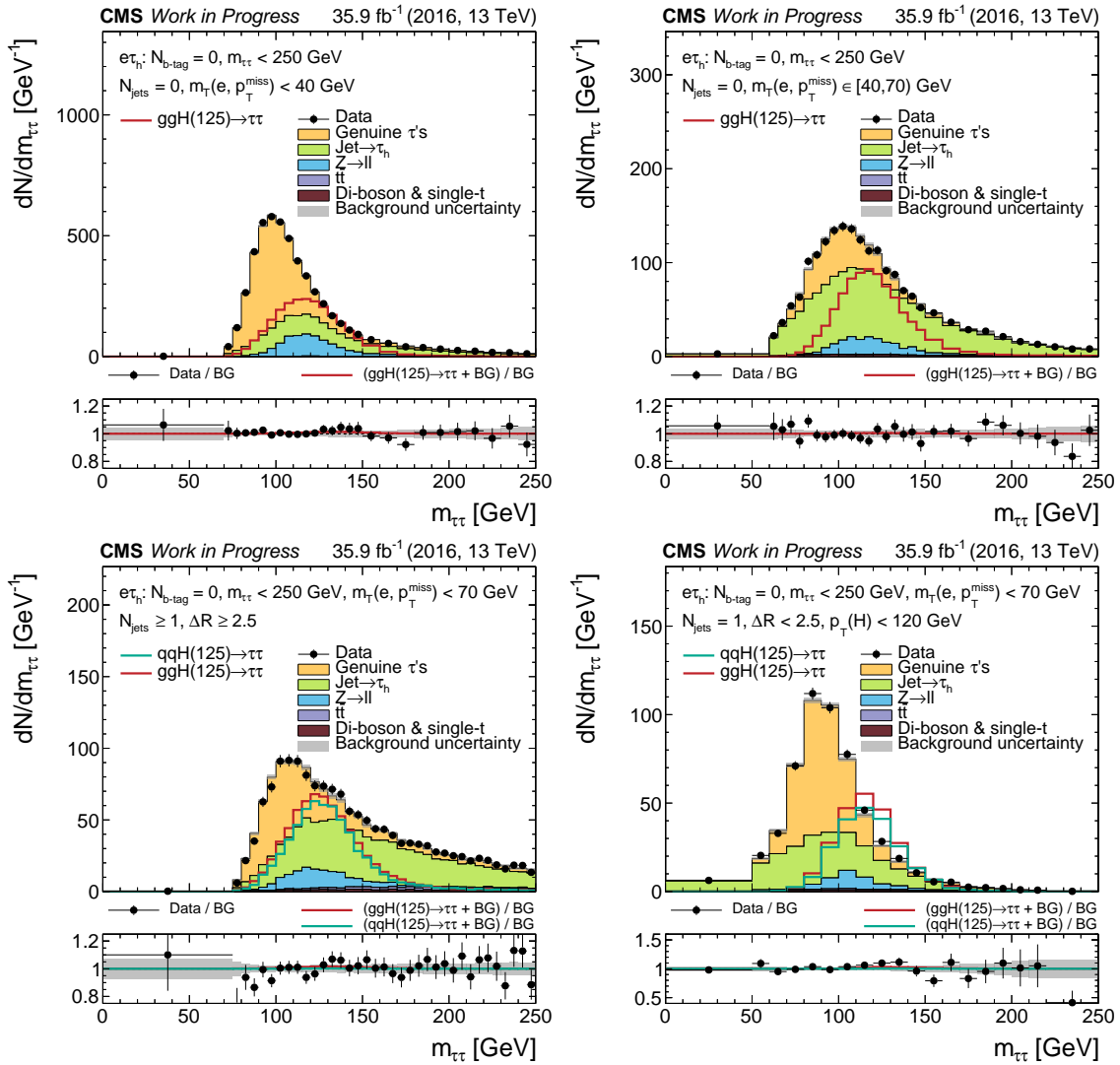
Figure A.16.: Distributions of $m_{\tau\tau}$ for the $e\tau_h$ final state. Expected SM H $\to \tau\tau$ signal, rescaled for shape comparison in the upper panels, is shown with data and stacked background (BG). Grey uncertainty bands illustrate the total BG uncertainty after a maximum likelihood fit for signal strength μ. In the lower panel, SM H $\to \tau\tau$ is scaled to SM expectation.
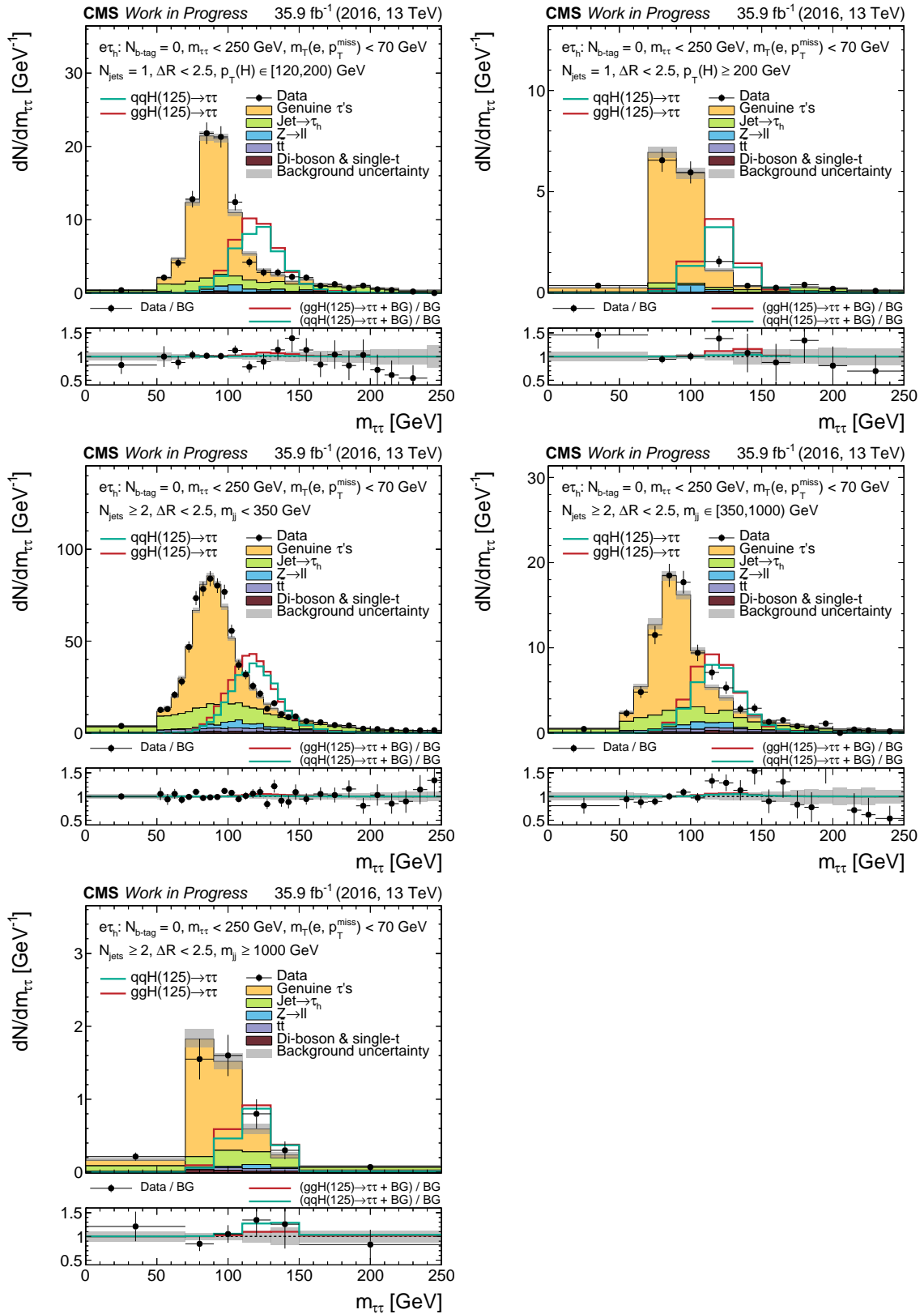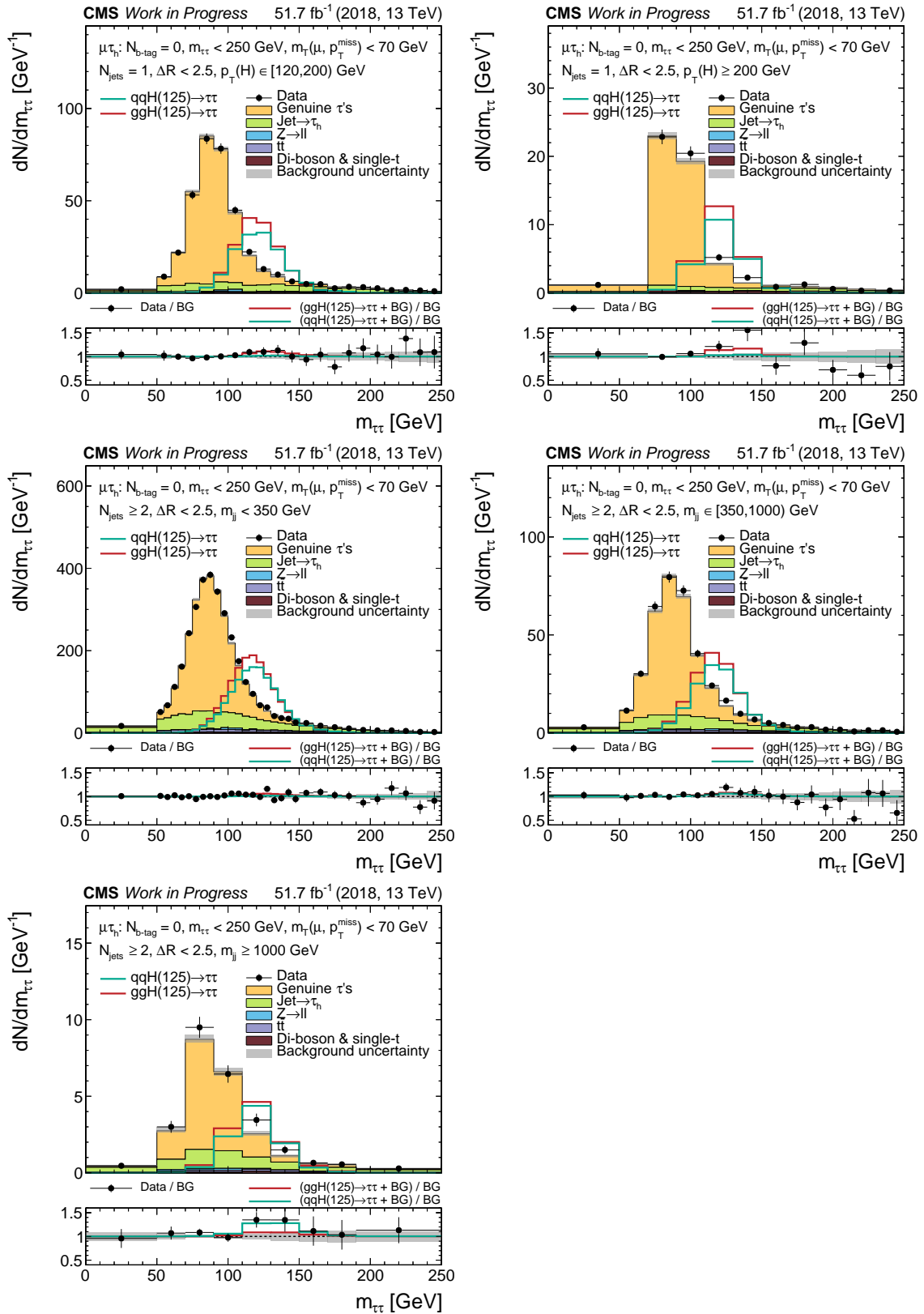
Figure A.17.: Distributions of $m_{\tau\tau}$ for the $e\tau_h$ final state. Expected SM $H \to \tau\tau$ signal, rescaled for shape comparison in the upper panels, is shown with data and stacked background (BG). Grey uncertainty bands illustrate the total BG uncertainty after a maximum likelihood fit for signal strength μ. In the lower panel, SM $H \to \tau\tau$ is scaled to SM expectation.
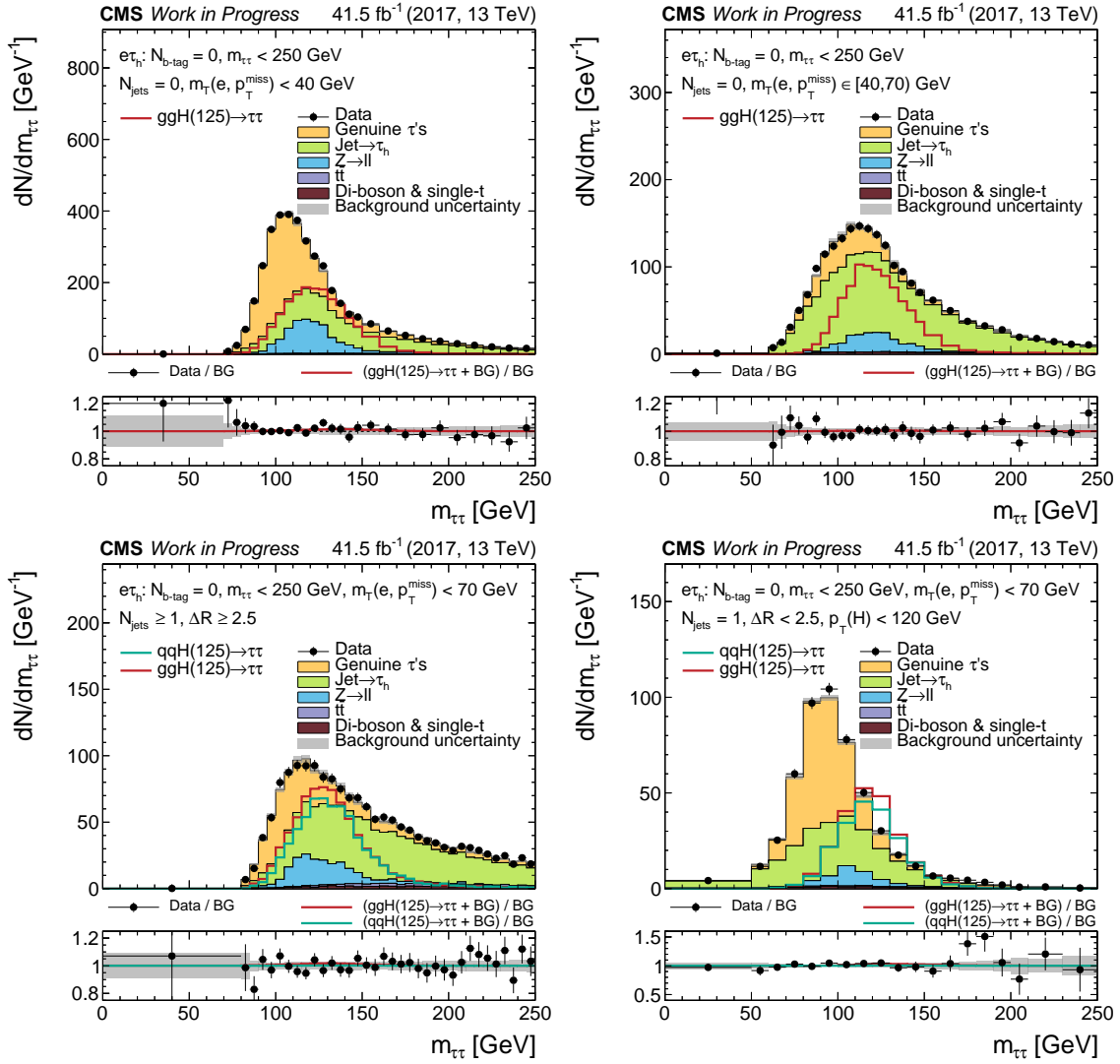
Figure A.18.: Distributions of $m_{\tau\tau}$ for the $e\tau_h$ final state. Expected SM $H \to \tau\tau$ signal, rescaled for shape comparison in the upper panels, is shown with data and stacked background (BG). Grey uncertainty bands illustrate the total BG uncertainty after a maximum likelihood fit for signal strength μ. In the lower panel, SM $H \to \tau\tau$ is scaled to SM expectation.
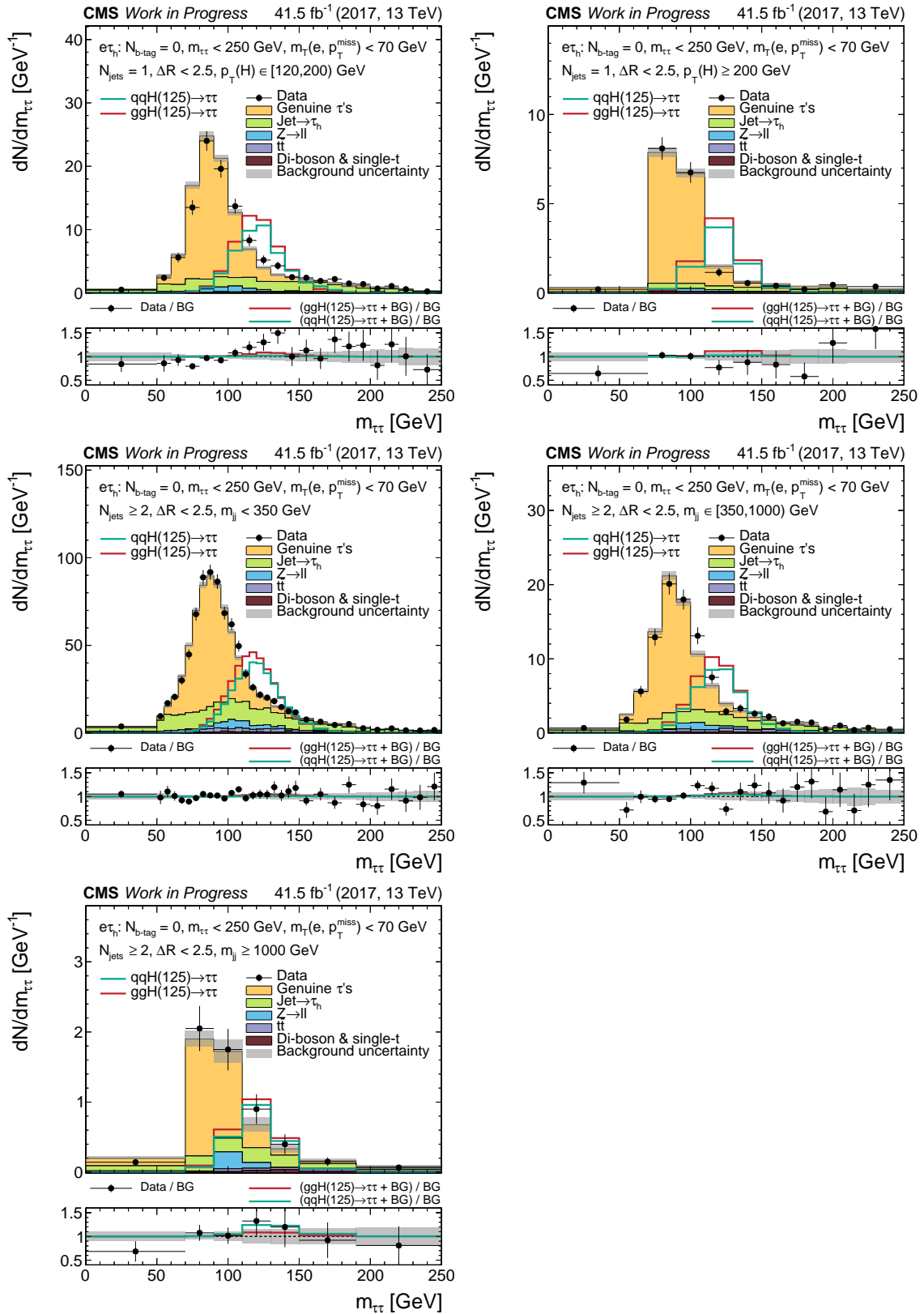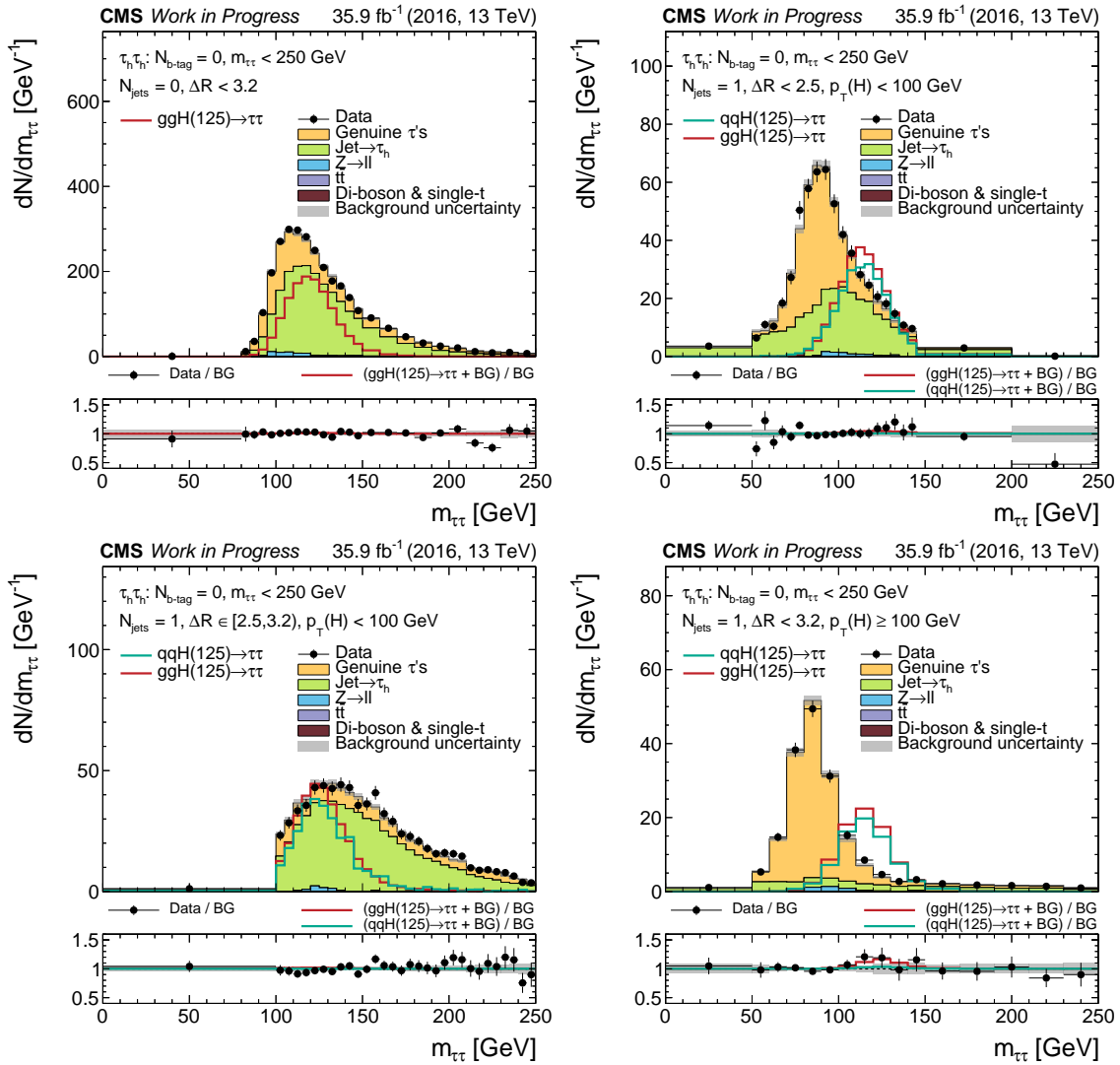
Figure A.19.: Distributions of $m_{\tau\tau}$ for the $e\tau_h$ final state. Expected SM H $\rightarrow \tau\tau$ signal, rescaled for shape comparison in the upper panels, is shown with data and stacked background (BG). Grey uncertainty bands illustrate the total BG uncertainty after a maximum likelihood fit for signal strength μ. In the lower panel, SM H $\rightarrow \tau\tau$ is scaled to SM expectation.
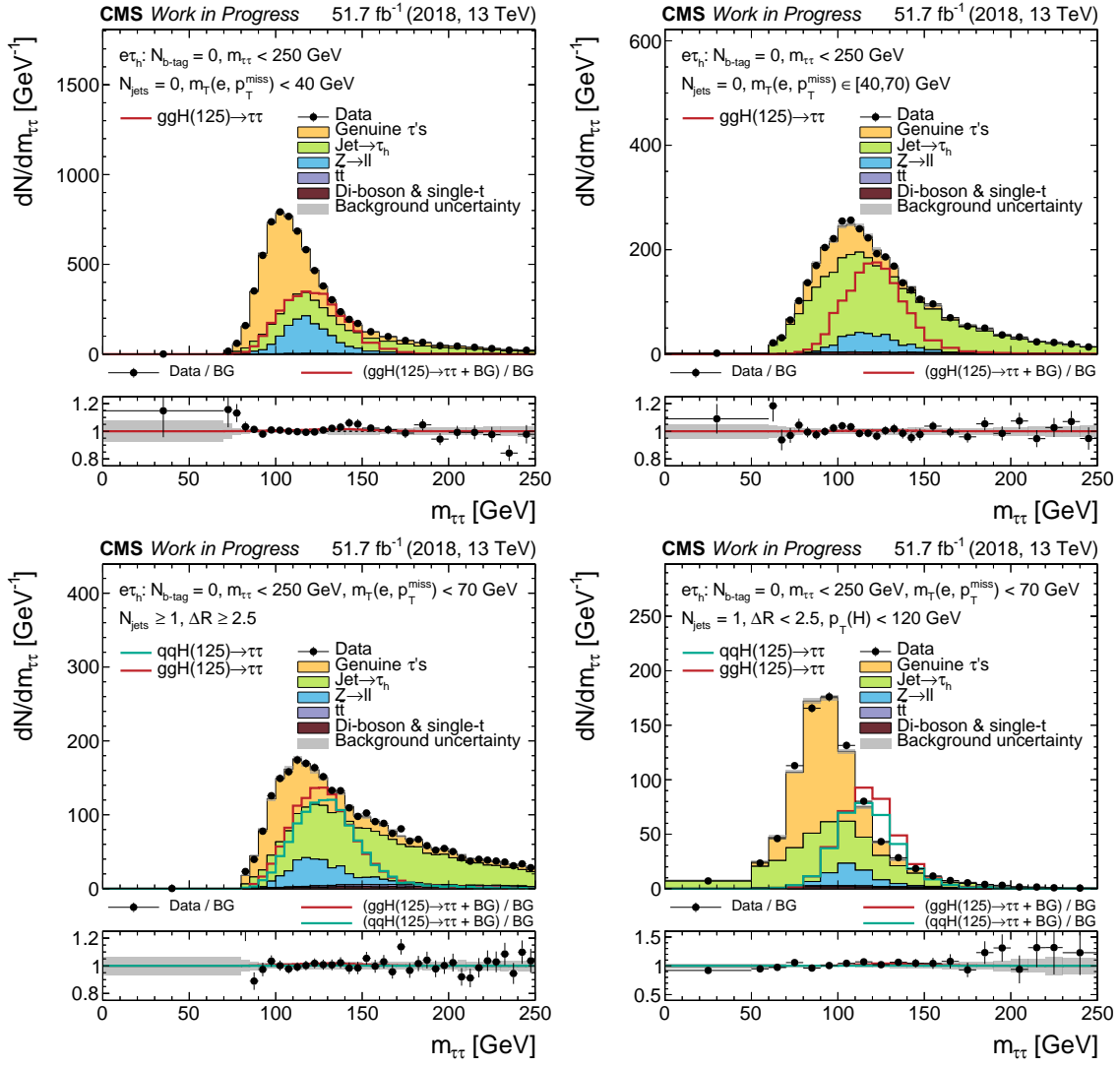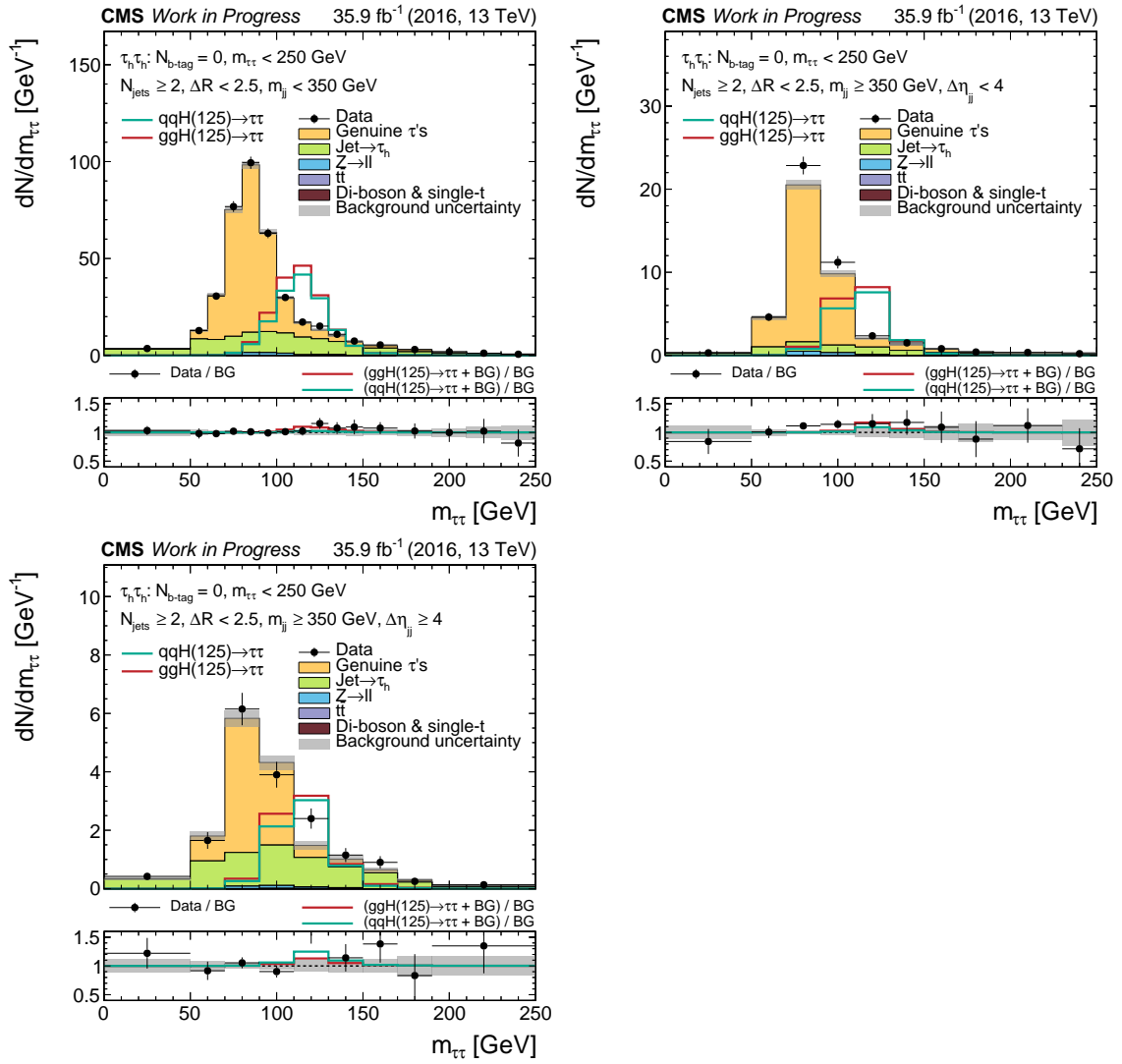
Figure A.20.: Distributions of $m_{\tau\tau}$ for the $e\tau_h$ final state. Expected SM $H \to \tau\tau$ signal, rescaled for shape comparison in the upper panels, is shown with data and stacked background (BG). Grey uncertainty bands illustrate the total BG uncertainty after a maximum likelihood fit for signal strength μ. In the lower panel, SM $H \to \tau\tau$ is scaled to SM expectation.
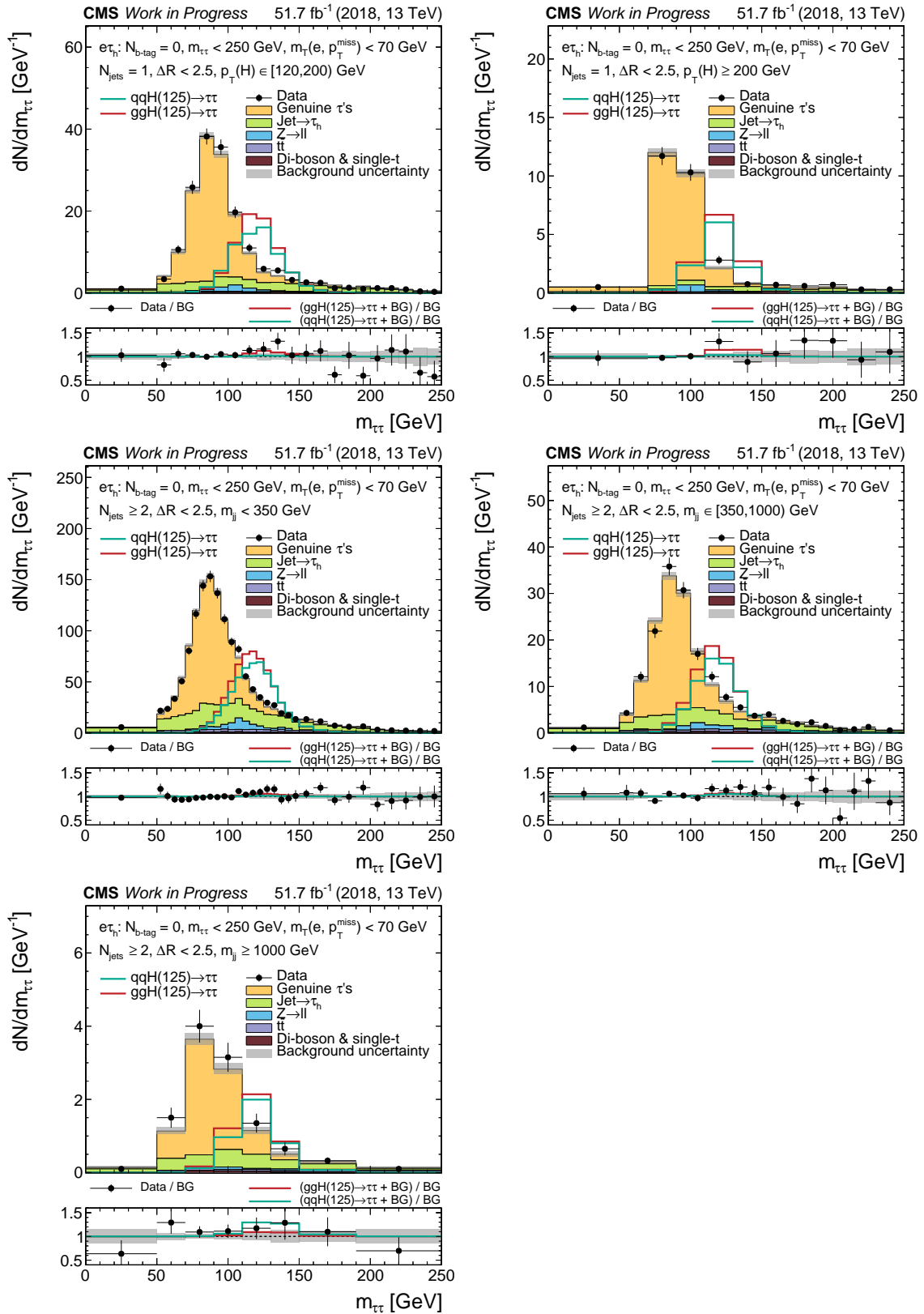
Figure A.21.: Distributions of $m_{\tau\tau}$ for the $e\tau_h$ final state. Expected SM $H \to \tau\tau$ signal, rescaled for shape comparison in the upper panels, is shown with data and stacked background (BG). Grey uncertainty bands illustrate the total BG uncertainty after a maximum likelihood fit for signal strength μ. In the lower panel, SM $H \to \tau\tau$ is scaled to SM expectation.

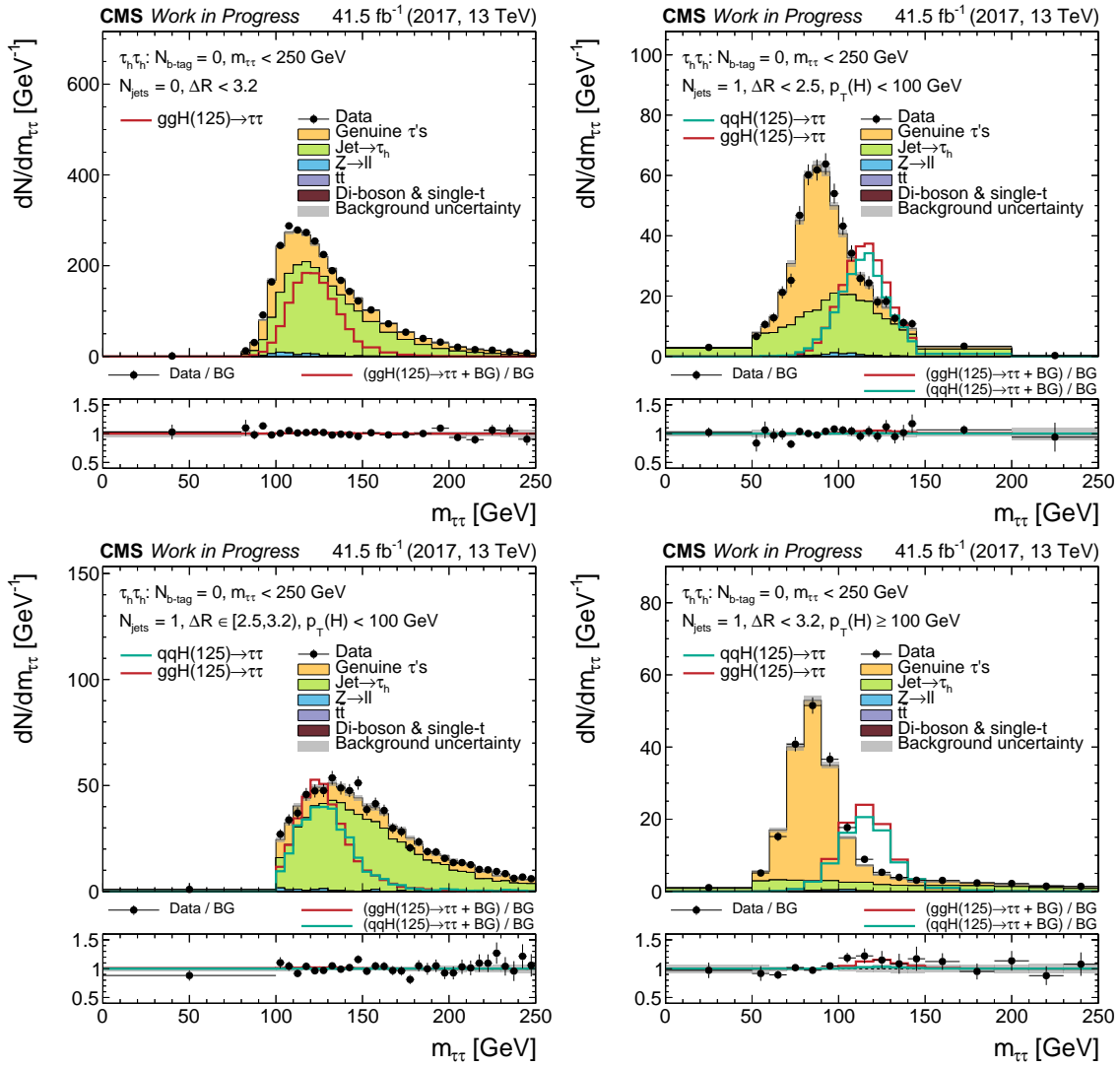## A.5. $m_{\tau\tau}$ in SM Categories ($\mu\tau_{\mathbf{h}}$)

Figure A.22.: Distributions of $m_{\tau\tau}$ for the $\mu\tau_h$ final state. Expected SM H $\to \tau\tau$ signal, rescaled for shape comparison in the upper panels, is shown with data and stacked background (BG). Grey uncertainty bands illustrate the total BG uncertainty after a maximum likelihood fit for signal strength μ. In the lower panel, SM H $\to \tau\tau$ is scaled to SM expectation.
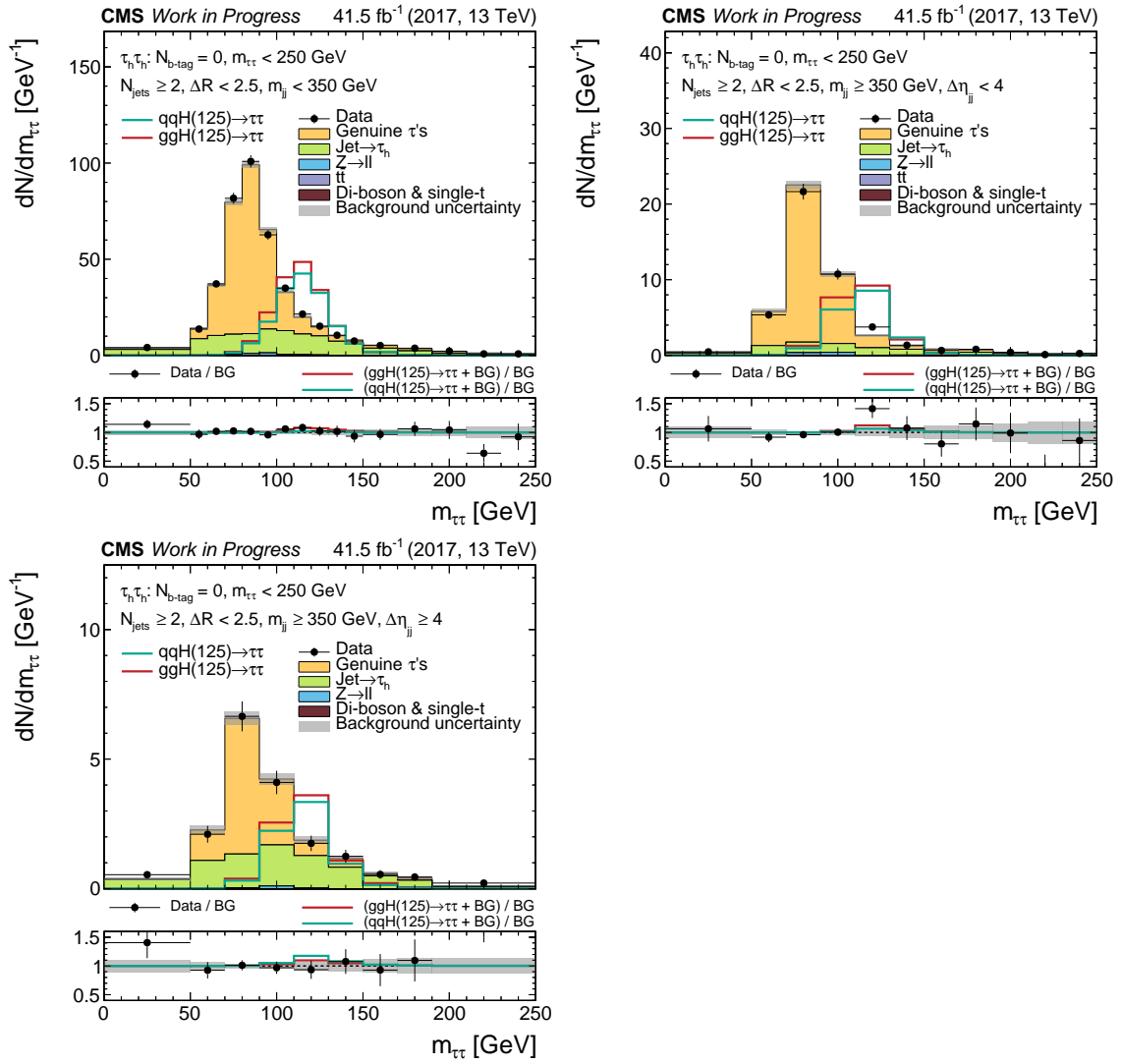
Figure A.23.: Distributions of $m_{\tau\tau}$ for the $\mu\tau_h$ final state. Expected SM H $\to \tau\tau$ signal, rescaled for shape comparison in the upper panels, is shown with data and stacked background (BG). Grey uncertainty bands illustrate the total BG uncertainty after a maximum likelihood fit for signal strength μ. In the lower panel, SM H $\to \tau\tau$ is scaled to SM expectation.
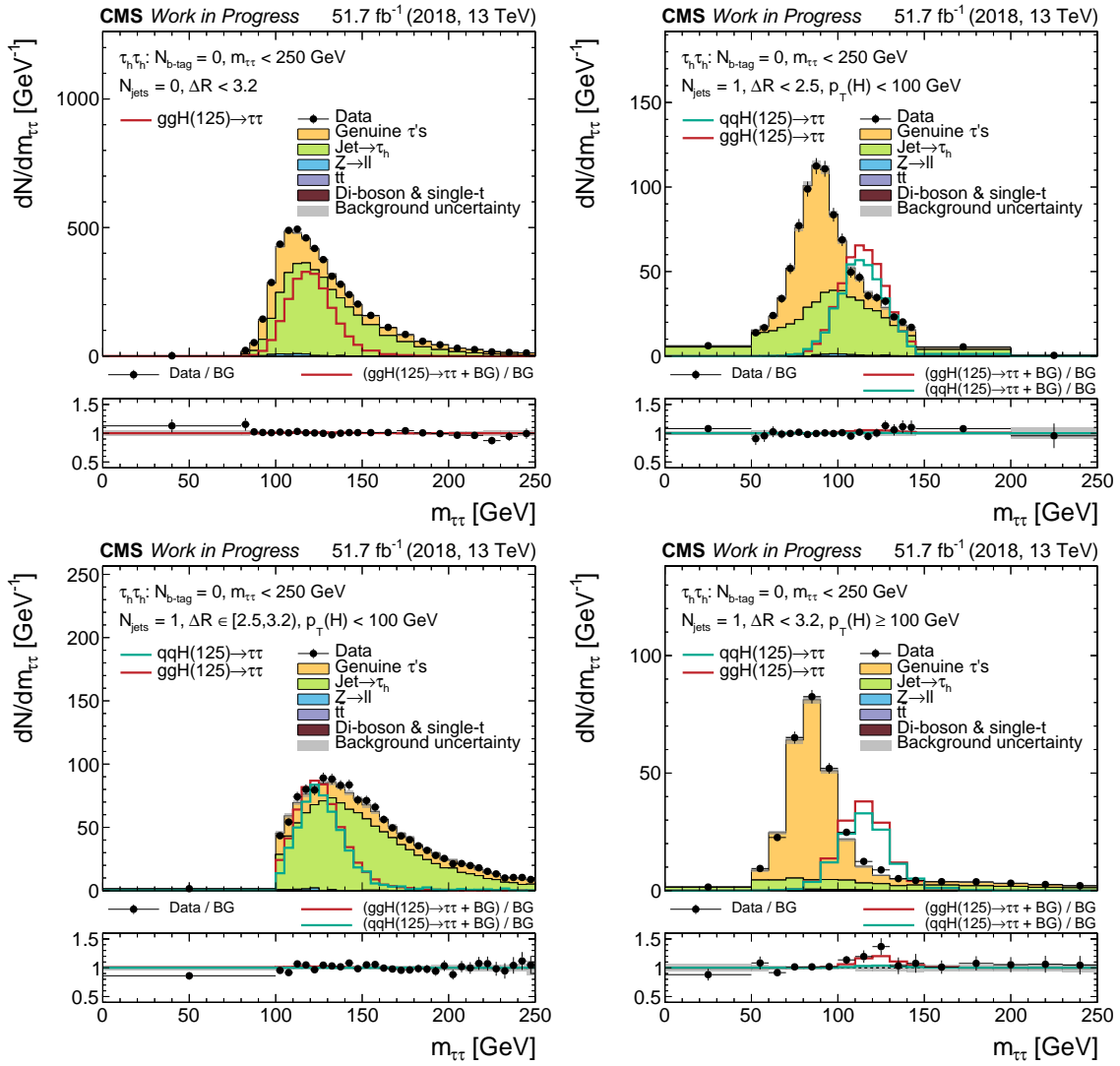
Figure A.24.: Distributions of $m_{\tau\tau}$ for the $\mu\tau_h$ final state. Expected SM $H \to \tau\tau$ signal, rescaled for shape comparison in the upper panels, is shown with data and stacked background (BG). Grey uncertainty bands illustrate the total BG uncertainty after a maximum likelihood fit for signal strength μ. In the lower panel, SM $H \to \tau\tau$ is scaled to SM expectation.

Figure A.25.: Distributions of $m_{\tau\tau}$ for the $\mu\tau_h$ final state. Expected SM $H \to \tau\tau$ signal, rescaled for shape comparison in the upper panels, is shown with data and stacked background (BG). Grey uncertainty bands illustrate the total BG uncertainty after a maximum likelihood fit for signal strength μ. In the lower panel, SM $H \to \tau\tau$ is scaled to SM expectation.
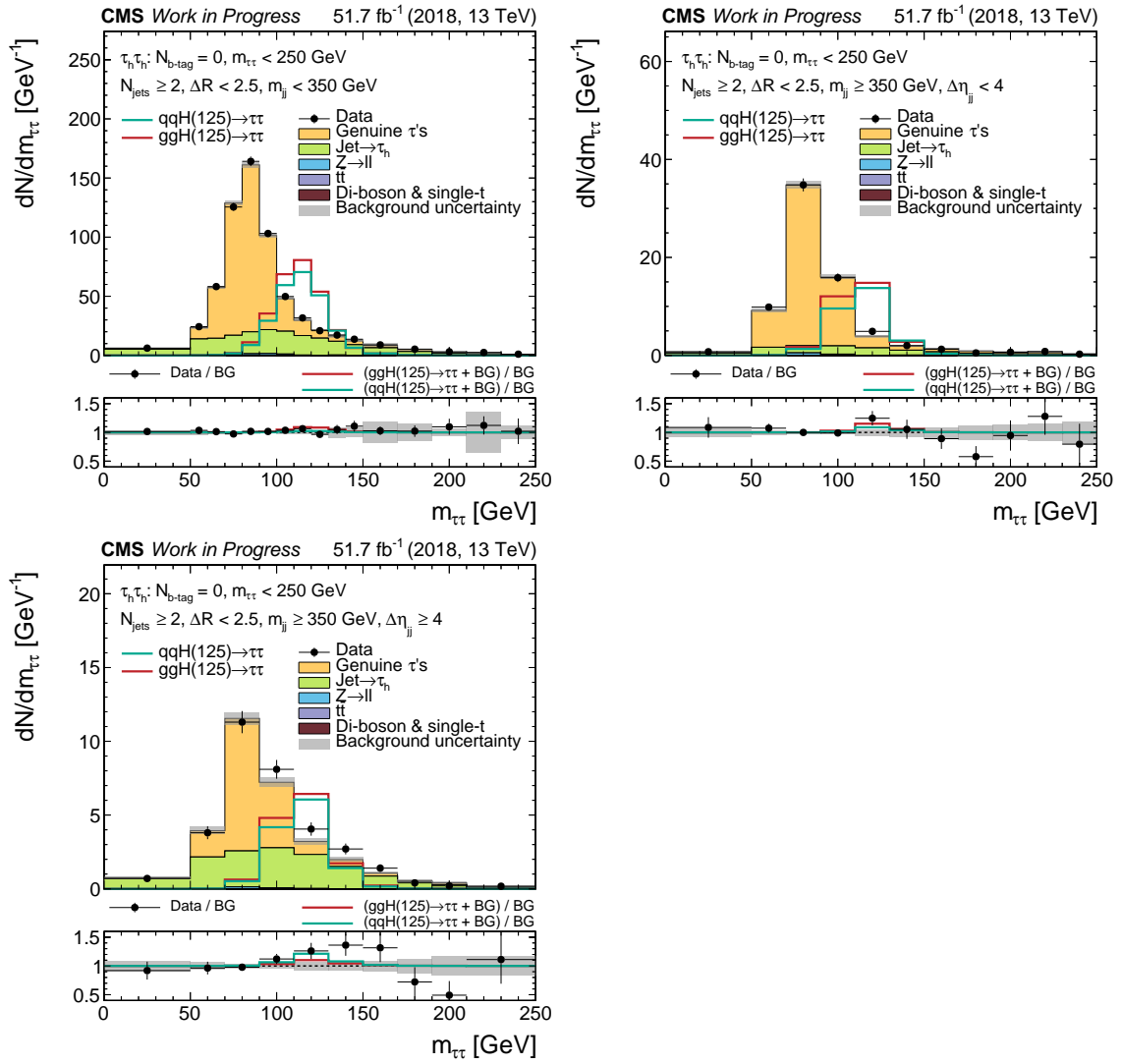
Figure A.26.: Distributions of $m_{\tau\tau}$ for the $\mu\tau_h$ final state. Expected SM H → $\tau\tau$ signal, rescaled for shape comparison in the upper panels, is shown with data and stacked background (BG). Grey uncertainty bands illustrate the total BG uncertainty after a maximum likelihood fit for signal strength μ. In the lower panel, SM H → $\tau\tau$ is scaled to SM expectation.

Figure A.27.: Distributions of $m_{\tau\tau}$ for the $\mu\tau_h$ final state. Expected SM $H \to \tau\tau$ signal, rescaled for shape comparison in the upper panels, is shown with data and stacked background (BG). Grey uncertainty bands illustrate the total BG uncertainty after a maximum likelihood fit for signal strength μ. In the lower panel, SM $H \to \tau\tau$ is scaled to SM expectation.

A.6. $m_{\tau\tau}$ in SM Categories ($\tau_h\tau_h$)

Figure A.28.: Distributions of $m_{\tau\tau}$ for the $\tau_h\tau_h$ final state. Expected SM H $\rightarrow \tau\tau$ signal, rescaled for shape comparison in the upper panels, is shown with data and stacked background (BG). Grey uncertainty bands illustrate the total BG uncertainty after a maximum likelihood fit for signal strength μ. In the lower panel, SM H $\rightarrow \tau\tau$ is scaled to SM expectation.

Figure A.29.: Distributions of $m_{\tau\tau}$ for the $\tau_h\tau_h$ final state. Expected SM H $\to \tau\tau$ signal, rescaled for shape comparison in the upper panels, is shown with data and stacked background (BG). Grey uncertainty bands illustrate the total BG uncertainty after a maximum likelihood fit for signal strength μ. In the lower panel, SM H $\to \tau\tau$ is scaled to SM expectation.

Figure A.30.: Distributions of $m_{\tau\tau}$ for the $\tau_h\tau_h$ final state. Expected SM H $\rightarrow \tau\tau$ signal, rescaled for shape comparison in the upper panels, is shown with data and stacked background (BG). Grey uncertainty bands illustrate the total BG uncertainty after a maximum likelihood fit for signal strength μ. In the lower panel, SM H $\rightarrow \tau\tau$ is scaled to SM expectation.

Figure A.31.: Distributions of $m_{\tau\tau}$ for the $\tau_h\tau_h$ final state. Expected SM H $\to \tau\tau$ signal, rescaled for shape comparison in the upper panels, is shown with data and stacked background (BG). Grey uncertainty bands illustrate the total BG uncertainty after a maximum likelihood fit for signal strength μ. In the lower panel, SM H $\to \tau\tau$ is scaled to SM expectation.

Figure A.32.: Distributions of $m_{\tau\tau}$ for the $\tau_h\tau_h$ final state. Expected SM H $\rightarrow \tau\tau$ signal, rescaled for shape comparison in the upper panels, is shown with data and stacked background (BG). Grey uncertainty bands illustrate the total BG uncertainty after a maximum likelihood fit for signal strength μ. In the lower panel, SM H $\rightarrow \tau\tau$ is scaled to SM expectation.

Figure A.33.: Distributions of $m_{\tau\tau}$ for the $\tau_h\tau_h$ final state. Expected SM $H \to \tau\tau$ signal, rescaled for shape comparison in the upper panels, is shown with data and stacked background (BG). Grey uncertainty bands illustrate the total BG uncertainty after a maximum likelihood fit for signal strength μ. In the lower panel, SM $H \to \tau\tau$ is scaled to SM expectation.

A.7. m_T^{tot} in BSM Categories (eμ)
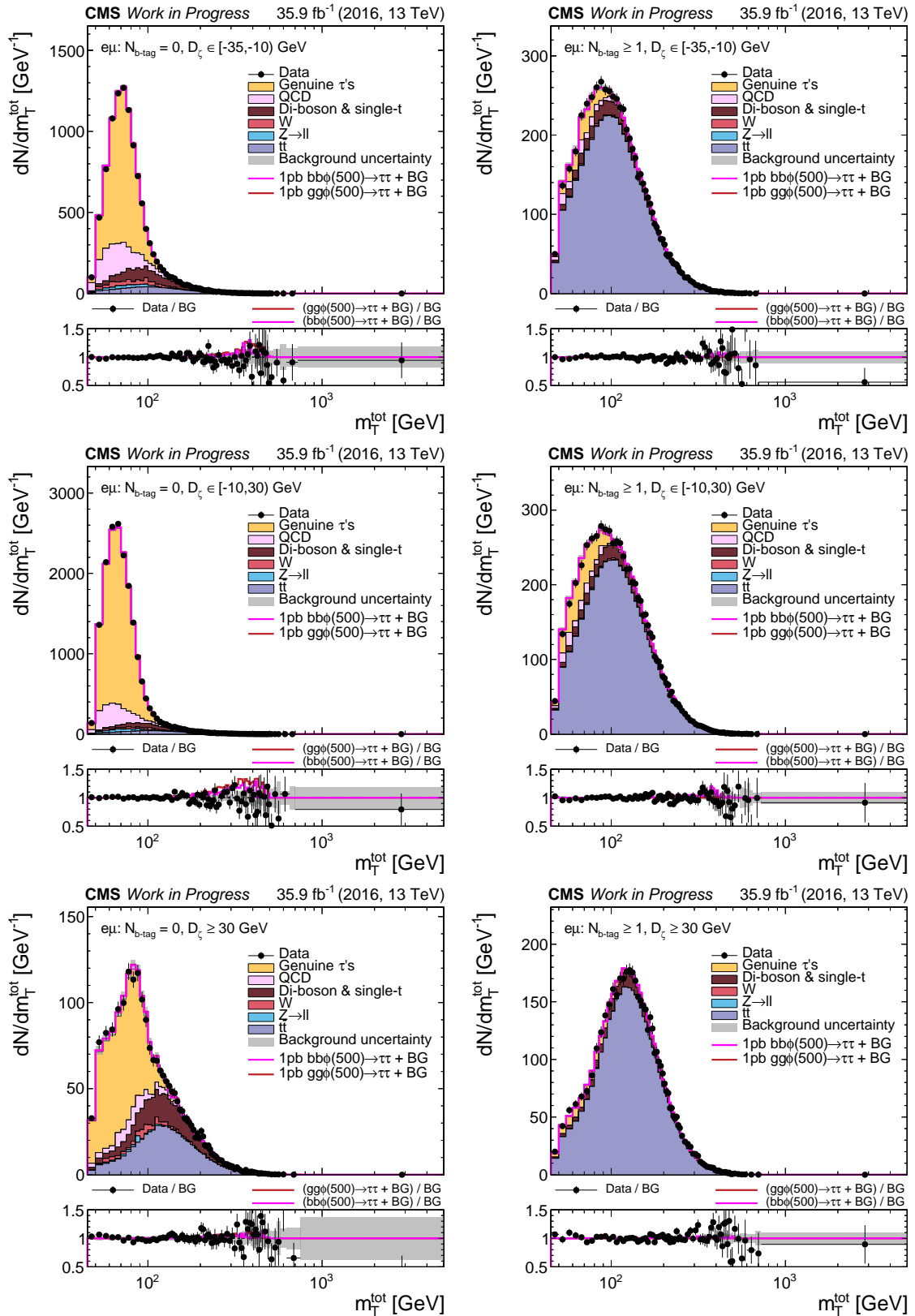
Figure A.34.: Distributions of m_T^{tot} in the BSM categories of the eµ final state. Stacked expected background (BG) and BSM signals ggφ and bbφ with $m_\phi = 500$ GeV and $\sigma \cdot BR = 1$ pb on top of BG are compared with data. Grey uncertainty bands illustrate the total BG uncertainty after a maximum likelihood fit for $\mu_{gg\phi}$ and $\mu_{bb\phi}$. In the lower panels, the ratio to BG is shown.
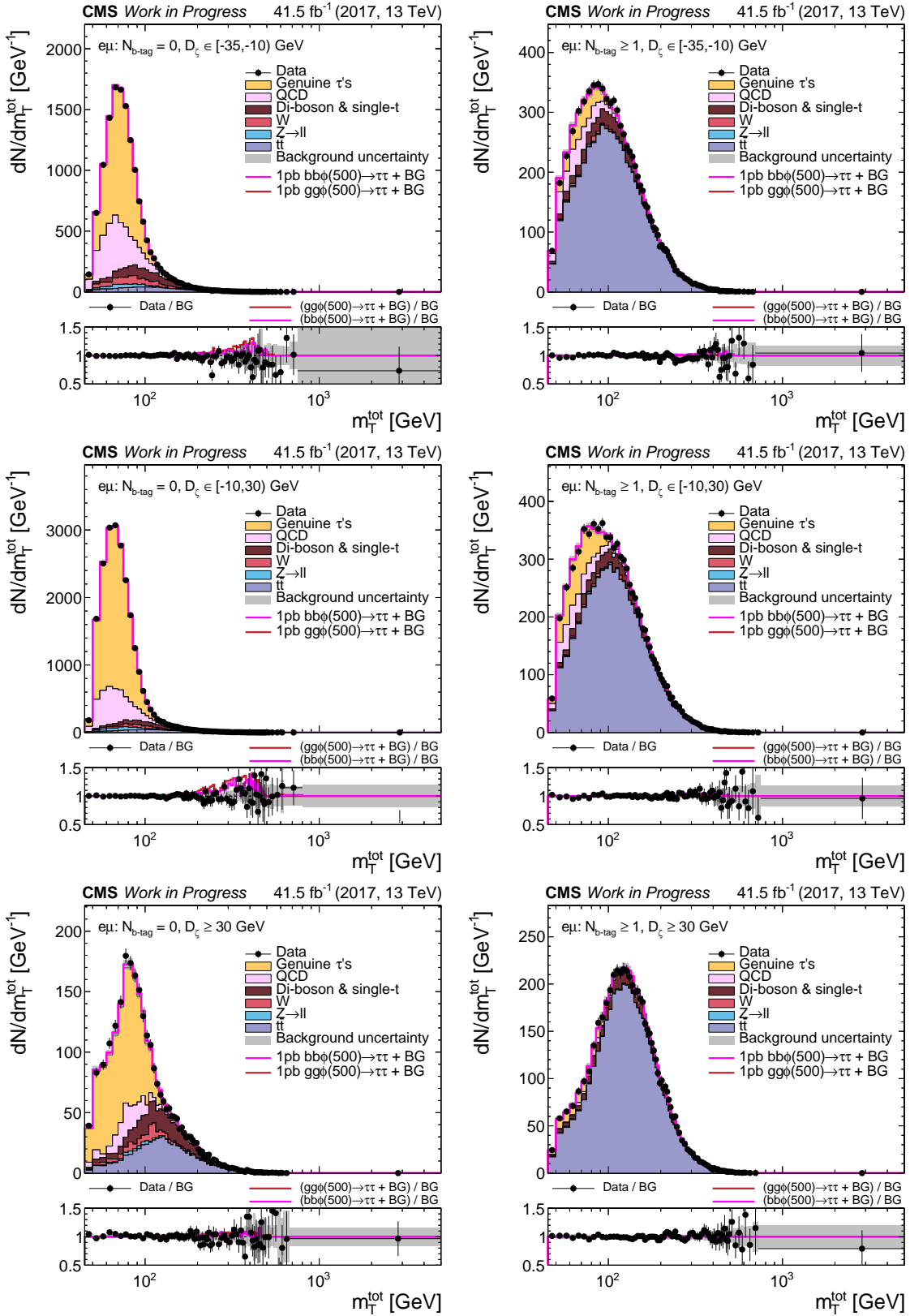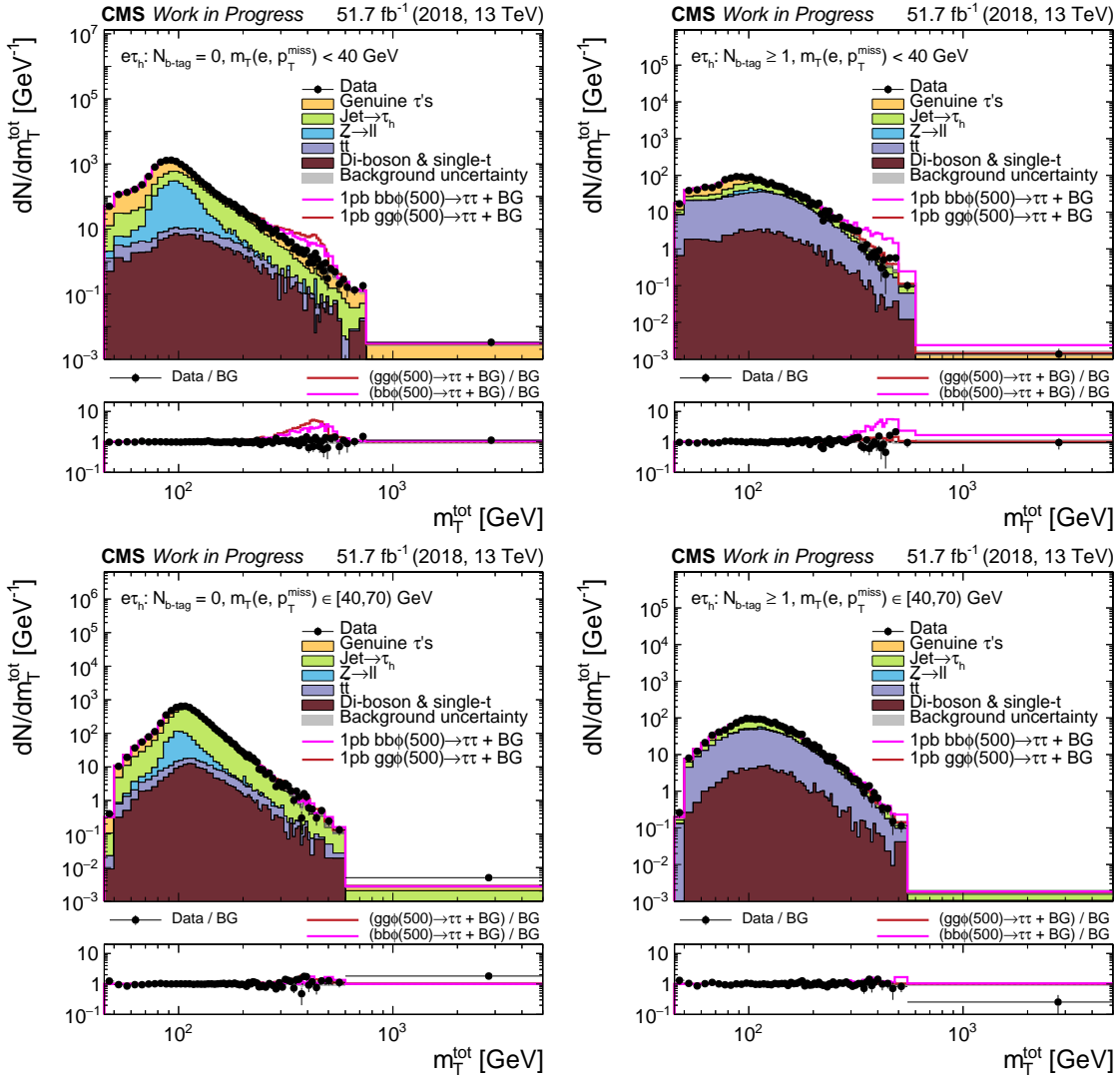
Figure A.35.: Distributions of m_T^{tot} in the BSM categories of the eμ final state. Stacked expected background (BG) and BSM signals ggφ and bbφ with $m_φ$ = 500 GeV and σ · BR = 1 pb on top of BG are compared with data. Grey uncertainty bands illustrate the total BG uncertainty after a maximum likelihood fit for $μ_{ggφ}$ and $μ_{bbφ}$. In the lower panels, the ratio to BG is shown.
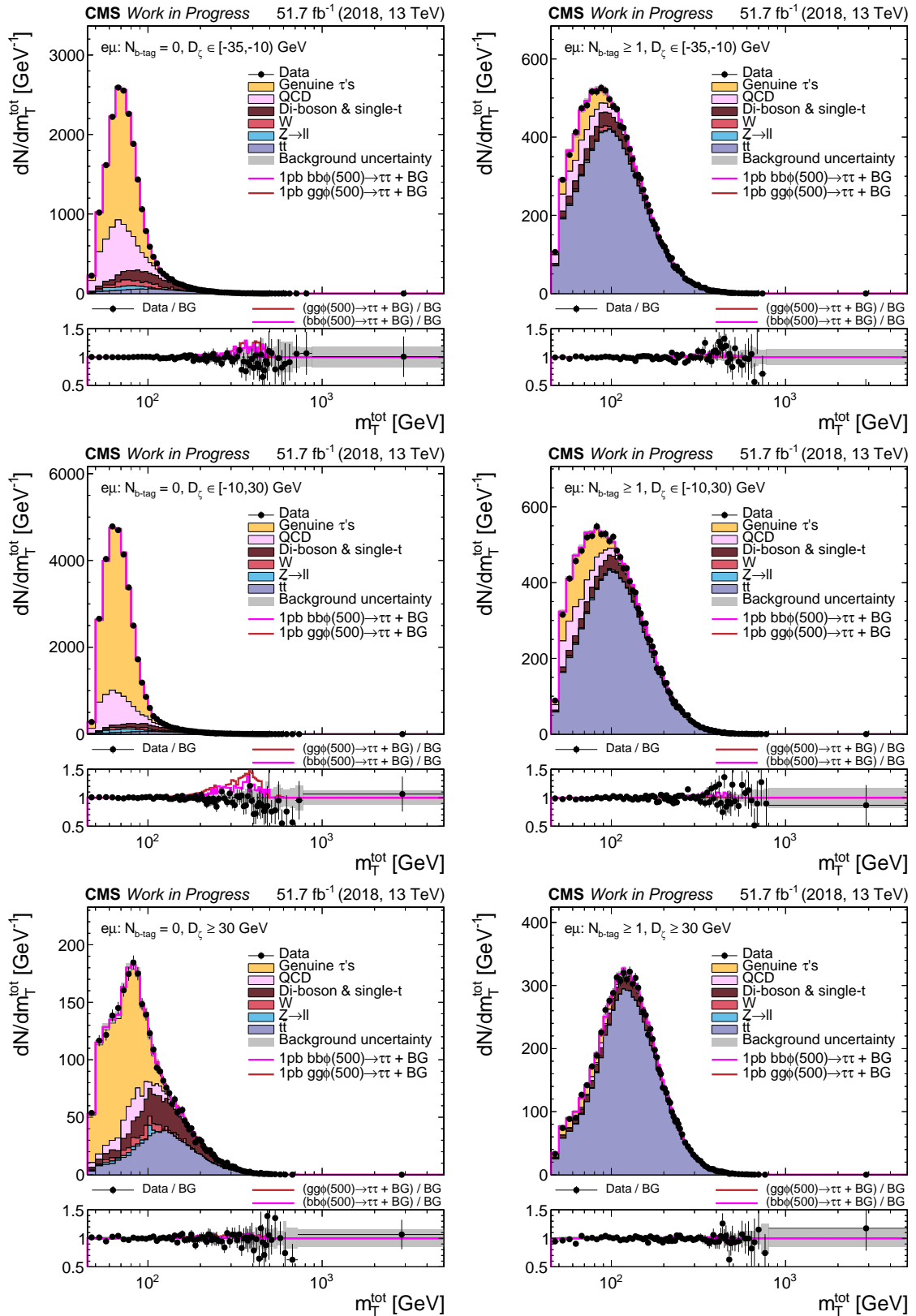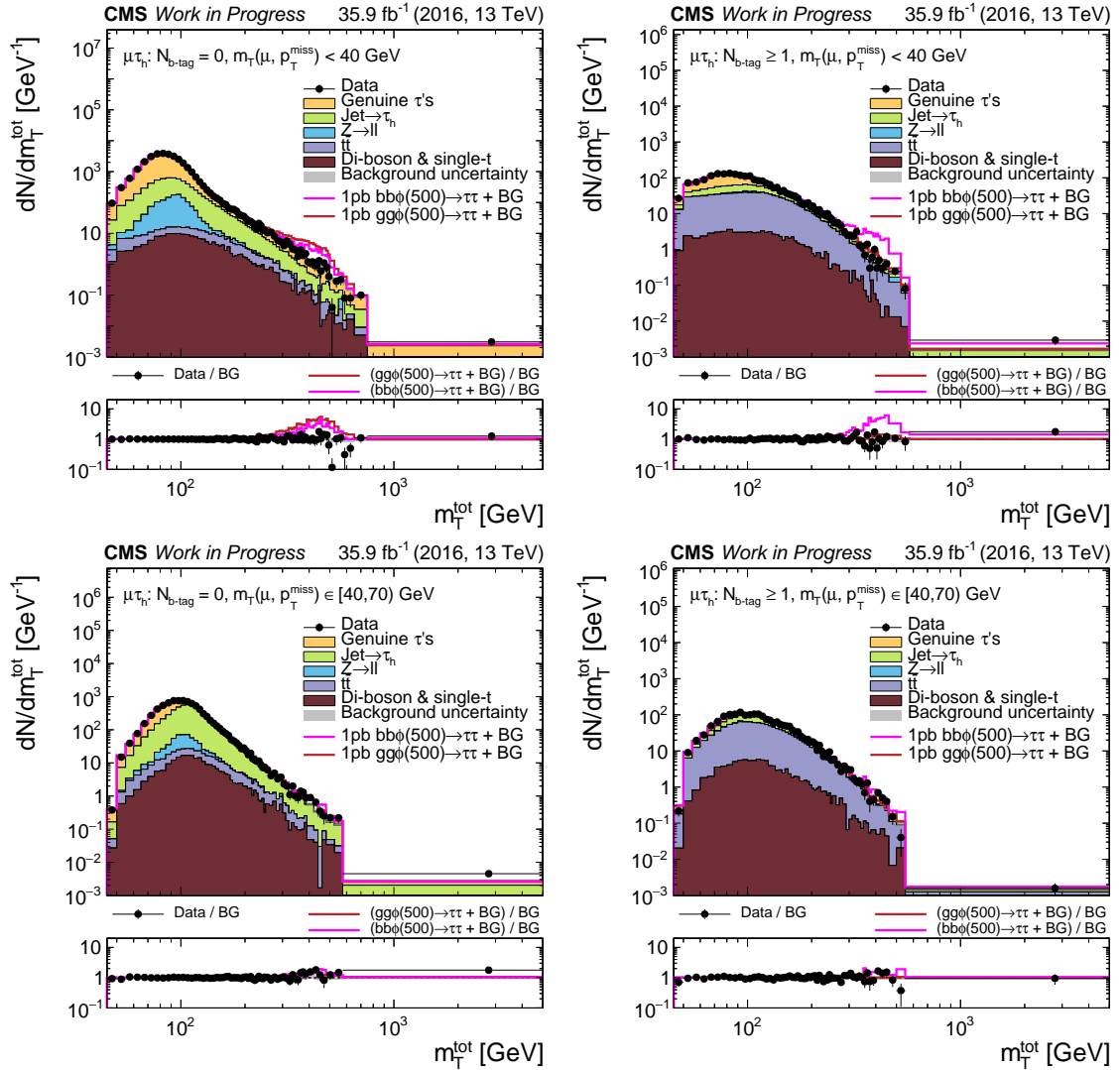
Figure A.36.: Distributions of m_T^{tot} in the BSM categories of the eµ final state. Stacked expected background (BG) and BSM signals ggφ and bbφ with $m_φ = 500$ GeV and $σ \cdot BR = 1$ pb on top of BG are compared with data. Grey uncertainty bands illustrate the total BG uncertainty after a maximum likelihood fit for $µ_{ggφ}$ and $µ_{bbφ}$. In the lower panels, the ratio to BG is shown.

A.8. m_T^{tot} in BSM Categories ($e\tau_h$)
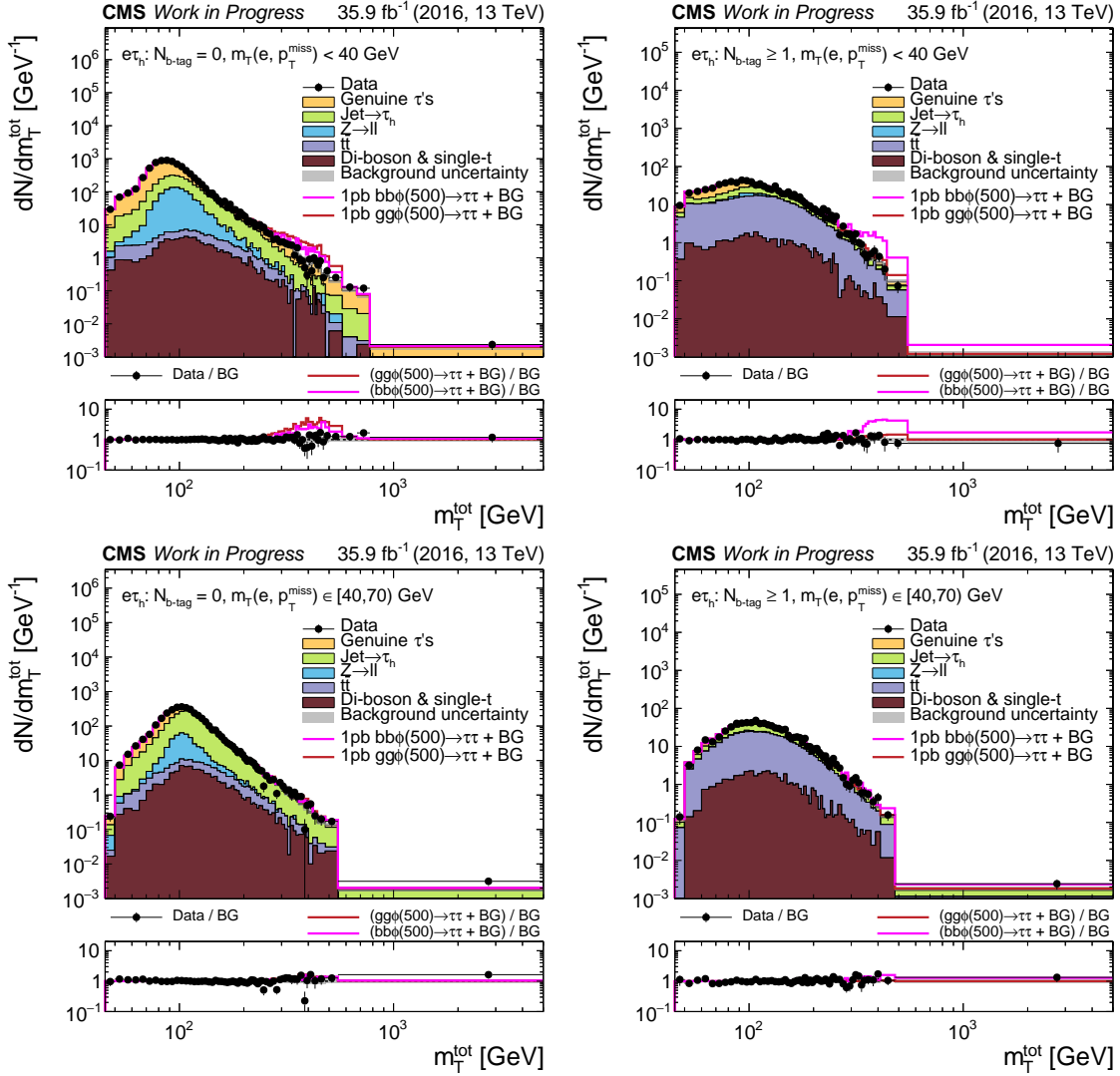
Figure A.37.: Distributions of m_T^{tot} in the BSM categories of the $e\tau_h$ final state. Stacked expected background (BG) and BSM signals $gg\phi$ and $bb\phi$ with $m_\phi = 500$ GeV and $\sigma \cdot BR = 1$ pb on top of BG are compared with data. Grey uncertainty bands illustrate the total BG uncertainty after a maximum likelihood fit for $\mu_{gg\phi}$ and $\mu_{bb\phi}$. In the lower panels, the ratio to BG is shown.
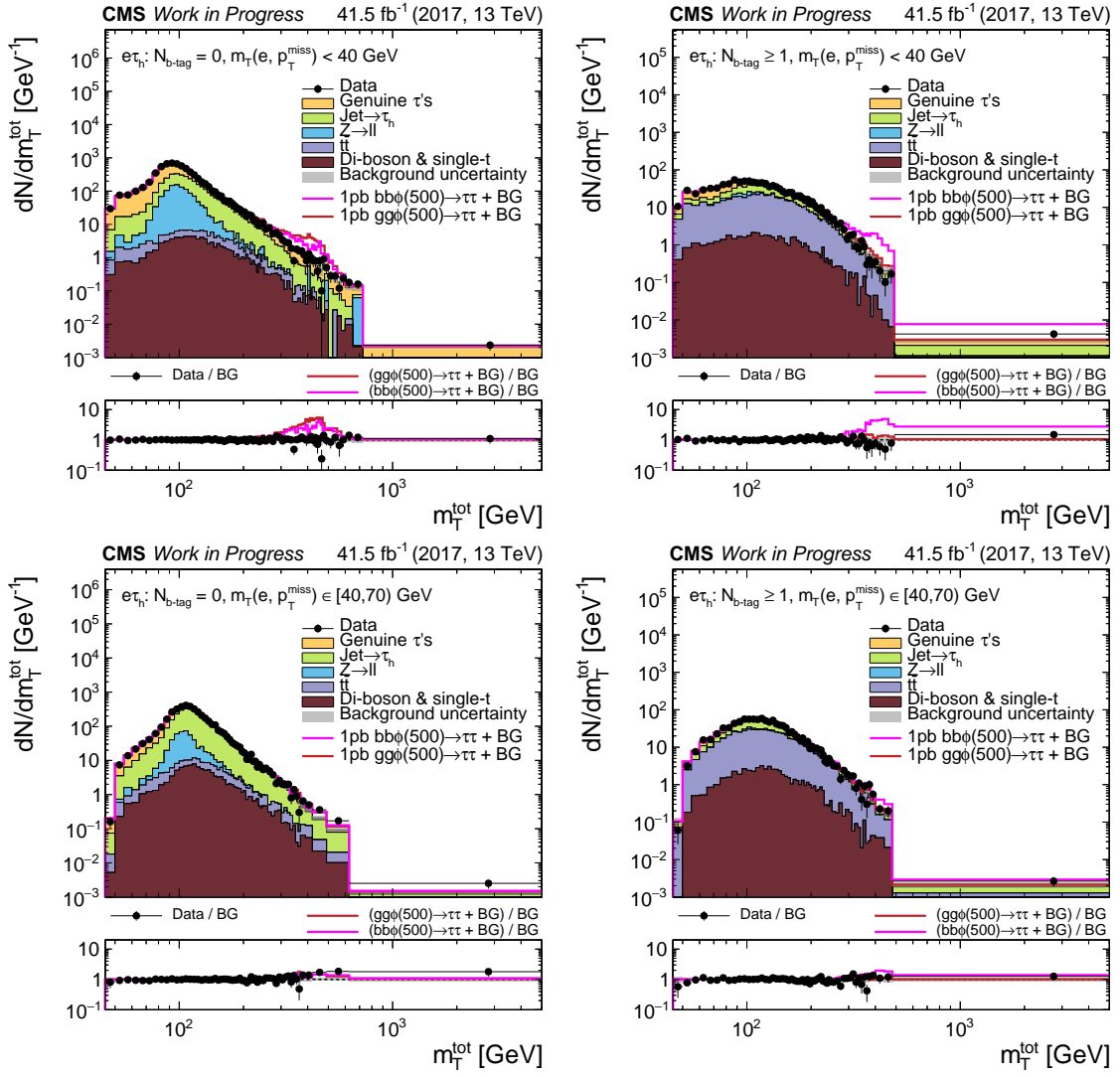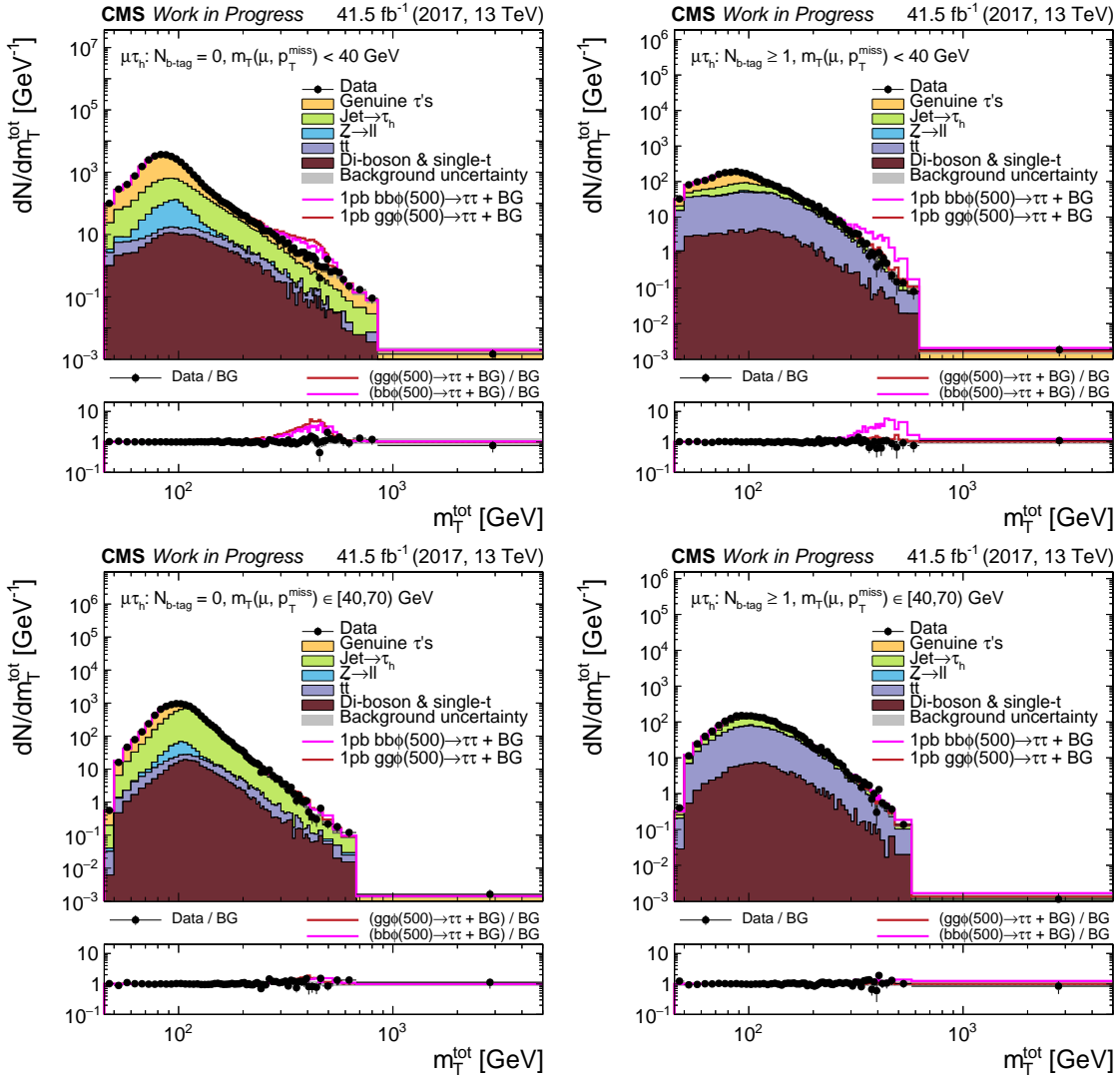
Figure A.38.: Distributions of m_T^{tot} in the BSM categories of the $e\tau_h$ final state. Stacked expected background (BG) and BSM signals $gg\phi$ and $bb\phi$ with $m_\phi = 500$ GeV and $\sigma \cdot BR = 1$ pb on top of BG are compared with data. Grey uncertainty bands illustrate the total BG uncertainty after a maximum likelihood fit for $\mu_{gg\phi}$ and $\mu_{bb\phi}$. In the lower panels, the ratio to BG is shown.
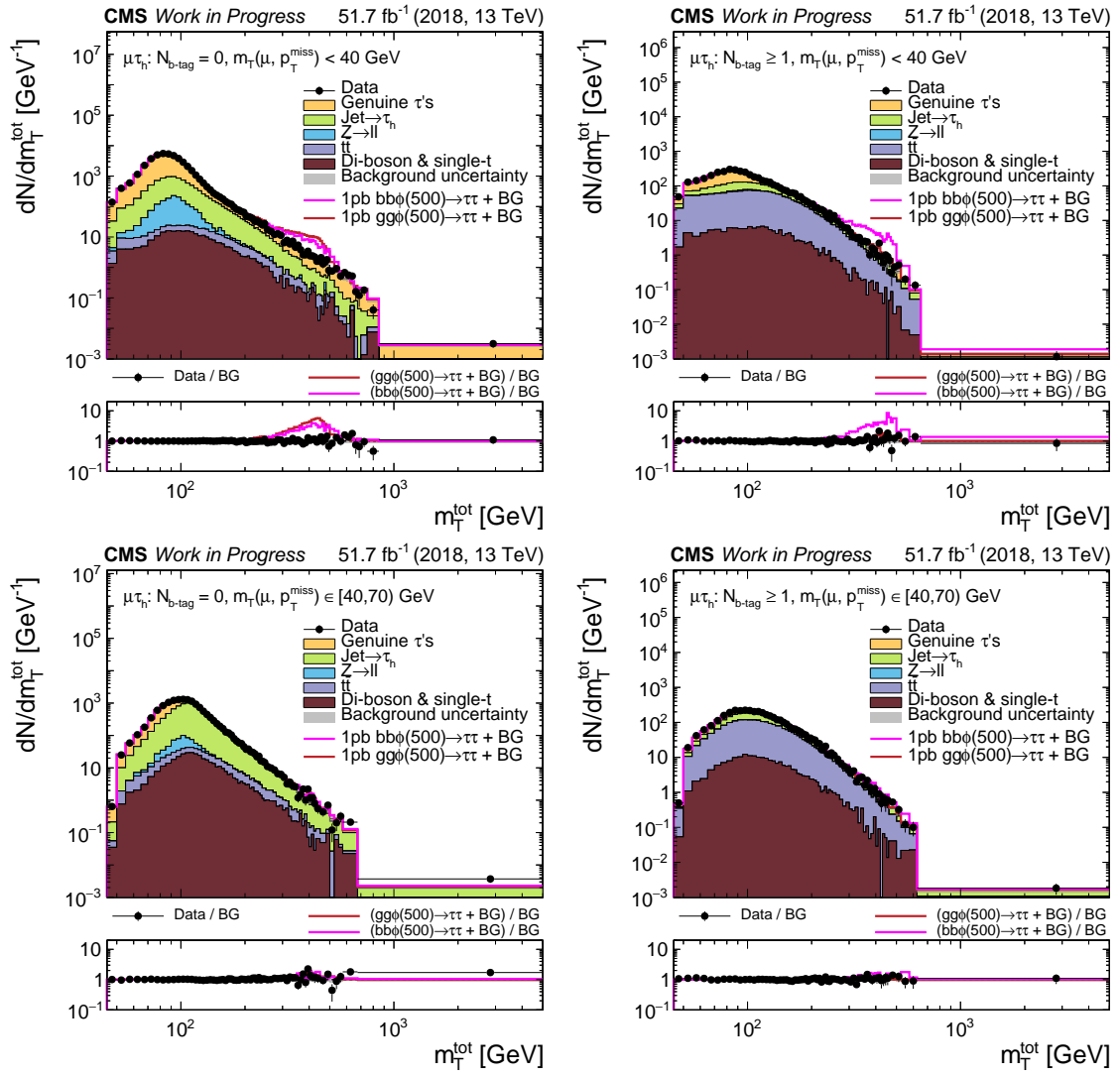
Figure A.39.: Distributions of m_T^{tot} in the BSM categories of the $e\tau_h$ final state. Stacked expected background (BG) and BSM signals $gg\phi$ and $bb\phi$ with $m_\phi = 500$ GeV and $\sigma \cdot BR = 1$ pb on top of BG are compared with data. Grey uncertainty bands illustrate the total BG uncertainty after a maximum likelihood fit for $\mu_{gg\phi}$ and $\mu_{bb\phi}$. In the lower panels, the ratio to BG is shown.
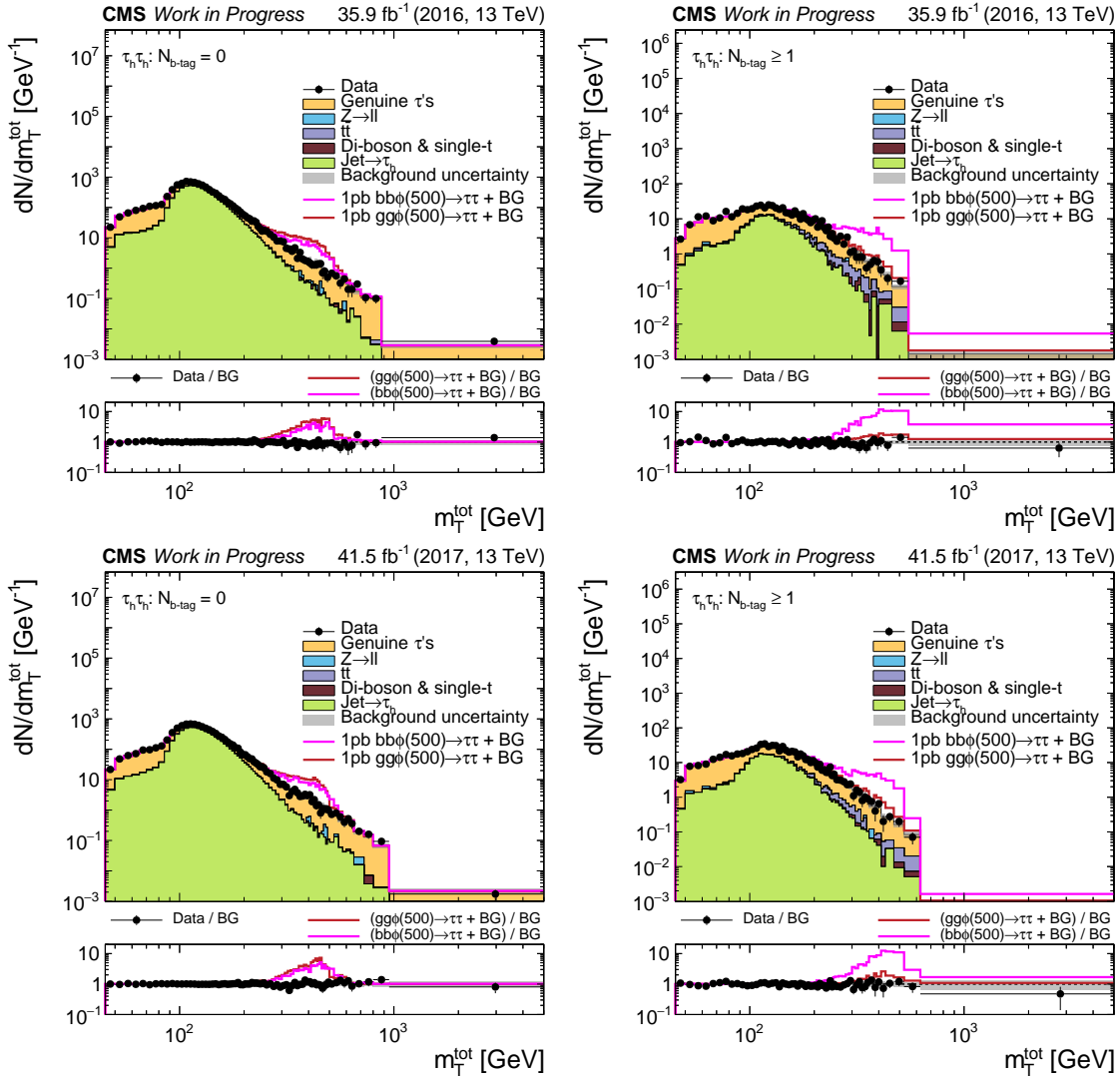
A.9. m_T^{tot} in BSM Categories ($\mu\tau_h$)

Figure A.40.: Distributions of m_T^{tot} in the BSM categories of the $\mu\tau_h$ final state. Stacked expected background (BG) and BSM signals ggϕ and bbϕ with m_ϕ = 500 GeV and $\sigma \cdot$ BR = 1 pb on top of BG are compared with data. Grey uncertainty bands illustrate the total BG uncertainty after a maximum likelihood fit for $\mu_{gg\phi}$ and $\mu_{bb\phi}$. In the lower panels, the ratio to BG is shown.

Figure A.41.: Distributions of m_T^{tot} in the BSM categories of the $\mu\tau_h$ final state. Stacked expected background (BG) and BSM signals $gg\phi$ and $bb\phi$ with $m_\phi = 500$ GeV and $\sigma \cdot BR = 1$ pb on top of BG are compared with data. Grey uncertainty bands illustrate the total BG uncertainty after a maximum likelihood fit for $\mu_{gg\phi}$ and $\mu_{bb\phi}$. In the lower panels, the ratio to BG is shown.
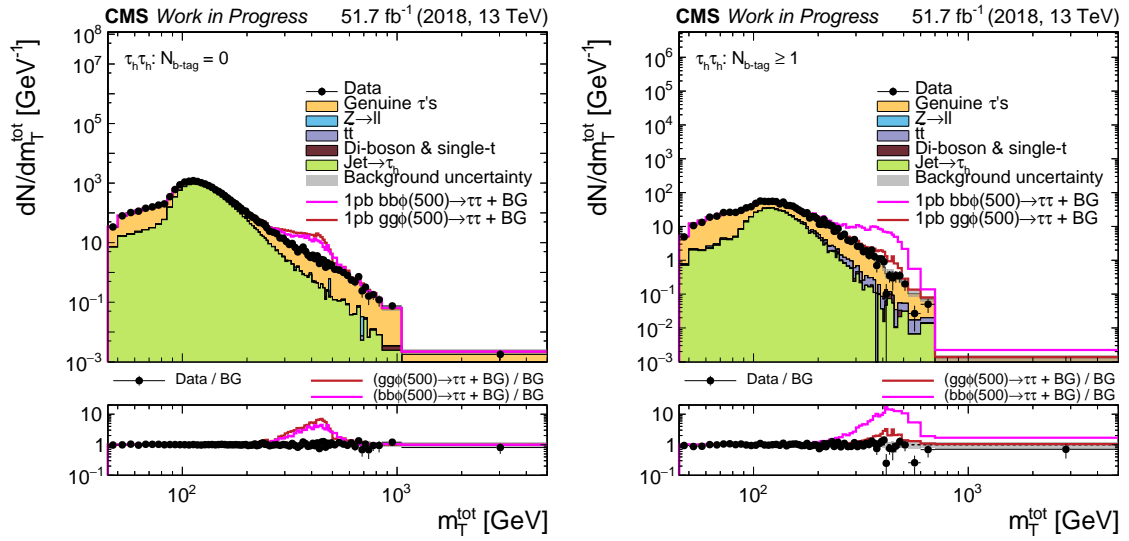
Figure A.42.: Distributions of m_T^{tot} in the BSM categories of the $\mu\tau_h$ final state. Stacked expected background (BG) and BSM signals $gg\phi$ and $bb\phi$ with $m_\phi = 500$ GeV and $\sigma \cdot BR = 1$ pb on top of BG are compared with data. Grey uncertainty bands illustrate the total BG uncertainty after a maximum likelihood fit for $\mu_{gg\phi}$ and $\mu_{bb\phi}$. In the lower panels, the ratio to BG is shown.

A.10. m_T^{tot} in BSM Categories ($\tau_h \tau_h$)

Figure A.43.: Distributions of m_T^{tot} in the BSM categories of the $\tau_h \tau_h$ final state. Stacked expected background (BG) and BSM signals $gg\phi$ and $bb\phi$ with $m_\phi = 500$ GeV and $\sigma \cdot BR = 1$ pb on top of BG are compared with data. Grey uncertainty bands illustrate the total BG uncertainty after a maximum likelihood fit for $\mu_{gg\phi}$ and $\mu_{bb\phi}$. In the lower panels, the ratio to BG is shown.

Figure A.44.: Distributions of m_T^{tot} in the BSM categories of the $\tau_h\tau_h$ final state. Stacked expected background (BG) and BSM signals $gg\phi$ and $bb\phi$ with $m_\phi = 500$ GeV and $\sigma \cdot BR = 1$ pb on top of BG are compared with data. Grey uncertainty bands illustrate the total BG uncertainty after a maximum likelihood fit for $\mu_{gg\phi}$ and $\mu_{bb\phi}$. In the lower panels, the ratio to BG is shown.

A.11. m_T^{tot} in BSM Categories (new approach)
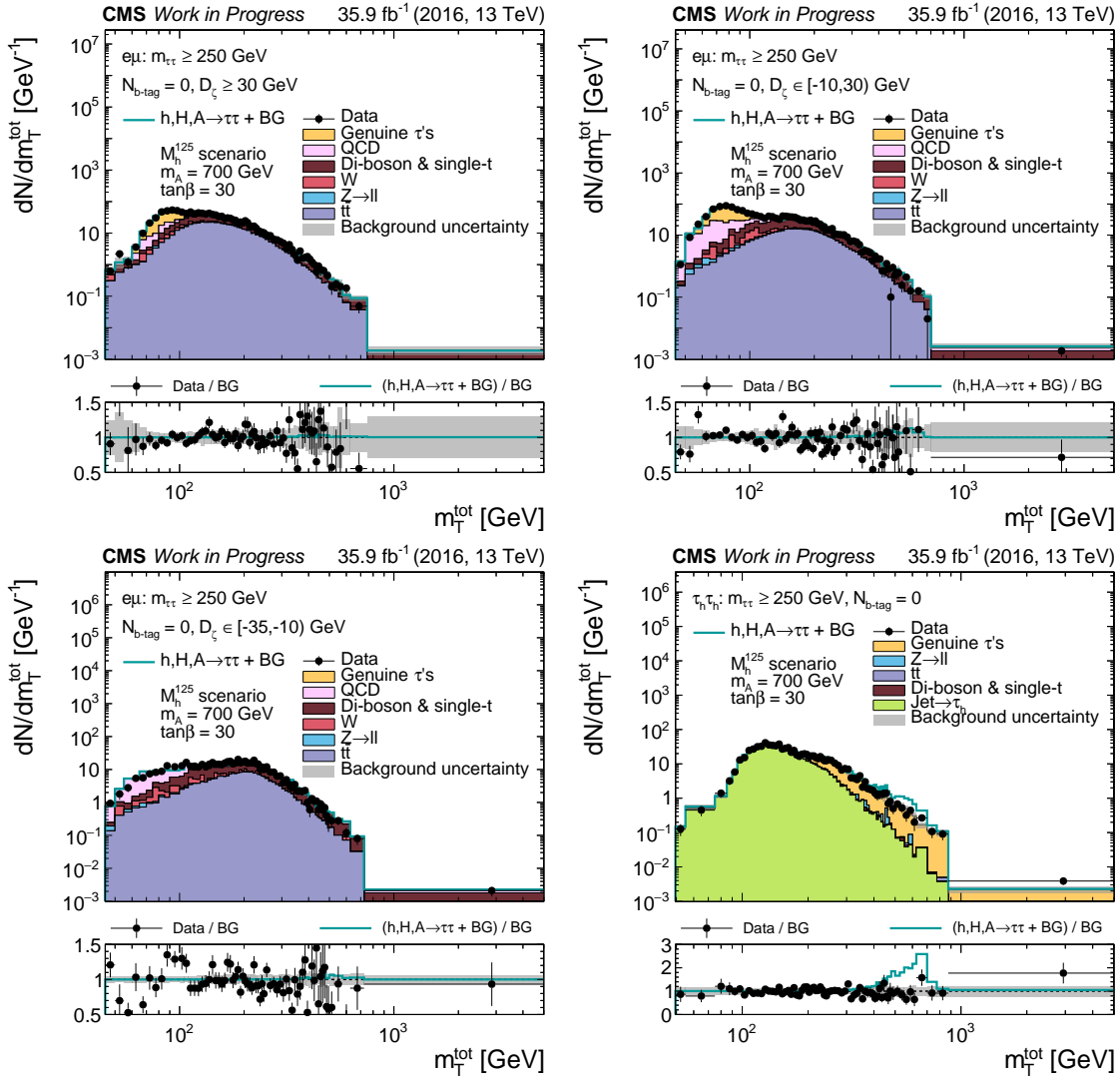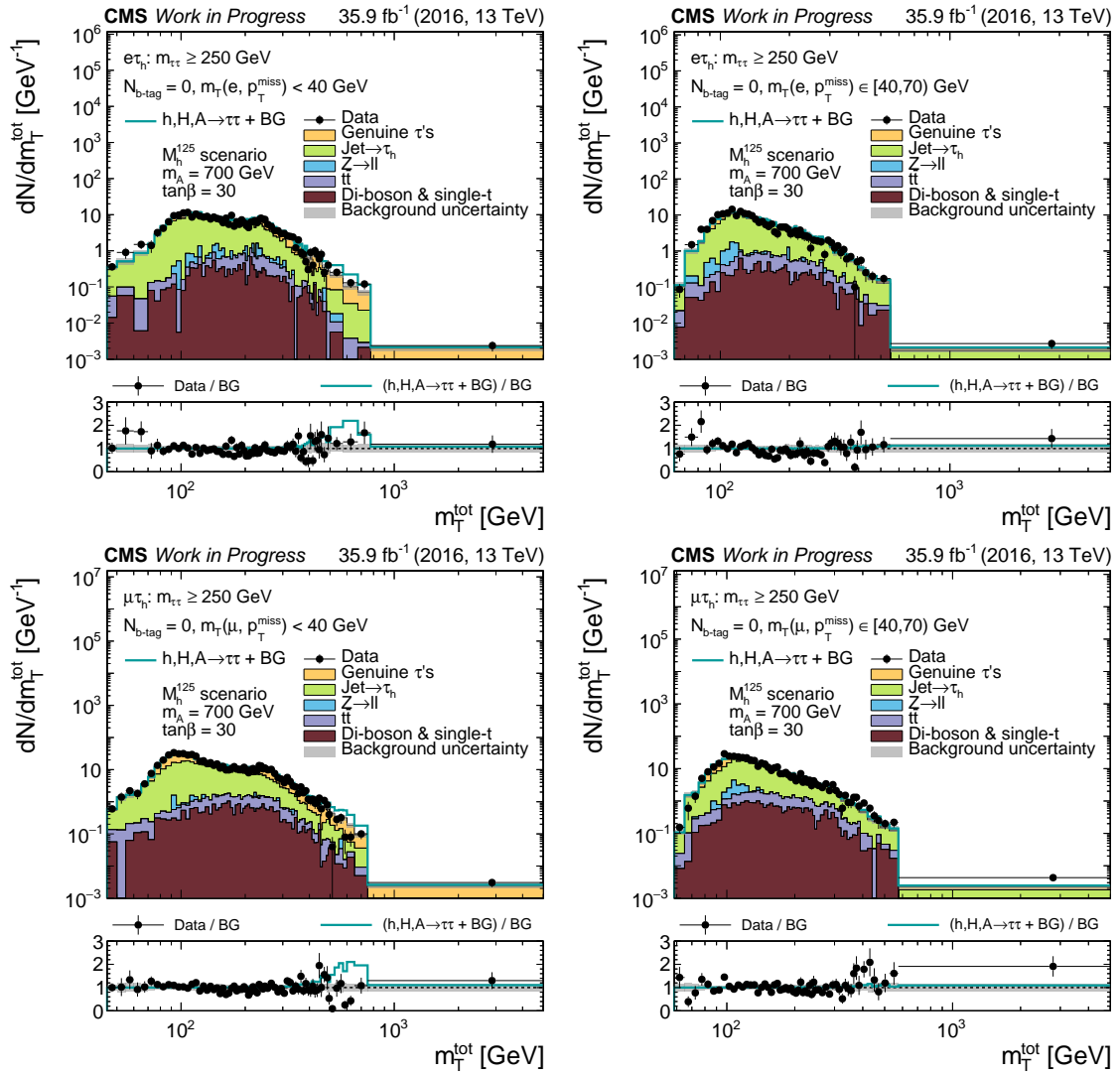

Figure A.45.: Distributions of m_T^{tot} in the BSM categories with $N_{b\text{-tag}} = 0$ and $m_{\tau\tau} \geq 250$ GeV of the (top and bottom left) $e\mu$ and (bottom right) $\tau_h\tau_h$ final states. The signal prediction of the M_h^{125} scenario at $(m_A, \tan\beta) = (700\text{ GeV}, 30)$ for the heavy Higgs bosons H and A is shown as signal, resulting in a single mass degenerate resonance dominated by the b-quark associated production. The signal is added on top of the stacked background expectation and compared with data. Grey uncertainty bands illustrate the total BG uncertainty after a maximum likelihood fit performed for the fixed $(m_A, \tan\beta)$ values.
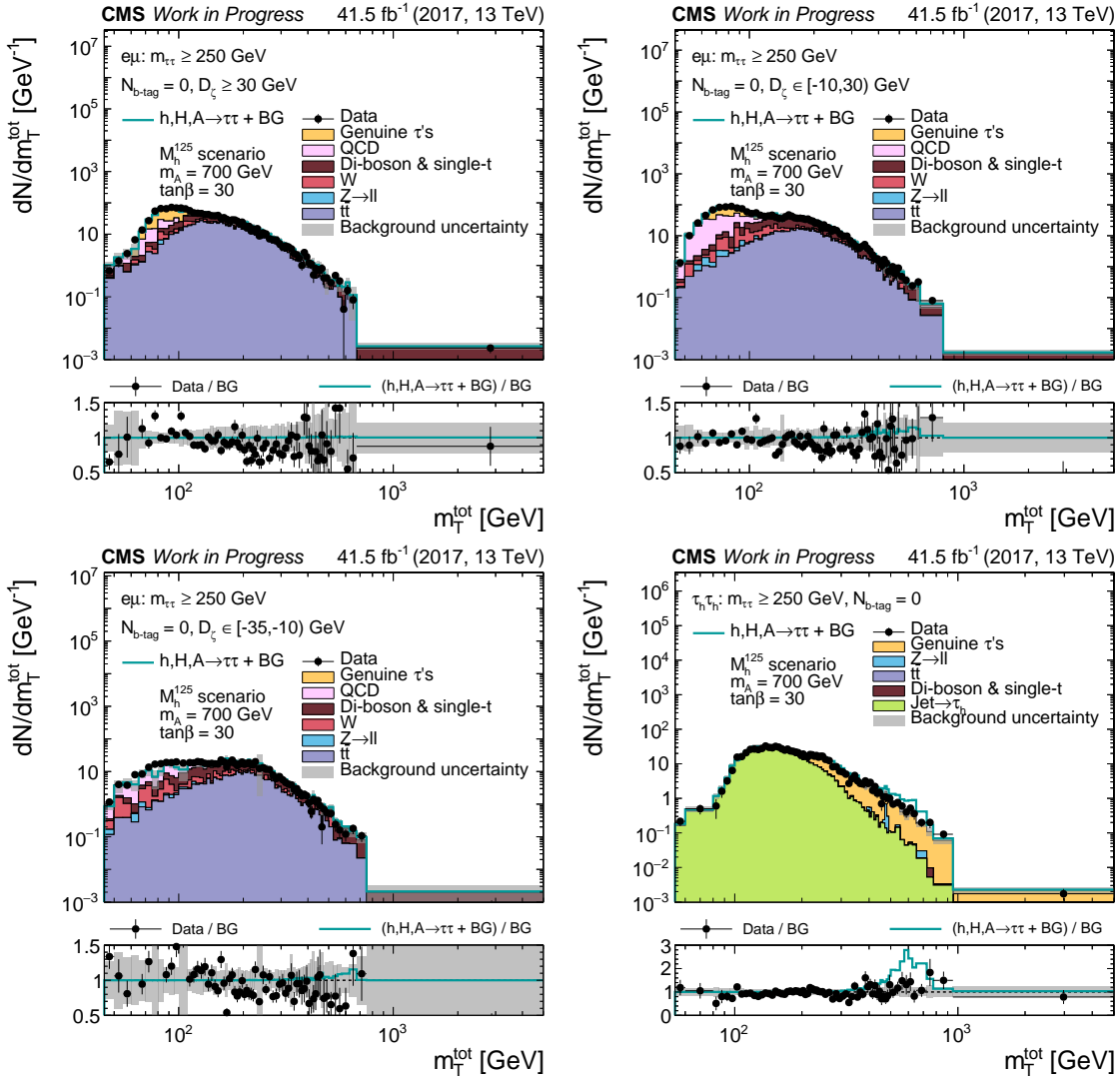
Figure A.46.: Distributions of m_T^{tot} in the BSM categories with $N_{b\text{-tag}} = 0$ and $m_{\tau\tau} \geq 250$ GeV of the (top) $e\tau_h$ and (bottom) $\mu\tau_h$ final states. The signal prediction of the M_h^{125} scenario at $(m_A, \tan\beta) = (700\text{ GeV}, 30)$ for the heavy Higgs bosons H and A is shown as signal, resulting in a single mass degenerate resonance dominated by the b-quark associated production. The signal is added on top of the stacked background expectation and compared with data. Grey uncertainty bands illustrate the total BG uncertainty after a maximum likelihood fit performed for the fixed $(m_A, \tan\beta)$ values.
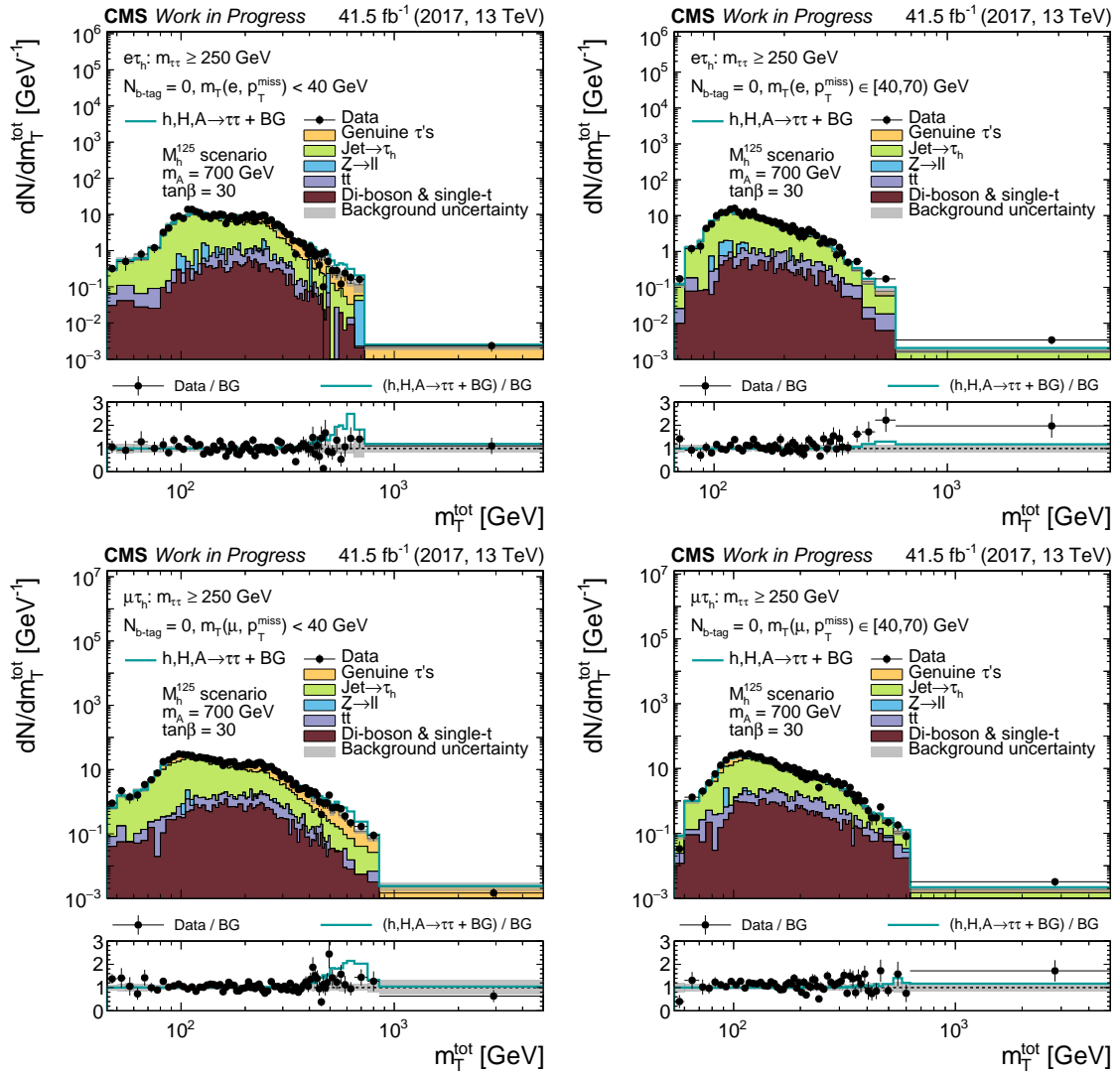
Figure A.47.: Distributions of m_T^{tot} in the BSM categories with $N_{b\text{-tag}} = 0$ and $m_{\tau\tau} \geq 250$ GeV of the (top and bottom left) eμ and (bottom right) $\tau_h\tau_h$ final states. The signal prediction of the M_h^{125} scenario at $(m_A, \tan\beta) = (700$ GeV, $30)$ for the heavy Higgs bosons H and A is shown as signal, resulting in a single mass degenerate resonance dominated by the b-quark associated production. The signal is added on top of the stacked background expectation and compared with data. Grey uncertainty bands illustrate the total BG uncertainty after a maximum likelihood fit performed for the fixed $(m_A, \tan\beta)$ values.
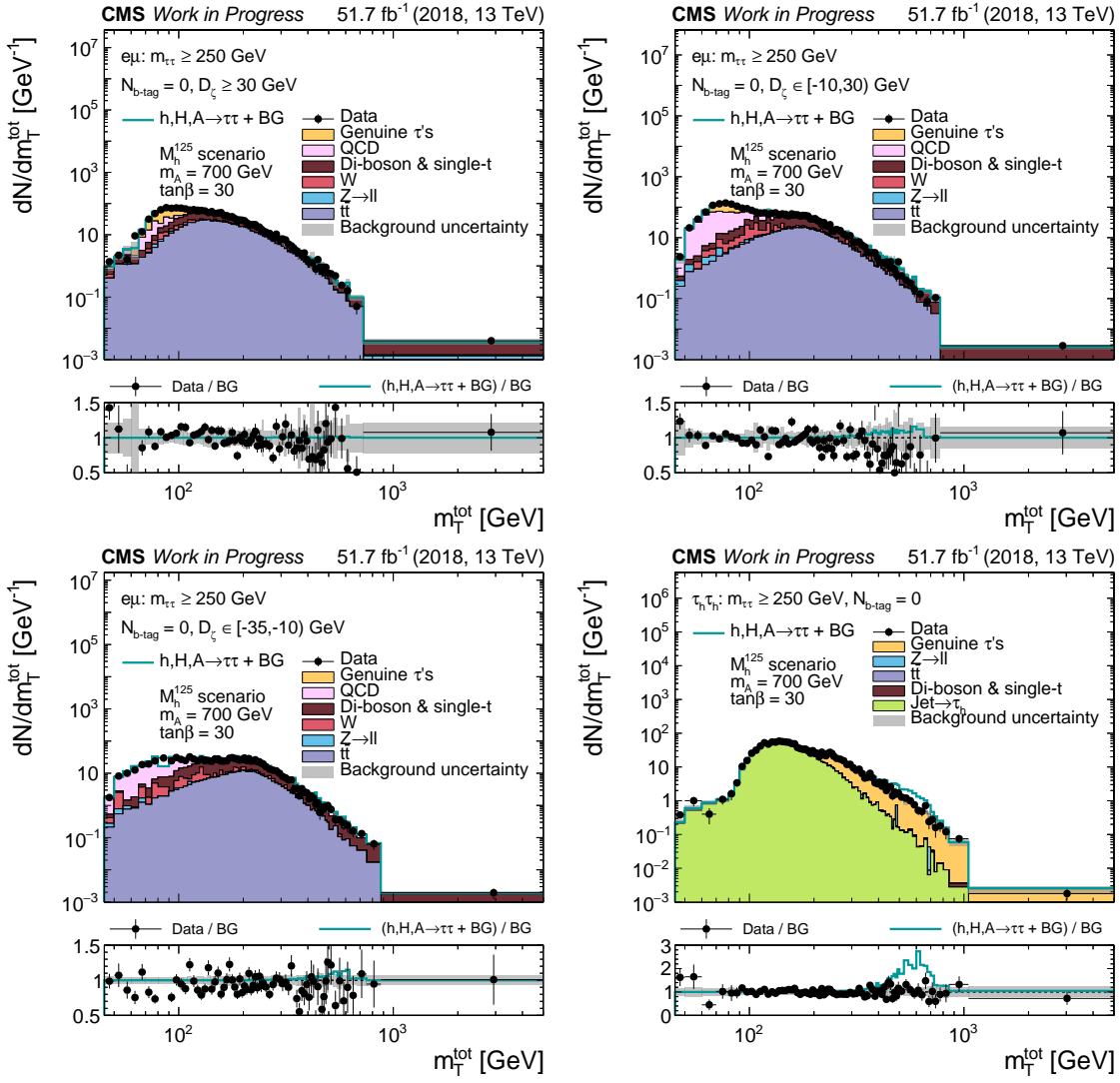
Figure A.48.: Distributions of m_T^{tot} in the BSM categories with $N_{b\text{-}tag} = 0$ and $m_{\tau\tau} \geq 250$ GeV of the (top) $e\tau_h$ and (bottom) $\mu\tau_h$ final states. The signal prediction of the M_h^{125} scenario at $(m_A, \tan\beta) = (700\,\text{GeV}, 30)$ for the heavy Higgs bosons H and A is shown as signal, resulting in a single mass degenerate resonance dominated by the b-quark associated production. The signal is added on top of the stacked background expectation and compared with data. Grey uncertainty bands illustrate the total BG uncertainty after a maximum likelihood fit performed for the fixed $(m_A, \tan\beta)$ values.

Figure A.49.: Distributions of m_T^{tot} in the BSM categories with $N_{b\text{-}tag} = 0$ and $m_{\tau\tau} \geq 250$ GeV of the (top and bottom left) $e\mu$ and (bottom right) $\tau_h\tau_h$ final states. The signal prediction of the M_h^{125} scenario at $(m_A, \tan\beta) = (700\text{ GeV}, 30)$ for the heavy Higgs bosons H and A is shown as signal, resulting in a single mass degenerate resonance dominated by the b-quark associated production. The signal is added on top of the stacked background expectation and compared with data. Grey uncertainty bands illustrate the total BG uncertainty after a maximum likelihood fit performed for the fixed $(m_A, \tan\beta)$ values.
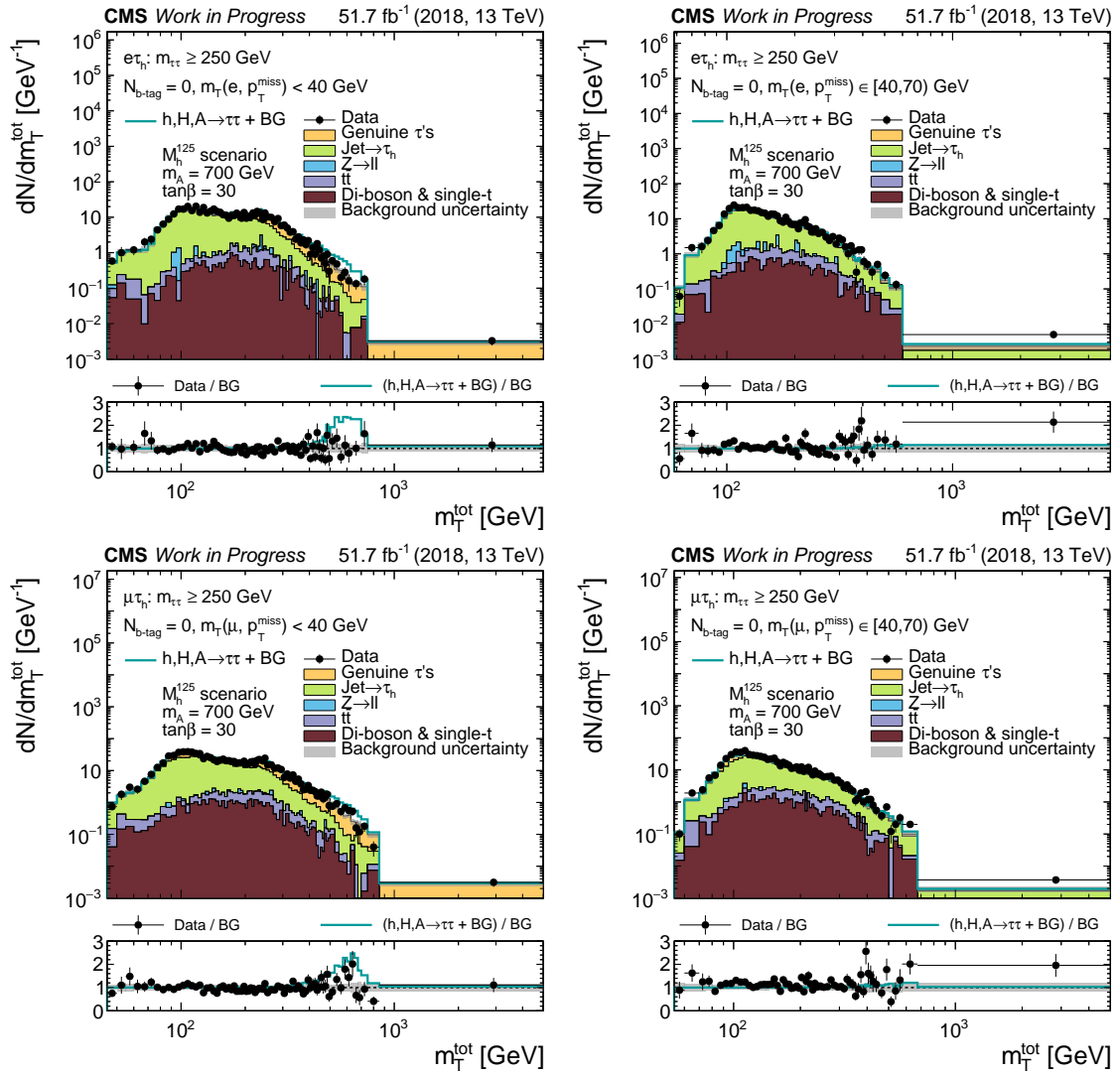
Figure A.50.: Distributions of m_T^{tot} in the BSM categories with $N_{b\text{-}tag} = 0$ and $m_{\tau\tau} \geq 250$ GeV of the (top) $e\tau_h$ and (bottom) $\mu\tau_h$ final states. The signal prediction of the M_h^{125} scenario at $(m_A, \tan\beta) = (700\,\text{GeV}, 30)$ for the heavy Higgs bosons H and A is shown as signal, resulting in a single mass degenerate resonance dominated by the b-quark associated production. The signal is added on top of the stacked background expectation and compared with data. Grey uncertainty bands illustrate the total BG uncertainty after a maximum likelihood fit performed for the fixed $(m_A, \tan\beta)$ values.
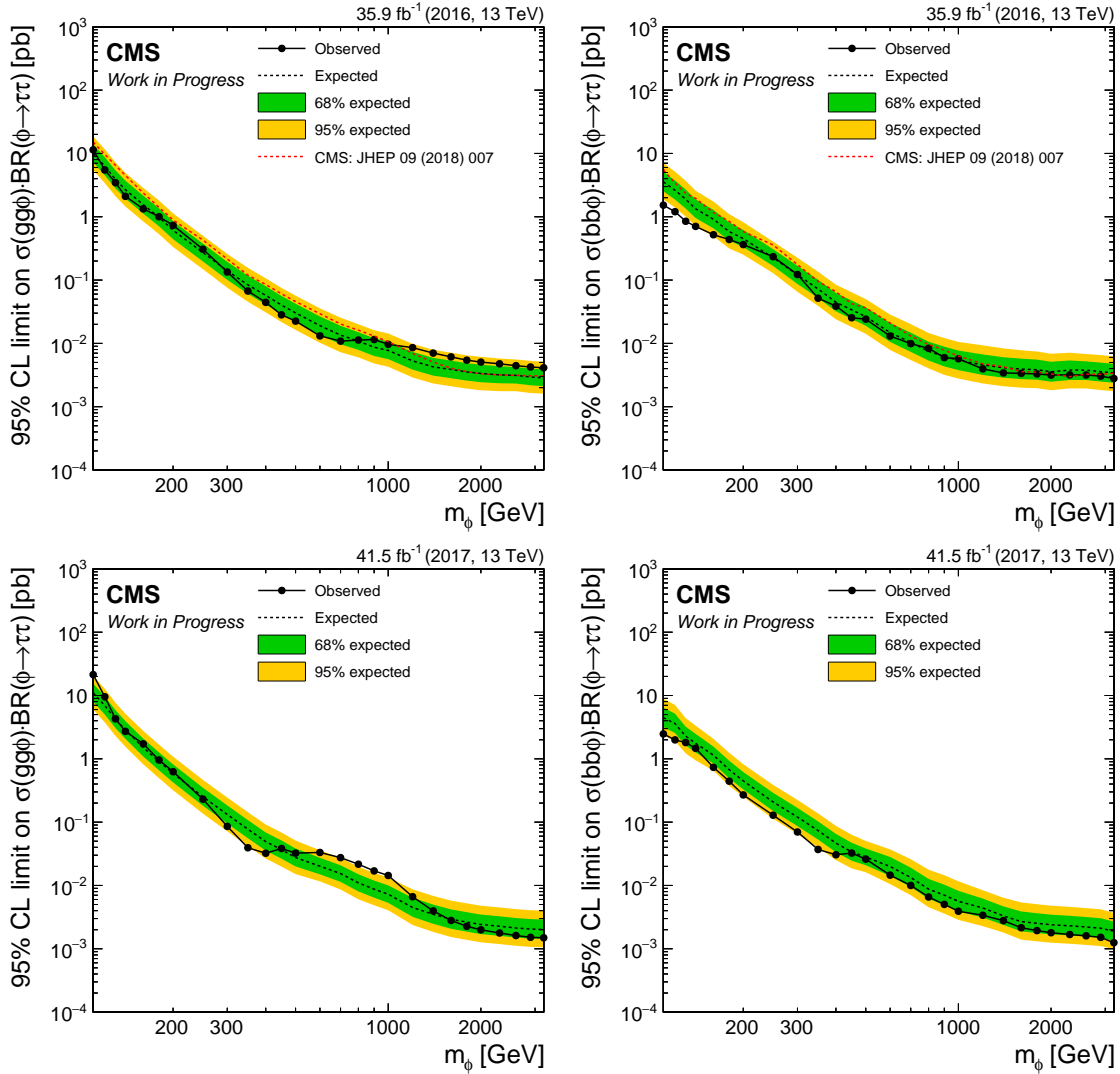
B. Model-Independent Limits

Figure B.1.: Model-independent upper limits at 95% confidence level on (left) gluon fusion and (right) b-associated production $\sigma \cdot BR$ of a Higgs boson ϕ with mass m_ϕ for (top) 2016 and (bottom) 2017 data. The black dashed line represents the median of the expected upper limit, while the green and yellow bands show the 68% and 95% confidence intervals for a given value of m_ϕ. Black dots connected with black solid lines correspond to observed limits. Expected results from CMS [19] are shown as a red dashed line for comparison with results for data-taking in 2016.
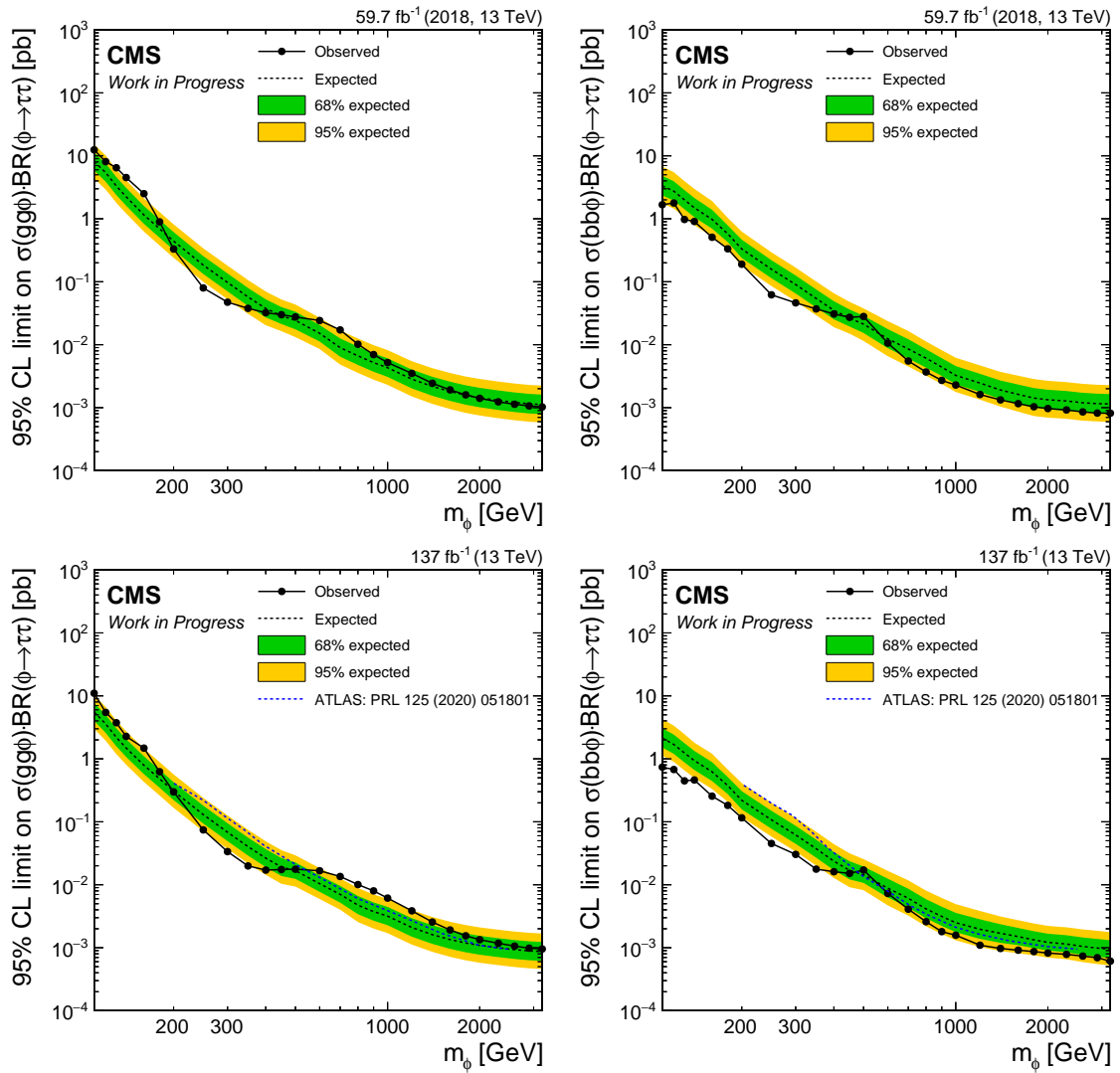
Figure B.2.: Model-independent upper limits at 95% confidence level on (left) gluon fusion and (right) b-associated production $\sigma \cdot BR$ of a Higgs boson ϕ with mass m_ϕ for (top) 2018 and (bottom) the entire Run 2 data. The black dashed line represents the median of the expected upper limit, while the green and yellow bands show the 68% and 95% confidence intervals for a given value of m_ϕ. Black dots connected with black solid lines correspond to observed limits. Expected results from ATLAS [170] are shown as a blue dashed line for comparison with results for full Run 2 data-taking.